Thermodynamic and geochemical modeling in metamorphic geology

Habilitationsschrift
vorgelegt bei der
Mathematisch-Naturwissenschaftlichen
Fakultät der
Universität Potsdam

von
Dr. rer. nat. Matthias Konrad-Schmolke
Potsdam, 2015

Published online at the
Institutional Repository of the University of Potsdam:
URN urn:nbn:de:kobv:517-opus4-101805
http://nbn-resolving.de/urn:nbn:de:kobv:517-opus4-101805

This work is dedicated to my parents

Content

Preface

In this Habilitationsschrift I have compiled nine published manuscripts that are concerned with the topic of thermodynamic forward modeling in geosciences in order to better understand lithosphere dynamics, mass transfer in the lithosphere and element transport properties of metamorphic rocks. None of the manuscripts were part of my PhD thesis or the result of works earlier than my PhD. I am the first author in six of these manuscripts and co-author in three of them. This Habilitationsschrift is divided into two parts: In the first part I give a conclusion of the results of the published manuscripts, an introduction into thermodynamics, thermodynamic modeling in geosciences as well as an overview of the combination of thermodynamic and geochemical models. In the second part, which contains the published manuscripts, I show with different case studies how the application of thermodynamic models in geosciences give new insights into the envisaged topic and helped to push science forward with respect to thermodynamic and geochemical modeling.

The publications included in this Habilitationsschrift address different topics of metamorphic petrology, but have in common the application of thermodynamic modelling and the comparison of model results with natural observations. In one of the papers included here (Konrad-Schmolke et al., 2007) thermodynamic modelling is not applied, but I have included this work as it demonstrates the potential pitfalls of interpreting and comparing compositional zonations in metamorphic minerals, an often used tracer for rock forming processes during metamorphism. The case studies in this compilation investigate rocks from different regions worldwide, which demonstrate the process oriented aim of all of my studies and the applicability of thermodynamic and geochemical modelling to different rocks and different petrological problems envisaged.

My first author publications are all based primarily on my own ideas and my own solution strategies for the addressed problems. In all of these works I have had fruitful co-operations with different researchers from various countries, which I want to thank for their constructive and helpful support. In the co-author publications included here the results of the thermodynamic modelling, which was designed and performed predominantly by myself, was an integral part of the interpretations and discussion. Thus, I have contributed significantly to the outcome and the interpretation of these manuscripts. I have detailed my intellectual and physical contributions to each of the papers included in this Habilitationsschrift in the conclusions of each work in chapter 6.

Summary

Quantitative thermodynamic and geochemical modeling is today applied in a variety of geological environments from the petrogenesis of igneous rocks to the oceanic realm. Thermodynamic calculations are used, for example, to get better insight into lithosphere dynamics, to constrain melting processes in crust and mantle as well as to study fluid-rock interaction. The development of thermodynamic databases and computer programs to calculate equilibrium phase diagrams have greatly advanced our ability to model geodynamic processes from subduction to orogenesis. However, a well-known problem is that despite its broad application the use and interpretation of thermodynamic models applied to natural rocks is far from straightforward. For example, chemical disequilibrium and/or unknown rock properties, such as fluid activities, complicate the application of equilibrium thermodynamics.

One major aspect of the publications presented in this Habilitationsschrift are new approaches to unravel dynamic and chemical histories of rocks that include applications to chemically open system behaviour. This approach is especially important in rocks that are affected by element fractionation due to fractional crystallisation and fluid loss during dehydration reactions. Furthermore, chemically open system behaviour has also to be considered for studying fluid-rock interaction processes and for extracting information from compositionally zoned metamorphic minerals. In this Habilitationsschrift several publications are presented where I incorporate such open system behaviour in the forward models by incrementing the calculations and considering changing reacting rock compositions during metamorphism. I apply thermodynamic forward modelling incorporating the effects of element fractionation in a variety of geodynamic and geochemical applications in order to better understand lithosphere dynamics and mass transfer in solid rocks.

I combine thermodynamic forward models with trace element calculations in three of the presented publications in order to enlarge the application of geochemical numerical forward modeling. In these publications a combination of thermodynamic and trace element forward modeling is used to study and quantify processes in metamorphic petrology at spatial scales from µm to km. In the thermodynamic forward models I utilize Gibbs energy minimization to quantify mineralogical changes along a reaction path of a chemically open fluid/rock system. These results are combined with mass balanced trace element calculations to determine the trace element distribution between rock and melt/fluid during the metamorphic evolution. Thus, effects of mineral reactions, fluid-rock interaction and element transport in metamorphic rocks on the trace element and isotopic composition of minerals, rocks and

percolating fluids or melts can be predicted.

One of the included publications shows that trace element growth zonations in metamorphic garnet porphyroblasts can be used to get crucial information about the reaction path of the investigated sample. In order to interpret the major and trace element distribution and zoning patterns in terms of the reaction history of the samples, we combined thermodynamic forward models with mass-balance rare earth element calculations. Such combined thermodynamic and mass-balance calculations of the rare earth element distribution among the modelled stable phases yielded characteristic zonation patterns in garnet that closely resemble those in the natural samples. We can show in that paper that garnet growth and trace element incorporation occurred in near thermodynamic equilibrium with matrix phases during subduction and that the rare earth element patterns in garnet exhibit distinct enrichment zones that fingerprint the minerals involved in the garnet-forming reactions.

In two of the presented publications I illustrate the capacities of combined thermodynamic-geochemical modeling based on examples relevant to mass transfer in subduction zones. The first example focuses on fluid-rock interaction in and around a blueschist-facies shear zone in felsic gneisses, where fluid-induced mineral reactions and their effects on boron (B) concentrations and isotopic compositions in white mica are modeled. In the second example, fluid release from a subducted slab and associated transport of B and variations in B concentrations and isotopic compositions in liberated fluids and residual rocks are modeled. I show that, combined with experimental data on elemental partitioning and isotopic fractionation, thermodynamic forward modeling unfolds enormous capacities that are far from exhausted.

In my publications presented in this Habilitationsschrift I compare the modeled results to geochemical data of natural minerals and rocks and demonstrate that the combination of thermodynamic and geochemical models enables quantification of metamorphic processes and insights into element cycling that would have been unattainable so far.

Thus, the contributions to the science community presented in this Habilitatonsschrift concern the fields of petrology, geochemistry, geochronology but also ore geology that all use thermodynamic and geochemical models to solve various problems related to geo-materials.

PART I

1 A (very) short outline of the history of Thermodynamics

Thermodynamics were always an integral part of the scientific examination of natural processes as it is concerned with heat and chemical reactions. Heat and the related chemical phenomenon of fire inspired humans from the beginning of civilization, but it took until the 17th century that scientists were able to describe natural processes in terms a comprehensive thermodynamic theory. The complexity of the science of thermodynamics is owing to the fact that it relates microscopic, i.e. atomistic processes with macroscopic, i.e. observable phenomena. Hence, the development in the understanding of thermodynamics is closely connected with the understanding that the motion of molecules is responsible for the heat content, the temperature and the volume of matter. In contrast to classical mechanics, magnetism or gravity the effects of thermodynamic processes are mostly hidden in substances and human beings do not have senses to detect thermodynamic properties of matter. For example, the weight of a cobblestone, although it is the result of a still unknown interaction of forces at the scale of elementary particles, can be easily measured with a balance or felt by lifting it from the floor. In contrast, the heat content of the same stone cannot be felt nor can it be easily measured with instruments of our daily life. It was then at the onset of the 17th century when scientists all over the world started to look at the phenomenon of heat and volume as well as their connection with energy from a more scientific point of view instead of a purely philosophical treatment of these properties of matter. Around 1600 the English philosopher and scientist Francis Bacon stated: “Heat itself, its essence and quiddity, is nothing but motion” and in 1646 Blaise Pascal the outstanding French physicist, mathematician and philosopher could experimentally show that a vacuum is not filled with a particular substance, as it was proposed by Aristotle, but rather the result of the absence of matter. With his experiments involving a quicksilver barometer he could further demonstrate the dependence of the air pressure on the height above sea level. His experiments inspired many later scientists, such as Otto von Guericke to follow the idea that volume and pressure are also the result of particle motion. With the physical explanation of the connection between particle motion, heat, volume and pressure the cornerstones of modern thermodynamics were laid.

The science of thermodynamics is often translated to German with the term “Wärmelehre”, which means the science of heat. This translation, of course, disregards one crucial aspect of thermodynamics, which is the observation that mechanical work can be transferred into heat and vice versa. The term “thermodynamics” was first used in 1849 by William Thompson –

better known as Lord Kelvin – and is ethymologically derived from the Greek words for "heat" (θέρμη, therme) and (δύναμις, dynamis), meaning "power".
A recent and comprehensive explanation of what thermodynamics is concerned with, is given by Reif (1965):

> *"Thermodynamics refers to a macroscopic description of bodies and processes".*

However, this sentence still leaves a fair amount of space for interpretations and thus, an anonymous, although slightly inaccurate, wit stated:

> *"Thermodynamics is the science of the impossible. It enables you to tell with certainty what cannot happen. Thermodynamics is noncommittal about the things that are possible. Thermodynamics is at its best when nothing can happen, a condition called equilibrium. The concept of equilibrium has been fruit fully extended to reversible processes. Here everything is impossible except one very specific process and even this process is on the verge of being impossible."*

In order to understand both statements one has to look back to the early days of the science of thermodynamics in the 17th century. After experiments of the French scientist Blaise Pascal a number of scientists were concerned with the construction of steam engines, compressors and vacuum pumps. Among these were Otto von Guericke (1602 – 1686) with his famous demonstration of the vacuum effect in Magdeburg (Fig. 1.1), Robert Boyle (1627 – 1692) and Robert Hooke (1635 – 1703) who were designing air and vacuum pumps.

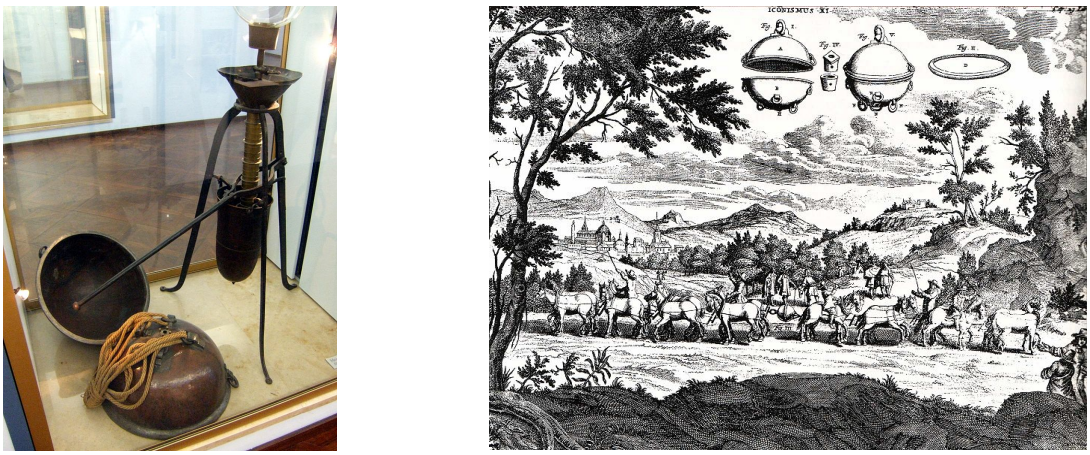

Fig. 1.1: *The original "Magdeburger Halbkugeln" used in the experiment of Otto von Guericke in 1656 and a historical illustration of Caspar Schott of the experiment in Magdeburg, Germany.* *Photography credits: LepoRello (Wikipedia)*

It was then Robert Boyle in 1656 who realized one fundamental aspect in thermodynamics, which is the correlation between pressure, temperature and volume of gases. His findings led

to a correlation, which is today known as the law of Boyle-Mariotte:

$$P \sim V^{-1} \ (T = \text{constant}) \qquad (1.1)$$

where P is pressure, V is volume and T is the temperature. Today such an observation seems to be ridiculously simple, but at that time, not even a proper steam engine was invented and Isaac Newton (1643 – 1727), the founder of the classical mechanics in physics, was 13 years old and likely concerned with puberty. Later, Boyle's observations were extended to the so-called ideal gas law:

$$PV = nRT \qquad (1.2)$$

where n is the number of moles of an ideal gas and R is the universal gas constant. This law is one of the fundamental correlations in thermodynamics and many thermodynamic equations of state of substances have been derived from it.

With the first (properly) working steam engines (Fig. 1.2), invented by Thomas Savery in 1697 followed by the Englishman Thomas Newcomen (1663 – 1729) in 1712, thermodynamics became an important branch in natural sciences as the efficiency of such engines was directly related to the work that can be done with that machines and that in turn was proportional to financial means. With the steam engines the definition of energy, i.e.:

"energy is the ability of objects to do work"

became manifest as they were the first objects that could do significant amounts of work in order to simplify peoples' lives and to produce large amounts of goods easily.

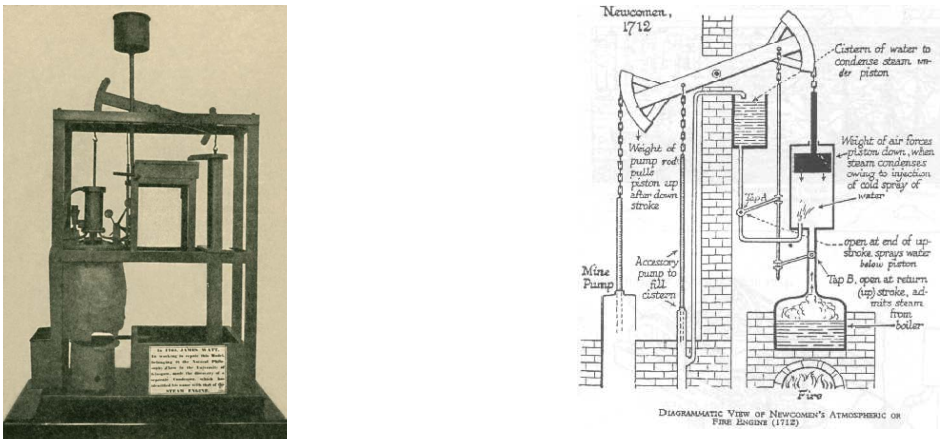

Fig. 1.2*: A model of Newcomen's steam engine and a historical description of its function.* From Burns (1910).

The steam engines and their efficiency inspired also Sadi Carnot (1796 - 1832), a French physicist and engineer, in his studies and with his work "*Réflexions sur la puissance motrice du feu et sur les machines propres à développer cette puissance*" published in 1824 he developed the idea that heat is converted into motion in steam engines and spent large effort in a proper description of that repeating process. He stated correctly that the process of energy transfer from one form (heat) to another (motion) is reversible and not restricted to steam engines, but that this concept can be expanded to any kind of "heat engine". Today, the so-called Carnot Cycle forms the basis for the construction and quantification of any periodically working heat engine. The first experimental quantification of that energy transfer - from kinetic energy to heat - was then performed by the English physicist James Prescott Joule (1818 – 1889) in 1845 where he could empirically show that "to raise the temperature of 1 pound of water by 1 °F you need the mechanical work equivalent represented by the fall of 772 pounds through 1 foot". The device with which he determined these values is shown in Fig. 1.3.

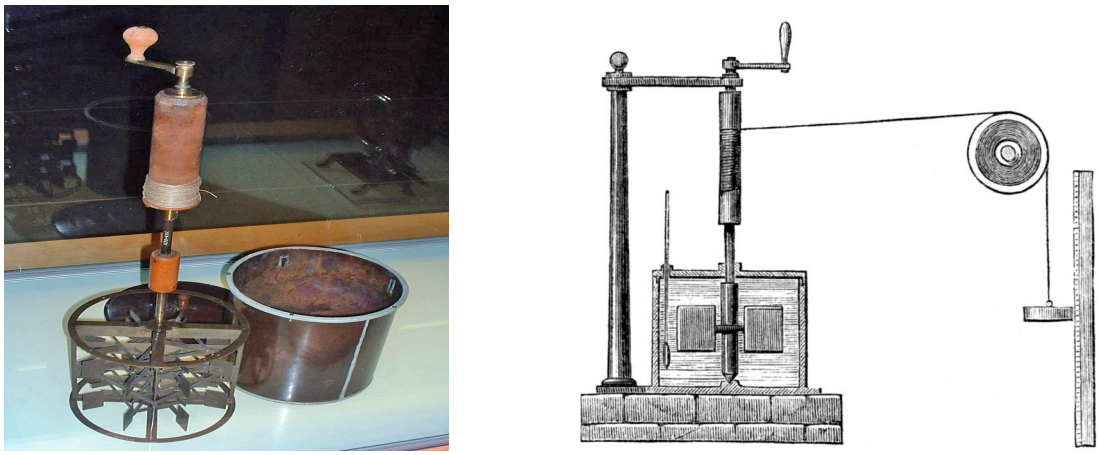

Fig. 1.3: *Joules heat apparatus in the Science Museum, London and its function principles. Pictures from Wikipedia.*

However, Joule's experiment was based on theoretical assumptions that came from the study of another thermodynamic property of substances: the heat capacity. The American-born British physicist Sir Benjamin Thompson (1753 – 1814) together with the Swedish physicist Johan Wilcke (1732 – 1792) studied how much energy is needed to raise the temperature of a solid substance by a certain amount and the French physicists Pierre Louis Delong and Alexis Thérèse Petit found that theoretically the molar heat capacity of any solid substance should be described by the relation:

$$C_{molar} = 3\, N_A k_B = 24.9 \text{ J mol}^{-1} \text{ K}^{-1} \qquad (1.3)$$

where C_{molar} is the molar heat capacity, N_A is the Avogadro number and k_B is the Boltzmann constant (1.361×10^{-23}). Although the so-called Dulong-Petit law is only obeyed at higher temperatures and only by some substances, such as pure heavy elements, it was an important observation for the understanding of the relation between heat, temperature and molecule motion in solid substances. However, the German Robert Mayer (1814 – 1878) studied an interesting aspect of the heat capacity of gases. In gases it was observed that the heat capacities of a particular gas differed in a way that if the heat capacity is measured at constant pressure (Cp) the values were always higher than those obtained from experiments performed at constant volume (Cv). Based on these observations Robert Mayer postulated in 1845 that the difference in the heat capacities (Cp and Cv) resulted from the fact that parts of the energy added to the gas in the constant pressure experiments was used by the gas to expand, which is a mechanical work, as the gas has to increase the volume against the surrounding air pressure. In his publication "Die organische Bewegung im Zusammenhang mit dem Stoffwechsel" he quantified the amount of mechanical work needed to raise the temperature of water and thus predicted the findings of James Joule in the same year. Combining the ideal gas law (1.2) and the energy-temperature relation based on the work of Ludwig Boltzmann

$$E_{kin} = f/2\ k_B\ T \qquad (1.4)$$

with E_{kin} being the kinetic energy ($1/2\ mv^2$) of the molecules, the degrees of freedom for each molecule (f) and T being the temperature, Robert Mayer could show that Cv and Cp must be related in a way that

$$Cp = Cv + nR = (f/2 + 1)\ nR \qquad (1.5)$$

with n being the number of moles of the ideal gas.

Further, he was the first who formulated the energetic equivalence of work and heat and went even further when he stated that the amount of energy in a system does not change if the forms of energy are converted into each other. The latter statement was published in 1847 by Hermann von Helmholtz and is known as the First Law of Thermodynamics

$$dU = \partial Q + \partial W = \text{constant} \qquad (1.6)$$

with U being the internal energy of the system, Q being the heat content and W being the work the system is doing or that is done on the system. One has to look quite sharp to understand the fundamental meaning of the equation (1.6) as it is obviously quite simple in form, but describes some interesting aspects of energy: (1) Energy is constant throughout a

closed system, i.e. a system that does not exchange any heat, matter or work with it's surrounding, and (2) the energy in that system can be described by it's heat content and the work that it is doing or that is done on the system. Not clearly visible from equation (1.6) but implicit in the first law is the observation that energy contained in the heat content of a system can be converted into mechanical work and vice versa. Also implicit in (1.6) is that energy cannot be created nor can it be destroyed or consumed somehow, which was at that time a groundbreaking postulate. It is notable here, that a description of the energy in a system as it is expressed in (1.6) is a purely macroscopic point of view. Due to the fact that at the middle of the 19th century little was known about the internal structure of matter, such as inter- and intra-atomic forces as well as electromagnetic forces, this simplification was mandatory. As thermodynamics are still applied in that way, it has been shown that this simplification was somewhat helpful. However, in equation (1.6) the differentials are expressed differently for the internal energy and heat as well as work. This is to point out that neither heat nor work are proper variables to describe the thermodynamic state of the system uniquely as they are a function of the "path" a system has taken to reach the state in which it is. Thus, it was necessary to find natural "state variables" that can properly describe the thermodynamic state of the system without being influenced by the systems thermodynamic history.

Resulting from the work of Robert Boyle, Sadi Carnot and James P. Joule it was already known that work a system can do or that can be done on the system can be described by a volume change against a surrounding pressure, which is the definition of the pressure-volume work

$$W = -PdV \tag{1.7}$$

where P is pressure and dV is the change in volume. The minus sign is conventionally showing that the system is doing work (and thus transferring energy to it's surroundings). The energy change of the entire system can therefore be described by

$$dU = \partial Q - PdV. \tag{1.8}$$

Rudolf Clausius (1822 – 1888) was a German physicist who was professor for physics in Berlin, Zürich, Würzburg and Bonn. During his studies of the relation between heat and work he recognized that heat, if supported to a heat engine can be more effectively converted into work if the heat engine is working at higher temperatures rather than at lower temperatures. He consequently stated that there must be a process, related to the temperature in a reciprocal way that lowers the amount of work that can be extracted from a certain heat amount. He

called that new state variable “entropy” (from the Greek “en” + “tropein”, which means “transformation content”) and gave it the unit “Clausius” (Cl) with 1 Cl being 1 cal/K. Later Cl was replaced by J/K. Clausius related the entropy difference of a system to the amount of heat that is added to (or subtracted from) the system in a way that

$$dS = dQ/T \tag{1.9}$$

where T is the absolute temperature at which the heat transfer occurs. Clausius also postulated in some way the second law of thermodynamics as he stated:

> “*The entropy of the Universe tends to a maximum*”.

A more precise formulation of his idea was later given by a number of physicists, Max Planck being one of the most famous:

> “*Every process occurring in nature proceeds in the sense in which the sum of the entropies of all bodies taking part in the process is increased. In the limit,* i.e. *for reversible processes, the sum of the entropies remains unchanged.”* Max Planck

It is notable here that together with the macroscopic description of the entropy like in equation (1.9) the Scottish mathematician James Clerk Maxwell studied thermodynamics at the microscopic, i.e. the molecular scale. His work on the so-called statistical thermodynamics led to the statistical formulation of the entropy by the Austrian physicist Ludwig Boltzmann

$$S = k_B \ln P \tag{1.10}$$

with P being the probability of a macroscopic state of a system. This definition, however, is interestingly much better accessible for many people as it relates entropy with order or disorder, a property of a system many people can imagine easily. The philosophical aspect of that formulation in combination with the second law of thermodynamics implies that Nature obviously tries to reach a most probable state if a system is able to transform. This circumstance, of course, excludes any pre-determination of macroscopic naturally occurring processes.

However, with the entropy being discovered the thermodynamic state of a system could be uniquely defined with so-called state variables and the expected change of the system with changing thermodynamic parameters could be predicted:

$$dU = TdS - PdV. \tag{1.11}$$

Furthermore, it was possible to define the amount of energy in a system that can be converted into mechanical work, an entity that is called the Helmholtz energy, or the free energy (F):

$$F = U - TS. \quad (1.12)$$

The only remaining major problem with equation (1.11) was that the variables (dS and dV) are not convenient for handling daily life's problems as they cannot be easily measured nor are they entities human beings have a good sense for. In contrast, temperature and pressure are much more convenient as both could be measured precisely even in the 19th century and they are related much more obviously to natural processes. Utilizing a mathematical operation called the Legendre-transformation, which enables the expression of a function $f(x)$ by its first derivative, Josiah Willard Gibbs (1839 – 1903), an outstanding American physicist, expressed the "enthalpy" (H) as "the heat function for constant pressure" (but without naming it "enthalpy"):

$$dH = TdS - VdP \quad (1.13)$$

and in the integrated form

$$H = U + PV. \quad (1.14)$$

Furthermore, in the same way Gibbs deduced the so-called "Gibbs energy" or "free enthalpy" (G):

$$dG = -SdT + VdP \quad (1.15)$$

and in integrated form at constant pressure and temperature:

$$G = H - TS. \quad (1.16)$$

With his compilation of papers "*On the Equilibrium of Heterogeneous Substances"* published between 1876 and 1878 he provided the basis for modern physical chemistry and enabled the application of thermodynamic concepts to chemical and mechanical systems. Today thermodynamic calculations are fundamental in many branches of natural, but also social sciences. Further, thermodynamics has provided the basis for the industrial revolution in the 19th century by enabling the construction of effective steam engines and still plays crucial roles in many industrial applications and the development of functional materials.

2 Application of thermodynamics in natural systems

2.1 Equations of state

Equation (1.16) can only be used to calculate the Gibbs energy in a system if the temperature and pressure dependencies of the Cp and volume functions are known. These dependencies are very simple in monoatomic gases whose behavior is close to that of an ideal gas. For such substances equation (1.2) describes the relation of the state variables P, V and T, which is sufficient to define the thermodynamic state of an ideal gas at any natural condition. Such equations that relate the state variables and enable to describe the state of a thermodynamic system under a given set of physical conditions are called "equations of state". For an ideal gas, this equation is quite simple but in most natural systems, especially those involving liquid and solid phases, the equations that accurately describe the thermodynamic properties of the considered system are more complex. In particular, complexities in describing thermodynamic systems arise during phase transitions, such as condensation or structural changes in solids, or in geologically relevant complex crystalline materials, such as minerals.

2.1.1. Equations of state for gases and fluids

As equation (1.2) was deduced for monoatomic ideal gases it fails to predict the thermodynamic properties of natural substances properly. Therefore, the ideal gas law had to be expanded in order to account for non-ideal behavior of natural substances. The first expansion of the ideal gas equation of state was given by Van der Waals in 1873. Van der Waals realized that in any polar substance the electromagnetic attractive and repulsive forces will influence the pressure of a certain amount of matter at given temperature. Consequently, the PV term in equation (1.2) must be modified in a way that it accounts for the attractive (P + x) and repulsive (V – y) forces. Van der Waals linked the material specific properties x and y to the molar volumes (V_c) at the pressure (P_c) and temperature (T_c) at the critical point of the substance and formulated his equation of state in the form:

$$(P + \frac{a}{V_m^2})(V_m - b) = RT \qquad (2.1)$$

where $a = 3P_cV_c^2$, $b = \frac{V_c}{3}$ and V_m = molar volume of the substance.

Although, this equation of state was a major enhancement regarding the prediction of the thermodynamic state of gases and fluids, the results of it still disagree with experimental

results and thus a number of improvements to the equation of state for gases and fluids were published. Today two approaches and modification of them are frequently used as equations of state for gases and fluids: (1) modifications of the Redlich-Kwong equation and (2) virial equations. The Redlich-Kwong equation (Redlich and Kwong 1949) is formulated as:

$$P = \frac{RT}{V_m - b} - \frac{a}{\sqrt{T}V_m(V_m + b)} \tag{2.2}$$

with $a = \frac{0.42748R^2T_c^{2.5}}{P_c}$ and $b = \frac{0.08662RT_c}{P_c}$.

The virial equations of state are given in the form of

$$\frac{PV_m}{RT} = 1 + \frac{B}{V_m} + \frac{C}{V_m^2} + \frac{D}{V_m^3} + \ldots \tag{2.3}$$

with the coefficients B, C, D etc. being a function of temperature and pressure independent. The term on the right side of the equation is often called the compressibility factor (Z).

2.1.2. Equations of state for solids

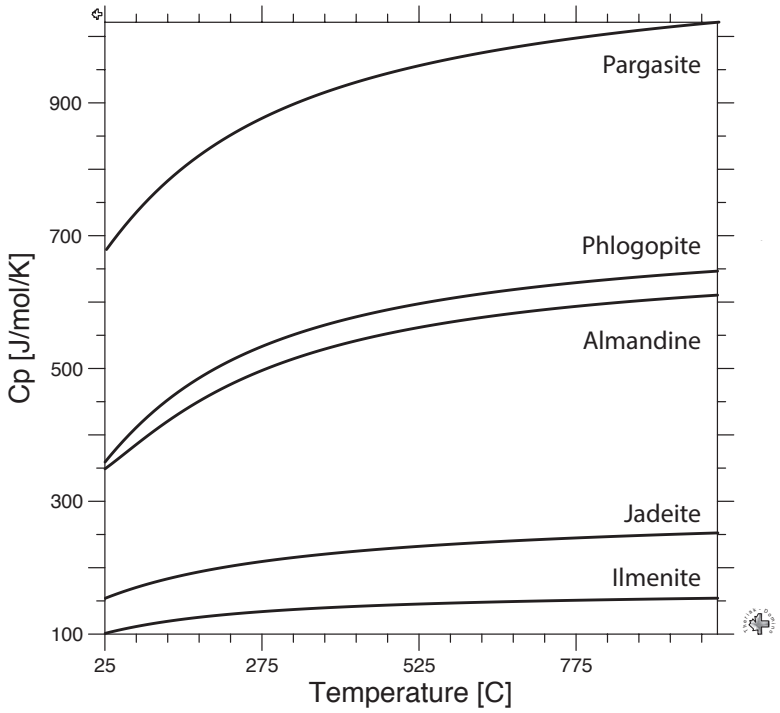

Fig. 2.1: *Temperature dependence of the Cp functions of various minerals calculated with the THERIAK algorithm (de Capitani and Brown 1987) and the JUN92 database from Berman 1988.*

In solids the intermolecular forces have a severe influence on the thermodynamic properties of the considered substances compared to gases and fluids. Hence, in order to predict the state of a given system with changing conditions the equations of state for solids must account for such strong deviation from the ideal gas behavior.

Figure 2.1 shows the temperature dependence of the Cp function for some selected minerals. Shapes and positions of these functions differ significantly from the Dulong-Petit law and have large differences among each other. Several approaches are published in order to fit the significantly different behavior of the Cp functions of solids to a single equation of state.

The heat capacities result from the fact that atoms in solids can be seen as harmonic oscillators. Based on this assumption Einstein (1907) and Debye (1912) formulated the quantum mechanical background for the understanding of heat capacities in natural solids. The first macroscopic formulations of the temperature dependence of the heat capacity were in the form of a power series, such as

$$Cp(T) = a + bT + cT^2 + \ldots \qquad (2.4)$$

with a, b and c being fit parameters and T being the absolute temperature. Maier and Kelley (1932) realized that this formulation did not sufficiently precise describe the heat capacities of solids especially at high temperatures, where the heat capacities increase nearly linear with temperature. Therefore, a subtractive term had to be incorporated into the heat capacity function and in their publication from 1932 Maier and Kelley formulated the first equation that was able to relate the heat capacities of solids with the temperature of interest properly. Their equation was in the form of

$$Cp = a + bT - cT^{-2}. \qquad (2.5)$$

Today, the Cp functions of minerals are commonly computed with equations following a power series with various numbers of coefficient and exponential terms. Berman and Brown (1985) for example suggested an equation of state in the form of

$$Cp = k_0 + k_1T^{-0.5} + k_2T^{-2} + k_3T^{-3} \qquad (2.6)$$

where $k1, k2 \leq 0$. This equation reproduces calorimetric measurements for most geologically relevant minerals within sufficient precision and is widely used in thermodynamic models of metamorphic rocks. Further, this equation ensures that the modeled heat capacities of solids approaches the high temperature limit given by the theoretical (lattice vibrational) theory,

which is

$$Cp \text{ (at high T)} = Cv + 3R = 3R + \alpha^2 VT/\beta \qquad (2.7)$$

where α is the coefficient of thermal expansion and β is the compressibility. Both values are given by the relations

$$\alpha = \left(\frac{\partial V}{\partial T}\right)_P \frac{1}{V} \qquad (2.8)$$

and

$$\beta = -\left(\frac{\partial V}{\partial P}\right)_T \frac{1}{V}, \qquad (2.9)$$

respectively.

Equations (2.8) and (2.9) can also be used to describe the volume of substances at given temperature and pressure. In general the volumetric change of a substance with changing temperature and pressure can be expressed by

$$V = V_0 \exp^{\alpha(T-T_0)-\beta(P-P_0)} \qquad (2.10)$$

with V_0, T_0 and P_0 being the initial volume, temperature and pressure and V, T, P being these parameters after temperature and pressure changes. However, as with the heat capacities the complex non-ideal behavior of many natural solid substances requires fitting of different parameters in order to describe the volume-temperature-pressure relations in minerals and other crystalline substances. A commonly used expression in thermodynamic models of geological processes is given in Berman (1988):

$$\frac{V^{P,T}}{V^{P_r,T_r}} = 1 + v_1(P - P_r) + v_2(P - P_r)^2 + v_3(T - T_r) + v_4(T - T_r)^2. \qquad (2.11)$$

In this equation v_1-v_4 are linear fit parameters, which facilitates the refinement process of these terms but allows sufficient extrapolation of the volume function to pressures up to 1.0 GPa (Berman 1988). However, several authors suggested more complex equations of state to describe volume changes in solids (e.g. Holland and Powell 1998, 2011; Stixrude and Lithgow-Bertollini 2005), but discussion of these are beyond the scope of this introductory chapter.

2.2. Thermodynamic treatment of polymorphic transformations

Several minerals of geoscientific interest undergo polymorphic transformations related to structural changes of the crystal lattice within a single phase. Examples of such transformations are the transitions among the quartz and alumosilicate polymorphs as well as the order-disorder transition in pyroxenes. Polymorphic transformations involve a drastic change in the thermodynamic properties of the phases in a relatively small pressure and temperature interval near the conditions of the transformation. These phase properties must be considered by the thermodynamic equations of state. Figure 2.2 shows the heat capacity of quartz between 25°C and 900°C. Between 275°C and 675°C the Cp function first changes its slope gently towards higher values and at the transition from α- to β-quartz suddenly steps back to lower values.

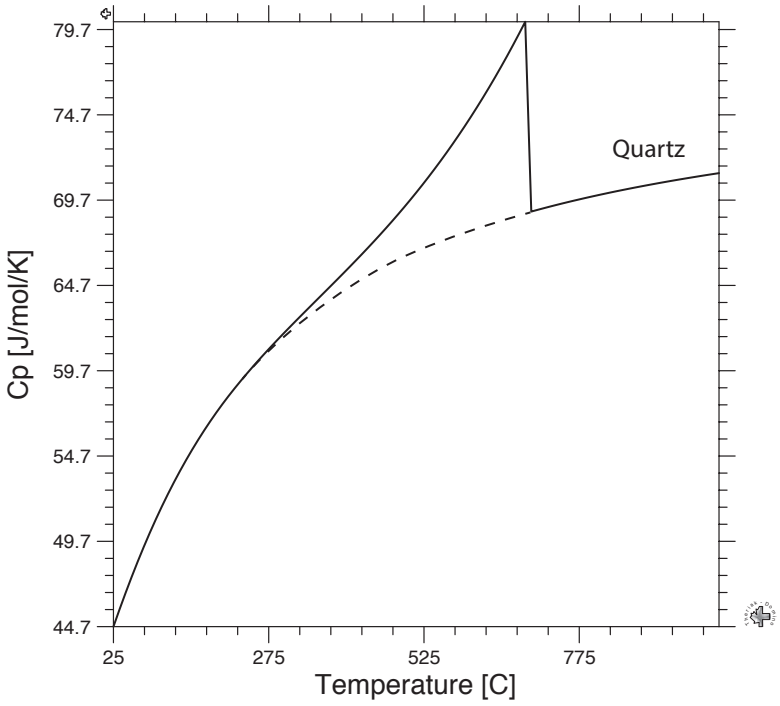

Fig. 2.2: Cp function of quartz between 25 and 900°C. Note the irregular behavior between 275 and 675°C resulting from the polymorphic transformation from α- to β-quartz. The stippled line marks the expected (regular) behavior. Diagram calculated with the THERIAK algorithm (de Capitani and Brown 1983) and the JUN92 database from Berman 1988.

According to Berman and Brown (1985) such polymorphic transitions are modeled by splitting the heat capacity into two parts, one part accounts for the "normal" lattice heat capacity, which is following the stippled line in Fig. 2.1 and a second part, which accounts for the heat capacity contribution from the polymorphic transformation. The latter is added to the lattice heat capacity between those temperatures at which the transition takes place. An extensive discussion about the general treatment of such continuous changes in the thermodynamic properties of phases is given in Landau (1937). Different approaches for the

mathematic treatment of such transformations are incorporated in various thermodynamic databases and computer algorithms (e.g., Berman 1988; Holland and Powell 1998; Holland and Powell 2011).

2.3. Application of thermodynamics to mineral equilibria

2.3.1. Calculation of heterogeneous phase equilibria among pure phases

Knowing the state functions for the heat capacity and the volume of substances equation (1.16) provides the basis for the calculation of the chemical energy in a system at given pressure and temperature. However, as can be seen from equation (1.15) the practical application of this equation to natural systems requires integration of the entropy over a certain temperature difference and integration of the volume over a pressure difference. In case of the entropy this integration can be defined to be from 0K to the temperature of interest, in case of the volume it is obvious that the initial volume of a substance at a certain pressure and temperature must be known. It is therefore convenient to define a common reference pressure and temperature, to determine the thermodynamic properties of the phases at this reference conditions and to integrate the entropy and volume function from this reference state to the pressure and temperature conditions of interest. Commonly, the reference temperature and pressure are 25°C and 1 bar, respectively. Standard state thermodynamic datasets commonly contain the properties of phases, such as enthalpy (H^0), entropy (S^0) and molar volume (V^0) at these standard state conditions. Based on these experimentally determined standard state values the Gibbs energy of a system can be calculated by integrating the system properties from standard state conditions to the temperature and pressure of interest. The general equation for this integration is

$$\Delta G^{P,T} = \Delta H_f^0 + \int_{T^0}^{T} Cp\,dT - T\Delta S_f^0 - T\cdot \int_{T^0}^{T} \frac{Cp}{T} dT + \int_{P^0}^{P} V\,dP \qquad (2.12)$$

where $\Delta G^{P,T}$ is the Gibbs free energy of the system at temperature T and pressure P and ΔH_f^0 and ΔS_f^0 are the enthalpy and entropy of formation from the elements at standard state temperature and pressure, respectively.

Applying this equation to natural systems we have to consider that the relations among the state variables as deduced in the first paragraphs considered only thermodynamic systems involving pure (i.e. consisting of one sort of molecules) phases. In heterogeneous thermodynamic systems, i.e. those containing multiple phases of different kind, we have to

define phases and their constituents in more detail:

> "Phases are parts of the system that consists of one type of molecules and that have the same physical and chemical properties. Components are the chemical constituents of phases or the system, such as atoms or molecules that are least necessary to describe the system".

The thermodynamic equilibrium in system containing multiple phases is controlled by the sum of the Gibbs energies of the phases coexisting in the system. For example, reactants and products in a chemical reaction are in thermodynamic equilibrium if the Gibbs energies of reactants ($G_{reactants}$) and products ($G_{products}$) are equal

$$\Delta G_{Reaction} = G_{products} - G_{reactants} = 0 \text{ (for thermodynamic equilibrium conditions).}$$

For reactions involving only pure phases the Gibbs energy of both, reactants and products can be calculated using equation (1.16), such that

$$\Delta G_{Reaction} = (H_{products} - TS_{products}) - (H_{reactants} - TS_{reactants}) = 0.$$

This equation defines a line in a P-T diagram along which reactants and products coexist in thermodynamic equilibrium. Using equation (1.15) the slope of this equilibrium line can be calculated with

$$d\Delta G = \Delta V dP - \Delta S dT. \qquad (2.13)$$

Rearranging this equation yields

$$dP/dT = \Delta S/\Delta V \qquad (2.14)$$

which is known as the Clausius-Clapeyron equation. With that simple relation the slope of a reaction among different phases can be judged from ΔS and ΔV of the reaction. For example, the Fe-Mg exchange reaction between garnet and clinopyroxene

$$2 \text{ pyrope} + 3 \text{ hedenbergite} \Leftrightarrow 2 \text{ almandine} + 3 \text{ diopside}$$

will certainly have a small volume change (ΔV), as on both sides of the reaction there is garnet and clinopyroxene. The entropy change is likely large, as Fe and Mg atoms are mixed in the solid solutions. Following the Clausius-Clapeyron equation, this reaction will have a steep slope in a pressure-temperature diagram and indeed the calibration of this reaction is a well-known geothermometer (e.g., Ravna 2000) being only moderately pressure sensitive. In

contrast, reactions with a large volume change, such as the transformation of sodic feldspar into clinopyroxene and quartz

albite ⇔ jadeite + quartz

will be good barometers as they have moderate slopes in a P-T diagram caused by the large volume difference between the two states of the system.

2.3.2. Calculation of heterogeneous phase equilibria including solution phases

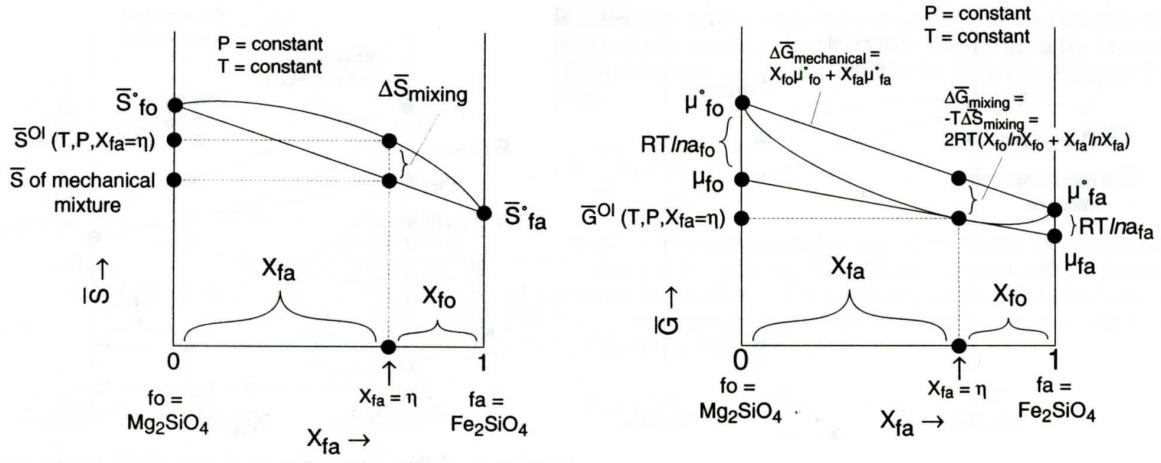

Fig. 2.3: Schematic illustration of the effect of chemical mixing in solid solutions on the entropy and the chemical potential in the solution phase (in this case olivine). Figure from Spear 1993.

In many natural systems the phases of interest do not consist of a single kind of molecules but are composed of chemical mixtures of different components. Such phases are called solutions and if solution phases are involved in a reaction the relation between the Gibbs energy of a phase and the composition of that phase must be quantified. In a first approximation the energetic contribution of the formation of solution phases, where different components are chemically mixed within one phase, is primarily by the entropy of mixing. Fig. 2.3 shows a S-X diagram for the olivine ($(Mg,Fe)_2SiO_4$) binary solid solution with two mixing sites. In a mechanical mixture the entropy of mixing (S_{mix}) would follow the straight line, but in case of a chemical solution, the entropy curve must be convex upward as the entropy (S) – composition (X_{fa}) relation of the solution follows the function

$$S_{mix} = -\alpha R \sum X_i \ln X_i. \qquad (2.15)$$

In this term X_i refers to the molar fraction of the component i in the solution phase and α is the site multiplicity on which the component substitutes. According to equation (1.16) the

Gibbs energy vs. composition curve of an ideal solid solution will be concave upward as the excess Gibbs energy (G_{excess}) contributed by the mixing entropy will be

$$G_{excess} = \alpha RT \sum X_i \ln X_i. \quad (2.16)$$

The relations of the above-described functions are visualized in Fig. 2.3.

Following the above arguments it is necessary in reactions involving solid solutions to define a molar Gibbs energy as the Gibbs energy of a solution phase is dependent of the mole fractions of the components in that solution. This molar Gibbs energy is often given the Greek letter μ and is defined as

$$\mu = dG/dn. \quad (2.17)$$

Where n is the number of moles in a substance. In analogy to other forms of energy, where spatial gradients in energy are called potentials, μ is called the chemical potential, as it relates changes in the Gibbs energy to changes in the amount of matter. For systems involving solution phases the contribution of the chemical potential resulting from chemical mixture of substances to the Gibbs energy must be considered so that the change in Gibbs energy with changing pressure, temperature and chemical composition of a solution phase can be written as

$$dG = -SdT + VdP + \sum \mu_i dn_i \quad (2.18)$$

where n_i is the number of moles of component i and μ_i is the chemical potential of that component in the solution phase. Following equation (2.17) the entire Gibbs energy of the system is defined as

$$G = \sum \mu_i n_i \quad (2.19)$$

the derivation of which yields

$$dG = \sum \mu_i dn_i + \sum n_i d\mu_i \quad (2.20)$$

combining equations (2.18) and (2.20) yields the so-called Gibbs-Duhem equation, which describes the thermodynamic equilibrium constraints in a single solution phase system as to be

$$0 = -SdT + VdP - \sum n_i d\mu_i. \qquad (2.21)$$

This equation implies that changes in the chemical potential can only occur as the result of changing pressure or temperature. Further it shows that at constant pressure and temperature there can be no change in the chemical potential of a solution phase. Also implicit in this equation is that at constant pressure and temperature the components of solution phases in a reaction, i.e. the moles of a particular component in the solution phase, cannot change independently, but in a related way such that

$$\sum n_i d\mu_i = 0. \qquad (2.22)$$

The Gibbs-Duhem equation is of particular interest, because in its application to multi phase systems it yields the so-called Gibbs phase rule, which defines the number of independently changeable variables in a system at thermodynamic equilibrium – the so-called degree of freedom (f) of a system.

$$f = c + 2 - p \qquad (2.23)$$

where c is the number of components and p is the number of coexisting phases at given pressure and temperature.

Equation (2.19) is sufficient to calculate modes and compositions of solution phases in thermodynamic equilibrium. However, for practical reasons it is convenient to divide the chemical potential of solution phases into one part that represents the chemical potential of the pure phase j (μ^0_j), often measured or calculated at specific conditions and a second part that refers to the contribution from chemical mixing within the solid solution ($RT\ln a_j$) yielding the chemical potential of the endmember j in an ideal solution phase to be

$$\mu_{j,ideal} = \mu_j^0 + RT \ln a_j. \qquad (2.24)$$

Here, a_j denotes the activity of the endmember j in the solution phase, which is accordingly defined as

$$a_j = \exp^{((\mu j - \mu j0)/RT)}. \qquad (2.25)$$

From equations (2.24) and (2.25) it is evident that the mathematical formulation of the relation between the composition of a solution phase and the resulting activity of the endmembers in that solution plays an enormous role in quantification of thermodynamic phase equilibria in natural systems and so-called solid solution models that provide this

mathematical connection are constantly discussed in the scientific literature.

Let's assume a reaction among the minerals A, B, C and D with the stoichiometric coefficients a, b, c and d, respectively. If the reaction can be written as

$$aA + bB \Leftrightarrow cC + dD \tag{2.26}$$

then the difference of the Gibbs energy of reactants and products can be written as

$$\Delta G_{Reaction} = c\mu_C + d\mu_D - a\mu_A - b\mu_B = \sum \nu_i \mu_i \tag{2.27}$$

where ν_I is the stoichiometric coefficient of phase i in the reaction and μ_i is the chemical potential, i.e. the molar Gibbs energy, of that phase. The reaction is at equilibrium if the sum of all chemical potentials of the reacting species in the reaction is zero:

$$0 = a\mu_A + b\mu_B - c\mu_C - d\mu_D = \sum \nu_i \mu_i \tag{2.28}$$

substituting equation (2.24) yields

$$0 = \sum \nu_i^0 \mu_i^0 + RT \sum \nu_i \ln a_i \tag{2.29}$$

and reformulation yields

$$0 = \sum \nu_i^0 \mu_i^0 + RT \prod a_i^{\nu} \tag{2.30}$$

The product $\Pi\, a_i^{\nu}$ is referred to as the equilibrium constant, which is commonly denoted K. As $\Sigma \nu_i^0 \mu_i^0$ refers to the chemical potentials of the pure phases at given pressure and temperature, the difference in Gibbs energy for the reaction (ΔG_R) resulting from the formation of solution phases equals

$$\Delta G_R^0 = -RT \ln K \tag{2.31}$$

where in case of reaction (2.27) K can be written as

$$K = \frac{a_C^c \cdot a_D^d}{a_A^a \cdot a_B^b} \tag{2.32}$$

and

$$\Delta G_R^0 = -RT \ln \frac{a_C^c \cdot a_D^d}{a_A^a \cdot a_B^b} \tag{2.33}$$

As an example of the application of that equation Figure 2.4 shows the K values for the reaction

3 anorthite = grossular + 2 kyanite + quartz

in a pressure-temperature diagram.

Two major implications are noteworthy regarding the calculation of phase equilibria using the equlibrium constant: (1) the chemical potential, i.e. the molar Gibbs energy, is split into two parts, one part that describes the chemical potential for the pure endmembers (μ_i^0), which can be experimentally determined, and a second part contributed from the chemical mixture in solution phases ($RT \ln K$). For this second part activity-composition relations must be known in order to correctly calculate the activity of the components in solution phases and thus the equilibrium constant. (2) In this approach the chemical equilibrium is calculated among pre-defined phases or a pre-defined reaction, but in complex chemically open systems it is often difficult to determine the phase assemblage expected to coexist at certain pressure and temperature conditions. This poses a major shortcoming of that method if applied to geoscientific problems, which will be discussed in a later chapter.

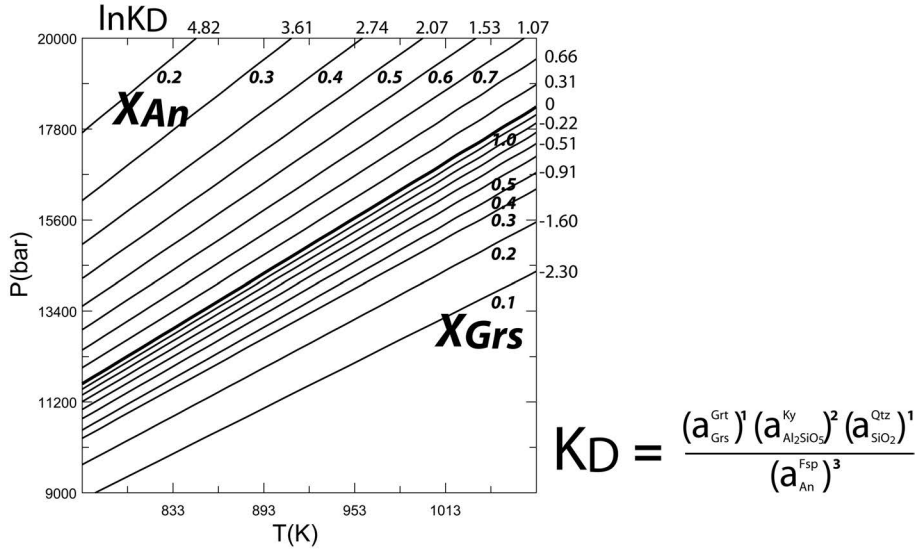

Fig. 2.4: K_D values for the reaction 3 anorthite = grossular + 2 kyanite + quartz and different feldspar and garnet compositions. The bold solid line ($\ln K_D=0$) marks the reaction of the pure phases. Calculated with the THERIAK algorithm (de Capitani and Brown 1987) and the JUN92 database from Berman 1988.

However, the concept of activity of a phase in a solution was developed for gaseous and liquid solutions and is based on the observation that partial pressure relations above a liquid solution reflect the fractions of endmembers in the liquid solution. Consequently, the activity of an endmember in a binary liquid solution was described as the partial pressure of that

endmember in the vapor pressure above the solution relative to the pressure of the endmember at reference conditions, which yields:

$$a = \frac{P}{P^{reference}} = \exp^{\frac{\mu^P - \mu^{P^{reference}}}{RT}} \qquad (2.34)$$

It is evident that this definition requires the definition of a reference vapor pressure for the phases of interest, without this definition the activity is also undefined. In solid solutions the chemical potential of an endmember is usually referenced to the chemical potential of the pure endmember at the pressure and temperature conditions of interest.

Alternatively, as mostly done for liquid and gaseous phases, the reference conditions are standard temperature and pressure (STP), i.e., 25°C at 1 bar (Fig. 2.5). In this case activity is usually referred to as "fugacity".

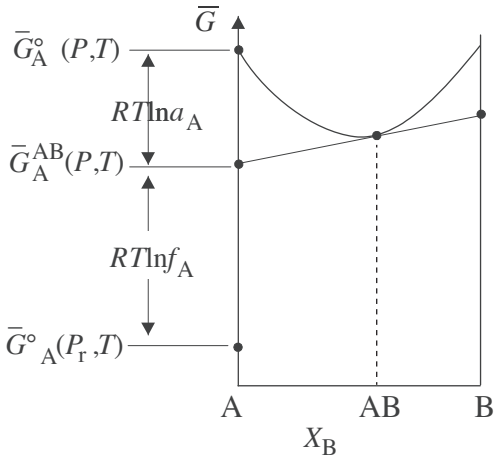

Fig. 2.5: The activity a_A of a solution endmember (A) is related to the difference in the partial molar Gibbs energy $G_A^{AB}(P,T)$ of the endmember in the solution and in its pure state at the same pressure and temperature $G_A^0(P,T)$. Alternatively, fugacity (f) is defined relative to the partial molar Gibbs energy $G_A^0(P_r,T)$ of the pure endmember at a different pressure. Modified from unpublished material of J.A.D. Connolly (ETH Zürich).

The development and understanding of thermodynamic processes and thermodynamic properties of matter were only possible by studying gases and fluids as in these substances the concept of the internal energy being the sum of the motion of particles holds largely true. In an "ideal gas" there is no mechanical, electro-magnetic or chemical interaction among the molecules, which allows the above-mentioned thermodynamic point of view. However, in fluids, this consideration is an oversimplification as electro-magnetic forces, such as Van der Waals forces are acting on the particles and when it comes to solids, these electro-magnetic forces are even stronger. As demonstrated above the effects of inter-molecular forces are contained in the expressions of heat and pressure-volume work in classical thermodynamics.

It is evident that the thermodynamic properties of solids – even more than those of fluids – deviate from the relatively simple thermodynamic relations obeyed by mono-atomic gases, although the theoretical background is the same for all substances. Investigation of thermodynamic processes involving fluids and solids therefore requires correcting functions in order to quantify the deviation in thermodynamic behavior of liquid and solid substances from those of "ideal gases". This circumstance holds true especially for thermodynamic calculations involving (poly-)crystalline materials, such as in material- and geosciences. To characterize such materials thermodynamically complex heat capacity and volume functions as well as sophisticated formulations for the thermodynamic behavior of solid solutions are necessary as will be demonstrated in the next paragraph.

2.3.3. Activity-composition (a-X) relations

Figure 2.6 shows the vapor pressures of water and dioxane over a water-dioxane solution. The composition-activity relations are linear only in regions near the endmember compositions, i.e. in cases where concentrations of the components are either very high or very low. In the cases, the composition-activity relations follow the Raoult's law

$$a_i = X_i \tag{2.35}$$

or the Henry's law

$$a_i = hX_i \tag{2.36}$$

where a_i is the activity of the endmember i in the solid solution, h is the Henry's law constant and X_i is the mole fraction of the endmember i. In between these regions the composition-activity relation follows a complex function, which is commonly described with a activity coefficient (γ):

$$a_i = \gamma X_i \tag{2.37}$$

where

$$\gamma = f(P,T). \tag{2.38}$$

Usually the pressure and temperature dependence of γ is expressed as

$$\gamma = \exp^{\left(\frac{(1-X_i)^2 W_{ij}}{\alpha RT}\right)} \tag{2.39}$$

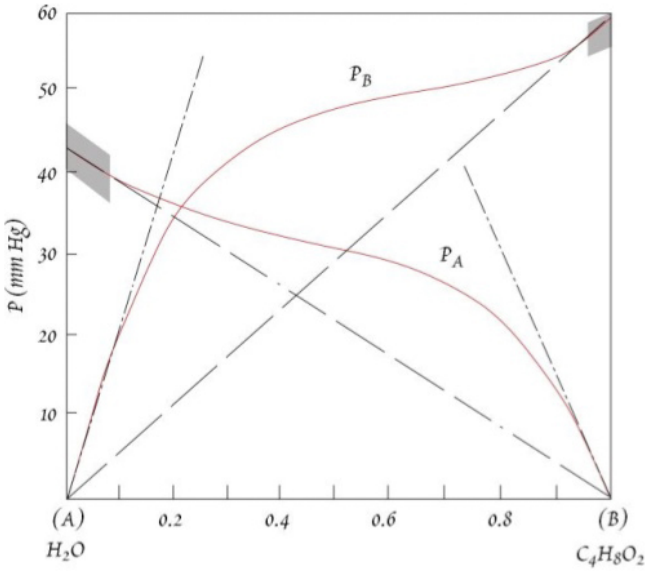

Fig 2.6: Vapor pressure (reflecting activity) of water and dioxane in a water-dioxane mixture. The measured values (red lines) deviate significantly from the theoretical values following the Raoult law (dashed lines) and the Henry law (dot-dashed lines). After Nordstrom and Munoz 1986.

where X_i is the mole fraction of the component i, α is the site multiplicity in the substance where i is incorporated and W_G denotes a so-called Margules parameter accounting for non-ideal solution behavior. Margules parameters are often used to introduce excess energies in solution models and as the Gibbs energy they must defined for non-ideal behavior of the substance with respect to enthalpy and entropy such that

$$W_G = W_H - TW_S. \qquad (2.40)$$

For solid and fluid solutions a number of a-X models are published and the datasets are continuously developed and improved. Regarding the calculation of complex phase diagrams they play a major role and are consequently a matter of intense debate especially in geosciences.

3 Thermodynamic forward modeling in geosciences

In this habilitation I present several publications that are concerned with the application of thermodynamic forward models to geoscientific problems as well as with combinations of thermodynamic and geochemical models in order to better understand lithosphere dynamics and element transfer in the lithosphere. Thermodynamic as well as geochemical models play a pivotal role in the simulation of natural processes and are therefore increasingly applied to a number of geoscientific questions.

In geosciences, field-based observations are fundamental for our interpretations of geological

processes. Quantitative models, which should be based on these observations, are essential to predict the evolution of geological systems and the outcome of geological processes (Albarède, 1995). As many disciplines in geosciences are faced with the fact that their study target, such as processes in the deep Earth, is either completely inaccessible, or that spatial or temporal scales at which the processes of interest operate do not allow direct observation, numerical and analogue models have become an indispensable tool to study, quantify and predict processes in Earth and environmental sciences. The development of high resolution - high precision analytical techniques to determine chemical and isotopic compositions of rocks and minerals, an increasing number of experimental data and advances in computational resources enhances our ability to simulate Earth processes and to test the results of these models against field-based observations.

Today predicting phase and chemical equilibria is extremely important in many industrial applications, such as gas distillation, cement production and the development of functional materials. In all of these applications, phase diagrams are used to predict physico-chemical processes in complex systems. Commonly phase diagrams display lines, which mark conditions at which multiple phases coexist in a thermodynamic equilibrium. Based on the thermodynamic state variables and on phase specific properties such diagrams can be used to predict how a system will change with changing thermodynamic variables. They were essential for the effective development of many functional materials, such as steel and plastics In general, the theoretical background for the prediction of phase equilibria in chemical systems is known since the groundbreaking papers of Josiah Willard Gibbs and the many works that these papers are based on (see above). However, modern thermodynamics deal with molecularly much more complex phases than those that were used to derive the theoretical backgrounds of thermodynamics, such as ideal gases and simple fluids. Therefore, modern thermodynamic calculations need to involve mathematical treatment of all kinds of non-ideal interactions and behaviors. Methods of calculation of phase diagrams (CALPHAD) have been successfully developed and are constantly improved.

Thermodynamic modeling is nowadays more frequently applied to geoscientific problems, although its application is far more complex than most approaches in material sciences. Challenges in geosciences arise from the fact that most geoscientific questions involve thermodynamic treatment of complex solid solution phases in multiphase systems, interaction of liquid and solid phases and consideration of open system behavior. The application of thermodynamic calculations to geoscientific problems became viable with the compilation of

extensive datasets for thermodynamic standard state properties (e.g. Helgeson et al., 1978; Robie and Hemingway, 1995; Holland and Powell, 1998; Berman, 1988; Gottschalk, 1997), reliable equations of state for geologically relevant phases and conditions (e.g., Kerrick and Jacobs, 1981; Berman, 1988, Stixrude and Lithgow-Bertelloni, 2005; Holland and Powell, 2011) and solid solution formulations for phases of geoscientific interest (e.g., Margules, 1895; van Laar, 1910; Holland and Blundy, 1984; Berman, 1990; Holland and Powell, 2003). Regarding the interpretation of thermodynamic calculations it is noteworthy that although many of the data incorporated in the available databases are based on experiments or have been numerically determined and are internally consistent, raw experimental data on standard state thermodynamic phase properties are still sparse and incomplete. The limited amount of experimental data together with an inappropriate use of thermodynamic variables (e.g., μ_{H2O} (chemical potential of water) vs. n_{H2O} (amount of water)) can result in significant misinterpretations of modeled thermodynamic equilibria in geosciences (Essene 1989, Powell et al., 2005). Therefore, it is of utmost importance that the formulation of the problem to be solved using thermodynamic modeling complies with limitations induced by the uncertainties implicit in the thermodynamic data and that the thermodynamic variables used to extract information from such models are carefully chosen.

In general, two different thermodynamic calculation approaches can be used to determine thermodynamic equilibria of mineral reactions ($\Delta G_R = 0$) among fluid and solid phase assemblages: (1) Solving the equilibrium constant (K) as demonstrated above and (2) minimization of the Gibbs energy in a system.

3.1. The global Gibbs energy minimization approach

The approach of Gibbs energy minimization for calculating amounts and composition of thermodynamically stable phases in a multicomponent multiphase system involving solution phases can be formulated as follows:

$$\text{minimize } G = \sum_{i=1}^{m} n_i \mu_i \qquad (3.1)$$

where n_i = molar amount of component i and μ_i = molar chemical potential of the i^{th} component. In this case the chemical potential is not split into a part for pure endmembers and the contribution from solutions, but the μ-X relations are directly determined from the mathematical formulation. The mathematical treatment of this approach involves (1) finding the phase assemblage with the lowest Gibbs energy among a large number of solid solution

phases (so called global Gibbs energy minimum) and (2) finding the tangent plane that touches the G-X curves of all stable solid solution phases, which is prerequisite for finding the thermodynamically stable compositions of solution phases (Fig. 3.1).

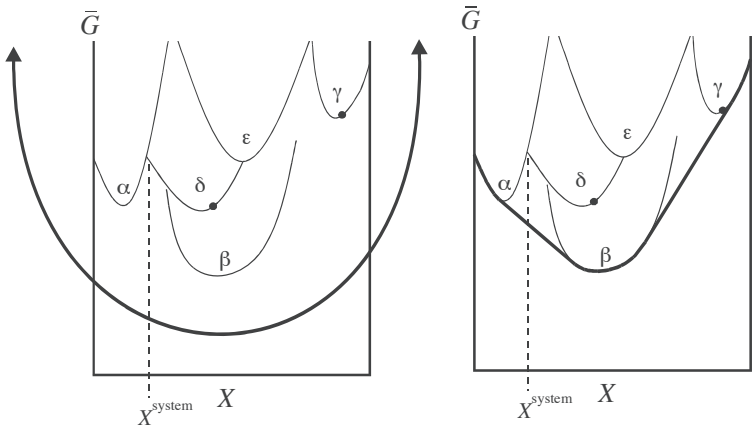

Fig. 3.1: *The stable states of a heterogeneous system can be determined conceptually by draping a rope under the G-X surfaces of the phases and then pulling upwards on the ends of the rope (left). When the rope is taut it defines the system minimum G surface (right). The stable assemblage is dependent on the system chemistry (X^{system}). Modified from unpublished material of J.A.D. Connolly (ETH Zürich).*

For both aspects, a number of mathematical approaches are published (see Koukarri and Pajarre (2011) for a detailed review) and are implemented into several commercial and open source software packages, including MELTS (Ghiorso and Sack, 1995; Asimow and Ghiorso, 1998), pMELTS (Ghiorso et al., 2002) PERPLE_X (Connolly, 2005), THERIAK/DOMINO (de Capitani and Brown, 1987) and GEM-Selektor (Kulik et al., 2004; 2013).

The equilibrium constant approach and the Gibbs energy minimization approach require knowledge about the Gibbs free energy of pure phases and a mathematical formulation of the relation between composition and activity/chemical potential in solution phases. Consequently, they both rely on thermodynamic data sets, which contain the standard state thermodynamic parameters and equations of state (EOS) for minerals, fluids and gases together with solution model formulations. The approach of solving the equilibrium constant furthermore requires that the phases among which the thermodynamic equilibria are calculated are pre-defined. This approach is widely utilized in aquatic geochemistry because the equilibrium constants of many aqueous reactions can be readily obtained from experiments (see Oelkers et al., 2009, and references therein). Several commercial and open source computer programs, such as PHREEQC (Parkhurst and Appelo, 1999), SUPCRT92 (Johnson et al., 1992) and THERMOCALC (Powell and Holland, 1988), are available for this

purpose.

In metamorphic petrology, element fractionation processes, e.g. fractional crystallization (e.g., Spear 1988; Marmo et al., 2002; Konrad-Schmolke et al., 2006; 2008a), water liberation (e.g., Hacker, 2008; Dragovic et al., 2012) and reactive fluid flow (e.g., Ferry and Gerdes 1998; Beinlich et al., 2010) require thermodynamic forward modeling of chemically open systems (e.g., Korzhinskii, 1965). In such open systems, coexisting phases cannot be predicted a priori – a prerequisite of the equilibrium constant approach – because they are a function of the pressure (P), temperature (T) and chemical (X) evolution of the rock. Therefore, the approach of global Gibbs energy minimization is preferable as it allows the calculation of thermodynamically stable phase assemblages among all phases available in the database.

Several pioneering works in the 1980s (Spear, 1988; Spear and Menard, 1989; Spear and Selverstone, 1983; Connolly and Kerrick, 1987; de Capitani and Brown, 1987) established the use of Gibbs energy minimization in petrologic modeling. These studies successfully demonstrated modeling of different rock-forming processes utilizing Gibbs energy minimization and yielded new insight into metamorphism. The basis for an important improvement in thermodynamic modeling of complex systems is implicit in equation (3.1), which implies that the Gibbs energy of a given system is dependent on the amount of matter within the considered system. In a chemically closed system, where no exchange of matter between the system and its surroundings occurs, the amount of matter and the element ratios in the system are fixed. This constraint can be used to calculate compositionally constrained phase diagrams that reflect phase relations in a particular chemical system. In geosciences such constrained chemical systems are specific rock types or even specific rock samples, for which individual phase diagrams can be calculated using the Lagrange method to solve matrices containing the thermodynamic parameters of the system. Such compositionally constrained phase diagrams are usually called “pseudosections” as they represent “cuts” at a certain chemical composition through the composition space. The prefix “pseudo” refers to the circumstance that not all phases considered in the system necessarily lie in one compositional plane, but are projected into it. In contrast to so-called petrogenetic grids, which are compositionally unconstrained phase diagrams, pseudosections contain additional information related to the specific chemical composition of the investigated sample (Powell et al., 2005). One very important difference between petrogenetic grids and pseudosections are the properties of the lines separating different phase fields. Whereas in case of petrogenetic grids these lines represent reaction lines along which one or more phases react to form other

phases, they represent lines where one or more phases disappear as their modal abundance becomes zero in case of pseudosections. Therefore they are often called “zero mode lines”.

In more recent publications, Gibbs energy minimization was used in a number of different contexts including precise correlations of the pressure-temperature evolution of metamorphic rocks with age determinations (e.g., Pollington and Baxter 2010), fluid-rock and melt-rock interaction (Nagel et al., 2012; Konrad-Schmolke et al., 2011a), deformation (Pearce and Wheeler 2010), fluid expulsion during metamorphic reactions in subduction zones (Dragovic et al., 2012; Connolly, 2005; Kerrick and Connolly, 2001; Gorman et al., 2008), element transport properties of metamorphic rocks (Skora et al., 2006; Konrad-Schmolke et al., 2008b), the prediction of compositional trends in arc melts (Hebert et al. 2009; Nagel et al., 2012) as well as quantification of reactive fluid flow during metamorphism (Beinlich et al., 2010).

4 Geochemical trace element modeling

Among the most important questions regarding modern geosciences are those related to mass transfer in solid materials. Mass transfer in the solid Earth is a social and economic problem as it is possibly resulting in ore deposit formation, volcanic eruptions or earthquake ruptures. The transport of matter is generally possible by two different processes, which are diffusion and passive transport in a transport agent, such as fluids or melts. As the latter is often several magnitudes faster the most effective way of element transport is as solutes in a fluid or a melt. Hence, effective element transport is directly connected with fluid transport mechanisms and –rates that are today in the focus of many geoscientific investigations. However, in most cases geoscientists are confronted with the fact that the object under investigation, which is the fluid phase, is not or only partially preserved in the investigated rock. Instead fluid pathways are characterized by newly precipitated solid phases or the chemical modification of pre-existing solids with which the fluid interacted during percolation. Transport mechanisms as well as amounts and rates of the percolating fluids can only be indirectly investigated by studying the relict affected phases or the newly precipitated minerals. For this purpose trace element concentrations as well as isotope characteristics of the solids are best suited.

Trace elements (elements that are present at concentrations of less than 0.1 wt.%) commonly substitute for major elements in rock-forming minerals. They have a negligible influence on the outcome of a particular process, but instead are passive recorders of the processes that the system has experienced (e.g., Blundy and Wood, 2003). The distinct geochemical behavior of

trace elements, which can be described by mathematical models, makes them particularly useful tracers. Depending on the process, trace elements behave in different, but predictable ways, which allows us to determine which processes have operated in a certain situation or setting.

In general, the incorporation of a certain trace element into a solid phase is strongly dependent on the size of the crystallographic site in the solid and the radius of the trace element cation (Onuma et al., 1968) and on the elastic properties of the solid (Blundy and Wood 1994). Unfortunately, comprehensive thermodynamic models to predict trace element concentrations in minerals still suffer from limited experimental and physical data. However, the low concentrations of trace elements cause them to be sufficiently diluted to follow simple relationships between composition and activity. For a wide range of trace element concentrations, Henry's Law applies, stating that the activity of a trace element is directly proportional to its composition (Fig. 2.6):

Commonly, the equilibrium distribution of trace elements between two phases is described by a distribution coefficient (or partition coefficient) (see White, 2013, for details). In geochemical applications, the Nernst partition coefficient (D) is used, which defines D as the ratio of the concentrations (c) of an element i between two phases A and B:

$$D_i^{A/B} = \frac{c_i^A}{c_i^B} \qquad (4.1)$$

Although D values are known to depend on temperature, pressure, and the compositions of the phases involved, P and T independent distribution coefficients are commonly used in magmatic and metamorphic petrology. This simplification is partly due to the limited pressure dependence of many partition coefficients under lithospheric conditions (Taura et al. 1998) and partly due to the lack of experimental data.

Quantitative models using trace elements were first applied in studies about the petrogenesis of igneous rocks. Gast (1968) and Shaw (1970) developed models for partial melting and fractional crystallization, in which they used concentrations of trace elements in liquid and solid phases in relation to the degree of partial melting of a rock and the degree of fractional crystallization, respectively. Later, assimilation of country rocks, combined assimilation – fractional crystallization processes, magma recharge, source rock heterogeneities and melt-rock reactions were all investigated using trace elements (O'Hara, 1977; De Paolo, 1981; Kelemen et al., 1992; McKenzie and O'Nions, 1991; Weaver, 1991). In recent years, trace

element models are combined with thermodynamic constraints to simulate the evolution of magmatic systems that simultaneously undergo a combination of fractional crystallization, recharge and assimilation processes (EC-cAFC; Bohrson and Spera, 2001, 2007).

Trace elements are also important petrogenetic tracers for the genesis of metamorphic rocks. Whole rock trace element concentrations are frequently used for the determination of protolith compositions and pre-metamorphic alteration processes (Pearce 2008; Altenberger et al., 2008; Bebout, 2007; Becker et al., 2000; Halama et al., 2013; John et al., 2010; van der Straaten et al., 2012) and the quantification of fluid infiltration and element transport (Nabelek 1987; Ague, 2003, 2011; John et al., 2004; Beinlich et al., 2010). Many experimental studies have focused on the partitioning of trace elements between solid and liquid phases during subduction (Kessel et al., 2005; Ayers and Eggler, 1995; Brenan et al., 1995), and these data were applied in numerous investigations about fluid-rock interaction during metamorphism (Bau, 1991; Brunsmann et al., 2001; Breeding et al., 2004; Beinlich et al., 2010). In metamorphic rocks, several phases of metamorphism may be recorded, and partial overprinting during metasomatism and/or retrogression may cause additional complexities. Therefore, *in situ* measurements that help to trace specific reactions and discern different episodes of equilibration are often crucial.

5 Combination of thermodynamic and geochemical models

The combination of thermodynamic and geochemical forward models has the distinct advantage of utilizing two independent sources of information about metamorphic processes. First, the thermodynamically modelled abundances and compositions of coexisting phases yield information about the major element distribution in a rock sample and second the geochemical modelling of trace elements I the same sample yields insight into the relation between thermodynamic equilibrium and kinetic effects during metamorphism. Thus, equilibrium and kinetic processes can be investigated by comparing modelled and observed phase assemblages, as well as the major and trace element composition of phases and whole rocks. I developed this approach as a consequent succession of my thermodynamic modelling experience and used this technique to study fluid migration and fluid-rock interaction in different tectonic settings and at different spatial scales.

In the following I will discuss two examples of the application of combined thermodynamic geochemical modelling in more detail. Applications of these approaches have been published in four of the attached manuscripts (Konrad-Schmolke et al., 2008b; Konrad-Schmolke et al., 2011b; Halama et al., 2014, Konrad-Schmolke and Halama 2014).

5.1. Introduction

As demonstrated by Goldschmidt (1954), physicochemical principles determine systematic compositional changes in rocks and minerals and are hence the key to understand geological processes. The combination of thermodynamic and geochemical forward modeling (e.g., Hebert et al., 2009; Kimura et al., 2009, 2010; Konrad-Schmolke et al., 2008b; Nagel et al., 2012) allows a more precise quantification of key geochemical parameters leading to an improved understanding of geodynamic mechanisms and enables to study and predict rates and kinematics of solid/fluid reactions. With such a combined approach, specific features in the trace element geochemistry of metamorphic minerals, such as garnet (Konrad-Schmolke et al., 2008b) or zircon and monazite (Hermann and Rubatto 2003), but also subduction-related rocks were successfully reproduced. Nagel et al. (2012), for example, combined the calculation of equilibrium assemblages in partially molten, mafic rocks with subsequent modeling of trace element fractionation between melt and residual phases to explain the formation of the Earth's oldest continental crust. Hebert et al. (2009) investigated slab fluid source lithologies and melt transport regimes in subduction zones using the GyPSM-S (Geodynamic and Petrological Synthesis Model for Subduction) modeling scheme, which couples a petrological with a thermal model to describe processes occurring in the supra-subduction zone (SSZ) mantle wedge, supplemented with models for trace element partitioning in the fluid phase and melt transport regimes. Kimura et al. (2009) developed the Arc Basalt Simulator (ABS) modeling scheme to predict the composition of primitive arc magmas. Application of the ABS models produced successful predictions of incompatible element and Sr-Nd-Pb isotopic compositions of distinct primitive magmas from the volcanic front and the rear-arc of the Izu arc (Kimura et al., 2010).

Hence, the above-mentioned works show the immense potential of thermodynamic and trace element modeling in comparison with natural rocks in terms of a better understanding and a quantification of rock-forming processes and their rates.

Depending on the choice of the boundary conditions of the thermodynamic models together with the chosen trace elements different metamorphic and magmatic processes can be investigated. In this habilitation I show how thermodynamic forward modeling, involving the simulation of chemically open systems, yield insight into a sample's metamorphic evolution (Konrad-Schmolke et al., 2008a; Konrad-Schmolke et al., 2011a), its fluid-rock history (Konrad-Schmolke et al., 2011b), the element transport properties of the sample (Konrad-Schmolke et al., 2005) and the influence of the bulk rock chemistry on the phase assemblage

(Scott et al., 2013; Konrad-Schmolke et al., 2008a). Further, I will show how thermodynamic models in combination with trace element modelling enables quantification of syn-metamorphic fluid fluxes (Konrad-Schmolke et al., 2011b, Halama et al., 2013) and the large scale water cycle in subduction zones (Konrad-Schmolke and Halama 2014). Regarding the trace element models, I predominantly concentrate on fluid-mobile elements (FME; Li, B, N, Cl, As, Rb, Sb, Cs, Ba as well as Pb and U), with a special emphasis on boron, and rare earth elements (REE), which can be excellently used for the study of fluid-rock interaction and reaction paths of the investigated samples, respectively. Furthermore, I show how microstructural investigations of the modeled samples can be used to constrain element fluxes in a sample down to the μm scale (Konrad-Schmolke et al., 2007).

5.2. FMEs – Boron and boron stable isotopes as tracers of fluid-rock interaction

As mentioned in the preceeding paragraphs indirect geochemical evidence for the presence of a fluid interacting with the host rock must be considered. Ideally, such indirect geochemical proxies for fluid-rock interaction are among the fluid mobile elements, have quick equilibration times and small equilibration volumes. Subsequent to fluid-rock interaction, the geochemical proxy must be stable and not prone to later, e.g. diffusional, re-equilibration. Furthermore, the proxy must be present in major phases in measurable quantities (see Ryan and Chauvel 2013 for a detailed review).

Boron is particularly useful for the investigation of fluid-rock interaction processes and dehydration because it is present in measurable quantities in several major mineral phases (white mica, tourmaline, amphibole, serpentine) as well as in hydrous fluids and its concentration is typically low enough to make it sensitive to fast equilibration at small fluid amounts. In most rock-forming minerals, including white mica, B substitutes for silica and occupies the tetrahedral position (Sanchez-Valle et al., 2005). If B diffuses similarly slow as Si, B concentrations are difficult to exchange after crystallization (Hervig et al., 2002), a prerequisite to preserve relevant information over geologic time scales. Furthermore, information from boron as fluid-mobile trace element can be combined with the isotopic information from B stable isotopes (e.g., Simon et al., 2006).

The observation of variations in the atomic weight of boron in minerals, made by Briscoe and Robinson (1925), was crucial for the recognition that physiochemical processes can cause isotopic fractionation of light elements in natural substances. It was therefore proposed that geologically relevant processes, including melting, crystallization, solution and volatilization,

would cause isotopic variations in nature (Briscoe and Robinson, 1925), leading the way for the widespread application of stable isotopes as tracers (Sharp, 2007). The value of the various stable isotope systems is based on the fact that distinct stable isotope signatures occur in different reservoirs, so that they can be used to trace the origin of rocks and fluids.

Boron has two stable isotopes, ^{10}B and ^{11}B, with relative abundances of 19.8% and 80.2%, respectively. The isotopic composition of a substance is usually expressed relative to a standard material. In case of boron this international standard material is boric acid NBS-SRM951 with a boron $^{11}B/^{10}B$ isotope ratio of 4.043627. The expression of the boron isotope composition of a substance relative to this standard material is commonly following the delta notation

$$\delta^{11}B = \left(\frac{\left(\frac{^{11}B}{^{10}B}\right)_{sample}}{\left(\frac{^{11}B}{^{10}B}\right)_{Std}} - 1\right) \cdot 1000 \qquad (5.1)$$

and this ratio is expressed in ‰.

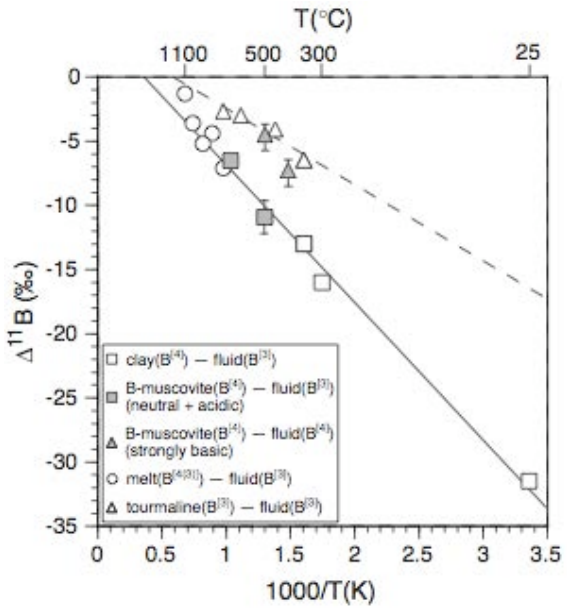

Fig. 4. Experimentally determined boron-isotope fractionation between solids, silicate melt, and fluid versus reciprocal temperature. Solid line is a least-squares linear regression of boron. Dashed line is for tourmaline–fluid. From Wunder et al., 2005

The large B isotopic variation in natural substances of almost 100‰ (Deyhle and Kopf, 2005) is dominantly due to differences in coordination between tetrahedral $B(OH)_4^-$ and trigonal $B(OH)_3$. Moreover, the B isotopic composition is influenced by temperature-dependent equilibrium fractionation between solid and fluid phases (Peacock and Hervig 1999; Hervig et

al., 2002; Wunder et al., 2005; Fig. 5.1) and it is also sensitive to changes in the pH value (Deyhle and Kopf, 2005). Temperature dependent equilibrium fractionation of boron between two phases is commonly expressed by the fractionation-induced differences in $\delta^{11}B$ values of the two phases A and B:

$$\Delta^{11}B_{A\text{-}B} = \delta^{11}B_A - \delta^{11}B_B \qquad (5.2)$$

or by using a fractionation factor α as

$$1000\ \ln\alpha_{A\text{-}B}. \qquad (5.3)$$

Boron preferentially partitions into the fluid phase (Brenan et al., 1998) with a concomitant enrichment of the heavy isotope ^{11}B relative to ^{10}B. The most striking example of coupled trends of elemental and isotopic variations occurs in arc lavas, where systematic across-arc trends of decreasing and isotopically lighter B with increasing slab depths (Ishikawa and Nakamura, 1994; Ishikawa et al., 2001; Moriguti et al., 2004; Fig. 5.2) are attributed to contributions from a slab-derived agent that successively reflects increasing degrees of slab dehydration and decreasing slab-to-arc element transfer (Bebout et al., 1999; Rosner et al., 2003; Marschall et al., 2007). In addition, several studies have emphasized the role of serpentinized mantle rocks, both in the supra-subduction zone wedge and in the subducting slab mantle, for boron cycling in subduction zones (Tonarini et al., 2007, 2011; Benton et al., 2001; Hattori and Guillot, 2003; Savov et al., 2007). Evidence for the sensitivity of the B system for fluid-rock interaction is provided by zoning patterns in various metamorphic minerals (white mica, amphibole, tourmaline), which retain information about the compositional evolution of metasomatic fluids through the metamorphic history (Bebout and Nakamura, 2003; Marschall et al., 2009; Konrad-Schmolke et al., 2011b; Halama et al., 2014).

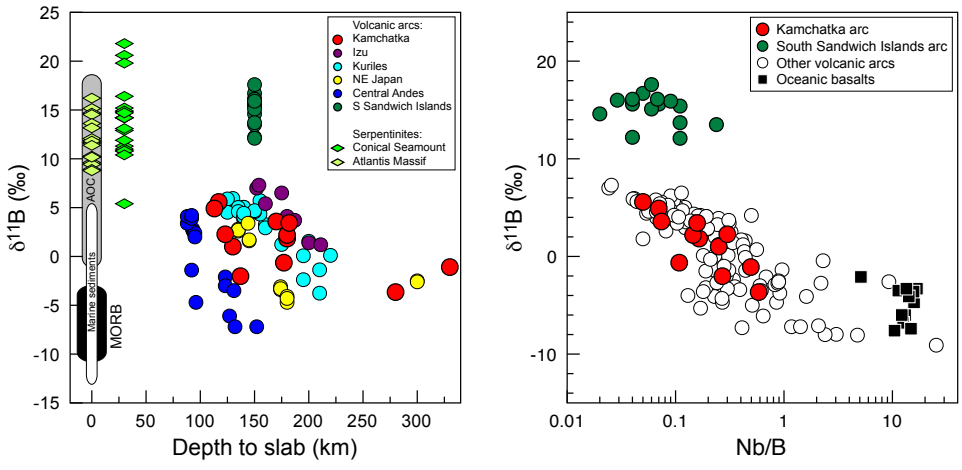

Fig. 5.2: (left) Boron isotope data from volcanic arcs in relation to the depth of the subducting slab. Notable exceptions from the general trends are the South Sandwich Islands arc, for which a constant depth is assumed, and the Kamchatka arc, for which $\delta^{11}B$ values are increasing following the typical $\delta^{11}B$ decrease across the volcanic front. (right) Trend of decreasing $\delta^{11}B$ with increasing Nb/B in arc volcanic rocks. The SSI arc deviates from the main trend due to elevated $\delta^{11}B$. Figure from Konrad-Schmolke and Halama 2014.

5.2.1. Geochemical modeling of B concentrations and B isotopic composition during fluid-rock interaction

The fluid mobility together with the temperature dependent isotopic fractionation of B qualifies B as an excellent tracer for fluid migration and fluid-rock interaction. However, as the general B budget during metamorphism is controlled by the fluid flux, but also by the coexisting phase assemblage combined thermodynamic-geochemical modeling of B are very versatile. This is demonstrated in three publications contained in this Habilitationsschrift (Konrad-Schmolke et al., 2011b, Halama et al., 2014; Konrad-Schmolke and Halama 2014). In these publications numerical models are used that utilize thermodynamic and mass balanced trace element calculations. Modeling generally consists of the following steps: (1) A thermal pattern or a pressure-temperature trajectory serves as input for a Gibbs energy minimization algorithm that simulates the passing of a rock sample through the pressure-temperature field or trajectory (dependent on whether the model is one- or two-dimensional. Based on the modeled pressure-temperature relations, phase relations are calculated at every P-T increment and water liberated by dehydration reactions is either released from the system or transported through the rock matrix. (2) The modeled phase relations at every calculated increment are used for a coefficient-based mass-balanced boron distribution among the stable solid and liquid phases. (3) A temperature-dependent fluid-solid boron isotope fractionation based on experimentally determined functions (e.g., Wunder et al., 2005) is calculated to determine the amounts of ^{10}B and ^{11}B in solids and fluid. Boron incorporated into the fluid phase is assumed to leave the system or migrate through the rock into the next calculated increment, where it is re-distributed. Elements retained in the solids are transported within the rocks and form the initial bulk rock composition in the next calculated increment. Therefore the models simulate fluid release, fluid migration, boron transport and boron isotope fractionation in a rock undergoing pressure- and temperature-controlled metamorphic transformation.

Under the assumption of thermodynamically independent trace element incorporation into stable phases it is possible to calculate trace element concentrations in coexisting phases by distributing a given amount of elements present in the bulk rock or effective (i.e. reacting)

bulk rock volume according to bulk distribution coefficients among the thermodynamically modeled stable phases. The fluid-solid boron distribution is done by calculating a Fluid/Matrix distribution coefficient ($D_B^{Fluid/Matrix}$) at each calculated increment, where

$$D_B^{Fluid/Matrix} = \frac{1}{\sum_{k=1} D_B^{Fluid/Mineral_k} \cdot X_{Mineral_k}} \quad (5.4)$$

with k denoting the stable minerals present at each calculation step and $D_B^{Fluid/Mineral}$ is the B distribution coefficient for the fluid with respect to a certain mineral.

Based on the bulk distribution coefficient the concentration of boron in the fluid and solids is calculated at each step by

$$C_B^{Fluid} = \frac{C_B^{Bulk}}{(X_{Solids}/(D_B^{Fluid/Matrix} \cdot X_{Fluid})) + 1} \quad (5.5)$$

Where C_B^{Bulk} is the B concentration in the bulk rock or effective bulk rock volume and X_{Solids} and X_{Fluid} being the weight proportions of the solids and the fluid. Element fractionation effects or fluid mediated element influx is modeled by changing the bulk rock or effective bulk rock composition at every calculated step.

Boron isotope composition in fluid and solids are calculated at every calculated increment based on the temperature-dependent fractionation function (Wunder et al., 2005):

$$\Delta^{11}B_{(Mineral\text{-}Fluid)} = -10.69\ (1000/T[K]) + 3.88 \quad (5.6)$$

where

$$\Delta^{11}B_{(Mineral\text{-}Fluid)} = \delta^{11}B_{(Mineral)} - \delta^{11}B_{(Fluid)}. \quad (5.7)$$

Knowing the initial $\delta^{11}B_{(Bulk)}$ at the beginning of the modeling, $\delta^{11}B_{(Solids)}$ and $\delta^{11}B_{(Fluid)}$ can be calculated at each step after boron distribution among the solids and the fluid.

5.3. REEs – Major- and trace element zoning in garnet porphyroblasts

Garnet is one of the most versatile minerals in petrology and geochronology. Garnet is stable over a large pressure and temperature range – largely independent of rock type – and thus occurs in many metamorphic, metasomatic and magmatic environments. Garnet has a wide

range of chemical compositions with complete solid solutions between most of its chemical endmembers and its major element composition well reflects the pressure (P), temperature (T) and chemical conditions (X) as well as the element transport kinetic properties of the host rock during growth (e.g., Berman 1990; Chernoff and Carlson 1997; Carlson 2002; Caddick et al., 2010). Because diffusional element transport in garnet is very sluggish even at elevated temperatures (e.g., Chakraborty and Ganguly 1991, Tirone et al., 2005) compositional growth zonations in garnet are very common (Hollister, 1966; Caddick et al., 2010). Information stored in these compositional variations makes garnet one of the most important recorders of geodynamic and element transport-processes in crust and mantle. Especially in subduction-related high pressure/low temperature rocks, such as eclogites, compositional growth zonations in garnet are commonly well preserved and display an important source of information about physico-chemical processes in the downgoing plate (e.g., Konrad-Schmolke et al., 2008a; Dragovic et al., 2012).

Garnet incorporates a large number of trace elements, such as high field strength elements (HFSEs), Y and Cr as well as measurable quantities of Li, B, Sc, V, Co, Ni and K (e.g., Kotkova and Harley 2010; Hauri et al., 1994; Paquin and Altherr 2001; 2004), but rare earth elements (REEs) are undoubtedly the most often analysed and interpreted trace elements in garnet. Especially with respect to the middle to heavy REEs garnet is the most important major phase in many rock types. Compositional REE variations in garnet bear information about scales of chemical equilibration and element transport properties in the host rock (e.g. Skora et al., 2006; Konrad-Schmolke et al., 2008b), they reflect fluid/melt-rock interaction (Jamtveit and Hervig 1994), and they can be used to decipher major- and accessory phase breakdown during a rock's metamorphic evolution (e.g., Konrad-Schmolke et al., 2008b; Moyen 2009; Yang and Rivers 2002; Mc Cammon and Kapylova 2004). Furthermore, REE patterns in garnet enable reconstructions of P-T-time trajectories (e.g., Hermann and Rubatto 2003; Whitehouse and Platt 2003) and, regarding the Lu/Hf and Sm/Nd dating methods, enable absolute age and growth rate determinations (e.g., Duchêne et al., 1997; Thöni et al., 2008, Schmidt et al., 2008; Pollington and Baxter 2010, Dragovic et al., 2012).

Information about all of the above mentioned rock forming processes as well as their rates could be extracted from garnet porphyroblasts if a particular process can be related to the REE composition or the compositional trend observed in natural samples.

As in all chemical reactions, the factors controlling the incorporation of REEs into the garnet crystal lattice can be divided into two parts, (1) a thermodynamic chemical equilibrium

contribution and (2) a kinetic contribution. In case of the interpretation of REE patterns in garnet, a distinction between and quantification of the two contributing factors is of crucial importance: whereas thermodynamically-controlled REE patterns will reflect the samples reaction path, e.g., a prerequisite for geodynamic interpretations, REE patterns controlled by kinetic factors, such as sluggish element transport in the interconnencted transport matrix (ITM) or intracrystalline diffusion, yield information about the element transport properties and permeability of the host rock during metamorphism (e.g., Spear and Daniel 2001; Baxter and De Paolo 2002; Carlson 2002; Skora et al., 2006; Carlson 2011; Ketcham and Carlson 2012).

Based upon the fact that many thermodynamic, geochemical and kinetic properties of garnet and the incorporated elements, such as standard state data and REE partition coefficients, are quantitatively well known, prediction and quantification of metamorphic garnet growth is possible utilizing thermodynamic and trace element forward models (e.g., Gaidies et al., 2006; Konrad-Schmolke et al., 2008b). Kinetic aspects of garnet growth can be simulated utilizing common diffusion equations and appropriate boundary conditions of the model approach (e.g., Skora et al., 2006). Consequently, information stored in compositional growth zonations can be related to rock forming processes by comparing the results of such forward models with natural observations (e.g., Spear and Selverstone 1983; Chernoff and Carlson 1997; Caddick et al., 2010; Dragovic et al., 2012).

In my works I combined different approaches of thermodynamic equilibrium calculations and mass balanced REE distribution among reactant and product phases with kinetic models that simulate diffusion-controlled element transport in the ITM. My model approaches envisage different element transport processes in the host rock and a comparison of the model results with natural rock samples enables detailed interpretation of commonly observed REE patterns in high-pressure garnet porphyroblast in terms of reaction paths and physico-chemical properties of the host rock.

In order to quantify garnet growth and to simulate the REE patterns in the growing porphyroblasts the following processes must be integrated into reliable growth models:

- **(1) fractional garnet crystallisation**, which continuously changes the effective, i.e. reacting, bulk rock chemistry (EBC; e.g., Hollister 1966, Otamendi et al., 2002, Konrad-Schmolke et al., 2008a), which in turn influences garnet growth and composition.
- **(2) reaction-controlled trace element availability** in the host rock can be predicted

and quantified by mass balanced trace element distribution among thermodynamically modelled mineral assemblages (e.g., Konrad-Schmolke et al., 2008b; 2011b; Nagel et al., 2013; Halama et al., 2014).

- **(3) element fractionation due to dehydration and open system behaviour**, such that water and trace elements therein are removed from the EBC simulating dehydration-induced element transport out of the system (e.g., Konrad-Schmolke et al., 2006).
- **(4) kinetically controlled element availability**, such that grain boundary diffusion in the host rock's interconnecting transport matrix (ITM) or surface processes in reacting phases cannot keep pace with the material required for garnet nucleation and growth in homogeneous thermodynamic equilibrium with the coexisting phase assemblage (e.g., Baxter and De Paolo 2002; Carlson 2002; Skora et al., 2006; Konrad-Schmolke et al., 2006; Carlson 2011; Ketcham and Carlson 2012).

5.3.1. Common REE zoning profiles in garnet

Although shapes and trends in major- and trace-element growth zonations in different high pressure garnets are varying in detail especially rare earth element zoning patterns commonly share some very characteristic features summarised below and shown in the representative examples in Fig. 5.3:

(1) The broad shape of the REE zoning changes with decreasing atomic number from bell-shaped patterns with a dominant central peak, often flanked by minor annular humps characteristic for the HREE, over a W-shaped pattern with a lower central and continuously higher annular peaks to a bowl-shaped pattern lacking a central peak but with dominant maxima near the garnet rims characteristic for the MREE and LREE.

(2) Superimposed on this broad pattern are distinct smaller peaks at fixed positions relative to the garnet radius that are developed to different extents but are visible in all REE profiles and on both sides of the garnet centre.

(3) The broad overall change from bell- to bowl-shaped pattern is the result of a significant decrease of the central peak and increasing intensities of the superimposed outer peaks that occur at fixed positions across the garnet grains.

(4) Concentrations of all REE decrease drastically at the outermost rims, sometimes with the position of the onset of that decrease shifting outward with decreasing atomic number.

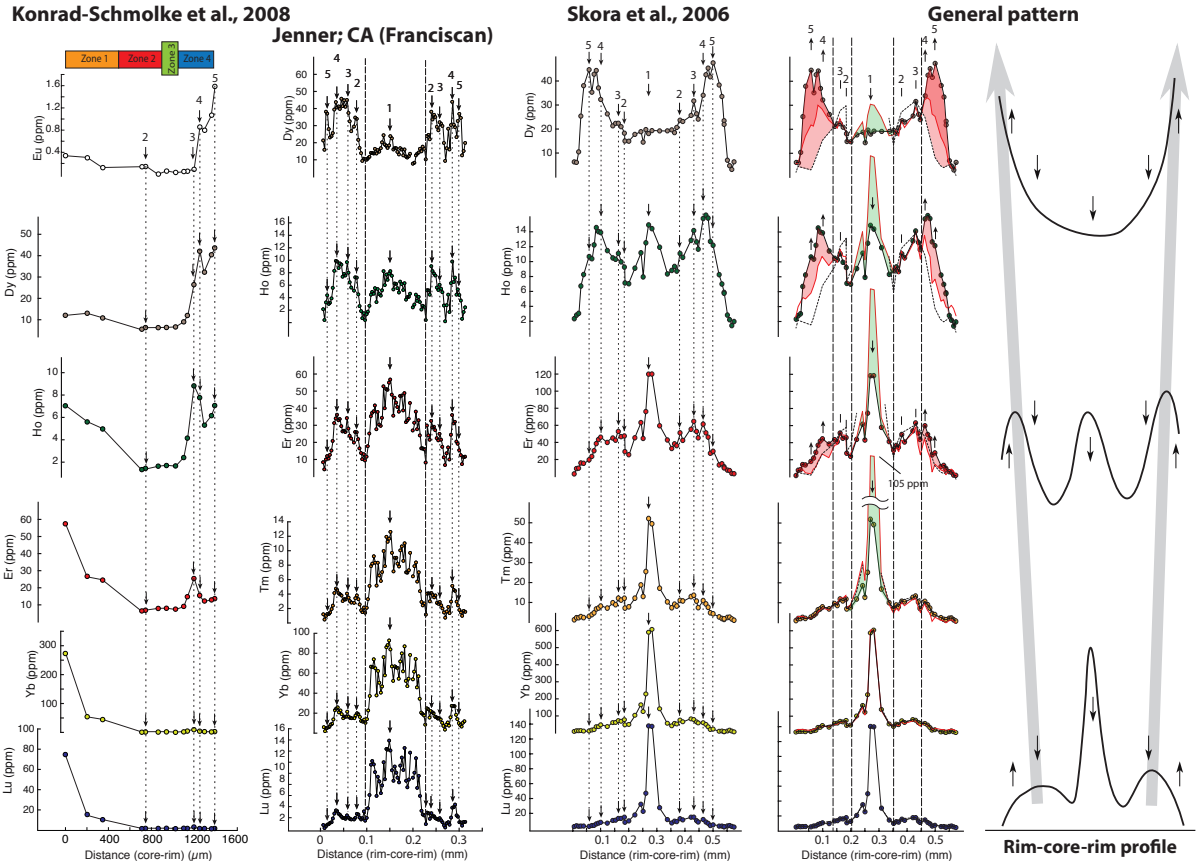

Fig. 5.3: Rare earth element zoning patterns in garnet commonly share characteristic features: (1) The shape of the REE zoning changes with decreasing atomic number from bell-shaped patterns with a dominant central peak, over a W-shaped pattern to a bowl-shaped pattern. (2) Superimposed on this pattern are smaller peaks at fixed positions on both sides of the garnet centre. (3) The change from bell- to bowl-shaped pattern is the result of a decrease of the central peak and increasing superimposed outer peaks. (4) Sometimes REE decrease at the outermost rims, with the position of the onset of that decrease shifting outward with decreasing atomic number.

5.3.2. Common REE patterns in garnet

The corresponding REE patterns also have striking similarities:

(1) from core to inner mantle, the REE pattern have a steep positve slope with HREE (Lu, Yb and Er) continuously decreasing as a result of Rayleigh fractionation, whereas the medium REE (MREE) content remains constant.

(2) In the inner part of the garnet mantle the decrease in HREE is amplified and also the MREE concentration slightly decreases resulting in a moderately folded pattern.

(3) Towards the outer part of the mantle the REE pattern is characterised by a drastic increase in Dy, Ho and Er whereas the increase in the heavier and lighter REE concentrations is only limited.

(4) In the outermost parts of the garnets, the REE pattern is characterised by an increase in the MREEs associated with a slight decrease in the HREEs resulting in a strongly folded pattern with a maximum between Tb and Dy.

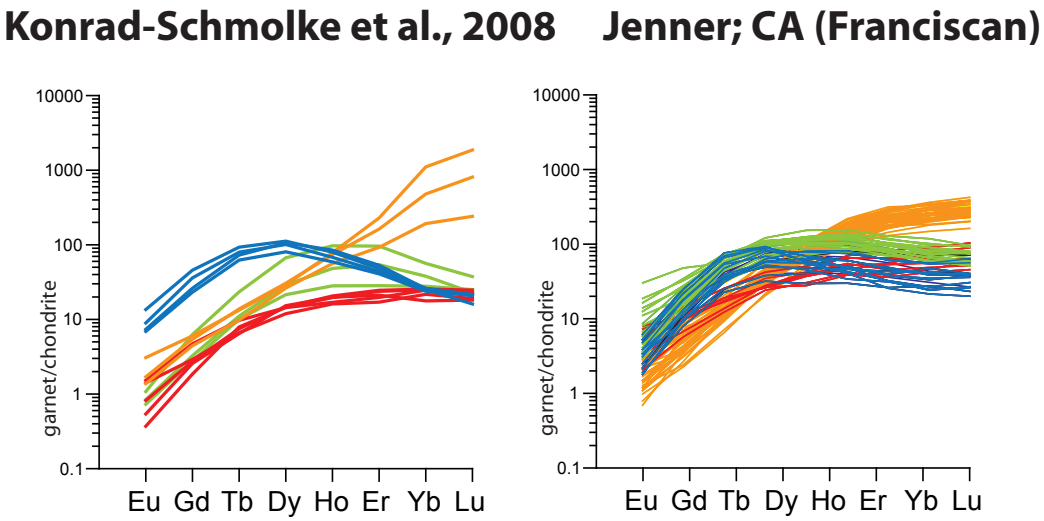

Fig. 5.4: The REE patterns corresponding to the profiles in Fig. 5.3 show also striking similarities: (1) From core to inner mantle, the REE pattern have a steep positve slope and decreasing HREEs (Rayleigh fractionation) (orange patterns). (2) In the inner part of the garnet mantle the decrease in HREE is amplified and also the MREE concentration slightly decreases (red). (3) Towards the outer part of the mantle the REE pattern is characterised by a significant increase in Dy, Ho and Er (green). (4) In the outermost parts of the garnets, MREEs and HREEs slightly decrease resulting in a strongly folded pattern with a maximum between Tb and Dy (blue patterns).

It is of crucial importance to understand and interpret these commonly observed trace element patterns in metamorphic garnets in order to investigate and quantify rock forming processes utilizing garnet porphyroblasts that often display the only remaining record in multiply overprinted metamorphic samples. In this Habilitation I present several contributions (Konrad-Schmolke et al., 2007; 2008a and b) to the science community that help to push forward our knowledge regarding this important topic in metamorphic petrology.

6 Conclusions of the results of the published manuscripts

6.1. Konrad-Schmolke et al., 2008a "Garnet growth at high- and ultra-high pressure metamorphism" published in Journal of Petrology

In this paper we show that thermodynamic forward modelling, using Gibbs energy minimisation with consideration of element fractionation into refractory phases and/or liberated fluids, is able to extract information about the complex physical and chemical evolution of deeply subducted rocks. By comparing complex compositional growth zonations in garnets from high- and ultra-high pressure (UHP) samples with those derived from thermodynamic forward modelling, we yield insight into the effects of element fractionation on composition and modes of the co-genetic metamorphic phase assemblage. Our results demonstrate that fractionation effects cause discontinuous growth and re-crystallisation of metamorphic minerals in high pressure rocks. The results clearly show that reduced or hindered mineral growth at UHP conditions can control the inclusion and preservation of minerals indicative for UHP metamorphism, such as coesite, and thus masking peak pressure conditions in subducted rocks. Further, our results demonstrate that fractional garnet crystallisation leads to strong compositional gradients and step-like zonation patterns in garnet, a feature often observed in high- and ultra-high pressure rocks. In this contribution it is shown that thermodynamic forward modelling allows the interpretation of commonly observed garnet growth zonation patterns in terms of garnet forming reactions and the relative timing of garnet growth with respect to the rock's pressure-temperature path. Such a correlation is essential for the determination of tectonic and metamorphic rates in subduction zones as well as for the understanding of trace element signatures in subduction related rocks.
My contribution to this publication in terms of ideas, data acquisition, interpretation and manuscript writing are 90%, 90%, 80% and 75%, respectively.

6.2. Konrad-Schmolke et al., 2008b "Thermodynamic and trace element modeling in high-pressure garnets from the WGR" published in Earth and Planetary Science Letters

This paper focuses on the idea that trace element growth zonations in metamorphic garnet porphyroblasts can be used to get crucial information about the reaction path of the investigated sample. We determined major- and trace element zonation patterns in ultra-high pressure eclogite garnets from the Western Gneiss Region (Norway) that show multiple growth zones and preserve complex growth zonation patterns with respect to both major and rare earth elements (REE). Due to chemical differences of the host rocks two types of major element compositional zonation patterns occur: (1) abrupt, step-like compositional changes corresponding with the growth zones and (2) compositionally homogeneous interiors,

independent of growth zones, followed by abrupt chemical changes towards the rims. Despite differences in major element zonation, the REE patterns are almost identical in all garnets and can be divided into four distinct zones with characteristic patterns. In order to interpret the major and trace element distribution and zoning patterns in terms of the subduction history of the rocks, we combined thermodynamic forward models for appropriate bulk rock compositions. This allowed us to obtain molar proportions and major element composition of stable phases along a pressure-temperature path from which we calculated the mass balance distribution of REE among the calculated stable phases during high-pressure metamorphism. The thermodynamic forward models applied in this work reproduce the complex major element zonation patterns and growth zones in the natural garnets, with garnet growth predicted during four different reaction stages: (1) chlorite breakdown, (2) epidote breakdown, (3) amphibole breakdown and (4) reduction in molar clinopyroxene at ultrahigh-pressure conditions. The phase relations along the prograde metamorphic path calculated with the thermodynamic model can be used to perform a mass balanced trace element distribution among the stable phases along the P-T trajectory. Such mass-balance calculations of the rare earth element distribution among the modelled stable phases yielded characteristic zonation patterns in garnet that closely resemble those in the natural samples. We conclude in that paper that garnet growth and trace element incorporation occurred in near thermodynamic equilibrium with matrix phases during subduction. The rare earth element patterns in garnet exhibit distinct enrichment zones that fingerprint the minerals involved in the garnet-forming reactions as well as local peaks that can be explained by fractionation effects and changes in the mineral assemblage.

My contribution to this publication in terms of ideas, data acquisition, interpretation and manuscript writing are 90%, 60%, 70% and 75%, respectively.

6.3. Konrad-Schmolke et al., 2007 "Garnet re-equilibration along sub-grain boundaries" published in European Journal of Mineralogy".

In this work we focus on the effect of diffusional equilibration of compositional growth zonations in metamorphic garnet. Diffusional re-equilibration of growth zonations can significantly bias the interpretation of P-T path calculations, geochronological investigations and geothermobarometrical results. Knowledge about the processes leading to diffusionally modified zoning patterns are therefore crucial for the use of growth zonations in metamorphic garnet. In this case study we investigated garnets from meta-granitoid high-pressure rocks from the Western Alpine Sesia Zone utilizing electron backscatter diffraction. All investigated garnets show complex internal sub-grain textures in electron forescatter images and consist of

a large number of sub-grains with different shapes and sizes. Some garnets exhibit a “core-mantle-structure” with very fine-grained (<20µm) sub-grains in their cores overgrown by palisade-like sub-grains in the rims. We could demonstrate that the observed sub-grain boundaries in these garnets have enabled diffusive element exchange between the garnet core and the surrounding matrix. Compositional X-ray mapping revealed zonation patterns of Mg that indicate modification of the garnet composition during prograde metamorphism. Our results indicate that the extent of diffusional re-equilibration is dependent on sub-grain size and element diffusivities. Our samples show that X_{Mg} is strongly influenced by diffusion along the sub-grain boundaries, whereas apparently slow diffusing elements, such as Ca, Ti and Y preserve their original concentric zonation pattern. This differential re-equilibration leads to very complex chemical zonation that cannot be easily interpreted in terms of simple prograde growth zonation or of commonly applied spherical diffusion models. The observation that almost all garnets in the investigated samples exhibit a sub-grain pattern suggests this might be a common feature in high pressure/low temperature rocks.
My contribution to this publication in terms of ideas, data acquisition, interpretation and manuscript writing are 90%, 60%, 75% and 80%, respectively.

6.4. Konrad-Schmolke et al., 2011a “Fluid migration above a subducted slab 1” published in the Journal of Petrology.

In this paper we investigated the effect of percolating fluids on modes and compositions of stable phases in exhumed high-pressure rocks. This work is the first part of two papers that focus on fluid migration processes and fluid-rock interaction in subduction zones. The rocks are from the Western Alpine Sesia Zone, which is well suited for that study as it is a sliver of eclogite-facies continental crust exhumed from mantle depths in the hanging wall of a subducting oceanic slab. Eclogite-facies felsic and basic rocks sampled across the internal SLZ show different degrees of retrograde metamorphic overprint associated with fluid influx. The weakly deformed samples preserve relict eclogite-facies mineral assemblages that show partial fluid-induced compositional re-equilibration along grain boundaries, brittle fractures and other fluid pathways. Multiple fluid influx stages are indicated by replacement of primary omphacite by phengite, albitic plagioclase and epidote as well as partial re-equilibration and/or overgrowths in phengite and sodic amphibole producing characteristic step-like compositional zoning patterns. The observed textures, together with the map-scale distribution of the samples, suggest an open system pervasive and reactive fluid flux across large rock volumes above the subducted slab. Thermodynamic modelling indicates a minimum amount of fluid of 0.1 to 0.5wt% interacting with the wall rocks. Phase relations

and reaction textures indicate mobility of K, Ca, Fe and Mg, whereas Al is relatively immobile in these medium-temperature–high-pressure fluids. Further, the thermodynamic models show that recycling of previously fractionated material, such as in cores of garnet porphyroblasts, largely controls the compositional re-equilibration of the exhumed rock body.
My contribution to this publication in terms of ideas, data acquisition, interpretation and manuscript writing are 90%, 90%, 80% and 75%, respectively.

6.5. Konrad-Schmolke et al., 2011b "Fluid migration above a subducted slab 2" published in Earth and Planetary Science Letters

This is the second part of the study about fluid migration processes in subduction zones. Here we focus on the trace element zonations in the partially overprinted rocks from the Sesia Zone. In this paper the amount and composition of subduction zone fluids and the effect of fluid-rock interaction at a slab-mantle interface has been constrained by thermodynamic and trace element modeling of partially overprinted blueschist-facies rocks. Deformation-induced differences in fluid flux led to a partial preservation of pristine mineral cores in weakly deformed samples that were used to quantify Li, B, Sr and Pb distribution during mineral growth, -breakdown and modification induced by fluid-rock interaction. Our results show that Li and B budgets are fluid-controlled, thus acting as tracers for fluid-rock interaction processes, whereas Sr and Pb budgets are mainly controlled by the fluid-induced formation of epidote. Our calculations show that fluid-rock interaction caused significant Li and B depletion in the affected rocks due to leaching effects, which in turn can lead to a drastic enrichment of these elements in the percolating fluid. Depending on available fluid-mineral trace element distribution coefficients modeled fluid rock ratios were up to 0.06 in weakly deformed samples and at least 0.5 to 4 in shear zone mylonites. These amounts lead to time integrated fluid fluxes of up to $1.4 \cdot 10^2$ m^3m^{-2} in the weakly deformed rocks and $1 – 8 \cdot 10^3$ m^3m^{-2} in the mylonites. Combined thermodynamic and trace element models can be used to quantify metamorphic fluid fluxes and the associated element transfer in complex, reacting rock systems and help to better understand commonly observed fluid-induced trace element trends in rocks and minerals from different geodynamic environments.
My contribution to this publication in terms of ideas, data acquisition, interpretation and manuscript writing are 90%, 60%, 70% and 75%, respectively.

6.6. Konrad-Schmolke and Halama 2014 "Combined thermodynamic-geochemical modeling in metamorphic geology" published as an invited review paper in Lithos

In this invited review paper we show how quantitative geochemical modeling is today applied

in a variety of geological environments from the petrogenesis of igneous rocks to radioactive waste disposal. We demonstrate that thermodynamic forward modeling unfolds enormous capacities if it is combined with experimental data on elemental partitioning and isotopic fractionation. In metamorphic petrology the combination of thermodynamic and trace element forward modeling can be used to study and to quantify processes at spatial scales from µm to km. The paper demonstrates how thermodynamic forward models that utilize Gibbs energy minimization can be used to quantify mineralogical changes along a reaction path of a chemically open fluid/rock system. These results are combined with mass balanced trace element calculations to determine the trace element distribution between rock and melt/fluid during the metamorphic evolution. Thus, effects of mineral reactions, fluid-rock interaction and element transport in metamorphic rocks on the trace element and isotopic composition of minerals, rocks and percolating fluids or melts can be predicted. We illustrate the capacities of combined thermodynamic-geochemical modeling based on two examples relevant to mass transfer during metamorphism. The first example focuses on fluid-rock interaction in and around a blueschist-facies shear zone in felsic gneisses, where fluid-induced mineral reactions and their effects on boron (B) concentrations and isotopic compositions in white mica are modeled. In the second example, fluid release from a subducted slab, the associated transport of B as well as variations in B concentrations and isotopic compositions in liberated fluids and residual rocks are modeled. We compare the modeled results of both examples to geochemical data of natural minerals and rocks and demonstrate that the combination of thermodynamic and geochemical models enables quantification of metamorphic processes and insights into element cycling that would have been unattainable if only one model approach was chosen.

My contribution to this publication in terms of ideas, data acquisition, interpretation and manuscript writing are 90%, 90%, 80% and 60%, respectively.

6.7. Wilke et al., 2010: "Multi-stage reaction history in different eclogite types from the Pakistan Himalaya and implications for exhumation processes". Published in Lithos.

In this work we investigate metabasites that were were sampled from rock series of the subducted margin of the Indian Plate, the so-called Higher Himalayan Crystalline, in the Upper Kaghan Valley, Pakistan. These rocks vary from corona dolerites, cropping out around Saif-ul-Muluk in the south, to coesite–eclogite close to the suture zone against rocks of the Kohistan arc in the north. We found that bulk rock major- and trace- element chemistry reveals essentially a single protolith as the source for five different eclogite types, which

differ in fabric, modal mineralogy as well as in mineral chemistry. Our study of newly-collected samples reveals coesite (confirmed by in situ Raman spectroscopy) in both garnet and omphacite. All eclogites show growth of amphiboles during exhumation. Within some coesite-bearing eclogites the presence of glaucophane cores to barroisite is noted whereas in most samples porphyroblastic sodic–calcic amphiboles are rimmed by more aluminous calcic amphibole (pargasite, tschermakite, and edenite). Eclogite facies rutile is replaced by ilmenite which itself is commonly surrounded by titanite. In addition, some eclogite bodies show leucocratic segregations containing phengite, quartz, zoisite and/or kyanite. The important implication is that the complex exhumation path shows stages of initial cooling during decompression (formation of glaucophane) followed by reheating: a very similar situation to that reported for the coesite-bearing eclogite series of the Tso Morari massif, India, 450 km to the south-east.

My contribution to this publication in terms of ideas, data acquisition, interpretation and manuscript writing are 10%, 10%, 20% and 10%, respectively.

6.8. Scott et al., 2013: "High-T, low-P formation of rare olivine-bearing symplectites in Variscan eclogite". Published in Journal of Petrology

This paper describes extremely rare veinlets and reaction textures composed of symplectites of olivine (~Fo_{50})-plagioclase±orthopyroxene±spinel±ilmenite, associated with more common clinopyroxene-plagioclase±orthopyroxene and amphibole-plagioclase varieties that occur within eclogites and pyroxenites across the Moldanubian Zone of the Bohemian Massif. In this contribution we focus on two topics, first to describe the unusual symplectites and to decipher their petrogenetic history and second we show the element transport in the interacting fluid, which was necessary to develop the observed textures. In the investigated samples the distribution of each symplectite type broadly reflects reactions that took place in micro-scale domains with chemically distinct compositions at ~ 850^{o}C and $\leq$ 6 kbar. We show that breakdown of high-*P* garnet strongly influenced the formation of the olivine-bearing and the amphibole-plagioclase varieties, and breakdown of high-*P* clinopyroxene controlled the distribution of pyroxene-plagioclase symplectites. Thermodynamically modeled isothermal *P-X* binary phase calculations for effective bulk compositions for micro-domains reveal that an influx of small volumes of an H- and Na-bearing fluid drove garnet dissolution-symplectite precipitation processes, even in symplectites that are now anhydrous. The olivine-bearing symplectites preferentially partitioned Fe and Mg from high-*P* garnet and clinopyroxene, but lost Si and Al to the simultaneously forming pyroxene-plagioclase and

amphibole-plagioclase symplectites. Where Na was available to the reacting system, plagioclase in the olivine-bearing symplectites shifted from pure anorthite to bytownite with the less calcic feldspar partitioning Si and inhibiting the formation of orthopyroxene. Breakdown of garnet to an outer olivine-bearing symplectite and an inner amphibole-plagioclase symplectite generated asymmetrical and symmetrical chemical gradients depending on whether the H- and Na-bearing fluid migrated along the rim or through the interior, respectively, of garnet. The partial preservation of earlier high-*P* textures, the high-*T* and moderate-*P* of symplectite formation, the narrow Mn- and Fe- enriched garnet steps immediately adjacent to the symplectites, and the evidence for a limited fluid flux, point to the symplectite-forming stage as taking place during a short-duration anomalously hot event in the shallow to middle Variscan crust. As the studied samples are not associated with the aureoles of plutonic rocks, the symplectite-causing event may have been due to advective heat loss from rapidly exhumed high-*T* high-*P* granulitic bodies that were emplaced into and over the middle crust during continent-continent collision.

My contribution to this publication in terms of ideas, data acquisition, interpretation and manuscript writing are 30%, 30%, 30% and 10%, respectively.

6.9. Halama and Konrad-Schmolke 2014: "Retrograde metasomatic effects on phase assemblages in an interlayered blueschist–greenschist sequence (Coastal Cordillera, Chile)". Published in Lithos.

This paper investigates interlayered blueschists and greenschists of the Coastal Cordillera in Chile that are part of a Late Palaeozoic accretionary complex. The focus of that work lies on the effect on retrograde mineral assemblages of metamorphic fluids. The interlayered greenschist-blueschist sequences represent metavolcanic rocks with oceanic affinities based on predominantly OIB-type REE patterns and immobile trace element ratios. Amphibole is the major mafic mineral and varies compositionally from glaucophane to actinolite. The presence of glaucophane relicts as cores in zoned amphiboles in both rock types is evidence for a pervasive high-pressure metamorphic stage. During exhumation, a retrograde greenschist-facies overprint stabilized phengitic white mica + chlorite + albite ± K-feldspar at 0.4±0.1 GPa. Geochemical variability can be ascribed to primary, magmatic and secondary, metasomatic processes. We used several adjacent blueschist-greenschist pairs with similar protolith geochemistry to evaluate metasomatic changes due to retrograde fluid-rock interaction at greenschist-facies conditions. Isocon diagrams show that the most important geochemical changes are depletion of Si and Na and addition of water in the greenschists compared to the blueschists. Transition metals and LILE are mobilized to varying degrees.

Both rock types of these adjacent pairs have a similar mineralogy, albeit with different mineral modal abundances, pointing to a selective infiltration overprinting process. We used pseudo-binary phase diagrams as a means to link bulk rock geochemical variability to changes in the modal abundance of minerals. These calculations show preferential formation of chlorite + albite and decrease in glaucophane abundance for greenschist compared to blueschist. Therefore, the fluid-induced metasomatic changes are the prime cause for the distinct visual appearance of the rocks as blue and green, respectively. Differences in protolith geochemistry become relevant when the entire outcrop-wide geochemical variation is considered. It is clear, however, that tectonic juxtaposition is an unlikely explanation for the cm-dm scale interlayering of blueschists and greenschists.
My contribution to this publication in terms of ideas, data acquisition, interpretation and manuscript writing are 10%, 20%, 20% and 10%, respectively.

In general, the various applications of thermodynamic forwards models, partly in combination with mass balanced trace element calculations, in the publications presented in this Habilitationsschrift, yielded crucial insight into rock-forming processes. All of these works demonstrate the enormous capacities arising from the application of thermodynamic and geochemical models in combination with natural observations to quantify metamorphic processes. All manuscripts are published in internationally highly ranked journals and their contribution to the scientific community is reflected in the frequent and continuous citations.

7 References Part I

Ague, J.J., 2003. Fluid infiltration and transport of major, minor, and trace elements during regional metamorphism of carbonate rocks, Wepawaug Schist, Connecticut, USA. American Journal of Science 303, 753-816.

Ague, J.J., 2011. Extreme channelization of fluid and the problem of element mobility during Barrovian metamorphism. American Mineralogist 96, 333-352.

Albarède, F., 1995. Introduction to Geochemical Modeling. Cambridge University Press, Cambridge, 543 pp.

Altenberger, U., Schmid, R., Oberhänsli, R., 2008. Composition and pre-metamorphic geodynamic setting of the ultrahigh-pressure metabasic rocks from Dabie Shan, E-China. International Journal of Earth Sciences 97, 1301-1314.

Asimow, P.D., Ghiorso, M.S., 1998. Algorithmic modifications extending MELTS to calculate subsolidus phase relations. American Mineralogist 83, 1127-1131.

Ayers, J.C., Eggler, D.H., 1995. Partitioning of elements between silicate melt and H_2O-NaCl fluids at 1.5 and 2.0 GPa pressure: Implications for mantle metasomatism. Geochimica et Cosmochimica Acta 59, 4237-4246.

Bau, M., 1991. Rare-earth element mobility during hydrothermal and metamorphic fluid-rock interaction and the significance of the oxidation state of europium. Chemical Geology 93, 219-230.

Baxter, E.F. and De Paolo, D.J., 2002. Field measurements of high temperature bulk reaction rates I: Theory and technique. American Journal of Science, 302: 442-464.
Bebout, G. E., 2007, Metamorphic chemical geodynamics of subduction zones: Earth and Planetary Science Letters, v. 260, p. 373-393.

Bebout, G. E., Ryan, J. G., Leeman, W. P. and Bebout, A. E. 1999. Fractionation of trace elements by subduction-zone metamorphism - effect of convergent-margin thermal evolution. Earth and Planetary Science Letters 171, (1): 63-81.

Bebout, G.E., Nakamura, E., 2003. Record in metamorphic tourmalines of subduction-zone devolatilization and boron cycling. Geology 31, 407-410.

Becker, H., Jochum, K.P., Carlson, R.W., 2000. Trace element fractionation during dehydration of eclogites from high-pressure terranes and the implications for element fluxes in subduction zones. Chemical Geology 163, 65-99.

Beinlich, A., Klemd, R., John, T. and Gao, J. 2010. Trace-element mobilization during Ca-metasomatism along a major fluid conduit: Eclogitization of blueschist as a consequence of fluid-rock interaction. Geochimica et Cosmochimica Acta 74(6): 1892-1922.

Benton, L. D., Ryan, J. G., Tera, F., 2001. Boron isotope systematics of slab fluids as inferred from a serpentine seamount, Mariana forearc. Earth and Planetary Science Letters 187, 273-282.

Berman, R. G., and Brown, T. H. 1985. Heat capacity of minerals in the system Na_2O-K_2O-CaO-MgO-FeO-Fe_2O_3-Al_2O_3-SiO_2-TiO_2-H_2O-CO_2: representation, estimation, and high temperature extrapolation. Contributions to Mineralogy and Petrology, 89(2-3), 168-183.

Berman, R. G., 1988. Internally-consistent thermodynamic data for minerals in the system Na_2O-K_2O-CaO-MgO-FeO-Fe_2O_3 -Al_2O_3 -SiO_2 -TiO_2 -H_2O-CO_2: Journal of Petrology, v. 29, p. 445-522.

Berman, R. G., 1990. Mixing properties of Ca-Mg-Fe-Mn garnets: American Mineralogist, v. 75, p. 328-344.

Blundy, J., and Wood, B. 1994. Prediction of crystal melt partition coefficients from elastic moduli.

Blundy, J. and Wood, B. 2003. Partitioning of trace elements between crystals and melts. Earth and Planetary Science Letters 210(3-4): 383-397.

Bohrson, W.A., Spera, F.J., 2001. Energy-constrained open-system magmatic processes II: Application of energy-constrained assimilation-fractional crystallization (EC-AFC) model to magmatic systems. Journal of Petrology 42, 1019-1041.

Bohrson, W.A., Spera, F.J., 2007. Energy-constrained recharge, assimilation, and fractional crystallization (EC-RAcFC): A Visual Basic computer code for calculating trace element and isotope variations of open-system magmatic systems. Geochemistry Geophysics Geosystems 8(11), Q11003, doi:10.1029/2007GC001781.

Breeding, C.M., Ague, J.J. and Bröcker, M. 2004. Fluid-metasedimentary rock interactions in subduction-zone mélange: Implications for the chemical composition of arc magmas. Geology, 32: 1041-1044.

Brenan, J.M., Neroda, E., Lundstrom, C.C., Shaw, H.F., Ryerson, F.J. and Phinney, D.L. 1998. Behaviour of boron, beryllium, and lithium during melting and crystallization: constraints from mineral-melt partitioning experiments. Geochimica et Cosmochimica Acta 62(12): 2129-2141.

Brenan, J.M., Shaw, H.F., Ryerson, F.J., Phinney, D.L., 1995. Mineral-aqueous fluid partitioning of trace elements at 900°C and 2.0 GPa: Constraints on the trace element chemistry of mantle and deep crustal fluids. Geochimica et Cosmochimica Acta 59, 3331-3350.

Briscoe, H.V.A., Robinson, P.L., 1925. A redetermination of the atomic weight of boron. Journal of the Chemical Society 127, 696-720.

Brunsmann, A., Franz, G., Erzinger, J., 2001. REE mobilization during small-scale high-pressure fluid-rock interaction and zoisite/fluid partitioning of La to Eu. Geochimica et Cosmochimica Acta 65, 559-570.

Burns, E.E. 1910. The Story of Great Inventions, Harper and Brothers, New York.

Caddick, M.J., Konopásek, J. and Thompson, A.B. 2010. Preservation of garnet growth zoning and the duration of prograde metamorphism. Journal of Petrology 53, (11): 2327-2347.

Carlson, W.D. 2002. Scales of disequilibrium and rates of equilibration during metamorphism. Amercan Mineralogist, 87: 185-204.

Carlson, W.D. 2011. Porphyroblast crystallization: linking processes, kinetics, and microstructures. International Geology Review 53: (3) 406-445.

Chernoff, C. B. and Carlson, W. D., 1999, Trace element zoning as a record of chemical disequilibrium during garnet growth: Geology (Boulder), v. 27, p. 555-558.

Chernoff, C. B. and Carlson, W. D., 1997, Disequilibrium for Ca during growth of pelitic garnet: Journal of Metamorphic Geology, v. 15, p. 421-438.

Chakraborty, S. and Ganguly, J. C. 1991: Compositional zoning and cation diffusion in garnets. in “Diffusion, atomic ordering and Mass Transport”. Ganguly, J., ed. Springer, New York: 120-175.

Connolly, J. A. D. 2005: Computation of phase equilibria by linear programming: A tool for geodynamic modeling and its application to subduction zone decarbonation. Earth and Planetary Science Letters, 236, 524-541.

Connolly, J. A. D., Kerrick, D. M., 1987. An algorithm and computer program for calculating composition phase diagrams. Calphad, 11(1), 1-55.

Debye, P. 1912. Zur theorie der spezifischen wärmen. Annalen der Physik, 344(14), 789-839.

de Capitani, C. and Brown, T. H. 1987. The computation of chemical equilibrium in complex systems containing non-ideal solutions. Geochimica et Cosmochimica Acta 51, (10): 2639-2652.

DePaolo, D.J., 1981. Trace element and isotopic effects of combined wallrock assimilation and fractional crystallization. Earth and Planetary Science Letters 53, 189-202.

Deyhle, A., Kopf, A., 2005. The use and usefulness of boron isotopes in natural silicate-water systems. Physics and Chemistry of the Earth 30, 1038-1046.

Deyhle, A., Kopf, A., Eisenhauer, A., 2001. Boron systematics of authigenic carbonates: a new approach to identify fluid processes in accretionary prisms. Earth and Planetary Science Letters, 187(1), 191-205.

Dragovic, B., Samanta, L.M., Baxter, E.F., Selverstone, J., 2012. Using garnet to constrain the duration and rate of water-releasing metamorphic reactions during subduction: An example from Sifnos, Greece. Chemical Geology 314-317, 9-22.

Duchêne, S., Blichert-Toft, J., Luais, B., Telouk, P., Lardeaux, J. M. and Albarede, F. 1997. The Lu-Hf dating of garnets and the ages of the Alpine high-pressure metamorphism. Nature, 387, 586-589.

Einstein, A. 1907. Planck's theory of radiation and the theory of specific heat. Annalen der Physik, 22, 180-190.

Essene, E.J., 1989. The current state of thermobarometry in metamorphic rocks. Geol. Soc. Spec. Publ. 43, 1-44.

Ferry, J.F. and Gerdes, M.L. 1998. Chemically reactive fluid flow during metamorphism. Annual reviews of earth and Planetary Sciences, 26: 255-287.

Gaidies, F., Abart, R., de Capitani, C., Schuster, R., Connolly, J. A. D. and Reusser, E., 2006, Characterisation of polymetamorphism in the Austroalpine basement east of the Tauern Window using garnet isopleth thermometry: Journal of Metamorphic Geology, v. 24, p. 451-475.

Garth, T., Rietbrock, A., 2014. Order of magnitude increase in subducted H_2O due to hydrated normal faults within the Wadati-Benioff zone. Geology, doi:10.1130/G34730.1.

Gast, P.W., 1968. Trace element fractionation and the origin of tholeiitic and alkaline magma types. Geochimica et Cosmochimica Acta 32, 1057-1086.

Ghiorso, M.S., Hirschmann, M.M., Reiners, P.W., Kress, V.C., 2002. The pMELTS: An revision of MELTS aimed at improving calculation of phase relations and major element partitioning involved in partial melting of the mantle at pressures up to 3 GPa. Geochemistry Geophysics Geosystems 3(5), DOI: 10.1029/2001GC000217.

Ghiorso, M.S., Sack, R.O., 1995. Chemical mass transfer in magmatic processes. IV. A revised and internally consistent thermodynamic model for the interpolation and extrapolation of liquid-solid equilibria in magmatic systems at elevated temperatures and pressures. Contributions to Mineralogy and Petrology 119, 197-212.

Goldschmidt, V.M., 1954. Geochemistry. Clarendon Press, Oxford, 730 pp.

Gorman, P. J., Kerrick, D. M., Connolly, J. A. D., 2006. Modeling open system metamorphic decarbonation of subducting slabs, Geochem. Geophys. Geosyst., 7, Q04007, doi:10.1029/2005GC001125.

Gottschalk, M., 1997, Internally consistent thermodynamic data for rock-forming minerals in the system SiO_2 -TiO_2 -Al_2O_3 -CaO-MgO-FeO-K_2O-Na_2O-H_2O-CO_2: European Journal of Mineralogy, v. 9, p. 175-223.

Hacker, B. R., 2008. H_2O subduction beyond arcs. Geochemistry, Geophysics, Geosystems, 9(3).

Halama, R., Savov, I.P., Garbe-Schönberg, D., Schenk, V., Toulkeridis, T., 2013. Vesuvianite in high-pressure-metamorphosed oceanic lithosphere (Raspas Complex, Ecuador) and its role for transport of water and trace elements in subduction zones. European Journal of Mineralogy 25, 193-219.

Halama, R., Konrad-Schmolke, M., Sudo, M., Marschall, H.R., Wiedenbeck, M., 2014. Effects of fluid-rock interaction on $^{40}Ar/^{39}Ar$ geochronology in high-pressure rocks (Sesia-Lanzo Zone, Western Alps). Geochimica et Cosmochimica Acta 126, 475-494.

Halama, R., and Konrad-Schmolke, M. 2015. Retrograde metasomatic effects on phase assemblages in an interlayered blueschist–greenschist sequence (Coastal Cordillera, Chile). Lithos, 216, 31-47.

Hattori, K., Guillot, S., 2003. Volcanic fronts form as a consequence of serpentinite dehydration in the forearc mantle wedge. Geology 31, 525-528.

Hauri, E.H., Wagner, T.P. and Grove, T.L. 1994. Experimental and natural partitioning of Th, U, Pb and other trace elements between garnet, clinopyroxene and basaltic melts. Chemical Geology, 117: 149-166.

Hebert, L.B., Asimow, P., Antoshechkina, P., 2009. Fluid source-based modeling of melt initiation within the subduction zone mantle wedge: Implications for geochemical trends in arc lavas. Chemical Geology 266, 297-310.

Hebert, L. B., Montési, L. G., 2013. Hydration adjacent to a deeply subducting slab: The roles of nominally anhydrous minerals and migrating fluids. Journal of Geophysical Research: Solid Earth, 118(11), 5753-5770.

Helgeson, H.C., Delany, J.M., Nesbitt, H.W., Bird, D.K., 1978. Summary and critique of the thermodynamic properties of rock-forming minerals. American Journal of Science 278-A, 1-229.

Hermann, J. and Rubatto, D. 2003: Relating zircon and monazite domains to garnet growth zones: age and duration of granulite facies metamorphism in the Val Malenco lower crust. J. Metamorphic Geol., 21, 833-852.

Hervig, R.L., Moore, G.M., Williams, L.B., Peacock, S.M., Holloway, J.R., Roggensack, K., 2002. Isotopic and elemental partitioning of boron between hydrous fluid and silicate melt. American Mineralogist 87, 769-774.

Holland, T. J. B. and Powell, R., 1998, An internally consistent thermodynamic data set for phases of petrological interest: Journal of Metamorphic Geology, v. 16, p. 309-343.

Holland, T.J.B. and Powell, R. 2011 An improved and extended internally consistent thermodynamic dataset for phases of petrological interest, involving a new equation of state for solids. Journal of Metamorphic Geology, DOI: 10.1111/j.1525-1314.2010.00923.x

Holland, T., and Blundy, J. 1994. Non-ideal interactions in calcic amphiboles and their bearing on amphibole-plagioclase thermometry. Contributions to Mineralogy and Petrology 116, 433-447.

Holland, T., Powell, R., 2003. Activity–composition relations for phases in petrological calculations: an asymmetric multicomponent formulation. Contributions to Mineralogy and Petrology, 145(4), 492-501.

Hollister, L.S., 1966. Garnet Zoning - an Interpretation Based on Rayleigh Fractionation Model. Science 154(3757): 1647-1649.

Ishikawa, T., Nakamura, E., 1994. Origin of the slab component in arc lavas from across-arc variation of B and Pb isotopes. Nature 370, 205-208.

Ishikawa, T., Tera, F., Nakazawa, T., 2001. Boron isotope and trace element systematics of the three volcanic zones in the Kamchatka arc. Geochimica et Cosmochimica Acta 65, 4523-4537.

Jamtveit, B. and Hervig, R.L. 1994. Constraints on Transport and Kinetics in Hydrothermal Systems from Zoned Garnet Crystals. Science 263(5146): 505-508.

John, T., Scherer, E.E., Haase, K., Schenk, V., 2004. Trace element fractionation during fluid-induced eclogitization in a subducting slab: trace element and Lu–Hf–Sm–Nd isotope systematics. Earth and Planetary Science Letters, 227(3), 441-456.

John, T., Scherer, E., Schenk, V., Herms, P., Halama, R., Garbe-Schönberg, D., 2010. Subducted seamounts in an eclogite-facies ophiolite sequence: The Andean Raspas Complex, SW Ecuador. Contributions to Mineralogy and Petrology 159, 265-284.

Johnson, J.W., Oelkers, E.H., Helgeson, H.C., 1992. SUPCRT92: A software package for calculating the standard molal thermodynamic properties of minerals, gases, aqueous species and reactions from 1 to 5000 bars and 0 to 1000 °C. Computers and Geosciences 18, 899-947.

Kelemen, P.B., Dick, H.J.B., Quick, J.E., 1992. Formation of harzburgite by pervasive melt/rock reaction in the upper mantle. Nature 358, 635-641.

Kerrick, D. M., Jacobs, G. K., 1981. A modified Redlich-Kwong equation for H_2O, CO_2, and H_2O-CO_2 mixtures at elevated pressures and temperatures. American Journal of Science, 281(6), 735-767.

Kerrick, D. M., and Connolly, J. A. D. 2001. Metamorphic devolatilization of subducted oceanic metabasalts: implications for seismicity, arc magmatism and volatile recycling. Earth and Planetary Science Letters, 189(1), 19-29.

Kessel, R., Schmidt, M. W., Ulmer, P. and Pettke, T., 2005, Trace element signature of subduction-zone fluids, melts and supercritical liquids at 120-180 km depth: Nature, v. 437, p. 724-727.

Ketcham, R.A. and Carlson, W.D. 2012. Numerical simulation of diffusion-controlled nucleation and growth of porphyroblasts. Journal of Metamorphic Geology, 30: 489-512.

Kimura, J.-I., Kent, A. J. R., Rowe, M. C., Katakuse, M., Nakano, F., Hacker, B. R., van Keken, P. E., Kawabata, H. and Stern, R. J. 2010. Origin of cross-chain geochemical variation in Quaternary lavas from the northern Izu arc: Using a quantitative mass balance approach to identify mantle sources and mantle wedge processes. Geochemistry Geophysics Geosystems 11 (10): doi:10.1029/2010GC003050

Kimura, J. I., Hacker, B. R., van Keken, P. E., Kawabata, H., Yoshida, T., Stern, R. J., 2009. Arc Basalt Simulator version 2, a simulation for slab dehydration and fluid-fluxed mantle melting for arc basalts: Modeling scheme and application. Geochemistry, Geophysics,

Geosystems, 10(9).

Konrad-Schmolke, M., Handy, M. R., Babist, J. and O'Brien, P. J. 2005: Thermodynamic modelling of diffusion-controlled garnet growth. Contrib. Mineral. Petrol., 149, 181-195.

Konrad-Schmolke, M., Babist, J., Handy, M. R. and O' Brien, P. J. 2006: The physico-chemical properties of a subducted slab from garnet zonation patterns (Sesia Zone, Western Alps). J. Petrol., 47, 2123-2148.

Konrad-Schmolke, M., O'Brien, P. J. and Heidelbach, F. 2007. Compositional re-equilibration of garnet: The importance of sub-grain boundaries. European Journal of Mineralogy 19, (4): 431-438.

Konrad-Schmolke, M., O'Brien, P. J., de Capitani, C. and Carswell, D. A. 2008a. Garnet growth at high- and ultra-high pressure conditions and the effect of element fractionation on mineral modes and composition. Lithos 103, (3-4): 309-332.

Konrad-Schmolke, M., Zack, T., O'Brien, P. J. and Jacob, D. E. 2008b. Combined thermodynamic and rare earth element modelling of garnet growth during subduction: Examples from ultrahigh-pressure eclogite of the Western Gneiss Region, Norway. Earth and Planetary Science Letters 272, (1-2): 488-498.

Konrad-Schmolke, M., O'Brien, P. J. and Zack, T. 2011a. Fluid Migration above a subducted slab – Constraints on amount, pathways and major element mobility from partially overprinted eclogite-facies rocks (Sesia Zone, Western Alps). Journal of Petrology. 52, (3): 457-486.

Konrad-Schmolke, M., Zack, T., O'Brien, P.J. and Barth, M. 2011b. Fluid migration above a subducted slab — Thermodynamic and trace element modelling of fluid–rock interaction in partially overprinted eclogite facies rocks (Sesia Zone, Western Alps). Earth and Planetary Science Letters, 311: 287-298.

Konrad-Schmolke, M., and Halama, R. 2014. Combined thermodynamic–geochemical modeling in metamorphic geology: Boron as tracer of fluid–rock interaction. Lithos, 208, 393-414.

Korzhinskii, D.S., 1965. The theory of systems with perfectly mobile components and processes of mineral formation. Am. J. Sci. 263: 193-205.

Kostenko, O., Jamtveit, B., Austrheim, H., Pollok, K. and Putnis, C. 2002. The mechanism of fluid infiltration in peridotites at Almklovdalen, Western Norway. Geofluids 2, (3): 203-215.

Koukarri, P., Pajarre, R. 2011. A Gibbs energy minimization method for constrained and partial equilibria. Pure and Applied Chemistry (83), 6: 1243-1254.

Kotková, J. and Harley, S.L. 2010. Anatexis during High-pressure Crustal Metamorphism: Evidence from Garnet-Whole-rock REE Relationships and Zircon-Rutile Ti-Zr Thermometry in Leucogranulites from the Bohemian Massif. Journal of Petrology, 51 (10): 1967-2001.

Kulik, D.A., Berner, U., Curti, E., 2004. Modelling chemical equilibrium partitioning with the GEMS-PSI code, Paul Scherrer Institute, Villigen, Switzerland.

Kulik, D.A., Wagner, T., Dmytrieva, S.V., Kosakowski, G., Hingerl, F.F., Chudnenko, K.V., Berner, U., 2013. GEM-Selektor geochemical modeling package: revised algorithm and GEMS3K numerical kernel for coupled simulation codes. Computational Geosciences 17, 1-24.

Landau, L. D. 1937. Zur Theorie der Phasenumwandlungen II. Phys. Z. Sowjetunion, 11, 26-35.

Moyen, J-F. 2009. High Sr/Y and La/Yb ratios: The meaning of the “adakitic signature”. Lithos, doi:10.1016/j.lithos.2009.04.001.

Maier, C.G., and Kelley, K.K. 1932. An equation for the representation of high-temperature heat content data1. Journal of the American chemical society, 54(8), 3243-3246.

Margules, M., 1895. Über die Zusammensetzung der gesättigten Dämpfe von Mischungen. Sitzungsberichte der Kaiserliche Akademie der Wissenschaften Wien Mathematisch-Naturwissenschaftliche Klasse II 104, 1243–1278.

Marmo, B. A., Clarke, G. L. and Powell, R., 2002, Fractionation of bulk rock composition due to porphyroblast growth: effects on eclogite facies mineral equilibria, Pam Peninsula, New Caledonia: Journal of Metamorphic Geology, v. 20, p. 151-165.

Marschall, H.R., Altherr, R. and Rüpke, L. 2007. Squeezing out the slab – modelling the release of Li, Be and B during progressive high-pressure metamorphism. Chemical Geology 239(3-4): 323-335.

Marschall, H., Altherr, R., Gméling, K. and Kasztovszky, Z. 2009. Lithium, boron and chlorine as tracers for metasomatism in high-pressure metamorphic rocks: a case study from Syros (Greece). Mineralogy and Petrology 95(3): 291-302.

McCammon, C and Kopylova, M.G. 2004. A redox profile of the Slave mantle and oxygen fugacity control in the cratonic mantle. Contrib Mineral. Petrol., 148: 55-68.

McKenzie, D., O'Nions, R.K., 1991. Partial melt distributions from inversion of Rare Earth Element concentrations. Journal of Petrology 32, 1021-1091.

Moriguti, T., Shibata, T., Nakamura, E., 2004. Lithium, boron and lead isotope and trace element systematics of Quaternary basaltic volcanic rocks in northeastern Japan: mineralogical controls on slab-derived fluid composition. Chemical Geology 212, 81-100.

Nabelek, P.I., 1987. General equations for modeling fluid/rock interaction using trace elements and isotopes. Geochimica et Cosmochimica Acta, 51(6), 1765-1769.

Nagel, T.J., Hoffmann, J.E., Münker, C., 2012. Generation of Eoarchean tonalite-trondhjemite-granodiorite series from thickened mafic arc crust. Geology 40, 375-378.

Nordstrom, D.K. and Munoz, J.L. 1986. Geochemical Thermodynamics. Blackwell Sci. Pub. (1986).

Oelkers, E.H., Bénézeth, P., Pokrovski, G.S., 2009. Thermodynamic databases for water-rock interaction. Reviews in Mineralogy and Geochemistry 70, 1-56.

O'Hara, M.J., 1977. Geochemical evolution during fractional crystallization of a periodically refilled magma chamber. Nature 266, 503-507.

Onuma, H. Higuchi, H. Wakita, H. Nagasawa 1968. Trace element partition between two pyroxenes and the host lava. Earth Planet. Sci. Lett., 5: 47–51

Otamendi J.E., de la Rosa J.D., Douce A.E.P. and Castro A., 2002, Rayleigh fractionation of heavy rare earths and yttrium during metamorphic garnet growth. Geology 30: 159-162.

Paquin, J., Altherr, R., and Ludwig, T., 2004. Li–Be–B systematics in the ultrahigh-pressure garnet peridotite from Alpe Arami (Central Swiss Alps): implications for slab-to-mantle wedge transfer. Earth and Planetary Science Letters, 218(3), 507-519.

Parkhurst, D.L., Appelo, C.A.J., 1999. User's guide to PHREEQC (version 2) - a computer program for speciation, batch-reaction, one-dimensional transport, and inverse geochemical calculations.

Peacock, S.M. and Hervig, R.L. 1999. Boron isotopic composition of subduction-zone metamorphic rocks. Chemical Geology 160(4): 281-290.

Pearce, J.A., 2008. Geochemical fingerprinting of oceanic basalts with applications to ophiolite classification and the search for Archean oceanic crust. Lithos, 100(1, 14-48.

Pearce, M.A., Wheeler, J., 2010. Modelling grain-recycling zoning during metamorphism. Journal of metamorphic Geology 28, 423-437.

Pollington, A.D., Baxter, E.F., 2010. High resolution Sm-Nd garnet geochronology reveals the uneven pace of tectonometamorphic processes. Earth and Planetary Science Letters 293, 63-71.

Powell, R., Holland, T.J.B., 1988. An internally consistent data set with uncertainties and correlations: 3. Applications to geobarometry, worked examples and a computer program. Journal of Metamorphic Geology 6, 173-204.

Powell, R., Guiraud, M. and White, R.W. 2005. Truth and beauty in metamorphic phase-equilibria: conjugate variables and phase diagrams. The Canadian Mineralogist 43(1): 21-33.

Ravna, K. 2000. The garnet–clinopyroxene Fe^{2+}–Mg geothermometer: an updated calibration. Journal of metamorphic Geology, 18(2), 211-219.

Reif, F. 1965. Fundamentals of Statistical and Thermal Physics, McGraw-Hill Book Company, New York, page 122.
Redlich, O. and Kwong, J.N.S., 1949. An equation of state. Fugacities of gaseous solutions. Chem. Rev. 44: 233-244.

Robie, R.A. and Hemingway, B.S. 1995. Thermodynamic Properties of Minerals and Related Substances at 298.15 K and 1 Bar (10^5 Pascals) Pressure and at Higher Temperature, U. S. Geological Survey, Washington, DC, 461 pp.

Rosner, M., Erzinger, J., Franz, G., Trumbull, R.B., 2003. Slab-derived boron isotope signatures in arc volcanic rocks from the Central Andes and evidence for boron isotope fractionation during progressive slab dehydration. Geochemistry Geophysics Geosystems 4(8), 9005, doi:10.1029/2002GC000438.

Ryan, J.G. and Chauvel, C., 2013. The Subduction Zone Conveyor and the Impact of Recycled Materials on the Evolution of the Mantle. Chapter 2.11 The Mantle and Core (Carlson, R. Ed.), Treatise on Geochemistry, Second Edition

Sanchez-Valle, C., Reynard, B., Daniel, I., Lecuyer, C., Martinez, I., Chervin, J.-C., 2005. Boron isotopic fractionation between minerals and fluids: New insights from in situ high pressure-high temperature vibrational spectroscopic data. Geochimica et Cosmochimica Acta 69, 4301-4313.

Savov, I.P., Ryan, J.G., D'Antonio, M., Fryer, P., 2007. Shallow slab fluid release across and along the Mariana arc-basin system: Insights from geochemistry of serpentinized peridotites from the Mariana fore arc. Journal of Geophysical Research 112, B09205, doi:10.1029/2006JB004749.

Scott, J.M., Konrad-Schmolke, M., O'Brien, P.J., Günter, C., 2013. High-T, low-P formation of rare olivine-bearing symplectites in Variscan eclogite. Journal of Petrology 54, 1375-1398.

Sharp, Z., 2007. Principles of Stable Isotope Geochemistry. Pearson Prentice Hall, Upper Saddle River, New Jersey, 344 pp.

Shaw, D.M., 1970. Trace element fractionation during anatexis. Geochimica et Cosmochimica Acta 34, 237-243.

Simon, L., Lécuyer, C., Maréchal, C., and Coltice, N., 2006. Modelling the geochemical cycle of boron: Implications for the long-term $\delta^{11}B$ evolution of seawater and oceanic crust. Chemical Geology 225(1), 61-76.

Skora, S., Baumgartner, L. P., Mahlen, N. J., Johnson, C. M., Pilet, S. and Hellebrand, E., 2006, Diffusion-limited REE uptake by eclogite garnets and its consequences for Lu-Hf and Sm-Nd geochronology: Contributions to Mineralogy and Petrology, v. 152, p. 703-720.

Spear, F. S. and Selverstone, J. 1983: Quantitative P-T path from zoned minerals; theory and tectonic applications. Contrib. Mineral. Petrol., 83, 348-357.

Spear, F. 1988. Metamorphic fractional crystallisation and internal metasomatism by diffusional homogenization of zoned garnets. Contributions to Mineralogy and Petrology, 99: 507-517.

Spear, F. S. and Menard, T., 1989, Program GIBBS; a generalized Gibbs method algorithm: American Mineralogist, v. 74, p. 942-943.

Spear, F. S. 1993. Metamorphic phase equilibria and pressure-temperaturetime paths. Mineral. Soc. America, Washington DC, 799p.

Spear, F. S. and Daniel, C. G., 2001, Diffusion control of garnet growth, Harpswell Neck, Maine, USA: Journal of Metamorphic Geology, v. 19, p. 179-195.

Stixrude, L., and Lithgow-Bertelloni, C., 2005. Thermodynamics of mantle minerals–I. Physical properties. Geophysical Journal International 162(2), 610-632.

Taura, H., Yurimoto, H., Kurita, K., Sueno, S., 1998. Pressure dependence on partition coefficients for trace elements between olivine and the coexisting melts. Contributions to Mineralogy and Petrology 25, 469-484.

Thöni, M., Miller, C., Blichert-Toft, J., Whitehouse, M.J., Konzett, J. and Zanetti, A. 2008. Timing of high-pressure metamorphism and exhumation of the eclogite type-locality (Kupplerbrunn–Prickler Halt, Saualpe, south-eastern Austria): constraints from correlations of the Sm–Nd, Lu–Hf, U–Pb and Rb–Sr isotopic systems. Journal of Metamorphic Geology, 26: 561-581.

Tirone, M., Ganguly, J., Dohmen, R., Langenhorst, F., Hervig, R. L. and Becker, H.-W., 2005, Rare earth element diffusion kinetics in garnet: Experimental studies and applications: Geochimica et Cosmochimica Acta, v. 69, p. 2385-2398.

Tonarini, S., Agostini, S., Doglioni, C., Innocenti, F., Manetti, P., 2007. Evidence for serpentinite fluid in convergent margin systems: The example of El Salvador (Central America) arc lavas. Geochemistry Geophysics Geosystems 8, Q09014, doi:10.1029/2006GC001508.

Tonarini, S., Leeman, W.P., Leat, P.T., 2011. Subduction erosion of forearc mantle wedge implicated in the genesis of the South Sandwich Island (SSI) arc: Evidence from boron isotope systematics. Earth and Planetary Science Letters 301, 275-284.

van der Straaten, F., Halama, R., John, T., Schenk, V., Hauff, F., Andersen, N., 2012. Tracing the effects of high-pressure metasomatic fluids and seawater alteration in blueschist-facies overprinted eclogites: Implications for subduction channel processes. Chemical Geology 292-293, 69-87.

Van Laar, J.J., 1910. Ueber Dampfspannung von binären Gemischen. Zeitschrift für Physikalische Chemie 72, 723-751.

Weaver, B.L., 1991. Trace element evidence for the origin of ocean-island basalts. Geology 19, 123-126.

Whitehouse, M. J. and Platt, J. P., 2003, Dating high grade metamorphism - constraints from rare-earth elements in zircon and garnet: Contributions to Mineralogy and Petrology, v. 145, p. 61-74.

White, W.M., 2013. Geochemistry. Wiley-Blackwell, Chichester, 660 pp.

Wilke, F. D. H., O'Brien, P. J., Altenberger, U., Konrad-Schmolke, M. and Khan, M. A. 2010. Multi-stage reaction history in different eclogite types from the Pakistan Himalaya and implications for exhumation processes. Lithos 114, (1-2): 70-85.

Wunder, B., Meixner, A., Romer, R.L., Wirth, R., Heinrich, W., 2005. The geochemical cycle of boron: Constraints from boron isotope partitioning experiments between mica and fluid. Lithos 84, 205-216.

Yang, P. and Rivers, T., 2001, Chromium and manganese zoning in pelitic garnet and kyanite; spiral, overprint, and oscillatory (?) zoning patterns and the role of growth rate: Journal of Metamorphic Geology, v. 19, p. 455-474.

PART II

Garnet growth at high- and ultra-high pressure conditions and the effect of element fractionation on mineral modes and composition

MATTHIAS KONRAD-SCHMOLKE[1], PATRICK J. O'BRIEN[1], CHRISTIAN DE CAPITANI[2] AND DENNIS A. CARSWELL[3,†]

[1] *Universität Potsdam, Institut für Geowissenschaften, Karl-Liebknecht-Straße 24-25, 14476 Golm, Germany*

[2]*Universität Basel, Institut für Mineralogie and Petrographie, Bernoullistrasse 30, CH-4056 Basel*

[3]*University of Sheffield, Department of Earth Sciences, Sheffield S3 7HF, England, UK*

[†] *deceased*

Abstract

In this paper we show that thermodynamic forward modelling, using Gibbs energy minimisation with consideration of element fractionation into refractory phases and/or liberated fluids, is able to extract information about the complex physical and chemical evolution of a deeply subducted rock volume. By comparing complex compositional growth zonations in garnets from high- and ultra-high pressure samples with those derived from thermodynamic forward modelling, we yield an insight into the effects of element fractionation on composition and modes of the co-genetic metamorphic phase assemblage. Our results demonstrate that fractionation effects cause discontinuous growth and re-crystallisation of metamorphic minerals in high pressure rocks. Reduced or hindered mineral growth at UHP conditions can control the inclusion and preservation of minerals indicative

for UHP metamorphism, such as coesite, thus masking peak pressure conditions reached in subducted rocks.

Further, our results demonstrate that fractional garnet crystallisation leads to strong compositional gradients and step-like zonation patterns in garnet, a feature often observed in high- and ultra-high pressure rocks. Thermodynamic forward modelling allows the interpretation of commonly observed garnet growth zonation patterns in terms of garnet forming reactions and the relative timing of garnet growth with respect to the rock's pressure-temperature path. Such a correlation is essential for the determination of tectonic and metamorphic rates in subduction zones as well as for the understanding of trace element signatures in subduction related rocks. It therefore should be commonplace in the investigation of metamorphic processes in subduction zones.

Keywords: *subduction zone; element fractionation; ultra-high pressure; garnet; thermodynamic modelling.*

Introduction

Advances in micro-analytical techniques in the last few decades have increasingly allowed precise and accurate determination of major and trace elements as well as isotope compositions of both rock-forming and accessory minerals. Consequently, inhomogeneity i.e. a lack of equilibrium in the form of compositional zoning, is now seen to be a normal feature of many metamorphic rocks and quantitative studies of major and trace element variations in metamorphic minerals have become key factors in deciphering rock pressure (P) and temperature (T) evolution (e.g. Spear and Selverstone 1983), determining element transport properties (e.g. Chernoff and Carlson 1997; Spear and Daniel 2001; Yang and Rivers 2001; Konrad-Schmolke et al., 2005; Inui 2006) as well as constraining the duration of metamorphic events (e.g. Lasaga and Jiang 1995; Ganguly et al., 1996; O'Brien, 1997). Modelling expected

mineral assemblages, phase compositions and modal proportions for a given rock composition at different P-T conditions with internally consistent thermodynamic data and computer programs such as e.g. Thermocalc (Powell et al., 1998), Perplex (Connolly and Kerrick, 1987) or Theriak/Domino (De Capitani and Brown, 1987) has now become commonplace. An advance on this static 'equilibrium' approach is to determine a whole series of 'equilibrium' stages along a P-T path by fractionating various proportions of refractory minerals (such as garnet) or reaction-produced fluids out of the reacting system and thus sequentially re-defining the effective reaction composition (e.g. Menard and Spear 1993; Connolly 2005; Konrad-Schmolke et al., 2005; 2006). In subduction zones for example, water fractionation during continuous dehydration of the subducted slab and fractional crystallisation of solids, due to sluggish volume diffusion, continuously change the chemical composition of the reacting rock volume (e.g. Marmo et al., 2002). Such fractionation processes are among the most important features during subduction, because they have a strong influence on major and trace element cycles in subduction zones. Thus, understanding and quantifying fractionation effects during the rocks metamorphic evolution is an important task in petrology and geochemistry. Calculating fractionation effects is a powerful extension of the thermodynamic modelling method and allows prediction of the timing of mineral growth, the evolution of compositional zonation and the nature of inclusion suites along chosen P-T paths and thus provides a direct comparison with such features recorded in natural samples.

In order to get an insight into the complex chemical and metamorphic evolution of a rock volume and to compare model results with nature it is most promising to investigate compositional growth zonations in minerals grown along the prograde P-T path, because the compositional variations in such phases reflect changes in the rocks P, T and chemical evolution and bear information about the temporal succession of different metamorphic stages. Garnet is best suited for this purpose because its sluggish intracrystalline element diffusion enables the preservation of chemical growth zonations even at elevated

metamorphic temperatures (e.g. O'Brien and Vrana, 1995). Especially in relatively cold metamorphic environments, such as subduction zones, garnet is very likely to preserve an almost unaffected chemical growth zonation pattern. Because garnet is one of the most abundant rock forming minerals in high pressure (HP) and ultra-high pressure (UHP) rocks and grows over a wide P-T range, its growth zonation preserves information about large parts of the rocks P-T and chemical (X) history. Additionally, UHP garnet often contains important mineral inclusions, like coesite and/or diamond: commonly the only indicators for UHP metamorphism.

In this paper we use thermodynamic forward models to investigate garnet growth and composition in UHP rocks in order to get an insight into the mineralogical processes that cause such complex growth zonation patterns and to study the influence of fractionation effects on garnet growth at UHP conditions.

Common growth zonation patterns in HP and UHP garnets

Many garnets in HP and UHP rocks preserve complex chemical zonation patterns that show multiple growth stages, often reflected in core-overgrowth differences both in main and trace element composition and in the inclusion assemblage (e.g. Vance and O'Nions 1990; Compagnoni and Hirajima 2001; Carswell et al., 2003b; Davis and Whitney 2006). The distinct growth zones are often bounded by strong compositional gradients and/or inclusion- and trace-element-enriched zones that indicate episodic garnet growth as well as growth interruptions during prograde metamorphism. A quantitative understanding of these distinct growth pulses enables the relationship between P-T path, age determinations in spatially controlled garnet domains or temperature-time constraints (from diffusion modelling) to be fully characterised.

Although in detail each garnet zoning pattern is unique and depends on rock chemistry and metamorphic evolution, broad similarities in the nature of overgrowths and compositional

100 trends have been recognised between zoning patterns of samples from different HP and UHP
101 belts. Generally two different prograde growth-zoning patterns occur in eclogite garnets, both
102 of which are characterised by increasing pyrope content and X_{Mg} and decreasing
103 almandine+spessartine content from core to rim, but which show a contrasting grossular
104 trend. The two trends are:

105 (1) slightly rising grossular content from core to an inner rim followed by a drastic
106 decrease towards the outer rim and

107 (2) increasing grossular content from core to inner rim followed by a further Ca-increase
108 towards the outermost-rim.

109 Examples of these two different zoning patterns from natural samples of eclogite (from
110 the Western Gneiss Region of Norway and from the Himalaya of Ladakh), were investigated
111 in detail with the aid of electron microprobe compositional mappings and line profiles. An
112 attempt was then made to try to reproduce the deduced zoning patterns by the use of
113 thermodynamic forward modelling.

114 **Samples**

115 *PAR 12 - UHP eclogite from Tso Morari (Western Himalaya, India)*

116 Sample PAR 12 (Fig. 1a) is an UHP eclogite from Tso Morari/Western Himalaya
117 (O'Brien and Sachan, 2001; Massonne and O´Brien, 2003). Garnet in this sample is
118 irregularly shaped and between 1 and 2 mm in diameter. Most grains show a conspicuous
119 boundary between inclusion-rich pale-red cores and inclusion-poor, colourless margins.
120 Inclusions in the core are epidote, omphacite, sodic-calcic amphibole, rare paragonite, rutile
121 and quartz whereas the margins are epidote- and amphibole-free and contain minor inclusions
122 of aegirine-poor omphacite and rutile (see Table 1 for inclusion compositions). Although the
123 matrix contains considerable sodic-calcic amphibole there are several domains where the

high-pressure amphibole-free omphacite-phengite-rutile-garnet-quartz assemblage is preserved.

Compositional mapping (Fig. 2a) reveals that the colour zoning in garnet is also reflected in major element chemistry. The maps show that there is often a very sharp compositional boundary between the internal (inclusion-rich) and the external (inclusion-poor) zones. The magnitude of the compositional variation can be seen in the compositional zoning profiles plotted in Fig. 2b, for the lines 'a' and 'b' located in Fig. 2a. Garnet core has a typical Mn peak, 20mol% or more, decreasing to below 1 mol% towards the rim as it is substituted by iron. The content of magnesium is remarkably low, around 5 mol%, for much of the interior and X_{Mg} (i.e. Mg/(Mg+Fe)) is around 0.1. At the rim of the garnet there is a very sharp rise in Mg countered by an equally sharp fall in Ca. Profile 1 of Fig. 2b, as evident in Fig. 2a, records a compositional profile in the garnet where the magnitude of the contrasting rim zone is relatively small. A more obvious compositional change is recorded by the Profile 2 marked in Fig. 2a as presented in Fig. 2b. There is no doubt in this profile that the outer zone of the garnet represents an overgrowth with a significantly different composition. From the inner to the outer zone Ca drops from 32 to 14 mol% and is countered by a rise in Mg from 6 to 25 mol%. Iron also shows a small rise but Mn, although already low, drops to virtually nothing.

The Mn profile suggests that the process leading to the garnet overgrowth was not Ostwald ripening as this would have freed Mn from the earlier-formed garnet. Note also the zoning towards higher X_{Mg} (i.e. reflecting higher temperature) in the overgrowth zone. Thus this garnet has at least two growth stages preserved – each with their own specific zoning pattern. The garnet pattern described above is a result of initial garnet growth at relatively low temperatures (core zone) followed by a second major growth stage at higher temperature and pressure conditions during which the garnet overgrowth occurred.

A 623 - UHP eclogite from the Nordfjord area (Norway)

Sample A 623 (Fig. 1b) stems from an eclogite lens from the HP to UHP transition zone near Krokken (Nordfjord/Norway). The sample is a medium-grained foliated eclogite with the matrix assemblage rt/tn-phng-qtz-zo-grt-cpx, in some cases elongate kyanite grains grow parallel to the weak main foliation, which is defined by a preferred orientation of omphacite. Quartz is common as inclusions in garnet but less abundant in the matrix. Although found in nearby samples, no coesite or polycrystalline quartz aggregates have been observed in this locality. The matrix minerals partly show symplectitic retrogression products along grain boundaries. Garnets in the sample display a very obvious prograde compositional zonation and clear indications of multi-stage growth (Fig. 3). Most garnets have idiomorphic outlines and clearly separated idiomorphic cores bounded by concentric inclusion trails that define the idiomorphic, mostly hexagonal shapes of the cores. In the cores, randomly oriented mineral inclusions are small and consist mostly of blue-green sodic-calcic amphibole, rutile, titanite, carbonate and quartz. Amphibole and rutile in places show signs of a retrograde transformation into chlorite, plagioclase and ilmenite. The concentric inclusion-rich zone between core and rim consists of quartz, rutile and minor omphacite. The first overgrowth zone has fewer but larger inclusions of sodic-calcic amphibole, omphacite and rutile/titanite (see Table 1 for inclusion compositions). The idiomorphic rims are partly overgrown by irregularly formed, almost inclusion-free small garnets that often form aggregates parallel to the main foliation (arrow in Fig. 3a) and textural relations that suggest equilibrium with cpx rims. If inclusions are found in the overgrowth, they consist of cpx and rutile.

Generally, the garnets have a patchy chemical zonation in some regions but compositional mapping as well as the profile show clear chemical trends (Fig.3a):

The cores have a compositional plateau in the inner regions with $Alm_{0.52}Grs_{0.25}Prp_{0.18}Sps_{0.05}$, but towards the outer part of the core region Grs and Prp sharply increase, whereas Alm and Sps decrease. Outside the inclusion trails that outline the cores,

garnet composition is more or less constant in the inner rim with the composition $Alm_{0.48}Grs_{0.3}Prp_{0.2}Sps_{0.02}$. Towards the outer rim Prp and Alm increase, whereas Grs slightly decreases. The irregularly-shaped small overgrowth zones, as well as the small matrix garnets, have a markedly different but mostly constant composition with lower Prp and Alm and significantly higher Grs content.

Settings of the thermodynamic forward models

P-T pseudosections and thermodynamic forward modelling was performed using the Gibbs energy minimisation algorithm THERIAK (de Capitani and Brown, 1987) and the thermodynamic database of Berman (1988) including more recent additions (e.g. Berman 1990; Mäder and Berman 1992). The solution models and the database used in this work as well as a comparison of the results derived with the Holland and Powell (1998) database can be found in the Appendix and in the electronic supplementary material. Forward modelling was performed by calculating the thermodynamic properties of a rock volume along a high pressure P-T trajectory under consideration of the elements Na, Ca, K, Fe, Mg, Al, Si, H and O (NCKFMASH-system). Whereas other works investigated the effect of different P-T trajectories on garnet growth (e.g. Konrad-Schmolke et al., 2006), in this study the same, simplified P-T trajectory was chosen for both samples in order to study the effect of different bulk rock compositions on garnet growth. As there are no detailed data on the shape of the prograde P-T paths of the two selected samples available, we modelled the thermodynamic evolution of the samples along a straight trajectory from 520°C at 1.5 GPa to 750°C at 3.5 GPa. The chosen path was divided into 100, regularly spaced P-T increments at each of which the thermodynamic properties of the system were determined. Modelling fractionation effects involved modifying the bulk rock composition between two calculated increments according to the predicted element incorporation in fractionated phases (in our case H_2O and garnet). Garnet zonation patterns were modelled with the calculated composition and amount of garnet

at every increment, assuming a spherical grain shape and no diffusive modification of growth zonation (cf. Konrad-Schmolke et al., 2005). The chemical potential of oxygen in the system was controlled by an ilmenite-magnetite-rutile (IMR) buffer in all calculations. The resulting chemical potential of oxygen, constrained by the chosen buffer, lies between the hematite-magnetite (HM) and nickel-nickel oxide (NNO) buffers (cf. Zhao et al., 1999).

Results

Sample PAR 12

Homogeneous equilibrium crystallisation with water in excess

The P-T pseudosections and the garnet growth diagrams in Fig. 4 are calculated for an average MORB composition (Schilling 1983) – a typical bulk composition for many eclogites and one corresponding roughly to that of sample PAR 12. Although it is evident that at UHP conditions water activity might be below unity (e.g. Hermann et al., 2006), water is assumed to be in access for simplicity reasons. Zero mode lines are labelled at the 'present' side of the mineral assemblage, the white arrow displays the path along which the thermodynamic forward modelling was performed.

The P-T diagrams reflect the phase relations commonly observed in a basaltic rock composition. Phase relations beyond the bold stippled line (wet basaltic solidus from Lambert and Wyllie, 1972) are shaded, because the presence of a melt phase might falsify the calculated stability fields. Along the considered P-T trajectory (arrow in Fig. 4), the rock crosses the zero mode lines of garnet, chlorite, omphacite, paragonite, epidote, kyanite and amphibole. Thus, the influence of these phases on garnet growth and garnet composition can be studied along the chosen P-T path. The isopleths in Fig. 4a, which display the calculated amount of garnet in the thermodynamic system, predict increasing amounts of garnet with increasing temperature and pressure across the entire grid. Along the P-T trajectory, garnet growth occurs in four distinct stages (Fig. 4a and b). The calculated garnet growth starts at P-

T increment # 11 at 545°C and 1.72 GPa. The first garnet grows from the reaction (Fig. 4c and d):

chlorite + epidote + quartz =

(almandine-rich) garnet (1) + calcic amphibole + water. (1)

Beyond the range of chlorite stability, garnet growth occurs by the reaction

(sodic-calcic) amphibole + epidote + quartz=

garnet (2) (increasing grossular content) + clinopyroxene (1) + kyanite + water (2)

The increase in Grs content during this reaction is evident from the Grs isopleths in Fig. 4c. In the small P-T segment between the 'epidote out' and 'amphibole out' univariant (see inset in Fig. 4e) the grossular content is predicted to decrease slightly along the considered path, because garnet in this assemblage grows predominantly from the reaction

Sodic-calcic amphibole + clinopyroxene (1) =

garnet (3) + clinopyroxene (2) + quartz + water. (3)

The last garnet growth stage produces only little garnet, again with increasing grossular component, and occurs by the consumption of omphacite:

Clinopyroxene (2) + kyanite = garnet (4) + clinopyroxene (3) + quartz (4)

Each of these garnet-forming reactions produces garnet with a characteristic chemical zonation pattern. Due to the large amount of garnet produced by the consumption of chlorite, the calculated pattern has a large, almandine-rich plateau in the core followed by smaller overgrowth zones resulting from the different garnet-producing reactions.

Fractional crystallisation and water fractionation

Comparing the diagrams in Figs. 4 and 5 demonstrates that the introduction of element fractionation in the model setting yields significantly different results compared with that

assuming homogeneous equilibrium crystallisation. The diagrams in Fig. 5 display garnet composition (a and d), garnet growth (b) and the co-genetic mineral paragenesis (c) along the considered P-T path, modelled with the consideration of fractional crystallisation and water fractionation. In case of fractional crystallisation, garnet grows in three, instead of four distinct episodes due to the modified bulk rock composition. The first two growth stages (reactions (1) and (2)), where garnet is predicted to grow from chlorite, epidote and amphibole are nearly unaffected by fractionation effects, but in contrast to homogeneous equilibrium crystallisation conditions, garnet growth from sodic-calcic amphibole (reaction (3)) occurs over a much larger P-T segment as in the previous calculations, resulting in a pronounced continuous decrease in grossular content towards the garnet rim. As a consequence of the bulk rock depletion due to enhanced garnet fractionation during the third growth stage, garnet growth from clinopyroxene (reaction (4)) is hindered. In case of fractional crystallisation, garnet stops growing at increment #47 (628°C at 2.44 GPa) just before the rock passes the quartz/coesite transition. The resulting zonation pattern (Fig. 5d) shows a markedly different shape compared to that calculated for homogeneous equilibrium crystallisation (Fig. 4d): Although the compositional trend in the garnet core is still the same as in the homogeneous crystallisation model (first two growth stages), the Grs content is now predicted to decrease rapidly at the outermost rim, due to the stronger contribution of garnet growth from sodic-calcic amphibole (Fig. 5c). The above calculations demonstrate that element fractionation has a significant influence on garnet growth, its compositional trend during metamorphism and also on the coexisting mineral paragenesis.

The influence of fractionation on garnet composition and garnet growth can also be demonstrated in a series of P-T pseudosections, such as in Fig. 6, which is calculated for different bulk rock compositions that result from element fractionation along the modelled path. Figs. 6a and b display the phase relations, the amount of garnet in the system (Fig. 6a) and the Grs content in garnet (Fig. 6b) calculated for the bulk rock composition at the end of

273 the second garnet growth stage (Fig. 5a, increment #33), where the compositional trend
274 changes at the outer rim of the modelled garnet. Because the bulk rock composition is a path-
275 dependent function, if element fractionation is considered, it is obvious that the diagrams in
276 Fig. 6 are only valid for a certain P-T evolution and a single calculated P-T increment. To
277 demonstrate this, contours are only drawn next to the P-T trajectory, whereas zero mode lines
278 are shown across the entire grid for a better overview. Two important fractionation effects are
279 visible. First, water fractionation has led to the situation whereby the system is water under-
280 saturated in large parts of the considered P-T space (to the left of, and below the zero mode
281 line of H_2O), which leads to a significant enlargement of the garnet stability towards lower
282 temperatures. Further, Grs- and modal isopleths in the water-under-saturated parts of the
283 system are strongly influenced by the absence of a free water phase. Second, the stability field
284 of sodic-calcic amphibole is slightly enlarged towards higher pressure and temperature,
285 enabling garnet growth with rapidly decreasing Grs content (Fig. 6b) as is observed in the
286 natural sample from the Himalayas (Fig. 2). Water under-saturation in parts of the considered
287 P-T space, differences in phase relations as well as modified grossular isopleths, result from
288 element fractionation along the modelled path. Nevertheless, in contrast to the diagrams in
289 Fig. 5, the equilibrium diagrams in Fig. 6a and b predict continuous garnet growth across the
290 entire grid, even at UHP conditions. Thus, further fractionation along the P-T trajectory must
291 be responsible for the garnet growth interruption that is predicted by the forward modelling
292 (Fig. 5).

293 The diagrams in Fig. 6c and d display the amount of garnet in the system and its Grs
294 content calculated for the bulk rock composition after the third stage of garnet growth along
295 the considered path (Fig. 5a, increment #47). Now, progressive bulk rock depletion led to a
296 large gap in the stability of the last-grown garnet along the considered path and new garnet
297 can only be generated if recycling of the interiors of already-grown garnet porphyroblasts
298 occurs. In other words, as coesite can only be enclosed in garnet during garnet growth

episodes, so long as metastable interiors of the garnet porphyroblasts remain isolated from the matrix, there would be no garnet growth and thus no potential for finding coesite inclusions in such garnets. This series of pseudosections clearly demonstrates the effect of element fractionation on the phase assemblage and phase composition in a rock during its metamorphic evolution.

Sample A 623

Homogeneous equilibrium crystallisation

Although the sample A 623 has a slightly different bulk rock composition than PAR 12 the differences in the P-T pseudosections calculated for water-saturated conditions and the initial bulk rock composition of sample A 623 (Fig. 7a and b) and those calculated for the sample PAR 12 (Fig. 4a and b) are only minor. In both cases, the amount of garnet is predicted to increase with increasing pressure and temperature (cf. Figs. 4a and 7a) and the Grs content in garnet (Figs. 4c and 7b) is expected to increase along the considered P-T path.

Nevertheless the calculated phase relations at the eclogite transition are slightly different in the pseudosections for sample A 623. Whereas in the pseudosections calculated for sample PAR 12 (Fig. 4), sodic-calcic amphibole is stable beyond the epidote stability field, in sample A 623 amphibole occurs only in co-existence with epidote along the considered P-T path. Although the calculated garnet composition (Fig. 7c) and the growth curve (Fig. 7d) calculated for water saturation and homogeneous equilibrium crystallisation are similar in both examples (cf. Figs. 4b and d), garnet growth by the reaction:

Sodic-calcic amphibole + clinopyroxene (1) =

garnet (3) + clinopyroxene (2) + water. (3)

is not expected in the Norwegian sample.

322 The larger stability of the assemblage epidote + amphibole in sample A 623 leads to a
323 steadily increasing grossular content from core to rim, because the fourth garnet forming
324 reaction (Cpx(2)=Grt(3)) also produces Grs-rich garnet. The resulting garnet zonation pattern
325 is shown in Fig. 7f. Interestingly, fractional crystallisation seems to have a minor influence on
326 the phase relations and phase compositions in this sample, compared to those modelled for
327 PAR 12 as will be demonstrated in the following calculations.

328 *Fractional crystallisation and water fractionation*

329 Fig. 8 shows the garnet composition (a and d), the garnet growth curve (b) and the co-
330 genetic mineral paragenesis (c) calculated with consideration of fractionation effects in
331 sample A 623. As in sample PAR 12, garnet growth in the first two stages is almost
332 unaffected by fractionation effects. But, in contrast to homogeneous equilibrium
333 crystallisation, the trend in garnet composition changes after the consumption of epidote,
334 because fractionation effects enables garnet growth at the expense of sodic-calcic amphibole
335 (reaction (3)), which causes a decrease in the grossular component in the newly formed garnet
336 (between P-T increments #36 and 39).

337 The predicted chemical trend shows a plateau in the core zone with a composition
338 around $Alm_{0.62}Grs_{0.2}Prp_{0.18}$, formed by the consumption of chlorite and epidote (reaction (1)).
339 Towards the outer core, Prp and Grs sharply increase and Alm decreases. In the rim
340 overgrowth the pattern again forms a plateau with a composition around $Alm_{0.5\text{-}0.4}Grs_{0.27\text{-}}$
341 $_{0.3}Prp_{0.23\text{-}0.3}$. This overgrowth zone mainly results from the consumption of epidote and sodic-
342 calcic amphibole, which form garnet and the first clinopyroxene. At the outermost rim,
343 pyrope increases sharply whereas almandine as well as grossular decreases as a result from
344 sodic-calcic amphibole consumption (reaction (3)). After that drastic change in garnet
345 composition, garnet growth is interrupted unless the rock reaches UHP conditions. At 3.1 GPa

346 garnet starts growing again (reaction (4)) with a significantly higher grossular content ($Alm_{0.2-0.15}Grs_{0.5}Prp_{0.3-0.35}$).

348 Apart from the similarities during the first garnet growth stages, there is an important
349 difference in garnet growth between the two samples at UHP conditions. Although the
350 amount of newly formed garnet and the shape of the garnet growth curve are similar in both
351 samples, there is, in contrast to sample PAR 12, a fourth growth stage (reaction (4)) in sample
352 A 623 starting at P-T increment #71 even if fractionation is considered along the modelled P-
353 T path. As in all calculations assuming homogeneous equilibrium crystallisation, there is
354 garnet growing from clinopyroxene at UHP conditions, which produces a grossular-pyrope-
355 rich overgrowth in equilibrium with clinopyroxene after a large interruption in garnet growth.
356 This growth interruption as well as the fourth garnet growth stage in sample A 623 has
357 important implications for the interpretation of peak metamorphic conditions in this sample. If
358 the transformation of pre-existing quartz inclusions into coesite during burial is neglected, the
359 grossular-rich garnet formed at this growth stage (reaction (4)) is the only garnet material in
360 this sample that might enclose coesite crystals or relics of these, because it is the only garnet
361 that grows at UHP conditions. The growth interruption, the third garnet growth stage as well
362 as the grossular isopleths are shown in the pseudosections in Fig. 9a and b, which are
363 calculated for the bulk rock composition after the first two garnet growth stages. Although the
364 phase relations are similar to that in the pseudosections calculated for the MORB
365 composition, the shape and position of the garnet growth interruption is slightly different,
366 which enables garnet growth at UHP conditions in this rock type.

367 **Discussion**

368 The results of the thermodynamic forward models in this work clearly show that
369 fractionation processes during subduction have a strong influence on garnet growth, its
370 composition and on the shape of its compositional growth zonation. Nevertheless, it is

371 obvious that the models are based on simplified assumptions with respect to the considered
372 chemical and physical parameters, which will be discussed in the following.

373 *Comparison of modelled and observed growth zonation patterns*

374 Despite the simplifications in our models a comparison of modelled and observed
375 growth zonation patterns in garnet helps us to understand the effect of fractionation processes
376 in natural rocks. The models show that the effect of fractional crystallisation on garnet
377 chemistry is strongest in the Himalayan sample (PAR 12). Although modelled and observed
378 garnet compositions differ slightly the compositional core-to-rim trends are characteristic for
379 each modelled scenario. The modelled growth zonation assuming homogeneous equilibrium
380 crystallisation (Fig. 4f) is characterised by a large plateau in the core, caused by the
381 consumption of chlorite, followed by a continuous grossular increase towards the outer rim.
382 This modelled profile only partly reflects the chemical trend in the Himalayan garnet (cf. Fig.
383 5e). The plateau-like core region, predicted by the model, is less well developed in the natural
384 sample. Also, the abrupt compositional change in the outer rim of the natural sample can not
385 be modelled with a constant bulk rock composition and water in access. In contrast, the
386 modelled pattern assuming fractional crystallisation and water fractionation (Fig. 5d), predicts
387 the sharply decreasing grossular content at the outer rim as observed in the natural sample
388 (Fig. 5e). Chemical depletion of the bulk rock composition due to fractionation effects hinders
389 garnet growth in this sample at UHP conditions and thus the formation of a Ca-rich
390 overgrowth as is predicted by the equilibrium crystallisation model. But, also in case of
391 fractional crystallisation, the large plateau in the garnet core caused by chlorite consumption,
392 is less well-developed in the natural sample, suggesting a lesser contribution of chlorite
393 (reaction 1) to the garnet forming reaction than that calculated by the model.

394 In case of sample A 623 the fractionation effect on garnet chemistry is less
395 pronounced but fractional crystallisation obviously enhances episodic, interrupted garnet

growth in this sample, which enables the formation of step-like zonation patterns. The major difference between the homogeneous equilibrium models (Fig. 7f) and those assuming fractional crystallisation (Fig. 8a and d) is the large growth interruption predicted along the modelled path, resulting in a characteristic zonation pattern at the outermost rim. A comparison of modelled and observed growth zonation pattern for sample A 623 and fractional crystallisation shows characteristic similarities (Fig. 8):

As in the natural sample, the predicted chemical trend shows a plateau in the core zone with a composition around $Alm_{0.62}Grs_{0.2}Prp_{0.18}$, followed by a sharp increase of Prp and Grs towards the outer core (Fig. 8d). The predicted composition in the outer core and in the first overgrowth zone largely resembles the observed shape of the natural pattern. The characteristic overgrowth zone is predicted to result from the consumption of epidote and sodic-calcic amphibole, which form garnet and the first clinopyroxene, whereas the outermost rim is modelled as a result from sodic-calcic amphibole consumption (reaction (3)). In the natural sample inclusions of epidote and amphibole can be found in the core and in the innermost part of the overgrowth zone, but not in the outer part of the overgrowth or in the rim. Instead, clinopyroxene is a common inclusion mineral in the outer parts of the garnets in this sample, which is in agreement with the modelled phase relations. The model predicts that garnet growth is interrupted at about 2.4 GPa and the outermost garnet rim, which starts growing at 3.1 GPa, is characterised by a high grossular and low almandine content ($Alm_{0.2-0.15}Grs_{0.5}Prp_{0.3-0.35}$). This trend is also observed in the natural sample, although the predicted grossular content is slightly higher than in the natural sample. As in the Himalayan sample the absolute values for the garnet composition differ slightly between predicted and observed zonations, but the compositional trends, caused by the garnet forming reactions and growth interruptions can be used to yield an insight into the garnet growth history and the sample's metamorphic evolution.

421 *Predicted garnet growth and phase relations*

422 Extracting information about a rock's temporal P-T-X evolution from
423 compositionally-zoned garnet is a technique that has been applied to a large number of
424 different rock types in many different metamorphic settings. Most of the investigated garnets
425 exhibit relatively simple, often continuous compositional growth zoning (e.g. Spear and
426 Selverstone 1983; Hoisch et al., 2002) that results from garnet growth in equilibrium with a
427 constant mineral assemblage. However, there are still many unresolved problems with respect
428 to more complexly-zoned garnets, such as those with multiple growth stages and abrupt
429 compositional changes, as it is the case in our samples. Such discontinuous zonation patterns
430 often contain important petrological information. On the one hand, the diffusional relaxation
431 of step-like chemical zonations can be used to determine the duration of metamorphic events
432 (e.g. Lasaga and Jiang 1995; Ganguly et al., 1996; O'Brien, 1997; Konrad-Schmolke et al.,
433 2006) and rates of tectonic processes (e.g. Philippot et al., 2001; Dachs and Proyer 2002;
434 Massonne and O'Brien, 2003), but on the other hand the duration of garnet growth
435 interruptions between the different growth stages is often hard to determine and might range
436 from several hundreds to millions of years (i.e. multiple growth during a single orogenic
437 event) or even longer (i.e. due to multiple orogenic events). Thus, the interpretation of
438 multiple garnet growth zones in terms of garnet forming reactions (single vs. multiple
439 metamorphic cycles) sets constraints on the broad metamorphic evolution of a rock body
440 (Ganné et al., 2006; Gaidies et al., 2006; Konrad-Schmolke et al., 2006).

441 Several authors have suggested that the reason for interrupted or strongly reduced
442 garnet growth during a single metamorphic cycle might be changing reaction assemblages or
443 changing abundances of co-genetic minerals that control garnet growth during the prograde
444 metamorphic evolution (e.g. O' Brien 1993; Carswell et al., 2003b). Also, diffusion-
445 controlled element availability has been proposed to be responsible for growth interruptions

446 during prograde metamorphism (Konrad-Schmolke et al., 2005). Our calculations show that
447 fractionation effects, like fractional crystallisation and the resulting bulk rock depletion, can
448 lead to reduced or hindered garnet growth along a prograde HP metamorphic P-T path (e.g.
449 Figs. 6 and 9) and might cause growth interruptions and strong compositional gradients within
450 a garnet grain. Because hiatuses in garnet growth can easily be detected, their temporal and
451 textural relation to other phases in a rock volume can be of essential importance for the
452 interpretation of the tectonometamorphic evolution of a sample (e.g. Spiess et al., 2000, Getty
453 et al., 1993). Growth interruptions might, for example, be marked by concentric inclusion
454 trails of accessory minerals (e.g. Olimpio and Anderson 1978; Spiess et al., 2000) that are
455 suitable for geochronology and thus act as P-T-t markers. In certain cases, growth
456 interruptions can be correlated with a certain tectonic event if the garnet crystal contains shear
457 sense indicators, such as sigmoidal inclusion trails or pre-existing foliations (e.g. Yang and
458 Rivers 2001; Biermeier and Stüwe 2003; Timms 2003).

459 Further, our results show that even without a suitable inclusion suite the garnet
460 zonation pattern can be interpreted with respect to the co-genetic mineral parageneses and
461 thus certain P-T stages, because each co-genetic mineral paragenesis and reaction assemblage
462 produces a characteristic chemical zonation pattern that can be interpreted in terms of the
463 rock's P-T-X evolution. For example, the predicted change in the Ca trend in both samples is
464 controlled by the disappearance of epidote at upper blueschist-facies conditions. Beyond
465 epidote stability, garnet growth occurs by the consumption of sodic-calcic amphibole, which
466 causes a strongly decreasing Ca content in garnet (Fig. 5). This predicted change in the
467 inclusion assemblage can be observed in both natural samples in this study. As in many HP
468 and UHP rocks, garnet in our samples is characterised by an inclusion-rich core containing
469 epidote, sodic-calcic amphibole and/or omphacite (Figs. 1, 2 and 3). In sample PAR 12 garnet
470 is characterised by steadily increasing Grs content in the epidote-inclusion rich core and a
471 strong decrease in Grs in the epidote-free overgrowth zones. The only enclosed minerals in

472 the grossular-poor parts of the rim is omphacite (and rutile) as predicted by the forward
473 models.

474 Interestingly, there is a difference in the correlation of the plateau-like core zones
475 modelled by the forward calculations and the natural zonations shown by the two samples.
476 Whereas the core zone, which is predicted to form by reaction (1), is almost absent or only
477 weakly developed in sample PAR 12, the modelled and observed core zonation correspond
478 well in sample A 623. Obviously the contribution of consumed chlorite to the newly formed
479 garnet material, which is responsible for the formation of the grossular-poorer, plateau-like
480 core zone, is larger in the Norwegian than in the Himalayan sample. This effect might by
481 indicative for a larger proportion of chlorite, and thus a higher amount of water during
482 subduction in sample A 623 than in sample PAR 12. Unfortunately, as in most HP and UHP
483 garnets, there are no chlorite inclusions preserved in the cores and information about the
484 water content of the samples at the onset of subduction must remain speculative. In fact, the
485 nature of the eclogite protolith is rarely known and can range from a metastable magmatic
486 assemblage (gabbro, dolerite) to hydrothermally-altered basalt. Another factor of importance
487 is the exact shape of the P-T path. Different subduction rates and angles can lead to different
488 heating and compression rates thus allowing a range of possible trajectories in P-T space to
489 the same peak assemblage field. However, the aim of this paper is to show the general trend
490 of fractionation processes allowing production of sharp, step-like zonation profiles and not the
491 fine-detail of exact P-T-t path determination.

492 *Regional implications*

493 The model results for sample A 623 can also be discussed in light of the regional
494 distribution of HP and UHP eclogites in the western part of the Western Gneiss Region
495 (WGR), Southern Norway. Wain (1997) describes a transitional zone between HP eclogites in
496 the southern part and UHP eclogites in the northern part of the WGR. In a several kilometre
497 wide zone at the northern bank of the Nordfjord, coesite- or polycrystalline quartz (PCQ)-

498 bearing UHP eclogites are closely associated with eclogites that contain no signs of UHP
499 metamorphism. Garnet in eclogites without UHP minerals shows well-preserved prograde
500 growth zoning (as in sample A 623), whereas garnet in UHP samples is commonly chemically
501 homogenised and sometimes encloses coesite relics or PCQ aggregates. Wain (1997) and
502 Wain et al., 2000 interpreted this HP/UHP transition zone to be the result of tectonic
503 juxtaposition of slices with different peak metamorphic conditions. Interestingly, Cuthbert et
504 al., 2001 report samples from this area that contain both idioblastic, compositionally-zoned,
505 coesite-free (HP) garnets as well as xenoblastic, chemically homogeneous garnet crystals that
506 contain PCQ after coesite. Even more remarkable is the observation of garnets with
507 idioblastic, chemically zoned cores that are overgrown by xenoblastic, Ca-rich rims that
508 preserve polycrystalline quartz inclusions after coesite (Cuthbert et al., 2001). This
509 observation suggests, in contrast to the interpretation of Wain et al., 2000, that the HP/UHP
510 transformation of the eclogites is kinetically hindered instead of the result of a tectonic
511 juxtaposition. The results of this study show that the mineral assemblage in sample A 623
512 does not significantly change between P-T increments #39 and 70, corresponding to pressures
513 between 2.3 and 3.1 GPa, due to the strongly depleted effective bulk rock composition after
514 fractional crystallisation of garnet (Figs.8 and 9). Neither garnet nor clinopyroxene, the rock
515 forming minerals at these P-T conditions, change significantly modal in abundance or
516 composition. In contrast, the models that assume homogeneous equilibrium crystallisation
517 indicate garnet growth as well as consumption of clinopyroxene over a large pressure range at
518 UHP conditions (Fig. 7). These results show that a kinetically-reduced element recycling from
519 garnet cores to the reacting bulk rock composition hinders significant changes in the phase
520 relations. Thus, our results support the interpretation of Cuthbert et al., 2001, who interpret
521 kinetic factors to be responsible for the close association of HP and UHP mineral assemblages
522 in the eclogites of the Nordfjord area in the WGR.

523 *Model settings and reproducibility*

524 The interpretation of results from thermodynamic forward modelling strongly depends
525 on the standard state thermodynamic dataset of the minerals as well as the thermodynamic
526 formulation of solid solutions. To test the influence of the standard state dataset on the
527 resulting mineral parageneses and the modelled garnet zonation patterns, we conducted
528 forward modelling utilising the Berman (1988) as well as the Holland and Powell (1998)
529 database. The comparison of the results showed that phase compositions and modal
530 abundances differ slightly between the different databases, but both datasets yielded
531 qualitatively the same results i.e. steps in garnet zoning profiles and fractionation effects (see
532 electronic Appendix). However, the aim of this work is to show the influence of changing
533 mineral paragenesis as well as fractionation effects on garnet growth and garnet chemistry.
534 Thus, the most important requirement of the models is to reproduce phase relations that are
535 commonly observed in high pressure metabasites, such as those shown in Figs. 5 and 8.
536 In order to test the ability of the model to predict the compositions of complex solution
537 phases, calculated and measured compositions of amphibole and clinopyroxene inclusions in
538 our samples are shown in Fig. 10. The compositions of calculated and observed amphibole
539 inclusions differ only slightly with respect to their tetrahedral aluminium content and their
540 sodium site distribution in sample PAR 12 and A 623 respectively (Fig. 10a and b). For the
541 calculated and measured clinopyroxene compositions the difference is mainly in the higher
542 X_{Mg} in the calculated pyroxenes, whereas the Jadeite content largely coincides between
543 measured and modelled compositions.

544 The slight mismatch between calculated and observed amphibole and clinopyroxene
545 compositions might have an influence on the amount and composition of garnet produced by
546 the consumption of these phases. A higher Al content and lower abundance of the co-existing
547 amphibole might result in a lower amount of newly formed garnet with a slightly higher Grs
548 component. However, the observed change in the Ca trend in garnet is mainly influenced by
549 the disappearance of epidote, which is much more calcic than the sodic-calcic amphibole.

550 Thus, we feel confident that the epidote-out reaction is mainly responsible for the changing
551 compositional trend in HP and UHP garnet. Another difference between calculated and
552 observed composition is the grossular content of the outermost garnet overgrowth, which is
553 slightly higher in the model (X_{Grs} = 0.5) than in the natural sample (X_{Grs} = 0.4). In our
554 opinion, this is due to the underestimated abundance of zoisite, which is predicted to be
555 consumed during UHP garnet growth (Fig. 8), but is observed in the natural sample.
556 Interestingly, the models calculated with the Holland and Powell (1998) database predict
557 zoisite to be stable and to coexist with a grossular-poorer (X_{Grs} = 0.4) garnet at UHP
558 conditions although the garnet composition in these calculations is too pyrope-rich (see
559 electronic Appendix). However, the slight differences between modelled and observed
560 absolute mineral compositions clearly demonstrate limitations of thermodynamic models at
561 present. Although the thermodynamic databases are rapidly evolving (e.g. Holland and Powell
562 1998; Berman and Aranovich 1996, Gottschalk 1997), the definitions of solution phases – the
563 majority of the considered minerals in this work – is still problematic. Problems arise mainly
564 from the lack of reliable thermodynamic data for certain minerals but also from the multiple
565 interactions between chemical and crystallographic parameters in complex solid solution, as
566 for example, amphibole, phengite, clinopyroxene and chlorite (e.g. Dale et al., 2005; Keller et
567 al., 2005; Meyre et al., 1997; Hunziker 2003). In order to minimise errors arising from these
568 uncertainties we concentrated on the interpretation of relative changes in phase compositions
569 and abundances.

570 In order to simplify the chemical system we omitted the elements Mn and Ti from the
571 bulk rock composition. As garnet is an important Mn-bearing mineral, the presence of
572 considerable amounts of Mn in the bulk rock composition expands the stability of garnet
573 towards lower temperatures especially at lower pressures (e.g. Droop and Harte 1995; Inui
574 and Toriumi 2004; Konrad-Schmolke et al., 2006). In our samples, the spessartine component
575 in the garnets is moderately low in the inner cores of the garnets (20% in PAR 12 and 8% in

576 A 625), thus indicating that Mn might have had only minor influence on initial garnet growth.
577 This is confirmed by our thermodynamic calculations, which show that the garnet stability
578 field is enlarged by less than 40°C towards lower temperatures between 1.5 and 3.5 GPa, but
579 does not significantly influence the modelled garnet zonation patterns (see electronic
580 Appendix). As this study concentrates on the relative changes of garnet composition along a
581 certain P-T trajectory rather than on the determination of exact P-T conditions, we assume
582 that influence to be negligible.

583 Another important simplification is the omission of titanium from the system, which
584 hinders modelling the sphene-rutile transition. This transition can influence the growth zoning
585 in garnet because it might liberate small amounts of calcium. Furthermore, the consumption
586 of sphene during garnet growth is an important factor for the rare earth element (REE) budget
587 in the rock (e.g. King et al., 2004) and might enlarge the stability of epidote or allanite during
588 garnet growth (Hermann 2002), which in turn will affect garnet composition. In case of
589 sample PAR 12, the sphene-out reaction might be of minor importance, because only rutile is
590 found as inclusion mineral in the garnets, suggesting that the onset of garnet growth was
591 outside the sphene stability field. In case of sample A 623 rutile and sphene can be found as
592 inclusions in the core and in the inner rim, whereas in the outer rim and in the matrix, only
593 rutile is present. Thus, it is evident that the sphene-out reaction must have occurred during
594 garnet growth. Unfortunately the thermodynamic models that included titanium did not
595 satisfactorily reproduce the observed mineral inclusion suite in sample A 623, which is why
596 we omitted Ti in this contribution. Nevertheless, further investigations including REE
597 measurements in garnet and inclusions could yield detailed insight into the complex growth
598 history in these samples but are beyond the scope of this paper.

599 Beside the effect of Mn and Ti in the system, oxygen fugacity, or: the chemical
600 potential of oxygen, plays an important role for the calculation of thermodynamic equilibria.

In our models we calculated phase equilibria assuming oxygen to be buffered by an ilmenite-magnetite-rutile buffer, which is modelled as a stable phase with a linear combination of the thermodynamic properties of the three phases (see electronic Appendix). The chemical potential of oxygen in the system is constrained by the forced presence of the buffer phase. In order to minimise the parameters in the model, we used the same buffer in all calculations. The chosen buffer constrains the chemical potential of oxygen between that of a nickel – nickel oxide (NNO) and a quartz – fayalite – magnetite (QFM) buffer. Nevertheless, it is clear that the choice of a buffer assemblage is arbitrary and it is very likely that the chemical potential of oxygen in subducted rocks cannot be described solely by an oxygen buffer. Most affected by a changing chemical potential of oxygen in our calculations are the epidote and omphacite solid solutions, because both minerals might contain considerable amounts of ferric iron. The reason for the presence of omphacite inclusions in the cores of the garnets in sample PAR 12, for example, might be due to the presence of a significant acmite component. Further, changing modal amounts of epidote due to a changing chemical potential of oxygen might strongly influence the grossular-content in the newly formed garnet. Thus, the chemical potential of oxygen in the system might have a strong influence on the Ca-pattern in the garnets, but the absence of appropriate solid solution models, e.g. for clinopyroxene with respect to the ferric iron-bearing component, hinders a more detailed forward modelling of ferric iron-bearing minerals at present. In order to achieve consistency and to allow a comparison of our model results with other calculations we used the same oxygen buffer in all our calculations. Comparison of the modelled patterns with that of natural samples allow the significance of different parameters of thermodynamic models to be ascertained.

Element transport during metamorphism

An important aspect of the modelling is to allow an evaluation of fractionation processes during subduction. Thermodynamic forward models have been used by several

626 authors to determine the physico-chemical properties of a subducted slab (e.g. Connolly 2005;
627 Konrad-Schmolke et al., 2006). Our calculations in this work have shown that element
628 fractionation affects garnet growth and composition as well as the phase relations during
629 progressive metamorphism. Thus, zoned metamorphic garnets can be used to constrain the in-
630 and output of matter in a subducted slab, by comparing modelled and observed
631 compositionally zoned metamorphic HP garnet (e.g. Konrad-Schmolke et al., 2005). The
632 importance of these fractionation effects on density and water content of a continentally-
633 derived subducted crustal segment has been shown by Konrad-Schmolke et al. (2006). As
634 shown in Fig. 4, the effect of water fractionation has severe consequences for the mineral
635 assemblage especially if the rock becomes water under-saturated by entering phase fields with
636 higher water contents. This is most likely the case in the lawsonite stability field, where the
637 rock needs intense re-hydration in order to form large amounts of highly hydrated minerals,
638 such as chlorite and lawsonite. The lack of water availability will be most accentuated in
639 subducted rocks that have already low water contents prior to subduction, such as gabbros or
640 granulites (e.g. Konrad-Schmolke et al., 2006). Water undersaturation has contrasting effects
641 with respect to garnet growth in a subducted slab that enters the lawsonite stability field. On
642 the one hand, reduced availability of fluids hinders effective element transport and thus might
643 disable garnet formation (Clarke et al., 2006), on the other hand, garnet stability is enlarged
644 towards lower temperatures (Fig. 6), which enables garnet growth at unusually low
645 temperatures as observed in lawsonite eclogites from Catalina Island (Tsujimori et al., 2006).

646 All of the results in this study show that a conventional thermodynamic approach, such
647 as interpretation of phase relations and isopleth pattern in pseudosections, might lead to
648 erroneous results with respect to a well-constrained P-, T- and chemical evolution of HP and
649 UHP rocks. This is because the mineral assemblage, as well as the compositional evolution of
650 phases, is a path-dependent function if the rock undergoes fractional crystallisation and water
651 fractionation. Marmo et al., 2002 already mentioned that fractionation effects might change

phase relations in metabasic HP rocks from New Caledonia but they applied conventional pseudosection calculation to better constrain the true metamorphic path of a subducted slice, similar to the situation envisaged in this work. Our work shows that a well-constrained mineralogical evolution can only be derived from thermodynamic forward modelling that considers fractional crystallisation and fluid fractionation. Although several studies (e.g. Spear et al., 1984) have shown the advantages of thermodynamic forward modelling this technique has only recently been applied to investigate geochemical (Connolly 2005; Konrad-Schmolke et al., 2005) and tectonophysical (e.g. Konrad-Schmolke et al., 2006) processes. Thus, this method should become a standard technique in metamorphic petrology in the future, especially as calculation routines become more and more suitable for solving complex mineralogical and petrological problems (e.g. Spear and Menard 1989; Connolly 2005; Konrad-Schmolke et al., 2005; Keller et al., 2006).

Conclusions

The thermodynamic forward models in this study use Gibbs energy minimisation and consider fractional crystallisation and water fractionation along the modelled P-T trajectory. The models are able to predict complex chemical zonation trends commonly observed in HP and UHP garnets and show that multi-stage garnet growth, which in the past has been suspected as evidence of polymetamorphism, is also possible along a single prograde PT-path as a result of changing effective bulk rock chemistry due to fractional crystallisation. Further, the models are able to predict the co-existing mineral parageneses during UHP metamorphism and show the influence of the bulk rock composition and fractionation effects on the likelihood of trapping coesite in garnet by predicting whether or not renewed garnet growth occurs in the UHP field.

Contrasting zoning trends commonly observed in HP and UHP eclogites, such as either increasing or decreasing grossular content from core to rim, are shown to be mainly due to

fractionation effects and slight differences in bulk rock compositions. Our results show that two dimensional P-T pseudosections that assume chemical equilibrium in a constant bulk rock composition might lead to considerable misinterpretation of garnet zonation patterns and P-T paths.

Acknowledgements

We thank the German Science Foundation (DFG) that supported the project. Further we are indebted to Ralf Milke who provided access to the electron microprobe lab at the Freie Universität Berlin. Rainer Abart and Romain Bousquet are thanked for their helpful discussions concerning the thermodynamic forward modelling. Jörg Hermann and Ian Buick are thanked for a detailed and constructive review and editorial handling of the manuscript respectively.

Appendix

Solid solution endmembers and mixing models

Garnet

Endmembers:

Almandine, pyrope, grossular.

Margules-type mixing model: Berman (1990)

Chlorite

Endmembers:

Amesite, ferroamesite, penninite, ferropenninite.

Mixing modell according to Hunziker (2003).

Clinopyroxene

Endmembers:

Diopside, hedenbergite, jadeite.

Margules-type mixing model: Meyre et al., 1997.

White mica

Endmembers:

Muscovite, celadonite, fe-celadonite, paragonite.

Margules-type mixing model: Keller et al., 2005.

Feldspar

Endmembers:

Albite, anorthite, K-feldspar.

Margules-type mixing model: Furman and Lindslay (1988).

Epidote

Endmembers:

Epidote, clinozoisite

Ideal mixing model.

Amphibole Model Appendix:

Amphibole

Endmembers:

Tremolite, ferroactinolite, tschermakite, ferrotschermakite, pargasite, glaucophane, ferroglaucophane.

Margules-type excess function based on Dale et al., 2005:

Margules parameters (J/mol)

	W^H	W^S	W^V
Tschermakite . Tremolite			
122	20000	5	0
Pargasite – Tremolite			
122	3000	10	0
Tremolite - Glaucophane			
12	25000	0	0
Tremolite - Ferroactinolite			
12	10000	0	0
Tremolite - Ferrotschermakite			
112	20000	5	0
Pargasite - Ferrotschermakite			
122	-38500	0	0
Glaucophane - Ferrotschermakite			
12	45900	0	0
Ferroactinolite - Ferrotschermakite			
112	12500	0	0
Pargasite - Tschermakite			
122	-38500	0	0
Glaucophane - Tschermakite			
12	25000	0	0
Ferroactinolite - Tschermakite			
112	15000	0.2	0
Pargasite - Glaucophane			
122	30000	10	0
Pargasite - Ferroactinolite			
122	-1900	10	0
Glaucophane - Ferroactinolite			
12	39300	0	0

Glaucophane - Ferroglaucophane			
12	-10000	0	0

726

727 *Bulk rock compositions used for the P-T diagram calculations*

Oxide (wt%)	Fig. 4	Fig. 6a and b	Fig. 6c and d	Fig. 7	Fig. 9
SiO_2	50.55	57.23	57.81	48.09	53.52
Al_2O_3	16.38	14.28	14.03	17.66	15.57
FeO	9.03	1.57	0.90	9.13	0.92
MgO	7.80	9.25	9.28	9.3	11.15
CaO	11.62	13.31	13.53	13.45	16.19
Na_2O	2.79	4.13	4.26	1.55	2.40
K_2O	0.09	0.13	0.14	0.14	0.22
H_2O	0.29	0.10	0.05	0.67	0.03
Sum	98.55	100.00(calc.)	100.00(calc.)	99.99	100.00(calc.)

728

Element (mol%)	Fig. 4	Fig. 6a and b	Fig. 6c and d	Fig. 7	Fig. 9
Si	18.622	17.867	18.065	16.120	17.129
Al	7.111	5.253	5.165	6.978	5.873
Fe	2.782	0.409	0.236	2.560	0.245
Mg	4.284	4.307	4.322	4.646	5.320
Ca	4.586	4.452	4.531	4.831	5.553
Na	1.993	2.502	2.584	1.010	1.487
K	0.042	0.054	0.055	0.062	0.091
H	saturated	0.213	0.111	saturated	0.055
O	60.580	64.838	64.84	61.540	64.219

729

730 **References**

731 Berman, R. G., 1988, Internally-consistent thermodynamic data for minerals in the system
732 Na2O-K2O-CaO-MgO-FeO-Fe2O3 -Al2O3 -SiO2 -TiO2 -H2O-CO2: Journal of
733 Petrology, v. 29, p. 445-522.

734 Berman, R. G., 1990, Mixing properties of Ca-Mg-Fe-Mn garnets: American Mineralogist, v.
735 75, p. 328-344.

736 Berman, R. G. and Aranovich, L. Y., 1996, Optimized standard state and solution properties
737 of minerals; I, Model calibration for olivine, orthopyroxene, cordierite, garnet, and
738 ilmenite in the system FeO-MgO-CaO-Al (sub 2) O (sub 3) -TiO (sub 2) -SiO (sub 2):
739 Contributions to Mineralogy and Petrology, v. 126, p. 1-24.

740 Biermeier, C. and Stüwe, K., 2003, Strain rates from snowball garnets: Journal of
741 Metamorphic Geology, v. 21, p. 253-268.

742 Carswell, D. A., Brueckner, H. K., Cuthbert, S. J., Mehta, K. and O'Brien, P. J., 2003b, The
743 timing of stabilisation and the exhumation rate for ultra-high pressure rocks in the
744 Western Gneiss Region of Norway: Journal of Metamorphic Geology, v. 21, p. 601-
745 612.

746 Chernoff, C. B. and Carlson, W. D., 1997, Disequilibrium for Ca during growth of pelitic
747 garnet: Journal of Metamorphic Geology, v. 15, p. 421-438.

748 Compagnoni, R. and Hirajima, T., 2001, Superzoned garnets in the coesite-bearing
749 Brossasco-Isasca Unit, Dora-Maira Massif, Western Alps, and the origin of the
750 whiteschists: Lithos, v. 57, p. 219-236.

751 Connolly, J. A. D. and Kerrick, D. M., 1987, An algorithm and Computer Program for
752 calculation Composition Phase Diagrams: Calphad, v. 11, p. 1-55.

753 Connolly, J. A. D., 2005, Computation of phase equilibria by linear programming: A tool for
754 geodynamic modeling and its application to subduction zone decarbonation: Earth and
755 Planetary Science Letters, v. 236, p. 524-541.

756 Cuthbert, S.J., Carswell, D.A. and O'Brien, P.J. (2001). HP-UHP transitions in the Western
757 Gneiss Complex, Norwegian Caledonides: Tectonics or kinetics? UHPM Workshop,
758 Waseda University, 4B07, p. 175-179.

759 Dachs, E. and Proyer, A., 2002, Constraints on the duration of high-pressure metamorphism
760 in the Tauern Window from diffusion modelling of discontinuous growth zones in
761 eclogite garnet: Journal of Metamorphic Geology, v. 20, p. 769-780.

762 Dale, J., Powell, R., White, L., Elmer, F. L. and Holland, T. J. B., 2005, A thermodynamic
763 model for Ca-Na-amphiboles in Na2O-CaO-FeO-MgO-Al2O3-SiO2-H2O-O for
764 prtrological calculations: Journal of Metamorphic Geology, v. 23, p. 771-791.

765 Davis, P. B. and Whitney, D. L., 2006, Petrogenesis of lawsonite and epidote eclogite and
766 blueschist, Sifrihisar Massif, Turkey: Journal of Metamorphic Geology, v. 24, p. 823-
767 849.

768 de Capitani, C. and Brown, T. H., 1987, The computation of chemical equilibrium in complex
769 systems containing non-ideal solutions: Geochimica et Cosmochimica Acta, v. 51, p.
770 2639-2652.

771 Droop, G. T. R. and Harte, B., 1995, The effect of Mn on the phase relations of medium-
772 grade metapelites: Constraints from natural assemblages on petrogenetic grid
773 topology. Journal of Petrology, v. 36: p.1549-1578.

774 Ducea, M. N., Ganguly, J., Rosenberg, E. J., Patchett, P. J., Cheng, W. J. and Isachsen, C.,
775 2003, Sm-Nd dating of spatially controlled domains of garnet single crystals: a new

776 method of high-temperature thermochronology: Earth and Planetary Science Letters,
777 v. 213, p. 31-42.

778 Fuhrman, M. L. and Lindsley, D. H., 1988, Ternary-Feldspar Modeling and Thermometry:
779 American Mineralogist, v. 73, p. 201-215.

780 Gaidies, F., Abart, R., de Capitani, C., Schuster, R., Connolly, J. A. D. and Reusser, E., 2006,
781 Characterisation of polymetamorphism in the Austroalpine basement east of the
782 Tauern Window using garnet isopleth thermometry: Journal of Metamorphic Geology,
783 v. 24, p. 451-475.

784 Ganguly, Y., Chakraborty, S., Sharp, T. G. and Rumble, D., 1996, Constraint on the time
785 scale of biotite-grade metamorphism during Acadian orogeny from a natural garnet-
786 garnet diffusion couple: American Mineralogist, v. 81, p. 1208-1216.

787 Ganné, J., Bussy, F. and Vidal, O., 2003, Multi-stage Garnet in the Internal Briançonnais
788 Basement (Ambin Massif, Savoy): New Petrological Constraints on the Blueschist-
789 facies Metamorphism in the Western Alps and Tectonic Implications: Journal of
790 Petrology, v. 44, p. 1281-1308.

791 Getty, S. R., Selverstone, J., Wernicke, B. P., Jacobson, S. B., Aliberti, E. and Lux, D., 1993,
792 Sm-Nd dating of multiple garnet growth events in an arc-continent collision zone,
793 northwestern U.S. Cordillera: Contributions to Mineralogy and Petrology, v. 115, p.
794 45-57.

795 Gottschalk, M., 1997, Internally consistent thermodynamic data for rock-forming minerals in
796 the system SiO2 -TiO2 -Al2O3 -CaO-MgO-FeO-K2O-Na2O-H2O-CO2: European
797 Journal of Mineralogy, v. 9, p. 175-223.

798 Hermann, J., 2002, Allanite: Thorium and light rare earth element carrier in subducted crust.
799 Chemical Geology, v. 192: p. 289-306.

800 Hermann, J. and Rubatto, D., 2003, Relating zircon and monazite domains to garnet growth
801 zones: age and duration of granulite facies metamorphism in the Val Malenco lower
802 crust: Journal of Metamorphic Geology, v. 21, p. 833-852.

803 Hermann, J., Spandler, C., Hack, A. and Korsakov, A. V., 2006, Aqueous fluids and hydrous
804 melts in high-pressure and ultra-high pressure rocks: Implications for element transfer
805 in subduction zones. Lithos, v. 92, p. 399-417.

806 Hoisch, T. D., Wells, M. L. and Hanson, L. M., 2002, Pressure-temperature paths from
807 garnet-zoning: Evidence for multiple episodes of thrust burial in the hinterland of the
808 Sevier orogenic belt: American Mineralogist, v. 87, p. 115-131.

809 Holland, T. J. B. and Powell, R., 1998, An internally consistent thermodynamic data set for
810 phases of petrological interest: Journal of Metamorphic Geology, v. 16, p. 309-343.

811 Hunziker, P., 2003, The stability of tri-octahedral Fe2+-Mg-Al chlorite. A combined
812 experimental and theoretical study. Ph D Thesis, University of Basel, 162 pp.

813 Inui, M., 2006, Forward calculation of zoned garnet growth with limited diffusion transport in
814 the matrix. Mineralogy and Petrology, v. 88: p. 29-46.

815 Inui, M. and Toriumi, M., 2004, A theoretical study on the formation of growth zoning in
816 garnet consuming chlorite. Journal of Petrology, v.45, p. 1369-1392.

817 Keller, L. M., De Capitani, C. and Abart, R., 2005, A Quaternary Solution Model for White
818 Micas Based on Natural Coexisting Phengite-Paragonite Pairs: Journal of Petrology, v.
819 46, p. 2129-2144.

820 Keller, L. M., Abart, R., Wirth, R. and Schmid, D. W., 2006, Enhanced mass transfer through
821 short-circuit diffusion: Growth of garnet reaction rims at eclogite facies conditions:
822 American Mineralogist, v. 91, p. 1024-1038.

King, R. L., Bebout, G. E., Kobayashi, K., Nakamura, E. and van der Klauw, S. N. G. C., 2004, Ultra-high pressure metabasaltic garnet as probes into deep subduction zone chemical recycling. Geochemistry, Geophysics, Geosystems, v. 5, Q12J14, DOI: 10.1029/2004GC000746.

Konrad-Schmolke, M., Handy, M. R., Babist, J. and O'Brien, P. J., 2005, Thermodynamic modelling of diffusion-controlled garnet growth. Contributions to Mineralogy and Petrology, v. 149, p. 181-195.

Konrad-Schmolke, M., Babist, J., Handy, M. R. and O'Brien, P. J., 2006, The physico-chemical properties of a subducted slab from garnet zonation patterns (Sesia Zone, Western Alps): Journal of Petrology, v. 47, p. 2123-2148.

Lasaga, A. C. and Jiang, J. X., 1995, Thermal History of Rocks - P-T-T Paths from Geospeedometry, Petrological Data, and Inverse-Theory Techniques: American Journal of Science, v. 295, p. 697-741.

Leake, B. E., Woolley, A. R., Arps, C. E. S., Birch, W. D., Gilbert, M. C., Grice, J. D., Hawthorne, F. C., Kato, A., Kisch, H. J., Krivovichev, V. G., Linthout, K., Laird, J., Mandarino, J. A., Maresch, W. V., Nickel, E. H., Rock, N. M. S., Schumacher, J. C., Smith, D. C., Stephenson, N. C. N., Ungaretti, L., Whittaker, E. J. W. and Guo, Y., 1997, Nomenclature of amphiboles; report of the subcommittee on amphiboles of the International Mineralogical Association, Commission on New Minerals and Mineral Names: The Canadian Mineralogist, v. 35, p. 219-246.

Marmo, B. A., Clarke, G. L. and Powell, R., 2002, Fractionation of bulk rock composition due to porphyroblast growth: effects on eclogite facies mineral equilibria, Pam Peninsula, New Caledonia: Journal of Metamorphic Geology, v. 20, p. 151-165.

Massonne, H.-J. and O'Brien, P. J. (2003). The Bohemian Massif and the Himalaya. In: Carswell, D.A. and Compagnoni, R. (eds.): EMU Notes in Mineralogy, UHP Metamorphism, v. 5, p. 145-187.

Mäder, U. K. and Berman, R. G. (1992). Amphibole thermobarometry; a thermodynamic approach. IGCP-304 Conference, Paper 92-1E, Geological Survey of Canada.

Menard, T. and Spear, F. S., 1993, Metamorphism of Calcic Pelitic Schists, Stratford Dome, Vermont - Compositional Zoning and Reaction History: Journal of Petrology, v. 34, p. 977-1005.

Meyre, C., de Capitani, C. and Partzsch, J. H., 1997, A ternary solid solution model for omphacite and its application to geothermobarometry of eclogites from the middle Adula Nappe (Central Alps, Switzerland): Journal of Metamorphic Geology, v. 15, p. 687-700.

Olimpio, J. C. and Anderson, D. E., 1978, The relationship between chemical and textural (optical) zoning in metamorphic garnets, South Morar, Scotland: American Mineralogist, v. 63, p. 677-689.

O'Brien, P. J., 1993, Partially retrograded eclogites of the Münchberg Massif, Germany: records of a multistage Variscan uplift history in the Bohemian Massif: Journal of Metamorphic Geology, v. 411, p. 241-260.

O'Brien, P. J. and Vrana, S., 1995, Eclogites with a short-lived granulite facies overprint in the Moldanubian Zone, Czech Republic: petrology, geochemistry and diffusion modelling of garnet zoning: Geologische Rundschau, v. 84, p. 473-488.

O'Brien, P. J., 1997, Garnet zoning and reaction textures in overprinted eclogites, Bohemian Massif, European Variscides; a record of their thermal history during exhumation: Lithos, v. 41, p. 119-133.

870 Philippot, P., Blichert-Toft, J., Perchuk, A., Costa, S. and Geerasimov, V., 2001, Lu-Hf and
871 Ar-Ar chronometry supports extreme rate of subduction zone metamorphism deduced
872 from geospeedometry: Tectonophysics, v. 342, p. 23-38.

873 Powell, R., Holland, T. and Worley, B., 1998, Calculating phase diagrams involving solid
874 solutions via non-linear equations, with examples using THERMOCALC: Journal of
875 Metamorphic Geology, v. 16, p. 577-588.

876 Schilling, J. G., Zajak, M., Evans, R., Johnston, T., White, W., Devine, J. D. and Kingsley, R.,
877 1983, Pettrologic and geochemical Variations along the Mid-atlantic Ridge from 27°N
878 to 73°N: American Journal of Science, v. 283, p. 510-586.

879 Spear, F. S. and Selverstone, J., 1983, Quantitative P-T path from zoned minerals; theory and
880 tectonic applications: Contributions to Mineralogy and Petrology., v. 83, p. 348-357.

881 Spear, F. S., Selverstone, J., Hickmott, D., Crowley, P. and Hodges, K. V., 1984, P-T paths
882 from garnet zoning; a new technique for deciphering tectonic processes in crystalline
883 terranes: Geology (Boulder), v. 12, p. 87-90.

884 Spear, F. S. and Menard, T., 1989, Program GIBBS; a generalized Gibbs method algorithm:
885 American Mineralogist, v. 74, p. 942-943.

886 Spear, F. S. and Daniel, C. G., 2001, Diffusion control of garnet growth, Harpswell Neck,
887 Maine, USA: Journal of Metamorphic Geology, v. 19, p. 179-195.

888 Spiess, R., Bertolo, B., Borghi, A., Chinellato, M. and Centi, M. T., 2000, Microtextures of
889 opaque inclusions: their use as indicators for hiatuses during garnet porphyroblast
890 growth: Journal of Metamorphic Geology, v. 18, p. 591-603.

891 Timms, N. E., 2003, Garnet porphyroblast timing and behaviour during fold evolutiuon:
892 implications from a 3-D geometric analysis of a hand-sample scale fold in a schist:
893 Journal of Metamorphic Geology, v. 21, p. 853-873.

894 Tsujimori, T., Sisson, V. B., Liou, J. G., Harlow, G. E. and Sorensen, S. S. (2006). Petrologic
895 characterisation of Guatemalian lawsonite eclogite: Eclogitisation of subducted
896 oceanic crust in a cold subduction zone. Ultrahigh-pressure metamorphism: Deep
897 continental subduction. B. R. Hacker, W. C. McClelland and J. G. Liou, Geological
898 Society of America. 403: 147-168.

899 Vance, D. and O'Nions, R. K., 1990, Isotopic Chronometry of Zoned Garnets - Growth-
900 Kinetics and Metamorphic Histories: Earth and Planetary Science Letters, v. 97, p.
901 227-240.

902 Wain, A. (1997). New evidence for coesite in eclogites and gneisses: Defining an ultrahigh-
903 pressure province in the Western Gneiss Region of Norway. Geology (Boulder), v. 25,
904 p. 927-930.

905 Wain, A. , Waters, D., Jephcoat, A. and Olijynk, H. (2000), The high-pressure to ultrahigh-
906 pressure eclogite transition in the Western Gneiss Region, Norway. European Journal
907 of Mineralogy, v.12, p. 667-687.

908 Whitehouse, M. J. and Platt, J. P., 2003, Dating high grade metamorphism - constraints from
909 rare-earth elements in zircon and garnet: Contributions to Mineralogy and Petrology,
910 v. 145, p. 61-74.

911 Yang, P. and Rivers, T., 2001, Chromium and manganese zoning in pelitic garnet and kyanite;
912 spiral, overprint, and oscillatory (?) zoning patterns and the role of growth rate:
913 Journal of Metamorphic Geology, v. 19, p. 455-474.

914 **Figure captions**

915 **Fig. 1**: Thin section photographs of the investigated samples. A) The irregularly-shaped
916 garnets in sample PAR 12 have inclusion-rich cores overgrown by inclusion-poor margins.
917 Inclusions in the core are epidote, omphacite, sodic-calcic amphibole, paragonite, rutile and
918 quartz. The margins contain inclusions of omphacite and rutile. The matrix contains

919 retrograde sodic-calcic amphibole but there are several domains where the high-pressure
920 assemblage is preserved. B) Most garnets in the weakly foliated sample A 623 have
921 idiomorphic cores bounded by concentric inclusion trails. Core inclusions consist of calcic
922 amphibole, rutile, titanite, carbonate and quartz. The inclusion-rich zone between core and
923 rim contains quartz, rutile and omphacite. The idiomorphic rims have inclusions of sodic-
924 calcic amphibole, omphacite and rutile/titanite. Rims are partly overgrown by irregularly
925 formed small garnets that form aggregates parallel to the main foliation (arrows). Scale bars
926 are 5 mm.
927
928 **Fig. 2:** a) The compositional X-ray mappings of a garnet from sample PAR 12 reveal a strong
929 zonation in major element chemistry with a very sharp compositional boundary between the
930 internal (inclusion-rich) and the external (inclusion-poor) zones. The magnitude of the
931 compositional variation is evident in the compositional profiles shown in b). Compositional
932 zoning in these garnets is characterised by slightly increasing grossular content from core to
933 inner rim followed by a drastic decrease towards the outer rim associated with a continuously
934 decreasing spessartine component and sharp increasing X_{Mg} at the outer rim.
935
936 **Fig. 3:** Compositional X-ray mappings (a) and electron microprobe profile (b) of a typical
937 garnet from sample A 623. The idiomorphic core is characterised by a homogeneous,
938 almandine-rich composition and is clearly separated by an inclusion-rich zone. In the core-
939 mantle transition zone, garnet chemistry changes drastically towards a more grossular- and
940 pyrope-rich composition. The idiomorphic grains are overgrown parallel to the weak foliation
941 by irregularly formed grossular-pyrope-rich aggregates (arrows).
942
943 **Fig. 4:** a) and b): Phase diagrams with contoured garnet mode (a) and grossular content in
944 garnet (b) calculated for a MORB chemistry representative for sample PAR 12. The white

arrows display the path along which the thermodynamic properties of the sample are modelled. The numbers along the arrows correspond with the P-T increments used for the calculations. The bold stippled line represents the solidus in a water saturated basaltic composition (Lambert and Wyllie, 1972, see text). c), d) and e): garnet chemistry (c), amount of newly formed garnet (d) and modal abundance of coexisting minerals (e) calculated along the selected P-T path assuming homogeneous equilibrium crystallisation and water saturation. f): Modelled garnet zonation displayed with a normalised radius. In contrast to the natural sample, the modelled garnet composition is characterised by continuously increasing grossular content from core to rim. See text for further discussion.

Fig. 5: Garnet chemistry (a), amount of newly formed garnet (b) and modal abundances of coexisting phases (c) modelled for sample PAR 12 along the selected P-T path assuming fractional garnet crystallisation and water fractionation. d) Resulting garnet zoning pattern displayed with a normalised radius. e) Measured garnet zonation in sample PAR 12 for comparison. In contrast to the models not considering fractionation effects, garnet growth stops at increment #48 and its composition towards the rim is characterised by strongly decreasing grossular content. See text for detailed discussion.

Fig. 6: P-T diagrams and contours for the modal amount of garnet (a and c) and grossular content in garnet (b and d) calculated for those bulk rock compositions that result from element fractionation along the considered P-T path till the sample reaches the epidote-out curve (a and b) and the garnet-out curve (c and d). The progression along the P-T trajectory is displayed by the solid arrows. Element fractionation along the P-T path influences the phase relations and garnet chemistry such that garnet growth from amphibole (a and b; causing decreasing grossular content) occurs over a larger P-T segment and stops shortly before the sample crosses the coesite/quartz transition (c and d). Note that contours are only drawn along

971 the P-T trajectory, because those diagrams are only valid along the modelled P-T path, as the
972 bulk rock composition is a path-dependent function. Zero mode lines are shown across the
973 entire grid for better overview.
974
975 **Fig. 7:** a) and b): Phase diagrams with contoured garnet mode (a) and grossular content in
976 garnet (b) calculated for the bulk rock composition of sample A 623. The white arrows
977 display the considered P-T path (same as in Fig. 4). c), d) and e): garnet chemistry (c), amount
978 of newly formed garnet (d) and modal abundance of coexisting minerals (e) calculated along
979 the selected P-T path assuming homogeneous equilibrium crystallisation and water saturation.
980 f): Modelled garnet zonation displayed with a normalised radius. As in the previous sample
981 garnet chemistry is characterised by steadily increasing grossular content from core to rim but
982 in contrast to sample PAR 12 the modelled composition assuming homogeneous
983 crystallisation largely resembles the naturally observed pattern in sample A 623.
984
985 **Fig. 8:** Garnet chemistry (a), amount of newly formed garnet (b) and modal abundances of
986 coexisting phases (c) modelled along the selected P-T path assuming fractional garnet
987 crystallisation and water fractionation. d) Resulting garnet zoning pattern displayed with a
988 normalised radius. e) Measured garnet rim-core-rim zonation in sample A 623 for
989 comparison. Due to the depleted bulk rock composition caused by element fractionation along
990 the P-T path garnet growth stops at increment #48 but, in contrast to sample PAR 12, restarts
991 at UHP conditions at increment #87 with a grossular-rich composition.
992
993 **Fig. 9:** P-T diagrams with contours for garnet mode (a) and grossular content in garnet (b)
994 calculated for the bulk rock composition at the end of the first garnet growth in sample A 623.
995 In contrast to sample PAR 12 the chosen P-T trajectory enters the garnet stability field at UHP
996 conditions above 3.0 GPa, where garnet is predicted to be grossular-rich (b).

997

998 **Fig. 10:** Comparison of modelled and measured compositions of amphibole (a) and

999 clinopyroxene (b) inclusions in garnet.

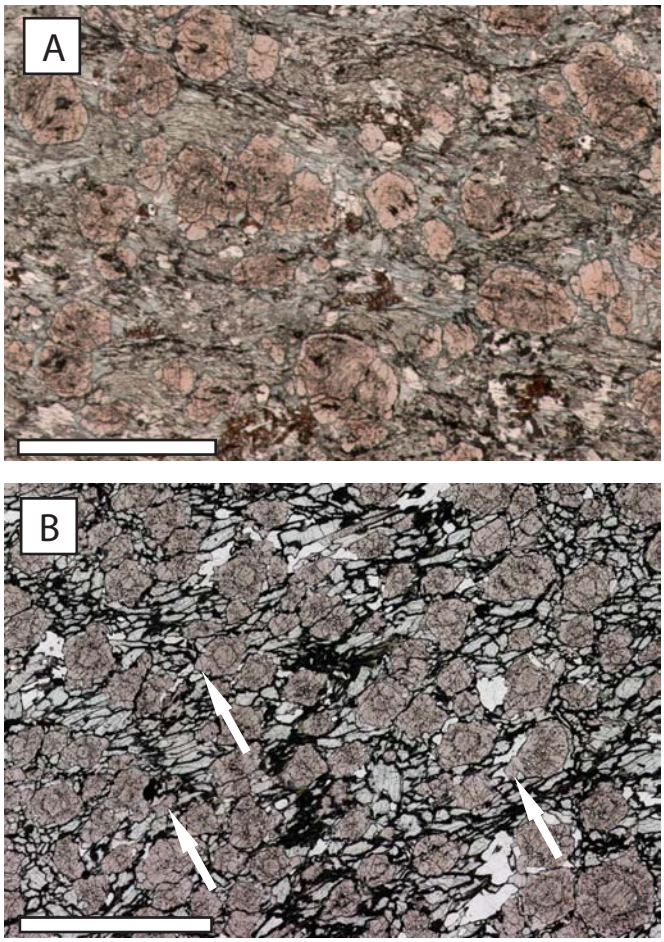
A
B

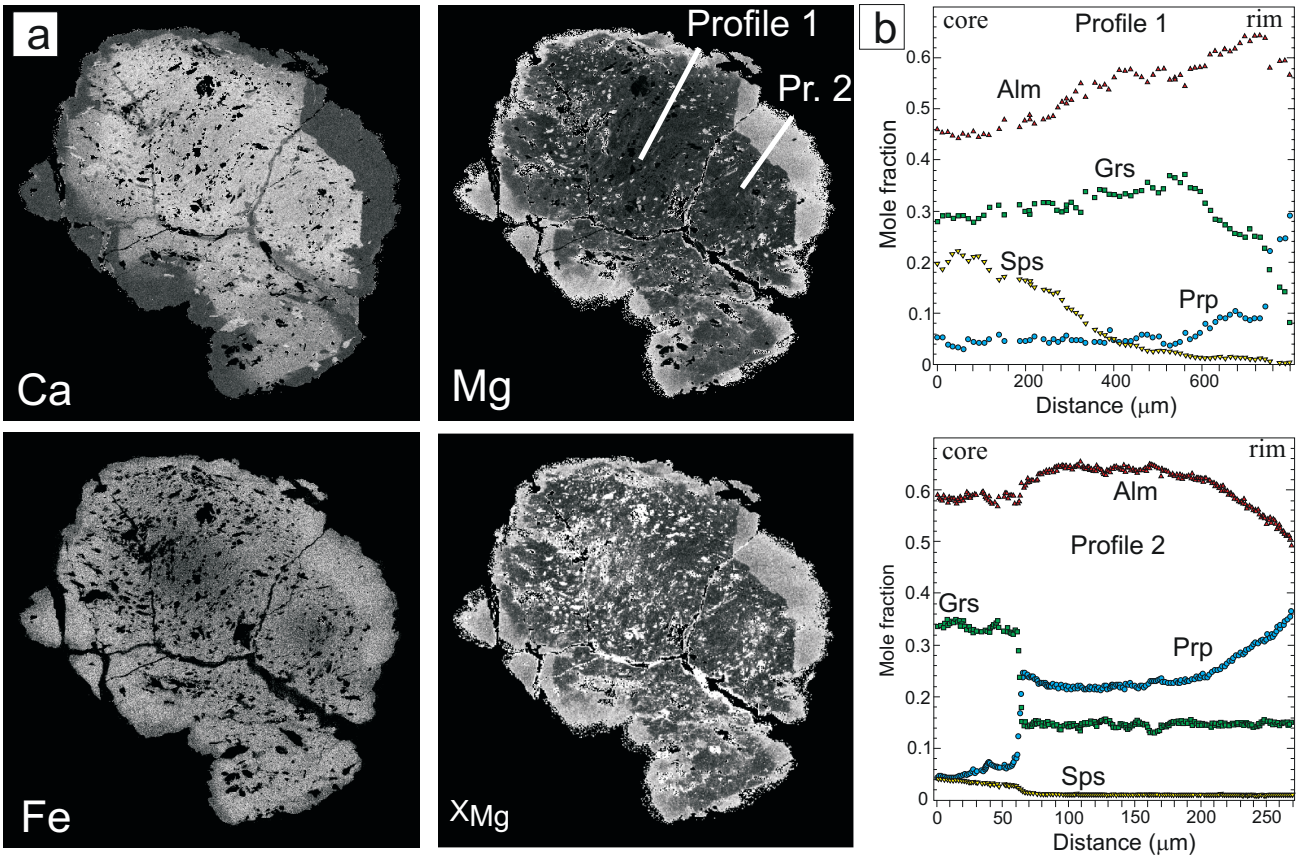
a
Ca
Mg
Profile 1
Pr. 2
Fe
XMg
b
core
Profile 1
rim
Alm
Grs
Sps
Prp
Mole fraction
Distance (μm)
core
rim
Alm
Profile 2
Grs
Prp
Sps
Mole fraction
Distance (μm)

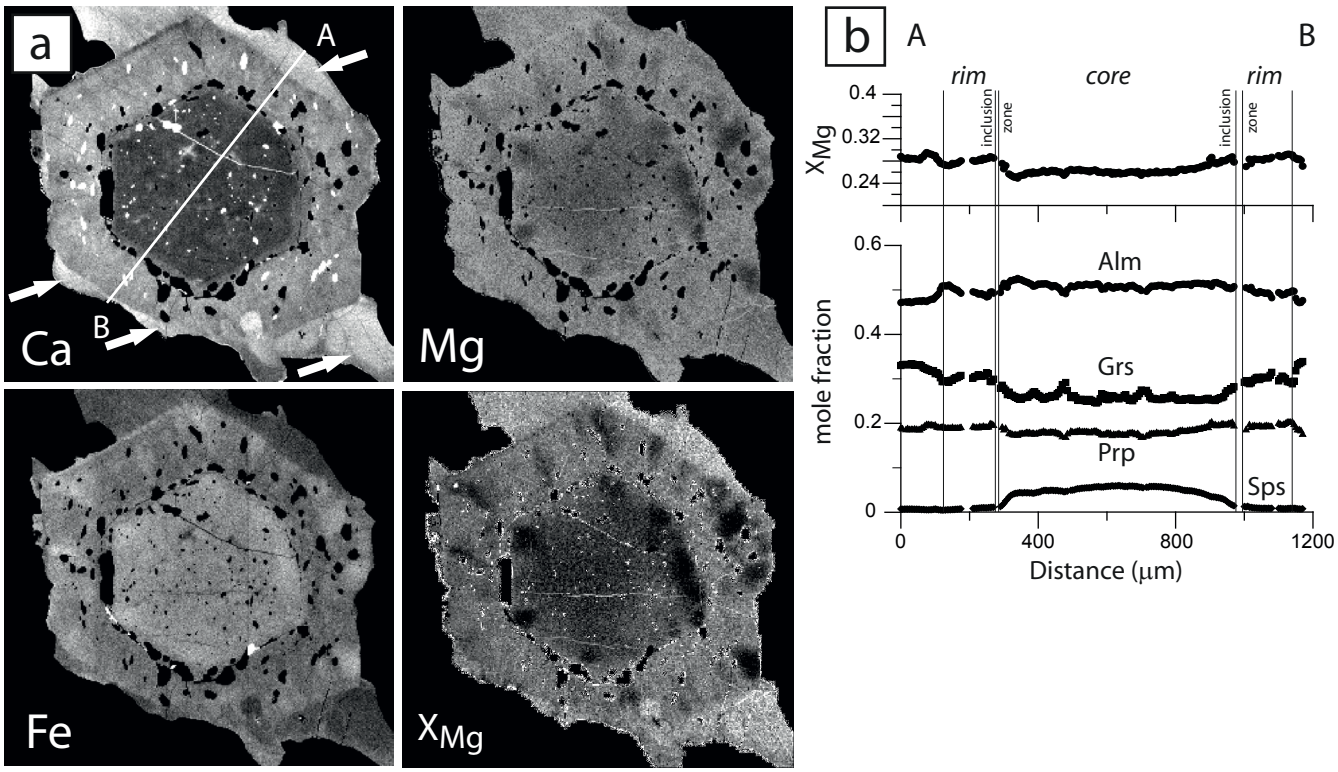
a
A
B
Ca
Mg
Fe
X_{Mg}
b
A
B
rim
core
rim
inclusion zone
inclusion zone
X_{Mg}
0.4
0.32
0.24
0.6
0.4
0.2
0
Alm
Grs
Prp
Sps
mole fraction
0
400
800
1200
Distance (μm)

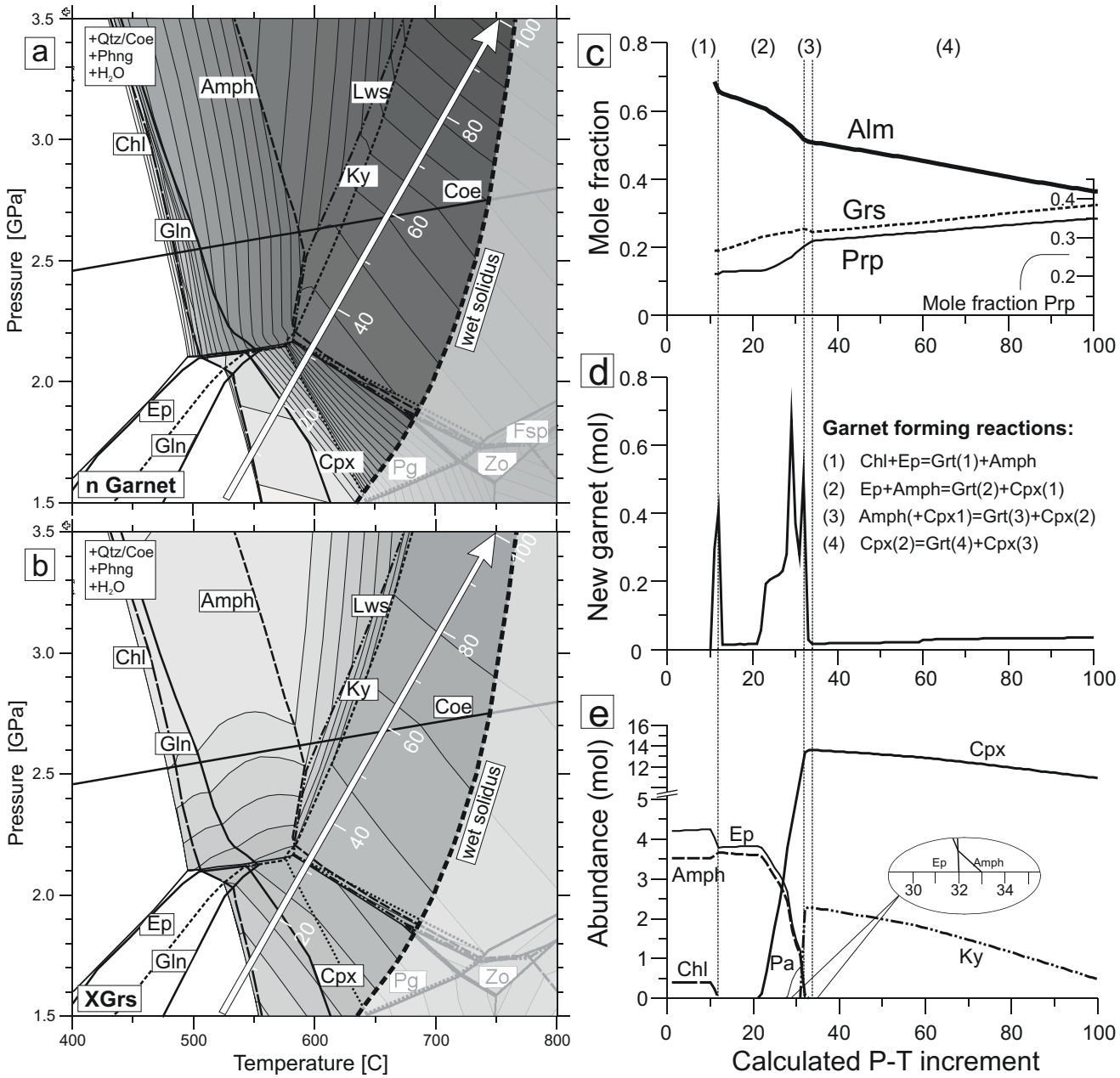
a
+Qtz/Coe
+Phng
+H2O
Amph
Lws
Chl
Ky
Coe
Gln
wet solidus
Ep
Gln
Cpx
Pg
Zo
Fsp
n Garnet
b
XGrs
Pressure [GPa]
Temperature [C]
c
(1) (2) (3) (4)
Alm
Grs
Prp
Mole fraction
Mole fraction Prp
d
New garnet (mol)
Garnet forming reactions:
(1) Chl+Ep=Grt(1)+Amph
(2) Ep+Amph=Grt(2)+Cpx(1)
(3) Amph(+Cpx1)=Grt(3)+Cpx(2)
(4) Cpx(2)=Grt(4)+Cpx(3)
e
Abundance (mol)
Cpx
Ep
Amph
Chl
Pa
Ky
Calculated P-T increment
f
Mole fraction
Normalised radius

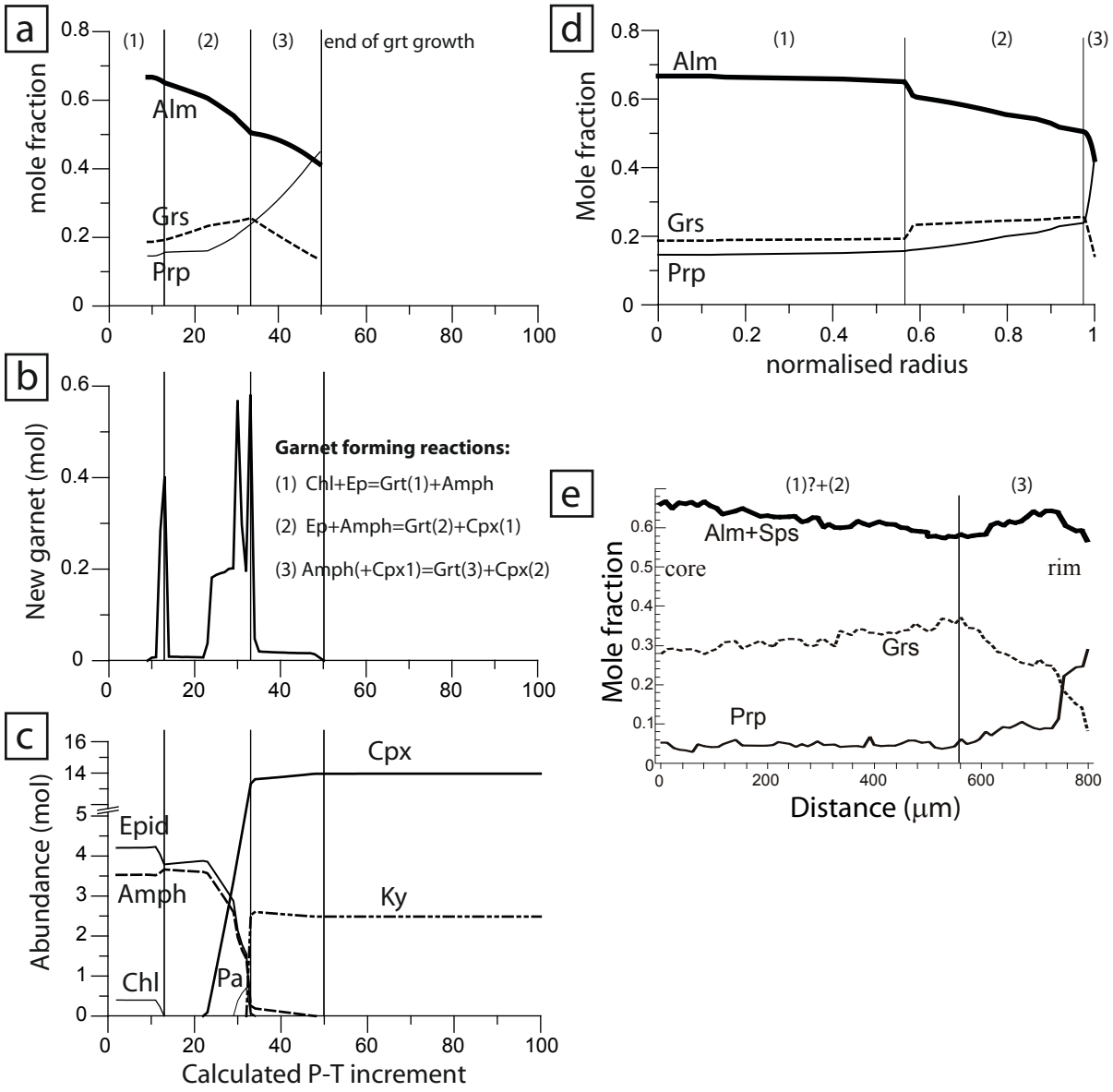
a
mole fraction
(1)
(2)
(3)
end of grt growth
Alm
Grs
Prp
b
New garnet (mol)
Garnet forming reactions:
(1) Chl+Ep=Grt(1)+Amph
(2) Ep+Amph=Grt(2)+Cpx(1)
(3) Amph(+Cpx1)=Grt(3)+Cpx(2)
c
Abundance (mol)
Epid
Amph
Chl
Pa
Cpx
Ky
Calculated P-T increment
d
Mole fraction
(1)
(2)
(3)
Alm
Grs
Prp
normalised radius
e
(1)?+(2)
(3)
Alm+Sps
core
rim
Grs
Prp
Mole fraction
Distance (μm)

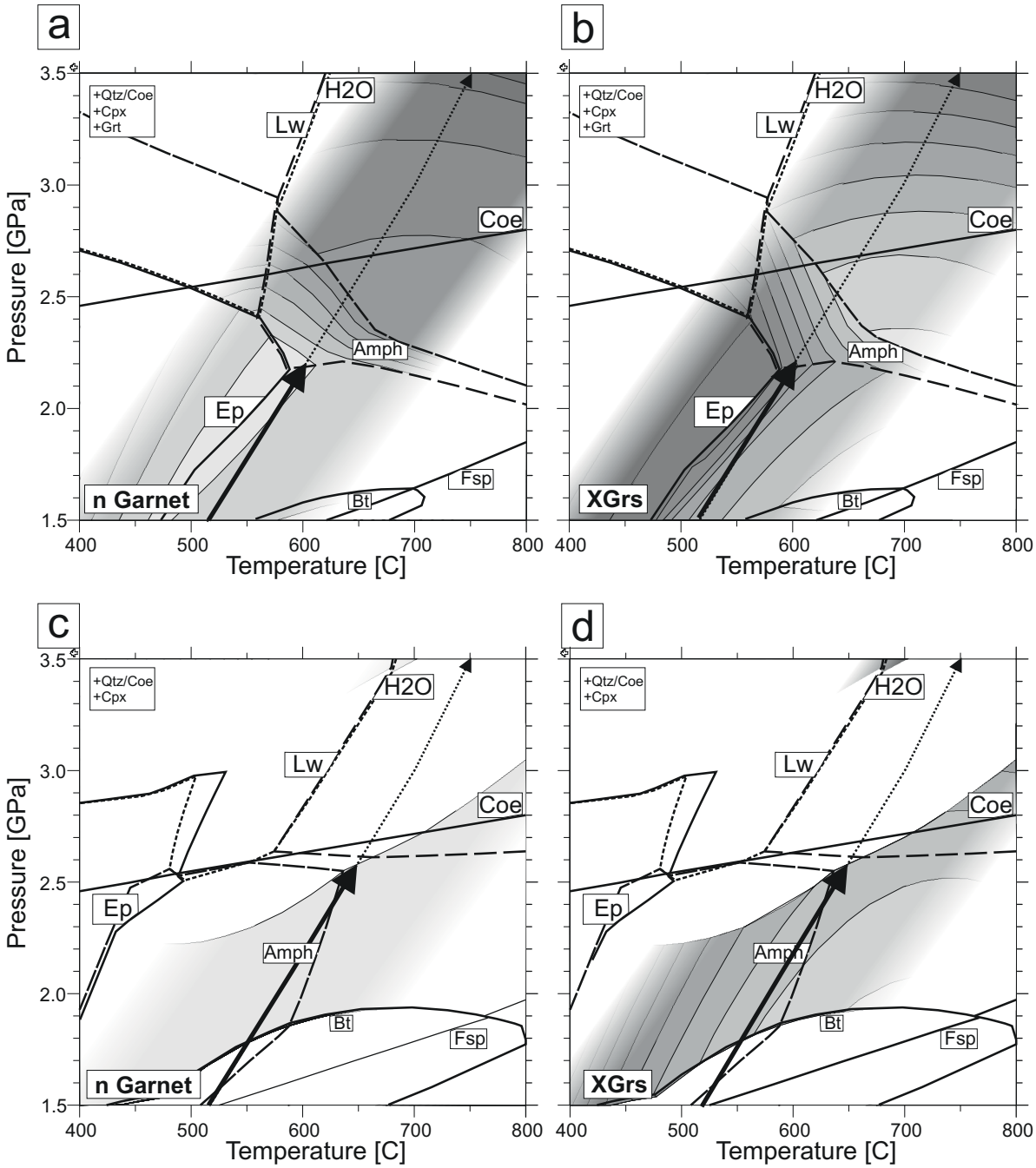
a
b
c
d
+Qtz/Coe
+Cpx
+Grt
H2O
Lw
Coe
Amph
Ep
Bt
Fsp
n Garnet
XGrs
Pressure [GPa]
Temperature [C]
3.5
3.0
2.5
2.0
1.5
400
500
600
700
800

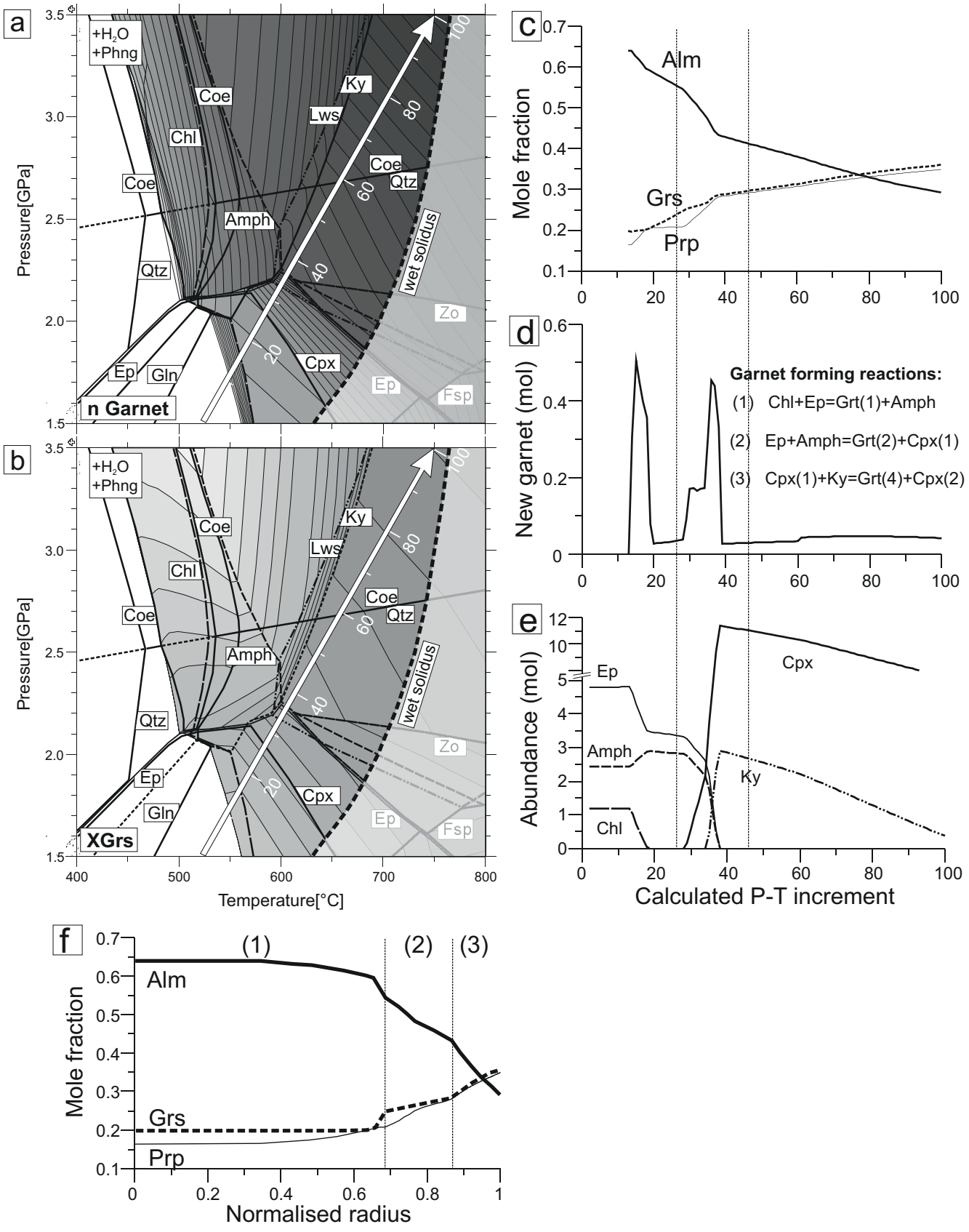
a
+H2O
+Phng
Coe
Chl
Coe
Amph
Qtz
Ep
Gln
Ky
Lws
Coe
Qtz
Cpx
Zo
Ep
Fsp
wet solidus
20
40
60
80
100
n Garnet
b
XGrs
Pressure[GPa]
Temperature[°C]
c
Alm
Grs
Prp
Mole fraction
d
New garnet (mol)
Garnet forming reactions:
(1) Chl+Ep=Grt(1)+Amph
(2) Ep+Amph=Grt(2)+Cpx(1)
(3) Cpx(1)+Ky=Grt(4)+Cpx(2)
e
Abundance (mol)
Ep
Amph
Chl
Cpx
Ky
Calculated P-T increment
f
(1)
(2)
(3)
Alm
Grs
Prp
Mole fraction
Normalised radius

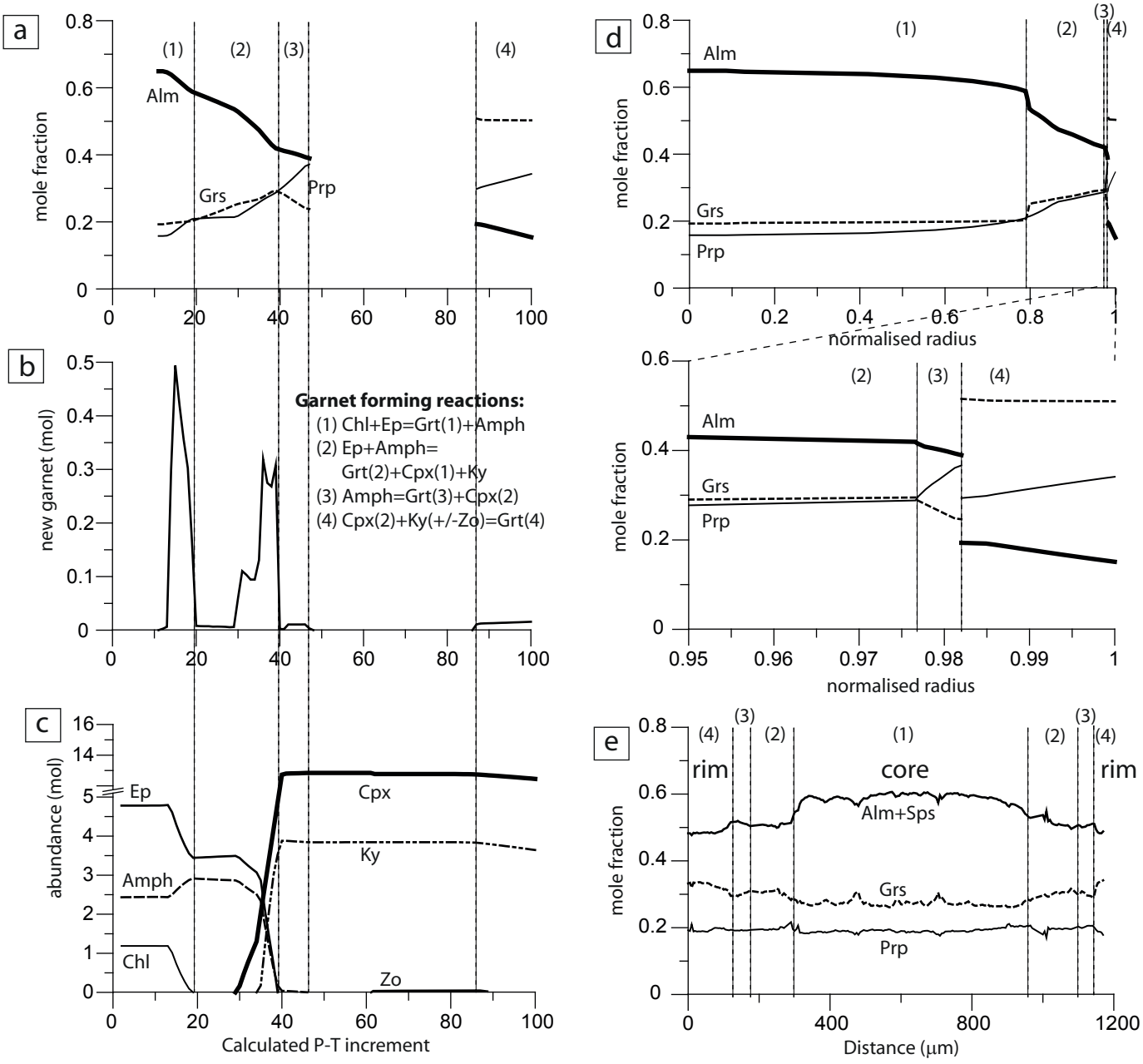
a
(1)
(2)
(3)
(4)
Alm
Grs
Prp
mole fraction
b
new garnet (mol)
Garnet forming reactions:
(1) Chl+Ep=Grt(1)+Amph
(2) Ep+Amph=
Grt(2)+Cpx(1)+Ky
(3) Amph=Grt(3)+Cpx(2)
(4) Cpx(2)+Ky(+/-Zo)=Grt(4)
c
abundance (mol)
Ep
Amph
Chl
Cpx
Ky
Zo
Calculated P-T increment
d
mole fraction
normalised radius
e
rim
core
rim
Alm+Sps
Grs
Prp
Distance (μm)

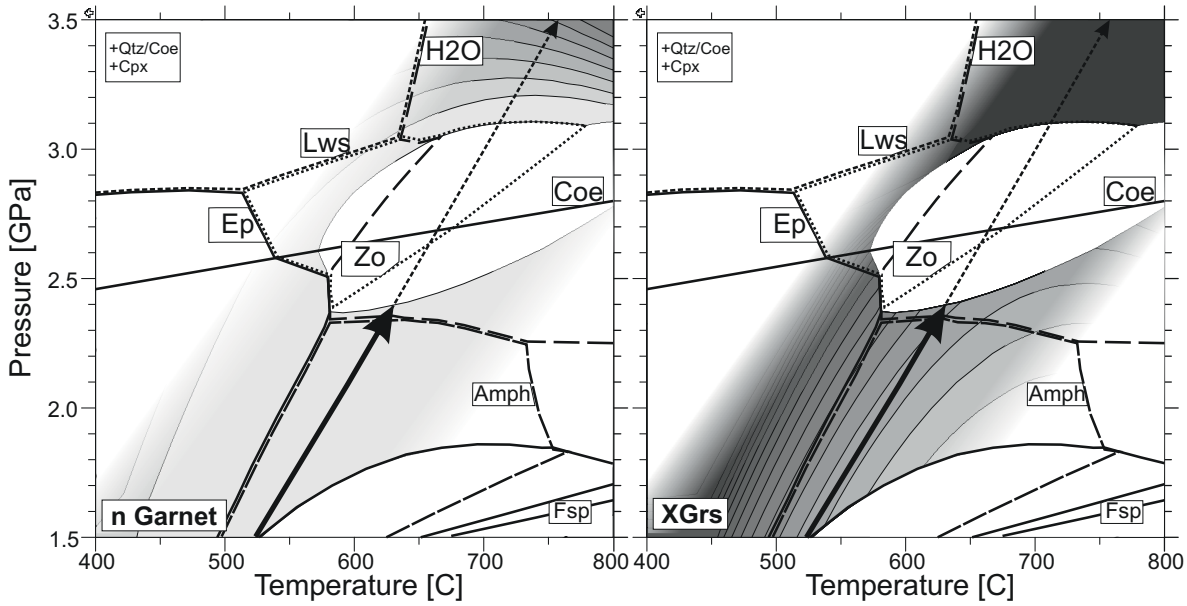
+Qtz/Coe
+Cpx
H2O
Lws
Coe
Ep
Zo
Amph
Fsp
n Garnet
XGrs
Pressure [GPa]
Temperature [C]
3.5
3.0
2.5
2.0
1.5
400
500
600
700
800

a) Ampohibole inclusions

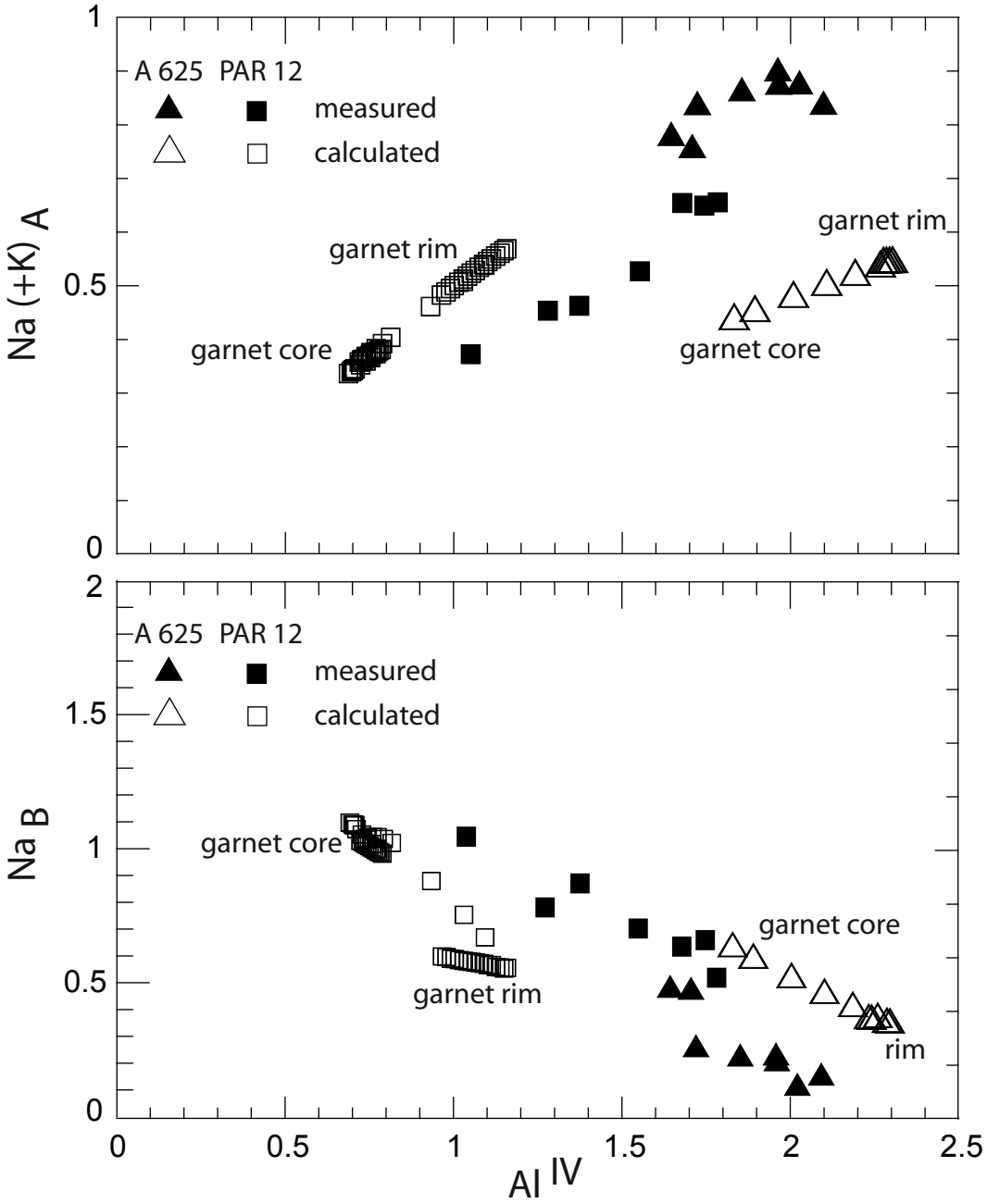

b) Clinopyroxene inclusions

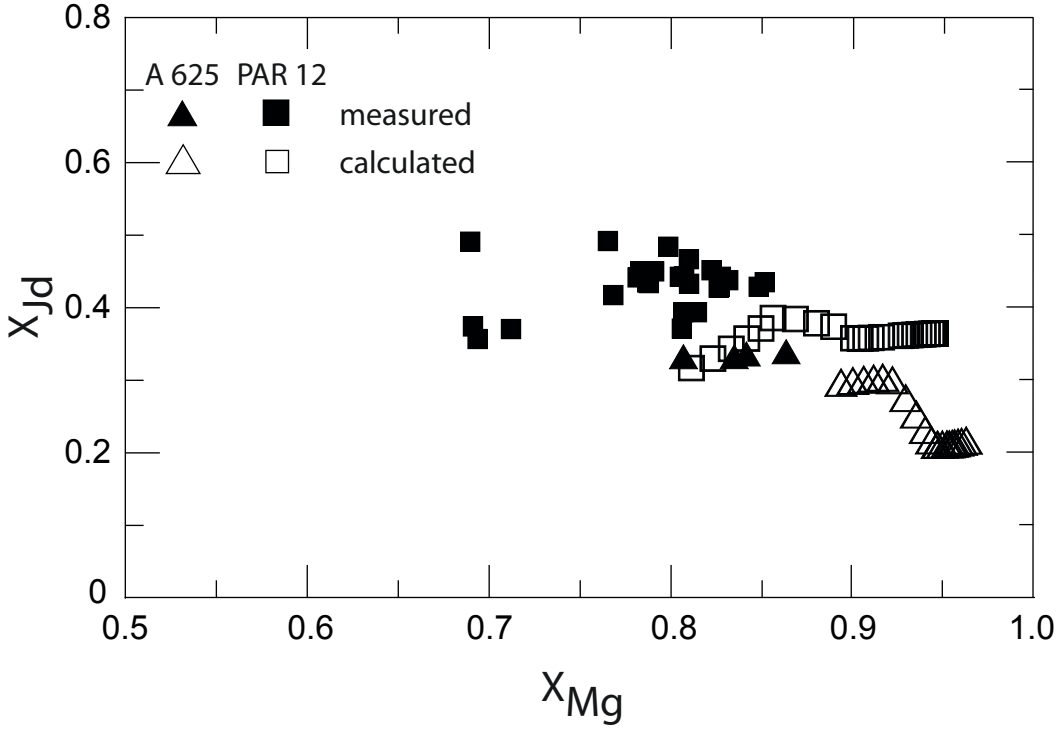

Elsevier Editorial System(tm) for Earth and Planetary Science Letters

Manuscript Draft

Manuscript Number: EPSL-D-08-00209R1

Title: Combined thermodynamic and rare earth element modelling of garnet growth during subduction: examples from ultrahigh-pressure eclogite of the Western Gneiss Region, Norway

Article Type: Regular Article

Keywords: ultrahigh-pressure metamorphism
garnet
trace elements
Western Gneiss Region
thermodynamic modelling
subdcution zone

Corresponding Author: Dr Matthias Konrad-Schmolke,

Corresponding Author's Institution: Universität Potsdam

First Author: Matthias Konrad-Schmolke

Order of Authors: Matthias Konrad-Schmolke; Thomas Zack; Patrick J O'Brien; Dorrit E Jacob

Abstract: Major- and trace element zonation patterns were determined in ultra-high pressure eclogite garnets from the Western Gneiss Region (Norway). All investigated garnets show multiple growth zones and preserve complex growth zonation patterns with respect to both major and rare earth elements (REE). Due to chemical differences of the host rocks two types of major element compositional zonation patterns occur: (1) abrupt, step-like compositional changes corresponding with the growth zones and (2) compositionally homogeneous interiors, independent of growth zones, followed by abrupt chemical changes towards the rims. Despite differences in major element zonation, the REE patterns are almost identical in all garnets and can be divided into four distinct zones with characteristic patterns.

In order to interpret the major and trace element distribution and zoning patterns in terms of the subduction history of the rocks, we combined thermodynamic forward models for appropriate bulk rock compositions to yield molar proportions and major element compositions of stable phases along the inferred pressure-temperature path with a mass balance distribution of REEs among the calculated stable phases during high pressure metamorphism. Our thermodynamic forward models reproduce the complex major element zonation patterns and growth zones in the natural garnets, with garnet growth predicted during four different reaction stages: (1) chlorite breakdown, (2) epidote breakdown, (3) amphibole breakdown and (4) reduction in molar clinopyroxene at ultrahigh-pressure conditions.

Mass-balance of the rare earth element distribution among the modelled stable phases yielded characteristic zonation patterns in garnet that closely resemble those in the natural samples. Garnet growth and trace element incorporation occurred in near thermodynamic equilibrium with matrix phases during subduction. The rare earth element patterns in garnet exhibit distinct enrichment zones that

fingerprint the minerals involved in the garnet-forming reactions as well as local peaks that can be explained by fractionation effects and changes in the mineral assemblage.

Combined thermodynamic and rare earth element modelling of garnet growth during subduction: examples from ultrahigh-pressure eclogite of the Western Gneiss Region, Norway

Matthias Konrad-Schmolke[1], Thomas Zack[2], Patrick J. O'Brien[1] and Dorrit E. Jacob[3]

[1]Universität Potsdam, Institut für Geowissenschaften, Karl-Liebknecht-Strasse 24-25, 14476 Potsdam, Germany

[2]Universität Heidelberg, Mineralogisches Institut, INF 236, 69120 Heidelberg, Germany

[3]Universität Mainz, Fachbereich Geowissenschaften, Becherweg 14, 55128 Mainz, Germany

Corresponding Author:

Matthias Konrad-Schmolke

Universität Potsdam

Institut für Geowissenschaften

Karl-Liebknecht-Strasse 24-25

14476 Potsdam

T: ++49 (0)331 977 5854

FAX: ++49 (0)331 977 5800

e-mail: mkonrad@geo.uni-potsdam.de

Abstract

Major- and trace element zonation patterns were determined in ultra-high pressure eclogite garnets from the Western Gneiss Region (Norway). All investigated garnets show multiple growth zones and preserve complex growth zonation patterns with respect to both major and rare earth elements (REE). Due to chemical differences of the host rocks two types of major element compositional zonation patterns occur: (1) abrupt, step-like compositional changes corresponding with the growth zones and (2) compositionally homogeneous interiors, independent of growth zones, followed by abrupt chemical changes towards the rims. Despite differences in major element zonation, the REE patterns are almost identical in all garnets and can be divided into four distinct zones with characteristic patterns.

In order to interpret the major and trace element distribution and zoning patterns in terms of the subduction history of the rocks, we combined thermodynamic forward models for appropriate bulk rock compositions to yield molar proportions and major element compositions of stable phases along the inferred pressure-temperature path with a mass balance distribution of REEs among the calculated stable phases during high pressure metamorphism. Our thermodynamic forward models reproduce the complex major element zonation patterns and growth zones in the natural garnets, with garnet growth predicted during four different reaction stages: (1) chlorite breakdown, (2) epidote breakdown, (3) amphibole breakdown and (4) reduction in molar clinopyroxene at ultrahigh-pressure conditions.

Mass-balance of the rare earth element distribution among the modelled stable phases yielded characteristic zonation patterns in garnet that closely resemble those in the natural samples. Garnet growth and trace element incorporation occurred in near thermodynamic equilibrium with matrix phases during subduction. The rare earth element patterns in garnet exhibit distinct enrichment zones that fingerprint the minerals involved in the garnet-forming reactions as well as local peaks that can be explained by fractionation effects and changes in the mineral assemblage.

Introduction

Input parameters for subduction zone models have so far primarily come from indirect evidence, such as the interpretation of geophysical observations and the elemental and isotopic signatures of subduction-related volcanic rocks (Gill, 1981; Tatsumi and Eggins, 1995), whereas the full potential of rock samples that were deeply subducted have not yet been greatly exploited for modelling parameters. In recent years, partly due to the rapid development of micro-analytical techniques enabling precise in situ analysis of trace elements and their isotopes, another source of information has become the focus of many investigations: namely exhumed high pressure (HP) and especially ultra-high pressure (UHP) metamorphic rocks (Bebout et al., 2007; Zack and John 2007). Such UHP rocks, formerly part of the downgoing slab, were subducted to depths of 100 km or more, where they underwent metamorphic reactions that result in complex element fractionation and mantle metasomatism inherent during subduction and thus record directly information about many subduction-related processes. However, extraction of information about high-pressure processes from exhumed subduction-zone rocks is not straightforward because chemical re-equilibration during pro- and retrograde metamorphism is commonly pervasive, thereby erasing large parts of the metamorphic record and the history of subduction.

On account of their refractory character and their propensity to preserve growth zoning, one of the best sources of information about the subduction process is commonly preserved in zoned metamorphic garnets formed on the prograde segment in HP and UHP settings (O'Brien 1997; King et al., 2004; Konrad-Schmolke et al., 2006). Due to sluggish intracrystalline diffusional equilibration the cores of garnet porphyroblasts become isolated from the reacting rock volume during garnet growth and thus preserve important information about previous stages in the metamorphic evolution. Because garnet chemistry is highly sensitive to physical and chemical changes in the host rock (Konrad-Schmolke et al., 2007), major element growth zonation in HP and UHP garnets can be used to determine the pressure,

temperature and chemical evolution of the sample in which it occurs (e.g., Spear 1988c). This is primarily achieved by thermodynamic forward modelling (e.g., Spear 1988b; Konrad-Schmolke et al., 2005) which, depending on the particular problem, can predict the physical-chemical properties of the downgoing slab along a defined subduction path (e.g., Connolly 2005; Konrad-Schmolke et al., 2006). With some simplifications and assumptions, the influence of intensive (e.g. pressure and temperature) and extensive (e.g. element fractionation) parameters on specific aspects of the system, such as garnet growth and composition, can be investigated. By comparing model results with the composition of natural garnets it is possible to interpret complex chemical growth and zonation patterns in terms of the pressure-, temperature- and bulk compositional evolution of their host rocks.

In addition to major-element compositional variations in (U)HP garnets there is commonly also a well developed trace element zonation that may provide information on element transport processes or mineral reactions in the host rock (e.g., Bollingberg and Bryhni 1972; Hickmott and Shimizu 1990). Trace element zonation in garnet is of particular importance for establishing rates of processes, because radiogenic isotopes used to determine absolute ages of growth steps, such as those of Sm and Lu, are especially enriched in garnet (Lapen et al., 2003; Kylander-Clark et al., 2007).

In this work we combine the results from thermodynamic forward models that yield detailed information on changing molar proportions and major element composition in garnet along a subduction-zone P-T path with a mass balance distribution of rare earth elements (REE) among the calculated stable phases. We will concentrate on a comparison of the modelled REE patterns with data from well-studied natural samples (garnet of eclogites from the Norwegian Western Gneiss Region) with the aim of interpreting both major- and trace element zonation patterns in terms of changing mineral assemblages and mineral proportions in a dynamic subduction-zone setting.

Analytical methods

Major element mapping and compositional profiles were carried out with a JEOL 8800 electron microprobe at the Mineralogisches Institut, Freie Universität Berlin equipped with five wave length dispersive spectrometers. For the analyses we used 1 μm beam size, calibration was carried out with natural standard materials and data correction involved the ZAF algorithm. Trace element contents were measured with the laser ablation ICP MS system at the Intitut für Geowissenschaften, Universität Mainz, equipped with a New Wave UP213 (Nd:YAG, 213 nm wavelength) laser system coupled to an Agilent 7500ce quadrupole inductively coupled plasma mass spectrometer (Jacob 2006). A total of 26 isotopes were selected for trace element analysis with a dwell time of 100 ms for each mass, 40 seconds of ablation, and a beam size of 50μm. For standardisation we used the NIST SRM 612 glass with Si as the normalizing element and the USGS BCR2-G glass was analysed as a secondary standard. Spot analysis quality was ensured by time-resolved signal analysis using the software "Glitter" and an analysis is only reported if a stable ablation signal of at least 10 seconds was recorded. We detected signals from inclusions by abnormally high and irregular counts rates for Sr (epidote, apatite), P (apatite), Zr (zircon) and Rb (fluid inclusions and cracks). Sections of a signal or a full analysis were discarded if ablation patterns of REE correlate with these elements. For further discussion on LA-ICP-MS quality controls in eclogitic assemblages see Zack et al., 2002. Note that REEs lighter than Eu were not considered in our interpretation because their abundances in garnet were too low to be precisely analysed in this mode of operation.

Sample description

For this study we investigated five samples from different UHP outcrops in the southern part of the Western Gneiss Region (WGR), Norway, where estimated peak conditions were 750-800°C and 3.0 GPa (Wain et al., 2000). Two of these samples, which show the most distinctive major and trace element zoning patterns, were selected to investigate their significance with respect to subduction processes.

Sample 714-3 was selected from the well-known outcrop near Verpenesset (Bryhni and Griffin 1971; Krogh 1982) and sample A 623 comes from an outcrop near Krokken, about 5 km west of the Verpenesset outcrop (Cuthbert et al., 2000). The eclogite in both outcrops occur as decametre-sized lenses within felsic gneisses. The Verpenesset samples are coarse-grained and preserve relics of coesite and/or polycrystalline quartz (PCQ) aggregates in matrix omphacites, whereas UHP metamorphism in the medium-grained Krokken sample can only be deduced from the interpretation of the garnet major element zonation patterns Konrad-Schmolke et al., 2007). All selected samples preserve the characteristic peak metamorphic assemblage garnet + clinopyroxene + rutile ± phengite ± quartz/coesite. The samples also contain kyanite and zoisite that both appear to be part of the stable peak metamorphic assemblage. Sample A 623 additionally contains calcite, which is found as inclusions in clinopyroxene and garnet as well as in the matrix. The peak assemblage in all samples is only weakly affected by later retrograde overprint, which mainly caused the development of amphibole-plagioclase symplectites along grain boundaries as well as narrow titanite ± ilmenite-rims around rutile grains.

Garnet

Garnet in the selected samples is idiomorphic to subidiomorphic, between 0.5 and 3 mm in diameter (depending on the overall sample grain size) and shows visible growth zones (Fig. 1) indicating multi-stage growth. Cores, commonly idiomorphic, are bounded by concentric inclusion trails that define mostly hexagonal shapes of the garnet interiors. Mineral inclusions in the cores are randomly oriented and consist of quartz, epidote, rutile and sodic-calcic amphibole and in sample A 623 also titanite. The concentric inclusion-rich zone between core and the first overgrowth zone contains predominantly quartz, minor rutile and omphacite. The first overgrowth zone has fewer but larger inclusions of quartz, omphacite, sodic-calcic amphibole and rutile (+ titanite in case of sample A 623). Along the rims of

several garnets, small irregularly-formed and almost inclusion-free overgrowth zones can also be found (white arrow in Fig. 1). Where present, inclusions in these overgrowth zones are clinopyroxene and rutile.

In samples from both locations, garnet reveals two different major element zonation patterns (Fig. 1). One type reflects a multi-stage growth with distinctive compositional trends within each growth zone and step-like compositional gradients between the different zones (Fig. 1, sample A 623). A second zoning pattern shows less significant compositional changes at the inclusion zone, but exhibits a dramatic compositional change at the outermost rims of the garnets (Fig. 1, sample 714-3).

The compositional maps and profiles of the garnets in sample A 623 clearly define a core and two overgrowth zones (Fig. 1). Cores have constant grossular and almandine contents and show increasing pyrope and X_{Mg} tied to decreasing spessartine towards the outer part of the core. Across the core-inner overgrowth transition marked by the inclusion trails, garnet composition changes abruptly: grossular increases to values around Grs_{33}, pyrope and almandine decrease to Prp_{17} and Alm_{45}. Garnet composition is more or less constant in the inner overgrowth zone but towards the rim of this zone pyrope and almandine increase sharply to values around Prp_{25} and Alm_{50}, whereas grossular decreases to values near Grs_{25}. The irregularly-shaped and discontinuous outer overgrowth zones show decreasing pyrope and almandine and increasing grossular content towards the rim.

Garnet in sample 714-3, typical of the second type of zonation pattern, also exhibits signs of multi-stage growth indicated by inclusion-rich cores outlined by concentric inclusion zones. However, in contrast to the garnets in sample A 623, the boundary is less pronounced and, apart from minor changes in Mg and Fe, not associated with an abrupt compositional change (Fig. 1). From the core to the inclusion-rich zone the composition is approximately constant ($Grs_{27}Alm_{45}Prp_{25}Sps_3$) and at the outer (overgrowth) zone grossular, almandine and

spessartine contents slightly decrease as pyrope increases. In the outermost 200 microns the fall in almandine and rise in pyrope is sharper. As in the previous sample, X_{Mg} is highest in the outermost parts of the garnet grains but in sample 714-3 it correlates with the lowest grossular contents whereas in A 623 the highest X_{Mg} values correlate with highest grossular contents.

Rare earth element zonation

Investigated garnets show significant core-to-rim changes in the REE profiles and normalised REE patterns but, despite the differences in major element zonation, the distribution of REE patterns is almost identical in both samples. The core-to-rim profiles (Fig. 2) for each individual element show certain variations depending on atomic number. HREEs, as typified by a plot of Lu, have high values in the core with a prominent maximum in the innermost core (arrow) and, apart from a small hump towards the outer part of the first overgrowth zone, significantly lower values towards the garnet rim. The profiles of the lighter REEs, such as Er, also have a maximum in the core and lower values in the overgrowth zones, albeit with a slightly climbing trend, but are characterised by a striking intermediate peak (arrow) near the rim of the first overgrowth zone. The profiles for Dy and Eu also show higher values in the core than in the overgrowth zones but here the dominant feature is the very sharp increase towards the rim which continues in the second overgrowth zone.

The REE core-to-rim variations can be divided into four distinct zones (Figs. 1 and 2), that are best visualised by normalised REE patterns from Eu to Lu, as demonstrated in Fig. 2. The core is characterised by steeply increasing normalised REE patterns from Eu to Lu and a strong, continuous HREE decrease towards the outer core (Zone 1). The medium REE (MREE) content remains constant in Zone 1. Towards the inner part of the first overgrowth zone (Zone 2) the HREEs show a sudden decrease of more than one order of magnitude. Also the MREE concentration slightly decreases, which results in a moderately convex upward

normalised REE pattern that hardly changes across the inner half of the first overgrowth zone (Zone 2). Towards the outer part of the first overgrowth zone (Zone 3) the REE pattern is characterised by a drastic increase in Dy, Ho and Er whereas the increase in the heavier and lighter REE concentrations is only limited. In the outermost parts of the first overgrowth zone, as well as in the small Ca-rich outer overgrowth zones, the REE pattern is characterised by an increase in the MREEs associated with a slight decrease in the HREEs resulting in a strongly convex upward pattern with a maximum between Tb and Dy (Zone 4).

Although the major element zonation in sample 714-3 is significantly different, the normalised REE patterns closely resemble that in sample A 623. Again four different zones with characteristic normalised REE patterns can be observed (Fig. 3). From the core to the inclusion-rich zone the REE patterns are characterised by strongly decreasing HREE contents (Zone 1). In contrast to the previous example, also the MREEs are continuously depleted from inner to outer core. At the innermost part of the overgrowth zone (Zone 2) the REE patterns start to change and Dy, Ho and Er start to increase towards the rim (Zone 3). The REE patterns in the rim are characterised by a drastic increase of MREEs associated with a strong decrease in the HREE. As in sample A 623 these REE patterns are also reflected in the REE profiles where the characteristic elements Lu, Er, Dy and Eu show broadly the same core-to-rim zonation as in the previous example.

Major and trace element forward modelling

Modal proportions and composition of stable phases were calculated at 100 increments along a high pressure P-T trajectory ($P(T) = 0{,}0278\ T^2$) that starts in the chlorite stability field at 530°C/1.8 GPa and ends at coesite-stable conditions at 830°C/3.3 GPa. It was chosen to cross the zero mode lines of the observed matrix and inclusion phases in our samples, such as garnet, epidote, amphibole, zoisite and coesite in order to study the effect of reactions among these phases on the trace element budget in UHP rocks. Phase relations were calculated by

thermodynamic forward modelling (cf. Spear et al., 1984; Konrad-Schmolke et al., 2005) with consideration of water fractionation and fractional garnet crystallisation in the chemical system Na, Ca, K, Fe, Mg; Al, Si, O, H (NCKFMASH) utilising Gibbs energy minimisation performed with the software package Perple_X (Connolly and Kerrick 1987) and the Holland and Powell (1998) database with recent updates (see electronic supplementary material for solid solution models). The chemical potential of oxygen was constrained by an ilmenite-magnetite-rutile buffer (cf. Konrad-Schmolke et al., 2007). The key aspects of the thermodynamic models are discussed in Konrad-Schmolke et al. (2007).

For REE modelling we assume that REEs in the system behave thermodynamically passively, i.e. without major influence on the composition and stability of the phases, and that the distribution of REEs among the stable phases can be described by bulk partition coefficients. With this assumption we calculated the REE distribution among the modelled phases at every calculated P-T increment using mass balance constraints and an internally consistent set of partition coefficients (Table 1). REEs incorporated in garnet and water were fractionated from the system according to the modelled modal amounts of these phases. Whereas the amount of REEs incorporated in the fluid phase (in our calculations between 0.002 ppm (Eu) and 0.05 ppm (Yb)) leads to bulk rock depletion, the REEs incorporated in refractory garnet (between 0.3 ppm (Eu) and 4.4 ppm (Dy)) only deplete the effective, i.e. the reacting bulk rock composition.

Sample A 623

Garnet growth calculated for sample A 623 along the considered P-T path is predicted to occur in three stages (Fig. 4) that can be correlated with four distinct garnet forming reactions. The first garnet (between increments #12 and 29) is predicted to form from chlorite, epidote and quartz by reaction (1):

chlorite + epidote + quartz =

(almandine-rich) garnet (1) + calcic amphibole + water. (1)

After chlorite consumption garnet growth is interrupted and restarts at increment #34 with reaction (2):

(sodic-calcic) amphibole + epidote = garnet (2) (with increasing grossular content)

+ clinopyroxene (1) + kyanite + quartz + water. (2)

This reaction forms a grossular-rich overgrowth zone with slightly lower pyrope content than the outer core. During the rapid epidote breakdown at the end of reaction (2) garnet composition becomes poorer in grossular and additional kyanite is formed. Beyond epidote stability the new garnet forming reaction is

Sodic-calcic amphibole + clinopyroxene (1) =

garnet (3) + clinopyroxene (2) + quartz + water. (3)

After the consumption of amphibole, garnet growth is again interrupted and restarts at UHP conditions with grossular-rich compositions formed by reaction (4):

Clinopyroxene (2) + kyanite = garnet (4) + clinopyroxene (3) + quartz (4)

Each of these garnet-forming reactions produces garnet with a characteristic chemical zonation pattern (Fig. 4).

Fig. 5a shows the calculated REE content in garnet, the abundances of coexisting phases and garnet composition modelled along the P-T trajectory. Mineral abundances and garnet composition are plotted relative to the normalised radius of a modelled garnet grain. The diagrams show a direct correlation among modelled garnet-forming reactions, garnet major element chemistry and its changing REE patterns. The almandine-rich garnet cores, formed mainly by the consumption of chlorite (reaction 1), are characterised by continuously decreasing HREE contents from inner to outer core. This HREE depletion is due to the continuous, preferential extraction of HREEs from the matrix, caused by fractional garnet

crystallisation and limited REE liberation from matrix phases due to the almost constant modal amounts of epidote and increasing modal amphibole. The effect of HREE fractionation can also be seen in the REE patterns in garnet shown in Fig. 5b. During the first part of reaction (2), where garnet grows from epidote and amphibole, the trend in the REE profile does not change significantly. At the onset of reaction (2), the effective bulk rock composition (EBC) is strongly depleted in HREE and the fractionation effect caused by garnet growth is limited, but towards the end of reaction (2) epidote and amphibole abundances change drastically, which causes liberation of predominantly medium to heavy REEs according to the REE patterns in these phases. As a result of epidote breakdown, the REE pattern in garnet changes significantly and the modelled REE profile is characterised by an increase in Er, Dy and, although less pronounced, in Lu (Fig. 5a). The REE pattern in garnet after the epidote-out reaction is characterised by a peak between Ho and Er and similar contents of MREE and HREE (Fig. 5b).

At the beginning of reaction (3) there is only little change in the REE pattern and in the REE profile in garnet. The sudden increase in Er and Dy at the end of reaction (2) is attenuated and Lu decreases. At the end of reaction (3), the MREE, displayed by Eu and Dy (Fig. 5a), show a drastic increase, whereas the increase in Er is only limited and Lu even further decreases. This trend is clearly visible in the changing REE pattern (Fig. 5b). At the end of reaction (3), i.e. beyond amphibole stability, the REE pattern shows a maximum at Tb and Dy and is characterised by more or less decreasing contents from MREE to HREE. At UHP conditions garnet grows from clinopyroxene and kyanite in the presence of a minor but constant amount of zoisite (reaction (4)). The modelled REE trend in garnet during this reaction is, similar to the chlorite breakdown reaction, characterised by a strong decrease of HREEs and a moderate change in MREEs. During reaction (4) the amount of zoisite in the assemblage largely controls the MREE concentration in garnet (small arrows in Fig. 5),

whereas the drastic change in the HREEs is controlled by EBC depletion due to fractional garnet crystallisation.

Sample 714-3

Due to small differences in bulk rock compositions, the modelled phase relations in sample 714-3 are slightly different to those in A 623 (Fig. 6a). In contrast to A 623, garnet growth in sample 714-3 occurs in two stages and there are only three garnet forming reactions involved. The first garnet in sample 714-3 is predicted to grow from chlorite, epidote and quartz (reaction 1), which form the almandine-rich garnet cores together with amphibole, kyanite and water. After chlorite consumption, garnet growth is interrupted and renewed garnet growth starts with the consumption of epidote and amphibole (reaction 2). As in sample A 623, epidote is completely consumed at increment #47, but the sudden rise in the grossular component is less pronounced in sample 714-3. Interestingly, amphibole stability in sample 714-3 is predicted to be larger than in A 623, resulting in a drastic grossular decrease during reaction (3), which ends at increment #80 shortly above the qtz/coe transition. Reaction (4) cannot be observed in this sample.

The phase relations in sample 714-3 determined by thermodynamic forward modelling, are similar to those in sample A 623 and although the resulting garnet composition is different, the same garnet forming reactions are involved. Consequently, the modelled REE profiles and the REE patterns in this sample broadly resemble those in A 623 (Fig. 6a and b). The garnet cores formed by reaction (1) are characterised by a strong HREE fractionation resulting in a drastic decrease in Lu from inner to outer core. This trend is, although still visible in the REE pattern, slightly attenuated during reaction (2). At the end of reaction (2), where epidote is completely consumed, the REE trend changes and develops its typical convex shape with a maximum between Dy and Er (Fig. 6b). During reaction (3) amphibole is

consumed and the resulting change in the REE profiles and the REE pattern is characterised by drastically increasing MREEs (Fig. 6b).

Discussion

Comparison and interpretation of modelled and observed zoning patterns

A comparison of modelled and observed garnet growth zonation patterns (cf. Figs. 2, 3, 5 and 6) reveals that the complex major- and REE growth zonation in the natural samples is accurately reproduced in our models. Additionally, the multistage garnet growth that is evident in the samples and the compositional trends within the different growth zones can be correlated with specific garnet-forming reactions that control the major-element and REE patterns in garnet. Thus, we conclude that the modelled features provide confirmation of the inferred reaction history during subduction.

Although our modelling shows that the M- and HREEs behave almost essentially passively with respect to their thermodynamic influence on the modes and compositions of stable phases, the petrologic interpretation of REE zoning patterns in metamorphic minerals, especially refractory phases, such as garnet, is not straightforward. Generally, four different chemical processes can significantly influence the REE zoning in refractory phases: (1) continuously changing REE concentrations in the rock and the EBC due to element fractionation processes (Hickmott and Shimizu 1990), (2) mineral reactions, including resorption of previously crystallised garnet, that liberate REEs or change their bulk partition coefficients (e.g., Hickmott et al., 1987; Spear 1988c; King et al., 2004), (3) diffusion- or surface-processes that hinder REE incorporation into garnet (e.g., Watson 1996; Chernoff and Carlson 1999; Skora et al., 2006) and (4) modification of growth zonation due to intracrystalline volume diffusion (e.g., Tirone et al., 2005). The focus of this work is on differentiating between the effects of element fractionation and mineral reactions on the REE pattern in garnet as well as a possible distinction between equilibrium and disequilibrium REE

distribution during subduction. Due to the preservation of step-like compositional gradients even in relatively fast diffusing elements such as Mg and Fe (Fig. 1) we assume that the effect of intracrystalline volume diffusion is minor in our samples, most likely reflecting the relatively low peak metamorphic temperatures.

The modelled changes in the REE pattern in garnet can be interpreted as a result of several effects. Firstly, the change in the REE pattern in garnet during reaction (1) is caused by the HREE depletion of the EBC as a result of fractional garnet crystallisation (Rayleigh fractionation; Otamendi et al., 2002) and the limited liberation of REE from the reactant phases (mainly chlorite). All modelled REE-bearing phases show the same normalised patterns, i.e. decreasing Dy/Lu during reaction (1) that is observed in the natural samples. The garnet cores in both samples as well as the measured matrix zoisites compared to the epidote inclusions show continuous HREE depletion with ongoing garnet crystallisation. A detailed comparison of measured and modeled phase compositions can be found in the electronic supplementary material.

Reaction (2) leads to a re-distribution of REE from epidote into amphibole and garnet, whereby, according to the partition coefficients, MREE are preferentially incorporated into amphibole rather than garnet, resulting in a modelled increase of MREEs in amphibole after the epidote-out reaction. Unfortunately, the amphibole inclusions were too small to extract precise REE concentrations, which hinders a reliable correlation of the model results with inclusion data. Due to the higher MREE/HREE ratio in epidote compared to garnet, epidote breakdown causes a compositional trend towards the incorporation of lighter REEs in refractory garnet that is reflected in the measured garnet REE composition (Figs. 2 and 3). We stress that accessory allanite was not observed in the investigated samples.

The change from fractionation- to mineral reaction-controlled REE incorporation in garnet during reaction (2) is also evident from the Y and Mn garnet zonation patterns in

sample A 623 (Fig. 7). Both elements are highly compatible in garnet and thus are direct indicators of the availability of these elements in the reacting rock volume (cf. Hickmott and Spear 1992). In the core of the natural sample the concentrations of both these elements continuously decrease outwards, indicating a progressive depletion of the EBC due to fractionation effects. At the core–overgrowth boundary there is a slight increase in Y but not in Mn, possibly indicating initial liberation of Y (but not Mn) from a REE-liberating mineral reaction. Most striking is the decoupling of Y and Mn towards the outer rim, just before the grossular trend in garnet starts to change due to the rapid consumption of epidote during reaction (2). Here, in Zone 3, Y increases sharply and forms a distinct spike, whereas Mn stays at low concentrations (Fig. 7). Such behaviour of two highly compatible elements is indicative for a drastic liberation of Yttrium during garnet growth, which can be correlated with the epidote-out reaction in our sample (cf. Hickmott and Spear 1992). This interpretation is further corroborated by the measured epidote inclusions, which contain up to twice as much Y as the garnet rim, but are almost Mn free (see Table Appendix).

During reaction (3) the last major MREE-bearing mineral (amphibole) is consumed, which results in a marked increase of MREE in garnet. The resulting, slightly MREE-enriched, strongly HREE-depleted pattern is thus characteristic of garnet material formed at UHP conditions in equilibrium with clinopyroxene (Fig. 5). Unfortunately, trace elements indicative of the net-transfer reaction (3) are not diagnostic, because amphibole and garnet have similar trace element characteristics and the elements enriched in amphibole, such as Li, Rb or Sr, are close to or below the detection limit in garnet. Scandium might provide the most sensitive fingerprint of amphibole breakdown. Sc is strongly partitioned into garnet (cf. Hickmott and Spear 1992) and should reflect the bulk rock composition or element availability during garnet growth, but amphibole contains Sc in sufficiently high concentrations that it can be analysed precisely. The Sc pattern in garnet shows a monotonic decrease from inner to outer core (Fig. 7), possibly caused by the depletion of Sc in the

reactant phases, in this case chlorite and epidote. At the core–overgrowth boundary the Sc trend changes and Sc rises to a maximum at the centre of the overgrowth and then decreases outwards. This change of slope can be interpreted as a result of a new garnet-forming reaction in which amphibole is now a reactant. In Zone 3 Sc increases again and forms another maximum. The decoupling of Sc from Mn might be interpreted in terms of element liberation due to amphibole breakdown, but the lack of independent indicators for net-transfer reactions, as during reaction (3), shows the importance of interpreting trace element patterns in garnet with a combination of thermodynamic modelling and quantitative trace element modelling.

During reaction (4), the shape of the REE pattern is influenced by two factors (Fig. 5): (1) the amount of zoisite in the assemblage and (2) HREE depletion in the EBC that is responsible for further HREE decrease in UHP garnet. Whereas the amount of zoisite present during reaction (3) and/or (4) controls the absolute MREE content, zoisite growth contemporaneous with garnet formation will result in a MREE decrease in garnet. Thus, detailed determination of REE trends in UHP garnet might yield information about the timing of zoisite growth in UHP rocks, essential for the understanding of de- and re-hydration processes during subduction.

Apart from the characteristic REE patterns in each growth zone, the modelled REE distribution leads to a characteristic trend in the core-to-rim normalised REE patterns in garnet. HREEs are predicted to have a maximum in the core followed by a continuous decrease towards the rim. Depending on EBC depletion and HREE content in amphibole and epidote, this decrease can be interrupted by an intermediate small peak towards the garnet rim (Fig. 2). The subsequent liberation and re-distribution of lighter REE during the epidote- and amphibole-out reactions (reactions (2) and (3)) associated with continuous depletion of the EBC in heavier REEs, leads to an intermediate peak of lighter REEs (Fig. 2). Due to the preferred partition of heavier REEs into garnet, this intermediate peak will form progressively

outward with decreasing atomic number, i.e. decreasing garnet/matrix partition coefficient, a feature, often observed in (U)HP garnets (e.g., Skora et al., 2006).

Accessory minerals

An important factor for the REE re-distribution during metamorphism is the presence of accessory phases, such as titanite and allanite that might contain significant amounts of REEs (King et al., 2004; Hermann 2002; Zack et al., 2002). Although the allanite component in the measured epidotes is quite small, there is evidence that titanite was stable during the onset of high pressure metamorphism. In one of our samples (A 623) titanite can be found in the cores and inner rims of the garnets. Because titanite is an important carrier of REEs, titanite-breakdown or -fractionation might have an important effect on the REE budget in the rocks and garnets therein (King et al., 2004; Sassi et al., 2002; Mulrooney and Rivers 2005). The measured REE patterns in titanite inclusions in sample A 623 resemble those observed in epidote, which show slight HREE depletions (see electronic supplementary material). Thus, titanite breakdown, which must have occurred in that sample, should have the same effect on the REE budget as the epidote-out reaction. Nevertheless, the calculated modal abundance of titanite is only about 10% of that of epidote. Thus, the quantitative effect of titanite-breakdown on the REE pattern in garnet will be much less than the epidote-breakdown reaction. Further, sample 714-3 does not contain titanite inclusions in the garnets, but shows the same REE pattern as sample A 623, thus confirming our assumption of a weak influence of titanite on the REE pattern in garnet. Nevertheless, it is obvious that breakdown of a phase with a high abundance of REE, despite occurring in low abundance, may give rise to a particular REE pattern, but the number of potential minerals is quite small, as the REE content in most phases (apart from those considered here) is limited in mafic systems.

Parameters

Our models are based on several simplified assumptions, such as equilibrium partitioning of REE among the stable phases, a limited influence of accessory phases on the REE budget and temperature- and composition-independent REE partition coefficients. Further, model results are mainly dependent on two parameters: the modelled mineral abundances and the partition coefficients, the first of which determines the amount of liberated REEs during the breakdown of a certain phase, the second controlling the pattern of the liberated REEs and their re-distribution among the refractory phases. Both parameters together define the characteristic change in the REE pattern in refractory garnet.

A comparison of modelled and observed REE patterns in amphibole and epidote coexisting with garnet showed that the characteristic REE trends can be modelled with the chosen dataset, although the absolute values of the REE contents might differ significantly (see electronic supplementary material). In epidote the REE content is slightly underestimated, whereas in case of zoisite and amphibole the model predicts higher REE contents. Because the overall trend of the modelled patterns match those observed in the garnet inclusions, we are confident that the effect of the over- and underestimation of the REE content will have only a limited effect on the resulting REE content in garnet and will not change the characteristic core-to-rim pattern. These results provide confidence for the assertion that the partition coefficients used for modelling the REE patterns in garnet are generally appropriate for mafic systems. However, reproduction of absolute REE values is expected to improve with more accurate partition coefficients determined from well-equilibrated natural assemblages.

Geochronology

Garnet is an important mineral for geochronology in HP rocks. The Sm-Nd and Lu-Hf isochron methods have been applied to many HP rocks (Lapen et al., 2003; Kylander-Clark 2007) and due to their high retentivity in garnet, both isotope systems are assumed to reflect

ages of metamorphism precisely (Ganguly and Tirone 1999). Apart from the initial isotope ratio of the daughter element the parent/daughter isotope ratio is the age controlling factor, i.e. the Sm/Nd and Lu/Hf ratios at the time of crystallisation. Due to the different bulk partition coefficients of these elements, their concentrations in garnet changes drastically from core to rim (Figs. 2 and 3). Lu is mostly concentrated in the cores, whereas Sm is concentrated in the rims of the garnet crystals (slope from Gd to Eu in Figs. 2, 3, 5 and 6 can be used to extrapolate Sm concentrations). Thus, depending on the chosen isotope system, the majority of the age information will be concentrated either in the cores, yielding an early crystallisation age in case of Lu/Hf, or in the rims, which will date a later stage of crystallisation as in case of Sm/Nd. In detail, both methods will yield isotope information about different stages of the metamorphic history. Because large amounts of Lu are incorporated during garnet growth from chlorite the Lu/Hf method will primarily yield information about the chlorite-out reaction, thus about the greenschist to amphibolite/blueschist facies transition. The majority of the lighter REEs is liberated during the epidote- and especially during the amphibole-out reaction. This liberation is reflected in the REE patterns in garnet, which are characterised by a drastic increase in lighter REEs in the outer parts of the garnet crystals (Figs. 5 and 6). Thus, the Sm/Nd system in garnet will be predominantly influenced by the amphibolite- to eclogite-facies transition. However, our models predict that beyond epidote- and amphibole-stability the majority of the LREE is stored in clinopyroxene and (at UHP conditions) zoisite. This is consistent with the observed LREE contents in matrix zoisite (see electronic supplementary material). Nevertheless, we state that further detailed analytical work is needed to constrain the partition of the lighter REEs, such as Sm and Nd, among the stable phases during subduction.

Conclusions

Our approach of combined major and trace element forward modelling in garnet from high pressure rocks offers the possibility to extract information about net-transfer mineral

reactions occurring during subduction on the basis of distinct trace element patterns in garnet and the coexisting mineral assemblage. This approach allows one to decipher chemical equilibrium domains in a reacting rock volume as well as to predict the distribution, fractionation and liberation of trace elements during subduction in both solid and fluid phases. Trace element zonation in garnet is stronger than major element zoning and allows a much clearer identification of phases contributing to garnet-forming reactions and thus a better-defined P-T path. All the investigated garnets have similar, complex REE patterns that can be interpreted with respect to sequential, garnet-producing mineral breakdown reactions occurring in thermodynamic equilibrium in a continuously depleted (due to fractionation) effective bulk rock composition during the subduction process.

We hope that findings of this study will encourage further investigation of trace element mobility. For example, REE distribution of phases included in garnet can be used to test if these are in chemical equilibrium with surrounding garnet. Undisturbed primary inclusions in garnet, like amphibole, epidote and phengite, may ultimately hold the key for the behaviour of a range of fluid-mobile elements (e.g., Li, B, Rb, Sr, LREE and Pb; all difficult to analyse in garnet directly) during prograde metamorphism.

Acknowledgements

We thank the German Science Foundation for the grant BR 1532/4 to MKS and PJO. Matthias Barth is thanked for help at the LA-ICP-MS facility in Mainz. Robbie King and an anonymous reviewer are kindly thanked for their detailed and very constructive reviews that improved style and content of the manuscript. Richard Carlson is thanked for his careful editorial handling.

References

Bebout, G. E., 2007, Metamorphic chemical geodynamics of subduction zones: Earth and Planetary Science Letters, v. 260, p. 373-393.

Bollingberg, H. J. and Bryhni, I., 1972, Minor element zoning in an eclogite garnet: Contributions to Mineralogy and Petrology, v. 36, p. 113-122.

Bryhni, I. and Griffin, W. L., 1971, Zoning in eclogite garnets from Nordfjord, West Norway: Contributions to Mineralogy and Petrology, v. 32, p. 112-125.

Chernoff, C. B. and Carlson, W. D., 1999, Trace element zoning as a record of chemical disequilibrium during garnet growth: Geology (Boulder), v. 27, p. 555-558.

Connolly, J. A. D. and Kerrick, D. M., 1987, An algorithm and Computer Program for calculation Composition Phase Diagrams: Calphad, v. 11, p. 1-55.

Connolly, J. A. D., 2005, Computation of phase equilibria by linear programming: A tool for geodynamic modeling and its application to subduction zone decarbonation: Earth and Planetary Science Letters, v. 236, p. 524-541.

Cuthbert, S. J., Carswell, D. A., Krogh Ravna, E. J. and Wain, A., 2000, Eclogites and eclogites in the Western Gneiss Region, Norwegian Caledonides: Lithos, v. 52, p. 165-195.

Ganguly, J. and Tirone, M., 1999, Diffusion closure temperature and age of a mineral with arbitrary extent of diffusion; theoretical formulation and applications: Earth and Planetary Science Letters, v. 170, p. 131-140.

Gill, J., 1981, Orogenic andesites and plate tectonics. Springer-Verlag, New York, 390 pp.

Hermann, J., 2002, Allanite: thorium and light rare earth element carrier in subdcuted crust: Chemical Geology, v. 192, p. 289-306.

Hickmott, D. D., Shimizu, N., Spear, F. S. and Selverstone, J., 1987, Trace-Element Zoning in a Metamorphic Garnet: Geology, v. 15, p. 573-576.

Hickmott, D. D. and Shimizu, N., 1990, Trace element zoning in garnet from the Kwoiek Area, British Columbia: disequilibrium partitioning during garnet growth?: Contributions to Mineralogy and Petrology, v. 104, p. 619-630.

Hickmott, D. and Spear, F. S., 1992, major- and trace-element zoning in garnets from calcerous pelites in the NW Shelburne Falls Quadrangle, Massachusetts: garnet growth histories in retrograded rocks: Journal of Petrology, v. 33, p. 965-1005.

Holland, T. J. B. and Powell, R., 1998, An internally consistent thermodynamic data set for phases of petrological interest: Journal of Metamorphic Geology, v. 16, p. 309-343.

Jacob, D. E., 2006, High sensitivity analysis of trace element-poor geological reference glasses by Laser ablation-inductively coupled plasma-mass spectrometry (LA-ICP-MS): Geostandards and Geoanalytical Research, v. 30, p. 221-235.

Kessel, R., Schmidt, M. W., Ulmer, P. and Pettke, T., 2005, Trace element signature of subduction-zone fluids, melts and supercritical liquids at 120-180 km depth: Nature, v. 437, p. 724-727.

King, R. L., Bebout, G. E., Kobayashi, K., Nakamura, E. and van der Klauw, S. N. G. C., 2004, Ultrahigh-pressure metabasaltic garnets as probes into deep subduction zone chemical cycling: Geochemistry Geophysics Geosystems, v. 5, p. 1-17.

Konrad-Schmolke, M., Handy, M. R., Babist, J. and O'Brien, P. J., 2005, Thermodynamic modelling of diffusion-controlled garnet growth: Contributions to Mineralogy and Petrology, v. 149, p. 181-195.

Konrad-Schmolke, M., Babist, J., Handy, M. R. and O´Brien, P. J., 2006, The physico-chemical properties of a subducted slab from garnet zonation patterns (Sesia Zone, Western Alps): Journal of Petrology, v. 47, p. 2123-2148.

Konrad-Schmolke, M., O'Brien, P. J., de Capitani, C. and Carswell, D. A., 2007, Garnet growth at high- and ultra-high pressure conditions and the effect of element fractionation on mineral modes and composition: Lithos, doi: 10.1016/j.lithos.2007.10.007.

Krogh, E. J., 1982, Metamorphic evolution of Norwegian country-rock eclogites, as deduced from mineral inclusions and compositional zoning in garnets: Lithos, v. 15, p. 305-321.

Kylander-Clark, R. C., Hacker, B., Johnson, C. M., Beard, B. L., Mahlen, N. J. and Lapen, T. J., 2007, Coupled Lu-Hf and Sm-Nd geochronology constrains prograde and exhumation histories of high- and ultrahigh-pressure eclogites from Western Norway: Chemical Geology, v. 242, p. 137-154.

Lapen, T. J., Johnson, C. M., Baumgartner, L. P., Mahlen, N. J., Beard, B. L. and Amato, J. M., 2003 Burial rates during prograde metamorphism of an ultra-high-pressure terrane: An example from Lago di Cignana, Western Alps, Italy: Earth and Planetary Science Letters v. 215: p. 57-72.

Mulrooney, D. and Rivers, T., 2005, Redistribution of the rare earth elements among coexisting minerals in metamafic rocks across the epidote-out isograd: an example from the St. Anthony Complex, Northern Newfoundland, Canada: Canadian Mineralogist, v. 43, p. 263-294.

O´Brien, P. J., 1997, Garnet zoning and reaction textures in overprinted eclogites, Bohemian Massif, European Variscides; a record of their thermal history during exhumation: Lithos, v. 41, p. 119-133.

Otamendi J.E., de la Rosa J.D., Douce A.E.P. and Castro A., 2002, Rayleigh fractionation of heavy rare earths and yttrium during metamorphic garnet growth. Geology 30: 159-162.

Sassi, R., Harte, B., Carswell, D. A. and Yujing, H., 2000, Trace element distribution in Central Dabie eclogites: Contributions to Mineralogy and Petrology, v. 139, p. 298-315.

Skora, S., Baumgartner, L. P., Mahlen, N. J., Johnson, C. M., Pilet, S. and Hellebrand, E., 2006, Diffusion-limited REE uptake by eclogite garnets and its consequences for Lu-Hf and Sm-Nd geochronology: Contributions to Mineralogy and Petrology, v. 152, p. 703-720.

Spear, F. S., Selverstone, J., Hickmott, D., Crowley, P. and Hodges, K. V., 1984, P-T paths from garnet zoning; a new technique for deciphering tectonic processes in crystalline terranes: Geology (Boulder), v. 12, p. 87-90.

Spear, F. S., 1988b, The Gibbs Method and Duhem Theorem - the Quantitative Relationships among P, T, Chemical-Potential, Phase-Composition and Reaction Progress in Igneous and Metamorphic Systems: Contributions to Mineralogy and Petrology, v. 99, p. 249-256.

Spear, F. S., 1988c, Metamorphic Fractional Crystallization and Internal Metasomatism by Diffusional Homogenization of Zoned Garnets: Contributions to Mineralogy and Petrology, v. 99, p. 507-517.

Tatsumi, Y., Eggins, S., 1995, Subduction zone magmatism, Blackwell Malden, Mass., 211 pp.

Tirone, M., Ganguly, J., Dohmen, R., Langenhorst, F., Hervig, R. L. and Becker, H.-W., 2005, Rare earth element diffusion kinetics in garnet: Experimental studies and applications: Geochimica et Cosmochimica Acta, v. 69, p. 2385-2398.

Wain, A., Waters, D., Jephcoat, A. and Olijynk, H., 2000, The high-pressure to ultrahigh-pressure eclogite transition in the Western Gneiss Region, Norway: European Journal of Mineralogy, v. 12, p. 667-687.

Watson, E. B., 1996, Surface enrichment and trace element uptake during crystal growth: Geochimica et Cosmochimica Acta, v. 60, p. 5013-5020.

Zack, T., Foley, S.F. and Rivers, T., (2002) Equilibrium and disequilibrium trace element partitioning in hydrous eclogites (Trescolmen, Central Alps). Journal of Petrology 43: 1947-1974.

Zack, T., John, T., 2007. An evaluation of reactive fluid flow and trace element mobility in subducting slabs: Chemical Geology, v. 239, p. 199-216.

Figure captions

Fig. 1: Compositional maps, major element profiles and laser ablation spots of investigated UHP eclogite garnet (Krokken and Verpenesset). Both garnets show multiple growth stages separated by inclusion trials. In sample A 623 (Krokken) the growth zones are marked by abrupt compositional gradients whereas in sample 714-3 (Verpenesset) only the rim shows a significant major element zoning. Rare earth element (REE) analyses revealed four different zones with distinct normalised REE patterns (see text).

Fig. 2: REE zoning in garnets from sample A 623 from Krokken. Individual REE profiles show characteristic shapes: HREE concentrations are highest in the core, lighter REEs have a peak towards the rim, which lies further outboard with decreasing atomic number (arrows). Normalised REE contents show four different zones with distinctive patterns.

Fig. 3: REE zoning in garnet from sample 714-3 from Verpenesset. Despite different major element zoning, the REEs show the same characteristics as in sample A 623. Four different REE patterns can be distinguished. As in the previous sample, the REE patterns correlate with certain major element growth zones (see text).

Fig. 4: Modelled garnet composition, garnet growth and phase relations in sample A 623 (Krokken), calculated along the prograde UHP trajectory. Garnet growth is predicted to occur in three distinct periods by four garnet-forming reactions. Each of the growth zones (shaded grey) is characterised by certain compositional trends that correlate well with the observed major element zonation in the natural sample.

Fig. 5: Calculated REE composition and zoning pattern of the modelled garnet from Krokken shown in Fig. 4. Characteristic REE profiles and patterns resulting from fractionation linked to different garnet-forming reactions are shown in black at each stage of garnet growth (see text).

Fig. 6: (a) Modelled garnet REE profiles, phase relations and garnet major-element composition in sample 714-3 (Verpenesset). Garnet growth occurs in two stages by three different reactions (reactions (1) – (3)). Despite different growth histories and differences in major element composition, the REE patterns (b) resemble those in the Krokken sample.

Fig. 7: Compositional profiles of Y, Mn and Sc in sample A 623 (Krokken). Decoupling of Y and Sc from Mn possibly indicates reaction-controlled REE uptake in garnet from the Krokken sample.

Figure 1

Click here to download Figure: Konrad-Schmolke et al. Fig. 01 revised.eps

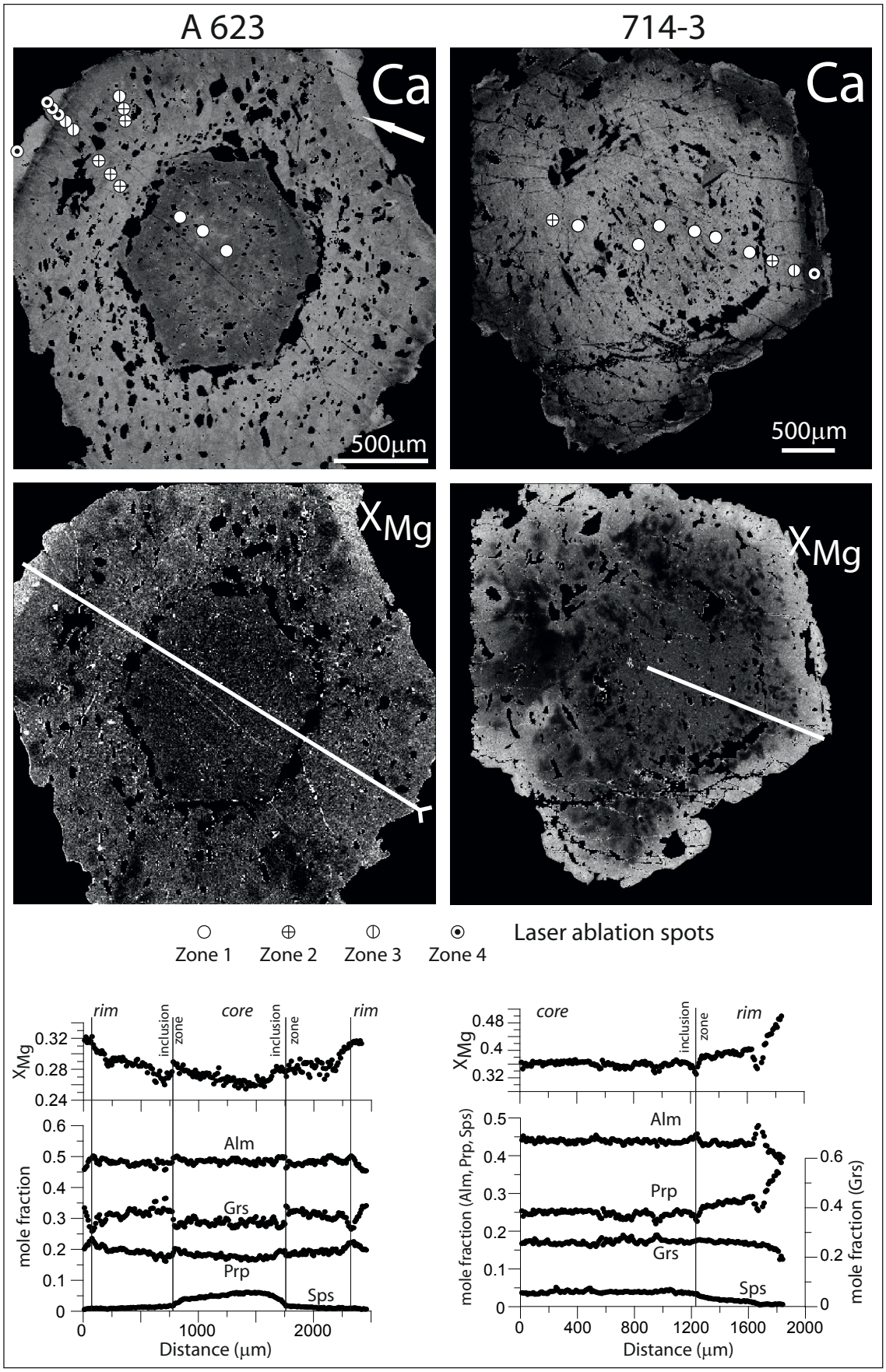

Figure 2

Click here to download Figure: Konrad-Schmolke et al. Fig. 02 revised.eps

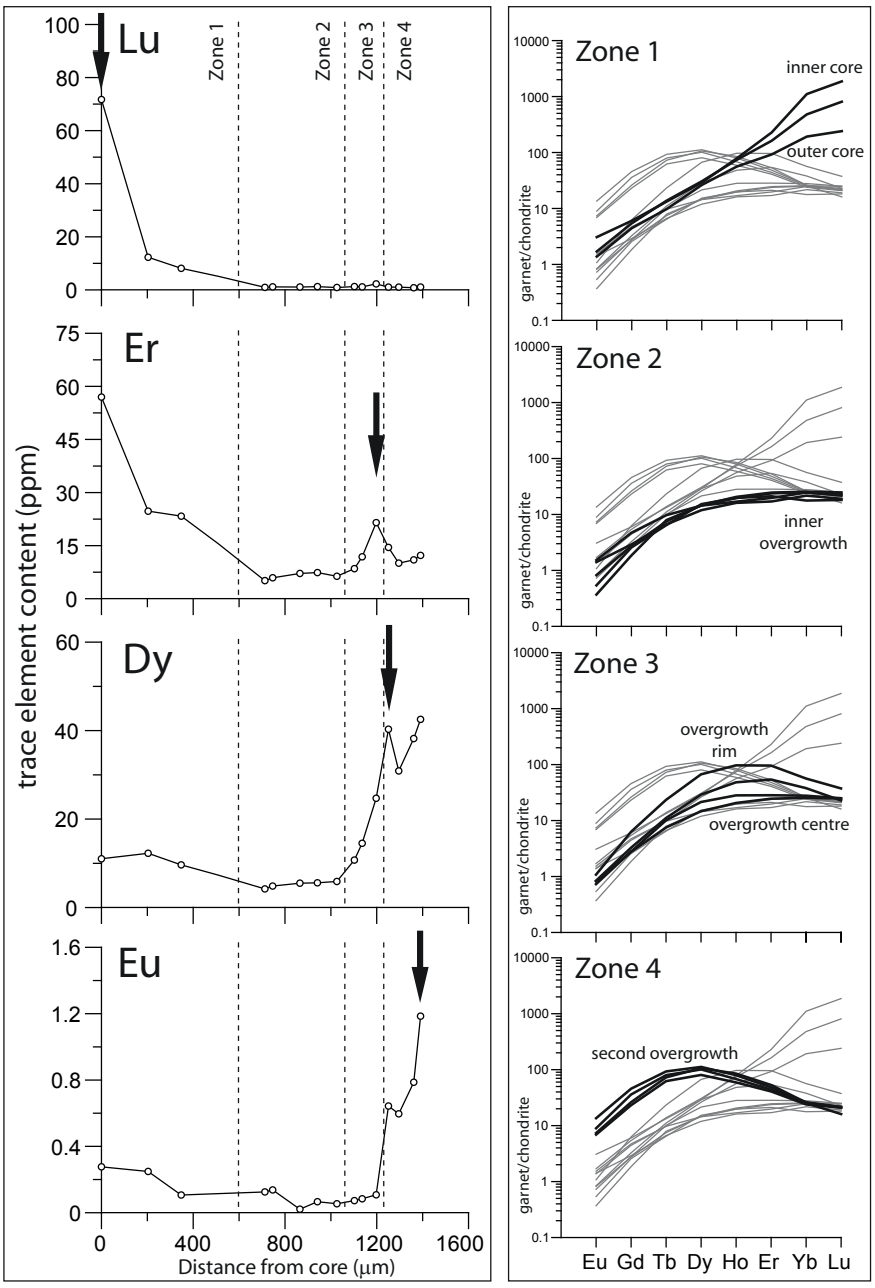

Figure 3

Click here to download Figure: Konrad-Schmolke et al. Fig. 03 revised.eps

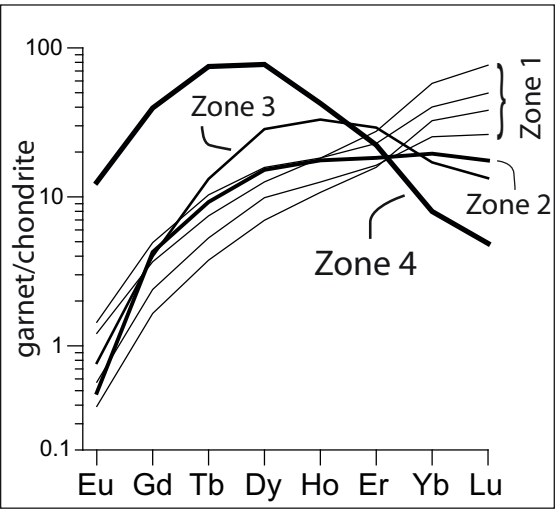

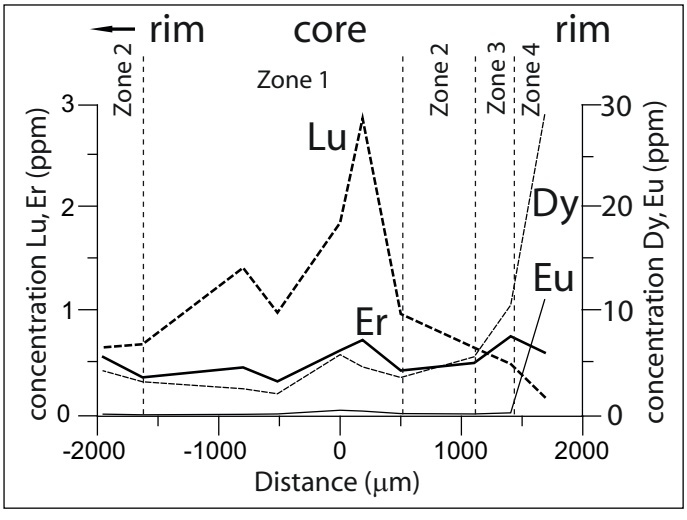

Figure 4

Click here to download Figure: Konrad-Schmolke et al. Fig. 04 revised.eps

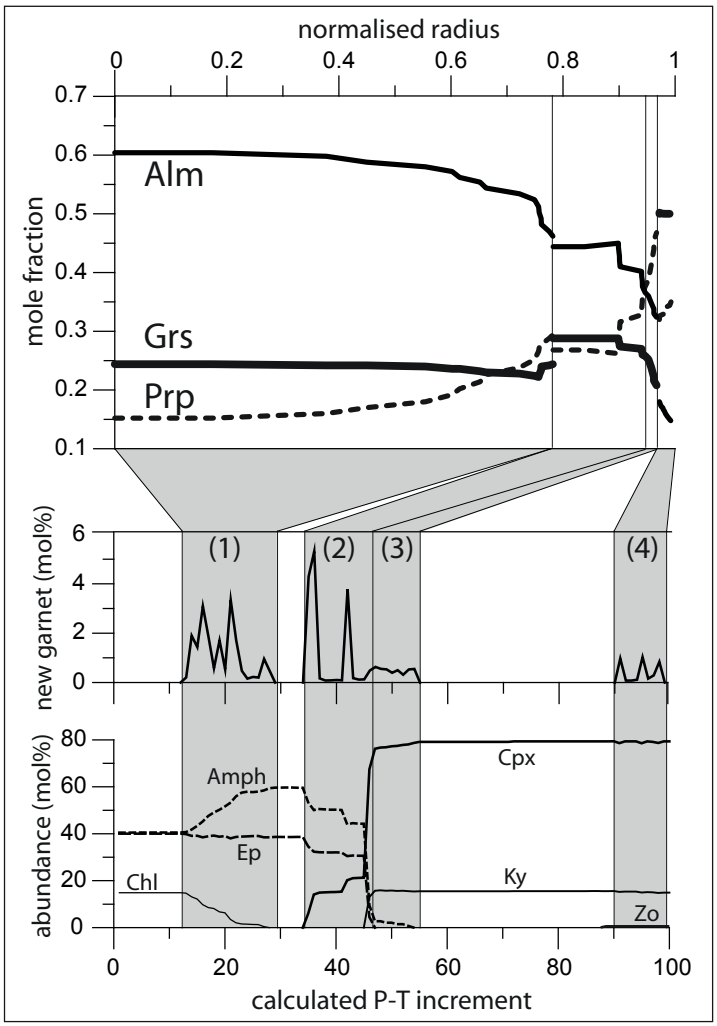

Figure 5

Click here to download Figure: Konrad-Schmolke et al. Fig. 05 revised.eps

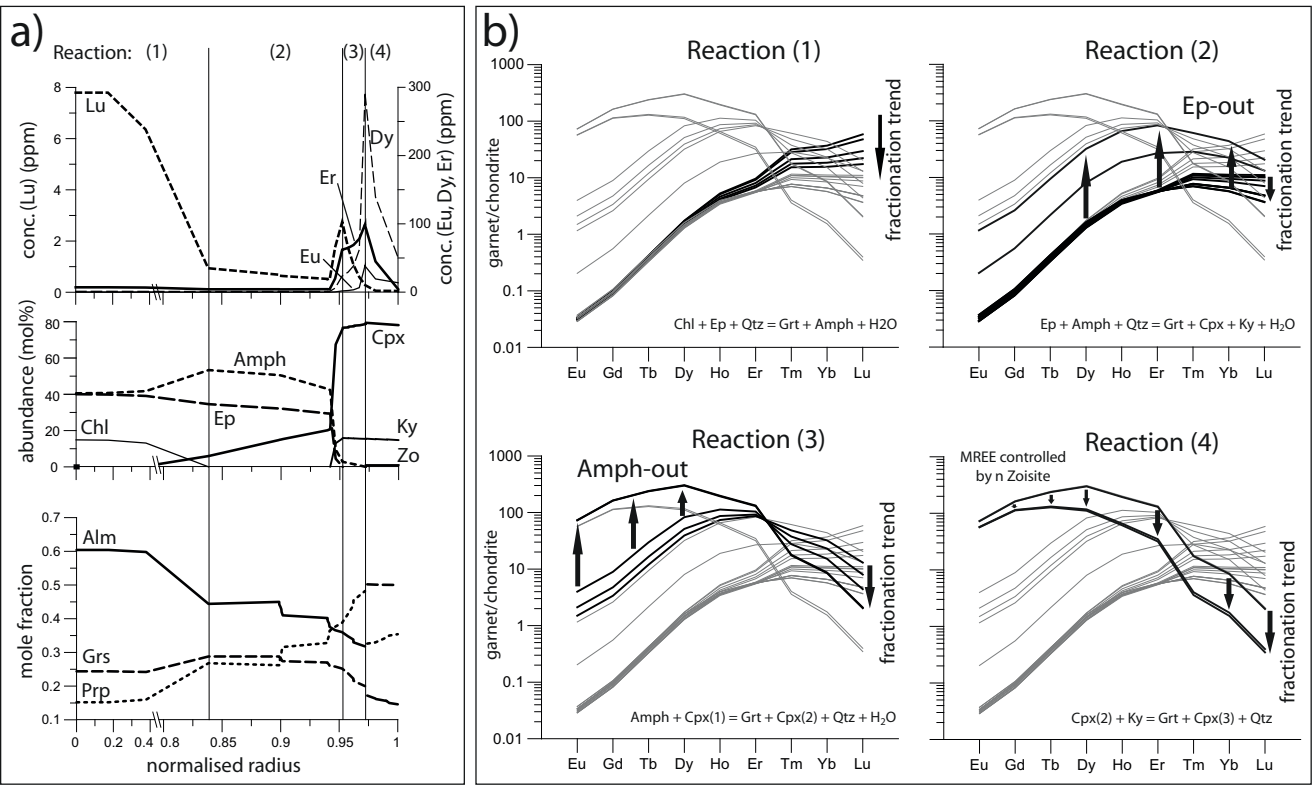

Figure 6

Click here to download Figure: Konrad-Schmolke et al. Fig. 06 revised.eps

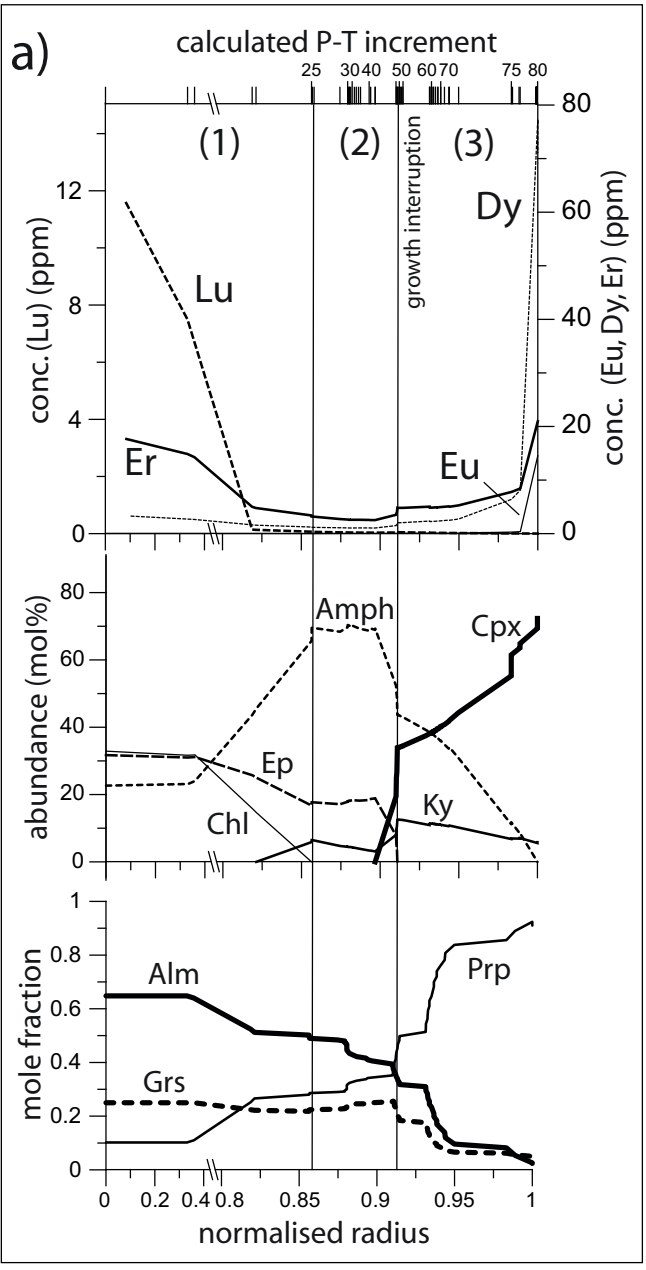

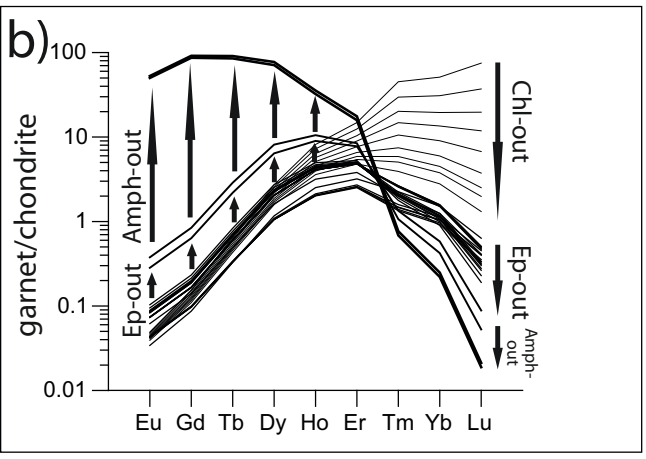

Figure 7

Click here to download Figure: Konrad-Schmolke et al. Fig. 07 revised.eps

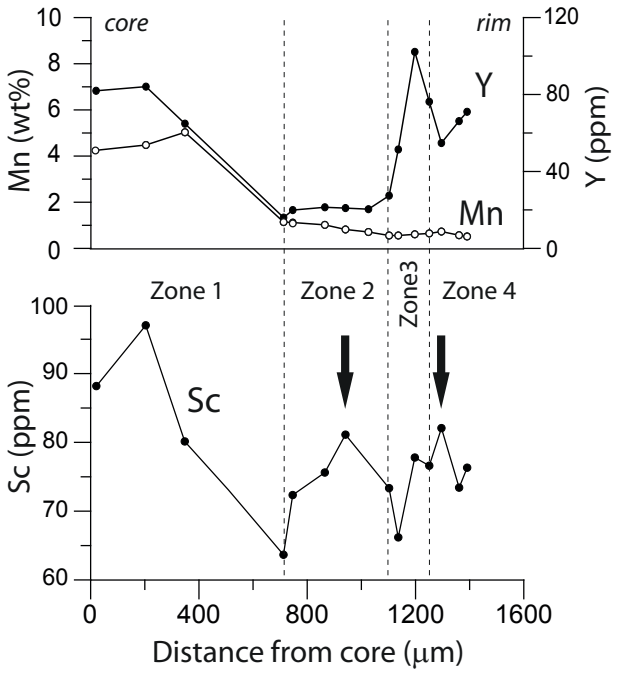

Table 1
Click here to download Table: Konrad-Schmolke et al. Table 1.doc

Table 1: Mineral/Mineral and Mineral/Fluid partition coefficients used to calculate REE patterns

	Eu	Gd	Tb	Dy	Ho	Er	Tm	Yb	Lu	source
Ep/Grt	224	70.2	12.1	2.61	0.731	0.348	0.097	0.071	0.042	1
Cpx/Grt	0.083	0.043	0.020	0.009	0.006	0.005	0.004	0.003	0.003	1
Grt/Fluid	109	199	250	285	350	425	500	552	608	2
Amph/Ep	0.73	1.3	1.68	2.02	2.42	3.03	3.54	3.87	4.31	3

Source: (1) Herrmann 2002; (2) Kessel et al.. 2005; (3) Mulrooney and Rivers 2005

Compositional re-equilibration of garnet: the importance of sub-grain boundaries

Matthias Konrad-Schmolke[1], Patrick J. O'Brien[1] & Florian Heidelbach[2]

[1]Universität Potsdam, Institut für Geowissenschaften, Karl-Liebknecht-Straße 24-25, 14476 Golm, Germany

E-mail: mkonrad@geo.uni-potsdam.de, obrien@geo.uni-potsdam.de

[2]Bayerisches Geoinstitut, Universität Bayreuth, 95440 Bayreuth, Germany

E-mail: Florian.Heidelbach@Uni-Bayreuth.de

Corresponding author:

Matthias Konrad-Schmolke

E-mail: *mkonrad@geo.uni-potsdam.de*

Abstract

Garnets from meta-granitoid high pressure rocks (Sesia Zone, Western Alps) show complex internal sub-grain textures in electron forescatter images. All investigated garnets consist of a large number of sub-grains with different shapes and sizes. Some garnets exhibit a sub-texture with very fine-grained (<20μm) sub-grains in their cores overgrown by palisade-like sub-grains in the rims. Sub-grain boundaries in these garnets have enabled diffusive element exchange between the garnet core and the surrounding matrix. Compositional mapping reveals zonation patterns of Mg that indicate modification of the garnet composition during prograde metamorphism. The extent of diffusional re-equilibration is dependent on sub-grain size and element diffusivities. Our samples show that X_{Mg} is strongly influenced by diffusion along the sub-grain boundaries, whereas apparently slow diffusing elements, such as Ca, Ti and Y preserve their original concentric zonation pattern. This differential re-equilibration leads to very complex chemical zonation that cannot be easily interpreted in terms of simple prograde growth zonation or of normally-applied spherical diffusion models. The observation that almost all garnets in the investigated samples exhibit a sub-grain pattern suggests this might be a common feature in high pressure/low temperature rocks.

Keywords: *garnet, microstructure, sub-grains, EBSD, diffusional equilibration, high pressure, subduction, Sesia Zone*.

Introduction

Understanding compositional re-equilibration of metamorphic minerals as a response to changing pressure (P), temperature (T) and/or chemical conditions is one of the most important aspects of metamorphic petrology. Diffusional relaxation of gradients in chemical potential within and among minerals is both a blessing and a curse for petrologists. On the one hand, relaxation of T- and P-dependent gradients in chemical compositions of minerals blurs information about previous metamorphic stages, thus complicating exact determination

of P-T-paths (e.g. Florence & Spear, 1991) or of growth and fractionation processes during metamorphism (e.g. Carlson 1989; Konrad-Schmolke *et al*., 2005). On the other hand, as long as the mechanism of diffusional relaxation and its parameters are known, characteristic diffusion-induced chemical zonation within mineral grains can be used to constrain temperature-time histories (e.g. Lasaga & Jiang 1995; Perchuk & Philippot 1997; Ganguly & Tirone 1999) by calculating the effects of diffusion on pre-existing growth patterns and comparing the so-modelled profiles with those in natural samples.

It is widely accepted that transport rates differ significantly between volume and grain-boundary diffusion, the latter being up to four orders of magnitude faster (e.g. Joesten, 1991). Thus, compositional resetting of mineral grains along fractures and sub-grain boundaries occurs rapidly, as long as fluids are available, because chemical potential gradients are maximised between the matrix and grain interiors. In addition, the presence of sub-grains markedly increases the reactive surface area thus enhancing solution-precipitation processes. Metamorphic garnets commonly preserve strong compositional growth zoning that at higher temperatures should begin to homogenise. Such homogenisation of zoned garnet is usually assumed to occur in a spherical grain with no directional variation in diffusivity. Such an assumption is invalidated if grain boundaries, fractures or interaction with inclusions allow preferential communication between garnet interior and exterior and thus faster diffusional relaxation (cf. Whitney 1991; Hames & Menard, 1993; Florence & Spear 1991). Some inclusions or fractures are easily detected by optical or electron microscopy, but sub-grain boundaries or sub-microscopic lattice defects (e.g. Hwang *et al,*. 2003), especially in cubic minerals such as garnet, are significantly harder to detect but may be large enough to enable considerable grain boundary diffusion. Several mechanisms for sub-grain development in low temperature garnets have been proposed. These include: amalgamation of separately formed nuclei (Spiess *et al.*, 2001; Dobbs *et al*., 2003; Okamoto & Michibayashi, 2006); brittle fracturing (Hames & Menard, 1993; Whitney, 1996; Prior 1993); and also diffusion-induced

grain boundary migration (e.g. Hwang *et al*., 2003), or even dislocation creep (e.g. Prior *et al*., 2000; Storey & Prior, 2005) at high metamorphic temperatures. However, the influence of these sub-textures on the diffusional re-equilibration of elements during metamorphism has not yet been investigated and is the focus of this study.

We investigated high-pressure garnets with electron microprobe and electron backscatter diffraction and found that many garnets consist of a large number of sub-grains with irregular boundaries as well as different grain sizes and shapes. In order to test whether this sub-grain network has enhanced element mobility and compositional relaxation we also undertook detailed compositional mapping of the same garnets. The effects on resetting of zoning patterns and consequences for geothermobarometry and geochronology will be discussed.

Results

Investigated samples

The investigated samples are meta-granitoid high pressure rocks from two different outcrops from the western part of the central Sesia Zone (see Konrad-Schmolke *et al*., 2006), Western Alps: an area famous for its well-preserved Alpine eclogite facies mineral assemblages in continentally derived rocks (e.g. Dal Piaz *et al*., 1978). Metamorphic peak conditions of 500-600°C, 1.5-2.0 GPa are deduced for the partly-preserved HP assemblage rutile+garnet+epidote/zoisite+sodic amphibole+omphacite+phengite+quartz (Koons 1986; Zucali *et al*., 2002). Sodic amphibole and omphacite are often strongly retrogressed to chlorite, albite +/-paragonite and epidote. Garnet forms clasts in a well-developed, blueschist- to greenschist-facies, retrograde foliation defined by phengite and/or sodic amphibole and/or chlorite, and is strongly zoned with respect to major and trace elements. In back-scattered electron (BSE) images (Fig. 1) some grains show domains with well-preserved concentric zoning whereas others parts of the same grains show an irregular, mesh-like zonation pattern.

Generally, garnet in our samples shows at least three growth zones, indicated by brightness variation in BSE images (cf. Konrad-Schmolke *et al*., 2006) and exhibits two different types of zonation pattern. Type 1 garnets have almandine-grossular-rich cores that appear dark in the BSE image (Grt 1.1), surrounded by a 'lighter' mantle (Grt 1.2) with significantly lower Ca and higher Fe, and a 'darker' outer rim (Grt 1.3; Fig. 1A, B) where Mg increases at the expense of Ca. Type 2 garnets have 'bright' almandine-rich, grossular-poor cores (Grt 2.1), overgrown by an almandine-grossular-rich mantle characterised by decreasing grossular and increasing almandine content (Grt 2.2). In some regions Grt 2.2 is overgrown by a small 'darker' rim (Grt 2.3) with higher grossular and pyrope and lower almandine content (Fig. 1D, E). Konrad-Schmolke *et al*., (2006) interpreted both types of zonation patterns to represent prograde growth, with the Type 2 patterns interpreted to result from water undersaturation of the host rock prior to and during prograde metamorphism.

High contrast BSE images reveal that both types of garnets often show internal modifications of the concentric zonation pattern. The right part of the mantle region of the Type 1 garnet in Fig. 1C shows a very patchy zonation, caused by a contrast between irregular 'bright' fragments separated by a network of 'darker' material, a feature frequently observed in garnets from HP and UHP rocks (e.g. Pennacchioni 1996; Austrheim *et al*., 1996; Inui & Toriumi, 2002; Zack *et al*., 2002; Janak *et al*., 2006; Hoschek 2007). The large Type 2 garnet crystal in Fig. 1F has 'bright' Grt 2.1 fragments in a 'darker' core, which is surrounded by a 'lighter' mantle and a 'darker' rim. The entire garnet grain is truncated by a complex, 'darker', in this case fracture-like radial pattern visible in the BSE image. The internal pattern reaches well into the garnet interior where it forms a dense network of 'darker' garnet material.

Correlation of internal garnet texture and chemistry

An orientation contrast (OC) image (Fig. 2A) of the “cloudy” area in the garnet shown in Fig. 1C reveals a complex internal sub-texture. Different shades of grey in the image

indicate a difference in crystallographic orientation of neighbouring areas (see e.g. Prior *et al*., 1999). The image shows that the outer part of the garnet crystal clearly consists of several crystallographically mis-oriented segments separated by sharp boundaries (arrows). Towards the more internal part of the garnet the crystallographic boundaries between these areas become more diffuse and differences in the mis-orientation of neighbouring segments, although still evident in some areas, become less pronounced. Comparison of OC images with major and trace element compositional maps (Figs. 2B-F respectively) shows that chemical modification of the originally concentric growth zonation correlates with the position of boundaries between crystallographically mis-oriented areas, if these are present (cf. arrows in A, B and C). In the upper left part of the crystal the lack of sub-structure boundaries hinders a correlation of the compositional mappings with the sub-structure pattern. Further, the compositional mappings show that the extent of chemical modification is element dependent.

The compositional patterns of Mg and X_{Mg} (=Mg/(Mg+Fe)) match the 'dark-light' pattern visible in the BSE image and correlate with the sub-structure pattern in the OC image, if developed. The concentration of Mg and the X_{Mg} value is similar along the entire sub-structure boundary network as well as at the outermost rim of the entire garnet grain (Fig. 2B and C) suggesting similar P-T conditions during the equilibration of the garnet rim and the modification of garnet interior along the sub-structure boundaries. In contrast, Ca, Ti and Y concentrations (Figs. 2D, E and F respectively) clearly still preserve a concentric pattern that is independent of the radially-oriented sub-structure boundary network. This observation suggests decoupling of relaxation of compositional gradients of relatively fast-diffusing elements (such as Mg) from that of slow-diffusing elements (such as Ca, Ti and Y). Further, the preservation of the original concentric zonation pattern demonstrates that the development of the sub-structure pattern postdates initial growth and that diffusional modification of the garnet interior occurs as a result of the presence of the sub-structure boundary network.

The OC image (Fig. 3A) of the large garnet grain shown in Fig. 1F reveals that the

garnet crystal shown in Fig. 1F exhibits a different, much more complex internal sub-structure pattern than the previous example: Whereas the core of the garnet crystal consists of a large number of small, mostly roundish sub-grains, the rim is made of larger elongate, sometimes palisade-like sub-grains. The close-up in Fig. 3B shows that the size of sub-grains in the fine-grained areas is between 1 and 10µm, whereas the palisade-like areas in the rim have diameters of at least 20 to 30, sometimes up to 100µm. As demonstrated by the electron backscatter diffraction (EBSD) mapping (Fig. 3C), the colour-coded pole plots (Fig. 3D) and the mis-orientation-angle diagram in Fig. 3E, the mis-orientation angle between most sub-grains is less than 5°, indicating the predominance of low angle grain boundaries among most of the crystallographic segments.

Due to the different diffusivities of elements in garnet, the size of the sub-grains is a critical factor with respect to the degree of re-equilibration of metastable interiors, as can be demonstrated with a comparison of the sub-grain pattern with compositional X-ray mappings. The compositional variations of Mg and the X_{Mg} value (Figs. 4A and B) correspond well with the sub-grain boundary pattern in the garnet crystal, i.e., it shows high values at the garnet rim and along the sub-grain boundaries throughout the interior. As a result of the small grain-size of sub-grains and thus high grain-boundary density, the core is almost entirely equilibrated at the same X_{Mg} level as the garnet rims. Compositional maps of Ca (Fig. 4C) and Fe (Fig. 4D) show markedly different patterns. Whereas the Fe pattern roughly corresponds with the grain boundaries of the palisade-like sub-grains in the rim of the large garnet, there is almost no correlation between Ca-content and the sub-grain pattern in this domain. In the core, Fe and Ca exhibit a completely different compositional pattern compared to that of Mg and X_{Mg}. Apart from the numerous Garnet 2.1 fragments Ca and Fe patterns allow recognition of two core regions with slightly higher Ca and lower Fe values (high grossular garnet 2.2), one in the upper left side and one in the lower left side of the map. This suggests the existence of two garnet nuclei that amalgamated during the growth process, a structure that is obviously

older than the Mg and X_{Mg} patterns, which equilibrated at or near peak metamorphic conditions. Differences in the re-equilibration between major elements are also evident in the composition of Grt 2.1 fragments. Whereas some of the grains (arrow 1 in Fig. 4) are nearly unchanged with respect to their original composition, other, smaller sub-grains show a complete re-equilibration with respect to Mg (although the Ca and Fe content is not exactly the same as at the rim, arrow 2, Fig. 4), which leads to a complex X_{Mg} pattern that cannot be simply interpreted in terms of a P and T evolution.

Interpretation and Discussion

The garnet crystals in this study exhibit different sub-grain textures both of which are responsible for internal compositional variations that significantly deviate from originally concentric or near-concentric growth zonations that are partly preserved in the samples. The results derived from Type 1 garnets show that the patchy compositional variations visible in BSE images of many HP and UHP garnets (e.g. Matthews *et al*., 1992; Austrheim *et al*., 1996; Zack *et al*., 2002) (Fig. 1C and F) are most likely the result of differential diffusive chemical re-equilibration of pre-existing growth zonations along sub-grain boundaries. Peak X_{Mg} values along grain and sub-grain boundaries in our samples indicate compositional re-equilibration during the prograde evolution or near peak metamorphic conditions. Further, there is a decoupling of chemical resetting between apparently fast diffusing elements, such as Mg, and slow diffusing elements such as Ca, Ti and Y during the re-equilibration process (Fig. 2). The importance of garnet fracturing associated with a chemical modification of garnet interiors during metamorphism has been addressed by various workers (e.g. Whitney 1996; Hames & Menard 1993; Hwang *et al*., 2003). It is obvious that diffusive modification of the zoned garnet has important implications for petrologic investigations, such that P-T estimations and postulated P-T trajectories might be misinterpreted (e.g. Chakraborty & Ganguly 1991; Florence & Spear 1991). Interestingly, the OC images and the compositional

mappings in Fig. 2 show that the sub-grain boundary pattern always coincides with chemical modifications of the growth zonation pattern, but that the pathways along which fast elemental exchange occurs not necessarily cause mis-orientations between neighbouring areas of the garnet crystal. This observation allows an interpretation of the sub-texture development. Obviously, the crystallographic anisotropies enabling directed element exchange allow, but not generally cause, neighbouring crystal segments to slightly rotate with respect to each other. Sub-grain rotation might only be enabled if the anisotropies form a three-dimensionally interconnected network but is hindered if the neighbouring segments are still crystallographically connected. Although several works (e.g. Vollbrecht *et al*., 2006) postulate dislocation mobility in terms of viscous deformation in garnet at relatively low temperatures around 650°C, we doubt a significant contribution of dislocation creep as a mechanism for the development of the sub-grain structure, because of the extremely low peak metamorphic temperatures (500-550°C) of our samples (cf. Zhang & Green 2007). Further, none of the investigated crystals in our sample shows significant elongation resulting from dynamic recrystallisation or cataclastic fragmentation as a response to host rock deformation. Thus, it is questionable whether dislocation creep and recovery (e.g. Prior *et al*., 2000), cataclastic deformation (e.g. Trepmann & Stöckhert 2002) or grain boundary sliding (e.g. Terry & Heidelbach 2004) can be responsible for the sub-texture development. This observation is important because deformation-controlled cation diffusion has been observed in plastically deformed tourmaline (Büttner 2005) and might also occur in garnet. Due to the absence of any signs of crystal-plastic deformation in our samples we favour the assumption that a diffusion induced dislocation migration and/or diffusion induced recrystallisation process (Hwang *et al*., 2003) is responsible for the development of the sub-grain texture. The preferred exchange of cations, as observed in our samples, and a resulting distortion of the crystal lattice might cause dislocation generation and facilitate dislocation migration. But to doubtlessly clarify the nature and development of the crystallograhic anisotropies that enable

fast and selective elemental exchange, further investigations utilising transmission electron microscopy are necessary but are beyond the scope of this paper.

Although the sub-grain boundary network in Type 2 garnets has similar effects on the diffusional re-equilibration of garnet interiors, the large textural difference between the internal sub-structures in Type 1 and 2 garnets suggest a different development of the sub-grain patterns in both types of garnet in our samples. The preservation of garnet 2.1 fragments as well as of compositional domains in the Fe and Ca mappings (Fig. 4) allows an interpretation of the development of the complex sub-grain texture in Type 2 garnets (Fig. 5): (1) In an initial stage fracturing and resorption of garnet 2.1 leads to differential preservation of larger and smaller garnet 2.1 fragments with similar crystallographic orientation inherited from the host grain (Fig. 5A). Examples of relatively well preserved but intensely fractured garnet 2.1 fragments are abundant in our samples (cf. BSE and OC images Fig. 5A). (2) Prograde metamorphism leads to the formation of a grossular-rich garnet 2.2 that fills the cracks between large garnet 2.1 fragments as well as overgrows smaller garnet 2.1 fragments, from which it inherits the crystallographic orientation (Fig. 5B,black arrows). Additionally, depending on fragment-size, sub-grain boundary density as well as element diffusivity, smaller garnet 2.1 fragments or areas within larger fragments are diffusionally homogenised (grey arrows in Fig. 5B). As a result of the amalgamation of the garnet 2.2 grains, a sub-grain boundary network develops within the large amalgamated grains. This stage is preserved in the compositional pattern of Ca and Fe as shown in Figs. 3 and 5C. (3) During the further prograde evolution garnet growth proceeds with grossular-poorer garnet 2.2, which also inherits the crystallographic orientation of pre-existing grains, but exhibits palisade-like radial growth as a result of the only possible growth direction (arrows in Fig. 5C). (4) During the last stage, but possibly also during all previous stages, selective compositional re-equilibration occurs along the sub-grain boundaries and progressively modifies garnet interiors with respect to Mg content and X_{Mg} value (Fig. 5D). Interestingly, the irregular

overgrowth of Grt 2.3, as observed along parts of the rim in the sample shown in Fig. 1D, is not observed in the highly re-equilibrated grain in Fig. 1F. A possible reason for this lack might be fractionation effects during prograde garnet growth, such that growth of Grt 2.3 is thermodynamically hindered in those samples with an intense element exchange between core and matrix due to small scale variations in the effective bulk rock composition around the garnet crystal (cf. Konrad-Schmolke *et al*., 2005). Thus, clarifying the influence of element recycling using thermodynamic forward modelling with the consideration of element fractionation (e.g. Spear & Selverstone 1983; Menard & Spear 1993, Connolly 2005; Konrad-Schmolke *et al*., 2006) should yield further important insight into garnet growth and composition in such partly re-equilibrated phase assemblages.

Conclusions

The examples in this work show that in contrast to the assumption of a spherical geometry for garnet, the presence of a complex, sub-grain texture may allow significant core-rim differences in diffusional re-equilibration. The result is a much faster homogenisation of cores and thus, if incorrectly modelled, a much longer timescale for peak metamorphism than actually experienced. Our samples indicate that the extent of diffusional resetting is clearly dependent on the size of sub-grains, which might have severe consequences for the interpretation of diffusional relaxation timescales for garnets with a critical sub-grain size. In our samples the size of the sub-grains in the garnet interior is small enough (<20μm) to enable almost complete resetting with respect to X_{Mg} whereas larger sub-grains still preserve lower X_{Mg} values.

Furthermore, chemical re-equilibration of existing garnets may influence the growth of new garnet in two ways. On the one hand, garnet growth might be enhanced by recycling of manganese from existing grains into the matrix. On the other hand, metastable cores of older garnets might be completely replaced by re-equilibration, thus leading to a situation where the garnet core is younger than the rim. An example of this phenomenon is the growth of newly

formed garnet in the lagoons of atoll-like garnets (e.g. Godard *et al*., 1981). In addition, differential resetting could cause major problems in the interpretation of isotopic ages of garnet as trace elements yielding age information will become decoupled from major element patterns used for geothermobarometry (e.g. Hermann & Rubatto 2003). The procedure for the determination of orientation contrast in natural garnet-bearing samples is now well developed and could become a standard technique in all studies of relaxation of compositional zoning where different diffusion mechanisms may be involved in different parts of the grains.

Acknowledgements

We thank the Deutsche Forschungsgemeinschaft (DFG) for financial support and Detlef Krauße (BGI Bayreuth) for his assistance with the electron microprobe analyses. FH acknowledges the support through the EU Marie Curie Research Training Network 'c2c' (contract MRTN-CT-2006-035957).

References cited

Austrheim, H., Erambert, M. & Boundy, T. M. (1996): Garnets recording deep crustal earthquakes: *Earth and Planetary Science Letters*, **139**, 223-238.

Büttner, S.H. (2005): Deformation-controlled cation diffusion in compositionally zoned tourmaline. *Mineral. Mag.*, **69**, 471-489.

Carlson, W. D. (1989): The significance of intergranular diffusion to the mechanism and kinetics of porphyroblast crystallization. *Contrib. Mineral. Petrol.*, **103**, 1-24.

Chakraborty, S. & Ganguly, J. C. (1991): Compositional zoning and cation diffusion in garnets. *in* "Diffusion, atomic ordering and Mass Transport". Ganguly, J., ed. Springer, New York: 120-175.

Connolly, J. A. D. (2005): Computation of phase equilibria by linear programming: A tool for geodynamic modeling and its application to subduction zone decarbonation. *Earth and Planetary Science Letters*, **236**, 524-541.

Dal Piaz, G. V., Hunziker, J. C. & Stern, W. B. (1978): The Sesia-Lanzo Zone, a slice of subducted continental crust?. *Open-File Report - U. S. Geological Survey*, 83-86.

Dobbs, H. T., Peruzzo, L., Seno, F., Spiess, R. & Prior, D. J. (2003): Unraveling the Schneeberg garnet puzzle: a numerical model of multiple nucleation and coalescence. *Contrib. Mineral. Petrol.*, **146**, 1-9.

Florence, F. P. & Spear, F. S. (1991): Effects of diffusional modification of garnet growth zoning on P-T path calculations: *Contrib. Mineral. Petrol.*, **107**, 487-500.

Ganguly, J. & Tirone, M. (1999): Diffusion closure temperature and age of a mineral with arbitrary extent of diffusion; theoretical formulation and applications. *Earth Planet. Sci. Lett.*, **170**, 131-140.

Godard, G., Kienast, J. R. & Lasnier, B. (1981): Retrogressive development of glaucophane in some eclogites from 'Massif Armoricain'. *Contrib. Mineral. Petrol.*, **78**, 126-135.

Hames, W. E. & Menard, T. (1993): Fluid-Assisted Modification of Garnet Composition Along Rims, Cracks, and Mineral Inclusion Boundaries in Samples of Amphibolite Facies Schists. *Am. Mineral.*, **78**, 338-344.

Hermann, J. & Rubatto, D. (2003): Relating zircon and monazite domains to garnet growth zones: age and duration of granulite facies metamorphism in the Val Malenco lower crust. *J. Metamorphic Geol.*, **21**, 833-852.

Hoschek, G. (2007): Metamorphic peak conditions of eclogites in the Tauern Window, Eastern Alps, Austria: Therbobarometry of the assemblage garnet + omphacite + phengite + kyanite + quartz. *Lithos*, **93**, 1-16.

Hwang, S. L., Shen, P., Yui, T. F. & Chu, H. T. (2003): On the mechanism of resorption zoning in metamorphic garnet. J. Metamorphic Geol., **21**, 761-769.

Inui, M. & Toriumi, M. (2002): Prograde pressure-temperature paths in the pelitic schists of the Sambagawa metamorphic belt, SW Japan. *J. Metamorphic Geol.*, **20**, 563-580.

Janak, M., Froitzheim, N., Vrabec, M., Krogh Ravna, E. J. & De Hoog, J. C. M. (2006): Ultrahigh-pressure metamorphism and exhumation of garnet peridotite in Pohorje, Eastern Alps. *J. Metamorphic Geol.*, **24**, 19-31.

Joesten, R. (1991): Grain boundary diffusion kinetics in silicate and oxide minerals. *in* "Diffusion, atomic ordering and Mass Transport", Ganguly, J., ed. Springer, New York, 345-395.

Konrad-Schmolke, M., Handy, M. R., Babist, J. & O'Brien, P. J. (2005): Thermodynamic modelling of diffusion-controlled garnet growth. *Contrib. Mineral. Petrol.*, **149**, 181-195.

Konrad-Schmolke, M., Babist, J., Handy, M. R. & O' Brien, P. J. (2006): The physico-chemical properties of a subducted slab from garnet zonation patterns (Sesia Zone, Western Alps). J. Petrol., **47**, 2123-2148.

Koons, P. O. (1986): Relative geobarometry from high-pressure rocks of quartzofeldspathic composition from the Sesia Zone, Western Alps, Italy. *Contrib. Mineral. Petrol.*, **93**, 322-334.

Lasaga, A. C. & Jiang, J. (1995): Thermal history of rocks; P-T-t paths for geospeedometry, petrologic data, and inverse theory techniques: *Am. J. Sci.*, **295**, 697-741.

Matthews, M., Harte, B. & Prior, D. J. (1992): Mantle garnets: a cracking yarn: Geochim. Cosmochim. Acta, **56**, 2633-2642.

Menard, T. & Spear, F. S. (1993): Metamorphism of Calcic Pelitic Schists, Stratford Dome, Vermont - Compositional Zoning and Reaction History. *J. Petrol.*, **34**, 977-1005.

Okamoto, A. & Michibayashi, K. (2006): Misorientations of garnet aggregate within a vein: an example from the Sanbagawa metamorphic belt, Japan. *J. Metamorphic Geol.*, **24**, 353-366.

Pennacchioni, G. (1996): Progressive eclogitization under fluid-present conditions of pre-Alpine mafic granulites in the Austroalpine Mt Emilius Klippe (Italian Western Alps). *J. Structural Geol.*, **18**, 549-561.

Perchuk, A. L. & Philippot, P. (1997): Rapid cooling and exhumation of eclogitic rocks from the Great Caucasus, Russia. *J. Metamorphic Geol.*, **15**, 299-310.

Prior, D. J. (1993): Sub-critical fracture and associated retrogression of garnet during mylonitic deformation: *Contrib. Mineral. Petrol.*, **113**, 545-556.

Prior, D. J., Boyle, A. P., Brenker, F., Cheadle, M. C., Day, A., Lopez, G., Peruzzi, L., Potts, G., Reddy, S., Spiess, R., Timms, N. E., Trimby, P., Wheeler, J. & Zetterstrom, L. (1999): The application of electron backscatter diffraction and orientation contrast imaging in the SEM to textural problems in rocks: *Am. Mineral.*, **84**, 1741-1759.

Prior, D. J., Wheeler, J., Brenker, F.E., Harte, B., & Matthews, M. (2000): Crystal plasticity of natural garnet: New microstructural evidence. *Geology*, **28**, 1003-1006.

Spear, F. S. & Selverstone, J. (1983): Quantitative P-T path from zoned minerals; theory and tectonic applications. *Contrib. Mineral. Petrol.*, **83**, 348-357.

Spiess, R., Peruzzo, L., Prior, D. J. & Wheeler, J. (2001): Development of garnet porphyroblasts by multiple nucleation, coalescence and boundary misorientation-driven rotations. *J. Metamorphic Geol.*, **19**, 269-290.

Storey, C. D. & Prior, D. J. (2005): Plastic deformation and recrystallization of garnet: A mechanism to facilitate diffusion creep. *J. Petrol.*, **46**, 2593-2613.

Terry, M. P., & Heidelbach, F. (2004): Superplasticity in garnet from eclogite facies shear zones in the Haram Gabbro, Haramsøya, Norway. *Geology*, **32**, 281-284.

Trepmann, C. A. & Stöckhert, B. (2002): Cataclastic deformation of garnet: a record of synseismic loading and postseismic creep. *J. Structural Geol.*, **24**, 1845-1856.

Vollbrecht, A., Pawlowski, Leiss, B., Heinrichs, T., Seidel, M. & Kronz, A.. (2006): Ductile deformation of garnet in mylonitic gneisses from the Münchberg Massif (Germany). *Tectonophysics*, **427**, 153-170.

Whitney, D.L. (1991): Calcium depletion halos and Fe-Mn-Mg zoning around faceted plagioclase inclusions in garnet from a high-grade pelitic gneiss. *Am. Mineral.*, **76**, 493-501.

Whitney, D. L. (1996): Garnets as open systems during regional metamorphism. *Geology*, **24**, 147-150.

Zack, T., Foley, S. F., & Rivers, T. (2002): Equilibrium and disequilibrium trace element partitioning in hydrous eclogites (Trescolmen, Central Alps). J. Petrol., **43**, 1947-1974..

Zhang, J. & Green, H. W. (2007): Experimental Investigation of Eclogite Rheology and Its Fabrics at High Temperature and Pressure. *J. Metamorphic Geol.*, **25**, 97-115.

Zucali, M., Spalla, M. I. & Gosso, G. (2002): Strain partitioning and fabric evolution as a correlation tool: the example of the Eclogitic Micaschists Complex in the Sesia-Lanzo Zone (Monte Mucrone-Monte Mars, Western Alps, Italy). *Schweiz. Mineral. Petro. Mitt.*, **82**, 429-454.

Figure captions

Fig. 1: Backscatter electron (BSE) images and compositional profiles of Type 1 (upper panel) and Type 2 (lower panel) garnet from metagranitoid samples from the Sesia Zone (Western Alps). A and B: Type 1 garnet unaffected by diffusional modification has almandine-grossular-rich cores (dark in BSE image, A) and almandine-rich rims (light in BSE image) with increasing pyrope and decreasing grossular content. C: BSE image of Type 1 garnet affected by diffusional modification indicated by a complex network of ‘darker’ garnet material in the ‘lighter’ rim (white rectangle). D and E: BSE image (D) and compositional

profile (E) of unmodified Type 2 garnet with almandine-rich, grossular-poor cores ('bright') and almandine-grossular-rich rims with increasing pyrope content. F: BSE image of a modified Type 2 garnet with radially oriented diffusion pathways ('dark' network) connecting the outer rim with the inner core.

Fig. 2: Orientation contrast (OC) image (A) and compositional mappings (B-E) of the area marked in Fig. 1 C. A: Different grey-shades in the OC image indicate a sub-grain pattern (traced by black lines) in the garnet. The superposed boundary pattern show that the compositional pattern of Mg and XMg largely correlate with the sub-grain pattern (B, D), whereas Ca, Ti and Y still preserve a concentric zonation (C, E, F).

Fig. 3: OC images (A and B) show a 'core-mantle' texture of the garnet crystal in Fig. 1F with fine-grained (<10 μm) sub-grains in the core and palisade-like, larger (>20 μm) sub-grains forming the rim. Compositional maps show that Mg (C) and XMg (D) have highest values along sub-grain boundaries and in the fine-grained core and correspond well with the sub-grain pattern. In contrast, Ca (E) and Fe (F) allow recognition of older compositional pattern in the core (white framed regions). Differential re-equilibration between major elements (arrows) leads to a complex XMg pattern that cannot be interpreted in terms of a P-T path (see text for further explanation).

Fig. 4: Compositional maps of the same area as shown in Fig. 3B show that Mg (A) and XMg (B) have highest values along sub-grain boundaries as well as in the fine-grained core and correspond well with the sub-grain pattern. In contrast, Ca (C) and Fe (D) allow recognition of older compositional pattern in the core (white framed regions). Differential re-equilibration between major elements (arrows) leads to a complex XMg pattern that cannot be interpreted in terms of a P-T path (see text for further explanation).

Fig. 5: Sub-texture development of Type 2 garnets. A) Fragmentation and resorption of garnet 2.1 grains without significant rotation of fragments. The comparison of BSE and OC images indicates that each subgrain contains a garnet 2.1 fragment in the core (see text). B) Overgrowth of Ca-rich garnet 2.2 inheriting the crystallographic orientation of garnet 2.1 fragments. The overgrowth stage is preserved in the Ca-rich amalgamated cores (X-ray mapping). C) Radial overgrowth of Ca-poorer, Fe-richer garnet 2.2 that forms palisade-like sub-grains. D) Differential compositional re-equilibration of all garnet generations along sub-grain boundaries. This stage is best preserved in the Mg and X_{Mg} mappings (see also Fig. 4).

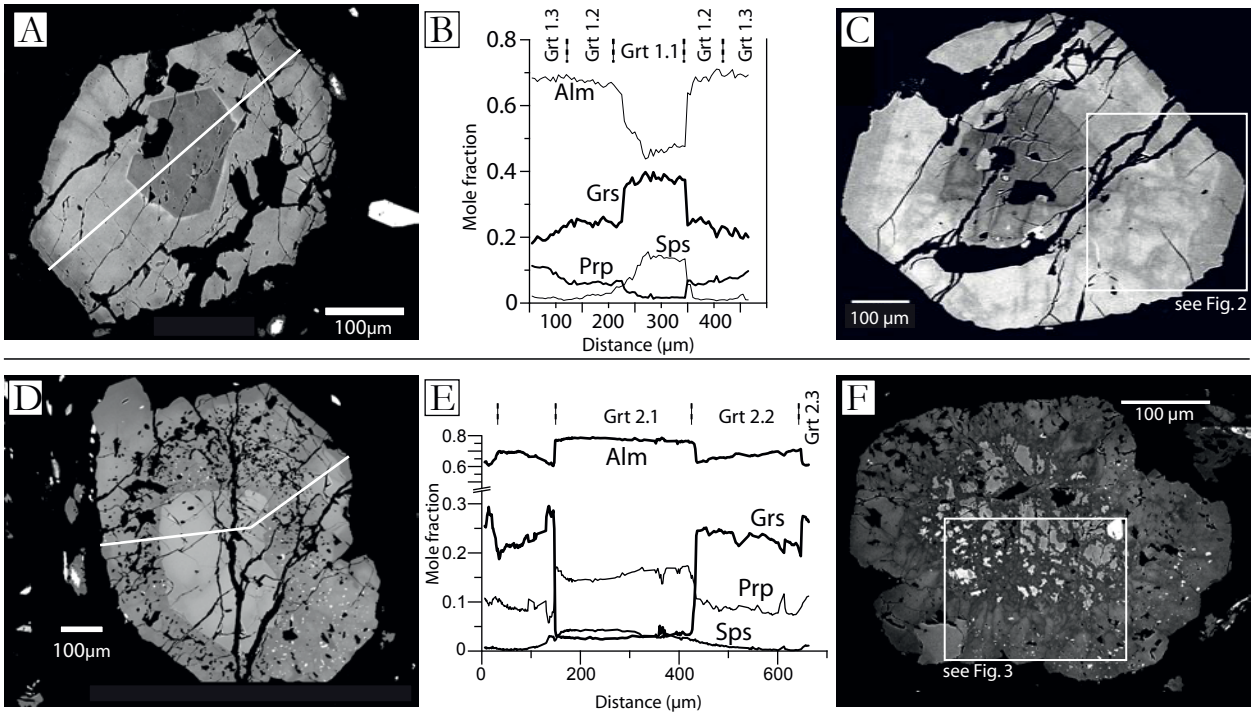

Fig. 1: Backscatter electron (BSE) images and compositional profiles of Type 1 (upper panel) and Type 2 (lower panel) garnet from metagranitoid samples from the Sesia Zone (Western Alps). A and B: Type 1 garnet unaffected by diffusional modification has almandine-grossular-rich cores (dark in BSE image, A) and almandine-rich rims (light in BSE image) with increasing pyrope and decreasing grossular content. C: BSE image of Type 1 garnet affected by diffusional modification indicated by a complex network of 'darker' garnet material in the 'lighter' rim (white rectangle). D and E: BSE image (D) and compositional profile (E) of unmodified Type 2 garnet with almandine-rich, grossular-poor cores ('bright') and almandine-grossular-rich rims with increasing pyrope content. F: BSE image of a modified Type 2 garnet with radially oriented diffusion pathways ('dark' network) connecting the outer rim with the inner core.

Konrad-Schmolke et al., Fig. 02 Top

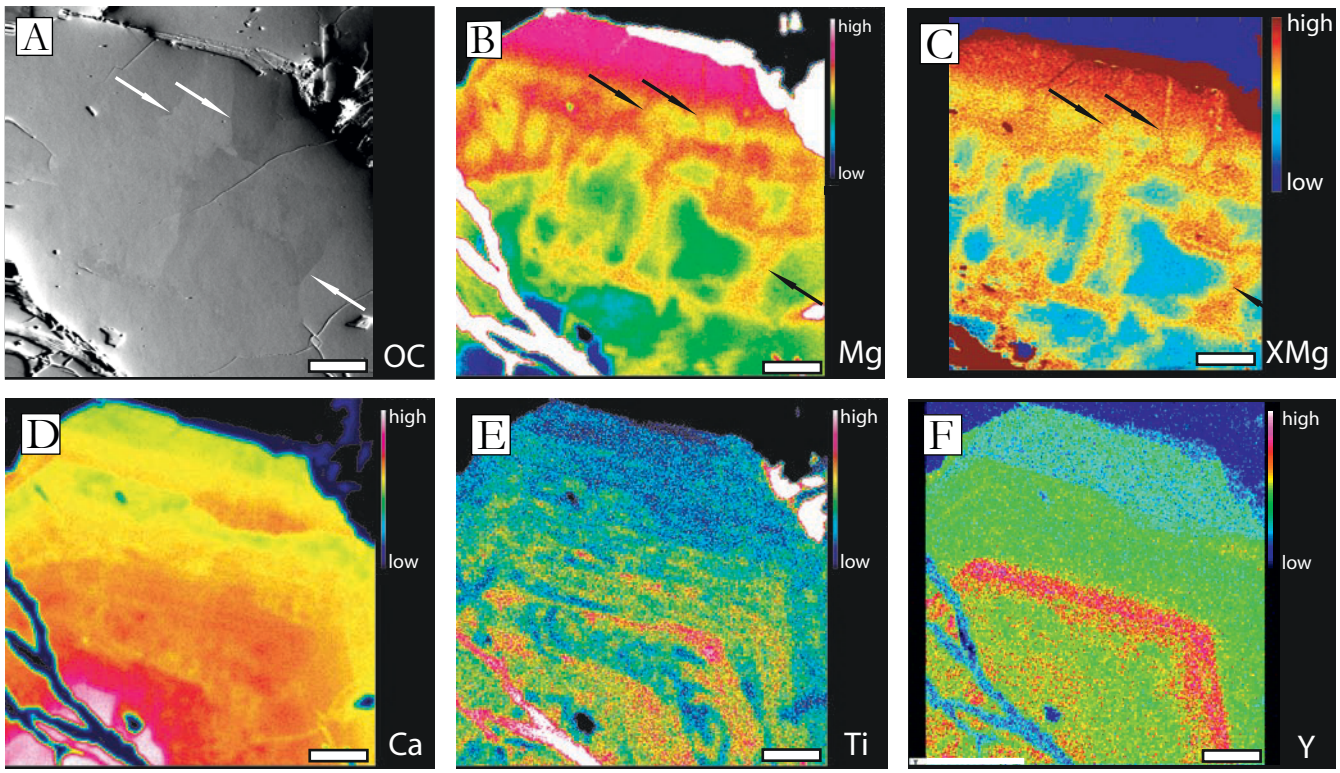

Fig. 2: Orientation contrast (OC) image (A) and compositional mappings (B-E) of the area marked in Fig. 1 C. A): The outer part of the garnet crystal consists of crystallographically mis-oriented segments separated by sharp boundaries (arrows). Towards the internal part the crystallographic boundaries are more diffuse and mis-orientations of neighbouring segments are less pronounced. The compositional pattern of Mg and X_{Mg} largely correlate with the sub-grain pattern (cf. arows in A, B and C), whereas Ca, Ti and Y still preserve a concentric zonation (D, E, F). Scale bars are 50μm.

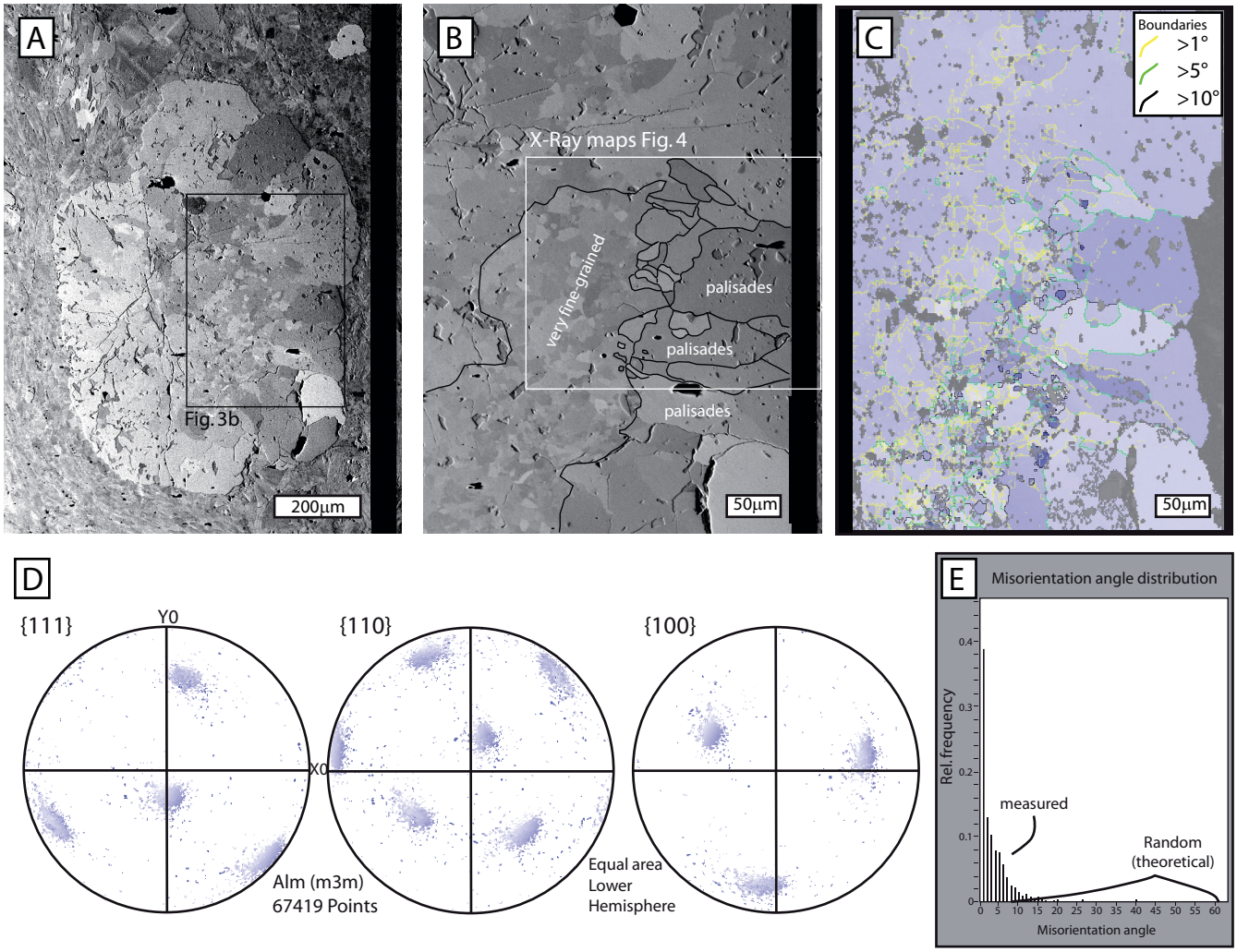

Fig. 3: Texture analysis of the Type 2 garnet crystal shown in Fig. 1F. A) The OC image of the entire grain shows that the core of the garnet crystal consists of a large number of small sub-grains, whereas the rim is made of larger elongate sub-grains. B) A close-up of the area shown in A) indicates that the sub-grains in the core are between 1 and 10µm, whereas those in the rim are up to several hundred µm in diameter. C) The EBSD mapping of the same area shows the predominance of low angle grain boundaries between the sub-grains. D) Corresponding color coded pole plots to the EBSD mapping in C). E) Corresponding mis-orientation angle diagram. Most sub-grains show a mis-orientation angle less than 10°.

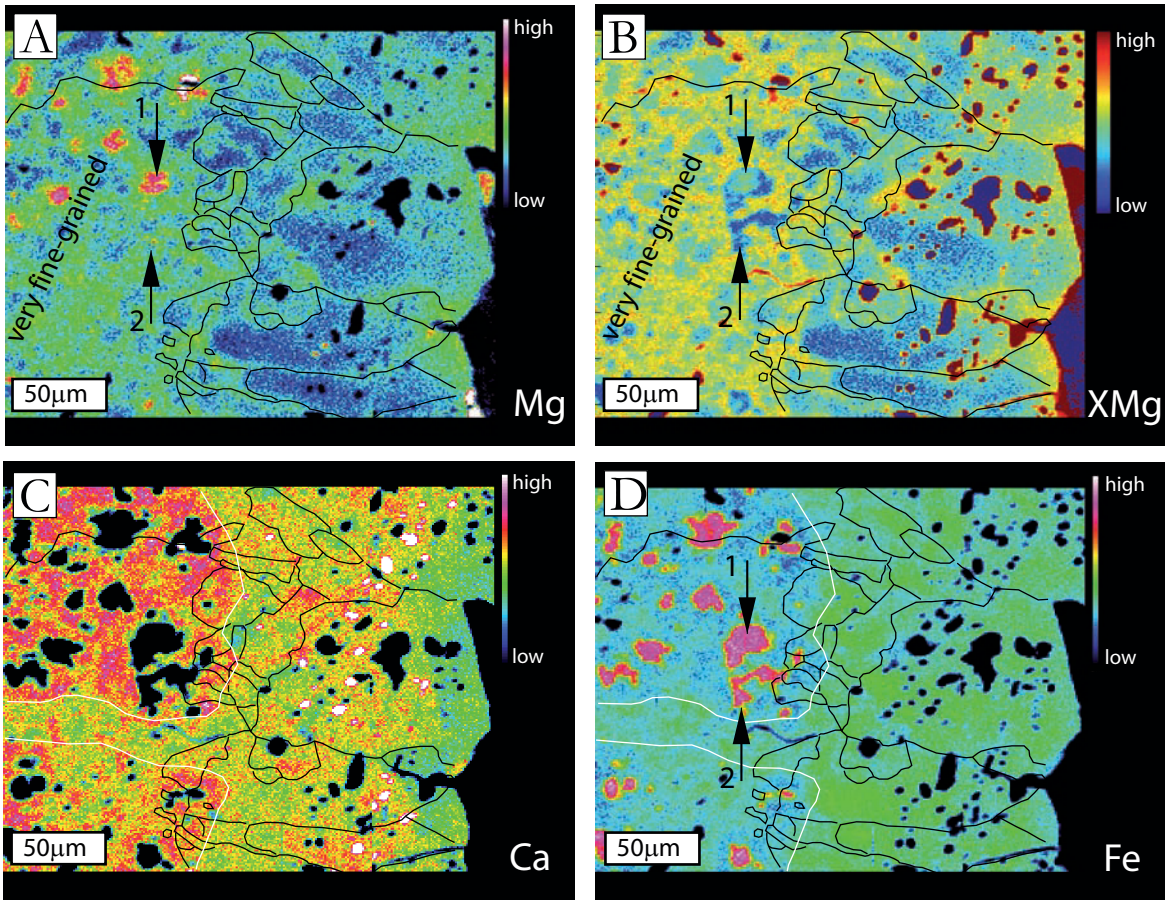

Fig. 4: Compositional maps of the same area as shown in Fig. 3B show that Mg (A) and XMg (B) have highest values along sub-grain boundaries as well as in the fine-grained core and correspond well with the sub-grain pattern. In contrast, Ca (C) and Fe (D) allow recognition of older compositional pattern in the core (white framed regions). Differential re-equilibration between major elements (arrows) leads to a complex XMg pattern that cannot be interpreted in terms of a P-T path (see text for further explanation).

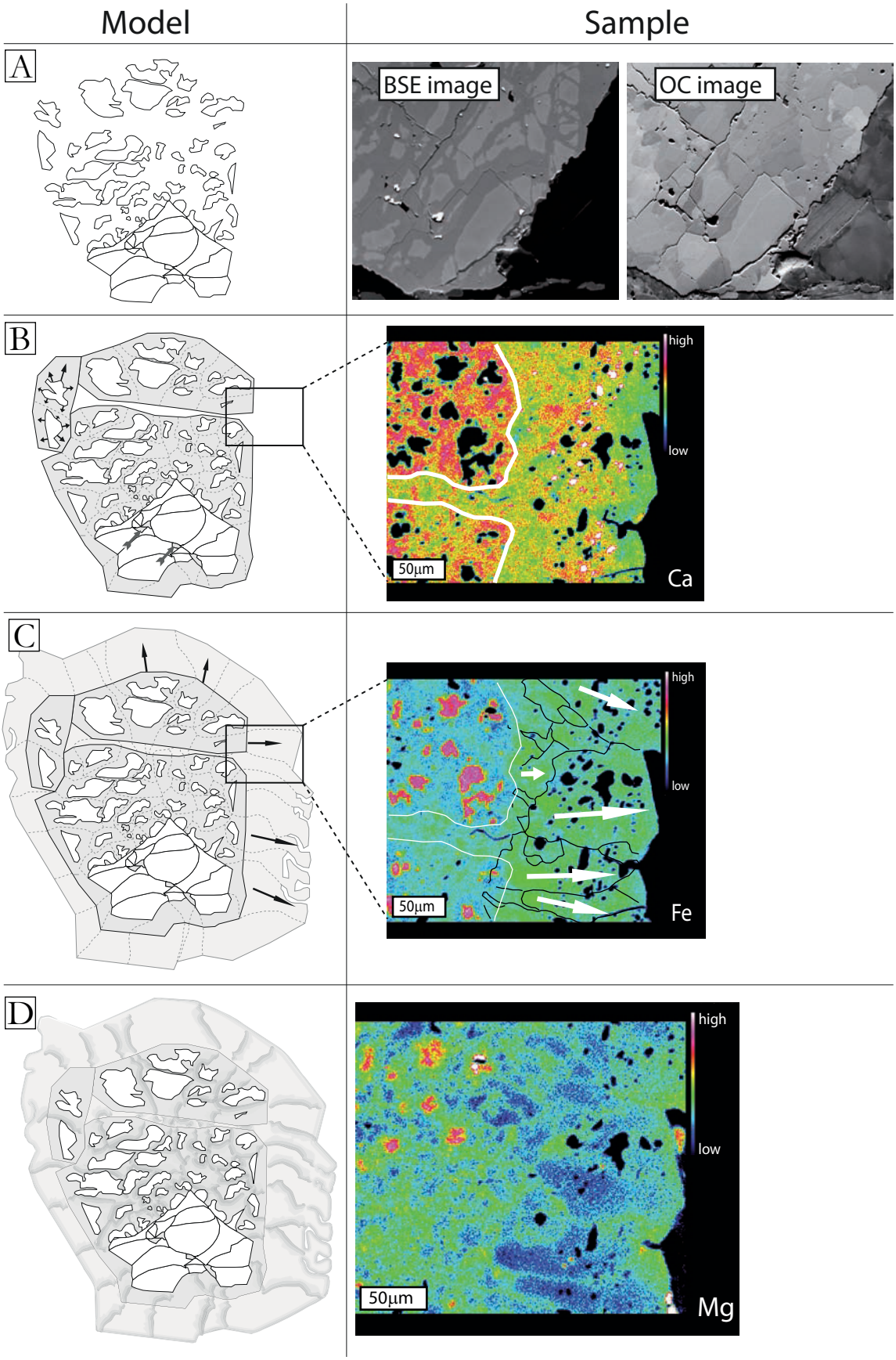

Fig. 5: Sub-texture development of Type 2 garnets. A) Fragmentation and resorption of garnet 2.1 grains without significant rotation of fragments. The comparison of BSE and OC images indicates that each subgrain contains a garnet 2.1 fragment in the core (see text). B) Overgrowth of Ca-rich garnet 2.2 inheriting the crystallographic orientation of garnet 2.1 fragments. The overgrowth stage is preserved in the Ca-rich amalgamated cores (X-ray mapping). C) Radial overgrowth of Ca-poorer, Fe-richer garnet 2.2 that forms palisade-like sub-grains. D) Differential compositional re-equilibration of all garnet generations along sub-grain boundaries. This stage is best preserved in the Mg and XMg mappings (see also Fig. 4).

Fluid migration above a subducted slab – Constraints on amount, pathways and major element mobility from partially overprinted eclogite-facies rocks (Sesia Zone, Western Alps)

Matthias Konrad-Schmolke, Patrick J. O'Brien and Thomas Zack

Department of Earth and Environmental Sciences, University of Potsdam, Germany

Corresponding Author:

Matthias Konrad-Schmolke
Universität Potsdam
Institut für Geowissenschaften
Karl-Liebknecht-Strasse 24-25
14476 Golm

e-mail: mkonrad@geo.uni-potsdam.de

ABSTRACT

The Western Alpine Sesia-Lanzo Zone (SLZ) is a sliver of eclogite-facies continental crust exhumed from mantle depths in the hanging wall of a subducted oceanic slab. Eclogite-facies felsic and basic rocks sampled across the internal SLZ show different degrees of retrograde metamorphic overprint associated with fluid influx. The weakly-deformed samples preserve relict eclogite-facies mineral assemblages that show partial fluid-induced compositional re-equilibration along grain boundaries, brittle fractures and other fluid pathways. Multiple fluid influx stages are indicated by replacement of primary omphacite by phengite, albitic plagioclase and epidote as well as partial re-equilibration and/or overgrowths in phengite and sodic amphibole producing characteristic step-like compositional zoning patterns. The observed textures, together with the map-scale distribution of the samples, suggest an open system pervasive and reactive fluid flux across large rock volumes above the subducted slab.

Thermodynamic modelling indicates a minimum amount of fluid of 0.1 to 0.5wt% interacting with the wall rocks. Phase relations and reaction textures indicate mobility of K, Ca, Fe and Mg, whereas Al is relatively immobile in these medium-temperature–high-pressure fluids. Further, the thermodynamic models show that recycling of previously fractionated material, such as in cores of garnet porphyroblasts, largely controls the compositional re-equilibration of the exhumed rock body.

INTRODUCTION

The migration of aqueous fluids and the associated major- and-trace element transport in metamorphic rocks, and particularly in subduction zones, has been a topic of intense research in the last decades (e.g., Zack and John 2007, Bebout et al., 1999, Poli and Schmidt 1997, Scambelluri and Phillippot 2001, Manning 2004). Migrating fluids released from the subducted slab as a result of devolatilisation of hydrous minerals are responsible for mantle metasomatism, the production of subduction-related magmatic activity (e.g., Schmidt and Poli

1998), the formation of large ore deposits (e.g., Rosenbaum et al., 2005) as well as for triggering earthquake ruptures (e.g., Hacker et al., 2003) and thus are of scientific, economic and social relevance. Further, slab-derived fluids are important carriers of major- and trace elements as well as isotopic signatures that contain encoded information about subduction-related processes in the downgoing slab, in the mantle wedge and in the lower crust (e.g., Sorensen et al., 1997, Ryan et al., 1995, Bouvier et al., 2008, Spandler et al., 2003, 2007, Kessel et al., 2005).

It is evident, however, that depending on the mode of fluid transport e.g., pervasive or channelized, the migrating fluids interact differently with the wall rocks during their ascent but, in any case, fluid-rock interaction will lead to a significant compositional modification of both wall rock and percolating fluids. Such fluid-rock interaction is often evident in exhumed high-pressure (HP) and ultrahigh-pressure (UHP) rocks as an incomplete retrogression and re-hydration of the primarily anhydrous eclogite-facies mineral assemblages (e.g., Schulte and Sindern 2002). Several recent works have shown the existence of a narrow, highly-strained mixing zone, often called “subduction channel”, between the subducted slab and the overlying mantle wedge (e.g., Lin et al., 1999, Bebout and Barton 2002), which is most likely the site of syn-convergent exhumation of deeply subducted material (e.g., Escher and Beaumont 1997). Within this zone, syn-kinematic fluid infiltration into metastable hot and dry (U)HP rocks on an exhumation path leads to a significant modification of rock- and fluid chemistry (e.g., Bebout and Barton 1993). Thus, fluids released from the subducted slab are likely modified during their ascent within such a highly reactive subduction channel depending on the intensity of rock deformation, the composition and amount of the infiltrated fluid, but also on reaction kinetics and permeability contrasts (Zack and John 2007, Ague 2007, van der Straaten et al., 2008). It is evident that any information about processes in the subducted slab, which might have been stored in the fluid properties, as well as fluid chemistry become heavily modified during the interaction with rocks undergoing exhumation in the hanging

wall of the downgoing plate. Therefore it is crucial to constrain the mode of fluid transport, to quantify the amount and composition of the infiltrated fluid and to understand the interplay between infiltrated fluid and wall rock above the subducted plate.

Rock samples that interacted with metamorphic fluids and still partly preserve information about the pre-influx metamorphic stage are of greatest importance for the quantification of fluid fluxes and associated element cycling in subduction zones. In such partly reacted rocks the effect of fluid influx on modes and compositions of newly-formed or recrystallized phases can be directly observed and, if the thermodynamic response of the coexisting mineral paragenesis during fluid infiltration is known, constraints on the amount, composition and possibly the origin of the infiltrated fluid can be made.

In this study we investigate four basic and felsic high-pressure metamorphic samples from the Western Alpine Sesia-Lanzo Zone (SLZ) that display excellent records of subduction zone fluid interaction with relatively dry wall rocks at lower crustal and mantle depths. Fluid infiltration at blueschist-facies conditions during the syn-convergent exhumation led to a partial compositional re-equilibration of hydrous high-pressure minerals, such as sodic amphibole and phengite, as well as to the formation of hydrous phases that partly replace the peak metamorphic eclogite-facies mineral assemblages.

In order to extract information about and to quantify the fluid-rock interaction from the compositionally zoned and newly formed minerals, we use various thermodynamic modelling techniques and compare modeled major element compositional trends and changing mineral paragenesis with those observed in our natural samples (cf. Konrad-Schmolke et al., 2008). We draw conclusions about the transport mode and amount as well as about the major element compositional effect of the infiltrating fluid on the wall rock.

TECTONIC AND GEOLOGICAL SETTING

The Sesia-Lanzo Zone (SLZ) consists mainly of continent-derived rocks that were subducted to depths between 50 and 70 km in the Late Cretaceous (e.g. Dal Piaz et al., 1972; Duchêne et al., 1997; Rubatto et al., 1999). Prior to subduction, the SLZ rocks occupied the distal part of the Apulian passive continental margin (e.g. Carraro et al., 1970) and were separated from the European continental margin by the Early Jurassic Piemont-Liguria Ocean. Large parts of the SLZ rocks underwent Permian and Jurassic amphibolite- to granulite-facies metamorphism resulting in relatively dry rock compositions prior to subduction (e.g., Lardeaux and Spalla 1991). The onset of convergence of the Apulian and European plates in the Cretaceous involved tectonic erosion and subduction of the SLZ rocks as well as subduction of the Piemont Ocean (e.g. Handy and Oberhänsli 2004 and references therein). During convergence, SLZ was exhumed in the hanging wall of the subducted oceanic plate prior to the continent-continent collision (Babist et al., 2006) and incorporated in the accretionary wedge-like Western Alpine nappe pile (Fig. 1a), within which it forms today the structurally uppermost segment.

The SLZ primarily consists of three large coherent metamorphic rock units (Fig. 1), namely the Mombarone and the Bard unit that are affected by Alpine metamorphic HP overprint (Babist et al., 2006) and the so-called II DK unit, which preserves mainly pre-Alpine granulite- and amphibolite-facies schist and gneiss, as well as several smaller lenses of gabbro and peridotite (e.g. Carraro et al., 1970; Dal Piaz et al., 1971). The internally only weakly deformed Mombarone Unit is separated from the other units by blueschist-facies mylonitic shear zones (e.g. Babist et al., 2006, Gosso et al., 1979; Fig. 1) and a band of Mesozoic metabasites and metacarbonates (Monometamorphic Cover Complex (MCC) of Venturini 1995) that is interpreted to form the nappe separator between the internal Mombarone and the external Bard unit.

Predominant rock types of the Mombarone unit are felsic quartz-rich coarse-grained garnet-omphacite-sodic amphibole-paragonite-phengite ortho- and para-gneisses and schists (e.g. Rubie 1983, Koons 1986), basic coarse-grained garnet-omphacite-sodic amphibole-paragonite-epidote gneisses, smaller lenses of sodic amphibole-bearing basic eclogite, omphacite-phengite-zoisite-bearing marble as well as subordinate quartzite and ultrabasic rocks (e.g. Compagnoni et al., 1977; Castelli 1991; Ferraris and Compagnoni, 2003). Peak metamorphic conditions of these rocks were about 500 to 600°C at pressures between 1.5 and 2.0 GPa (Pognante 1989; Tropper et al, 1999; Zucali et al., 2002). Blueschist-facies viscous deformation at the contact between the Mombarone and the Bard Units (Tallorno Shear Zone) affected felsic and basic rock types and led to well-equilibrated ± garnet-bearing albitic plagioclase-epidote-sodic amphibole-paragonite-phengite mylonites (e.g., Gosso et al., 1979; Babist et al., 2006). In the more external Bard unit Alpine greenschist-facies overprint is more thorough, reflected in fine-grained albitic plagioclase-white mica-epidote-biotite-gneisses with minor intercalations of chlorite-calcic amphibole gneiss and subordinate phengite-bearing quartzite. Alpine peak metamorphic conditions attained in the Bard unit are estimated to have been 1.0-1.5 GPa at 500-550°C (Lardeaux and Spalla 1991).

SAMPLES

We investigated four samples that were collected within the Mombarone Unit (Fig. 1b). The samples represent two major rock types of the SLZ and can be divided into two chemically different groups: two samples are characterised by higher K, Al and Si concentrations, thus reflecting felsic precursor and two are characterised by high Ca, Na and Mg and lower K and Si contents, thus reflecting a more basic composition of the protolith. Representative examples of both felsic and mafic rocks types will be described in greater detail. Major and trace element bulk rock compositions are given in the electronic supplementary material.

Mineral assemblages and –chemistry in samples (MKS-52-1 and MKS-55-1)

The weakly deformed samples are moderately foliated and fine- to medium-grained (Fig. 2). The weak foliation in the basic sample (MKS-52-1, Fig. 2a) is parallel to a compositional banding defined by garnet-, sodic amphibole-, quartz- and mica-rich layers. The metapelitic sample (Fig. 2b), containing sodic amphibole, white mica and omphacite (or pseudomorphs after omphacite) in a quartz-rich matrix, is more homogeneous with a moderate foliation defined by sodic amphibole and white mica. In both samples the foliation is interpreted to be syn-kinematic with respect to the mylonitic blueschist-facies shear zone at the contact between the Mombarone and Bard Units (cf. Babist et al., 2006).

The samples have a high-pressure mineral assemblage, the oldest preserved stage, of quartz (predominant in the felsic sample) + phengitic white mica + omphacite + sodic amphibole + garnet + rutile + paragonite with differences being restricted to variation in modal proportions. The felsic sample (MKS-55-1) is quartz and mica-rich whereas the basic sample (MKS-52-1) is dominated by sodic amphibole, garnet and, if preserved, omphacite.

In all samples three major stages of retrograde metamorphic overprint associated with fluid influx are evident from the textural phase relations (Fig. 3). Each of the overprinting stages is preserved in the samples either in the form of compositional zonation in phengite and sodic amphibole or by the preservation of characteristic mineral assemblages (Table 1). The first two overprinting stages that occurred in the stability field of sodic amphibole are obvious in all samples, whereas the third, greenschist-facies overprint is only weakly developed and restricted to few areas in each thin section.

If preserved, primary ***omphacite*** (cpx) forms grains up to 5 mm long, which commonly contain numerous inclusions of garnet, rutile and quartz. Compositional variations are only minor ranging between Jd_{30} and Jd_{40} in the basic samples and between Jd_{50} and Jd_{60} in the felsic samples (Fig. 5a). The first retrograde compositional resetting of omphacite starts at

the rims of large grains and produces patchy omphacite with lower jadeite content along a complex intra-grain network (Fig. 3a). In some places newly formed diopsidic omphacite overgrowths are found. In the next stage omphacite shows a characteristic and unusual replacement by pseudomorphs containing phengite, epidote, quartz and albitic plagioclase (Fig. 3b). The extent of the replacement and the amounts of replacement products vary within a single thin section. The relative amounts of pseudomorph phases vary from phengite-rich to albitic plagioclase-rich, but always with only small amounts of epidote (Fig. 3a and b). Interestingly, in some places epidote shows a topotactic replacement of the earlier pseudomorph texture, thus suggesting epidote growth after the phengite-bearing pseudomorph stage (Fig. 3b). Phengite in the pseudomorphs has lower Na but higher Fe than cores of large matrix grains. Symplectite plagioclase is almost pure albite and epidote is zoned to slightly more Fe-rich rims. The third stage of omphacite modification is characterised by the formation of a finger-like vein network within the relict omphacite crystals that consists of sodic-calcic amphibole, mostly concentrated in the middle of the veins and sometimes arranged *en echelon*, and albitic plagioclase (Fig. 3a). None of the replacement textures show signs of a deformation after formation.

Primary ***phengite*** (phe) forms grains up to 3 mm long, in places intergrown with paragonite, and containing minor inclusions of garnet and quartz (Fig. 3). Primary phengite has between 3.3 and 3.5 Si per formula unit, X_{Mg} between 0.6 and 0.7, and shows slightly higher celadonite content in the basic samples (Fig. 5b). Chemical modifications of phengite due to retrograde equilibration are visible in high contrast BSE images (Fig. 3) and in compositional X-ray mappings (Fig. 4). The BSE images show darker-coloured cores surrounded by brighter zones that are concentrated at the tips and grain boundaries (Figs. 3c and 4a), around inclusions (Figs. 3e and 4a) and in deformed parts (Fig. 3d) of many grains. The BSE images and X-ray mappings reveal one, in some places two different overprinting zones (Figs. 3c and 4), which likely correspond to two different overprinting events. The

boundary between unaffected and overprinted parts can be relatively sharp but especially in deformed grains also diffuse transitions occur (Fig. 5b). The compositional variation between the homogeneous cores and the rims is mainly characterised by a Fe-Mg exchange and an associated decrease in the X_{Mg} value (Figs. 4b and 5b). A slight decrease in the Si-content associated with an increase in tetrahedrally-coordinated Al (Tschermak-substitution) is sometimes observable (Fig. 4c). Further, overprinted areas are characterised by lower Na and Sr and higher Ba and Cl contents (Fig. 4). During the last overprinting event phengite is rimmed by biotite and oxide phases (Fig. 3).

Sodic amphibole (gln) grains, up to 5 mm long, commonly contain garnet, omphacite and quartz inclusions (Fig. 3). Primary sodic amphibole can be characterised by a solid solution between glaucophane and Fe-glaucophane with X_{Mg} between 0.55 and 0.7 (Fig. 5c). During initial retrogression sodic amphibole adjusts compositionally with a characteristic chemical trend in overgrowth zones as well as in intra-grain re-crystallisation and diffusion zones. The chemical modification of affected amphibole grains is reflected, in high-contrast BSE images, as a network of brighter (compared to the unaffected areas) amphibole material, varying in width and emanating from grain boundaries, brittle fractures and cleavage planes. The affected areas often have sharp boundaries towards the unaffected cores, but also more diffuse transitions between affected and unaffected parts occur. In the modified parts two, in places three, compositional variations can be observed. The first compositional overprint occurs only along grain boundaries and is emanating mainly sub-parallel to the grain boundaries into the interior of the amphibole grains (Fig. 3f). It can be seen in weakly retrogressed samples that this overprinting is related to the first retrograde metamorphic event as modified sodic amphibole rims coexist with retrogressed omphacite. The second stage of overprint is indicated by sodic amphibole with slightly brighter appearance in the BSE images, which has a more diffuse pattern although it seems to be concentrated along the grain boundaries as well (Fig. 3g). The third retrogression stage is characterised by the “brightest”

sodic amphibole composition and occurs mainly along brittle fractures that clearly postdate the two earlier overprint stages (Fig. 3g).

As in phengite, the compositional change across the boundary to the affected rims can be mainly characterised by Mg and Fe exchange (Fig. 4b). Mg contents change drastically and drop from values around 2.2 to 1.6 cations per formula unit (c.p.f.u.) followed by a further decreases to values around 1.45. The change in the Fe content is inverse with a sharp increase from 0.9 to 1.4 c.p.f.u. and a further increase towards the rim. Although Ca is minor it shows a slight increase, as does calculated tetrahedral Al, whereas octahedral Al shows a slight decrease towards the overprinting zones. Si and Na show no significant differences between cores and overprinted rims (Fig. 4c and d). In contrast to phengite, sodic amphibole in places exhibits oscillatory growth zonation (Fig. 3h).

A last retrogression of sodic amphibole is in some areas visible at the outermost rims of the amphibole grains, where it is often replaced by chlorite, calcic amphibole and albitic plagioclase indicating a static greenschist-facies overprint (Figs. 3d and f).

The numerous idiomorphic to sub-idiomorphic, almost inclusion-free ***garnet*** (grt) grains vary in size from 50 µm to 200 µm in diameter and preserve compositional growth zonation (Fig. 5d). In most cases the variation is only a minor increase in Prp and X_{Mg} ($Mg/Mg+Fe^{2+}$) associated with a decrease in Alm and Grs from core to rim. Sps content in all investigated garnets is low ranging from 1 to 10 mol%. Garnet shows signs of resorption, indicated by crosscutting relations between grain boundary and zonation pattern, but without obvious replacement by other phases (Fig. 4h). In sample MKS-52-1 newly formed garnet, with higher Mn and lower Ca, overgrew rims of large porphyroblasts and infiltrated the interior of the porphyroblasts along a sub-grain boundary networks (Fig. 4h, c.f. Konrad-Schmolke et al., 2007). The overgrowth zones are characterised by sharp compositional

gradients towards the host grains. In the latest preserved metamorphic stage garnet is partly replaced by chlorite.

Paragonite (pg) occurs in all samples either in mica-rich layers or associated, sometimes intergrown, with phengite (Fig 3e). Paragonite is more abundant in the felsic samples where it forms up to several hundreds of micron large grains with uniform composition. In a few areas paragonite replacement by albitic plagioclase can be observed.

Epidote (ep) occurs in the matrix as well as in pseudomorphs and aggregates together with phengite that replace omphacite. In the matrix epidote forms grains up to 300µm that are mostly rounded, but sometimes occur also as elongate grains grown parallel to the main foliation. Epidote in pseudomorphs and phengite-epidote aggregates is often hypidiomorphic and forms grains up to 200µm. Epidote composition is quite uniform with X_{Ep} between 0.6 and 0.7.

Calcic amphibole (cam) occurs as small acicular grains that are often associated with chlorite and albitic plagioclase along the rims of sodic amphibole as well as within relict omphacite grains (Fig 3a and f). Chemically calcic amphibole is tremolite sometimes magnesiohornblende, but commonly has moderate Na(A) between 0.1 and 0.15 cations per formula unit and tetrahedral Al contents ranging between 0.25 and 0.35 cations per formula unit.

Textural relations indicate that ***rutile*** (rt) is the stable Ti phase at peak conditions in both rock types. Rutile is found as inclusions in garnet – where it occurs predominantly in the outer cores and near the rims – omphacite, sodic amphibole and phengite. Rutile has grain sizes between 10 (small inclusions) and 200 µm (matrix grains aligned parallel to the foliation) and is generally more abundant in the basic than in the felsic samples. In the basic samples rutile is replaced by ***ilmenite*** along rims and cracks whereas in the felsic samples rutile is overgrown by titanite.

In both rock types ***apatite*** and ***pyrite*** occur as accessory phases. Apatite is usually inclusion-free and occurs in the matrix as well as inclusions in garnet. Apatite forms elongate roundish grains of up to 300 μm. Pyrite is more abundant in the basic samples than in the felsic ones and usually forms grains of up to 100μm. Together with ilmenite, forming around rutile in the basic samples, pyrite is the major iron-rich accessory phase in the samples.

In summary, three retrogression stages control the paragenesis and mineral compositions in the samples (Table 1). The first retrogression drives omphacite, sodic amphibole and phengite rims to become more Fe-rich, whereas net transfer reactions are not evident. During the second retrogression omphacite is replaced by phengite-epidote-albitic plagioclase pseudomorphs, whereas sodic amphibole and phengite re-crystallise and again shift towards more Fe-rich compositions. Garnet is resorbed and forms, together with omphacite, sodic amphibole and epidote. The last visible overprint produces calcic amphibole + albitic plagioclase from omphacite and calcic amphibole + chlorite + albitic plagioclase from sodic amphibole. During that stage garnet is replaced by chlorite, paragonite decomposes to albitic plagioclase and phengite forms biotite. Measured electron microprobe analyses and calculated mineral compositions are included in the electronic supplementary material.

RELATION BETWEEN COMPOSITIONAL MINERAL ZONING AND P-T-X EVOLUTION

To correlate the growth and recrystallization zones in sodic amphibole and phengite with the pressure-temperature and chemical evolution as well as to constrain the modal changes of stable solid and fluid phases we calculated contoured P-T- and P-XH_2O-phase diagrams for the specific bulk rock compositions of a basic (MKS-52-1) and a felsic (MKS-55-1) sample. Additionally, in order to constrain fluid in- and output as well as the effect of fractional crystallisation on the phase assemblage we performed thermodynamic forward modelling along a specified P-T path representing the metamorphic evolution of the SLZ

(Babist et al., 2006 and references therein). In contrast to isochemical phase diagrams, such forward models are suitable for modeling non-isochemical metamorphic rock evolutions.

Forward modelling involved calculation of sample-specific thermodynamic properties at 25 P-T increments along the prograde segment of the P-T trajectory as well as at 100 increments along the retrograde branch (see arrow in Fig. 6). We utilised Gibbs energy minimisation, and modification of the effective bulk rock composition between two P-T increments according to the amount of elements incorporated in those phases that are assumed to undergo fractional crystallisation (garnet) or that are assumed to enter or leave the system (water) using the THERIAK algorithm (De Capitani and Brown, 1987; Konrad-Schmolke et al., 2005, 2006). Further details, such as solid solution formulations and bulk rock chemistries used for the models are given in the electronic supplementary material. In order to validate model settings we compare modelled major element compositional changes in garnet, sodic amphibole and phengite with the actual, measured compositional changes in these phases. The thermodynamic models were applied for different boundary conditions of the fluid budget during subduction and subsequent exhumation based on naturally occurring situations:

On the prograde path we assume that any fluid liberated during dehydration reactions leaves the (rock-) system. Garnet undergoes fractional crystallisation and elements incorporated into the stable amount of garnet are removed from the effective bulk rock composition (EBC). On the retrograde branch of the P-T trajectory the effects of two different processes on the samples are modelled: 1) the effect of water-fractionation, water under-saturation and re-hydration on the samples and 2) the effect of refractory garnet material being recycled into the EBC or staying isolated without thermodynamically equilibrating with the EBC.

Modeling results

Fig. 6 shows the calculated phase relations in P-T diagrams for the two selected samples in the temperature and pressure range of interest (a) as well as contours for the amount of water in the stable solid phases (b) and for X_{Mg} in sodic amphibole (c) and phengite (d). The stability fields of the observed coexisting phase assemblages in our samples are indicated by the shaded areas in Fig. 6a. Although different in detail, both diagrams show broadly similar topologies.

At peak conditions (ca. 2.0 GPa at 550°C) the equilibrium assemblage in both samples is predicted to contain garnet + omphacite + sodic amphibole + phengite + quartz. Paragonite is calculated to be stable at peak conditions in sample MKS-55-1 (Fig. 6a). The large multivariant stability fields are constrained by the zero mode lines of lawsonite and plagioclase, which are absent in the observed assemblage, and by the stability of omphacite, which was stable at peak conditions. The retrograde path of the P-T trajectory (arrow) crosses the stability fields of all the observed retrogressional mineral assemblages (shaded areas in Fig. 6a) in our samples.

An important feature of the metamorphic history of our samples is demonstrated by the isopleth patterns in these diagrams relative to the followed P-T path. The isopleths for the water content have a positive slope below 1.1 GPa and a negative slope at higher pressures. At peak conditions the basic and felsic rocks are predicted to contain ca. 0.65 and 1.5 wt% water, respectively. Thus, it is possible that decompression from the pressure peak, if not associated with a significant temperature increase, would result in water under-saturation of our samples if no external fluid is entrained above 1.1 GPa. The omphacite-free retrogressional mineral assemblage sodic amphibole + phengite + epidote ± garnet ± albitic plagioclase contains, at water saturation, about 1.8 wt% water in case of the basic sample (Fig. 6c) and about 2.2 wt% water in case of the felsic sample (Fig. 6d). Thus, to maintain

water saturation and to produce the retrograde mineral assemblages observed in our samples a significant amount of water must have been added.

The X_{Mg} isopleths in amphibole (shown in Fig. 6b in those areas where the stable amphibole is sodic in composition) and phengite (Fig. 6c) lie sub-parallel to those for the water content but show an opposite pattern with respect to the quantitative values. Whereas the calculated water content of our samples shows a characteristic increase along the retrograde branch of the P-T path associated with the formation of epidote and the breakdown of omphacite, the X_{Mg} patterns of amphibole and phengite are characterised by a large area with low X_{Mg} in both phases that stretches from 400 to 550°C at 1.2 GPa in all diagrams. The X_{Mg} isopleths are closely spaced in those areas where amphibole coexists with clinopyroxene and/or plagioclase and are more widely spaced where sodic amphibole coexists with garnet and paragonite in the absence of omphacite and plagioclase. Generally, the isopleth patterns indicate a continuous decrease in the glaucophane component with decreasing pressure along the P-T trajectory up to 1.1 GPa. Comparing the calculated and observed compositional trends indicates that the Fe enrichment in amphibole and phengite of the natural samples is compatible with a decompression of the samples, although the calculated X_{Mg} values in phengite are slightly lower than those observed in the natural samples. In contrast to X_{Mg}, the calculated and observed Si content in phengite (between 3.5 and 3.4 in sample MKS-52-1 and MKS-55-1, respectively) are in agreement with postulated peak pressures between 1.8 and 2.0 GPa (Fig. 6d) and the widely spaced pattern of Si-isopleths, especially in phase fields with coexisting paragonite (sample MKS-55-1) explains the minor silicon core-to-rim difference in the natural samples. However, it is evident that the step-like compositional zoning in the natural samples contradicts a continuous thermodynamic equilibration during exhumation.

The diagrams in Fig. 7 display the relation between modal changes in the phase assemblage (a), the compositional trends in phengite (b) and amphibole (c) as well as the

water content and volume of solids (d) calculated along the retrograde segment of the P-T trajectory. Homogeneous equilibrium crystallisation and water saturation are assumed. During the initial stages of the decompression sodic amphibole and, in sample MKS-55-1, paragonite is formed from omphacite and garnet. Around 1.5 GPa also epidote forms which leads to a drastic decrease in modal omphacite and garnet, both of which are completely consumed at 1.3 GPa (Fig. 7a). These phase transitions are associated with a continuous X_{Mg} decrease in phengite and amphibole, which leads to a minimum X_{Mg} of around 0.5 between 1.4 and 1.2 GPa. This X_{Mg} minimum corresponds with the highest modal amounts of sodic amphibole in both samples. Amphibole consumption associated with the formation of plagioclase and/or magnetite leads to slightly increasing X_{Mg} in phengite and amphibole. The diagrams in Fig. 7d show, that, depending on bulk rock chemistry, and influx of water between 0.6 and 1.5 wt% are necessary to ensure water saturation of the samples along the decompression path. Depending on rock composition decompression and rehydration is associated with up to 17 % volume increase that occurs in two stages in both samples (Fig. 7d). Eclogite- to blueschist-facies transition (between 1.4 and 1.2 GPa) is associated with 8 and 5% expansion in the basic and felsic sample respectively, the blueschist- to greenschist-facies transition contributes another 5 % volume increase.

Nevertheless, the presence of large, compositionally zoned garnet porphyroblasts in both samples suggests fractional garnet crystallisation during the prograde metamorphic evolution of the samples. As a consequence, the diagrams in Figs. 5 and 6 might not correctly represent the crystallisation sequence along the retrograde P-T segment, as they assume homogeneous equilibrium crystallisation across the entire grid: a process contradicted by the occurrence of large garnet cores that are isolated from the EBC (cf., Marmo et al., 2002; Konrad-Schmolke et al., 2007). Further, it is likely that water liberated during the prograde devolatilisation of the samples left the rocks, which also might have influenced the crystallisation history of the samples. To account for element fractionation along the prograde

segment of the P-T trajectory we performed thermodynamic forward modelling under consideration of fractional garnet crystallisation and water fractionation. The results of these models are shown in Fig. 8.

Prograde evolution

The diagrams in Fig. 8 show the modal abundances of the stable phases of interest (a) as well as the compositional evolution of phengite (b), amphibole (c) and garnet (d) calculated for the two chosen samples along the prograde branch of the P-T trajectory shown in Fig. 6. Both samples undergo significant dehydration indicated by the drastic decrease of hydrous phases and the increase of (accumulated) liberated water. Interestingly, dehydration occurs in two stages, one between 1.2 and 1.3 GPa and a second between 1.5 and 1.8 GPa, associated with the breakdown of chlorite, epidote and amphibole. The compositional evolution of phengite in both samples is characterised by an increase in the celadonite component indicated by an increase in the Si content associated with a decrease in tetrahedral Al (Fig. 8b). This exchange is more pronounced in the basic sample. Additionally, X_{Mg} in phengite increases in both samples, a feature also more pronounced in the basic sample. In both samples X_{Mg} in amphibole changes towards higher values with increasing metamorphic grade. The Ca content of amphibole in both samples decreases slightly.

Garnet growth in both samples is connected with dehydration and the compositional change in garnet involves a continuous slight decrease in the almandine component associated with a slight increase of grossular and pyrope towards the inner rim (Fig. 8d). In the outer rim the trend changes and almandine and pyrope are increasing sharply, whereas grossular decreases. It is notable that the modelled trend in garnet chemistry correlates well with the observed compositional zoning in the garnet crystals in both samples (cf., Figs. 7 and 4), which in turn indicates a potentially good correlation of assumed and real metamorphic evolution.

Fractional garnet crystallisation and water liberation along the prograde P-T path significantly changes the composition of the EBC of the samples (see also electronic supplementary material). Therefore, we calculated P-T pseudosections (Fig. 9) as well as isopleths for the amount of H_2O in solid phases (a) and X_{Mg} in amphibole (b) for the chosen samples with the EBC at peak metamorphic conditions. Differences between the initial bulk rock composition and the EBC used in these calculations are due to the fractional crystallisation of garnet, which is present in our samples as compositionally zoned porphyroblasts, and due to the liberation of water during prograde dehydration reactions. This element fractionation led to a significant modification of the phase topology compared to the diagrams in Fig. 6. It is, of course, notable that the P-T diagrams in Fig. 9 (as are those in Fig. 6) are isochemical and do not reflect the effect of metasomatism during the rock's retrograde evolution and thus are only used to demonstrate the potential effect of element fractionation on the retrograde metamorphic evolution.

The major difference in the phase relations between fractionated (Fig. 8) and unfractionated (Fig. 6) bulk rock compositions are the restricted stabilities of epidote, chlorite and garnet, the absence of paragonite in the basic sample as well as the enlarged stability field of omphacite in a fractionated EBC. Further, the distance between the X_{Mg} isopleths for sodic amphibole is much larger and amphibole is generally more Mg rich. X_{Mg} in amphibole does not significantly change above the plagioclase stability boundary. In the large multivariant phase field of omphacite + sodic amphibole + phengite in case of sample MKS-52-1 and omphacite + sodic amphibole + phengite + paragonite in case of sample MKS-55-1, which stretches across almost the entire upper half of the diagrams, X_{Mg} in amphibole varies only by 0.02 in both samples, with a minimum of 0.6 and 0.68 in the basic and felsic sample respectively. Thus, fractional garnet crystallisation and water liberation have significant influence on the composition of the coexisting phases. In the following sections we will

demonstrate how this effect on amphibole and phengite can be used to reconstruct the evolution of solid and fluid phases during decompression of the samples.

Retrograde evolution

To study the influence of water infiltration on the amount and composition of stable phases during decompression we calculated isothermal P-XH_2O phase diagrams at 550°C for our samples (Figs. 10 and 11). The diagrams in Fig. 10 are calculated for the unfractionated compositions of the samples those in Fig. 11 are calculated for the EBC at peak metamorphic conditions. The diagrams show contours for X_{Mg} in amphibole (a) and phengite (b). Although these two dimensional isothermal diagrams cannot fully display the retrograde evolution of our samples as they ignore the assumed temperature decrease associated with the decompression, several important constraints on the rock evolution can be made.

The diagrams in Fig. 10 show that water saturation in the samples during decompression assuming homogeneous equilibrium crystallisation can only be attained if significant amounts of water are added (see also Fig. 7d). Assuming the rock to be on the water saturation curve at peak conditions, which is likely if continuous dehydration occurred along the prograde path, the samples need between 1.5 and 1.0 wt% H_2O added to attain water saturation at lower pressures. Further, the stability fields of epidote, omphacite, paragonite and garnet are strongly dependent on the water content. The same control accounts for sodic amphibole at very low water contents. In contrast, the occurrence of plagioclase is independent of the water content and strongly pressure sensitive even under water under-saturated conditions. Interestingly, omphacite breakdown occurs at water saturated conditions well above plagioclase stability, thus producing paragonite, epidote, garnet and/or sodic amphibole. At water under-saturated conditions, omphacite breakdown coincides with plagioclase formation or occurs at lower pressures, thus predominantly producing plagioclase during decompression. This indicates that the reaction products of decomposing omphacite

during decompression are dependent on the H_2O content of the rock, and might include (albitic) plagioclase, paragonite, epidote, garnet and sodic amphibole.

Especially indicative for the water content of the samples are the X_{Mg} patterns of amphibole and phengite. X_{Mg} isopleths are near vertical in most water under-saturated fields above plagioclase stability. The steep isopleths indicate that amphibole as well as phengite composition at water under-saturated conditions are very sensitive indicators for the addition of H_2O at any pressure. Increasing H_2O contents at elevated pressures cause drastically decreasing X_{Mg} values in these phases. Further, the calculated X_{Mg} isopleths have contrasting orientations depending on the coexisting phases. A drastic change in the X_{Mg} isopleth patterns occurs if an iron- and/or aluminium-rich phase, such as garnet, epidote or magnetite enters or leaves the mineral assemblage. This effect is visible in the diagrams in Figs. 10 and 11, where the formation of epidote and magnetite in the basic and felsic sample, respectively, strongly deflect the X_{Mg} isopleths.

The effect on the composition of amphibole and phengite of the coexisting mineral assemblage is even more evident in a comparison of the P-H_2O diagrams calculated with and without fractionation effects (Figs. 9 and 10). Fig. 11 shows that due to fractional crystallisation the stability of garnet, doubtless the most important Fe-Al phase in the rocks, is restricted to highly water under-saturated conditions in both samples. In the presence of garnet + magnetite, best visible in case of the basic sample, the X_{Mg} isopleths are near horizontal, whereas those in the garnet- or magnetite-absent fields are subvertical or steeply dipping. Furthermore, X_{Mg} in amphibole and phengite is much higher and the compositional variations in both phases are much smaller in the diagrams calculated for the fractionated EBC, even at water-saturated conditions. However, the absence of magnetite in the natural samples is likely due to the fact that iron liberated by garnet and omphacite forms (apart from the X_{Mg} modification of phengite and amphibole) titanite, pyrite and epidote, whereas in the

models, which do not consider Ti and S, partition of iron occurs mainly into epidote and magnetite.

Three different retrograde evolution scenarios can be extracted from the P-H_2O diagrams: (1) homogeneous equilibrium crystallisation without water re-saturation (i.e. the samples follow the red stippled line given in Fig. 10b and c). This evolution implies complete equilibration of all minerals and recycling of previously fractionated garnet material into the EBC. In this case the observed retrograde mineral paragenesis epidote + paragonite and the observed amphibole and phengite compositions cannot be generated, due to the lack of water influx during decompression. (2) Homogeneous equilibrium crystallisation with water re-saturation (the samples follow the water saturation curves given in Fig. 10). This scenario implies addition of H_2O where the water saturation curve has a negative slope. In this case compositional re-equilibration of amphibole and phengite and thus the compositional zoning, if developed, is unlikely to be step-like. (3) conservation of the peak EBC and peak water content without garnet resorption (samples follow the red stippled line given in Fig. 11b and c). This last case would indeed maintain water saturation during decompression, but the refractory garnet material hinders the formation of the observed compositional re-equilibration of amphibole and phengite as well as the formation of paragonite in the basic sample.

The forward models for the different scenarios along the retrograde P-T trajectory, which reflect a more detailed evolutionary model of the samples, are shown in the following figures. In contrast to the diagrams in Figs. 9 and 10, the diagrams in Fig. 12 reflect the effect of decreasing temperatures during decompression. The diagrams in Fig. 12 show changes in the phase assemblage (a) as well as in phengite (b) and amphibole (c) compositions assuming homogeneous equilibrium crystallisation without water influx, i.e. fractionated garnet material is resorbed, but the H_2O contents of the samples remain constant at peak metamorphic values.

The most important effect during this scenario is that at the initial stages of the exhumation the samples are water saturated and garnet material is available for the compositional equilibration of the phase assemblage (Fig. 12a). The amount of garnet decreases during decompression and sodic amphibole is formed. Associated with this reaction is a slight decrease in X_{Mg} in phengite and amphibole. As both product phases are hydrous and the amount of water is restricted, the rocks become water under-saturated around 1.8 (felsic sample) or 1.6 GPa (basic sample). Thus, resorption of garnet and the associated formation of hydrous phases consume the entire available amount of free water. The resulting water under-saturation hinders further compositional re-equilibration of amphibole and phengite during decompression.

The diagrams in Fig. 12 have shown the importance of water saturation on the mineral assemblage and composition. In the following calculations we demonstrate the effect of resorption of previously fractionated garnet material on the re-equilibration of phases and phase compositions. The diagrams in Fig. 13 are calculated for the assumption of a "rehydrating system". The samples stay water saturated during their retrograde evolution, but refractory garnet does not dissolve or react during decompression. Interestingly, the calculated amount of newly formed sodic amphibole is very small (a) and the compositional trends of phengite (b) and sodic amphibole (c) are almost constant, which indicates that water influx into the dehydrated and depleted bulk rock volume without remobilisation of the fractionated elements in refractory garnet does not lead to a significant change in the retrograde metamorphic rock evolution. The depleted effective (i.e., reacting) bulk rock composition, despite being water present, hinders the compositional re-equilibration of phengite and sodic amphibole.

DISCUSSION

The preservation of multiple stages of retrogression in the mineral assemblages as well as compositional differences within mineral grains allows detailed reconstruction of the retrograde metamorphic evolution of our samples. Comparing the results of the thermodynamic modelling with the observed features in our samples yields important insights into the effect of fluid infiltration on the mineral parageneses and on the major element compositions of the coexisting phases. Further, the pattern of restricted compositional resetting of sodic amphibole (cf., Faryad and Hoinkes 2004) and phengite (cf., Dempster 1992 and Giorgis et al., 2000), visible in high-contrast BSE images, allows tracing of the fluid pathways and the regional distribution of fluid influx above a subducted slab.

It is notable that our thermodynamic calculations are performed in a simplified chemical system (NCKFMASH) with the chemical potential of oxygen (μ_O) being controlled by an ilmenite-magnetite-rutile (IMR) buffer, which constrains the oxidation state of the rocks between the hematite-magnetite (HM) and quartz-fayalite-magnetite (QFM) buffers (cf. Konrad-Schmolke et al., 2008). Ferric iron is considered in the epidote solid solution as well as in endmember magnetite. It is questionable whether buffering μ_O can adequately describe the oxidation state of a rock (e.g. Diener and Powell 2010) but in the absence of a complete set of thermodynamic data for ferric iron-bearing solid solution phases and under consideration of an open system behavior of our samples, buffering μ_O seems a reasonable compromise. Further, ignoring ferric iron in omphacite and amphibole solid solutions might underestimate the extent of stability of both phases. Whereas ferric iron in amphibole is quite low in our samples (usually <10% Fe_{tot}) it is present in considerable amounts in omphacite from the felsic sample (Fig. 4). However, calculations utilising the latest thermodynamic data for ferric iron endmembers in omphacite (Green et al., 2007) and amphibole (Diener et al., 2007) solid solutions show that omphacite might be stable in all plagioclase-absent assemblages (i.e., above 1.0-1.4 GPa, depending on temperature), but, similar to our simplified calculations, giving way to an assemblage with increasing epidote, sodic amphibole

and plagioclase during breakdown (see electronic supplementary material). As the focus of this work is on the effect of water influx on changes in the mineral assemblage rather than on specifying exact metamorphic P-T conditions of our samples, we assume that a slightly underestimated stability of omphacite has only minor effect on our conclusions.

Water re-saturation and amount of infiltrated fluid

At peak metamorphic conditions the stable mineral paragenesis of the samples was garnet + omphacite + glaucophane-rich sodic amphibole + phengite + quartz ± epidote ± paragonite. This assemblage is only partly preserved in the samples. The calculated water content of these assemblages at peak conditions was around 1.5 wt% in the felsic samples and between 0.6 and 1.3 wt% in the basic samples (Fig. 6). Most interesting is the partial re-equilibration of our samples during exhumation. The observed modal relations in the overprinted areas, i.e. the formation of hydrous phases such as phengite and epidote after omphacite, as well as the characteristic often step-like compositional trends in phengite and sodic amphibole, are clear evidence for one or more discrete fluid influx stages during decompression. As it is shown in the P-XH_2O diagrams in Fig. 10, the observed compositions of the overprinted areas of sodic amphibole (X_{Mg} = 0.5) and phengite (X_{Mg} = 0.6) are highly indicative of the coexistence of these phases in specific stability fields where both phases form a characteristic X_{Mg} minimum. The observed compositions of phengite and sodic amphibole are calculated to be stable at (near-) water saturated conditions between 1.4 and 1.2 GPa only. The diagrams in Fig. 7, which display the calculated compositional evolution of phengite and sodic amphibole at water-saturated conditions along the proposed P-T trajectory, also show this distinct X_{Mg} minimum. However, the modelled, relatively smooth compositional trends in phengite and sodic amphibole are in contrast to the observed trends, which show drastic, step-like core-to-rim transitions from high to low-X_{Mg} values (Figs. 3 and 4). Assuming a continuous metamorphic evolution and homogeneous equilibrium

crystallisation both phases would exhibit either no or only smooth compositional gradients even in the case of sluggish diffusional relaxation and the development of compositional growth zonation. Thus, it is much more likely that the observed compositional trends are the result of a discontinuous compositional equilibration. Following the thermodynamic calculations, such a discontinuity can be best explained by an initial decompression without water addition, which led only to moderate compositional changes in amphibole and phengite (e.g., Fig. 11), followed by one or more discrete fluid influx events between 1.4 and 1.2 GPa, which enabled rapid water re-saturation and (partial) compositional equilibration of the mineral assemblage. It is likely that during initial decompression and cooling the rocks became water under-saturated due to the limited external water influx. This effect is evident from the preservation of the Mg-rich compositions of phengite and sodic amphibole. Limited water availability additionally hindered the compositional re-equilibration due to sluggish reaction kinetics and slow element transport (e.g. Rubie 1986, Stünitz 1989).

Some constraints on the amount of fluid necessary to re-establish water saturation in the overprinted areas of the samples can be estimated. It is important to note that all thermodynamic calculations in this work are based on a normalisation of the coexisting phases to represent 100% of the reacting rock volume. Thus, quantification of absolute amounts of fluids and solids must take into account that only a fraction of the entire rock volume has reacted during the fluid influx. This is critical if we quantify the absolute amount of infiltrated fluid or a fluid-rock ratio. It is evident that the amount of the infiltrated fluid led to a water saturation only in the overprinted rims, but was not large enough – or reaction kinetics too sluggish – to re-equilibrate the entire rock volume.

Nevertheless, rough estimates can be made for the amount of the infiltrating fluid during metamorphism. It can be seen in the thin sections as well as in the BSE images that (1) almost the entire amount of omphacite in our samples has been consumed by retrograde

reactions, (2) estimating from the BSE images shows that about 10% of mica and 20% of the sodic amphibole by volume are overprinted and recrystallized and (3) the amount of the greenschist facies overprint is clearly below 5% of the entire rock volume. A conservative estimate of the reacted rock volume during the blueschist facies fluid influx is around 20% of the entire rock volume. The isothermal P-XH_2O Diagrams in Fig. 10 as well as the forward model results shown in Fig. 7 display that about 1.2 and 0.6 wt% water must be added in sample MKS-52-1 and MKS-55-1 respectively, to re-saturate the entire rock with respect to water, to yield the stability of the observed assemblage and to produce the observed Mg trends in mica and sodic amphibole (cf., Figs. 4 and 6). Assuming about 20% of the entire rock to be re-equilibrated during fluid influx the amount of the percolating fluid in these samples must be around 0.2 and 0.1 wt% in sample MKS-52-1 and MKS-55-1 respectively to ensure water re-saturation in the affected areas. Following the results shown in Fig. 10, this fluid influx occurred between 1.4 and 1.2 GPa. However, these values give not a clear idea about the time integrated fluid flux as they do not involve the length scale of the fluid migration, estimation of which is difficult due to the large scale structures in the SLZ (e.g. Gosso et al., 1979; Zucali et al., 2002; Babist et al., 2006). A minimum length scale is given by the vertical distance of overprinted samples in an observable, structurally coherent profile, which is in the order of 2 km. This would correspond to a time integrated fluid flux of about 15 m^3m^{-2}. A less conservative estimation would assume the length scale of fluid migration being constrained by the present vertical extent of the SLZ, which can only be estimated from seismic profiles (e.g. Schmid and Kissling 2000) and is in the order of 10 km. This vertical column would require a time integrated fluid flux of 75 m^3m^{-2} to produce the observed re-equilibration textures. Both estimations yield fairly moderate fluid fluxes through the moderately deformed internal SLZ, although the intensity of fluid migration and fluid-rock interaction might change depending on the mode of fluid transport, which is discussed in the following paragraphs.

Regional fluid flux and fluid pathways

Fluid flux in metamorphic rocks might be related to brittle deformation, such as veins (e.g., Cartwright and Buick 2000; Oliver and Bons 2001), to ductile deformation, e.g., shear zones (e.g., Bebout and Barton 1993, Austrheim 1987) or pervasive by an interconnected fluid film along grain boundaries and other microstructures (Keller et al., 2006; de Meer et al., 2005). Deformation-induced fluid flux is often associated with limited fluid-rock interaction in undeformed areas and allows large quantities of fluid to migrate through a rock volume without significant compositional effects on fluid and wall rock (e.g., Austrheim 1987; Barnicoat and Cartwright 1995). In contrast, large-scale pervasive fluid flux along grain boundaries, as in our samples, allows intense fluid-rock interaction with strong chemical and physical effects on fluid and wall rock. The consequences of a reactive fluid flux above a subducted slab have been demonstrated by many trace element and isotopic investigations in melange zones and exhumed high-pressure sequences (e.g., Sorensen et al., 1997, Marschall et al., 2006, Penniston-Dorland et al., 2010), which show that pervasive fluid fluxes heavily modify the elemental and isotopic composition of wall rocks and fluid. Due to the fact that compositional re-equilibration of our samples is incomplete and that newly-formed as well as re-equilibrated phases can be easily distinguished in high-contrast BSE images, our samples are excellently suited to study regional scale fluid infiltration and fluid-rock interaction, which is important for the general understanding of fluid-driven mass transfer in the Earth's crust and, in particular, in subduction zones.

There are four different types of fluid-assisted re-equilibration textures visible in our samples: (1) brittle fracturing within amphiboles with subsequent precipitation of new equilibrated amphibole material (Fig. 3a), (2) precipitation of new phengite and amphibole material along grain boundaries (Fig. 3c, d and h), (3) migration of reaction fronts from grain boundaries concentrically into undeformed grains (Fig. 3d, e and f) and (4) re-equilibration by

volume diffusion that produces a continuous compositional change perpendicular to the grain boundaries (arrows in Fig. 3c, d and h). Many of the re-equilibrated areas in our samples are of type (2) and (3), both of which occur along almost all grain boundaries (Fig. 3c, d, e and f). The observation that this kind of overprinting occurs along almost the entire grain boundary network, together with our thermodynamic calculations, that show a fluid influx being necessary to produce the newly-formed rim compositions and overgrowth, suggest the presence of an interconnected network, likely wetted by a free fluid phase, along the grain boundaries (cf., Rubie 1986). Such a regional scale, open system pervasive and reactive fluid flux (e.g. Ferry 1987, 1992) allowed effective elemental exchange and compositional re-equilibration of fluids and wall rocks.

Many experimental works and natural examples (e.g. Holness 1993, Mancktelow and Pennacchioni 2004, Hippertt 1994) suggest the existence of non-interconnected porosity along grain boundaries in undeformed rocks that might become interconnected during deformation and changing confining pressure (e.g. Holness 1993, Fusseis et al., 2009). Recent works also suggest the existence of a several nm-wide continuous fluid film along grain boundaries under static metamorphic conditions (e.g. Keller et al., 2006, de Meer et al., 2005). Nakamura and Watson (2001) could experimentally show that due to dissolution-precipitation processes, wetting fluids, such as aqueous solutions, can migrate in form of advancing high-porosity zones in quartzites. These findings are similar to our observation of newly precipitated sodic amphibole material along existing grains (Fig. 3h) and the occurrence of re-equilibration fronts that migrate into older grains (Fig. 3f).

However, the development of micro-porosity is difficult to explain in rocks undergoing mineral reactions with a positive volume change. In our samples, rock volume due to retrograde mineral reactions increases from eclogite-to blueschist-facies conditions by 5 % in the felsic and 8 % in the basic sample. Up to greenschist-facies conditions the volume

increases by 10 and 17 % in the felsic and basic sample, respectively (Fig. 7d). The fluid influx event and the associated mineral reactions alone are associated with a volume increase of about 1.8%. Thus dilatancy due to negative volume changes seems to be unlikely for the generation of any permeability, but recent works (e.g., Jamtveit et al., 2008) show evidence for the development of an extensive network of brittle fractures and/or sub-grain boundaries developing in initially low-permeability rocks by mineral reactions that are associated with a volume increase. It is notable that the microfractures and/or interconnected sub grain boundaries shown in Fig. 3h, are very similar to the textures developed in the models of Jamtveit et al., (2008) as well as in several other experiments (e.g., Putnis 2002; Milke and Wirth 2003) and seem to be common in naturally occurring high-pressure/low temperature rocks (e.g., Konrad-Schmolke et al., 2007). However, the existence of an interconnected fluid film along grain boundaries in our samples is contrary to the observations in many retrograded high-pressure rocks from within the subducted slab, where fluid migration is often connected to brittle fracturing or restricted to shear zones (e.g. Austrheim 1987, John and Schenk 2003, Cartwright and Buick 2000, Franz et al., 2001). This is, of course, important for the extent of the fluid-rock interaction in our samples, but also for the initiation of solution/re-precipitation processes (e.g. de Meer et al., 2005) that might explain the observed intra-grain step-like re-equilibration features in our samples.

Open system pervasive fluid flow is important in mid and upper crustal levels and in hydrothermal systems associated with regional metamorphism (e.g., Ferry 1987, 1988, 1992, Cartwright et al., 1995, St-Onge and Lukas 1995), but similar examples are given for subduction zone settings, such as the mantle wedge (e.g. Peacock 1987, Kostenko et al., 2002) or the slab-mantle interface (e.g., Bebout and Barton 1993). In the hanging wall of a subducted slab, where strong thermally induced gradients in hydraulic head exist and where buoyancy-driven upward migration of fluids liberated by dehydration reactions in the downgoing slab is a likely process, the prerequisites for a pervasive fluid flux along grain

boundaries are generally met (e.g., Oliver 1996). Thus, pervasive fluid flow might be a common mechanism especially in larger, weakly deformed coherent blocks that undergo exhumation on top of the subducted slab and thus, interpretations of trace element and isotopic patterns in subduction related volcanic rocks must consider a significant compositional modification of primary devolatilisation fluids already at the slab-mantle interface.

Generally, there is likely a drastic change in the overall fluid flow mechanism from within the subducted slab, across the slab-mantle interface into the hanging wall mantle wedge (Fig. 14). In the downgoing subducted slab most prograde mineral reactions are associated with a negative volume change, which enables the formation of open fractures that channelize fluid fluxes (e.g., John and Schenk 2003; Zack and John 2007). In contrast, as demonstrated by our examples, rocks in the hanging wall of the subducted slab are often affected by retrograde and/or re-hydration reactions, due to decompression or fluid infiltration, or both. Such reactions are often associated with a positive volume change (Fig. 7d) and thus, dilatancy and the possibility of vein formation is limited. In this setting, fluid migration is controlled either by viscous deformation and channelized in ductile shear zones or by the development of microfractures as a response to the internal strain distributed among and around mineral grains. Several authors (e.g., Sorensen 1988; Sorensen et al., 1997; Breeding et al., 2003) have shown inhomogeneous and incomplete retrogression of high-pressure rocks in melange blocks that are interpreted to represent parts of the slab-mantle interface. Fluid flux in these examples is concentrated around low permeability regions ranging from cm- to decametre-sized undeformed blocks of eclogite material that is surrounded by a highly deformed and highly permeable matrix (e.g. Ague 2007).

Our samples represent a similar situation, although at a different scale: During exhumation of the Mombarone Unit strain was partitioned between large-scale blueschist-

facies shear zones bounding the Mombarone unit and weakly-deformed rocks in the internal parts (Babist et al., 2006). Mylonitic rocks are well equilibrated under retrograde blueschist facies conditions (Stünitz 1989; Babist et al., 2006), whereas our samples from weakly deformed, internal, initially less permeable, regions of the Mombarone Unit reflect only moderate fluid influx, although associated with intense retrograde overprint in the affected areas. Although fluids might be carried away fast and without strong interaction from the subducting slab, (e.g., Zack and John (2007)), it is evident that intense fluid-rock interaction occurs on top of the slab, which significantly modifies the trace element information of the subduction-related fluid in the highly reactive slab-mantle transition zone.

Above the slab-mantle transition zone the mode of fluid migration and therefore the extent of fluid-rock interaction in the mantle wedge is crucial for the understanding of mantle hydration, major- and trace-element transfer, melt generation and migration as well as for the boundary conditions of numerical thermal models of subduction zones (e.g., Iwamori 1998, Arcay et al., 2005). Here, pervasive fluid flux seems to be a common mechanism for fluid- and also melt migration in the mantle wedge (e.g., Kostenko et al., 2002; Lundstrom 2000), although some examples also exist for a channelized fluid influx into the mantle wedge (e.g., Bodinier et al., 1990). Following the interpretation of seismic observations (Bostock et al., 2002; Xia et al., 2008) the hydration of the mantle wedge above the subducted slab seems to be inhomogeneous, which is evidence for inhomogeneous fluid fluxes but, unfortunately, yields only little constraints on the mode of fluid migration on a larger scale.

Rate-controlling processes

Interesting with respect to the rate-controlling factor of rock retrogression and of fluid-rock interaction is the reaction-controlled element availability and the limited compositional resetting of phengite and sodic amphibole during the fluid influx. Fig. 13 shows the calculated phase assemblages and amphibole compositions of the effective bulk rock composition at

peak metamorphic conditions of the two selected samples in P-T space and along the specified P-T trajectory, respectively. The calculations assume fractionated garnet does not back-react and thus all elements incorporated into the garnet interiors are isolated from the reacting bulk rock volume, thus implying garnet-absent conditions during decompression, as the material in the interiors of the porphyroblasts is not available for thermodynamic equilibration. A comparison of the results shown in Fig. 12 indicates that even with a re-saturation of the rocks with respect to water there is no thermodynamically controlled Fe-enrichment predicted in phengite and amphibole. In contrast, as shown in the calculations in Fig. 7, recycling of garnet material is the controlling factor for the stabilisation of iron-rich areas in phengite and amphibole. Thus, the kinetically most retentive phase, in our samples garnet, controls the extent of re-crystallisation and re-equilibration in our samples. In other words, resorption of garnet material from the porphyroblasts, i.e. recycling of garnet material into the EBC, is necessary to enable compositional re-equilibration of amphibole and phengite and to produce the observed X_{Mg} decrease in the natural samples. In turn, the spatial extend of phengite and amphibole overprinting can give information about the transport distances and -properties of recycled garnet material (e.g. iron) in the samples. Although Mn backdiffusion and newly-formed Mn-rich overgrowth zones in garnets from our samples (Fig. 4h) are clear indications of garnet resorption during fluid infiltration, textural relations do not allow a spatial correlation of garnet resorption sites and intensity of X_{Mg} reequilibration in phengite and sodic amphibole.

The above observation leads to the fact that garnet porphyroblasts have a multiple importance in high-pressure rocks. On the one hand they might trigger the physical behaviour of the rock (e.g. Groome et al., 2006), they might control element recycling into the mantle (e.g. Konrad-Schmolke et al., 2008) and they might further control the extent of preservation of high-pressure assemblages in exhumed rocks because of their sluggish reaction rates, which in turn significantly influences the coexisting phases.

Major element transport in the fluid

The compositional profiles and mappings of phengite and amphibole (Figs. 4 and 5b and c) show a predominant Fe-Mg exchange towards higher Fe contents in the overprinted areas of both minerals. Ca is also slightly enriched in the overprinted areas of sodic amphibole. As the overprinting effect is fluid controlled, all three elements must be sufficiently present in the transport agent to enable re-equilibration of the affected areas. The length scale of the element transport is at least at thin section-scale, because there is no preferential overprinting of phengite and amphibole around Fe- and Ca-rich minerals such as omphacite and garnet. There is still too little knowledge about the properties of subduction related fluids (Manning 2004) and the solubility and transport of different elements in such fluids is difficult to constrain experimentally. Several studies on fluid inclusions from high-pressure veins in exhumed eclogitic rocks as well as data from forearc serpentinites exist (e.g. Franz et al., 2001, Gao and Klemd 2001, Becker et al., 1999, Fryer et al., 1999). Most of these studies show a significant mobilisation of major elements, such as Si, Al, Na, Ca and Mg, but none of these concentrates on the amount of dissolved iron, which is clearly mobile in our samples. However, the formation of Fe-rich minerals, such as omphacite and garnet, within high-pressure veins suggests a significant fluid-bound transport of Fe in subduction zone fluids (Philippot and Selverstone 1991; Franz et al., 2001).

Furthermore, there is an obvious addition of potassium during the fluid influx, which is evident from the formation of phengite-rich pseudomorphs after omphacite (cf. Rubie 1986). Interestingly, newly-formed phengite does not precipitate along the edges of existing grains, which would be the favoured site of precipitation considering the surface energy constraints, but has formed preferentially at omphacite reaction sites. We interpret the replacement of omphacite by phengite as a result of the limited availability of Al in the percolating fluid. It is likely that the K/Al ratio in the fluid is too large to allow phengite

precipitation along existing phengite grain boundaries. Only at those sites where Al is available due to retrograde net-transfer reactions, such as the omphacite breakdown location, new phengite can form. This observation suggests a limited mobility of Al in our samples but abundant K needs to be present in the fluid (e.g., Philippot and Selverstone 1991). Rubie (1986) attributed the observed K-metasomatism to a large fluid/rock ratio that might partially be present in these rocks. It is obvious that water saturation must have prevailed during this non-isochemical reaction as hydrous K-bearing phases formed from omphacite, which did not contain K or even inclusions of phengite prior to the fluid influx (cf. Rubie 1986). However, the presence of chlorine in the fluid, which is indicated by the higher Cl contents in the overprinted phengite rims (Fig. 4g), certainly plays a major role regarding the relatively high solubility and transport of major elements in our samples (e.g., Manning 2004).

Conclusions

The Western Alpine Sesia Zone is a segment of continentally derived high-pressure rocks that were exhumed in the hanging wall of a subducted oceanic plate. Fluid infiltration into the previously dehydrated rocks led to a partial retrogression during exhumation. Weakly deformed samples from the internal part of the SLZ well preserve relict eclogite facies mineral assemblages. Limited fluid influx into relatively dry high-pressure rocks led to complex and characteristic compositional zonation patterns in phengite and sodic amphibole that is best visible in high contrast back scattered electron images. The effect of the fluid influx is reflected in a complex network of modified amphibole and phengite material that appears brighter in BSE images and has sharp boundaries to the unaffected cores. Differences between overprinted and shielded areas in both minerals are mainly in the X_{Mg} value with lower X_{Mg} in the overprinted rims as well as in the concentrations of fluid-mobile trace elements, such as Ba and Sr, which increase and decrease from core to rim, respectively. Further, fluid infiltration caused the formation of unusual phengite-epidote-albitic plagioclase

pseudomorphs after omphacite. A comparison of the observed textural and compositional changes in our samples with thermodynamic models yields insight into the amount and major element composition of the infiltrated fluid. Only approximately 0.1 – 0.5 wt% fluid relative to the entire rock was added during exhumation. Further, the observation of the fluid induced retrogression features over map-scale distances indicates an open system pervasive fluid infiltration and intense fluid-rock interaction at blueschist facies conditions above the subducted slab. Fluid infiltration caused Potassium-metasomatism, enabled an intense Fe-Mg exchange among coexisting minerals, but did not enable mobilisation of large amounts of Al. We propose that these samples are excellently suited for the investigation of fluid-triggered high-pressure processes in a subduction zone from (sub-)grain- to regional-scale and that the compositional resetting of sodic amphibole as well as phengite can be used as an excellent tracer of the fluid-rock interaction.

ACKNOWLEDGEMENTS

We thank Horst Marschall (Woods Hole) and Michel Marks (Tübingen) for inspiring discussions about fluid migration. James Scott and Christina Günter are thanked for assistance with the EMPA analyses. We additionally thank Jörg Herrman for thoughtful editorial handling as well as Jay Ague, Daniele Castelli and Peter Tropper for thorough, critical and constructive reviews.

REFERENCES

Ague, J. J. (2007). Models of permeability contrasts in subduction zone mélange: Implications for gradients in fluid fluxes, Syros and Tinos islands, Greece. Chemical Geology 239, (3-4): 217-227.

Arcay, D., Tric, E. and Doin, M.-P. (2005). Numerical simulation of subduction zones. Effect of slab dehydration on the mantle wedge dynamics. Physics of the Earth and Planetary Interiors 149: 133-153.

Austrheim, H. (1987). Eclogitization of lower crustal granulites by fluid migration through shear zones. Earth and Planetary Science Letters 81, (2-3): 221-232.

Ayers, J. (1998). Trace element modeling of aqueous fluid-peridotite interaction in the mantle wedge of subduction zones. Contributions to Mineralogy and Petrology 132, (4): 390-404.

Babist, J., Handy, M. R., Konrad-Schmolke, M. and Hammerschmidt, K. (2006). Precollisional, multistage exhumation of subducted continental crust: The Sesia Zone, Western Alps. Tectonics 25, (6): TC6008.

Barnicoat, A. C. and Cartwright, I. (1995). Focused fluid flow during subduction: Oxygen isotope data from high-pressure ophiolites in the Western Alps. Earth and Planetary Science Letters 132: 53-61.

Bebout, G. E. and Barton, M. D. (1993). Metasomatism during subduction: Products and possible paths in the Catalina schist, California. Chemical Geology 108, (1-4): 61-92.

Bebout, G. E., Ryan, J. G., Leeman, W. P. and Bebout, A. E. (1999). Fractionation of trace elements by subduction-zone metamorphism - effect of convergent-margin thermal evolution. Earth and Planetary Science Letters 171, (1): 63-81.

Bebout, G. E. and Barton, M. D. (2002). Tectonic and metasomatic mixing in a high-t, subduction-zone mélange - insights into the geochemical evolution of the slab-mantle interface. Chemical Geology 187, (1-2): 79-106.

Becker, H., Jochum, K. P. and Carlson, R. W. (1999). Constraints from high-pressure veins in eclogites on the composition of hydrous fluids in subduction zones. Chemical Geology 160, (4): 291-308.

Bodinier, J. L., Vasseur, G., Vernieres, J., Dupuy, C. and Fabries, J. (1990). Mechanisms of mantle metasomatism: Geochemical evidence from the Lherz orogenic peridotite. Journal of Petrology 31, (3): 597-628.

Bostock, M. G., Hyndman, R. D., Rondenay, S. and Peacock, S. M. (2002) An inverted continental Moho and serpentinization of the forearc mantle. Nature 417: 536-538.

Bouvier, A.-S., Metrich, N. and Deloule, E. (2008). Slab-derived fluids in the magma sources of st. Vincent (Lesser Antilles arc): Volatile and light element imprints. Journal of Petrology 49, (8): 1427-1448.

Breeding, C. M., Ague, J. J., Bröcker, M. and Bolton, E. W. (2003). Blueschist preservation in a retrograded, high-pressure, low-temperature metamorphic terrane, Tinos, Greece: Implications for fluid flow paths in subduction zones. Geochem. Geophys. Geosyst. 4, (1): 9002.

Carraro, F., Dal Piaz, G. V. and Sacchi, R. (1970). Serie di Valpelline e II Zona Diorito-Kinzigitica sono i relitti di un ricoprimento proveniente dalla Zona Ivrea-Verbano. Memorie della Societa Geologica Italiana 9: 197-224.

Cartwright, I., Vry, J. and Sandiford, M. (1995). Changes in stable isotope ratios of metapelites and marbles during regional metamorphism, Mount Lofty Ranges, South Australia: Implications for crustal scale fluid flow. Contributions to Mineralogy and Petrology 120, (3): 292-310.

Cartwright, I. and Buick, I. S. (2000). Fluid generation, vein formation and the degree of fluid-rock interaction during decompression of high-pressure terranes: The Schistes Lustrés, Alpine Corsica, France. Journal of Metamorphic Geology 18, (6): 607-624.

Castelli, D. (1991). Eclogitic metamorphism in carbonate rocks; the example of impure marbles from the Sesia-Lanzo Zone, Italian Western Alps. Journal of Metamorphic Geology 9, (1): 61-77.

Compagnoni, R., Dal Piaz, G. V., Hunziker, J. C., Gosso, G., Lombardo, B. and Williams, P. F. (1977). The Sesia-Lanzo Zone, a slice of continental crust with Alpine high pressure-low temperature assemblages in the Western Italian Alps. Rendiconti della Societa Italiana di Mineralogia e Petrologia 33, (2): 335-374.

Connolly, J. A. D. (1997) Mid-crustal focussed fluid movement: thermal consequences and silica transport. In: Fluid Flow and Transport in Rocks (eds. Jamtveit B, Yardley BWD), pp. 235–50. Chapman and Hall, London.

Dal Piaz, G. V., Gosso, G. and Martinotti, G. (1971). La II Zona Diorito-Kinzigitica tra la Valle Sesia e la Valle d´Ayas (Alpi Occidentali). Memorie della Societa Geologica Italiana 11: 433-460.

Dal Piaz, G. V., Hunziker, J. C. and Martinotti, G. (1972). La Zona Sesia-Lanzo e l'evoluzione tettonico-metamorfica delle Alpi Nordoccidentali interne. Memorie della Societa Geologica Italiana 11: 433-466.

de Capitani, C. and Brown, T. H. (1987). The computation of chemical equilibrium in complex systems containing non-ideal solutions. Geochimica et Cosmochimica Acta 51, (10): 2639-2652.

de Meer, S., Spiers, C. J. and Nakashima, S. (2005). Structure and diffusive properties of fluid-filled grain boundaries: An in-situ study using infrared (micro) spectroscopy. Earth and Planetary Science Letters 232, (3-4): 403-414.

Dempster, T. J. (1992). Zoning and recrystallization of phengitic micas: Implications for metamorphic equilibration. Contributions to Mineralogy and Petrology 109, (4): 526-537.

Diener, J.F.A., Powell, R., White, R.W. and Holland T.J.B. (2007). A new thermodynamic model for clino- and orthoamphibole in the system Na_2O-CaO-FeO-MgO-Al_2O_3-SiO_2-H_2O-O. Journal of Metamorphic Geology 25: 631-656.

Diener, J.F.A. and Powell, R. (2010). Influence of ferric iron on the stability of mineral assemblages. Journal of Metamorphic Geology 28: 599-613.

Duchêne, S., Blichert-Toft, J., Luais, B., Telouk, P., Lardeaux, J. M. and Albarede, F. 1997. The Lu-Hf dating of garnets and the ages of the Alpine high-pressure metamorphism. Nature, 387, 586-589.

Escher, A. and Beaumont, C. (1997). Formation, burial and exhumation of basement nappes at crustal scale: A geometric model based on the Western Swiss-Italian Alps. Journal of Structural Geology 19, (7): 955-974.

Faryad, S. W. and Hoinkes, G. (2004). Complex growth textures in a polymetamorphic metabasite from the Kraubath Massif (Eastern Alps). Journal of Petrology 45, (7): 1441-1451.

Ferraris, C. and Compagnoni, R. (2003). Metamorphic evolution and significance of a serpentinized peridotite slice within the Eclogitic Micaschist Complex of the Sesia-zone (Western Alps - Italy). Schweizerische Mineralogische und Petrographische Mitteilungen 83, (1): 3-13.

Ferry, J. M. (1987). Metamorphic hydrology at 13-km depth and 400-550 °C. American Mineralogist 72, (1-2): 39-58.

Ferry, J. M. (1988). Infiltration-driven metamorphism in northern New England, USA. Journal of Petrology 29, (6): 1121-1159.

Ferry, J. M. (1992). Regional metamorphism of the Waits River Formation, Eastern Vermont: Delineation of a new type of giant metamorphic hydrothermal system. Journal of Petrology 33, (1): 45-94.

Franz, L., Romer, R. L., Klemd, R., Schmid, R., Oberhänsli, R., Wagner, T. and Shuwen, D. (2001). Eclogite-facies quartz veins within metabasites of the Dabie Shan (eastern China): Pressure-temperature-time-deformation path, composition of the fluid phase and fluid flow during exhumation of high-pressure rocks. Contributions to Mineralogy and Petrology 141, (3): 322-346.

Fryer, P. (1992). A synthesis of leg 125 drilling of serpentine seamounts on the Mariana and Izu-Bonin forearcs. Proceedings of the Ocean Drilling Program, Scientific Results 125: 593-614.

Fusseis, F., Regenauer-Lieb, K., Liu, J., Hough, R. M. and De Carlo, F. (2009). Creep cavitation can establish a dynamic granular fluid pump in ductile shear zones. 459, (7249): 974-977.

Gao, J. and Klemd, R. (2001). Primary fluids entrapped at blueschist to eclogite transition: Evidence from the Tianshan meta-subduction complex in northwestern China. Contributions to Mineralogy and Petrology 142, (1): 1-14.

Giorgis, D., Cosca, M. and Li, S. (2000). Distribution and significance of extraneous argon in UHP eclogite (Sulu Terrain, China) : Insight from in situ $^{40}Ar/^{39}Ar$ UV-laser ablation analysis. Earth and Planetary Science Letters 181: 601-615.

Gosso, G., Dal Piaz, G. V., Piovano, V. and Polino, R. (1979). High pressure emplacement of early-Alpine nappes, post-nappe deformations and structural levels (internal northwestern Alps). Memorie degli Instituti di Geologia e Mineralogia dell∩Universita di Padova 32: 5-15.

Green, E.C.R., Holland, T.J.B and Powell, R. (2007). An order-disorder model for omphacite pyroxenes in the system jadeite-diopside-hedenbergite-acmite with applications to eclogitic

rocks. American Mineralogist 92:1181-1189.

Groome, W. G., Johnson, S. E. and Koons, P. O. (2006). The effects of porphyroblast growth on the effective viscosity of metapelitic rocks: Implications for the strength of the middle crust. Journal of Metamorphic Geology 24, (5): 389-407.

Hacker, B. R., Peacock, S. M., Abers, G. A. and Holloway, S. D. (2003). Subduction factory - 2. Are intermediate-depth earthquakes in subducting slabs linked to metamorphic dehydration reactions? Journal of Geophysical Research-Solid Earth 108, (B1).

Handy, M. R. and Oberhänsli, R. (2004). Age map of the metamorphic structure of the Alps - tectonic interpretation and outstanding problems. Mitteilungen der Österreichischen Mineralogischen Gesellschaft 149: 97-121.

Hippertt, J. F. M. (1994). Grain boundary microstructures in micaceous quartzite: Significance for fluid movement and deformation processes in low metamorphic shear zones. The Journal of Geology, 102: 331-348.

Holness, M. B. (1993). Temperature and pressure dependence of quartz-aqueous fluid dihedral angles: The control of adsorbed H_2O on the permeability of quartzites. Earth and Planetary Science Letters 117, (3-4): 363-377.

Iwamori, H. (1998). Transportation of H_2O and melting in subduction zones. Earth and Planetary Science Letters 160, (1-2): 65-80.

Jamtveit, B., Malthe-Sørenssen, A. and Kostenko, O. (2008). Reaction enhanced permeability during retrogressive metamorphism. Earth and Planetary Science Letters 267, (3-4): 620-627.

John, T. and Schenk, V. (2003). Partial eclogitisation of gabbroic rocks in a late Precambrian subduction zone (Zambia): Prograde metamorphism triggered by fluid infiltration. Contributions to Mineralogy and Petrology 146, (2): 174-191.

Keller, L. M., Abart, R., Wirth, R., Schmid, D. W. and Kunze, K. (2006). Enhanced mass transfer through short-circuit diffusion: Growth of garnet reaction rims at eclogite facies conditions. American Mineralogist 91, (7): 1024-1038.

Kessel, R., Schmidt, M. W., Ulmer, P. and Pettke, T. (2005). Trace element signature of subduction-zone fluids, melts and supercritical liquids at 120-180 km depth. 437, (7059): 724-727.

Konrad-Schmolke, M., Handy, M. R., Babist, J. and O`Brien, P. J. (2005). Thermodynamic modelling of diffusion-controlled garnet growth. Contributions to Mineralogy and Petrology 149, (2): 181-195.

Konrad-Scmolke, M., Babist, J., Handy, M. R. and O`Brien, P. J. (2006). The physico-chemical properties of a subducted slab from garnet zonation patterns (Sesia Zone, Western Alps). Journal of Petrology 47, (11): 2123-2148.

Konrad-Schmolke, M., O'Brien, P. J. and Heidelbach, F. (2007). Compositional re-equilibration of garnet: The importance of sub-grain boundaries. European Journal of Mineralogy 19, (4): 431-438.

Konrad-Schmolke, M., Zack, T., O'Brien, P. J. and Jacob, D. E. (2008). Combined thermodynamic and rare earth element modelling of garnet growth during subduction: Examples from ultrahigh-pressure eclogite of the Western Gneiss Region, Norway. Earth and Planetary Science Letters 272, (1-2): 488-498.

Konrad-Schmolke, M., O'Brien, P. J., de Capitani, C. and Carswell, D. A. (2008b). Garnet growth at high- and ultra-high pressure conditions and the effect of element fractionation on mineral modes and composition. Lithos 103, (3-4): 309-332.

Koons, P. O. (1986). Relative geobarometry from high-pressure rocks of quartzofeldspathic composition from the Sesia Zone, Western Alps, Italy. Contributions to Mineralogy and Petrology. 93, (3): 322-334.

Kostenko, O., Jamtveit, B., Austrheim, H., Pollok, K. and Putnis, C. (2002). The mechanism of fluid infiltration in peridotites at Almklovdalen, Western Norway. Geofluids 2, (3): 203-215.

Lardeaux, J.-M. and Spalla, M. I. (1991). From granulites to eclogites in the Sesia zone (Italian Western Alps); a record of the opening and closure of the Piedmont ocean. Journal of Metamorphic Geology 9, (1): 35-59.

Lin, C. H., Huang, B. S. and Rau, R. J. (1999). Seismological evidence for a low-velocity layer within the subducted slab of southern Taiwan. Earth and Planetary Science Letters 174, (1-2): 231-240.

Lundstrom, C. C. (2000). Rapid diffusive infiltration of sodium into partially molten peridotite. Nature 403, (6769): 527-530.

Mancktelow, N. S. and Pennacchioni, G. (2004). The influence of grain boundary fluids on the microstructure of quartz-feldspar mylonites. Journal of Structural Geology 26, (1): 47-69.

Manning, C. E. (2004). The chemistry of subduction-zone fluids. Earth and Planetary Science Letters 223, (1-2): 1-16.

Marmo, B. A., Clarke, G. L. and Powell, R. (2002). Fractionation of bulk rock composition due to porphyroblast growth: Effects on eclogite facies mineral equilibria, Pam Peninsula, New Caledonia. Journal of Metamorphic Geology 20, (1): 151-165.

Marschall, H. R., Ludwig, T., Altherr, R., Kalt, A. and Tonarini, S. (2006). Syros metasomatic tourmaline: Evidence for very high-$\delta^{11}B$ fluids in subduction zones. Journal of Petrology 47, (10): 1915-1942.

Milke, R. and Wirth, R. (2003). The formation of columnar fibre texture in wollastonite rims by induced stress and implications for diffusion-controlled corona growth. Physics and Chemistry of Minerals, 30: 230-242.

Mukherjee, B. K., Sachan, H. K., Ogasawara, Y., Muko, A. and Yoshioka, N. (2003). Carbonate-bearing UHPM rocks from the Tso-Morari region, Ladakh, India: Petrological implications. International Geology Review, 45: 49-69.

Nakamura, M. and Watson, E. B. (2001). Experimental study of aqueous fluid infiltration into quartzite: Implications for the kinetics of fluid redistribution and grain growth driven by interfacial energy reduction. Geofluids 1, (2): 73-89.

Oliver, N. H. S. (1996). Review and classification of structural controls on fluid flow during regional metamorphism. Journal of Metamorphic Geology 14, (4): 477-492.

Oliver, N. H. S. and Bons, P. D. (2001). Mechanisms of fluid flow and fluid-rock interaction in fossil metamorphic hydrothermal systems inferred from vein-wallrock patterns, geometry and microstructure. Geofluids 1, (2): 137-162.

Peacock, S. M. (1987). Serpentinization and infiltration metasomatism in the Trinity peridotite, Klamath Province, northern California: Implications for subduction zones. Contributions to Mineralogy and Petrology 95, (1): 55-70.

Penniston-Dorland, S. C., Sorensen, S. S., Ash, R. D. and Khadke, S. V. (2010). Lithium isotopes as a tracer of fluids in a subduction zone mélange: Franciscan complex, Ca. Earth and Planetary Science Letters 292, (1-2): 181-190.

Philippot, P. and Selverstone, J. (1991). Trace element-rich brines in eclogitic veins: implications for fluid composition and transport during subduction. Contributions to Mineralogy and Petrology 106: 417-430.

Pognante, U. (1989). Tectonic implications of lawsonite formation in the Sesia zone (Western Alps). Tectonophysics 162, (3-4): 219-227.

Poli, S. and Schmidt, M. W. (1997). The high-pressure stability of hydrous phases in orogenic belts: An experimental approach on eclogite-forming processes. Tectonophysics 273, (1-2): 169-184.

Putnis, A. (2002). Mineral replacement reactions: From macroscopic observations to microscopic mechanisms. Mineralogical Magazine 66, (5): 689-708.

Rosenbaum, G., Giles, D., Saxon, M., Betts, P.G., Weinberg, R.F. and Duboz, C. (2005). Subduction of the Nazca Ridge and the Inca Plateau: Insights into the formation of ore deposits in Peru. Earth and Planetary Science Letters 239 (1): 18-32.

Rubatto, D., Gebauer, D. and Compagnoni, R. 1999. Dating of eclogite facies zircons: the age of Alpine metamorphism in the Sesia-lanzo Zone (Western Alps). Earth and Planterary Science Letters, 167, 141-158.

Rubie, D. C. (1983). Reaction-enhanced ductility: The role of solid-solid univariant reactions in deformation of the crust and mantle. Tectonophysics 96, (3-4): 331-352.

Rubie, D. C. (1986). The catalysis of mineral reactions by water and restrictions on the presence of aqueous fluid during metamorphism. Mineralogical Magazine, 50: 399-415.

Ryan, J. G., Morris, J., Tera, F., Leeman, W. P. and Tsvetkov, A. (1995). Cross-arc geochemical variations in the Kurile arc as a function of slab depth. Science 270, (5236): 625-627.

Scambelluri, M. and Philippot, P. (2001). Deep fluids in subduction zones. Lithos 55, (1-4): 213-227.

Schmid, S. M. and Kissling, E. (2000). The arc of the western Alps in the light of geophysical data on deep crustal structures. Tectonics 19, (1): 62-85.

Schmidt, M. W. and Poli, S. (1998). Experimentally based water budgets for dehydrating slabs and consequences for arc magma generation. Earth and Planetary Science Letters 163, (1-4): 361-379.

Schulte, B. and Sindern, S. (2002). K-rich fluid metasomatism at high-pressure metamorphic conditions: Lawsonite decomposition in rodingitized ultramafite of the Maksyutovo Complex, Southern Urals (Russia). Journal of Metamorphic Geology 20, (6): 529-541.

Sorensen, S. S. (1988). Petrology of amphibolite-facies mafic and ultramafic rocks from the Catalina schist, southern California: Metasomatism and migmatization in a subduction zone metamorphic setting. Journal of Metamorphic Geology 6, (4): 405-435.

Sorensen, S. S., Grossman, J. N. and Perfit, M. R. (1997). Phengite-hosted LILE enrichment in eclogite and related rocks: Implications for fluid-mediated mass transfer in subduction zones and arc magma genesis. Journal of Petrology 38, (1): 3-34.

Spandler, C., Hermann, J. r., Arculus, R. and Mavrogenes, J. (2003). Redistribution of trace elements during prograde metamorphism from lawsonite blueschist to eclogite facies; implications for deep subduction-zone processes. Contributions to Mineralogy and Petrology 146, (2): 205-222.

St-Onge, M. R. and Lucas, S. B. (1995). Large-scale fluid infiltration, metasomatism and re-equilibration of Archean basement granulites during palaeoproterozoic thrust belt construction, Ungava Orogen, Canada. Journal of Metamorphic Geology 13, (4): 509-535.

Stünitz, H. (1989). Partitioning of metamorphism and deformation in the boundary region of the "Seconda Zona Diorito-Kinzigitica", Sesia Zone, Western Alps. PhD Thesis, Zürich, Swiss Federal Institute of Technology: 244.

Tropper, P., Essene, E. J., Sharp, Z. D. and Hunziker, J. C. (1999). Application of K-feldspar-jadeite-quartz barometry to eclogite facies metagranites and metapelites in the Sesia Lanzo Zone (Western Alps, Italy). Journal of Metamorphic Geology 17, (2): 195-209.

van der Straaten, F., Schenk, V., John, T. and Gao, J. (2008). Blueschist-facies rehydration of eclogites (Tian Shan, NW-China): Implications for fluid-rock interaction in the subduction channel. Chemical Geology 255, (1-2): 195-219.

Venturini, G. (1995). Geology, geochemistry and geochronology of the inner central Sesia Zone (Western Alps, Italy). PhD Thesis, Lausanne, Universite de Lausanne, Institut de Geologie et Paleontologie.

Wain, A. (1997). New evidence for coesite in eclogite and gneisses: Defining an ultrahigh-pressure province in the Western Gneiss region of Norway. Geology, 25 (10): 927-930.

Wilke, F. D. H., O'Brien, P. J., Altenberger, U., Konrad-Schmolke, M. and Khan, M. A. (2010). Multi-stage reaction history in different eclogite types from the Pakistan Himalaya and implications for exhumation processes. Lithos 114, (1-2): 70-85.

Zack, T. and John, T. (2007). An evaluation of reactive fluid flow and trace element mobility in subducting slabs. Chemical Geology 239, (3-4): 199-216.

Zucali, M., Spalla, M. I. and Gosso, G. (2002). Strain partitioning and fabric evolution as a correlation tool: The example of the Eclogitic Micaschists complex in the Sesia-Lanzo Zone (Monte Mucrone-Monte Mars, Western Alps, Italy). Schweizerische Mineralogische und Petrographische Mitteilungen 82, (3): 429-454.

Figure captions

Fig. 1: a) Simplified geological map of the Sesia-Lanzo Zone (SLZ) and adjacent areas. b) Structural profile along the section shown in a) and geological sketch representing the exhumation of the SLZ in Late Cretaceous time. Sample sites are along a transect across the Mombarone Unit. Figure modified from Babist et al., 2006.

Fig. 2: Thin section photographs of the selected samples. Both samples have similar phase assemblages but differ in modal amounts of the phases. Sample MKS-52-1 (a) has a compositional layering.and a parallel, weak foliation. Within quartz-rich layers phengite-epidote-albitic plagioclase pseudomorphs after omphacite (bold arrows) are abundant. The weakly foliated sample MKS-55-1 (b) has also a weak foliation, but a more homogeneous texture. Abbreviations: garnet (grt), sodic amphibole (gln), phengite (phe), epidote (ep). Long side of the images is 2.5 cm.

Fig. 3: Back scattered electron images of minerals affected by the fluid influx. a) and b) Relict omphacite is compositionally modified and replaced by phengite, epidote, albitic plagioclase and, later, by calcic amphibole (arrows). c), d) and e) Phengite shows modified (brighter) areas along grain boundaries and deformed parts. f), g) and h) Overprinting features in sodic amphibole along fluid pathways, such as grain boundaries ((f) and (g)) and microcracks ((g) and (h)) as well as overgrowth zones (h). See text for further description. Arrows in (d) and (g) indicate positions of the compositional profiles in Fig. 5. Cam = calcic amphibole.

Fig. 4: a-g) Back scattered electron image and compositional mappings of sodic amphibole and phengite from sample MKS-55-1. The back scattered electron image (a) correlates inverse with the XMg pattern (b), which in turn mimics the compositional maps of Na (d) and Sr (f), all of which show significantly lower values along the rims. In contrast, the concentrations Ba (e) and Cl (g) are higher in the overprinted rims than in the cores. Variations in Si (c) content are only minor in both phases. Note that the Na mapping (d) is a composite image focusing on Na concentrations in sodic amphibole and phengite respectively. h) The manganese pattern in garnet shows a sharp, sometimes diffusive enrichment in the rim, along microcracks and subgrain boundaries, indicating garnet resorption, overgrowth and Mn backdiffusion.

Fig. 5: Compositional profiles across representative grains of omphacite, phengite, sodic amphibole and garnet from both samples. a) Omphacite composition shows minor irregular

variations without clear core-to-rim trend. b) The affected areas in phengite show a sharp shift towards more iron-rich compositions, other elements are largely unaffected. In deformed areas (left side of the profile) compositional transitions are smoother. c) Sodic amphibole is also more iron-rich in the overprinted areas. Ca is increasing in some grains, but does not correlate with X_{Mg}. Garnets preserve compositional growth zonations with a trend towards more Grs-poor and Prp-rich compositions.

Fig. 6: P-T diagrams calculated for the bulk rock compositions of the two samples. a) Phase relations labelled for each field. The shaded areas correspond to the three parageneses that represent different metamorphic overprinting stages preserved in the samples. b) Contours for the water content in solids calculated for the same diagram. Stability fields correspond to those in a). c) Contours for X_{Mg} in sodic amphibole are sub-parallel to those in b), but show an inverse correlation. d) Contours for X_{Mg} in phengite have a similar pattern than those in sodic amphibole. The stippled arrow in a) marks the P-T trajectory used for the thermodynamic forward models.

Fig. 7: Phase relations, phengite and amphibole compositions as well as water content and volumes of the solid phases calculated for the two samples along the retrograde segment of the P-T trajectory shown in Fig. 6. Homogeneous equilibrium crystallisation and water saturation are assumed. The drastic change in the phase assemblage between 1.6 and 1.3 GPa marks the transition from eclogite- to blueschist-facies associated with the formation of sodic amphibole and epidote and the breakdown of omphacite and garnet. The transformation is associated with a continuous decrease in X_{Mg} in phengite (b) and amphibole (c), which shows a characteristic minimum around 1.3 GPa. d) The continuous increase of H_2O in the solids (bold solid lines) indicates the need of water influx to maintain water-saturation along the retrograde path. Rehydration and decompression is associated with a volume increase of 17 and 10% in the basic and felsic sample respectively (stippled lines).

Fig. 8: Phase relations, phengite and amphibole compositions as well as water content of the solid phases calculated for the two samples along the prograde segment of the P-T trajectory shown in Fig. 6. Fractional garnet crystallisation and release of liberated water are assumed. a) Curves for accumulated amount of water and garnet indicate two stages of dehydration and

garnet formation. b) and c) Phengite and sodic amphibole become more Mg-rich. d) Garnet zonation patterns resemble those observed in the natural samples.

Fig. 9: P-T diagrams calculated for the effective bulk rock compositions (EBC) of the samples at peak metamorphic conditions (after fractional garnet crystallisation and water release). a) Phase relations, b) contours for water content of the stable phases and c) contours for X_{Mg} in amphibole. Phase relations in b) and c) are as indicated in a). Note that water saturation (stable H_2O) is restricted due to dehydration during prograde metamorphism. See text for discussion.

Fig. 10: P-H_2O diagrams calculated for the bulk rock composition of the samples. a) Phase relations. The stability field of a certain phase is displayed by the zero mode line and the label of the mineral shown on the "present" side. b) Contours for X_{Mg} in amphibole. c) Countours for X_{Mg} in phengite. Phase fields are as shown in a). Note the restricted stability of low-X_{Mg} amphibole and phengite in assemblages close to water-saturation.

Fig. 11: P-H_2O diagrams calculated for the effective bulk rock composition of the samples at peak metamorphic conditions. a) Phase relations, b) X_{Mg} in amphibole and c) X_{Mg} in phengite. Without recycling of the fractionated material (garnet) amphibole and phengite do not develop the low X_{Mg} values observed in the natural samples.

Fig. 12: Phase relations (a), amphibole X_{Mg} (b) and phengite X_{Mg} calculated along the retrograde P-T segment assuming peak EBC and peak water content of the samples but re-equilibration of fractionated garnet material.

Fig. 13: Same calculations as in Fig. 13, but without recycling of fractionated garnet material. See text for discussion.

Fig. 14: Schematic illustration of fluid migration modes in a subduction zone. Within the slab fluid flux is channelized and fluid-rock interaction limited due to the development of veins by prograde mineral reactions with negative volume change. In the slab-mantle transition zone fluid flux is controlled by the extent of viscous deformation and mostly parallel to the slab-mantle interface. Pervasive fluid flux is possible due to retrograde mineral reactions with

positive volume change. In the mantle wedge fluid flux is pervasive or might regionally be controlled by viscous deformation.

Table 1: Changing mineral assemblages in the samples at peak metamorphic conditions, during fluid influx and static greenschist-facies overprint.

Elsevier Editorial System(tm) for Earth and Planetary Science Letters
Manuscript Draft

Manuscript Number: EPSL-D-11-00491R1

Title: Fluid migration above a subducted slab - Thermodynamic and trace element modeling of fluid-rock interaction in partially overprinted eclogite-facies rocks (Sesia Zone, Western Alps)

Article Type: Regular Article

Keywords: fluid-rock interaction
subduction zone
fluid migration
slab-mantle interface
trace element transport

Corresponding Author: Dr Matthias Konrad-Schmolke,

Corresponding Author's Institution: Universität Potsdam

First Author: Matthias Konrad-Schmolke

Order of Authors: Matthias Konrad-Schmolke; Thomas Zack; Patrick J O'Brien; Matthias Barth

Abstract: The amount and composition of subduction zone fluids and the effect of fluid-rock interaction at a slab-mantle interface has been constrained by thermodynamic and trace element modeling of partially overprinted blueschist-facies rocks from the Sesia Zone (Western Alps). Deformation-induced differences in fluid flux led to a partial preservation of pristine mineral cores in weakly deformed samples that were used to quantify Li, B, Sr and Pb distribution during mineral growth, -breakdown and modification induced by fluid-rock interaction. Our results show that Li and B budgets are fluid-controlled, thus acting as tracers for fluid-rock interaction processes, whereas Sr and Pb budgets are mainly controlled by the fluid-induced formation of epidote. Our calculations show that fluid-rock interaction caused significant Li and B depletion in the affected rocks due to leaching effects, which in turn can lead to a drastic enrichment of these elements in the percolating fluid. Depending on available fluid-mineral trace element distribution coefficients modeled fluid rock ratios were up to 0.06 in weakly deformed samples and at least 0.5 to 4 in shear zone mylonites. These amounts lead to time integrated fluid fluxes of up to 1.4 . 102 m3m-2 in the weakly deformed rocks and 1 - 8 . 103 m3m-2 in the mylonites. Combined thermodynamic and trace element models can be used to quantify metamorphic fluid fluxes and the associated element transfer in complex, reacting rock systems and help to better understand commonly observed fluid-induced trace element trends in rocks and minerals from different geodynamic environments.

Fluid migration above a subducted slab – Thermodynamic and trace element modeling of fluid-rock interaction in partially overprinted eclogite-facies rocks (Sesia Zone, Western Alps)

Matthias Konrad-Schmolke[1], Thomas Zack[2], Patrick J. O'Brien[1] and Matthias Barth[2]

[1]*Institut für Erd- und Umweltwissenschaften, Universität Potsdam, Karl-Liebknecht-Straße 24-25, 14476 Potsdam, Germany*

[2]*Universität Mainz, Fachbereich Geowissenschaften, Becherweg 14, 55128 Mainz, Germany*

Corresponding Author:

Matthias Konrad-Schmolke
Universität Potsdam
Institut für Geowissenschaften
Karl-Liebknecht-Strasse 24-25
14476 Potsdam

e-mail: mkonrad@geo.uni-potsdam.de

Abstract

The amount and composition of subduction zone fluids and the effect of fluid-rock interaction at a slab-mantle interface has been constrained by thermodynamic and trace element modeling of partially overprinted blueschist-facies rocks from the Sesia Zone (Western Alps). Deformation-induced differences in fluid flux led to a partial preservation of pristine mineral cores in weakly deformed samples that were used to quantify Li, B, Sr and Pb distribution during mineral growth, -breakdown and modification induced by fluid-rock interaction. Our results show that Li and B budgets are fluid-controlled, thus acting as tracers for fluid-rock interaction processes, whereas Sr and Pb budgets are mainly controlled by the fluid-induced formation of epidote. Our calculations show that fluid-rock interaction caused significant Li and B depletion in the affected rocks due to leaching effects, which in turn can lead to a drastic enrichment of these elements in the percolating fluid. Depending on available fluid-mineral trace element distribution coefficients modeled fluid rock ratios were up to 0.06 in weakly deformed samples and at least 0.5 to 4 in shear zone mylonites. These amounts lead to time integrated fluid fluxes of up to $1.4 \cdot 10^2$ m^3m^{-2} in the weakly deformed rocks and 1 – $8 \cdot 10^3$ m^3m^{-2} in the mylonites. Combined thermodynamic and trace element models can be used to quantify metamorphic fluid fluxes and the associated element transfer in complex, reacting rock systems and help to better understand commonly observed fluid-induced trace element trends in rocks and minerals from different geodynamic environments.

Introduction

Fluid fluxes and associated mass transfer in subduction zones are of significant importance for scientific research. Fluids released from the subducted slab trigger earthquake rupture (e.g., Hacker et al., 2003), are responsible for arc-related magma generation and volcanism (e.g., Wyllie 1983, Tatsumi et al., 1986), enable ore deposit

55 formation (e.g., Sillitoe 1972; Sawkins 1972; Rosenbaum et al., 2005) and trigger one of
56 the most important element cycles on Earth that connects the subducted plate with the
57 overlying mantle, the crust and the atmosphere. Characterisation and quantification of
58 this fluid-mediated mass transfer in subduction zones is a prerequisite to our
59 understanding of the above-mentioned processes and our ability to accurately model
60 and thus predict their consequences.

61 Potential indicators for fluid processes are the concentrations and isotopic
62 compositions of Li and B (e.g., Bebout et al., 1993; Marschall et al., 2006, 2009; King et
63 al., 2007; Penniston-Dorland et al., 2010; Elliott et al., 2004; Peacock and Hervig 1999;
64 Zack et al., 2003) as well as Sr and Pb (e.g., Bickle and Teagle 1992; Beinlich et al., 2010),
65 in rocks and minerals, the latter being of particular interest in geochronology. All of
66 these elements are potentially fluid mobile (e.g. Ryan and Langmuir 1988, Brenan et al.,
67 1998; Najorka et al., 1999; Kessel et al., 2005), are abundant in common metamorphic
68 minerals such as phengite, amphibole or epidote and therefore can act as tracers for
69 fluid fluxes and fluid-rock interaction.

70 Quantification of fluid fluxes and associated trace element transport in
71 subduction zones must consider fluid-rock interaction, because the percolating fluids
72 interact with the wall rocks, leading to a compositional modification of solid and fluid
73 phases. However, the element distribution between fluid and wall rock during fluid-rock
74 interaction is controlled by a complex interdependence of mineral reactions as well as
75 the amount and physico-chemical properties of the percolating fluid. On the one hand,
76 mineral reactions in the wall rocks control the distribution of trace elements between
77 fluids and solids (e.g., Spandler et al., 2003; John et al., 2008), whereas on the other hand
78 changing pressure, temperature and bulk chemistry of the fluid-rock system modify
79 fluid properties (e.g., Manning 2004), which in turn influences the trace element

distribution between solid and liquid phases. Thus, fluid-mediated element transport is a function of pressure, temperature and bulk chemistry of the system as well as of the mineral paragenesis coexisting with the fluid phase. Prediction of element transport and -distribution in subduction zones requires quantification of all of the above-mentioned parameters.

In this paper we study partially overprinted eclogite facies rocks from the Western Alpine Sesia zone that were exhumed from mantle depths on top of a dehydrating subducted oceanic plate where they directly interacted with percolating fluids at blueschist-facies conditions. The effect of the fluid influx on major- and trace element compositions of newly formed or recrystallized phases can be directly observed in our samples and changes in the mineral paragenesis and –compositions can be quantified. Thus, the amount and composition of the infiltrated fluid and its effects on the trace element bulk rock chemistry can be constrained.

We use a combined approach of thermodynamic and trace element modeling that considers element fractionation to interpret the compositional trends of Li, B, Sr and Pb in phengite and sodic amphibole from both partially and well re-equilibrated, mylonitic samples in terms of the trace element compositional evolution of fluid and wall rock during fluid infiltration and percolation. This combined method makes the valuable information that is stored in disequilibrium textures resulting from fluid-rock interactions accessible.

Tectonic and Geological Setting

The Sesia-Lanzo Zone (SLZ) consists predominantly of felsic rocks that were subducted to depths between 60 and 70 km in the Late Cretaceous (e.g. Dal Piaz et al., 1972; Duchêne et al., 1997; Rubatto et al., 1999). Convergence of the Apulian and European plates involved subduction of the SLZ rocks that were part of the distal

105 Apulian continental margin as well as subduction of the Piemont Ocean that separated
106 Apulia from the European continent (e.g. Handy and Oberhänsli 2004). During
107 convergence, the SLZ was exhumed in the hanging wall of the subducted Piemont
108 oceanic plate prior to continent-continent collision (Babist et al., 2006) and
109 incorporated into the Western Alpine nappe pile (Fig. 1), within which it forms today the
110 structurally uppermost segment.

111 In the investigated area the SLZ consists primarily of two large coherent blocks
112 (Fig. 1a), the Mombarone and the Bard unit that were affected by Alpine eclogite-facies
113 metamorphism (Babist et al., 2006) followed by a partial blueschist-facies re-
114 equilibration (Konrad-Schmolke et al., 2011). The weakly-deformed Mombarone Unit is
115 separated from the Bard Unit by a blueschist-facies mylonite zone (Tallorno Shear Zone,
116 Fig. 1b), interpreted to be responsible for significant parts of the initial exhumation of
117 the Mombarone Unit (e.g. Gosso et al., 1979; Babist et al., 2006).

118 The Mombarone unit comprises predominantly eclogite-facies (T=500-600°C,
119 P=1.5-2.0 GPa; Pognante 1989; Tropper et al, 1999; Zucali et al., 2002) felsic ortho- and
120 para-gneisses and schists, metabasites and minor impure marbles as well as
121 subordinate quartzite and ultrabasic rocks (e.g. Koons 1986; Compagnoni et al., 1977;
122 Castelli 1991; Ferraris and Compagnoni, 2003). Blueschist-facies viscous deformation in
123 the Tallorno shear zone affected felsic and basic rock types and led to well-equilibrated
124 felsic and basic mylonites (e.g., Gosso et al., 1979; Babist et al., 2006). In the more
125 external Bard unit (peak conditions 500-550°C at 1.0-1.5 GPa; Lardeaux and Spalla
126 1991) an Alpine greenschist-facies overprint is more thorough.

127 Retrograde fluid influx into the Mombarone Unit occurred at pressures between
128 1.3 and 1.1 GPa (Konrad-Schmolke et al., 2011). In the internal, weakly deformed part,
129 fluid-rock interaction at blueschist facies conditions led to a partial re-hydration and re-

equilibration of the eclogite-facies mineral assemblages (Konrad-Schmolke et al., 2011). In contrast, blueschist-facies mylonites at the base of the Mombarone Unit are well equilibrated and contain compositionally more homogeneous minerals (Babist et al., 2006; Gosso et al., 1979). Compositional and textural contrasts between weakly-deformed, partially overprinted rocks and well-equilibrated highly strained mylonites enables a detailed investigation and quantification of fluid fluxes and associated mass transfer in the hanging wall of a subducted oceanic plate. Further, deformation-induced differences in fluid fluxes around a large-scale high-pressure shear zone can be studied.

Mineral assemblages and major element mineral chemistry of the samples

Samples for this study were collected along a strain gradient from the internal Mombarone Unit into the Tallorno shear zone (Fig. 1b). We investigated four samples in detail, one felsic (TSZR-1) and one basic (MKS-99-1) mylonite as well as one felsic (MKS-30-1) and one basic (MKS-52-1) weakly-deformed gneiss.

The weakly-deformed samples are moderately foliated and medium- to fine-grained. The foliation in the metabasic sample is parallel to a compositional banding defined by garnet-, sodic amphibole-, quartz- and mica-rich layers. The metapelitic samples, containing sodic amphibole, white mica and ±omphacite (or pseudomorphs after omphacite) in a quartz-rich matrix, are more homogeneous with a foliation defined by sodic amphibole and white mica. All samples partly preserve the high-pressure mineral assemblage of quartz (predominant in the felsic sample) + phengite + omphacite + sodic amphibole + garnet + rutile + paragonite with differences being restricted to variation in modal proportions. The felsic samples are quartz- and mica-rich whereas the metabasic sample is dominated by sodic amphibole, garnet and, if preserved, omphacite.

154 Retrogression of the eclogite facies mineral assemblages in all weakly-deformed
155 samples shows similar features. Initial retrogression is associated with the re-
156 equilibration of primary omphacite (Jd_{40}-Jd_{60}) towards lower jadeite contents, followed
157 by pseudomorphic replacement by phengite, albite and epidote (cf. Rubie 1983).
158 Omphacite breakdown is further associated with the formation of matrix epidote and
159 new sodic amphibole. Eclogite facies garnet grains that preserve prograde growth
160 zonation are partially resorbed during the fluid influx, indicated by cross-cutting
161 relations between grain boundaries and zonation patterns. In some places newly-
162 formed garnet, with higher Mn and lower Ca, overgrew rims of large porphyroblasts and
163 infiltrated the interior of the porphyroblasts along a sub-grain boundary network (cf.
164 Konrad-Schmolke et al., 2007).

165 During fluid infiltration primary *phengite* (3.3 - 3.5 Si p.f.u., X_{Mg} between 0.6 and
166 0.7) is compositionally modified along fluid pathways (Fig. 2a and b). Retrograde
167 equilibration of phengite involves a major decrease in X_{Mg} and is visible in high contrast
168 BSE images, which show darker-coloured cores surrounded by brighter zones that are
169 concentrated at the tips and grain boundaries, around inclusions and in deformed parts
170 (Fig. 2a). The BSE images show one, in some places two different replacement zones
171 (e.g., Putnis 2002) as well as areas with diffuse transitions, but oscillatory zoning is
172 missing.

173 S*odic amphibole* grains adjust compositionally with a characteristic
174 compositional trend in affected areas. Primary grains are predominantly glaucophane–
175 Fe-glaucophane solid solutions with X_{Mg} between 0.75 and 0.65 and show multiple,
176 sometimes oscillatory, overprinting and overgrowth textures (Fig. 2b). Major element
177 modification in the overprinted areas is restricted, as in phengite, to Fe-Mg exchange
178 with most other components being largely unchanged. The modifications are visible in

high-contrast BSE images as a network of brighter, more Fe-rich amphibole material, varying in width and emanating from grain boundaries, brittle fractures and cleavage planes. The affected areas often have sharp boundaries towards the unaffected cores, but also more diffuse transitions occur.

Epidote occurs in the matrix as well as in pseudomorphs and aggregates together with phengite that replace omphacite. In the matrix epidote forms grains up to 300μm that are mostly rounded, but sometimes occur also as elongate grains grown parallel to the main foliation. Epidote in pseudomorphs and phengite-epidote aggregates is often hyp-idiomorphic and forms grains up to 200μm. Epidote major element composition is quite uniform with X_{Ep} between 0.6 and 0.7.

In addition, blueschist-facies retrogression also involves the formation of *paragonite,* occurring in all samples, as well as growth of *ilmenite* and *titanite* around *rutile* in the basic and felsic samples, respectively.

The mylonites are fine-grained garnet-epidote-albite-phengite-sodic amphibole±chlorite schists with only scarce relics of older minerals, such as garnet clasts and/or cores to phengite and sodic amphibole. Omphacite has not been observed and a greenschist facies overprint is restricted to the static replacement of garnet and sodic amphibole by chlorite and albite + chlorite, respectively. The foliation in the mylonites is defined by quartz-rich layers that alternate with phengite-paragonite-epidote-rich layers in the felsic sample and layers with oriented sodic amphibole, epidote, paragonite and phengite grains in the basic sample. Elongate albite and epidote aggregates aligned parallel to the foliation are common in mica- and amphibole-rich layers.

Phengite, apart from subordinate mm-sized clasts, is fine-grained (5-200μm) and forms up to several mm wide layers. Phengite clasts are weakly zoned compositionally,

whereas fine-grained matrix phengite is homogeneous (Fig. 2c) with Si contents between 3.3 and 3.5 Si p.f.u. in the felsic and basic samples, respectively. A core-rim trend of X_{Mg} in the large porphyroclasts ranges from 0.8-0.6 and small mylonitic phengite grains have major element compositions corresponding to the rims of larger grains with lower X_{Mg} values.

Sodic amphibole grains in the mylonites are up to 500µm large, aligned parallel to the foliation, and contain inclusions of garnet, epidote and rutile. Most grains are compositionally homogeneous with respect to major elements, but some preserve an irregular or patchy appearance in BSE images indicating slight compositional variations similar to those observed in the weakly deformed samples (Fig. 2c).

Epidote is abundant and occurs as strongly elongate grains with lengths up to 500µm, which grow always parallel to the main foliation (Fig. 2c). Epidote is slightly chemically zoned with more iron-rich compositions at the rim.

In addition, the mylonitic samples contain *paragonite*, mostly in fine-grained mica-rich layers aligned parallel to the foliation. Paragonite tips are sometimes replaced by phengite or by aggregates of albite + phengite. *Garnet* occurs in two size fractions. Large (up to 2 mm) elongate, almost inclusion-free clasts are rimmed by inclusion-rich up to 100µm wide polycrystalline garnet overgrowths. The two garnet generations are compositionally distinct with lower Grs and higher Alm and Prp contents in the large porphyroblasts and Grs-Alm-rich overgrowths. Matrix *rutile* is always rimmed by *titanite* and/or *ilmenite*.

Trace element mineral compositions

We determined trace element concentrations using an Agilent 7500ce quadrupole ICPMS at the Universität Mainz, equipped with a New Wave UP213 (213 nm

wavelength) laser system. Spot sizes varied between 25 and 80 µm. For the smallest spot sizes, the element menu was reduced down to 10 elements to maximize signal intensities of the most relevant trace elements. In order to detect accidentally measured inclusions or contamination we measured Be, Ti, Rb, Y, Cs, Ba, Ce, Th, and U in addition to Li, B, Sr and Pb and carefully examined the time resolved ablation signals. For further details see Konrad-Schmolke et al. (2008a). A table of representative mineral analyses can be found in the electronic supplementary material.

The trace element concentrations in phengite show two distinct core-rim trends. The contents of Li, B, Ti, Sr and Pb decrease significantly in the overprinted rims, whereas concentrations of Ba, Cs and Rb have constant values or increase slightly. Be concentrations decrease slightly from core to rim. These trends are characteristic for all overprinted phengites from the weakly deformed samples. Apart from Li, all trace element concentrations in *sodic amphibole* are significantly lower than in phengite and core-to-rim trace element variations in the weakly deformed samples are less prominent than those in phengite.

Fig. 3 shows the Li, B, Sr and Pb concentrations of all measured phengites and sodic amphiboles. Pristine phengite cores in the weakly deformed samples overlap within a scatter between 60 and 80 µg/g Li and 35 to 55 µg/g B. The concentrations of both elements are significantly lower in the overprinted rims of both samples. Whereas phengite rims in the felsic samples fall within a small range of 35 to 45 µg/g Li and 20 to 40 µg/g B, the scatter in the basic sample is larger and the rim concentrations of Li are slightly higher than in the felsic sample. Mylonitic phengites have no or very limited core-to-rim compositional variations and have markedly lower trace element concentrations than cores and rims of the weakly-deformed samples. Core and rim

compositions of the weakly deformed samples define compositional trends in Li, B, Sr and Pb that lead towards the compositions of the mylonitic phengites.

Li concentrations in sodic amphiboles from the weakly-deformed samples are almost unchanged in the overprinted rims, whereas B concentrations decrease slightly in the affected areas. Sr and Pb contents are very low and scatter over a wide range, although a slight core-to-rim trend towards lower values is visible. As in case of phengite, sodic amphibole in the mylonitic samples have the lowest concentrations of all measured trace elements and fall within a smaller range than amphiboles in the weakly-deformed samples.

Epidote has high concentrations of Sr and Pb and negligible contents of Li and B in both weakly-deformed and mylonitic samples. The highest Sr and Pb concentrations can be found in the epidote cores of the mylonitic samples, with up to 2000 µg/g Sr and 200 µg/g Pb. Epidote in the weakly-deformed samples is compositionally unzoned with respect to trace elements, whereas Sr and Pb concentrations decrease slightly from core to rim in the mylonitic samples.

Apart from phengite and sodic amphibole, *paragonite* is the major Li- and B-bearing phase in our samples. Compared to phengite, paragonite has similar concentrations in all investigated trace elements, but does not show significant compositional core-to-rim variations. *Garnet* contains up to 20 µg/g Li but the concentrations of all other considered elements are negligible. Albite does not contain significant amounts of trace elements relevant for this study. It is notable that tourmaline, also a major carrier of B and, to a limited extend, Li was not found in our samples. A complete list of mineral compositions as well as calculated bulk rock trace element mass balances can be found in the electronic supplementary material.

Model description

277 Stable phases and compositions are modeled with the Gibbs energy minimisation
278 algorithm THERIAK (de Capitani and Brown 1987) with the updated (ds55 from 2003)
279 Holland and Powell (1998) standard state database. Solid solution models are those
280 described in Konrad-Schmolke et al., (2011). Forward models are calculated along a
281 prograde P-T segment from 500°C/1.1 GPa to peak metamorphic conditions at
282 575°C/2.0 GPa and a retrograde segment from peak conditions to 535°C/1.0 GPa. This
283 P-T path was divided into 100 increments (45 and 55 along the pro- and retrograde
284 paths, respectively) at each of which the thermodynamic properties of the system were
285 calculated. Compositional changes of the effective, i.e. reacting, bulk rock composition
286 (EBC) were modeled by recalculating the bulk rock composition at every increment
287 considering element fractionation into garnet porphyroblasts, water release during
288 prograde dehydration reactions as well as garnet resorption and water influx along the
289 retrograde P-T trajectory (cf. Konrad-Schmolke et al., 2008b).

290 To model fluid influx the retrograde path was divided into two segments: From
291 peak conditions to 550°C at 1.35 GPa (30 increments) the thermodynamic parameters
292 are calculated utilising the EBC at peak conditions (c.f. Konrad-Schmolke et al., 2011). At
293 550°C and 1.35 GPa water influx leads to water re-saturation of the samples during the
294 second segment of the P-T path (25 increments), causes garnet resorption and drives
295 the major element EBC back to the whole rock composition. Trace element distribution
296 among the stable phases followed the thermodynamic modeling at every increment and
297 involved calculation of bulk distribution coefficients based on the thermodynamically
298 modeled mineral abundances and published distribution coefficients.

299 **Trace element model approaches**

300 Two major factors influencing the trace element budget during fluid-rock
301 interaction are envisaged in our models: (1) fluid-induced mineral reactions lead to

redistribution of trace elements among newly formed phases, and (2) fluid-mediated trace element transport enriches or depletes the reacting rock volume depending on composition and amount of the percolating fluid. These processes are reflected in our model approaches: In the first case the infiltrated fluid is completely consumed by re-hydration reactions, the mineral assemblage gets water-saturated and trace element distribution occurs only among the newly-formed solid phases. The second case involves percolation of a free fluid phase and is modeled in two steps. First, the infiltrating fluid interacts and equilibrates with the reacting rocks. Second, the equilibrated fluid leaves the model system after fluid-rock interaction, thus carrying a certain amount of trace elements out of the rock.

However, as it is impossible in such partly reacted rocks to constrain the pristine chemical bulk rock composition, initial trace element content of the rock was chosen to reproduce the phengite core composition of the respective sample. Fluid-induced bulk rock enrichment or depletion was then modeled in three steps at every increment: (1) elements infiltrated by the fluid phase are added to the initial bulk rock composition, (2) the new bulk rock trace element amount is distributed among the modeled stable fluid and solid phases, (3) trace elements distributed into the fluid phase are assumed to leave the system, whereas trace elements incorporated into the solid phases display the mineral and bulk rock chemistry after fluid rock interaction and are used to model compositional trends in minerals and rocks. These modeled trends are then compared to the natural samples in order to quantify the effect of fluid percolation on mineral, bulk rock and fluid composition.

The distribution coefficients used in this study are based on experimentally determined $D^{Cpx/Fluid}$ values of Brenan et al., (1998) and $D^{Min/Cpx}$ values from natural rocks from Marschall et al. (2007). The experimental partition coefficients are far from

perfect as the P-T-X conditions are very different from samples of this study. However, mineral-fluid experiments under natural conditions are notoriously difficult and published results are scarce. We chose values from Brenan et al. (1998) as they explicitly concentrated on Li and B, two analytically challenging trace elements.

In the following we show the results for the weakly-deformed felsic sample that are considered to be representative for the investigated processes. Calculations for the basic sample yield similar results, which are shown in the electronic supplementary material.

Results

Fig. 4 shows a correlation of the phase relations (a) and the trace element evolution of phengite (b) and sodic amphibole (c) modeled for the chosen sample along the P-T-X trajectory, assuming no fluid percolation. This model setting reflects a simplified scenario of internal trace element redistribution among all phases in a homogeneously equilibrated system.

The modeled modal mineral abundances along the retrograde path show three different stable phase assemblages. The assemblage prior to the fluid influx, represents isochemical decompression and cooling from peak P-T-conditions, contains garnet (Grt), omphacite (Omph), sodic amphibole (Gln), phengite (Phe) and paragonite (Pg) as well as quartz (not shown) and does not change significantly until fluid influx. Water-re-saturation causes rapid omphacite and garnet breakdown and the formation of new sodic amphibole, paragonite and epidote. Below 1.2 GPa, feldspar (Fsp) forms at the expense of sodic amphibole. The fluid-induced mineral reactions produce a typical epidote-blueschist facies phase assemblage, stable between 1.35 and 1.1 GPa, which is the observed mineral assemblage in the mylonites, therefore representing P-T conditions of the highly strained samples and bracketing the pressure range within

which the effect of fluid percolation on coexisting phases was modeled in later calculations. Below 1.1 GPa the greenschist facies assemblage calcic amphibole (Cam) + chlorite (Chl) + epidote + feldspar is stable. In the following, we refer to phengite and sodic amphibole compositions coexisting with the mineral assemblage prior to the fluid influx as core compositions and to those after water-re-saturation as rim compositions.

The fluid influx initially causes omphacite and garnet breakdown resulting in the formation of sodic amphibole, paragonite and epidote. This transformation re-distributes Li and B, present in reacting omphacite and garnet, into paragonite, amphibole and phengite reflected in slightly decreasing, in the case of B, or increasing concentrations, in the case of Li, in overprinted phengite and amphibole. Due to the fluid-induced formation of epidote, Sr and Pb are strongly partitioned into this phase resulting in a drastic decrease of these elements in phengite and sodic amphibole. At pressures below 1.1 GPa paragonite and amphibole breakdown causes a drastic increase of Li and B in phengite and relict sodic amphibole.

The modeled Li and B trends are opposite to those observed in measured phengite, but partly resemble those in measured sodic amphibole, such as the decreasing B content associated with relatively constant Li concentrations in the rims of amphiboles (Fig. 3). It is notable that modeled Li and B concentrations in amphibole show an offset with respect to the observed values, which is constrained by the partition coefficients.

Fig. 5 shows the same correlation as in Fig. 4, but modeled with 0.1 wt% free H_2O in equilibrium with the solid phases at every calculated step. After infiltration and compositional equilibration, H_2O leaves the system and trace elements incorporated in the fluid phase are subtracted from the bulk rock composition (see model description above).

In contrast to the calculations involving water re-saturation only (Fig. 4) the concentrations of all considered trace elements in phengite and sodic amphibole decrease strongly after fluid infiltration as a response to the compositional fluid-mineral equilibration and the fractionation effect of the fluid that leaves the system after equilibration. In contrast to the previous calculations, no core-to-rim increase of Li and B is observed and the concentration of these elements in phengite and amphibole is dominated by the leaching effect of the fluid. However, the evolution of Sr and Pb does not significantly differ between both models (Figs. 4 and 5), which demonstrates that the fluid percolation effect on these elements is negligible as the concentration of both in phengite and sodic amphibole is dominated by the formation of epidote.

The plots in Fig. 6 show the observed compositional core-to-rim variations in phengites and amphiboles from the weakly deformed and the mylonitic samples (shaded areas). Further, the trends marked by open circles display the results from the forward models assuming percolation of 0.1 wt% pure H_2O. The effect of the fluid on phengite and amphibole compositions occurs in two steps. After fluid infiltration phengite and amphibole composition equilibrates with the coexisting fluid, which drives their compositions towards the observed rim values. With ongoing fluid percolation Li and B in both minerals is continuously depleted due to the leaching effect of the percolating fluid. The equilibration of Sr and Pb with newly-formed epidote after initial fluid infiltration drives phengite and amphibole compositions already to the observed values in the overprinted rims and in the mylonitic samples. The leaching effect of the subsequent percolating fluid is negligible, which is why we do not consider Sr and Pb for quantitative calculations involving a percolating fluid.

In contrast to the models assuming internal trace element distribution (Fig. 4), those assuming fluid percolation reproduce the observed core-to-rim trace element

decrease in phengite from the weakly deformed samples and also the low Li, B, Sr and Pb concentrations in the mylonitic samples. Interestingly, the modeled Li and B concentrations in amphibole reflect well the trend between unaffected cores and mylonitic samples, but only partly correspond to the Li trend in the weakly overprinted samples.

However, it is evident (Fig. 6) that the modeled leaching effect of the fluid in case of Li and B is overestimated compared to the natural samples. The reason for that is an overestimated amount of percolating fluid – the amount of 0.1 wt% fluid in the previous calculations was chosen as an arbitrary starting value to demonstrate the leaching effect generally – and/or an underestimated trace element load of the fluid, which will have a counter effect on element leaching. With two assumptions it is possible to model the trace element content of the infiltrated fluid and the resulting compositional trends in phengite and amphibole as a function of the amount of infiltrated fluid i.e. (1) mineral compositions in the mylonitic samples reflect (near) chemical equilibrium between fluid and solid phases, which enables calculation of the fluid composition and (2) pre-deformational trace element contents of the mylonites' precurser have been at least similar to the weakly deformed samples. If this holds true our models can determine the fluid amount that is necessary to reproduce the observed compositional trends from unaffected cores to overprinted rims and to the well-equilibrated mylonitic samples.

The trends marked by filled circles in Fig. 6 display the results from forward models assuming percolation of 0.1 wt% H_2O with 250 µg/g Li and 25 µg/g B, which reflects chemical equilibrium composition of the fluid with the rims of the mylonitic phengites, assuming $D^{Phe/Fluid}$ values of 0.1 and 0.2 for Li and B, respectively (see appendix). Sr and Pb were not considered in these calculations, as their distribution is mainly controlled by the amount of newly-formed epidote, rather than reflecting

427 transport in the percolating fluid. Compared to the calculations involving pure H_2O
428 (open circles), the leaching effect on the affected minerals of a trace element bearing
429 fluid is reduced and the modeled trends (filled circles) reproduce the compositional
430 change between unaffected cores, overprinted rims and phengites as well as amphiboles
431 in the mylonitic samples.

432 The Li-B diagram in Fig. 7 shows the resulting phengite composition in the
433 chosen sample after percolation of a fluid with constant composition of 250 µg/g Li and
434 25 µg/g B, but varying fluid-rock ratios, which are calculated as to be the sum of the
435 amounts of water coexisting with the solid phases at every calculated increment. This
436 diagram shows that the extent of Li and B depletion is dependent on the amount of the
437 percolating fluid and that the compositions of phengite cores, overprinted rims and
438 mylonitic phengites can be explained by different fluid-rock ratios (bold numbers)
439 percolating through the host rocks. The observed rim compositions in the felsic sample
440 are the result of fluid-rock interaction with fluid-rock ratios between 0.1 and 0.3. In
441 contrast, fluid-rock ratios not less than 0.5 to 4 are necessary to drive the initial
442 phengite compositions towards those in the mylonitic samples.

443 Fig. 8a shows the modeled change in fluid composition due to fluid-rock
444 interaction. Whereas the infiltrated fluid has a composition of 250 µg/g Li and 25 µg/g
445 B, the trace element content of the percolating fluid is significantly enriched during the
446 initial stages of the fluid-rock interaction and can reach values of up to 900 µg/g Li and
447 250 µg/g B. The calculated leaching effect of fluid percolation on the bulk rock chemistry
448 is shown in Fig. 8b. Li and B are continuously depleted and the modeled B/Be ratio is
449 decreasing with ongoing fluid percolation. The dependence of the trace element
450 distribution on the mineral assemblage is demonstrated by the Li curve. The sodic
451 amphibole- and paragonite-rich rocks retain Li until both phases break down at 1.0 GPa,

452 which enhances Li liberation, reflected in enhanced bulk rock depletion and in slightly
453 increasing Li concentrations in the fluid outflux (Fig. 8a).

454 **Discussion**

455 Thermodynamic forward calculations to investigate compositional
456 disequilibrium textures in reacting rock systems (e.g., Spear 1988; Florence and Spear
457 1991) are a common technique for petrological and geodynamic research (e.g., Connolly
458 2005; Konrad-Schmolke et al., 2008b; Caddick et al., 2010; Pearce et al., 2010). However,
459 thermodynamic equilibrium calculations assume equilibrated chemical potentials
460 among all stable phases within a compositionally homogeneous rock volume.
461 Compositional disequilibrium effects, such as fractional crystallisation, devolatilisation
462 and metasomatism are usually modeled by incrementing a P-T trajectory of the
463 considered rock volume and manipulating the compositional parameters between every
464 calculated increment (e.g., Konrad-Schmolke et al., 2005; 2006). It is notable, that the
465 size of the considered equilibration domain, which is often unknown in Nature, defines
466 the length scale over which interpretations of the modeled data are reliable. In our case,
467 the size of the equilibrated rock volume defines the length scale of fluid-rock interaction
468 in our models, as the fluid is considered to leave the model system after equilibration.
469 Compositional disequilibrium effects that result from fluid percolation through a rock
470 column (e.g., Breeding et al., 2004) as well as temperature and pressure differences
471 along the flow path are not considered in this study, but are the topic of a subsequent
472 work (Pöhle et al., 2011). Our aim is to present a new approach for the quantification of
473 trace element budgets and fluid fluxes during fluid-rock interaction in reacting and
474 deforming rocks as well as for the distinction between chemically open and closed
475 metamorphic systems.

476 Relative changes of abundances or isotopic compositions of light fluid-mobile
477 elements, such as Li and B, are often used to trace fluid-rock interaction processes in
478 subduction zones (e.g. Marschall et al., 2006; Penniston-Dorland 2010). Several works
479 show that decreasing concentrations of Li and B, as well as decreasing B/Be in bulk rock
480 samples and specific minerals are the result of progressive rock dehydration (e.g.
481 Bebout et al., 2007). In turn, positive correlations between H_2O content of the rock and
482 these parameters are commonly associated with fluid-influx events (e.g. Marschall et al.,
483 2009). However, quantification of the fluid influx is of crucial importance to understand
484 the associated element transfer as well as to quantify its effect on the physical behaviour
485 of crustal and mantle rocks (e.g., Regenauer-Lieb et al., 2001).
486 Quantitative constraints on metamorphic fluid fluxes in natural rock systems
487 usually come from fluid-induced mineralogical, isotopic or chemical changes in the
488 investigated rocks (see Ferry and Gerdes 1998 for a detailed review). Although Li and B
489 are increasingly used as tracers for fluid-rock interaction, quantification of fluid
490 amounts based on these trace elements have not been performed so far. Our models
491 demonstrate that percolation of relatively Li- and B-rich fluids can result in depletion of
492 these elements in metamorphic rock and minerals (Figs. 6 and 8), depending on fluid-
493 and bulk rock chemistry, mineral reactions, fluid-solid trace element distribution, but
494 most strongly on the amount of percolating fluid that enables continuous leaching of the
495 affected wall rock. In turn, this leaching effect leads to a major transport of Li, less
496 pronounced B, into the fore-arc mantle wedge. The relation between amount of
497 percolating fluid and the effect on phengite chemistry is shown in Fig. 7. This relation
498 can be used to infer the amount of percolating fluid through our samples.
499 Konrad-Schmolke et al., (2011) showed that, assuming a structurally coherent
500 section affected by fluid influx with a vertical extent of 2 km (e.g., Gosso et al., 1979;

501 Babist et al., 2006), a fluid influx of 15 m^3m^{-2} is needed for partial water re-saturation of
502 the weakly overprinted samples and 75 m^3m^{-2} for a complete resetting of the rocks,
503 reflected in the mylonitic samples. The constant or even slightly increasing Li
504 concentrations in the amphiboles of the weakly-deformed samples indicate that during
505 this re-hydration process trace element distribution was mostly internal, i.e. trace
506 elements were transferred from reactant into product phases (Figs. 2 and 6). Further, Li
507 and B concentrations in the rims of the weakly-deformed phengites and amphiboles
508 reflect equilibration with an infiltrated fluid rather than a leaching effect of a percolating
509 fluid (Fig. 6). Maximum fluid percolation in the weakly deformed samples, assuming
510 about 20% of the entire rock volume to be affected by fluid-induced reactions (Konrad-
511 Schmolke et al., 2011) results in a total fluid-rock ratio of up to 0.06 (Fig. 7) leading to a
512 maximum time integrated fluid flux of 140 m^3m^{-2}, a value close to the amount necessary
513 for re-hydration. Interestingly, the percolating fluid amount did not fully rehydrate the
514 weakly deformed samples indicating either that the fluid flux was even lower than these
515 estimates or that a kinetically hindered re-equilibration during short-lived fluid pulses
516 occurred (e.g., van Haaren et al., 1996; Camacho et al., 2005). In contrast, minumum
517 fluid-rock ratios in the mylonites are as high as 0.5 to 4 (Fig. 7), equivalent to time
518 integrated fluid fluxes of at least $1 - 8 \cdot 10^3$ m^3m^{-2} thus, more than one order of
519 magnitude larger than in the weakly deformed areas. However, our models allow
520 quantification of fluid-rock interaction only in a chemically equilibrated domain, the
521 vertical extent of which is not well constrained as our samples were collected along a
522 near horizontal rather than a vertical profile (Fig. 1). Nevertheless, the large relative
523 differences in fluid percolation through weakly and strongly deformed rocks from the
524 sample area are significant and most likely reflect different modes of fluid migration
525 (e.g. Zack and John 2007).

526 Enhanced permeability in highly strained rocks has been demonstrated in
527 numerical models (e.g., Ord and Oliver 1997; Ague 2007) and natural observations (e.g.,
528 Fusseis et al., 2009). Our calculated values of time integrated fluid fluxes in the
529 mylonites fall within the lower end of the observed range, i.e. 10^4 – 10^6 m^3m^{-2}, postulated
530 for ductile shear zones active at similar temperatures (e.g., Dipple and Ferry 1992;
531 Selverstone et al., 1991). In contrast, calculated fluid fluxes in the weakly deformed
532 samples are lower than commonly calculated and observed fluid fluxes in regionally
533 metamorphosed areas (e.g., Baumgartner and Ferry 1991; Ferry 1992; Ferry and Gerdes
534 1998) and most likely reflect pervasive fluid flux along grain boundaries in high-
535 pressure rocks with low permeabilities (e.g., Ague 2007). Interestingly, the estimated
536 values for the weakly deformed samples are close to the boundary between open and
537 closed system behavior in fluid systems (~100 m^3m^{-2}; Oliver 1996; Zack & John, 2007),
538 loosely defined as an amount below which detection by classic methods like oxygen
539 isotopes are difficult.
540 Such heterogeneous fluid fluxes on top of the subducted slab may have major
541 implications for the fluid and trace element entrainment into the mantle wedge (cf.
542 Beinlich et al., 2010). Whereas large amounts of fluids percolating in high strain zones
543 entrain the mantle in discrete areas, those pervasively migrating through low permeable
544 rock volumes will have lower amounts, or will even be completely consumed by re-
545 hydration reactions in the exhuming high- and ultra-high pressure rock bodies. Such
546 fluid consuming re-hydration, e.g. retrograde formation of amphibole, is a commonly
547 observed feature in exhumed eclogites (e.g., Carson et al., 2000; Wilke et al., 2010). Both,
548 discrete dehydration reactions as well as deformation induced fluid channelling produce
549 inhomogeneous fluid fluxes at the slab-mantle interface, which complicate the
550 quantification of mass transfer from the slab into the mantle wedge.

551 Furthermore, fluid-rock interaction and associated mineral reactions can result
552 in discrete strong trace element variations in the fluid, such as shown in Fig. 8a. Trace
553 element leaching and mineral reactions in the fluid affected rocks, such as the
554 breakdown of paragonite and sodic amphibole, cause sharp changes in the fluid
555 composition reflected in jumps in the fluid evolution plots. Although the total amount of
556 fluid mobile trace elements entering the mantle wedge is dependent on the absolute
557 amount of fluid and on its trace element composition, such strong local variations
558 resulting from interactions in the subduction channel might have a distinct surface
559 expression in subduction zones. This is even more critical when considering accessory
560 and/or trace-element-rich phases. Figs. 4 and 5 show that the budget of Sr and Pb in our
561 samples is largely controlled by the formation of epidote, demonstrating that even small
562 amounts of trace element-rich phases, such as allanite, monazite and titanite, in reacting
563 rocks might govern the trace element budget during metamorphism (e.g., Hermann
564 2002; Hermann and Rubatto 2003; King et al., 2004) and thus influence the composition
565 of slab-derived fluids and arc volcanics (e.g., Plank et al., 2009). As quantitative
566 thermodynamic models of accessory phases are continuously developed (e.g. Kelsey and
567 Powell 2010; Evans et al., 2010), better constraints of their effect on the trace element
568 budget can be obtained utilising combined thermodynamic and trace element models.
569 All of the above observations demonstrate that the interplay between amounts and
570 compositions of fluid and solid phases, partition coefficients as well as mineral reactions
571 occurring in a discrete rock volume can lead to complex compositional effects in rocks
572 and minerals during fluid-rock interaction, which can be quantified with our model
573 approach.

574 However, to interpret our model results quantitatively critical parameters must
575 be studied thoroughly. In contrast to the thermodynamic datasets and modeling

576 techniques, which have been continuously improved over the last decade (e.g. Holland
577 and Powell 1998; Evans et al., 2010; Holland and Powell 2011; Connolly 2005),
578 knowledge of parameters that control trace element distribution and transport has not
579 kept pace with the analytical techniques (Blundy and Wood 2003). Solid/fluid trace
580 element partition coefficients are generally scarce (Brenan et al., 1998; Kessel et al.,
581 2005; Keppler 1996; Johnson and Plank 1999; Najorka et al., 1999; Melzer and Wunder
582 2000), especially at low temperatures as experienced by our samples.

583 The bulk partition coefficients calculated in our models reflect high fluid mobility
584 of Li and B with $D^{Fluid/Rock}$-values of 3.5 – 25 for Li and 1.8 – 11 for B, depending on the
585 coexisting phase assemblage. Indeed, high fluid mobility of Li and B is evident from
586 other natural observations (e.g. You et al., 1993; 1995; Ryan et al., 1995) and although
587 our calculated $D^{Fluid/Mineral}$-values might not exactly quantify the fluid mobility of both
588 elements, it is obvious that the percolating fluid led to a decrease of these elements in
589 the overprinted rims of the investigated grains (Figs. 3). $D^{Fluid/Phe}$-values used in this
590 study are calculated from $D^{Cpx/Fluid}$ values (Brenan et al., 1998) and $D^{Cpx/Phe}$ (Marschall et
591 al., 2007). In contrast, the experiments by Kessel et al., (2005) suggest a more refractory
592 behaviour of both elements with $D^{Cpx/Fluid}$ of 1.6 and 0.28 for Li and B, respectively, thus
593 implying B to be relatively immobile in subduction zone fluids. In the case of Li the
594 calculated fluid fluxes using the Kessel et al., (2005) data are slightly higher, with up to 6
595 $\cdot 10^3$ m^3m^{-2} in the weakly deformed samples and up to $1.1 \cdot 10^4$ m^3m^{-2} in the mylonites.
596 For B, the observed trends in our samples cannot be reproduced, as a refractory
597 behaviour of B will lead to increasing concentrations in the bulk rock, phengite and
598 amphibole (see electronic supplementary material). However, it is evident that better
599 quantitative constraints about trace element distribution during metamorphism are
600 needed to strengthen the potential of numerical models (e.g. Marschall et al., 2007;

Konrad-Schmolke et al., 2008a; Kimura et al., 2010), as a comparison with natural rocks will then become more reliable.

Acknowledgements

We thank Horst Marschall and Michel Marks for stimulating discussions as well as Christina Günter for help with the electron microprobe analyses. Further, we would like to thank Rick Carlson for his editorial handling and Jay Ague for a very thorough and helpful review. Additionally, comments by two anonymous reviewers helped to improve the manuscript.

References

Ague, J.J. (2007). Models of permeability contrasts in subduction zone mélange: Implications for gradients in fluid fluxes, Syros and Tinos Islands, Greece. Chemical Geology, 239(3-4): 217-227.

Babist, J., Handy, M. R., Konrad-Schmolke, M. and Hammerschmidt, K. (2006). Precollisional, multistage exhumation of subducted continental crust: The Sesia Zone, Western Alps. Tectonics 25, (6): TC6008.

Baumgartner, L. and Ferry, J. (1991). A model for coupled fluid-flow and mixed-volatile mineral reactions with applications to regional metamorphism. Contributions to Mineralogy and Petrology 106(3): 273-285.

Bebout, G.E., Ryan, J.G. and Leeman, W.P. (1993). B – Be systematics in subduction-related metamorphic rocks: Characterization of the subducted component. Geochimica et Cosmochimica Acta 57(10): 2227-2237.

Bebout, G.E., Bebout, A.E. and Graham, C.M. (2007). Cycling of B, Li and LILE (K, Cs, Rb, Ba, Sr) into subduction zones: SIMS evidence from micas in high-P/T metasedimentary rocks. Chemical Geology 239: 284-304.

Beinlich, A., Klemd, R., John, T. and Gao, J. (2010). Trace-element mobilization during Ca-metasomatism along a major fluid conduit: Eclogitization of blueschist as a consequence of fluid-rock interaction. Geochimica et Cosmochimica Acta 74(6): 1892-1922.

Bickle, M. J. and Teagle, D. A. H. (1992). Strontium alteration in the Troodos ophiolite: implications for fluid fluxes and geochemical transport in mid-ocean ridge hydrothermal systems. Earth and Planetary Science Letters, 113: 219-237.

Blundy, J. and Wood, B. (2003). Partitioning of trace elements between crystals and melts. Earth and Planetary Science Letters 210(3-4): 383-397.

Breeding, C.M., Ague, J.J. and Bröcker, M. (2004). Fluid-metasedimentary rock interactions in subduction-zone mélange: Implications for the chemical composition of arc magmas. Geology, 32: 1041-1044.

Brenan, J.M., Neroda, E., Lundstrom, C.C., Shaw, H.F., Ryerson, F.J. and Phinney, D.L. (1998). Behaviour of boron, beryllium, and lithium during melting and crystallization:

638 constraints from mineral-melt partitioning experiments. Geochimica et Cosmochimica
639 Acta 62(12): 2129-2141.Camacho et al., 2005

640 Caddick, M.J., Konopásek, J. and Thompson, A.B. (2010). Preservation of garnet growth
641 zoning and the duration of prograde metamorphism. Journal of Petrology 53, (11):
642 2327-2347.

643 Camacho, A., Lee, J.K.W., Hensen, B.J. and Braun, J. (2005). Short-lived orogenic cycles
644 and the eclogitization of cold crust by spasmodic hot fluids. 435, (7046): 1191-1196.

645 Carson, C.J., Clarke, G. L. & Powell, R. (2000). Hydration of eclogite, Pam Peninsula, New
646 Caledonia. Journal of Metamorphic Geology 18, (1): 79-90.

647 Castelli, D. (1991). Eclogitic metamorphism in carbonate rocks; the example of impure
648 marbles from the Sesia-Lanzo Zone, Italian Western Alps. Journal of Metamorphic
649 Geology 9, (1): 61-77.

650 Compagnoni, R., Dal Piaz, G. V., Hunziker, J. C., Gosso, G., Lombardo, B. and Williams, P. F.
651 (1977). The Sesia-Lanzo Zone, a slice of continental crust with Alpine high pressure-low
652 temperature assemblages in the Western Italian Alps. Rendiconti della Societa Italiana di
653 Mineralogia e Petrologia 33, (2): 335-374.

654 Connolly, J.A.D. (2005). Computation of phase equilibria by linear programming: A tool
655 for geodynamic modeling and its application to subduction zone decarbonation. Earth
656 and Planetary Science Letters 236: 524-541.

657 Dal Piaz, G.V., Hunziker, J.C. and Martinotti, G. (1972). La Zona Sesia-Lanzo e l'evoluzione
658 tettonico-metamorfica delle Alpi nordoccidentali interne. Memorie della Societa
659 Geologica Italiana 11: 433-466.

660 de Capitani, C. and Brown, T. H. (1987). The computation of chemical equilibrium in
661 complex systems containing non-ideal solutions. Geochimica et Cosmochimica Acta 51,
662 (10): 2639-2652.

663 Dipple, G.M. and Ferry, J.M. (1992). Fluid flow and stable isotopic alteration in rocks at
664 elevated temperatures with applications to metamorphism. Geochimica et
665 Cosmochimica Acta 56(9): 3539-3550.

666 Duchêne, S., Blichert-Toft, J., Luais, B., Telouk, P., Lardeaux, J. M. and Albarede, F. 1997.
667 The Lu-Hf dating of garnets and the ages of the Alpine high-pressure metamorphism.
668 Nature, 387, 586-589.

669 Elliott, T., Jeffcoate, A. and Bouman, C. (2004). The terrestrial Li isotope cycle: light-
670 weight constraints on mantle convection. Earth and Planetary Science Letters 220(3-4):
671 231-245.

672 Evans, K.A., Powell, R. and Holland, T.J.B., 2010. Internally consistent data for sulphur-
673 bearing phases and applications to the constructions for mafic greenschists facies rocks
674 in Na2O-CaO-K2O-FeO-MgO-Al2O3-SiO2-CO2-O-S-H2O. Journal of Metamorphic
675 Geology, 28, 667–687.

676 Ferraris, C. and Compagnoni, R. (2003). Metamorphic evolution and significance of a
677 serpentinized peridotite slice within the Eclogitic Micaschist Complex of the Sesia-zone
678 (Western Alps - Italy). Schweizerische Mineralogische und Petrographische Mitteilungen
679 83, (1): 3-13.

680 Ferry, J.F. (1992). Overview of the petrologic record of fluid flow during regional
681 metamorphism in northern New England. American Journal of Science, 294: 905-988.

682 Ferry, J.F. and Gerdes, M.L. (1998). Chemically reactive fluid flow during metamorphism.
683 Annual reviews of earth and Planetary Sciences, 26: 255-287.

684 Florence, F. P. and Spear, F. S. (1995). Intergranular diffusion kinetics of Fe and Mg
685 during retrograde metamorphism of a pelitic gneiss from the Adirondack Mountains.
686 Earth and Planetary Science Letters, 134: 329-340.

687 Fusseis, F., Regenauer-Lieb, K., Liu, J., Hough, R.M. and De Carlo, F. (2009). Creep
688 cavitation can establish a dynamic granular fluid pump in ductile shear zones.
689 459(7249): 974-977.

690 Gosso, G., Dal Piaz, G. V., Piovano, V. and Polino, R. (1979). High pressure emplacement of
691 early-Alpine nappes, post-nappe deformations and structural levels (internal
692 northwestern Alps). Memorie degli Instituti di Geologia e Mineralogia dell'Universita di
693 Padova 32: 5-15.

694 Hacker, B. R., Peacock, S. M., Abers, G. A. and Holloway, S. D. (2003). Subduction factory -
695 2. Are intermediate-depth earthquakes in subducting slabs linked to metamorphic
696 dehydration reactions? Journal of Geophysical Research-Solid Earth 108, (B1).

697 Handy, M. R. and Oberhänsli, R. (2004). Age map of the metamorphic structure of the
698 Alps - tectonic interpretation and outstanding problems. Mitteilungen der
699 Österreichischen Mineralogischen Gesellschaft 149: 97-121.

700 Hermann, J. (2002). Allanite: thorium and light rare earth element carrier in subducted
701 crust. Chemical Geology 192: 289-306.

702 Hermann, J. and Rubatto, D. (2003). Relating zircon and monazite domains to garnet
703 growth zones: age and duration of granulite facies metamorphism in the Val Malenco
704 lower crust. Journal of Metamorphic Geology 21: 833-852.

705 Holland, T.J.B. and Powell, R. (1998). An internally consistent thermodynamic data set
706 for phases of petrological interest. Journal of Metamorphic Geology 16(3): 309-343.

707 Holland, T.J.B. and Powell, R. (2011) An improved and extended internally consistent
708 thermodynamic dataset for phases of petrological interest, involving a new equation of
709 state for solids. Journal of Metamorphic Geology, DOI: 10.1111/j.1525-
710 1314.2010.00923.x

711 John T., Klemd R., Gao J. and Garbe-Schönberg C.D. (2008) Trace-element mobilization in
712 slabs due to non steady-state fluid–rock interaction: constraints from an eclogite-facies
713 transport vein in blueschist (Tianshan, China). Lithos 103: 1–24.

714 Johnson, M. C. and Plank, T. (1999). Dehydration and melting experiments constrain the
715 fate of subducted sediments: Geochemistry, Geophysics, Geosystems, v. 1,
716 1999GC000014.

717 Keppler, H. (1996). Constraints from partitioning experiments on the composition of
718 subduction-zone fluids. Nature 380(6571): 237-240.

719 Kelsey, D. E. and Powell, R. (2010). Progress in linking accessory mineral growth and
720 breakdown to major mineral evolution in metamorphic rocks: a thermodynamic
721 approach in the Na_2O-CaO-K_2O-FeO-MgO-Al_2O_3-SiO_2-H_2O-TiO_2-ZrO_2 system. Journal of
722 Metamorphic Geology, 29, (1): 151-166.

723 Kessel, R., Schmidt, M. W., Ulmer, P. and Pettke, T. (2005). Trace element signature of
724 subduction-zone fluids, melts and supercritical liquids at 120-180 km depth. Nature
725 437, (7059): 724-727.

726 Kimura, J.-I., Kent, A. J. R., Rowe, M. C., Katakuse, M., Nakano, F., Hacker, B. R., van Keken,
727 P. E., Kawabata, H. and Stern, R. J. (2010). Origin of cross-chain geochemical variation in
728 Quaternary lavas from the northern Izu arc: Using a quantitative mass balance approach
729 to identify mantle sources and mantle wedge processes. Geochemistry Geophysics
730 Geosystems 11 (10): doi:10.1029/2010GC003050

731 King, R.L., Bebout, A.E., Kobayashi, K., Nakamura, E. and van der Klauw, S.N.G.C. (2004).
732 Ultrahigh-pressure metabasaltic garnets as probes into deep subduction zone chemical
733 cycling. Geochemistry Geophysics Geosystems 5 (12) doi:10.1029/2004GC000746

734 King, R.L., Bebout, G.E., Grove, M., Moriguti, T. and Nakamura, E. (2007) Boron and lead
735 isotope signatures of subduction-zone mélange formation: Hybridization and
736 fractionation along the slab–mantle interface beneath volcanic arcs. Chemical Geology
737 239: 305 – 322.

738 Konrad-Schmolke, M., Handy, M. R., Babist, J. and O'Brien, P. J. (2005). Thermodynamic
739 modelling of diffusion-controlled garnet growth. Contributions to Mineralogy and
740 Petrology, 149: 181-195.

741 Konrad-Schmolke, M., Babist, J., Handy, M. R. and O Brien, P. J. (2006). The physico-
742 chemical properties of a subducted slab from garnet zonation patterns (Sesia Zone,
743 Western Alps). Journal of Petrology, 47, (11): 2123-2148.

744 Konrad-Schmolke, M., O'Brien, P. J. and Heidelbach, F. (2007). Compositional re-
745 equilibration of garnet: The importance of sub-grain boundaries. European Journal of
746 Mineralogy 19, (4): 431-438.

747 Konrad-Schmolke, M., Zack, T., O'Brien, P. J. and Jacob, D. E. (2008a). Combined
748 thermodynamic and rare earth element modelling of garnet growth during subduction:
749 Examples from ultrahigh-pressure eclogite of the Western Gneiss Region, Norway. Earth
750 and Planetary Science Letters 272, (1-2): 488-498.

751 Konrad-Schmolke, M., O'Brien, P. J., de Capitani, C. and Carswell, D. A. (2008b). Garnet
752 growth at high- and ultra-high pressure conditions and the effect of element
753 fractionation on mineral modes and composition. Lithos 103, (3-4): 309-332.

754 Konrad-Schmolke, M., O'Brien, P. J. and Zack, T. (2011). Fluid Migration above a
755 subducted slab – Constraints on amount, pathways and major element mobility from
756 partially overprinted eclogite-facies rocks (Sesia Zone, Western Alps). Journal of
757 Petrology. 52, (3): 457-486.

758 Koons, P. O. (1986). Relative geobarometry from high-pressure rocks of
759 quartzofeldspathic composition from the Sesia Zone, Western Alps, Italy. Contributions
760 to Mineralogy and Petrology. 93, (3): 322-334.

761 Lardeaux, J.-M. and Spalla, M. I. (1991). From granulites to eclogites in the Sesia zone
762 (Italian Western Alps); a record of the opening and closure of the Piedmont ocean.
763 Journal of Metamorphic Geology 9, (1): 35-59.

764 Manning, C.E. (2004). The chemistry of subduction-zone fluids. Earth and Planetary
765 Science Letters 223(1-2): 1-16.

766 Marschall, H. R., Ludwig, T., Altherr, R., Kalt, A. and Tonarini, S. (2006). Syros
767 metasomatic tourmaline: Evidence for very high-$\delta^{11}B$ fluids in subduction zones. Journal
768 of Petrology 47, (10): 1915-1942.

769 Marschall, H.R., Altherr, R. and Rüpke, L. (2007). Squeezing out the slab – modelling the
770 release of Li, Be and B during progressive high-pressure metamorphism. Chemical
771 Geology 239(3-4): 323-335.

772 Marschall, H., Altherr, R., Gméling, K. and Kasztovszky, Z. (2009). Lithium, boron and
773 chlorine as tracers for metasomatism in high-pressure metamorphic rocks: a case study
774 from Syros (Greece). Mineralogy and Petrology 95(3): 291-302.

775 Melzer, S. and Wunder, B. (2000). Island-arc basalt alkali ratios: Constraints from
776 phengite-fluid partitioning experiments. Geology 28(7): 583-586.

777 Najorka, J., Gottschalk, M., Franz, G. and Heinrich, W. (1999). Ca-Sr distribution among
778 amphibole, clinopyroxene, and chloride-bearing solutions. American Mineralogist 84(4):
779 596-606.Peacock, S.M. and Hervig, R.L. (1999). Boron isotopic composition of
780 subduction-zone metamorphic rocks. Chemical Geology 160(4): 281-290.

781 Ord, A. and Oliver, N.H.S. (1997). Mechanical controls on fluid flow during regional
782 metamorphism: some numerical models. Journal of Metamorphic Geology, 15: 345-359.

783 Peacock, S.M. and Hervig, R.L. (1999). Boron isotopic composition of subduction-zone
784 metamorphic rocks. Chemical Geology 160(4): 281-290.

785 Penniston-Dorland, S. C., Sorensen, S. S., Ash, R. D. and Khadke, S. V. (2010). Lithium
786 isotopes as a tracer of fluids in a subduction zone mélange: Franciscan complex, Ca.
787 Earth and Planetary Science Letters 292, (1-2): 181-190.

788 Plank, T., Cooper, L.B. and Manning, C.E. (2009). Emerging geothermometers for
789 estimating slab surface temperatures. Nature Geoscience 2(9): 611-615.

790 Pöhle, M., Konrad-Schmolke, M. and Jahn, S. (2011). 2-D Thermodynamic and trace
791 element models of subduction zones. Mineralogical Magazine, 75 (3): 1652.

792 Pognante, U. (1989). Tectonic implications of lawsonite formation in the Sesia zone
793 (Western Alps). Tectonophysics 162, (3-4): 219-227.

794 Putnis, A. (2002). Mineral replacement reactions: From macroscopic observations to
795 microscopic mechanisms. Mineralogical Magazine. 66,(5): 689-708.

796 Regenauer-Lieb, K., Yuen, D.A. and Branlund, J. (2001). The initiation of subduction:
797 Criticality by addition of water? Science, 294: 578-580.

798 Rosenbaum, G., Giles, D., Saxon, M., Betts, P.G., Weinberg, R.F. and Duboz, C. (2005).
799 Subduction of the Nazca Ridge and the Inca Plateau: Insights into the formation of ore
800 deposits in Peru. Earth and Planetary Science Letters 239 (1): 18-32.

801 Rubatto, D., Gebauer, D. and Compagnoni, R. 1999. Dating of eclogite facies zircons: the
802 age of Alpine metamorphism in the Sesia-lanzo Zone (Western Alps). Earth and
803 Planterary Science Letters, 167, 141-158.

804 Rubie, D. C. (1983). Reaction-enhanced ductility: The role of solid-solid univariant
805 reactions in deformation of the crust and mantle. Tectonophysics 96, (3-4): 331-352.

806 Ryan, J.G. and Langmuir, C.H. (1988). Beryllium systematics in young volcanic rocks:
807 Implications for 10Be. Geochimica et Cosmochimica Acta 52(1): 237-244.

808 Ryan, J. G., Morris, J., Tera, F., Leeman, W. P. and Tsvetkov, A. (1995). Cross-arc
809 geochemical variations in the Kurile arc as a function of slab depth. Science 270, (5236):
810 625-627.

811 Sawkins, F.J. (1972). Sulfide ore deposits in relation to plate tectonics. The Journal of
812 Geology, 80 (4): 377-397.

813 Selverstone, J., Morteani, G. and Staude, J.-M. (1991). Fluid channelling during ductile
814 shearing: transformation of granodiorite into aluminous schist in the Tauern Window,
815 Eastern Alps. Journal of Metamorphic Geology, 9: 419-431.

816 Sillitoe, R.H. (1972). A plate tectonic model for the origin of porphyry copper ore
817 deposits. Economic Geology, 67 (2): 184-197.

818 Spandler, C., Hermann, J. r., Arculus, R. and Mavrogenes, J. (2003). Redistribution of trace
819 elements during prograde metamorphism from lawsonite blueschist to eclogite facies;
820 implications for deep subduction-zone processes. Contributions to Mineralogy and
821 Petrology 146, (2): 205-222.

822 Spear, F. (1988). Metamorphic fractional crystallisation and internal metasomatism by
823 diffusional homogenization of zoned garnets. Contributions to Mineralogy and
824 Petrology, 99: 507-517.

825 Tatsumi, Y., Hamilton, D.L. and Nesbitt, R.W. (1986). Chemical characteristics of fluid
826 phase released from a subducted lithosphere and origin of arc magmas: Evidence from
827 high-pressure experiments and natural rocks. Journal of Volcanology and Geothermal
828 Research 29(1-4): 293-309.

829 Tropper, P., Essene, E. J., Sharp, Z. D. and Hunziker, J. C. (1999). Application of K-
830 feldspar-jadeite-quartz barometry to eclogite facies metagranites and metapelites in the
831 Sesia Lanzo Zone (Western Alps, Italy). Journal of Metamorphic Geology 17, (2): 195-
832 209.

833 van Haren, J.L.M., Ague, J.J. and Rye, D.M. (1996). Oxygen isotope record of fluid
834 infiltration and mass transfer during regional metamorphism of pelitic schists,
835 Conneticut, USA. Geochimica Cosmochimica Acta, 60 (18): 3487- 3504.

836 Wilke, F. D. H., O'Brien, P. J., Altenberger, U., Konrad-Schmolke, M. and Khan, M. A.
837 (2010). Multi-stage reaction history in different eclogite types from the Pakistan
838 Himalaya and implications for exhumation processes. Lithos 114, (1-2): 70-85.

839 Wyllie, PJ (1983) Experimental and thermal constraints on the deep-seated parentage of
840 some granitoid magmas in subduction zones. In: Atherton MP, Gribble CD (eds)
841 Migmatites, melting, and metamorphism. Shiva, Orpington, pp 37-51.

842 You, C.-F., Spivack, A.J., Smith, J.H. and Gieskes, J.M. (1993). Mobilization of boron in
843 convergent margins: Implications for the boron geochemical cycle. Geology 21(3): 207-
844 210.

845 You, C.-F., Spivack, A.J., Gieskes, J.M., Rosenbauer, R. and Bischoff, J.L. (1995).
846 Experimental study of boron geochemistry: implications for fluid processes in
847 subduction zones. Geochimica et Cosmochimica Acta 59(12): 2435-2442.

848 Zack, T., Tomascak, P.B., Rudnick, R.L., Dalpé, C. and McDonough, W.F. (2003). Extremely
849 light Li in orogenic eclogites: The role of isotope fractionation during dehydration in
850 subducted oceanic crust. Earth and Planetary Science Letters 208(3-4): 279-290.

851 Zack T. and John T. (2007). An evaluation of reactive fluid flow and trace element mobility
852 in subducting slabs. Chemical Geology 239: 199-216.

853 Zucali, M., Spalla, M. I. and Gosso, G. (2002). Strain partitioning and fabric evolution as a
854 correlation tool: The example of the Eclogitic Micaschists complex in the Sesia-Lanzo

855 Zone (Monte Mucrone-Monte Mars, Western Alps, Italy). Schweizerische Mineralogische
856 und Petrographische Mitteilungen 82, (3): 429-454.
857

858 **Figure captions**

859

860 Fig. 1: a) Tectonometamorphic map of the Sesia-Lanzo zone (SLZ) and adjacent units.
861 The samples were collected along a profile parallel to a strain gradient in the southern
862 SLZ. b) Schematic exhumation sketch and structural profile along the white line shown
863 in a). The two weakly deformed samples are from within the Mombarone Unit, the
864 mylonites were sampled within the Tallorno shear zone.

865

866 Fig. 2: High contrast back scattered electron (BSE) images from phengites and sodic
867 amphiboles in the weakly deformed samples (a and b) and the mylonites (c). Fluid-
868 induced compositional variations (Fe-Mg exchange) are well preserved in coarse-
869 grained weakly deformed samples (bright zones in a and b), whereas the smaller
870 mylonitic grains are compositionally more homogeneous (c). Black dots are laser
871 ablation pits.

872

873 Fig. 3: Results of in situ laser ablation measurements in pristine cores, overprinted rims
874 and mylonitic phengites and sodic amphiboles. In phengite Li, B, Sr and Pb
875 concentrations define a clear trend between relict cores, overprinted rims and mylonitic
876 samples. In sodic amphibole only B shows a clear core-rim-mylonites trend towards
877 lower values. Li is almost unchanged in the overprinted rims but significantly lower in
878 the mylonitic grains. Sr and Pb concentrations scatter in the overprinted rims but a
879 weak trend towards the mylonitc samples is visible.

880

881 Fig. 4: Results from thermodynamic and trace element modeling for the selected felsic
882 sample (MKS-30-1). a) Modeled molar phase abundances assuming isochemical
883 decompression and cooling from peak conditions to the fluid influx event (stippled line).
884 After fluid influx the rock is assumed to be water saturated, but no free fluid phase is
885 affecting the trace element composition of phengite and sodic amphibole. Trace element
886 redistribution without percolation of a free fluid phase causes at first slight variations in
887 Li and B concentrations in phengite (b) and sodic amphibole (c) and then a drastic
888 increase of both elements during paragonite and sodic amphibole breakdown. In
889 contrast, Sr and Pb concentrations decrease drastically after the fluid-induced formation
890 of epidote. See text for further details.

891

892 Fig. 5: Same plots as in Fig. 4, but calculated with 0.1 wt% free H_2O in equilibrium with
893 the solid phases after fluid infiltration. The percolating fluid has a significant leaching
894 effect on Li and B, reflected in drastically decreasing concentrations of both elements in
895 phengite (b) and sodic amphibole (c) during fluid infiltration. The Sr and Pb evolution is
896 similar as in Fig. 4 indicating a limited fluid effect on these elements.
897
898 Fig. 6: Element-element plots showing the results of the modeled trace element
899 evolution in phengite and sodic amphibole assuming a percolation of 0.1 wt% pure H_2O
900 (open circles) as well as percolation of 0.1 wt% H_2O with 250 µg/g Li and 25 µg/g B. The
901 Li and B compositional fluid effect on phengite and amphibole is controlled by the
902 equilibration with the fluid phase and the leaching effect of the percolating fluid. In
903 contrast, Sr and Pb compositional trends are mainly controlled by the formation of
904 epidote. The observed trends in our samples (shaded areas) can be modeled assuming a
905 Li- and B-bearing percolating fluid.
906
907 Fig. 7: Modeled compositional Li and B variations in phengite dependent on the fluid-
908 rock ratio during fluid percolation. The observed rim compositions in the weakly
909 deformed samples can be explained by fluid percolation with fluid-rock ratios between
910 0.15 and 0.3, whereas modeling of the composition of the mylonitic samples requires
911 fluid-rock ratios between 0.5 and 4.0. SZ = shear zone samples.
912
913 Fig. 8: Modeled effects on fluid (a) and bulk rock (b) composition of the fluid-rock
914 interaction. The composition of the infiltrated fluid (250 µg/g Li, 25 µg/g B) is strongly
915 modified at the initial stages of the fluid-rock interaction and shows a slight response to
916 mineral reactions in the wall rock. Li and B concentrations as well as the B/Be ratio are
917 strongly decreasing in the affected host rock due to the fluid-induced trace element
918 leaching during fluid-rock interaction.

Figure 1

Click here to download Figure: Fig_01.eps

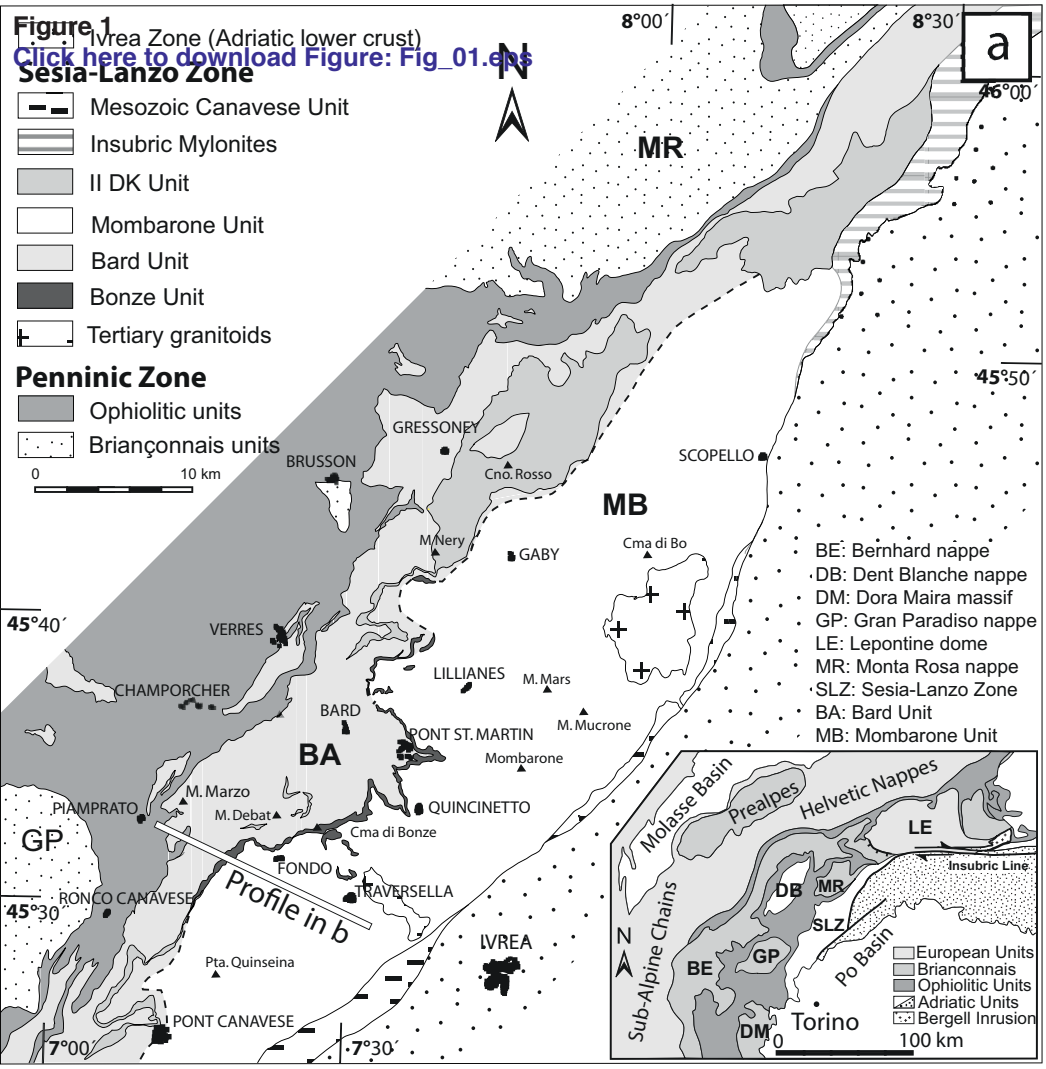

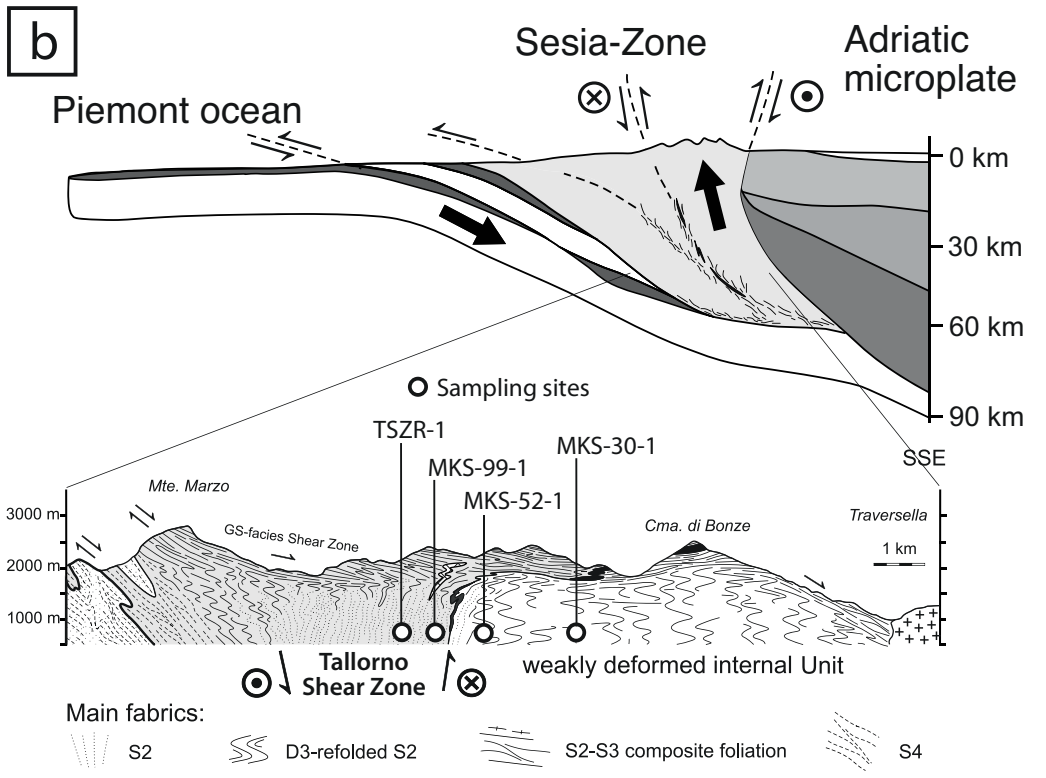

Fig. 1

Figure 2
Click here to download high resolution image

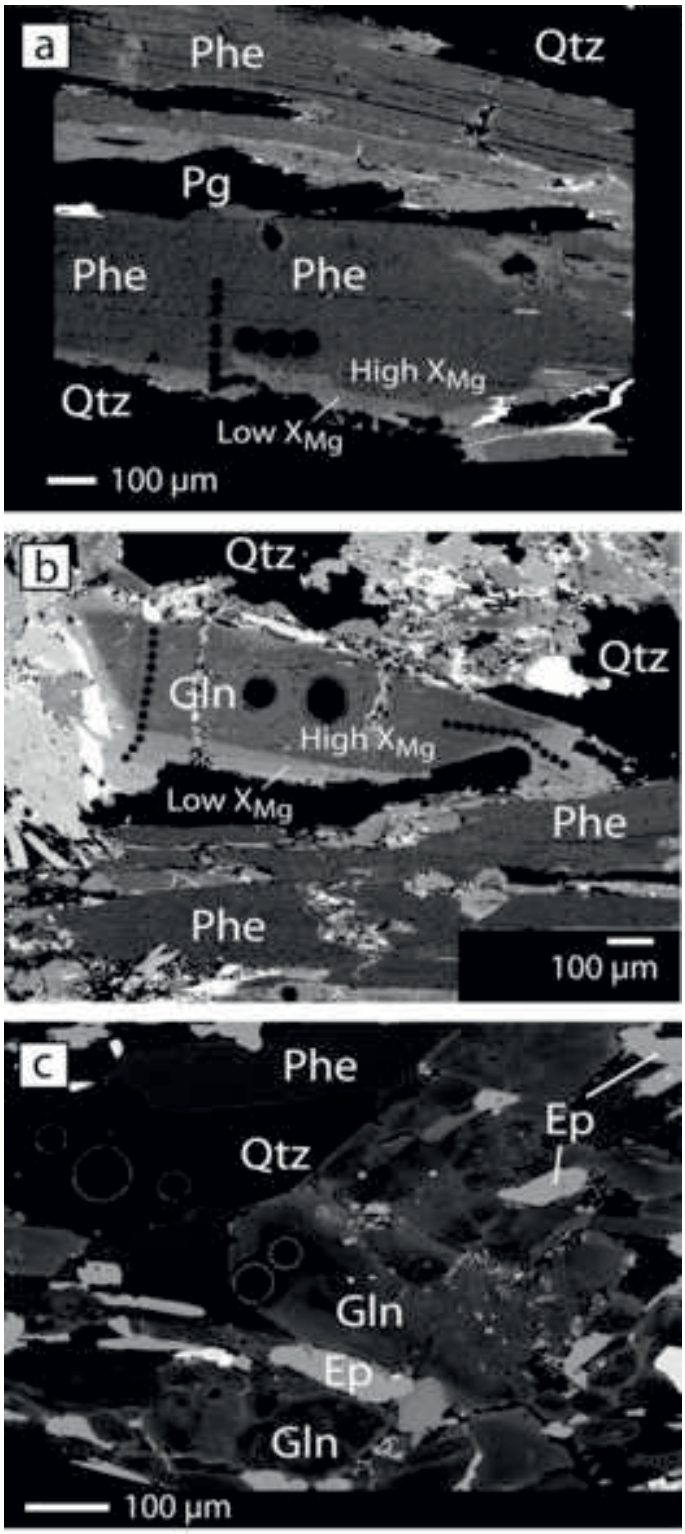

Fig. 2

Figure 3
Click here to download Figure: Fig_03.eps

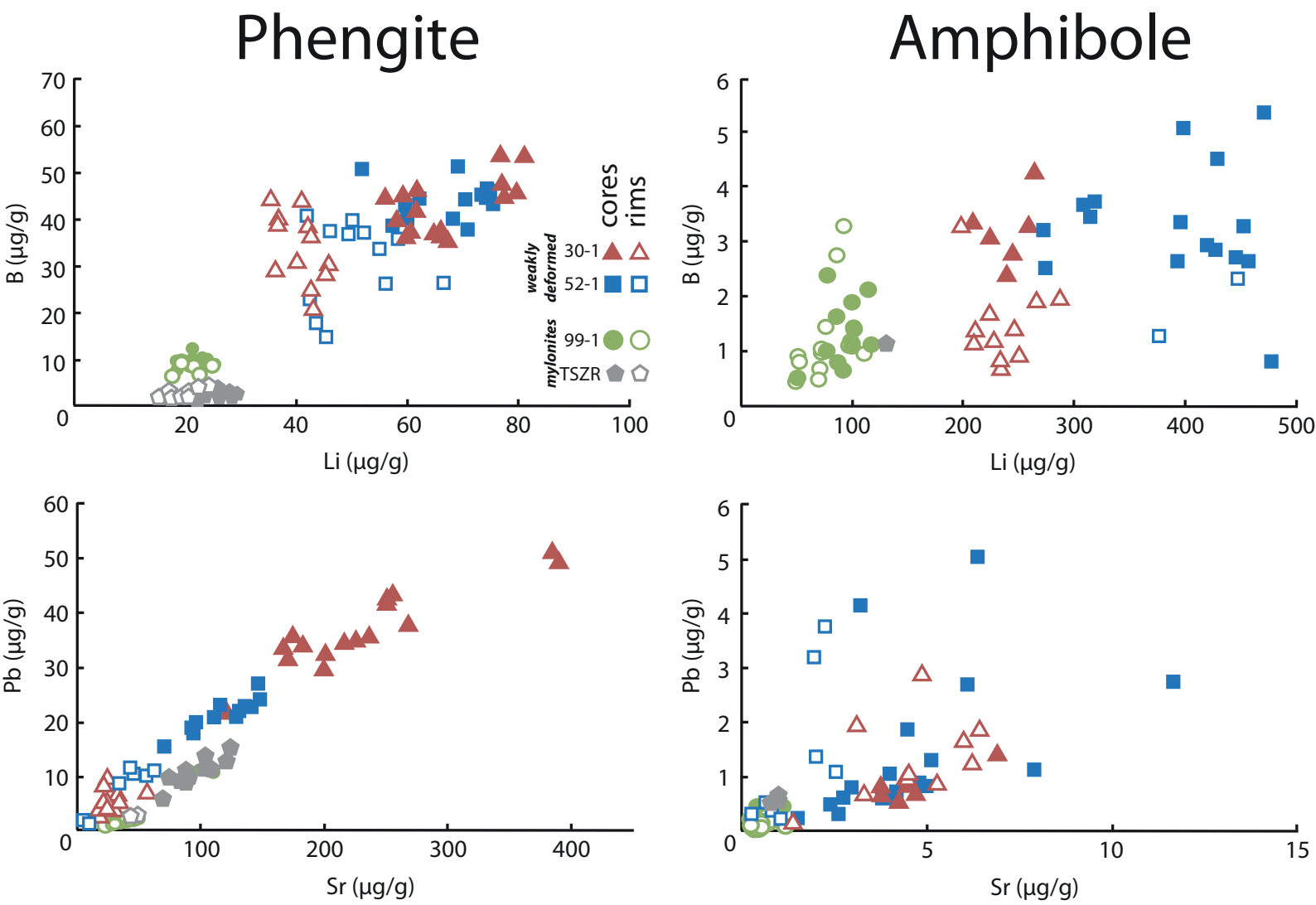

Fig. 3

Figure 4
Click here to download Figure: Fig_04.eps

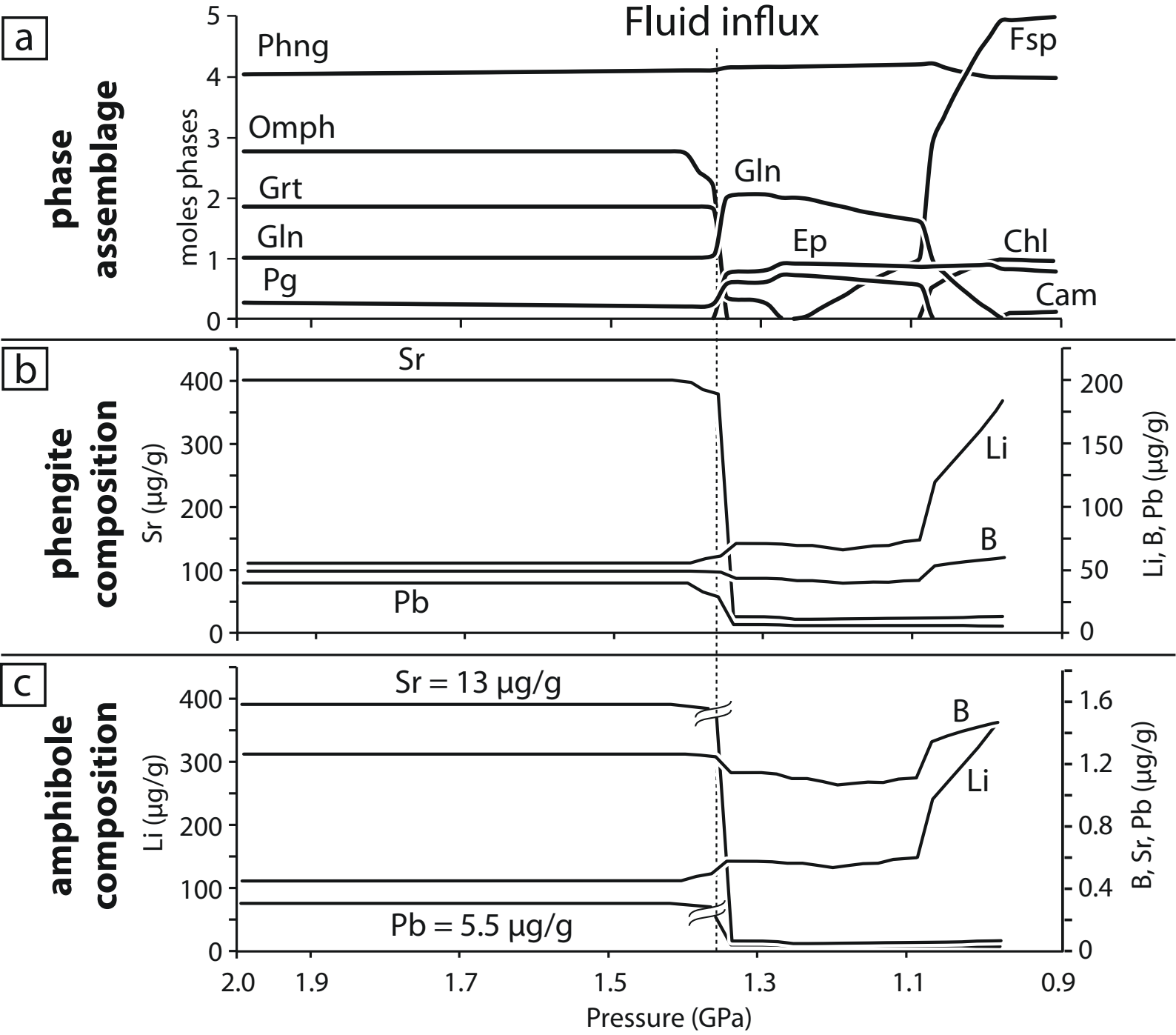

Fig. 4

Figure 5
Click here to download Figure: Fig_05.eps

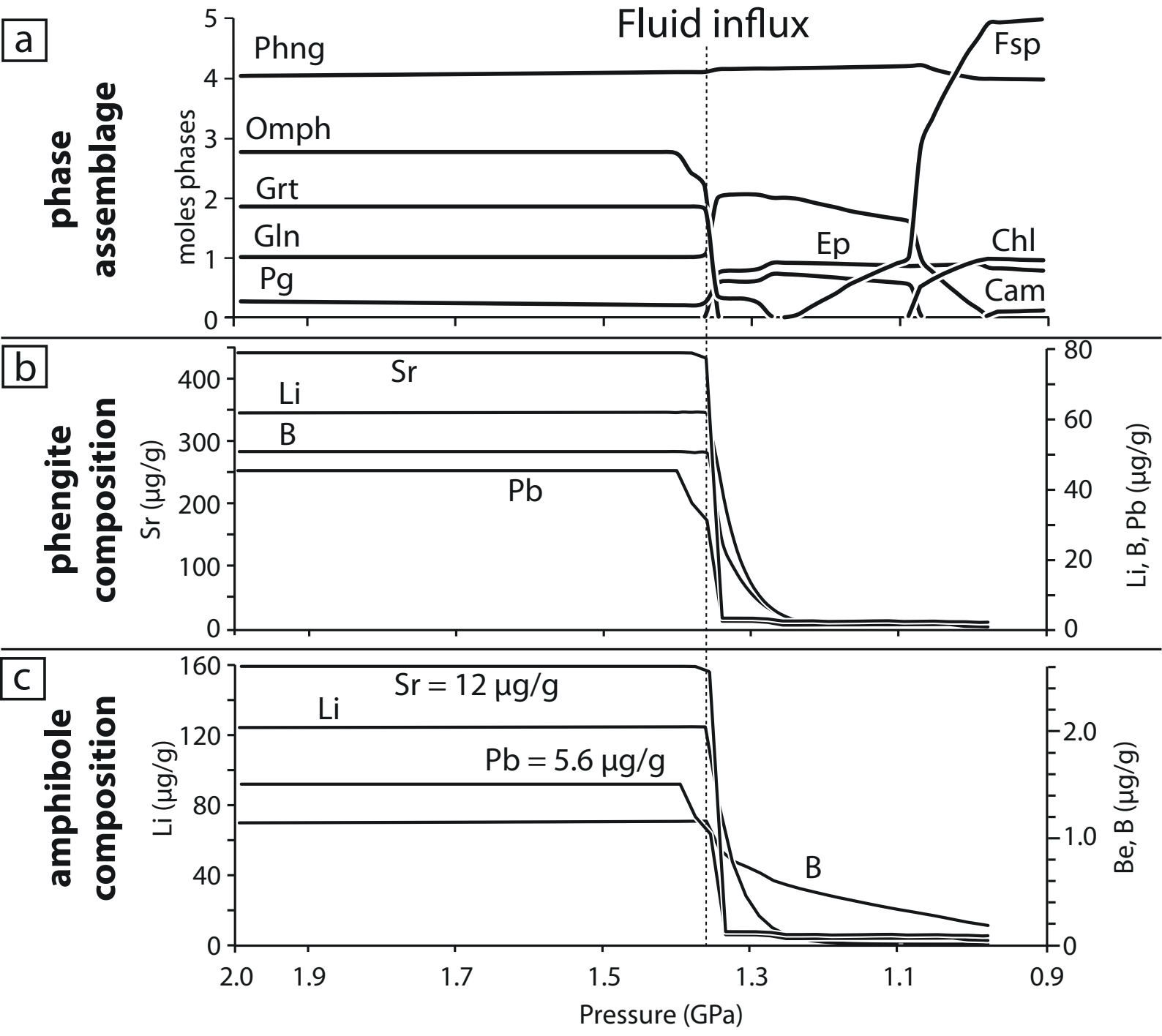

Fig. 5

Figure 6
Click here to download Figure: Fig_06.eps

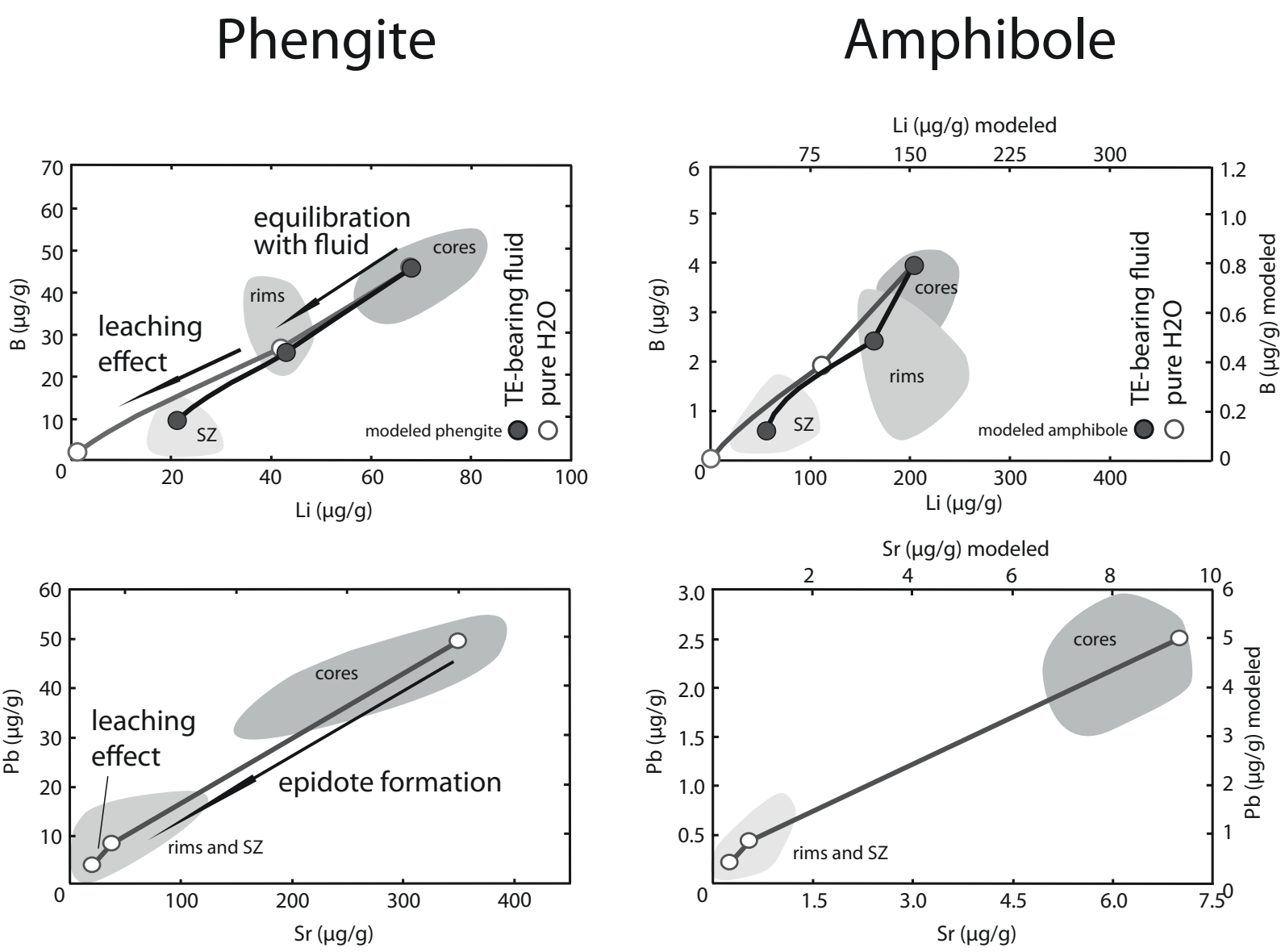

Fig. 6

Figure 7
Click here to download Figure: Fig_07.eps

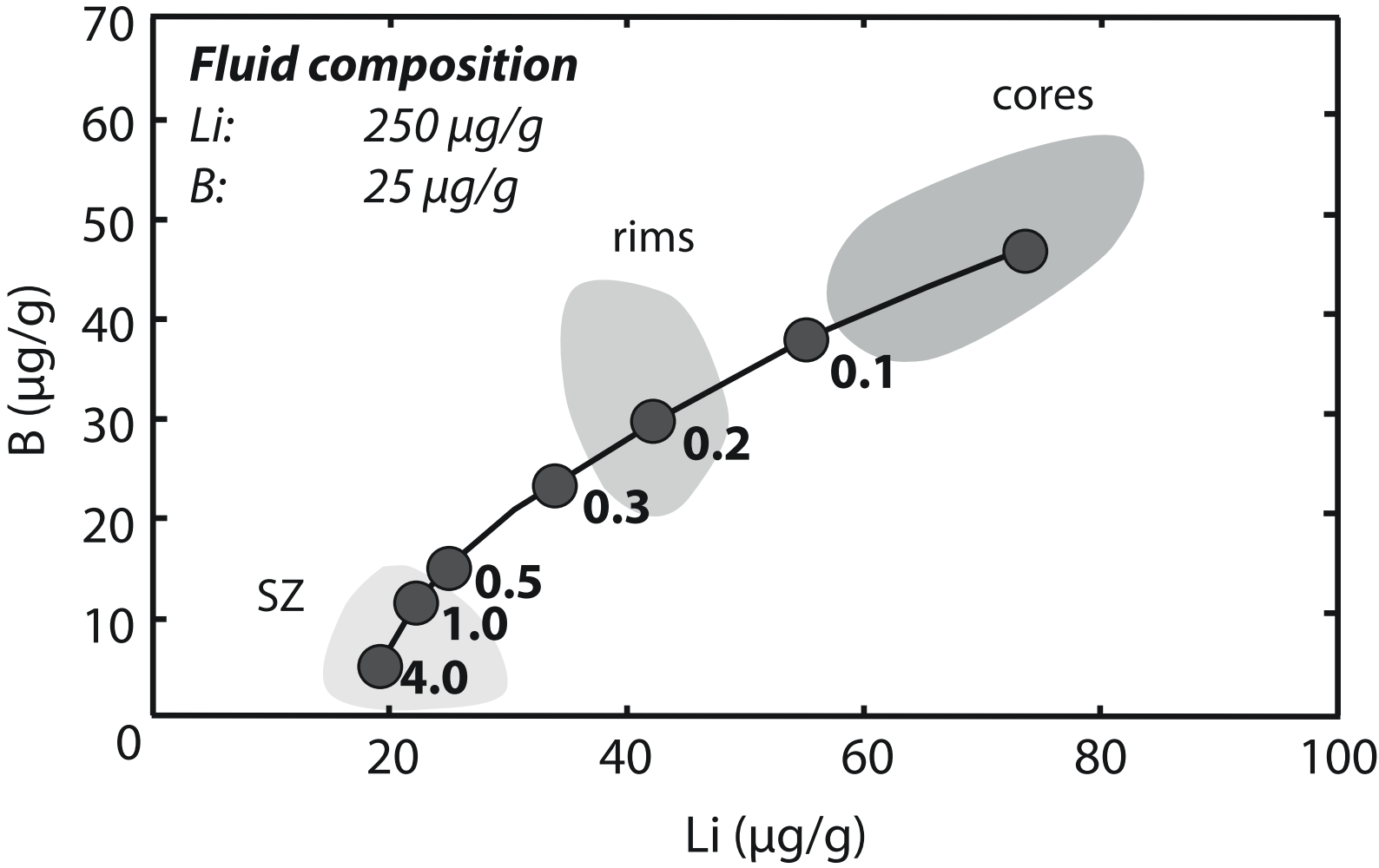

Fig. 7

Figure 8
Click here to download Figure: Fig_08.eps

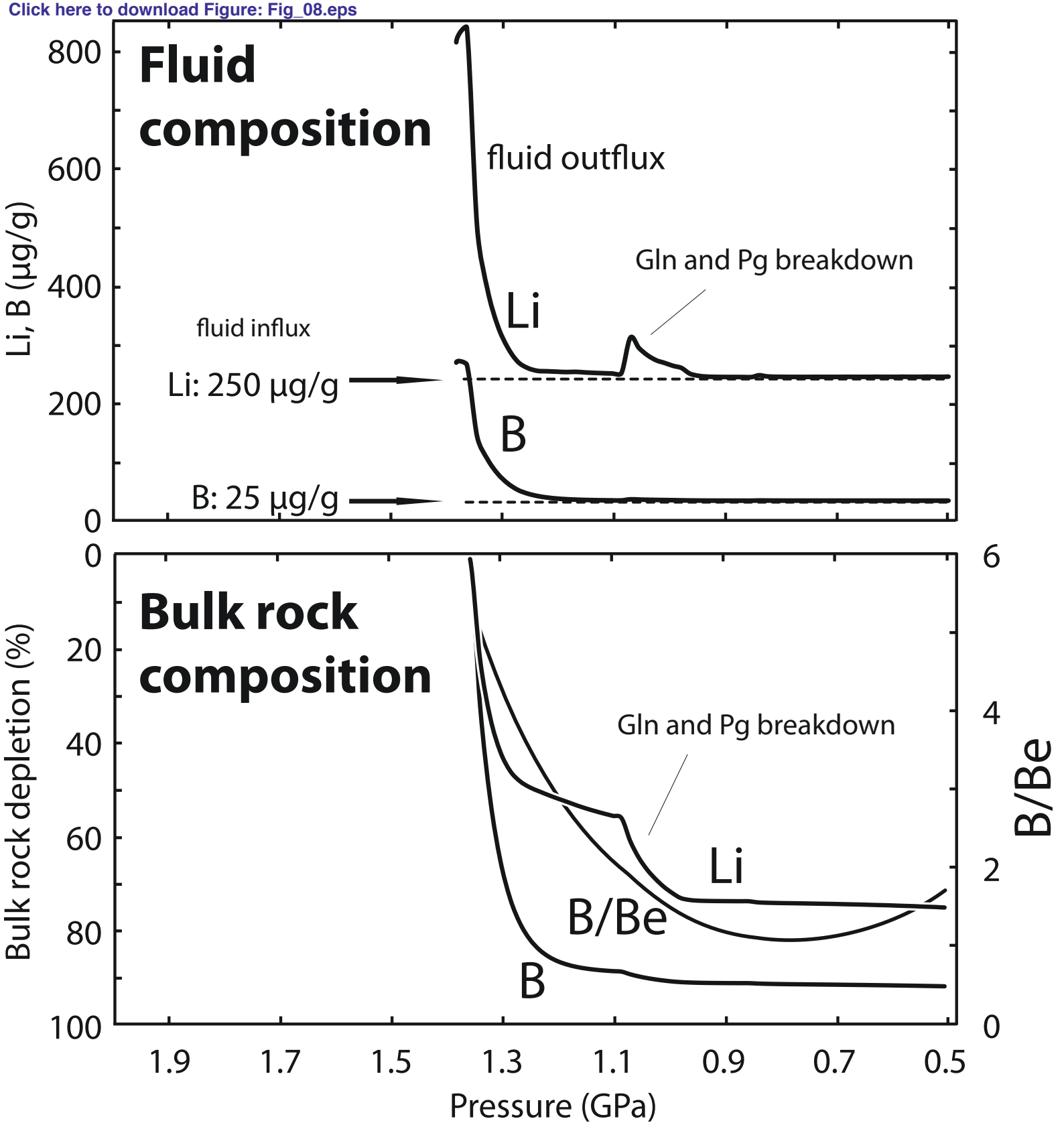

Fig. 8

Combined thermodynamic - geochemical modeling in metamorphic geology: Boron as tracer of fluid-rock interaction

Matthias Konrad-Schmolke* **and Ralf Halama**

Institute of Earth and Environmental Science, University of Potsdam, Karl-Liebknecht-Str. 24-25, 14476 Potsdam, Germany

* Corresponding author contact information:

Matthias Konrad-Schmolke

University of Potsdam

Institute of Earth and Environmental Science

Karl-Liebknecht-Str. 24-25

14476 Potsdam

E-mail: mkonrad@geo.uni-potsdam.de

Tel: +49-331-977-5854

Fax: +49-331-977-5700

ABSTRACT

Quantitative geochemical modeling is today applied in a variety of geological environments from the petrogenesis of igneous rocks to radioactive waste disposal. In addition, the development of thermodynamic databases and computer programs to calculate equilibrium phase diagrams have greatly advanced our ability to model geodynamic processes. Combined with experimental data on elemental partitioning and isotopic fractionation, thermodynamic forward modeling unfolds enormous capacities that are far from exhausted.

In metamorphic petrology the combination of thermodynamic and trace element forward modeling can be used to study and to quantify processes at spatial scales from µm to km. The thermodynamic forward models utilize Gibbs energy minimization to quantify mineralogical changes along a reaction path of a chemically open fluid/rock system. These results are combined with mass balanced trace element calculations to determine the trace element distribution between rock and melt/fluid during the metamorphic evolution. Thus, effects of mineral reactions, fluid-rock interaction and element transport in metamorphic rocks on the trace element and isotopic composition of minerals, rocks and percolating fluids or melts can be predicted.

Here we illustrate the capacities of combined thermodynamic-geochemical modeling based on two examples relevant to mass transfer during metamorphism. The first example focuses on fluid-rock interaction in and around a blueschist-facies shear zone in felsic gneisses, where fluid-induced mineral reactions and their effects on boron (B) concentrations and isotopic compositions in white mica are modeled. In the second example, fluid release from a subducted slab, the associated transport of B as well as variations in B concentrations and isotopic compositions in liberated fluids and residual rocks are modeled. We compare the modeled results of both examples to geochemical data of natural minerals and rocks and demonstrate that the combination of thermodynamic and geochemical models enables quantification of metamorphic processes and insights into element cycling that would have been unattainable if only one model approach was chosen.

1. Introduction

In geosciences, field-based observations are fundamental for our interpretations of geological processes. Quantitative models, which should be based on these observations, are essential to predict the evolution of geological systems and the outcome of geological processes (Albarède, 1995). As many disciplines in geosciences are faced with the fact that their study target, such as processes in the deep Earth, is either completely inaccessible, or that spatial or temporal scales at which the processes of interest operate do not allow direct observation, numerical and analogue models have become an indispensable tool to study, quantify and predict processes in Earth and environmental sciences. The development of high resolution - high precision analytical techniques to determine chemical and isotopic compositions of rocks and minerals, an increasing number of experimental data and advances in computational resources enhances our ability to simulate Earth processes and to test the results of these models against field-based observations. As demonstrated by Goldschmidt (1954), physicochemical principles determine systematic compositional changes in rocks and minerals and are hence the key to understand geological processes. The combination of thermodynamic and geochemical forward modeling (e.g., Hebert et al., 2009; Kimura et al., 2009, 2010; Konrad-Schmolke et al., 2008b; Nagel et al., 2012) allows a more precise quantification of key geochemical parameters leading to an improved understanding of geodynamic mechanisms and enables to study and predict rates and kinematics of solid/fluid reactions.

1.1. Thermodynamic equilibrium forward modeling in geosciences

Predicting phase and chemical equilibria is extremely important in many industrial applications, such as gas distillation, cement production and the development of functional materials. Therefore, methods of calculation of phase diagrams (CALPHAD) have been successfully developed and constantly improved. Thermodynamic modeling is nowadays more frequently applied to geoscientific problems, although its application is far more complex than most approaches in material sciences. Challenges in geosciences arise from the fact that most geoscientific questions involve thermodynamic treatment of complex solid solution phases in multiphase systems, interaction of liquid and solid phases and consideration of open system behavior. The application of thermodynamic calculations to geoscientific problems became viable with the compilation of extensive datasets for thermodynamic standard state properties (e.g. Helgeson, 1978; Robie and Hemingway, 1995; Holland and Powell, 1998; Berman, 1988; Gottschalk, 1997), reliable equations of state for

geologically relevant phases and conditions (e.g., Kerrick and Jacobs, 1981; Berman, 1988, Stixrude and Lithgow-Bertelloni, 2005; Holland and Powell, 2011) and solid solution formulations for phases of geoscientific interest (e.g., Margules, 1895; van Laar, 1910; Holland and Blundy, 1984; Berman, 1990; Holland and Powell, 2003). Regarding the interpretation of thermodynamic calculations it is noteworthy that although many of the data incorporated in the available databases are based on experiments or have been numerically determined and are internally consistent, raw experimental data on standard state thermodynamic phase properties are still sparse and incomplete. The limited amount of experimental data together with an inappropriate use of thermodynamic variables (e.g., μ_{H2O} (chemical potential of water) vs. n_{H2O} (amount of water)) can result in significant misinterpretations of modeled thermodynamic equilibria in geosciences (Essene 1989, Powell et al., 2005). Therefore, it is of utmost importance that the formulation of the problem to be solved using thermodynamic modeling complies with limitations induced by the uncertainties implicit in the thermodynamic data and that the thermodynamic variables used to extract information from such models are carefully chosen.

In general, two different thermodynamic calculation approaches can be used to determine thermodynamic equilibria ($\Delta G_R = 0$) among fluid and solid phase assemblages:

1) Solving the equilibrium constant (K)

$$0 = \Delta\mu_0 + RT\ln K$$

where R = gas constant (in J K^{-1} mol^{-1}), T = temperature (in K) and $\Delta\mu_0 = \sum_{i=1}^{m} \upsilon_i \mu_i^0$ = free energy change for the reaction for the species in the standard state with μ_i^0 = standard state molar chemical potential of species i and υ_i = stoichiometric coefficient of species i in the reaction. The equilibrium constant is defined as

$$K = \prod_{i=1}^{m} \left(a_i^{\upsilon_i}\right)$$

where a_i = activity of species i.

2) Global Gibbs energy minimization

$$\text{minimize } G = \sum_{i=1}^{m} n_i \mu_i$$

where n_i = molar amount of component i and μ_i = molar chemical potential of the i^{th} component.

Both approaches require knowledge about the Gibbs free energy of pure phases and a mathematical formulation of the relation between composition and activity/chemical potential in solution phases. Consequently, they both rely on thermodynamic data sets, which contain the standard state thermodynamic parameters and equations of state (EOS) for minerals, fluids and gases together with solution model formulations. The approach of solving the equilibrium constant furthermore requires that the phases among which the thermodynamic equilibria are calculated are pre-defined. This approach is widely utilized in aquatic geochemistry because the equilibrium constants of many aqueous reactions can be readily obtained from experiments (see Oelkers et al., 2009, and references therein). Several commercial and open source computer programs, such as PHREEQC (Parkhurst and Appelo, 1999), SUPCRT92 (Johnson et al., 1992) and THERMOCALC (Powell and Holland, 1988), are available for this purpose.

In metamorphic petrology, element fractionation processes, e.g. fractional crystallization (e.g., Spear 1988; Marmo et al., 2002; Konrad-Schmolke et al., 2006; 2008a), water liberation (e.g., Hacker, 2008; Dragovic et al., 2012) and reactive fluid flow (e.g., Ferry and Gerdes 1998; Beinlich et al., 2010) require thermodynamic modeling of chemically open systems (e.g., Korzhinskii, 1965). In such open systems, coexisting phases cannot be predicted a priori – a prerequisite of the equilibrium constant approach – because they are a function of the pressure (P), temperature (T) and chemical (X) evolution of the rock. Therefore, the approach of global Gibbs energy minimization is preferable as it allows the calculation of thermodynamically stable phase assemblages among all phases available in the database. The mathematical treatment of this approach involves (1) finding the phase assemblage with the lowest Gibbs energy among a large number of solid solution phases (so called global Gibbs energy minimum) and (2) finding the tangent plane that touches the G-X curves of all stable solid solution phases, which is prerequisite for finding the thermodynamically stable compositions of solution phases. For both aspects, different mathematical approaches are published (see Koukarri and Pajarre (2011) for a detailed review) and are implemented into a number of commercial and open source software packages, including MELTS (Ghiorso and Sack, 1995; Asimow and Ghiorso, 1998), pMELTS (Ghiorso et al., 2002) PERPLE_X (Connolly, 2005), THERIAK/DOMINO (de Capitani and Brown, 1987) and GEM-Selektor (Kulik et al., 2004; 2013).

Several pioneering works in the 1980s (Spear, 1988; Spear and Menard, 1989; Spear and Selverstone, 1983; Connolly and Kerrick, 1987; de Capitani and Brown, 1987) established the use of Gibbs energy minimization in petrologic modeling. These studies successfully demonstrated modeling of different rock-forming processes utilizing Gibbs energy minimization and yielded new insight into metamorphism. In more recent publications, Gibbs energy minimization was used in a number of different contexts including precise correlations of the pressure-temperature evolution of metamorphic rocks with age determinations (e.g., Pollington and Baxter 2010), fluid-rock and melt-rock interaction (Nagel et al., 2012; Konrad-Schmolke et al., 2011a), deformation (Pearce and Wheeler 2010), fluid expulsion during metamorphic reactions in subduction zones (Dragovic et al., 2012; Connolly, 2005; Kerrick and Connolly, 2001; Gorman et al., 2008), element transport properties of metamorphic rocks (Skora et al., 2006; Konrad-Schmolke et al., 2008b), the prediction of compositional trends in arc melts (Hebert et al. 2009; Nagel et al., 2012) as well as quantification of reactive fluid flow during metamorphism (Beinlich et al., 2010).

1.2. Geochemical trace element modeling

Trace elements (elements that are present at concentrations of less than 0.1 wt.%) commonly substitute for major elements in rock-forming minerals. They have a negligible influence on the outcome of a particular process, but instead are passive recorders of the processes that the system has experienced (e.g., Blundy and Wood, 2003). The distinct geochemical behavior of trace elements, which can be described by mathematical models, makes them particularly useful tracers. Depending on the process, trace elements behave in different, but predictable ways, which allows us to determine which processes have operated in a certain situation or setting.

The low concentrations of trace elements cause them to be sufficiently diluted to follow simple relationships between composition and activity. For a wide range of trace element concentrations, Henry's Law applies, stating that the activity of a trace element is directly proportional to its composition:

$$a_i^A = h_i^A X_i^A,$$

where a_i^A is the activity of the trace element in phase A, h_i^A is Henry's Law constant (a proportionality constant or activity coefficient), and X_i^A is the composition of phase A. Commonly, the equilibrium distribution of trace elements between two phases is described by a distribution coefficient (or partition coefficient) (see White, 2013, for details). In

geochemical applications, the Nernst partition coefficient (D) is used, which defines D as the ratio of the concentrations (c) of an element i between two phases A and B:

$$D_i^{A/B} = \frac{c_i^A}{c_i^B}.$$

Although D values are known to depend on temperature, pressure, and the compositions of the phases involved, P and T independent distribution coefficients are commonly used in magmatic and metamorphic petrology. This simplification is partly due to the limited pressure dependence of many partition coefficients under lithospheric conditions (Taura et al. 1998) and partly due to the lack of experimental data.

Quantitative models using trace elements were first applied in studies about the petrogenesis of igneous rocks. Gast (1968) and Shaw (1970) developed models for partial melting and fractional crystallization, in which they used concentrations of trace elements in liquid and solid phases in relation to the degree of partial melting of a rock and the degree of fractional crystallization, respectively. Later, assimilation of country rocks, combined assimilation – fractional crystallization processes, magma recharge, source rock heterogeneities and melt-rock reactions were all investigated using trace elements (O'Hara, 1977; De Paolo, 1981; Kelemen et al., 1992; McKenzie and O'Nions, 1991; Weaver, 1991). In recent years, trace element models are combined with thermodynamic constraints to simulate the evolution of magmatic systems that simultaneously undergo a combination of fractional crystallization, recharge and assimilation processes (EC-χAFC; Bohrson and Spera, 2001, 2007).

Trace elements are also important petrogenetic tracers for the genesis of metamorphic rocks. Whole rock trace element concentrations are frequently used for the determination of protolith compositions and pre-metamorphic alteration processes (Pearce 2008; Altenberger et al., 2008; Bebout, 2007; Becker et al., 2000; Halama et al., 2013; John et al., 2010; van der Straaten et al., 2012) and the quantification of fluid infiltration and element transport (Nabelek 1987; Ague, 2003, 2011; John et al., 2004; Beinlich et al., 2010). Many experimental studies have focused on the partitioning of trace elements between solid and liquid phases during subduction (Kessel et al., 2005; Ayers and Eggler, 1995; Brenan et al., 1995), and these data were applied in numerous investigations about fluid-rock interaction during metamorphism (Bau, 1991; Brunsmann et al., 2001; Breeding et al., 2004; Beinlich et al., 2010). In metamorphic rocks, several phases of metamorphism may be recorded, and partial overprinting during metasomatism and/or retrogression may cause additional

complexities. Therefore, *in situ* measurements that help to trace specific reactions and discern different episodes of equilibration are often crucial.

Significant advances in modeling were achieved by the combination of thermodynamically constrained equilibrium assemblage calculations with trace element fractionation models between fluid/melt and residual phases. With this approach, specific features in the trace element geochemistry of subduction-related rocks were successfully reproduced. Nagel et al. (2012) combined the calculation of equilibrium assemblages in partially molten, mafic rocks with subsequent modeling of trace element fractionation between melt and residual phases to explain the formation of the Earth's oldest continental crust by melting arc tholeiites within a tectonically thickened mafic island-arc crust (Fig. 1a). Hebert et al. (2009) investigated slab fluid source lithologies and melt transport regimes in subduction zones using the GyPSM-S (Geodynamic and Petrological Synthesis Model for Subduction) modeling scheme, which couples a petrological with a thermal model to describe processes occurring in the supra-subduction zone (SSZ) mantle wedge, supplemented with models for trace element partitioning in the fluid phase and melt transport regimes. They interpreted geochemical characteristics of across-arc and along-arc lavas in relation to distinct shallow and deep slab fluid sources and found that melt migration through the mantle wedge preserves spatial distinctions among melts initiated in different areas of the wedge (Hebert et al., 2009). Focusing on the distribution of fluids in the mantle adjacent to a subducting slab, Hebert and Montési (2013) modeled fluid transport and mantle hydration related to deep dehydration reactions in subducted serpentinized mantle and effects on hydration of the transition zone. Kimura et al. (2009) developed the Arc Basalt Simulator (ABS) modeling scheme to predict the composition of primitive arc magmas (Fig. 1b). This simulation scheme initially included slab dehydration and fluid-fluxed mantle melting and was subsequently modified to incorporate slab melting and melt-fluxed mantle melting (Kimura et al., 2010) and, most recently, separate P-T paths for distinct slab layers, yielding more liquid-solid interaction within the 1-D vertical column (Kimura et al., 2014). Application of the ABS models produced successful predictions of incompatible element and Sr-Nd-Pb isotopic compositions of distinct primitive magmas from the volcanic front and the rear-arc of the Izu arc (Kimura et al., 2010).

1.3. Boron and boron stable isotopes as tracers of fluid-rock interaction

One of the key aspects in metamorphic petrology is to trace and quantify liquid phases percolating through solid rocks. Liquid phases, such as aqueous fluids or melts, are the major

transport agents in the solid Earth and thus quantification of the fluxes of liquid phases enables tracing of the mass transfer in the solid Earth. In contrast to a melt phase, which might crystallize *in situ* and can then be directly investigated, fluids can only be passively trapped as inclusions in solid phases and in most cases have left the rock at the time of investigation. Thus, indirect geochemical evidence for the presence of a fluid interacting with the host rock must be considered. Ideally, such indirect geochemical proxies for fluid-rock interaction are among the fluid mobile elements (FME), have quick equilibration times and small equilibration volumes. Subsequent to fluid-rock interaction, the geochemical proxy must be stable and not prone to later, e.g. diffusional, re-equilibration. Furthermore, the proxy must be present in major phases in measurable quantities. Elements often used for this purpose are Li, B, N, Cl, As, Rb, Sb, Cs, Ba as well as Pb and U (see Ryan and Chauvel 2013).

Boron is particularly useful for the investigation of fluid-rock interaction processes and dehydration because it is present in measurable quantities in several major mineral phases (white mica, tourmaline, amphibole, serpentine) as well as in hydrous fluids and its concentration is typically low enough to make it sensitive to fast equilibration at small fluid amounts. In most rock-forming minerals, including white mica, B substitutes for silica and occupies the tetrahedral position (Sanchez-Valle et al., 2005). If B diffuses similarly slow as Si, B concentrations are difficult to exchange after crystallization (Hervig et al., 2002), a prerequisite to preserve relevant information over geologic time scales. Furthermore, information from boron as fluid-mobile trace element can be combined with the isotopic information from B stable isotopes (e.g., Simon et al., 2006).

The observation of variations in the atomic weight of boron in minerals, made by Briscoe and Robinson (1925), was crucial for the recognition that physiochemical processes can cause isotopic fractionation of light elements in natural substances. It was therefore proposed that geologically relevant processes, including melting, crystallization, solution and volatilization, would cause isotopic variations in nature (Briscoe and Robinson, 1925), leading the way for the widespread application of stable isotopes as tracers (Sharp, 2007). The value of the various stable isotope systems is based on the fact that distinct stable isotope signatures occur in different reservoirs, so that they can be used to trace the origin of rocks and fluids.

Boron has two stable isotopes, ^{10}B and ^{11}B, with relative abundances of 19.8% and 80.2%, respectively. The large B isotopic variation in natural substances of almost 100‰ (Fig. 2; Deyhle and Kopf, 2005) is dominantly due to differences in coordination between tetrahedral

$B(OH)_4^-$ and trigonal $B(OH)_3$. Moreover, the B isotopic composition is influenced by temperature-dependent equilibrium fractionation between solid and fluid phases (Peacock and Hervig 1999; Hervig et al., 2002; Wunder et al., 2005) and it is also sensitive to changes in the pH value (Deyhle and Kopf, 2005). Boron preferentially partitions into the fluid phase (Brenan et al., 1998) with a concomitant enrichment of the heavy isotope ^{11}B relative to ^{10}B. The most striking example of coupled trends of elemental and isotopic variations occurs in arc lavas, where systematic across-arc trends of decreasing and isotopically lighter B with increasing slab depths (Fig. 2; Ishikawa and Nakamura, 1994; Ishikawa et al., 2001; Moriguti et al., 2004) are attributed to contributions from a slab-derived agent that successively reflects increasing degrees of slab dehydration and decreasing slab-to-arc element transfer (Bebout et al., 1999; Rosner et al., 2003; Marschall et al., 2007). In addition, several studies have emphasized the role of serpentinized mantle rocks, both in the supra-subduction zone wedge and in the subducting slab mantle, for boron cycling in subduction zones (Tonarini et al., 2007, 2011; Benton et al., 2001; Hattori and Guillot, 2003; Savov et al., 2007). Evidence for the sensitivity of the B system for fluid-rock interaction is provided by zoning patterns in various metamorphic minerals (white mica, amphibole, tourmaline), which retain information about the compositional evolution of metasomatic fluids through the metamorphic history (Bebout and Nakamura, 2003; Marschall et al., 2009; Konrad-Schmolke et al., 2011b; Halama et al., 2014).

In the following sections we will show two examples of combined thermodynamic-geochemical models that focus on the mass transfer in subduction zones at different spatial scales (Fig. 3). The first model simulates fluid-rock interaction at grain-scale and investigates the effect of fluid percolation on B concentrations and B isotopic compositions in partially overprinted phengites. In the second example, fluid release from a subducted slab, the associated transport of B and variations in B concentrations and isotopic compositions in liberated fluids and residual rocks are modeled. We compare the results of both examples with observations in natural minerals and rocks in order to quantify fluid fluxes and element cycling.

2. Example 1: Boron and boron isotopes in white mica during high-pressure fluid-rock interaction

2.1. Observations in natural samples

Fluid-induced metasomatic overprinting is a common feature in many metamorphic terranes

303 (e.g., Sorensen and Grossman, 1989; John et al., 2004; Bebout, 2007; Beinlich et al., 2010;
304 Halama et al., 2011). Partial re-equilibration of metamorphic rocks, immensely important to
305 trace the rocks' metamorphic evolution, results in whole rock geochemical and isotopic
306 variations and in compositional changes in individual metamorphic minerals (Spear and
307 Selverstone 1983; Thompson and England 1984; Yardley et al., 1991; Kohn 2003; Habler et
308 al., 2007; Konrad-Schmolke et al., 2011a,b; Pearce and Wheeler, 2010; Goncalves et al.,
309 2012). Since white mica is ubiquitous in metamorphic rocks of both igneous and sedimentary
310 origin and stable over a wide P-T range, especially in high pressure rocks (Domanik and
311 Holloway, 1996; Hermann and Spandler, 2008), it is well suited to investigate fluid-rock
312 interaction processes during metamorphism. Chemical variations in white mica depend on P-
313 T conditions, bulk rock composition and syn-kinematic mass transfer and fluid conditions
314 (Velde, 1965; Massonne and Schreyer, 1987; Guidotti et al., 1994; Goncalves et al., 2012).
315 Diffusion-controlled exchange reactions in white mica have relatively high closure
316 temperatures below which major element exchange is effectively impossible, so that
317 preserved chemical variations predominantly reflect deformation and recrystallization
318 controlled equilibria (Dempster, 1992). Potassic white mica is also amenable to age dating
319 using both the $^{40}Ar/^{39}Ar$ and Rb-Sr methods and hence provides a means to directly link age
320 information to the metamorphic evolution of a rock (Di Vincenzo et al., 2001; Glodny et al.,
321 2002; Bröcker et al., 2013; Halama et al., 2014; Warren et al., 2011, 2012). White mica is also
322 an important carrier of fluid-mobile trace elements including B, lithium (Li) and the large ion
323 lithophile elements (LILE; K, Cs, Rb, Ba, Sr; Bebout et al., 1999, 2007, 2013; Konrad-
324 Schmolke et al. 2011b; Hermann and Rubatto, 2009). Boron is concentrated in white mica
325 (phengite and paragonite), compared to all other major phases, except tourmaline (Domanik et
326 al., 1993; Marschall et al., 2006). Hence, white mica dominates the B budget in most
327 tourmaline-free rocks and its B isotopic composition can be considered as representative of
328 the bulk rock (Peacock and Hervig, 1999). During subduction, the presence of white mica
329 critically determines retention and release of B as well as the B isotopic composition of
330 released fluids (Marschall et al., 2007). Therefore, B elemental and isotopic changes in white
331 mica are ideally suited to trace compositional changes due to fluid-mediated metasomatism.
332 However, B isotope data in white mica are still relatively rare (Peacock and Hervig, 1999;
333 Pabst et al., 2012; Angiboust et al., 2014) as many B isotope studies concentrated on
334 tourmaline (Bebout and Nakamura, 2003; Trumbull et al., 2008, 2009; Marschall et al., 2009).

335 In this example, we present a detailed study of high-pressure metamorphosed felsic rocks of
336 the Western Alpine Sesia Zone (SZ) that were exhumed from mantle depths on top of a

dehydrating subducted oceanic plate where they directly interacted with percolating fluids at blueschist-facies conditions. A sampling profile across a deformation gradient around a major blueschist-facies shear zone showed several remarkable compositional features in texturally different phengite grains and domains (Konrad-Schmolke et al., 2011a,b, Halama et al., 2014).

2.1.1. Phengite chemistry in the Sesia Zone samples

Fluid infiltration in weakly deformed rocks modified primary phengite (3.3 - 3.5 Si p.f.u., X_{Mg} = 0.6 - 0.7) compositionally along fluid pathways (Fig. 4a and b). Fluid-induced retrograde major element equilibration of phengite involves a major decrease in X_{Mg} and is visible in high contrast BSE images, which show darker-colored cores surrounded by brighter zones that are concentrated at the tips and grain boundaries, around inclusions and in deformed parts (Fig. 4a). The BSE images show one, in some places two different replacement zones as well as areas with diffuse transitions, but oscillatory zoning is missing.

Phengite cores in weakly deformed samples have variable $\delta^{11}B$ values (-18 to -10‰) that were interpreted to reflect the lack of km scale B homogenization during HP crystallization (Fig. 4c). Corresponding overprinted phengite rims have lower B abundances but overlapping $\delta^{11}B$ values (-15 to -9‰), thought to reflect predominantly internal redistribution of B and internal buffering of the B isotopic compositions during recrystallization of the rims (Halama et al., 2014). In contrast, fine-grained mylonitic phengites are compositionally homogeneous in their major and trace element concentrations. X_{Mg} and Si p.f.u. in the syn-kinematic phengites correspond to the values observed in the overprinted phengite rims of the weakly deformed samples. Boron is almost completely removed in the mylonitic phengites (1-10 µg/g). The boron isotopic compositions in the mylonitic phengites are significantly heavier than in those from the weakly deformed samples, indicating an external control by a high-$\delta^{11}B$ fluid ($\delta^{11}B$ = +7±4‰). The compositional trend leads from relict cores via overprinted rims towards the mylonitic phengites (Fig. 4c). Based on estimates of the time-integrated fluid fluxes, which are more than one order of magnitude higher in the mylonites (Konrad-Schmolke et al. 2011b), the B removal was related to fluid-induced phengite recrystallization.

The sample profile, with presumably unmodified peak P-T phengite cores in weakly deformed samples, a partial metasomatic overprint represented by the phengite rims, and a strong deformation coupled to intense fluid-rock interaction in the mylonitic phengite provide the conceptual basis for fluid-rock interaction modeling along a distnct P-T path (Fig. 5). In

particular, we focus on the apparent paradox of lower B contents at similar $\delta^{11}B$ values in the overprinted areas. Moreover, we want to evaluate to which degree the accurate determination of the two parameters [B] and $\delta^{11}B$ allows a quantification of fluid amounts that have interacted with the rock.

2.2. Thermodynamic-geochemical modeling of B concentrations and isotopic compositions in phengite

The boundary conditions for the thermodynamic model that has been performed with the THERIAK algorithm (de Capitani and Brown 1987) in the NCKFMASH chemical system comprise the following assumptions: Along the prograde P-T path, the samples underwent fractional garnet crystallization, indicated by large, compositionally zoned garnet porphyroblasts in the natural samples, and water fractionation due to devolatilization reactions (Konrad-Schmolke et al., 2011a). Thus, calculation of the effective bulk rock composition (EBC) at the start of the retrograde P-T trajectory must consider a prograde segment accounting for the element fractionation processes. Along the retrograde P-T path, from 2.0 GPa and 575°C to 1.1 GPa and 500°C (Fig. 5), a fluid influx event occurs at about 1.35 GPa and 550°C, which causes water re-saturation in the affected areas of our samples.

The mineralogical evolution of the samples in the P-T-X-space can be displayed with two compositionally constrained P-T equilibrium assemblage diagrams (P-T pseudosections) (Fig. 5a) and a P-X diagram (Fig. 5b). Fractional garnet crystallization and water fractionation along the prograde P-T path continuously modified the EBC. At peak conditions (left diagrams in Fig. 5a), the rock is water-saturated and becomes water under-saturated along the first segment of the retrograde P-T trajectory. The diagram calculated for the EBC at peak conditions shows that there is no significant change in the phase assemblage (pg+gln+cpx+phng+qtz) along the retrogade path until fluid influx at 1.35 GPa and 550°C. The fluid influx causes water re-saturation of the EBC and changing phase relations (right diagrams in Fig. 5a) that are then applicable for the second part of the retrograde P-T trajectory. The P-H_2O diagram (Fig. 5b) highlights the compositional plane in the P-T-X space together with the retrograde P-X trajectory of our samples (red arrow). Below the water saturation line (bold blue) X_{Mg} in phengite strongly depends on the H_2O content indicated by the sub-vertical X_{Mg} isopleths. The compositional correlation between H_2O content and X_{Mg} in phengite is reflected in the fluid-induced overprinting zones in the mica grains of the natural samples (Fig. 4a). The modeled phase relations and phengite compositions along the retrograde P-T trajectory demonstrate that the fluid influx causes drastic changes in both

modal mineralogy and phase chemistry (Fig. 6).

Phengite amount decreases by about 10 wt.%, whereas the abundances of glaucophane and paragonite increase. Omphacite is no longer stable and epidote joins the stable phase assemblage. In phengite, the model indicates a slight decrease in Si_T due to the fluid influx, unrelated to the continuous pressure decrease (Fig. 6a). The negative correlation between decreasing celadonite (X_{Cel}) and increasing ferroceladonite (X_{Fcel}) components reflects the sudden increase in X_{Fe} in the overprinted zones. These modal and chemical phase changes reflect the blueschist-facies overprint as observed in the shear zone (Konrad-Schmolke et al., 2011a).

Boron concentrations [B] and isotopic compositions ($\delta^{11}B$) of phengite (phng) are modeled along the retrograde P-T path. Boron distribution among fluid and stable mineral phases is calculated using partitioning data of Brenan et al. (1998) and Marschall et al. (2007). Specifically, the $D^{fluid\text{-}phng}$ value was derived from $D^{cpx\text{-}fluid}$ (Brenan et al., 1998) and $D^{cpx\text{-}phng}$ (Marschall et al., 2007). Experimentally determined B isotope fractionation data were taken from Wunder et al. (2005). Initial values for [B] and $\delta^{11}B$ in the host rock are chosen to reflect the composition of the phengite cores, whereas [B] and $\delta^{11}B$ in the infiltrating fluid (27 µg/g and +7‰) were calculated assuming chemical equilibrium with the mylonites in the shear zone. A detailed modeling description together with a software package including the Gibbs energy minimization algorithm THERIAK (de Capitani and Brown 1987) together with a MatLab® script for B and $\delta^{11}B$ calculations are given in the electronic supplementary material.

2.3. Geochemical model results

The modeling of [B] and $\delta^{11}B$ in phengite relates the amount of water that percolated through the rock to the structural and textural characteristics of phengite in the natural samples (Fig. 7). High-pressure conditions at P > 1.35 GPa – before the fluid influx – are represented by relict, unmodified phengite cores. Predominantly internal B redistribution and low amounts of water influx are mirrored in the overprinted rims, whereas high amounts of water reflect conditions in the shear zone. The model shows that with increasing water flux, [B] in phengite decreases (Fig. 7a) due to the preferential partitioning of B into the fluid. The redistribution of B is quite efficient even at low amounts of water influx, so that a constant [B] value is reached after only 0.5 wt.% accumulated water influx. The changes in $\delta^{11}B$, caused by the preferential partitioning of ^{11}B into the fluid, are more sluggish (Fig. 7b). At very low water

fluxes the isotopic composition of white mica is even driven towards slightly lower $\delta^{11}B$ values, a trend that is reversed after ~0.1 wt% water influx. About 1 wt.% H_2O is required before a constant $\delta^{11}B$ value is reached in the model.

When distinct amounts of water influx (0, 0.09 and 1.5 wt.%) for the given P-T path are compared, the rapid chemical and isotopic changes of the predicted B equilibrium concentrations and isotope compositions become even more apparent (Fig. 7c,d). If no water is added, representing a completely internal redistribution of boron, the model predicts a small increase of [B] in phengite associated with unchanged $\delta^{11}B$ compared to the pre-influx values. Low water influx (0.09 wt.%) causes a 20% decrease in [B], consistent with B concentrations measured in the overprinted rims. The modeled $\delta^{11}B$ in phengite resulting from fluid-rock interaction at these low fluid fluxes is much less affected and changes by less than 1‰. The modeled B isotopic variation is within analytical uncertainty and natural inhomogeneity between different samples. Indeed, most samples do not show B isotopic differences between relict cores and rims, albeit a tendency towards higher $\delta^{11}B$ values is recognizable for some. High fluid influx (1.5 wt.% accumulated water flux) results in an 80% decrease in [B], whereas $\delta^{11}B$ increases toward the equilibrium value determined by the external fluid. Again, both features agree well with the field-based observations in the SZ.

The interplay of the two parameters [B] and $\delta^{11}B$ during progressive fluid influx allows a quantification of the amounts of fluid absorbed by the rocks. The evolution of [B] and $\delta^{11}B$ in the percolating fluid are decoupled at low amounts of H_2O. Whereas removal of B from the interacting host rock leads to a continuous decrease in [B] immediately after infiltration of the first increment of fluid, $\delta^{11}B$ initially slightly decreases. With increasing fluid amount, the trend in $\delta^{11}B$ reverses. In our example, the amount of water in the weakly deformed samples is limited to a maximum of ~0.25 wt.%. In the mylonites, at least 0.75 wt.% water must have been percolating through the rock to explain the changes in both [B] and $\delta^{11}B$. One of these parameters alone would not suffice to quantify fluid amounts.

Decreasing B concentrations in minerals and rocks are commonly attributed to dehydration reactions as evident in figures 2 and 8 whereas in the chosen example decreasing B concentrations in phengite are the result of the fluid infiltration and fluid-rock interaction leading to a B redistribution and precipitation of phengite material with lower B concentration. In contrast to dehydration that is associated with decreasing $\delta^{11}B$ values, fluid-rock interaction in the investigated samples causes an increase in $\delta^{11}B$ in the affected phengite grains, which demonstrates that only the combination of the two parameters [B] and $\delta^{11}B$

allows distinction between the two contrasting processes.

It is notable that in our samples overprinted phengite areas are visible in BSE images due to their significantly higher Fe concentrations and B measurements can be correlated with these zones. To evaluate whether the B compositional and isotopic zoning in the investigated phengites fully correlates with the major element zonation, qualitative mappings of single grains are necessary. Such mappings of trace element compositional variations in metamorphic minerals are crucial to increase our knowledge about the fluid-rock interaction and associated processes in metamorphic phases (e.g., Papst et al., 2011; Valle et al., 2011). At present, relatively large analytical uncertainties for B isotope compositions measured in natural phengite (2s uncertainty = 1-5 ‰) make it difficult to detect intra-grain variations in samples with low B concentrations and small grain sizes (Aggarwal and Palmer, 1995; Jacob, 2006; Rosner et al., 2008), but in contrast to B-rich phases, such as tourmaline, white mica has the advantage that it is a rock-forming phase in many metamorphic rocks and its compositional variations can easily linked with its metamorphic evolution (e.g., Massonne and Schreyer 1987). Our example shows the capacity of B concentrations and the isotopic composition of B in phengite to record fluid influx and fluid-rock interaction in metamorphic rocks (e.g., Angiboust et al., 2014). Qualitatively, the results of this example demonstrate that the effects of fluid-rock interaction during fluid percolation on the trace element transport may be profound and need to be considered in large-scale subduction zone models, which will be delineated below.

3. Example 2: Boron release in subduction zones

3.1. Observations in natural samples

Subduction of hydrated oceanic lithosphere is the main process that allows element transfer from the Earth's surface to the deeper mantle. Devolatilization of the subducted slab leads to partitioning of elements into the upward migrating fluid and subducting solid phases. Whereas the former are recycled into the upper plate or the atmosphere, the latter are deeply subducted and assimilated into the deep mantle (Elliott et al., 2004; Peacock and Hervig, 1999; Hofmann, 1997; Hacker, 2008). Knowledge about and quantification of this element partitioning is crucial for the understanding of global scale element distribution between crust, mantle and atmosphere (e.g., Connolly, 2005; Kerrick and Connolly, 2001; Spandler and Pirard 2013). As we have no direct access to the subducting rocks, elemental and isotopic signatures in arc volcanic rocks are interpreted in terms of processes occurring in the

499 downgoing slab (Pearce and Peate, 1995), although the extent to which slab contributions
500 control geochemical characteristics of arc magmas is disputed (Elliott, 2003). However, there
501 are several examples where across-arc geochemical variations in arc lavas appear to reflect
502 changes in the subducting slab as a function of depth (Fig. 2), which in turn control slab-to-
503 arc mass transfer (Ishikawa and Nakamura, 1994; Ryan et al., 1995, 1996; Moriguti and
504 Nakamura, 1998). Geochemical reservoirs in the slab that potentially leave their imprints in
505 arc volcanic signatures include all lithological layers of the subducting lithosphere: sediments,
506 igneous oceanic crust and the hydrated slab mantle (Ryan et al., 1995; Plank and Langmuir,
507 1993; Morris et al., 1990; John et al., 2004; Herms et al., 2012). If seawater is able to infiltrate
508 the upper oceanic mantle (Ranero et al., 2003; Ranero and Sallarès, 2004; Garth and
509 Rietbrock, 2014), serpentinites formed by this process can theoretically absorb up to 13 wt%
510 of water and may therefore be effective carriers of water (Schmidt and Poli 1998; Rüpke et
511 al., 2004; Hacker, 2008) and certain fluid-mobile elements (FME) to sub-arc depths (Ulmer
512 and Trommsdorff, 1995; Scambelluri et al., 2001; Hattori and Guillot, 2003). Additionally,
513 the supra subduction zone (SSZ) wedge mantle, which is hydrated by fluids liberated from the
514 subducted slab, may also be an important reservoir of water and trace elements delivered to
515 greater depth (Tatsumi, 1986; Hyndman and Peacock, 2003; Straub and Layne, 2002; Hattori
516 and Guillot, 2003; Kawamoto et al., 2013), although both water and FME are originally
517 derived from the slab itself. If SSZ mantle is dragged down along the slab-wedge interface
518 towards sub-arc depth (Savov et al., 2005, 2007), and if temperatures remain cold enough so
519 that relevant dehydration reactions are delayed until these depths are reached (Grove et al.,
520 2009; Till et al., 2012), geochemical signals from SSZ mantle-derived fluids may be
521 incorporated into arc melt sources. A thermodynamic-geochemical model reflecting fluid
522 liberation and reactive fluid flow (Zack and John 2007) in subduction zones must incorporate
523 fluid production and fluid-rock interaction in all of the above-mentioned reservoirs.

524 Regarding the use of B as tracer for subduction zone processes, Ryan and Langmuir (1993)
525 first noted that B is a useful proxy in across-arc studies by observing systematically lower B
526 contents in arcs where volcanoes sample deeper portions of the slab. As B concentrations in
527 dry mantle rocks are extremely low (<1 μg/g), B is flushed through the SSZ mantle wedge
528 without significant modification of the B slab signal during fluid ascent (Ryan and Langmuir,
529 1993). Compared to the mantle wedge, B is concentrated in several slab lithologies, including
530 subducted sediment (Ishikawa and Nakamura, 1993), altered oceanic crust (AOC) (Spivack
531 and Edmond, 1987; Yamaoka et al., 2012) and serpentinized mantle rocks (Benton et al.,
532 2001; Boschi et al., 2008; Vils et al., 2009; Scambelluri et al. 2004). Arc lavas are generally

533 enriched in B, as shown by elevated B/Nb and B/Be ratios compared to oceanic basalts (Fig.
534 2a). The B/Nb ratio is used as tracer of B enrichment because B/Nb is considered as
535 unfractionated during partial melting based on similarity in mineral-melt partition coefficients
536 (Brenan et al., 1998). Arc lavas are also relatively enriched in ^{11}B (Fig. 2b), suggesting fluid-
537 mediated slab-to-arc B transfer via a B-rich, high-$\delta^{11}B$ slab fluid (Scambelluri and Tonarini,
538 2012). In many cases, the B isotopic compositions systematically vary with B enrichment as
539 higher B/Nb ratios are coupled to higher $\delta^{11}B$ values (Fig. 2a; Spandler and Pirard, 2013).
540 Consequently, across-arc trends with increasingly lower B concentrations and isotopically
541 lighter compositions with increasing slab-surface depths, as observed in many subduction
542 zones (Fig. 8b; Ishikawa and Nakamura, 1994; Ishikawa et al., 2001; Ishikawa and Tera,
543 1999; Rosner et al., 2003), are interpreted to directly reflect increasing degrees of slab
544 dehydration and decreasing slab-to-arc element transfer. However, several subduction zones
545 show unusually high $\delta^{11}B$ and B/Nb values or reversals in the across-arc trends of these
546 values (Moriguti et al., 2004; Ishikawa et al., 2001; Tonarini et al., 2001), but the reasons for
547 these exceptions are still debated. Among the most interesting of the deviating examples are
548 the South Sandwich Islands (SSI) arc and the Kamchatka subduction zone. In the SSI arc,
549 anomalously high $\delta^{11}B$ and B/Nb are observed throughout the entire volcanic arc and
550 interpreted to reflect dehydration of the SSZ wedge mantle (Tonarini et al., 2011). Across the
551 Kamchatka peninsula, arc volcanic rocks from three successive volcanic chains yield a
552 complex $\delta^{11}B$ and B/Nb pattern (Fig. 2; Ishikawa et al., 2001), the reason for this complexity
553 being unclear so far, but possibly related to dehydration of subducted slab mantle. Slab
554 mantle dehydration is difficult to detect in arc volcanic rocks by geochemical means because
555 ultramafic rocks are typically poor in many trace elements. Arsenic, antimony and boron are
556 among the few elements characteristic for serpentinites and geochemical trends of these
557 elements (Spandler and Pirard, 2013) as well as the isotopic composition of boron in arc lavas
558 are interpreted to reflect serpentinite dehydration (Tonarini et al., 2011). However,
559 geochemical models alone cannot discriminate between dehydration of upper- and lower-plate
560 serpentinites. If and to which degree slab mantle dehydration influences $\delta^{11}B$ and B/Nb in
561 across-arc profiles can be tested with a combined thermodynamic-geochemical model, which
562 utilizes boron and its isotopic composition to model slab fluid release and fluid rock
563 interaction in the downgoing slab and the mantle wedge.

564 *3.2. Modeling B concentrations and isotopic compositions in a subduction zone*

565 Marschall et al. (2007) modeled B concentrations in subducting rocks and released fluids

566 during subduction by combining the B distribution among the minerals present with
567 temperature-dependent fractionation of B isotopes, corroborating the proposed continuous
568 decrease in B and $\delta^{11}B$ in both residual rocks and released fluids (Fig. 8). These one-
569 dimensional models predict that white mica plays a crucial role in the B geochemical cycling.
570 The more white mica is present in the rock, the more B is retained in the slab down to subarc
571 depths and beyond, and the more positive are the $\delta^{11}B$ values of the released fluids (Marschall
572 et al., 2007). Based on this pioneering work, our models additionally incorporate a
573 sedimentary layer, a layer of oceanic mantle in the subducting slab as well as a SSZ mantle
574 wedge layer (Fig. 9a), thus expanding the model to a second dimension (cf. Connolly, 2005;
575 Rüpke et al., 2006). Moreover, interaction between the liberated water and the wall rock
576 during the ascent of the fluid phase is taken into account because fluid-rock interaction within
577 the slab, at the slab-wedge interface (Marschall et al., 2006) and in the overlying mantle
578 wedge can lead to significant modifications of both percolating fluid and the affected wall
579 rock with respect to [B] and $\delta^{11}B$. In our model, a thermal subduction zone pattern (Fig. 9a) of
580 the Kamchatka subduction zone derived from finite element thermomechanical modeling
581 (Manea and Manea, 2007) is used as pressure-temperature input for a Gibbs energy
582 minimization algorithm (PERPLE_X; Connolly 2005) that simulates the passing of a vertical
583 rock column within the subducted slab through the steady state thermal pattern. The thermal
584 pattern is modeled with a finite element grid extending from 25 km seaward of the
585 Kamchatkan trench up to 600 km landward of it. The numerical scheme solves a 2D Navier-
586 Stokes equation and a 2D steady state heat transfer equation. Shape and dip of the subducting
587 plate beneath the active arc are constrained by the earthquake hypocenter distribution (see
588 Manea and Manea 2007 for further details). Phase relations within the rock column that
589 consists of a SSZ mantle wedge layer (10 km; Primitive Upper Mantle from Workman and
590 Hart, 2005), a sediment pile (625 m; GLOSS from Plank and Langmuir, 1998), igneous
591 basaltic crust (6.4 km; N-MORB from Workman and Hart, 2005) and a variably hydrated slab
592 mantle (18.5 km; Depleted Mantle from Workman and Hart, 2005) are calculated with a
593 resolution of 250 x 250m. A more detailed description of the model and input parameters
594 together with a MatLab® script can be found in the electronic supplement. Water liberated by
595 dehydration reactions is transported vertically upward, equilibrating at every calculated
596 increment within the column, thus reflecting a high ratio of fluid/slab migration velocity. The
597 modeled phase relations at every calculated increment are used for a coefficient-based mass-
598 balanced B distribution (Brenan et al., 1998) and a temperature-dependent fluid-solid B
599 isotope fractionation (Fig. 9b; Wunder et al., 2005). The model simulates fluid release, fluid

migration, fluid-rock interaction and boron transport in a subducted slab and the overlying mantle wedge. Comparison of modeled and observed B concentrations and isotopic patterns help to constrain initial hydration of the slab and the dehydration behavior of wedge mantle and slab during subduction.

3.3. Model results

The dehydration model of the subduction zone shows that water release from the slab is controlled by thermally induced breakdown of the hydrous minerals brucite, antigorite, chlorite and lawsonite (Figs. 10 and 11). In case of a dry slab mantle dehydration occurs up to 250 km slab surface depth and is characterized by a continuous crustal signal and superimposed dehydration spikes resulting from discontinuous wedge mantle and slab crust dehydration (Fig. 11a). Breakdown of brucite and antigorite with minor contributions from chlorite and amphibole in the SSZ wedge mantle dominates water release in the fore-arc region. In the sub-arc region, water is delivered by continuous chlorite dehydration from the crust and the chlorite-out reaction in the SSZ mantle wedge that causes a characteristic dehydration peak at ~130 km slab surface depth. As predicted by the models of Marschall et al. (2007), continuous dehydration of the slab leads to a drastic decrease of the B concentrations (Fig. 11b) as well as to decreasing $\delta^{11}B$ values (Fig. 11c) in the residual rocks. However, depending on the depth within the slab crust the B concentrations in different rocks from the same layer can have significantly different values and a concentration gradient within the slab is maintained up to 200 km slab surface depth. This circumstance is the result of the interplay between the predominantly temperature-controlled dehydration pattern that is skewed relative to the surfaces of the lithological layers and the leaching effect resulting from fluid percolation within the slab. The effect of fluid-rock interaction on the subducted rocks is also clearly visible in the $\delta^{11}B$ values at different positions within the slab. Differences in the $\delta^{11}B$ values between the slab surface and in the SSZ mantle wedge subsequent to fluid-rock interaction can be as large as 10‰ in shallower regions and are about 5‰ at greater slab surface depths. These results show the need for two or three-dimensional models regarding the prediction of B concentrations and $\delta^{11}B$ values in subduction-related fluids and rocks.

Utilizing the same model setup, the effect on [B] and $\delta^{11}B$ values in the fluids released by slab mantle dehydration can be studied. In contrast to the preceding model, the slab mantle is now initially hydrated to a depth of 15 km perpendicular to the slab mantle surface. This is the maximum depth to which hydrous phases are thermodynamically stable at the beginning of the model run. The pseudosection (Fig. 10b) shows that chlorite and serpentine are the stable

633 hydrous phases in the slab mantle up to 175 km slab surface depth. Depending on the thermal
634 pattern within the slab there is an overlap of the stability fields of antigorite and phase A,
635 enabling the transfer of H_2O into the deeper mantle beyond sub-arc depths (cf. Hacker, 2008).
636 As there is no water release from the slab mantle at slab surface depths less than 175 km, the
637 dehydration pattern of the hydrated slab mantle up to this depth is the same as in the dry slab
638 mantle case (Fig. 12a). Water released by chlorite breakdown in the slab mantle is directly
639 transferred into serpentine at slab depth of about 150 km. Subsequently, the antigorite
640 breakdown reaction is the key factor regarding water release from the slab mantle (Fig. 12a).
641 The antigorite-out reaction starts at the bottom of the hydrated slab mantle part at ~130 km
642 slab surface depth. The liberated water migrates into the water-undersaturated overlying part
643 of the slab mantle, where it is resorbed and dragged down until the thermal stability limit of
644 antigorite is reached at ~175 km slab surface depth. The model shows that large amounts of
645 water are liberated at the terminal antigorite-out reaction, causing a massive fluid flux into the
646 overlying slab crust and wedge mantle. This dehydration burst is responsible for the second,
647 most prominent peak superimposed on the crustal dehydration pattern (Fig. 12a). Beyond the
648 antigorite-out reaction in the slab mantle, minor water release continues by lawsonite
649 breakdown in the crustal part of the slab. Phengitic white mica remains stable in the crustal
650 parts of the slab and does not significantly contribute to water release.

651 Based on the mass balanced boron distribution, the mass of boron (kg B/m^3 rock) released
652 from the slab is calculated (Fig. 12b). These values show a drastic decrease across the profile
653 down to ~170 km slab surface depth, followed by a characteristic and spike-like increase
654 where antigorite dehydration takes place in the slab mantle. The continuous water release
655 from SSZ wedge serpentinites and slab crust explains the strongly decreasing B supply with
656 increasing slab depth because the fluid-mobile B is flushed out with the water. Thus, our
657 model reproduces the decreasing B/Nb ratios observed in various across-arc trends that were
658 attributed to continuous dehydration reactions in the oceanic crust (Ryan et al., 1995;
659 Marschall et al., 2007). At the tip of the antigorite-out reaction in the slab mantle, the transfer
660 of large amounts of boron into the hanging wall plate is predicted, causing B enrichment in
661 arc melts generated there. In terms of B isotope composition, our model shows high $\delta^{11}B$
662 values in the fore-arc region, followed by a continuous linear decrease in $\delta^{11}B$ from ~110 to
663 ~175 km slab surface depth and a distinct increase where the terminal antigorite-out reaction
664 in the slab mantle is located (Fig. 12c). Initially, dehydration of sediments and SSZ wedge
665 serpentinites releases extremely heavy boron into the fore-arc region, as observed in fore-arc
666 slab fluids from serpentinite seamounts (Benton et al., 2001). Subsequently, dehydration of

667 the igneous oceanic crust exemplifies the continuous dehydration-induced ^{11}B depletion in the
668 residual rocks leading to a decreasing $\delta^{11}B$ trend in the released fluids (Marschall et al., 2007;
669 Rosner et al., 2003). This trend has not only been observed in Kamchatka, but also in the
670 Kurile (Ishikawa and Tera, 1997), West Pacific (Ishikawa and Nakamura, 1994) and Chile
671 (Rosner et al., 2003) subduction zones (Fig. 2). Finally, the high-B fluid released by antigorite
672 breakdown in the slab mantle directly transfers a high-$\delta^{11}B$ signature towards the surface due
673 to the high water flux and the finite capability of the crust to incorporate B. Continuing
674 dehydration of slab crust alone is not able to deliver any significant amounts of water or
675 boron at that depth. A major implication of our model is that the absolute $\delta^{11}B$ values
676 expected where antigorite breaks down depend on the hydration state of the slab mantle. In
677 the slab crust, refertilization leads to an additional decreasing $\delta^{11}B$ trend caused by the
678 lawsonite-out reaction between 200 and 250 km slab depth, although this trend is blurred at
679 the model surface by fluid-rock interaction.

680 If we assume unmodified transport of the B signal from the top of the model surface through
681 the upper part of the SSZ wedge mantle and the continental crust, the distinct [B] – $\delta^{11}B$
682 relationship of fluids derived from wedge mantle, crust and slab mantle may be used to
683 identify fluid source lithologies in arc lavas (Fig. 13). It is notable that the position of the slab
684 mantle dehydration is primarily dependent on the stability of antigorite. In our
685 thermodynamic model we use a binary Fe-Mg, Al-free solid solution model of antigorite,
686 which might underestimate the upper stability limit, as Al incorporation into antigorite can
687 result in an increase of the maximum stability in the order of 30°C (Padrón-Navarta et al.,
688 2013). Regarding the spatial scale of our model, together with the fact that Al solution into
689 antigorite has insignificant effects on the co-existing phase relations, we assume this
690 uncertainty to be of minor importance for our interpretation. As pointed out by Scambelluri
691 and Tonarini (2012), arc lavas with $\delta^{11}B$ greater than that of slab fluids require serpentinite as
692 source component. The relatively B-rich, high-$\delta^{11}B$ nature of the South Sandwich lavas (Fig.
693 2) was attributed to the influence of serpentinite-derived fluids from the mantle wedge
694 (Tonarini et al., 2011), in agreement with the characteristics of the modeled mantle wedge –
695 derived fluids. In contrast, slab-derived fluids are expected to have lower B contents. Fluids
696 derived from the slab crust trend toward negative $\delta^{11}B$ values, whereas those from the slab
697 mantle have positive $\delta^{11}B$ values (Fig. 13). For each individual subduction zone modeled,
698 thermal constraints and variations in the input parameters need to be taken into account when
699 evaluating the calculated values. Using the additional constraints of the location relative to the
700 trench and the depth to the slab, which are available for natural samples, the pattern modeled

here may serve as a useful guide in evaluating fluid sources. For the Kamchatka subduction zone model, the difference in $\delta^{11}B$ between fluids derived from slab crust compared to slab mantle is on average about 10‰, but importantly, at 175 km depth-to-slab where the CKD volcanoes are located, crustal fluids would have highly negative $\delta^{11}B$ values. Hence, a fluid contribution from the hydrated slab mantle is indicated. Such serpentinite-derived fluid fluxes at eclogite-facies conditions from the subducted slab mantle have also been postulated in several case studies (Herms et al., 2012; John et al., 2004; Martin et al., 2014), corroborating our interpretation that hydrated slab mantle plays an important role for the water budget in subduction zones.

4. Discussion and Outlook

Both of the examples given in this paper show the immense capacity of combined thermodynamic and trace element models to investigate fluid-rock interaction processes in metamorphic geology. Further, we have shown that boron is a well-suited trace element to trace and quantify fluid-rock interaction at various scales. Our results therefore corroborate the findings of earlier investigations (Bebout and Nakamura 2003; Bebout et al., 2007; Boschi et al., 2008; Bouvier et al., 2008; Brenan et al., 1998; Deyhle et al., 2001; Halama et al., 2014; Ishikawa and Nakamura 1993; Ishikawa and Tera 1997; King et al., 2007; Konrad-Schmolke et al., 2011b; Leeman et al., 1994; Marschall et al., 2007; Nabelek et al., 1990; Pabst et al., 2012; Paquin et al., 2004; Peacock and Hervig 1999; Rose et al., 2000; Sano et al., 2001; Scambelluri et al., 2004; Spivack and Edmond, 1987; Straub and Layne 2002; Tonarini et al., 2001; Wunder et al., 2005) and emphasize the need of more detailed geochemical models that use trace elements and their isotopic composition as a proxy for fluid-rock interaction. At present such complex combined numerical models that focus on the simulation of mass transfer in the solid Earth are at the beginning of unfolding their capacities and more detailed experiments require integration of data and modeling techniques that are still under development.

The two examples presented in this paper diverge in a pivotal aspect: whereas the results of the first example can be directly compared to natural rocks affected by the fluid-rock interaction process, and thus most model parameters can be linked to natural observations, this is not the case in the second, large scale example. Subduction zone models focusing on deep-seated processes, such as the thermal evolution of the subducted slab, the water release and water migration at elevated depth, have generally a large number of unknowns in the

boundary conditions of the models, which leads to a high degree of freedom with respect to the interpretation of the model results. Relevant parameters for the mechanical model that is used as basis for the thermodynamic-geochemical model of the Kamchatkan subduction zone comprise rheological parameters, lithological slab structure and the coupling between the slab and the overriding mantle, all of which are specifically discussed in Manea and Manea (2007) and generally in a number of recent papers that concentrate on benchmarking numerical subduction zone models in order to make different approaches comparable (Gerya and Yuen 2007; Van Keken et al., 2008; Syracuse et al., 2010). It is beyond the scope of this contribution to test the influence of various parameters on the result of the thermo-mechanical model, but rather to demonstrate the potential of coupled geochemical-thermo-mechanical models to properly interpret geochemical data from arc volcanic rocks – data that is abundant in the literature, but has not yet been implemented into thermo-mechanical subduction zone models (Gerya 2011). As shown in our second example, the implementation of thermomechanical models into thermodynamic and geochemical calculations is crucial for the quantification large-scale elemental fluxes (e.g., Rüpke et al., 2004; Hacker, 2008; Van Keken et al., 2011). The striking coincidence between the water release pattern, the position of volcanic centers in the Kamchatkan arc as well as the B concentration and isotope patterns in the arc volcanic rocks should therefore be seen as stimulation for further research in that field, but also to point out the importance of the subducted slab mantle for the water budget in subduction zones. Furthermore we would like to stress that B and its isotopic composition serve as excellent tracer for these processes. However, the combination of thermomechanical, thermodynamic and trace element models still faces computational obstacles that hinder a complete implementation into a single model. Most thermomechanical models use thermodynamic lookup-tables to constrain mineralogically controlled rheological parameters (e.g., Iwamori, 2007; Arcay et al., 2005) and, in turn, thermodynamic and geochemical models use the thermal pattern from thermomechanical models as basis for their thermodynamic predictions (this study). However, in order to fully quantify mass transfer in three dimensions it will be a major task in geodynamic-geochemical modeling to implement fluid-mediated element transport into thermomechanical models.

4.1. Constraints on fluid migration processes

The mode of fluid transport, e.g. channelized vs. pervasive, as well as the volume and intensity of the fluid-rock interaction process predominantly control the amount and rate of transported solutes (Zack and John 2007). For a correct numerical formulation of

766 thermodynamic-geochemical models the fluid migration mechanism plays a crucial role. In
767 turn, variation of the boundary conditions of such combined models can be used to constrain
768 possible modes of fluid percolation in a particular setting. In nature there are examples of
769 both highly channelized fluid flux in brittle and ductile shear zones (e.g., Bebout and Barton
770 1993, Austrheim 1987) as well as pervasive fluid flux by interconnected fluid films along
771 grain boundaries (Keller et al., 2006; de Meer et al., 2005, Konrad-Schmolke et al., 2011a,
772 example 1 in this work; see also Oliver 1996 for a detailed review) reflecting a broad range of
773 fluid flow mechanisms in natural rocks that might be active at the same time in a single
774 sample (Fusseis and Handy 2008). Several works provide a theoretical background for fluid
775 flux in metamorphic rocks (Connolly and Podlachikov 2007, Fusseis et al., 2009, Kruhl et al.,
776 2013) and numerical thermomechanical models increasingly focus on the prediction and
777 quantification of fluid fluxes in metamorphic rocks, especially in subduction zones (see Gerya
778 2011 and references therein). As metamorphic porosity and thus permeability is transient in
779 most rocks, unequivocal evidence for a certain fluid-migration mode is lacking in most
780 natural samples.

781 Besides experiments that provide insight into porosity development and fluid-induced mineral
782 replacement mechanisms (Putnis and Mezger 2004), natural samples that preserve areas that
783 are unaffected by fluid infiltration together with overprinted parts, such as the samples in our
784 first example, are crucial for the investigation of fluid migration during metamorphism and
785 for the validation of numerical models (Jamtveit et al., 2008; Putnis and Austrheim 2010;
786 Konrad-Schmolke et al., 2011a). Although sensitivity tests allow determination of the critical
787 parameters and give insight into the robustness and validity of numerical model results (e.g.,
788 Spakman and Wortel 2004; Martí et al., 2009; Gray and Pysklywec, 2012), comparison of the
789 modeled processes with their effect on natural rocks is, whenever possible, indispensible. As
790 fluid-rock interaction processes in natural rocks must be investigated from km- to nm-scale
791 and comprise chemical effects that often require high precision combined with high spatial
792 resolution scientific advances in this field are directly coupled with technical innovations
793 (Gianuzzi and Stevie 1999; Albarède et al., 2004; Fusseis et al., 2009; Kylander-Clark et al.,
794 2013). For example, with high-resolution analytical techniques, such as TEM, X-ray
795 tomography using synchrotron radiation or dual beam focused ion beam investigations, syn-
796 metamorphic porosity development can be visualized in natural samples and experiments
797 (e.g., Fusseis et al., 2009, Kruhl et al., 2013) and the sites of fluid rock interaction can be
798 chemically analyzed. However, proper sample selection is of utmost importance in order to
799 trace the effects of fluid rock interaction at various scales. Fig. 14 shows an example of

800 porosity formation in a natural rock from the Franciscan mélange complex at Jenner,
801 California. A metre-sized block of eclogite is partly transformed into blueschist with a clearly
802 visible reaction front running through the block (Fig. 14a). The sharp reaction front separates
803 a moderately affected area where the assemblage clinopyroxene+garnet+rutile is well
804 preserved from a strongly overprinted part with the assemblage
805 glaucophane+plagioclase+titanite (Fig. 14b). One of the strongly zoned clinopyroxene
806 crystals points into the reacted part and the reaction front is running through the lowermost
807 edge of the crystal (Fig. 14c). The electron transparent slice, taken perpendicular to the
808 reaction front (red line in c), shows a µm-sized pore that comprises a dark rim, dark worm-
809 like precipitates and bright Ga precipitate from the FIB sectioning in its interior (Fig. 14d).
810 The dark rim consists of amorphous Si-rich material and is connected with the worm-like
811 material in the interior of the pore (Fig. 14e) that has approximately the same major element
812 composition as the amorphous rim (Fig. 14f and Fig. 15). Precise measurements of major and
813 trace element concentrations and the isotopic compositions in such µm- to nm-scale features
814 displays a challenging task for future analytical developments as such features will reveal the
815 connection between the processes of porosity formation, fluid migration, fluid-rock
816 interaction and metamorphism.

817 Regarding the quantification of element transport – often in the focus of combined
818 thermodynamic-geochemical models – aqueous fluids and hydrous melts have a fundamental
819 importance with respect to the mass transfer in geological systems (e.g., Hermann et al.,
820 2006). In many metamorphic environments, pressures and temperatures exceed the critical
821 point of water resulting in a drastic increase of dissolved material in the transport agent
822 compared to ambient pressures and temperatures (e.g., Manning 1994). Consequently, the
823 thermodynamic and chemical properties of supercritical fluids and hydrous melts control
824 large parts of the mass transfer in the lithosphere. Experiments have shown that the solubility
825 of major and trace elements in supercritical fluids is also strongly dependent on fluid
826 chemistry (e.g., Manning et al., 2008; Wilke et al., 2012). Moreover, solubilities of several
827 elements are enhanced by the addition of ligands (Cl^-, F^-, CO_3^{2-} and SO_4^{2-}) and by complexing
828 with major rock-forming constituents (Antignano and Manning 2008; Tsay et al., 2014). In
829 turn, the fluid chemistry might change along its migration path as a result of the interaction
830 with the wall rock and/or due to changing chemistry of the rock column. Thus, the interaction
831 between fluid chemistry – that may comprise a complete miscibility between hydrous melts
832 and dilute aqueous solutions (Manning, 2004; Hermann et al., 2006) – soluble metal
833 compounds, dissolved trace elements and host rock chemistry controls the fluid-mediated

mass transfer in metamorphic systems. Such reactive fluid flow systems can be quantified with combined thermodynamic-geochemical models. To develop more reliable models additional experimental data as well as knowledge of thermodynamic properties and equations of state of supercritical fluids and the solutes therein are needed (e.g., Hauthal, 2001; Gottschalk et al., 2007; Dolejis and Manning, 2010). Improved analytical instrumentation and experimental setups will allow determination of more precise distribution coefficients, especially those between solid and liquid phases (e.g., Kessel et al., 2005), which are most critical for such trace element models. Determining and quantifying a potential pressure, temperature and host mineral chemistry dependence of the trace element distribution will be essential for forward models that span large pressure and temperature ranges, such as the subduction zone model shown above. Integrating these data in Gibbs energy minimization algorithms, reactive-flow models (e.g. Baumgartner and Ferry 1991) or combined thermodynamic-trace element models (this study) will enable a full quantification of reactive fluid flow and the associated mass transfer in the solid Earth.

4.2. Constraints on thermodynamic and geochemical model parameters

In contrast to most applications in material sciences, simulations of natural processes in geosystems are confronted with complications arising from multiphase-multicomponent chemically open systems that must be simplified in order to be mathematically feasible. In terms of the thermodynamic treatment of the envisaged process much attention must be paid to set appropriate simplified boundary conditions of the model. At first, this concerns the choice of an appropriate chemical system, the selection of thermodynamic datasets and solution models as well as the choice of appropriate thermodynamic variables, such that the boundary conditions of the model reflect the envisaged geological process (e.g., Connolly 2005; Powell et al., 2005). In case of chemically open systems element fractionation processes, such as fluid percolation and fractional crystallization, must be reflected in the models. This circumstance is often disregarded, but has to be considered in order to avoid misinterpretations of thermodynamic equilibrium calculations (Marmo et al., 2002; Konrad-Schmolke et al., 2008a).

The increasing use of phase diagrams in progressively complex chemical systems in the geoscientific literature suggests a rapid development with respect to the understanding of the metamorphic evolution of rock samples. However, as concluded nicely in Powell and Holland (2005), thermodynamic models can be excellently used to solve metamorphic-geodynamic problems as long as the limitations of the available thermodynamic data are known. For

867 example, significant simplifications must be made with respect to the chemical composition
868 of geosystems in order to make them feasible for mathematic treatment. On the other hand,
869 constraining the chemical system has the disadvantage that the effects of omitted chemical
870 components on the stability of solution phases cannot be predicted. This circumstance is well
871 known for the garnet solid solution, where Mn has a profound influence on garnet stability
872 (e.g., Marmo et al., 2002; Konrad-Schmolke et al., 2005). Furthermore, compositional
873 simplifications of the investigated system often require omission of accessory phases that can
874 play an important role for the trace element budget in metamorphic rocks (e.g., Hermann,
875 2002). Since thermodynamic data as well trace element distribution coefficients for accessory
876 phases are scarce and contain large uncertainties, incorporation of such phases into
877 thermodynamic and trace element models remains an important task for the future (e.g.,
878 Kelsey and Powell, 2010; van Hinsberg et al., 2011).

879 Many thermodynamic standard state data for chemical endmembers as well as reliable solid
880 solution models for complex phases, such as amphibole and chlorite, are missing and research
881 in this field is work in progress. Modern analytical technology allows determination of
882 precise thermodynamic properties of geologically relevant phases (e.g., Dachs et al., 2009) in
883 calorimetric experiments and improvements have been made to derive more precise activity-
884 composition relationships (e.g., Powell and Holland 2008 and references therein) and
885 equations of state for different geologic environments (e.g., Stixrude and Lithgow-Bertelloni,
886 2005; Holland and Powell, 2011; Holland et al., 2013). However, none of the published
887 datasets covers the entire range of pressure-, temperature- and compositional variations in
888 geosystems. Regarding the rapidly evolving computational capacities it seems likely that
889 numerical simulations of geomaterials will enable significant developments in
890 thermodynamic applications in geosciences (e.g., van Hinsberg et al., 2005).

891 Especially in material science and industrial applications (e.g., Dixon and Gutowski 2005) the
892 study of thermodynamic and physical properties of solid and liquid phases involves molecular
893 dynamic and *ab initio* models (e.g., Prausnitz, 1969; Belonoshko and Saxena, 1991;
894 Kalinichev 2001; Cygan, 2001). Both approaches minimize the energy of a given system that
895 is controlled by the electromagnetic forces within and between molecules. Whereas molecular
896 dynamic models require empirical data to model the intra- and intermolecular forces, *ab initio*
897 or quantum mechanical models are directly based on wave functions that describe electron
898 orbitals on the basis of the Schrödinger equations. Consequently, these mathematical
899 approaches require a minimum of empirical data to obtain fundamental thermodynamic

properties of phases, equations of state, physico-chemical properties as well as trace element partition and isotope fractionation coefficients (e.g., Jahn and Wunder 2009; Ottonello et al., 2010; Kowalski et al., 2013; Haigis et al., 2013). Especially the thermodynamic properties of fluids and aqueous species are increasingly simulated utilizing molecular dynamics or *ab initio* models (e.g., Kalinichev 2001 and references therein; Sedlbauer et al., 2000). Due to the immense computational resources needed for these simulations, recent research is focused on simple chemical systems, such as phases in the Earth's mantle or core (e.g., Matsui et al., 2000), but in the near future, numerical atomistic simulations will lead to a better understanding and a prediction of processes in more complex geosystems (e.g., Cruz et al., 2005). In combination with the approach described in van Hinsberg et al., 2005, who derive thermodynamic properties of complex phases by combining the fractional properties of their constituent chemical compounds, *ab inito* models might soon become valuable sources of thermodynamic data for complex phases relevant for geological processes.

Acknowledgements

We thank Vlad Manea for generously providing the thermal model of the Kamchatkan subduction zone and Richard Wirth as well as Anja Schreiber for the TEM analyses and FIB sectioning, respectively. Further, we thank Marco Scambelluri for the invitation to that Review Article and for the editorial handling of the manuscript. We also thank Timm John and an anonymous reviewer for their critical and constructive comments that significantly improved the manuscript. Funding of this work by the Deutsche Forschungsgemeinschaft (grant KO-3750/2-1) is gratefully acknowledged.

923

924

925 **Figure captions**

926 Fig. 1:

927 Two examples of combined thermodynamic-geochemical modeling applied to the
928 petrogenesis of Archean tonalite-trondhjemite-granodiorite (TTG) series rocks (a) and
929 primitive arc magmas (b), respectively. (a) Primitive mantle–normalized trace element
930 patterns of measured Archean TTG rocks from the Isua Supracrustal Belt (gray area) and
931 modeled primitive melt compositions (modified from Nagel et al., 2012). Colored dashed
932 lines represent trace element compositions of the two protoliths considered in the modeling,
933 present-day normal mid-ocean ridge basalt (N-MORB) and Isua tholeiite. Colored solid lines
934 indicate compositions of TTGs modeled for 10% melting at different melting pressures.
935 Characteristic trace element features of natural TTG, including negative Ti and positive Zr-Hf
936 anomalies, are best reproduced by melting of Archean tholeiite at 10-14 kbar, which was
937 considered to represent the source lithology for Archean TTG rocks by Nagel et al. (2012).
938 (b) N-MORB–normalized trace element patterns of arc basalts from the NE Japan arc (red
939 circles) and modeled results from Arc Basalt Simulator (ABS) (modified from Kimura et al.,
940 2009). The thin blue lines mark the minimum and maximum fits calculated by the ABS
941 algorithm. Compositions for the volcanic front were calculated using the Tohoku (NE Japan
942 arc) slab surface trajectory (SST), whereas rear arc compositions were modeled using the
943 Cascadia SST.

944 Fig. 2:

945 (a) Boron isotope data from volcanic arcs in relation to the depth of the subducting slab.
946 Several arcs display decreasing $\delta^{11}B$ values with increasing depth to slab. Notable exceptions
947 are the South Sandwich Islands arc, for which a constant depth is assumed, and the
948 Kamchatka arc, for which $\delta^{11}B$ values are increasing following the typical $\delta^{11}B$ decrease
949 across the volcanic front. (b) Trend of decreasing $\delta^{11}B$ with increasing Nb/B in arc volcanic
950 rocks. The SSI arc deviates from the main trend due to elevated $\delta^{11}B$. Data sources:
951 Kamchatka – Ishikawa et al., 2001; Izu – Ishikawa and Nakamura, 1994; Kuriles – Ishikawa
952 & Tera, 1999; NE Japan – Moriguti et al., 2004; Central Andes – Rosner et al., 2003; South
953 Sandwich Islands –Tonarini et al., 2011; Conical Seamount – Benton et al., 2001; Atlantis
954 Massif – Boschi et al., 2008; MORB – Shaw et al., 2012; AOC – Yamaoka et al., 2012;

955 Marine sediments – Tonarini et al., 2011; Oceanic basalts – Turner et al., 2007. In (b), data of
956 the other arcs include data shown in (a) and additional data from Smith et al. (1997) and
957 Leeman et al. (2004).

958 Fig. 3:

959 Schematic cross section through a subduction zone (modified from Wunder et al., 2005) and
960 sketches of the fluid-rock interaction scenario modeled in this study. Areas of interest are
961 marked by rectangles in the upper sketch. The two lower images show fluid-rock interaction
962 at the slab-wedge interface and recrystallization of phengite and amphibole on the µm to mm
963 scale, as observed in samples from the Sesia Zone. Boron concentrations and $\delta^{11}B$ values
964 typical for natural reservoirs were taken from Wunder et al. (2005) with additional data from
965 Leeman et al. (2004) and Tonarini et al. (2011) for marine sediments and from Spivack and
966 Edmond (1987), Boschi et al. (2008) and Vils et al. (2009) for serpentinized oceanic mantle.
967

968 Fig. 4:

969 a) Back-scattered electron image of partially overprinted phengite from eclogites-facies rocks
970 of the Sesia Zone. Phengite and sodic amphibole grains are compositionally modified along
971 grain boundaries and other fluid pathways. b) Major element microprobe profile along the
972 arrow shown in a). Compositional variations comprise predominantly a Fe-Mg exchange with
973 the other elements being largely unaffected. c) Boron isotopic and concentration data from
974 phengites of the EMS unit in the Sesia Zone (data from Konrad-Schmolke et al., 2011b and
975 Halama et al., 2014). Overprinted areas have consistently lower B contents than the
976 corresponding relict cores, but $\delta^{11}B$ values are similar. Note the coupled decrease in [B] and
977 increase in $\delta^{11}B$ in mylonitic phengite from the shear zone (green arrow).

978

979 Fig. 5:

980 (a) Phase relations and water content in solids in equilibrium assemblage diagrams for sample
981 MK-55 from the Eclogitic Micaschist unit of the Sesia Zone. The diagrams on the left hand
982 side were calculated for peak P-T and water-saturated conditions. The diagrams on the right
983 hand side were calculated with excess H_2O, simulating the fluid influx at 1.35 GPa. (b) X_{Mg} in
984 phengite depending on P and X_{H2O}. The red arrow marks the retrograde path and the blue line
985 represents the water saturation line. Initially, decompression leads to increasingly water-

986 undersaturated conditions in the rock until fluid influx at 1.35 GPa occurs. At these pressures,
987 increasing X_{H2O} causes a significant decrease in X_{Mg}. Mineral abbreviations: qtz = quartz,
988 phng = phengite, pg = paragonite, gln = glaucophane, cpx = clinopyroxene, ep = epidote, lws
989 = lawsonite, pl = plagioclase, chl = chlorite, bt = biotite, cam = clinoamphibole, grt = garnet,
990 mt = magnetite.

991 Fig. 6:

992 Compositional evolution in phengite and modal phase abundances along the retrograde P-T
993 path from 1.45 to 1.1 GPa. Drastic compositional changes are associated with fluid influx at
994 1.35 GPa, causing a decrease in Si_T and X_{Cel} in phengite. Glaucophane, epidote and
995 paragonite abundances increase, whereas omphacite and phengite abundances decrease due to
996 the fluid influx. Mineral abbreviations as in Fig. 1.

997 Fig. 7:

998 Fluid-rock interaction model. The evolution of $[B]_{phng}$ and $\delta^{11}B_{phng}$ are shown depending on
999 the amount of accumulated water (left column) and with decreasing pressure along the
1000 retrograde P-T path (middle column). The range of observed compositional features in relict
1001 phengite cores (green), overprinted phengite rims (red) and mylonitic phengite (blue) are
1002 shown for comparison. In the right column, the relevant parameters are combined to illustrate
1003 how the curves shown in (a) and (b) are linked. The dashed line labeled “fluid influx” marks
1004 the maximum amount of water available before the influx that is consistent with the
1005 composition of the overprinted rims (left column) and the position of the influx on the
1006 retrograde path (middle column).

1007 Fig. 8:

1008 Summary of modeled trends of B release and B isotope fractionation in a slab-derived fluid
1009 during subduction of oceanic crust as modeled by Marschall et al. (2007). Solid lines are B
1010 concentrations, dashed lines are $\delta^{11}B$ values. During subduction, both B concentrations and
1011 $\delta^{11}B$ decrease with increasing pressure. The decrease is particularly strong if there is no
1012 phengite present in the rock.

1013 Fig. 9:

1014 a) A thermal pattern for the Kamchatkan subduction zone derived from the thermomechanical
1015 models of Manea and Manea (2007) was used as basis for the pressure and temperature

1016 relations in the thermodynamic model. The structure of the modeled slab includes all
1017 lithologies relevant for the B budget in our models. b) Isotopic fractionation values calculated
1018 for the thermal pattern in a) with the data from Wunder et al., 2005.

1019

1020 Fig. 10:

1021 Contoured pseudosection of the modeled slab, subdivided into SSZ wedge mantle, sediments,
1022 igneous oceanic crust for dry (a) and hydrated (b) slab mantle. Colored contours show the
1023 amount of water in solid phases. Mineral abbreviations as in Fig. 1.

1024 Fig. 11:

1025 Modeled (a) boron concentrations and (b) corresponding $\delta^{11}B_{rock}$ values assuming water-
1026 saturated sediments and oceanic crust and a dry slab mantle. The input parameters for wedge
1027 mantle (50 µg/g B, $\delta^{11}B = +15$), sediments (40 µg/g B, $\delta^{11}B = +5$) and oceanic crust (25 µg/g
1028 B, $\delta^{11}B = +0.8$‰) change during forward modeling due to the fluid-solid B elemental and
1029 isotopic fractionation. For the slab mantle, constant values of 0.1 µg/g B and $\delta^{11}B = -10$‰ are
1030 assumed.

1031 Fig. 12:

1032 Modeled dehydration, release of boron and corresponding $\delta^{11}B_{fluid}$ values. (a) SSZ wedge
1033 mantle dehydration dominates water release in the forearc. Chlorite breakdown in crust and
1034 wedge mantle is the dominant water source at shallow depths down to ~150 km. The marked
1035 peak at ~175 km slab surface depth results from serpentine breakdown in the slab mantle. (b)
1036 The boron pattern mimics the water release, including high concentrations in the forearc and a
1037 prominent peak at ~175 km slab surface depth. (c) High $\delta^{11}B_{fluid}$ values characterize water
1038 release into the forearc, followed by a systematic decrease in $\delta^{11}B_{fluid}$ values, reflecting
1039 continuous dehydration. The increase in $\delta^{11}B_{fluid}$ at ~175 km slab surface depth is coupled to
1040 serpentine dehydration in the slab mantle, and the height of the $\delta^{11}B$ curve depends on water
1041 contents in the slab mantle. For a slab mantle hydrated to a depth of 15 km, the best fit is
1042 obtained for ~2.5 wt.% H_2O. In all figures, a simplified topographic profile across Kamchatka
1043 is shown for comparison. Boron concentration data in (b) are given as B/Nb ratios to
1044 eliminate fractionation effects in natural samples. Data from Kamchatka samples are from
1045 Ishikawa et al. (2001). Please note that the high frequency variations in the water release are
1046 the result of the incremented thermal pattern and does not reflect distinct fluid pulses.

1047 Fig. 13:

1048 Composition of fluids released at the upper boundary of the model into the overlying mantle
1049 wedge. Distinct areas can be defined depending on the dominant water and boron source
1050 lithologies. Fluids derived from the SSZ wedge mantle have the highest B concentrations and
1051 the highest $\delta^{11}B$ values, and all fluids released by mantle deserpentinization have strongly
1052 positive $\delta^{11}B$ values distinct from crustal fluids.

1053 Fig. 14:

1054 Investigation of fluid-rock interaction processes from m- to nm-scale, exemplified by a fluid-
1055 induced blueschist-facies overprint of eclogite from a subduction mélange (Jenner, California,
1056 USA). See text for details.

1057 Fig. 15:

1058 TEM-EDX analyses from areas shown in Fig. 14f. Both the overprinted rim as well as worm-
1059 like structures in the pore interior consist of an amorphous silica-rich material with minor
1060 concentrations of Al, Ca and Fe. Ga and Cu peaks result from the Ga-beam used for FIB
1061 sectioning and the sample holder, respectively.

1062

1063 **References**

1064 Aggarwal, J. K., Palmer, M. R., 1995. Boron isotope analysis. A review. Analyst, 120(5),
1065 1301-1307.

1066 Ague, J.J., 2003. Fluid infiltration and transport of major, minor, and trace elements during
1067 regional metamorphism of carbonate rocks, Wepawaug Schist, Connecticut, USA. American
1068 Journal of Science 303, 753-816.

1069 Ague, J.J., 2011. Extreme channelization of fluid and the problem of element mobility during
1070 Barrovian metamorphism. American Mineralogist 96, 333-352.

1071 Albarède, F., 1995. Introduction to Geochemical Modeling. Cambridge University Press,
1072 Cambridge, 543 pp.

1073 Albarede, F., Telouk, P., Blichert-Toft, J., Boyet, M., Agranier, A., Nelson, B., 2004. Precise
1074 and accurate isotopic measurements using multiple-collector ICPMS. Geochimica et
1075 Cosmochimica Acta, 68(12), 2725-2744.

1076 Altenberger, U., Schmid, R., Oberhänsli, R., 2008. Composition and pre-metamorphic
1077 geodynamic setting of the ultrahigh-pressure metabasic rocks from Dabie Shan, E-China.
1078 International Journal of Earth Sciences 97, 1301-1314.

1079 Angiboust, S., Pettke, T., De Hoog, J.C., Caron, B., Oncken, O., 2014. Channelized Fluid
1080 Flow and Eclogite-facies Metasomatism along the Subduction Shear Zone. Journal of
1081 Petrology, 55(5), 883-916.

1082 Antignano, A., Manning, C.E., 2008. Rutile solubility in H_2O, H_2O–SiO_2, and H_2O–
1083 $NaAlSi_3O_8$ fluids at 0.7–2.0 GPa and 700–1000 C: implications for mobility of nominally
1084 insoluble elements. Chemical Geology, 255, 283-293.

1085 Arcay, D., Tric, E., Doin, M.P., 2005. Numerical simulations of subduction zones: effect of
1086 slab dehydration on the mantle wedge dynamics. Physics of the Earth and Planetary Interiors,
1087 149(1), 133-153.

1088 Asimow, P.D., Ghiorso, M.S., 1998. Algorithmic modifications extending MELTS to
1089 calculate subsolidus phase relations. American Mineralogist 83, 1127-1131.

1090 Austrheim, H., 1987. Eclogitization of lower crustal granulites by fluid migration through
1091 shear zones. Earth and Planetary Science Letters, 81(2), 221-232.

1092 Ayers, J.C., Eggler, D.H., 1995. Partitioning of elements between silicate melt and H_2O-NaCl
1093 fluids at 1.5 and 2.0 GPa pressure: Implications for mantle metasomatism. Geochimica et
1094 Cosmochimica Acta 59, 4237-4246.

1095 Bau, M., 1991. Rare-earth element mobility during hydrothermal and metamorphic fluid-rock
1096 interaction and the significance of the oxidation state of europium. Chemical Geology 93,
1097 219-230.

1098 Baumgartner, L.P., Ferry, J.M., 1991. A model for coupled fluid-flow and mixed-volatile
1099 mineral reactions with applications to regional metamorphism. Contributions to Mineralogy
1100 and Petrology, 106(3), 273-285.

1101 Bebout, G.E., 2007. Metamorphic chemical geodynamics of subduction zones. Earth and
1102 Planetary Science Letters 260, 373-393.

1103 Bebout, G. E., 2013. Metasomatism in subduction zones of subducted oceanic slabs, mantle
1104 wedges, and the slab-mantle interface. In *Metasomatism and the Chemical Transformation of*
1105 *Rock* (pp. 289-349). Springer Berlin Heidelberg.

1106 Bebout, G.E., Barton, M.D., 1993. Metasomatism during subduction: products and possible

1107 paths in the Catalina Schist, California. Chemical Geology, 108(1), 61-92.

1108 Bebout, G.E., Nakamura, E., 2003. Record in metamorphic tourmalines of subduction-zone
1109 devolatilization and boron cycling. Geology 31, 407-410.

1110 Bebout, G.E., Ryan, J.G., Leeman, W.P., Bebout, A.E., 1999. Fractionation of trace elements
1111 during subduction-zone metamorphism: Impact of convergent margin thermal evolution.
1112 Earth and Planetary Science Letters 171, 63-81.

1113 Becker, H., Jochum, K.P., Carlson, R.W., 2000. Trace element fractionation during
1114 dehydration of eclogites from high-pressure terranes and the implications for element fluxes
1115 in subduction zones. Chemical Geology 163, 65-99.

1116 Beinlich, A., Klemd, R., John, T., Gao, J., 2010. Trace-element mobilization during Ca-
1117 metasomatism along a major fluid conduit: Eclogitization of a blueschist as a consequence of
1118 fluid-rock interaction. Geochimica et Cosmochimica Acta 74, 1892-1922.

1119 Belonoshko, A., Saxena, S. K., 1991. A molecular dynamics study of the pressure-volume-
1120 temperature properties of super-critical fluids: I. H_2O. Geochimica et Cosmochimica Acta 55,
1121 381-387.

1122 Benton, L. D., Ryan, J. G., Tera, F., 2001. Boron isotope systematics of slab fluids as inferred
1123 from a serpentine seamount, Mariana forearc. Earth and Planetary Science Letters 187, 273-
1124 282.

1125 Berman, R.G., 1988. Internally-consistent thermodynamic data for minerals in the system
1126 Na_2O-K_2O-CaO-MgO-FeO-Fe_2O_3-Al_2O_3-SiO_2-TiO_2-H_2O-CO_2. Journal of Petrology 29, 445-
1127 522.

1128 Berman, R.G. (1990). Mixing properties of Ca-Mg-Fe-Mn garnets. American Mineralogist
1129 75(3-4): 328-344.

1130 Blundy, J., Wood, B., 2003. Partitioning of trace elements between crystals and melts. Earth
1131 and Planetary Science Letters 210, 383-397.

1132 Bohrson, W.A., Spera, F.J., 2001. Energy-constrained open-system magmatic processes II:
1133 Application of energy-constrained assimilation-fractional crystallization (EC-AFC) model to
1134 magmatic systems. Journal of Petrology 42, 1019-1041.

1135 Bohrson, W.A., Spera, F.J., 2007. Energy-constrained recharge, assimilation, and fractional
1136 crystallization (EC-RAχFC): A Visual Basic computer code for calculating trace element and

1137 isotope variations of open-system magmatic systems. Geochemistry Geophysics Geosystems
1138 8(11), Q11003, doi:10.1029/2007GC001781.

1139 Boschi, C., Dini, A., Früh-Green, G.L., Kelley, D.S., 2008. Isotopic and element exchange
1140 during serpentinization and metasomatism at the Atlantis Massif (MAR 30°N): Insights from
1141 B and Sr isotope data. Geochimica et Cosmochimica Acta 72, 1801-1823.

1142 Bouvier, A. S., Metrich, N., Deloule, E., 2008. Slab-derived fluids in the magma sources of
1143 St. Vincent (Lesser Antilles Arc): volatile and light element imprints. Journal of Petrology,
1144 49, 1427-1448.

1145 Breeding, C.M., Ague, J.J., Bröcker, M., 2004. Fluid-metasedimentary rock interactions in
1146 subduction-zone mélange: Implications for the chemical composition of arc magmas.
1147 Geology 32, 1041-1044.

1148 Brenan, J.M., Ryerson, F.J., Shaw, H.F., 1998. The role of aqueous fluids in the slab-to-
1149 mantle transfer of boron, beryllium, and lithium during subduction: Experiments and models.
1150 Geochimica et Cosmochimica Acta 62, 3337-3347.

1151 Brenan, J.M., Shaw, H.F., Ryerson, F.J., Phinney, D.L., 1995. Mineral-aqueous fluid
1152 partitioning of trace elements at 900°C and 2.0 GPa: Constraints on the trace element
1153 chemistry of mantle and deep crustal fluids. Geochimica et Cosmochimica Acta 59, 3331-
1154 3350.

1155 Briscoe, H.V.A., Robinson, P.L., 1925. A redetermination of the atomic weight of boron.
1156 Journal of the Chemical Society 127, 696-720.

1157 Bröcker, M., Baldwin, S., Arkudas, R., 2013. The geological significance of $^{40}Ar/^{39}Ar$ and
1158 Rb-Sr white mica ages from Syros and Sifnos, Greece: a record of continuous
1159 (re)crystallization during exhumation? Journal of Metamorphic Geology 31, 629-646.

1160 Brunsmann, A., Franz, G., Erzinger, J., 2001. REE mobilization during small-scale high-
1161 pressure fluid-rock interaction and zoisite/fluid partitioning of La to Eu. Geochimica et
1162 Cosmochimica Acta 65, 559-570.

1163 Connolly, J.A.D., 2005. Computation of phase equilibria by linear programming: A tool for
1164 geodynamic modeling and its application to subduction zone decarbonation. Earth and
1165 Planetary Science Letters 236, 524-541.

1166 Connolly, J. A. D., Kerrick, D. M., 1987. An algorithm and computer program for calculating
1167 composition phase diagrams. Calphad, 11(1), 1-55.

1168 Connolly, J.A.D., Podladchikov, Y.Y., 2007. Decompaction weakening and channeling
1169 instability in ductile porous media: Implications for asthenospheric melt segregation. Journal
1170 of Geophysical Research: Solid Earth (1978–2012), 112(B10).

1171 Cruz, F. J., Canongia Lopes, J. N., Calado, J. C., & Minas da Piedade, M. E. (2005). A
1172 molecular dynamics study of the thermodynamic properties of calcium apatites. 1. Hexagonal
1173 phases. The Journal of Physical Chemistry B, 109(51), 24473-24479.

1174 Dachs, E., Geiger, C. A., Withers, A. C., Essene, E. J., 2009. A calorimetric investigation of
1175 spessartine: Vibrational and magnetic heat capacity. Geochimica et Cosmochimica Acta
1176 73(11), 3393-3409.

1177 De Capitani, C., Brown, T.H., 1987. The computation of chemical equilibrium in complex
1178 systems containing non-ideal solutions. Geochimica et Cosmochimica Acta 51, 2639-2652.

1179 Cygan, R. T., 2001. Molecular modeling in mineralogy and geochemistry. Reviews in
1180 Mineralogy and Geochemistry, 42(1), 1-35.

1181 de Meer, S., Spiers, C.J., Nakashima, S., 2005. Structure and diffusive properties of fluid-
1182 filled grain boundaries: An in-situ study using infrared (micro) spectroscopy. Earth and
1183 Planetary Science Letters, 232(3), 403-414.

1184 Dempster, T. J., 1992. Zoning and recrystallization of phengitic micas: implications for
1185 metamorphic equilibration. Contributions to Mineralogy and Petrology, 109(4), 526-537.

1186 DePaolo, D.J., 1981. Trace element and isotopic effects of combined wallrock assimilation
1187 and fractional crystallization. Earth and Planetary Science Letters 53, 189-202.

1188 Deyhle, A., Kopf, A., 2005. The use and usefulness of boron isotopes in natural silicate-water
1189 systems. Physics and Chemistry of the Earth 30, 1038-1046.

1190 Deyhle, A., Kopf, A., Eisenhauer, A., 2001. Boron systematics of authigenic carbonates: a
1191 new approach to identify fluid processes in accretionary prisms. Earth and Planetary Science
1192 Letters, 187(1), 191-205.

1193 Di Vincenzo, G., Ghiribelli, B., Giorgetti, G., Palmeri, R., 2001. Evidence of a close link
1194 between petrology and isotope records: constraints from SEM, EMP, TEM and in situ ^{40}Ar-
1195 ^{39}Ar laser analyses on multiple generations of white micas (Lanterman Range, Antarctica).
1196 Earth and Planetary Science Letters 192, 389-405.

1197 Dixon, D. A., Gutowski, M., 2005. Thermodynamic properties of molecular borane amines
1198 and the [BH4-][NH4+] salt for chemical hydrogen storage systems from ab initio electronic
1199 structure theory. The Journal of Physical Chemistry A, 109(23), 5129-5135.

1200 Dolejš, D., Manning, C. E., 2010. Thermodynamic model for mineral solubility in aqueous
1201 fluids: theory, calibration and application to model fluid-flow systems. Geofluids, 10(1-2),
1202 20-40.

1203 Domanik, K.J., Hervig, R.L., Peacock, S.M., 1993. Beryllium and boron in subduction zone
1204 minerals: An ion microprobe study. Geochimica et Cosmochimica Acta 57, 4997-5010.

1205 Domanik, K.J., Holloway, J.R., 1996. The stability and composition of phengitic muscovite
1206 and associated phases from 5.5 to 11 GPa: Implications for deeply subducted sediments.
1207 Geochimica et Cosmochimica Acta 60, 4133-4150.

1208 Dragovic, B., Samanta, L.M., Baxter, E.F., Selverstone, J., 2012. Using garnet to constrain
1209 the duration and rate of water-releasing metamorphic reactions during subduction: An
1210 example from Sifnos, Greece. Chemical Geology 314-317, 9-22.

1211 Elliott, T., 2003. Tracers of the slab. In: J. Eiler (Editor), Inside the Subduction Factory.
1212 Geophysical Monograph. American Geophysical Union, Washington, DC, pp. 23-45.

1213 Elliott, T., Jeffcoate, A., Bouman, C., 2004. The terrestrial Li isotope cycle: light-weight
1214 constraints on mantle convection. Earth and Planetary Science Letters, 220(3), 231-245.

1215 Essene, E.J., 1989. The current state of thermobarometry in metamorphic rocks. Geol. Soc.
1216 Spec. Publ. 43, 1-44.

1217 Ferry, J.M., Gerdes, M.L., 1998. Chemically reactive fluid flow during metamorphism.
1218 Annual Review of Earth and Planetary Sciences, 26(1), 255-287.

1219 Fusseis, F., Handy, M.R., 2008. Micromechanisms of shear zone propagation at the brittle–
1220 viscous transition. Journal of Structural Geology, 30(10), 1242-1253.

1221 Fusseis, F., Regenauer-Lieb, K., Liu, J., Hough, R.M., De Carlo, F., 2009. Creep cavitation
1222 can establish a dynamic granular fluid pump in ductile shear zones. Nature, 459(7249), 974-
1223 977.

1224 Garth, T., Rietbrock, A., 2014. Order of magnitude increase in subducted H_2O due to
1225 hydrated normal faults within the Wadati-Benioff zone. Geology, doi:10.1130/G34730.1.

1226 Gast, P.W., 1968. Trace element fractionation and the origin of tholeiitic and alkaline magma

1227 types. Geochimica et Cosmochimica Acta 32, 1057-1086.

1228 Ghiorso, M.S., Hirschmann, M.M., Reiners, P.W., Kress, V.C., 2002. The pMELTS: An
1229 revision of MELTS aimed at improving calculation of phase relations and major element
1230 partitioning involved in partial melting of the mantle at pressures up to 3 GPa. Geochemistry
1231 Geophysics Geosystems 3(5), DOI: 10.1029/2001GC000217.

1232 Ghiorso, M.S., Sack, R.O., 1995. Chemical mass transfer in magmatic processes. IV. A
1233 revised and internally consistent thermodynamic model for the interpolation and extrapolation
1234 of liquid-solid equilibria in magmatic systems at elevated temperatures and pressures.
1235 Contributions to Mineralogy and Petrology 119, 197-212.

1236 Giannuzzi, L.A., Stevie, F.A., 1999. A review of focused ion beam milling techniques for
1237 TEM specimen preparation. Micron, 30(3), 197-204.

1238 Glodny, J., Bingen, B., Austrheim, H., Molina, J.F., Rusin, A., 2002. Precise eclogitization
1239 ages deduced from Rb/Sr mineral systematics: The Maksyutov complex, Southern Urals,
1240 Russia. Geochimica et Cosmochimica Acta 66, 1221-1235.

1241 Goldschmidt, V.M., 1937. The principles of distribution of chemical elements in minerals and
1242 rocks. Journal of the Chemical Society 37, 655-673.

1243 Goldschmidt, V.M., 1954. Geochemistry. Clarendon Press, Oxford, 730 pp.

1244 Goncalves, P., Oliot, E., Marquer, D., Connolly, J.A.D., 2012. Role of chemical processes on
1245 shear zone formation: an example from the Grimsel metagranodiorite (Aar massif, Central
1246 Alps). Journal of metamorphic Geology 30, 703-722.

1247 Gorman, P. J., Kerrick, D. M., Connolly, J. A. D., 2006. Modeling open system metamorphic
1248 decarbonation of subducting slabs, Geochem. Geophys. Geosyst., 7, Q04007,
1249 doi:10.1029/2005GC001125.

1250 Gottschalk, M., 1997. Internally consistent thermodynamic data for rock forming minerals.
1251 European Journal of Mineralogy 9, 175-223.

1252 Gottschalk, M., 2007. Equations of state for complex fluids. Reviews in Mineralogy and
1253 Geochemistry, 65(1), 49-97.

1254 Grove, T.L., Till, C.B., Lev, E., Chatterjee, N., Médard, E., 2009. Kinematic variables and
1255 water transport control the formation and location of arc volcanoes. Nature 459, 694-697.

1256 Guidotti, C.V., Sassi, F.P., Blencoe, J.G., Selverstone, J., 1994. The paragonite-muscovite
1257 solvus: I. P-T-X limits derived from the Na-K compositions of natural, quasibinary

paragonite-muscovite pairs. Geochimica et Cosmochimica Acta 58, 2269-2275.

Habler, G., Thöni, M., Miller, C., 2007. Major and trace element chemistry and Sm-Nd age correlation of magmatic pegmatite garnet overprinted by eclogite-facies metamorphism. Chemical Geology 241, 4-22.

Hacker, B. R., 2008. H_2O subduction beyond arcs. Geochemistry, Geophysics, Geosystems, 9(3).

Haigis, V., Salanne, M., Simon, S., Wilke, M., Jahn, S., 2013. Molecular dynamics simulations of Y in silicate melts and implications for trace element partitioning. Chemical Geology, 346, 14-21.

Halama, R., John, T., Herms, P., Hauff, F., Schenk, V., 2011. A stable (Li, O) and radiogenic (Sr, Nd) isotope perspective on metasomatic processes in a subducting slab. Chemical Geology 281, 151-166.

Halama, R., Savov, I.P., Garbe-Schönberg, D., Schenk, V., Toulkeridis, T., 2013. Vesuvianite in high-pressure-metamorphosed oceanic lithosphere (Raspas Complex, Ecuador) and its role for transport of water and trace elements in subduction zones. European Journal of Mineralogy 25, 193-219.

Halama, R., Konrad-Schmolke, M., Sudo, M., Marschall, H.R., Wiedenbeck, M., 2014. Effects of fluid-rock interaction on $^{40}Ar/^{39}Ar$ geochronology in high-pressure rocks (Sesia-Lanzo Zone, Western Alps). Geochimica et Cosmochimica Acta 126, 475-494.

Hattori, K., Guillot, S., 2003. Volcanic fronts form as a consequence of serpentinite dehydration in the forearc mantle wedge. Geology 31, 525-528.

Hauthal, W. H., 2001. Advances with supercritical fluids [review]. Chemosphere, 43(1), 123-135.

Hebert, L.B., Asimow, P., Antoshechkina, P., 2009. Fluid source-based modeling of melt initiation within the subduction zone mantle wedge: Implications for geochemical trends in arc lavas. Chemical Geology 266, 297-310.

Hebert, L. B., Montési, L. G., 2013. Hydration adjacent to a deeply subducting slab: The roles of nominally anhydrous minerals and migrating fluids. Journal of Geophysical Research: Solid Earth, 118(11), 5753-5770.

Helgeson, H.C., Delany, J.M., Nesbitt, H.W., Bird, D.K., 1978. Summary and critique of the

thermodynamic properties of rock-forming minerals. American Journal of Science 278-A, 1-229.

Hermann, J., 2002. Allanite: thorium and light rare earth element carrier in subducted crust. Chemical Geology 192: 289-306.

Hermann, J., Rubatto, D., 2009. Accessory phase control on the trace element signature of sediment melts in subduction zones. Chemical Geology 265, 512-526.

Hermann, J., Spandler, C.J., 2008. Sediment melts at sub-arc depths: an experimental study. Journal of Petrology 49, 717-740.

Hermann, J., Spandler, C., Hack, A., Korsakov, A.V., 2006. Aqueous fluids and hydrous melts in high-pressure and ultra-high pressure rocks: Implications for element transfer in subduction zones. Lithos 92, 399-417.

Herms, P., John, T., Bakker, R.J., Schenk, V. 2012. Evidence for channelized external fluid flow and element transfer in subducting slabs (Raspas Complex, Ecuador). Chemical Geology, 310, 79-96.

Hervig, R.L., Moore, G.M., Williams, L.B., Peacock, S.M., Holloway, J.R., Roggensack, K., 2002. Isotopic and elemental partitioning of boron between hydrous fluid and silicate melt. American Mineralogist 87, 769-774.

Hofmann, A.W., 1997. Mantle geochemistry: the message from oceanic volcanism. Nature, 385, 219-229.

Holland, T. J., Hudson, N. F., Powell, R., Harte, B., 2013. New Thermodynamic Models and Calculated Phase Equilibria in NCFMAS for Basic and Ultrabasic Compositions through the Transition Zone into the Uppermost Lower Mantle. Journal of Petrology, 54(9), 1901-1920.

Holland, T., Blundy, J., 1994. Non-ideal interactions in calcic amphiboles and their bearing on amphibole-plagioclase thermometry. Contributions to Mineralogy and Petrology, 116(4), 433-447.

Holland, T.J.B., Powell, R., 1998. An internally consistent thermodynamic data set for phases of petrologic interest. Journal of metamorphic Geology 16, 309-343.

Holland, T., Powell, R., 2003. Activity–composition relations for phases in petrological calculations: an asymmetric multicomponent formulation. Contributions to Mineralogy and Petrology, 145(4), 492-501.

1318 Holland, T.J.B., Powell, R., 2011. An improved and extended internally consistent
1319 thermodynamic dataset for phases of petrological interest, involving a new equation of state
1320 for solids. Journal of Metamorphic Geology, 29(3), 333-383.

1321 Holloway, J.R., 1977. Fugacity and activity of molecular species in supercritical fluids. In:
1322 Thermodynamics in Geology (ed. Fraser, D) Reidel, Boston, 161-181

1323 Hyndman, R. D., Peacock, S. M., 2003. Serpentinization of the forearc mantle. Earth and
1324 Planetary Science Letters 212(3), 417-432.

1325 Ishikawa, T., Nakamura, E., 1994. Origin of the slab component in arc lavas from across-arc
1326 variation of B and Pb isotopes. Nature 370, 205-208.

1327 Ishikawa, T., Tera, F., 1997. Source, composition and distribution of the fluid in the Kurile
1328 mantle wedge: Constraints from across-arc variations of B/Nb and B isotopes. Earth and
1329 Planetary Science Letters 152, 123-138.

1330 Ishikawa, T., Tera, F., 1999. Two isotopically distinct fluid components involved in the
1331 Mariana arc: Evidence from Nb/B ratios and B, Sr, Nd, and Pb isotope systematics. Geology
1332 27, 83-86.

1333 Ishikawa, T., Tera, F., Nakazawa, T., 2001. Boron isotope and trace element systematics of
1334 the three volcanic zones in the Kamchatka arc. Geochimica et Cosmochimica Acta 65, 4523-
1335 4537.

1336 Iwamori, H., 2007. Transportation of H_2O beneath the Japan arcs and its implications for
1337 global water circulation. Chemical Geology, 239(3), 182-198.

1338 Jacob, D.E., 2006. High sensitivity analysis of trace element-poor geological reference glasses
1339 by Laser ablation-inductively coupled plasma-mass spectrometry (LA-ICP-MS).
1340 Geostandards and Geoanalytical Research 30(3): 221-235.

1341 Jahn, S., Wunder, B., 2009. Lithium speciation in aqueous fluids at high P and T studied by
1342 ab initio molecular dynamics and consequences for Li-isotope fractionation between minerals
1343 and fluids. Geochimica et Cosmochimica Acta, 73(18), 5428-5434.

1344 Jamtveit, B., Malthe-Sørenssen, A., Kostenko, O. 2008. Reaction enhanced permeability
1345 during retrogressive metamorphism. Earth and Planetary Science Letters, 267(3), 620-627.

1346 John, T., Scherer, E.E., Haase, K., Schenk, V., 2004. Trace element fractionation during fluid-
1347 induced eclogitization in a subducting slab: trace element and Lu–Hf–Sm–Nd isotope

systematics. Earth and Planetary Science Letters, 227(3), 441-456.

John, T., Scherer, E., Schenk, V., Herms, P., Halama, R., Garbe-Schönberg, D., 2010. Subducted seamounts in an eclogite-facies ophiolite sequence: The Andean Raspas Complex, SW Ecuador. Contributions to Mineralogy and Petrology 159, 265-284.

John, T., Gussone, N., Podladchikov, Y.Y., Bebout, G.E., Dohmen, R., Halama, R., Klemd, R., Magna, T., Seitz, H.M., 2012. Volcanic arcs fed by rapid pulsed fluid flow through subducting slabs. Nature Geoscience, 5(7), 489-492.

Johnson, J.W., Oelkers, E.H., Helgeson, H.C., 1992. SUPCRT92: A software package for calculating the standard molal thermodynamic properties of minerals, gases, aqueous species and reactions from 1 to 5000 bars and 0 to 1000 °C. Computers & Geosciences 18, 899-947.

Kalinichev, A. G., 2001. Molecular simulations of liquid and supercritical water: thermodynamics, structure, and hydrogen bonding. Reviews in Mineralogy and Geochemistry, 42(1), 83-129.

Kawamoto, T., Yoshikawa, M., Kumagai, Y., Mirabueno, M.H.T., Okuno, M., Kobayashi, T., 2013. Mantle wedge infiltrated with saline fluids from dehydration and decarbonation of subducting slab. Proceedings of the National Academy of Sciences 110, 9663-9668.

Kelemen, P.B., Dick, H.J.B., Quick, J.E., 1992. Formation of harzburgite by pervasive melt/rock reaction in the upper mantle. Nature 358, 635-641.

Keller, L.M., Abart, R., Wirth, R., Schmid, D.W., Kunze, K., 2006. Enhanced mass transfer through short-circuit diffusion: growth of garnet reaction rims at eclogite facies conditions. American Mineralogist, 91(7), 1024-1038.

Kelsey, D.E. and Powell, R., 2010. Progress in linking accessory mineral growth and breakdown to major mineral evolution in metamorphic rocks: a thermodynamic approach in the Na_2O-CaO-K_2O-FeO-MgO-Al_2O_3-SiO_2-H_2O-TiO_2-ZrO_2 system. Journal of Metamorphic Geology 29(1), 151-166.

Kerrick, D. M., Jacobs, G. K., 1981. A modified Redlich-Kwong equation for H_2O, CO_2, and H_2O-CO_2 mixtures at elevated pressures and temperatures. American Journal of Science, 281(6), 735-767.

Kessel, R., Schmidt, M. W., Ulmer, P., and Pettke, T., 2005. Trace element signature of subduction-zone fluids, melts and supercritical liquids at 120–180 km depth. Nature, 437(7059), 724-727.

1379 Kimura, J. I., Hacker, B. R., van Keken, P. E., Kawabata, H., Yoshida, T., Stern, R. J., 2009.
1380 Arc Basalt Simulator version 2, a simulation for slab dehydration and fluid-fluxed mantle
1381 melting for arc basalts: Modeling scheme and application. Geochemistry, Geophysics,
1382 Geosystems, 10(9).

1383 Kimura, J. I., Kent, A. J., Rowe, M. C., Katakuse, M., Nakano, F., Hacker, B. R., Stern, R. J.,
1384 2010. Origin of cross-chain geochemical variation in Quaternary lavas from the northern Izu
1385 arc: Using a quantitative mass balance approach to identify mantle sources and mantle wedge
1386 processes. Geochemistry, Geophysics, Geosystems, 11(10).

1387 Kimura, J.I., Gill, J.B., Kunikiyo, T., Osaka, I., Shimoshioiri, Y., Katakuse, M., Kakubuchi,
1388 S., Nagao, T., Furuyama, K., Kamei, A., Kawabata, H., Nakajima, J., van Keken, P.E., Stern,
1389 R.J., 2014. Diverse magmatic effects of subducting a hot slab in SW Japan: results from
1390 forward modeling. Geochemistry Geophysics Geosystems, doi: 10.1002/2013GC005132.

1391 King, R. L., Bebout, G. E., Grove, M., Moriguti, T., and Nakamura, E., 2007. Boron and lead
1392 isotope signatures of subduction-zone mélange formation: hybridization and fractionation
1393 along the slab–mantle interface beneath volcanic arcs. Chemical Geology 239(3), 305-322.

1394 Kohn, M.J., 2003. Geochemical zoning in metamorphic minerals. In: Rudnick, R.L. (Ed), *The*
1395 *Crust*, Treatise on Geochemistry, 3, Elsevier, pp. 229-261.

1396 Konrad-Schmolke, M., Handy, M. R., Babist, J., O'Brien, P. J., 2005. Thermodynamic
1397 modelling of diffusion-controlled garnet growth. Contributions to Mineralogy and Petrology,
1398 149(2), 181-195.

1399 Konrad-Schmolke, M., O'Brien, P. J., Heidelbach, F., 2007. Compositional re-equilibration of
1400 garnet: The importance of sub-grain boundaries. European Journal of Mineralogy 19(4), 431-
1401 438.

1402 Konrad-Schmolke, M., O'Brien, P.J., De Capitani, C., Carswell, D.A., 2008a. Garnet growth
1403 at high- and ultra-high pressure conditions and the effect of element fractionation on mineral
1404 modes and composition. Lithos 103, 309-332.

1405 Konrad-Schmolke, M., O'Brien, P.J., Zack, T., 2011a. Fluid migration above a subducted slab
1406 - constraints on amount, pathways and major element mobility from partially overprinted
1407 eclogite-facies rocks (Sesia Zone, Western Alps). Journal of Petrology 52, 457-486.

1408 Konrad-Schmolke, M., Zack, T., O'Brien, P.J., Barth, M., 2011b. Fluid migration above a

1409 subducted slab - thermodynamic and trace element modelling of fluid-rock interaction in
1410 partially overprinted eclogite-facies rocks (Sesia Zone, Western Alps). Earth and Planetary
1411 Science Letters 311, 287-298.

1412 Konrad-Schmolke, M., Zack, T., O'Brien, P.J., Jacob, D., 2008b. Combined thermodynamic
1413 and rare earth element modelling of garnet growth during subduction: Examples from
1414 ultrahigh-pressure eclogite of the Western Gneiss Region, Norway. Earth and Planetary
1415 Science Letters 272, 488-498.

1416 Korzhinskii, D.S., 1965. The theory of systems with perfectly mobile components and
1417 processes of mineral formation. Am. J. Sci. 263: 193-205.

1418 Koukarri, P., Pajarre, R. 2011. A Gibbs energy minimization method for constrained and
1419 partial equilibria. Pure and Applied Chemistry (83), 6: 1243-1254.

1420 Kowalski, P. M., Wunder, B., Jahn, S., 2013. Ab initio prediction of equilibrium boron
1421 isotope fractionation between minerals and aqueous fluids at high P and T. Geochimica et
1422 Cosmochimica Acta, 101, 285-301.

1423 Kruhl, J. H., Wirth, R., Morales, L. F. (2013): Quartz grain boundaries as fluid pathways in
1424 metamorphic rocks. - Journal of Geophysical Research, 118, 5, p. 1957-1967.

1425 Kulik, D.A., Berner, U., Curti, E., 2004. Modelling chemical equilibrium partitioning with the
1426 GEMS-PSI code, Paul Scherrer Institute, Villigen, Switzerland.

1427 Kulik, D.A., Wagner, T., Dmytrieva, S.V., Kosakowski, G., Hingerl, F.F., Chudnenko, K.V.,
1428 Berner, U., 2013. GEM-Selektor geochemical modeling package: revised algorithm and
1429 GEMS3K numerical kernel for coupled simulation codes. Computational Geosciences 17, 1-
1430 24.

1431 Kylander-Clark, A.R., Hacker, B.R., Cottle, J.M., 2013. Laser-ablation split-stream ICP
1432 petrochronology. Chemical Geology, 345, 99-112.

1433 Leeman, W. P., Carr, M. J., Morris, J. D., 1994. Boron geochemistry of the Central American
1434 volcanic arc: Constraints on the genesis of subduction-related magmas. Geochimica et
1435 Cosmochimica Acta, 58(1), 149-168.

1436 Leeman, W.P., Tonarini, S., Chan, L.-H., Borg, L.E., 2004. Boron and lithium isotopic
1437 variations in a hot subduction zone - the southern Washington Cascades. Chemical Geology
1438 212, 101-124.

1439 Manea, V.C., Manea, M., 2007. Thermal models beneath Kamchatka and the Pacific plate

1440 rejuvenation from a mantle plume impact. In: J. Eichelberger, P. Izbekov, N. Ruppert, E.
1441 Gordeev and J. Lees (Editors), Volcanism and Tectonics of the Kamchatka peninsula and
1442 adjacent arcs, Geophysical Monograph Series. Geophysical Monograph Series, pp. 77-90.

1443 Manning, C. E., 2004. The chemistry of subduction-zone fluids. Earth and Planetary Science
1444 Letters 223, (1-2): 1-16.

1445 Manning, C.E., Wilke, M., Schmidt, C., Cauzid, J., 2008. Rutile solubility in albite-H_2O and
1446 $Na_2Si_3O_7$-H_2O at high temperatures and pressures by in-situ synchrotron radiation micro-
1447 XRF. Earth and Planetary Science Letters, 272(3-4), 730-737.

1448 Margules, M., 1895. Über die Zusammensetzung der gesättigten Dämpfe von Mischungen.
1449 Sitzungsberichte der Kaiserliche Akademie der Wissenschaften Wien Mathematisch-
1450 Naturwissenschaftliche Klasse II 104, 1243–1278.

1451 Marmo, B.A., Clarke, G.L., Powell, R., 2002. Fractionation of bulk rock composition due to
1452 porphyroblast growth: effects on eclogite facies mineral equilibria, Pam Peninsula, New
1453 Caledonia. Journal of Metamorphic Geology 20(1): 151-165.

1454 Marschall, H.R., Altherr, R., Gméling, K., Kasztovszky, Z., 2009. Lithium, boron and
1455 chlorine as tracers for metasomatism in high-pressure metamorphic rocks: a case study from
1456 Syros (Greece). Mineralogy and Petrology.

1457 Marschall, H.R., Altherr, R., Ludwig, T., Kalt, A., Gméling, K., Kasztovszky, Z., 2006.
1458 Partitioning and budget of Li, Be and B in high-pressure metamorphic rocks. Geochimica et
1459 Cosmochimica Acta 70, 4750-4769.

1460 Marschall, H.R., Altherr, R., Rüpke, L., 2007. Squeezing out the slab - modelling the release
1461 of Li, Be and B during progressive high-pressure metamorphism. Chemical Geology 239,
1462 323-335.

1463 Martin, L.A., Rubatto, D., Crépisson, C., Hermann, J., Putlitz, B., Vitale-Brovarone, A., 2014.
1464 Garnet oxygen analysis by SHRIMP-SI: Matrix corrections and application to high-pressure
1465 metasomatic rocks from Alpine Corsica. Chemical Geology, 374, 25-36.

1466 Massonne, H.-J., Schreyer, W., 1987. Phengite geobarometry based on the limiting
1467 assemblage with K-feldspar, phlogopite, and quartz. Contributions to Mineralogy and
1468 Petrology 96, 212-224.

1469 Matsui, M., Parker, S. C., & Leslie, M. (2000). The MD simulation of the equation of state of
1470 MgO: Application as a pressure calibration standard at high temperature and high pressure.
1471 American Mineralogist, 85(2), 312-316.

1472 McKenzie, D., O'Nions, R.K., 1991. Partial melt distributions from inversion of Rare Earth
1473 Element concentrations. Journal of Petrology 32, 1021-1091.

1474 Moriguti, T., Nakamura, E., 1998. Across-arc variation of Li isotopes in lavas and
1475 implications for crust/mantle recycling at subduction zones. Earth and Planetary Science
1476 Letters 163, 167-174.

1477 Moriguti, T., Shibata, T., Nakamura, E., 2004. Lithium, boron and lead isotope and trace
1478 element systematics of Quaternary basaltic volcanic rocks in northeastern Japan:
1479 mineralogical controls on slab-derived fluid composition. Chemical Geology 212, 81-100.

1480 Morris, J.D., Leeman, W.P., Tera, F., 1990. The subducted component in island arc lavas:
1481 constraints from Be isotopes and B-Be systematics. Nature 344, 31-36.

1482 Nabelek, P.I., 1987. General equations for modeling fluid/rock interaction using trace
1483 elements and isotopes. Geochimica et Cosmochimica Acta, 51(6), 1765-1769.

1484 Nabelek, P. I., Denison, J. R., Glascock, M. D., 1990. Behavior of boron during contact
1485 metamorphism of calc-silicate rocks at Notch Peak, Utah. American Mineralogist, 75(7-8),
1486 874-880.

1487 Nagel, T.J., Hoffmann, J.E., Münker, C., 2012. Generation of Eoarchean tonalite-
1488 trondhjemite-granodiorite series from thickened mafic arc crust. Geology 40, 375-378.

1489 O'Hara, M.J., 1977. Geochemical evolution during fractional crystallization of a periodically
1490 refilled magma chamber. Nature 266, 503-507.

1491 Oelkers, E.H., Bénézeth, P., Pokrovski, G.S., 2009. Thermodynamic databases for water-rock
1492 interaction. Reviews in Mineralogy and Geochemistry 70, 1-56.

1493 Oliver, N.H.S., 1996. Review and classification of structural controls on fluid flow during
1494 regional metamorphism. Journal of Metamorphic Geology, 14(4), 477-492.

1495 Ottonello, G., Civalleri, B., Ganguly, J., Perger, W.F., Belmonte, D., Zuccolini, M.V., 2010.
1496 Thermo-chemical and thermo-physical properties of the high-pressure phase anhydrous B
1497 ($Mg_{14}Si_5O_{24}$): An ab-initio all-electron investigation. American Mineralogist, 95(4), 563-573.

1498 Pabst, S., Zack, T., Savov, I.P., Ludwig, T., Rost, D., Vicenzi, E.P., 2011. Evidence for boron
1499 incorporation into the serpentine crystal structure. American Mineralogist 96, 1112-1119.

Pabst, S., Zack, T., Savov, I.P., Ludwig, T., Rost, D., Tonarini, S., Vicenzi, E.P., 2012. The fate of subducted oceanic slabs in the shallow mantle: Insights from boron isotopes and light element composition of metasomatized blueschists from the Mariana forearc. Lithos 132-133, 162-179.

Padrón-Navarta, J. A., Sánchez-Vizcaíno, V. L., Hermann, J., Connolly, J. A., Garrido, C. J., Gómez-Pugnaire, M. T., & Marchesi, C. (2013). Tschermak's substitution in antigorite and consequences for phase relations and water liberation in high-grade serpentinites. Lithos, 178, 186-196.

Paquin, J., Altherr, R., and Ludwig, T., 2004. Li–Be–B systematics in the ultrahigh-pressure garnet peridotite from Alpe Arami (Central Swiss Alps): implications for slab-to-mantle wedge transfer. Earth and Planetary Science Letters, 218(3), 507-519.

Parkhurst, D.L., Appelo, C.A.J., 1999. User's guide to PHREEQC (version 2) - a computer program for speciation, batch-reaction, one-dimensional transport, and inverse geochemical calculations.

Peacock, S.M., Hervig, R.L., 1999. Boron isotopic composition of subduction-zone metamorphic rocks. Chemical Geology 160, 281-290.

Pearce, J.A., Peate, D.W., 1995. Tectonic implications of the composition of volcanic arc magmas. Annu. Rev. Earth Planet. Sci. 23, 251-285.

Pearce, J.A., 2008. Geochemical fingerprinting of oceanic basalts with applications to ophiolite classification and the search for Archean oceanic crust. Lithos, 100(1), 14-48.

Pearce, M.A., Wheeler, J., 2010. Modelling grain-recycling zoning during metamorphism. Journal of metamorphic Geology 28, 423-437.

Plank, T., Langmuir, C.H., 1993. Tracing trace elements from sediment input to volcanic output at subduction zones. Nature 362, 739-743.

Plank, T., Langmuir, C. H. 1998. The chemical composition of subducting sediment and its consequences for the crust and mantle. Chem. Geol. 145, 325-394.

Pollington, A.D., Baxter, E.F., 2010. High resolution Sm-Nd garnet geochronology reveals the uneven pace of tectonometamorphic processes. Earth and Planetary Science Letters 293, 63-71.

Powell, R., Holland, T.J.B., 1988. An internally consistent data set with uncertainties and correlations: 3. Applications to geobarometry, worked examples and a computer program.

1531 Journal of Metamorphic Geology 6, 173-204.

1532 Powell, R., Holland, T. J. B., 2008. On thermobarometry. Journal of Metamorphic Geology,
1533 26(2), 155-179.

1534 Powell, R., Guiraud, M., White, R.W., 2005. Truth and beauty in metamorphic phase-
1535 equilibria: conjugate variables and phase diagrams. The Canadian Mineralogist, 43(1), 21-33.

1536 Prausnitz, J.M., 1969. Molecular Thermodynamics of Fluid-Phase Equilibria, 523 pp.
1537 Prentice-Hall.

1538 Putnis, C.V., Mezger, K., 2004. A mechanism of mineral replacement: isotope tracing in the
1539 model system KCl-KBr-H_2O. Geochimica et Cosmochimica Acta, 68(13), 2839-2848.

1540 Putnis, A., Austrheim, H., 2010. Fluid-induced processes: metasomatism and metamorphism.
1541 Geofluids, 10(1-2), 254-269.

1542 Ranero, C.R., Phipps Morgan, J., McIntosh, K., Reichert, C., 2003. Bending-related faulting
1543 and mantle serpentinization at the Middle American trench. Nature 425, 367-373.

1544 Ranero, C.R., Sallarès, V., 2004. Geophysical evidence for hydration of the crust and mantle
1545 of the Nazca plate during bending at the north Chile trench. Geology 32, 549-552.

1546 Redlich, O. and Kwong, J.N.S., 1949. An equation of state. Fugacities of gaseous solutions.
1547 Chem. Rev. 44: 233-244.

1548 Robie, R.A. and Hemingway, B.S. 1995. Thermodynamic Properties of Minerals and Related
1549 Substances at 298.15 K and 1 Bar (10^5 Pascals) Pressure and at Higher Temperature, U. S.
1550 Geological Survey, Washington, DC, 461 pp.

1551 Rose, E. F., Chaussidon, M., France-Lanord, C., 2000. Fractionation of boron isotopes during
1552 erosion processes: the example of Himalayan rivers. Geochimica et Cosmochimica Acta
1553 64(3), 397-408.

1554 Rosner, M., Erzinger, J., Franz, G., Trumbull, R.B., 2003. Slab-derived boron isotope
1555 signatures in arc volcanic rocks from the Central Andes and evidence for boron isotope
1556 fractionation during progressive slab dehydration. Geochemistry Geophysics Geosystems
1557 4(8), 9005, doi:10.1029/2002GC000438.

1558 Rosner, M., Wiedenbeck, M., and Ludwig, T., 2008. Composition-induced variations in SIMS
1559 instrumental mass fractionation during boron isotope ratio measurements of silicate glasses.
1560 Geostandards and Geoanalytical Research 32(1), 27-38.

1561 Rüpke, L. H., Morgan, J. P., Hort, M., and Connolly, J. A., 2004. Serpentine and the
1562 subduction zone water cycle. Earth and Planetary Science Letters 223(1), 17-34.

1563 Rüpke, L., Phipps Morgan, J., and Eaby Dixon, J., 2006. Implications of subduction
1564 rehydration for Earth's deep water cycle. Geophysical Monograph Series, 168, 263-276.

1565 Ryan, J., Morris, J., Bebout, G.E., Leeman, W.P., 1996. Describing chemical fluxes in
1566 subduction zones: insights from "depth-profiling" studies of arc and forearc rocks. In: G.E.
1567 Bebout, D.W. Scholl, S.H. Kirby and J.P. Platt (Editors), Subduction top to bottom. American
1568 Geophysical Union Monograph, pp. 263-268.

1569 Ryan, J., Morris, J., Tera, F., Leeman, W.P., Tsvetkov, A., 1995. Cross-arc geochemical
1570 variations in the Kurile arc as a function of slab depth. Science 270, 625-627.

1571 Ryan, J.G., Langmuir, C.H., 1993. The systematics of boron abundances in young volcanic
1572 rocks. Geochimica et Cosmochimica Acta 57, 1489-1498.

1573 Ryan, J.G. and Chauvel, C., 2013. The Subduction Zone Conveyor and the Impact of
1574 Recycled Materials on the Evolution of the Mantle. Chapter 2.11 The Mantle and Core
1575 (Carlson, R. Ed.), Treatise on Geochemistry, Second Edition (in press)

1576 Sanchez-Valle, C., Reynard, B., Daniel, I., Lecuyer, C., Martinez, I., Chervin, J.-C., 2005.
1577 Boron isotopic fractionation between minerals and fluids: New insights from in situ high
1578 pressure-high temperature vibrational spectroscopic data. Geochimica et Cosmochimica Acta
1579 69, 4301-4313.

1580 Sano, T., Hasenaka, T., Shimaoka, A., Yonezawa, C., and Fukuoka, T., 2001. Boron contents
1581 of Japan Trench sediments and Iwate basaltic lavas, Northeast Japan arc: estimation of
1582 sediment-derived fluid contribution in mantle wedge. Earth and Planetary Science Letters,
1583 186(2), 187-198.

1584 Savov, I.P., Ryan, J.G., D'Antonio, M., Fryer, P., 2007. Shallow slab fluid release across and
1585 along the Mariana arc-basin system: Insights from geochemistry of serpentinized peridotites
1586 from the Mariana fore arc. Journal of Geophysical Research 112, B09205,
1587 doi:10.1029/2006JB004749.

1588 Savov, I.P., Ryan, J.G., D'Antonio, M., Kelley, K., Mattie, P., 2005. Geochemistry of
1589 serpentinized peridotites from the Mariana Forearc Conical Seamount, ODP Leg 125:
1590 Implications for the elemental recycling at subduction zones. Geochemistry Geophysics
1591 Geosystems 6, Q04J15, doi:10.1029/2004GC000777.

1592 Scambelluri, M., Bottazzi, P., Trommsdorff, V., Vannucci, R., Hermann, J., Gómez-Pugnaire,
1593 M.T., López-Sánchez Vizcaíno, V., 2001. Incompatible element-rich fluids released by
1594 antigorite breakdown in deeply subducted mantle. Earth and Planetary Science Letters 192,
1595 457-470.

1596 Scambelluri, M., Müntener, O., Ottolini, L., Pettke, T., Vannucci, R., 2004. The fate of B, Cl
1597 and Li in the subducted oceanic mantle and in antigorite breakdown fluids. Earth and
1598 Planetary Science Letters 222, 217-234.

1599 Scambelluri, M., Tonarini, S., 2012. Boron isotope evidence for shallow fluid transfer across
1600 subduction zones by serpentinized mantle. Geology 40, 907-910.

1601 Schmidt, M.W., Poli, S. 1998. Experimentally based water budgets for dehydrating slabs and
1602 consequences for arc magma generation. Earth and Planetary Science Letters, 163(1), 361-
1603 379.

1604 Sedlbauer, J., O'Connell, J.P., Wood, R.H., 2000. A new equation of state for correlation and
1605 prediction of standard molal thermodynamic properties of aqueous species at high
1606 temperatures and pressures. Chemical Geology, 163(1), 43-63.

1607 Selverstone, J., Morteani, G., Staude, J.-M., 1991. Fluid channelling during ductile shearing:
1608 transformation of granodiorite into aluminous schist in the Tauern Window, Eastern Alps.
1609 Journal of metamorphic Geology 9, 419-431.

1610 Sharp, Z., 2007. Principles of Stable Isotope Geochemistry. Pearson Prentice Hall, Upper
1611 Saddle River, New Jersey, 344 pp.

1612 Shaw, D.M., 1970. Trace element fractionation during anatexis. Geochimica et
1613 Cosmochimica Acta 34, 237-243.

1614 Shaw, A.M., Hauri, E.H., Behn, M.D., Hilton, D.R., Macpherson, C.G., Sinton, J.M., 2012.
1615 Long-term preservation of slab signatures in the mantle inferred from hydrogen isotopes.
1616 Nature Geoscience 5, 224-228.

1617 Simon, L., Lécuyer, C., Maréchal, C., and Coltice, N., 2006. Modelling the geochemical cycle
1618 of boron: Implications for the long-term $\delta^{11}B$ evolution of seawater and oceanic crust.
1619 Chemical Geology 225(1), 61-76.

1620 Skora, S., Baumgartner, L. P., Mahlen, N. J., Johnson, C. M., Pilet, S., and Hellebrand, E.,
1621 2006. Diffusion-limited REE uptake by eclogite garnets and its consequences for Lu–Hf and
1622 Sm–Nd geochronology. Contributions to Mineralogy and Petrology, 152(6), 703-720.

1623 Smith, H.J., Leeman, W.P., Davidson, J., Spivack, A.J., 1997. The B isotopic composition of
1624 arc lavas from Martinique, Lesser Antilles. Earth and Planetary Science Letters 146, 303-314.

1625 Sorensen, S.S., Grossman, J.N., 1989. Enrichment of trace elements in garnet amphibolites
1626 from a paleo-subduction zone: Catalina Schist, southern California. Geochimica et
1627 Cosmochimica Acta 53, 3155-3177.

1628 Spandler, C., Pirard, C., 2013. Element recycling from subducting slabs to arc crust: A
1629 review. Lithos 170-171, 208-223.

1630 Spear, F.S., 1988. Metamorphic fractional crystallization and internal metasomatism by
1631 diffusional homogenization of zoned garnets. Contributions to Mineralogy and Petrology 99,
1632 507-517.

1633 Spear, F.S., Menard, T., 1989. Program GIBBS: A generalized Gibbs method algorithm.
1634 American Mineralogist 74, 942-943.

1635 Spear, F.S., Selverstone, J., 1983. Quantitative P-T paths from zoned minerals: Theory and
1636 tectonic applications. Contributions to Mineralogy and Petrology 83, 348-357.

1637 Spivack, A.J., Edmond, J.M., 1987. Boron isotope exchange between seawater and the
1638 oceanic crust. Geochimica et Cosmochimica Acta 51, 1033-1043.

1639 Stixrude, L., and Lithgow-Bertelloni, C., 2005. Thermodynamics of mantle minerals–I.
1640 Physical properties. Geophysical Journal International 162(2), 610-632.

1641 Straub, S.M., Layne, G.D., 2003. The systematics of chlorine, fluorine, and water in Izu arc
1642 front volcanic rocks: Implications for volatile recycling in subduction zones. Geochimica et
1643 Cosmochimica Acta 67, 4179-4203.

1644 Tatsumi, Y., Hamilton, D.L., Nesbitt, R.W., 1986. Chemical characteristics of fluid phase
1645 released from a subducted lithosphere and origin of arc magmas: evidence from high-pressure
1646 experiments and natural rocks. Journal of Volcanology and Geothermal Research 29, 293-
1647 309.

1648 Taura, H., Yurimoto, H., Kurita, K., Sueno, S., 1998. Pressure dependence on partition
1649 coefficients for trace elements between olivine and the coexisting melts. Contributions to
1650 Mineralogy and Petrology 25, 469-484.

1651 Taylor, J.H.P., Epstein, S., 1962. Relationship between O^{18}/O^{16} ratios in coexisting minerals
1652 of igneous and metamorphic rocks, Part 2: Application to petrologic problems. . Geological
1653 Society of America Bulletin 73, 675-694.

1654 Thompson, A.B., England, P.C., 1984. Pressure—Temperature—Time Paths of Regional
1655 Metamorphism II. Their Inference and Interpretation using Mineral Assemblages in
1656 Metamorphic Rocks. Journal of Petrology, 25(4), 929-955.

1657 Till, C.B., Grove, T.L., Withers, A., 2012. The beginnings of hydrous mantle wedge melting.
1658 Contributions to Mineralogy and Petrology 163, 669-688.

1659 Tonarini, S., Armienti, P., D'Orazio, M., Innocenti, F., 2001. Subduction-like fluids in the
1660 genesis of Mt. Etna magmas: evidence from boron isotopes and fluid mobile elements. Earth
1661 and Planetary Science Letters 192, 471-483.

1662 Tonarini, S., Agostini, S., Doglioni, C., Innocenti, F., Manetti, P., 2007. Evidence for
1663 serpentinite fluid in convergent margin systems: The example of El Salvador (Central
1664 America) arc lavas. Geochemistry Geophysics Geosystems 8, Q09014,
1665 doi:10.1029/2006GC001508.

1666 Tonarini, S., Leeman, W.P., Leat, P.T., 2011. Subduction erosion of forearc mantle wedge
1667 implicated in the genesis of the South Sandwich Island (SSI) arc: Evidence from boron
1668 isotope systematics. Earth and Planetary Science Letters 301, 275-284.

1669 Trumbull, R.B., Krienitz, M.-S., Gottesmann, B., Wiedenbeck, M., 2008. Chemical and
1670 boron-isotope variations in tourmalines from an S-type granite and its source rocks: the
1671 Erongo granite and tourmalinites in the Damara Belt, Namibia. Contributions to Mineralogy
1672 and Petrology 155, 1-18.

1673 Trumbull, R.B., Krienitz, M.-S., Grundmann, G., Wiedenbeck, M., 2009. Tourmaline
1674 geochemistry and $d^{11}B$ variations as a guide to fluid-rock interaction in the Habachtal emerald
1675 deposit, Tauern Window, Austria. Contributions to Mineralogy and Petrology 157, 411-427.

1676 Tsay, A., Zajacz, Z., Sanchez-Valle, C., 2014. Efficient mobilization and fractionation of rare-
1677 earth elements by aqueous fluids upon slab dehydration. Earth and Planetary Science Letters,
1678 398, 101-112.

1679 Turner, S., Tonarini, S., Bindeman, I., Leeman, W.P., Schaefer, B.F., 2007. Boron and
1680 oxygen isotope evidence for recycling of subducted components over the past 2.5 Gyr. Nature
1681 447, 702-705.

1682 Ulmer, P., Trommsdorff, V., 1995. Serpentine stability to mantle depths and subduction-
1683 related magmatism. Science 268, 858-861.

1684 Valle, N., Drillet, J., Pic, A., Migeon, H. N., 2011. Nano-SIMS investigation of boron

distribution in steels. Surface and Interface Analysis 43(1-2), 573-575.

van der Straaten, F., Halama, R., John, T., Schenk, V., Hauff, F., Andersen, N., 2012. Tracing the effects of high-pressure metasomatic fluids and seawater alteration in blueschist-facies overprinted eclogites: Implications for subduction channel processes. Chemical Geology 292-293, 69-87.

Van Hinsberg, V. J., Vriend, S. P., Schumacher, J. C. (2005). A new method to calculate end-member thermodynamic properties of minerals from their constituent polyhedra I: enthalpy, entropy and molar volume. Journal of Metamorphic Geology 23(3), 165-179.

Van Hinsberg, V. J., Henry, D. J., Dutrow, B. L., 2011. Tourmaline as a petrologic forensic mineral: A unique recorder of its geologic past. Elements 7(5), 327-332.

van Keken, P. E., Hacker, B. R., Syracuse, E. M., Abers, G. A., 2011. Subduction factory: 4. Depth-dependent flux of H_2O from subducting slabs worldwide. Journal of Geophysical Research 116, B01401.

Van Laar, J.J., 1910. Ueber Dampfspannung von binären Gemischen. Zeitschrift für Physikalische Chemie 72, 723-751.

Velde, B., 1965. Phengite micas: Synthesis, stability, and natural occurrence. American Journal of Science 263, 886-913.

Vils, F., Tonarini, S., Kalt, A., Seitz, H.-M., 2009. Boron, lithium and strontium isotopes as tracers of seawater-serpentinite interaction at Mid-Atlantic ridge, ODP leg 209. Earth and Planetary Science Letters 286, 414-425.

Warren, C.J., Kelley, S.P., Sherlock, S.C., McDonald, C.S., 2012. Metamorphic rocks seek meaningful cooling rate: Interpreting $^{40}Ar/^{39}Ar$ ages in an exhumed ultra-high pressure terrane. Lithos 155, 30-48.

Warren, C.J., Sherlock, S.C., Kelley, S.P., 2011. Interpreting high-pressure phengite $^{40}Ar/^{39}Ar$ laserprobe ages: an example from Saih Hatat, NE Oman. Contributions to Mineralogy and Petrology 161, 991-1009.

Weaver, B.L., 1991. Trace element evidence for the origin of ocean-island basalts. Geology 19, 123-126.

White, W.M., 2013. Geochemistry. Wiley-Blackwell, Chichester, 660 pp.

Wilke, M., Schmidt, C., Dubrail, J., Appel, K., Borchert, M., Kvashnina, K., Manning, C.E.,

2012. Zircon solubility and zirconium complexation in H_2O+ Na_2O+ SiO_2±Al_2O_3 fluids at high pressure and temperature. Earth and Planetary Science Letters, 349, 15.

Workman, R. K., Hart, S. R. 2005. Major and trace element composition of the depleted MORB mantle (DMM). Earth Planet. Sci. Lett. 231, 53-72.

Wunder, B., Meixner, A., Romer, R.L., Wirth, R., Heinrich, W., 2005. The geochemical cycle of boron: Constraints from boron isotope partitioning experiments between mica and fluid. Lithos 84, 205-216.

Yamaoka, K. et al., 2012. Boron and oxygen isotope systematics for a complete section of oceanic crustal rocks in the Oman ophiolite. Geochimica et Cosmochimica Acta 84, 543-559.

Yardley, B.W.D., Rochelle, C.A., Barnicoat, A.C., Lloyd, G.E., 1991. Oscillatory zoning in metamorphic minerals: an indicator of infiltration metasomatism. Mineralogical Magazine, 55(380), 357-365.

Zack, T., John, T. 2007. An evaluation of reactive fluid flow and trace element mobility in subducting slabs. Chemical Geology 239, 199-216.

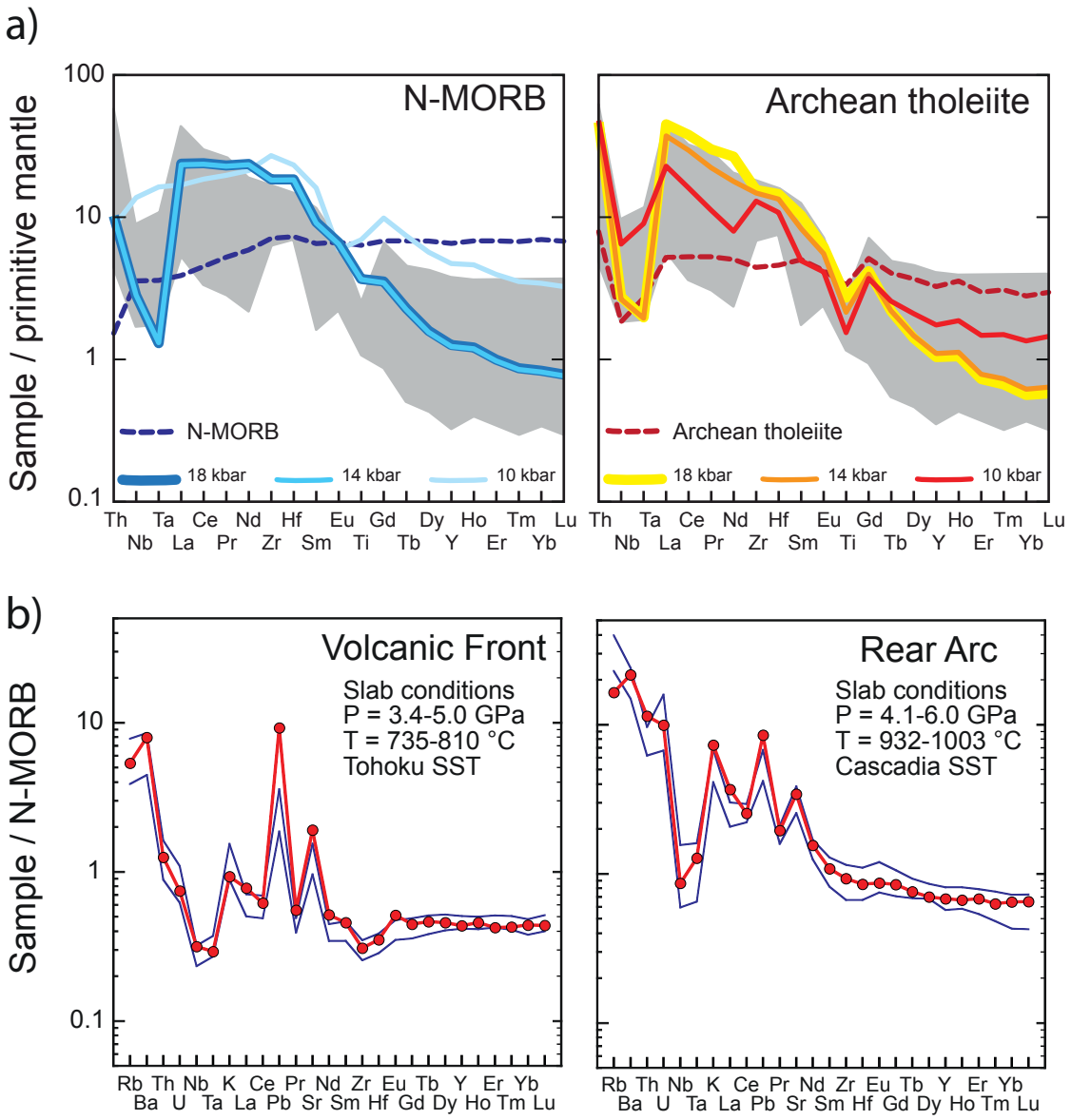
a)
Sample / primitive mantle
100
10
1
0.1
N-MORB
N-MORB
18 kbar
14 kbar
10 kbar
Archean tholeiite
Archean tholeiite
18 kbar
14 kbar
10 kbar
Th Ta Ce Nd Hf Eu Gd Dy Ho Tm Lu
Nb La Pr Zr Sm Ti Tb Y Er Yb
b)
Sample / N-MORB
10
1
0.1
Volcanic Front
Slab conditions
P = 3.4-5.0 GPa
T = 735-810 °C
Tohoku SST
Rear Arc
Slab conditions
P = 4.1-6.0 GPa
T = 932-1003 °C
Cascadia SST
Rb Th Nb K Ce Pr Nd Zr Eu Tb Y Er Yb
Ba U Ta La Pb Sr Sm Hf Gd Dy Ho Tm Lu

Fig. 01

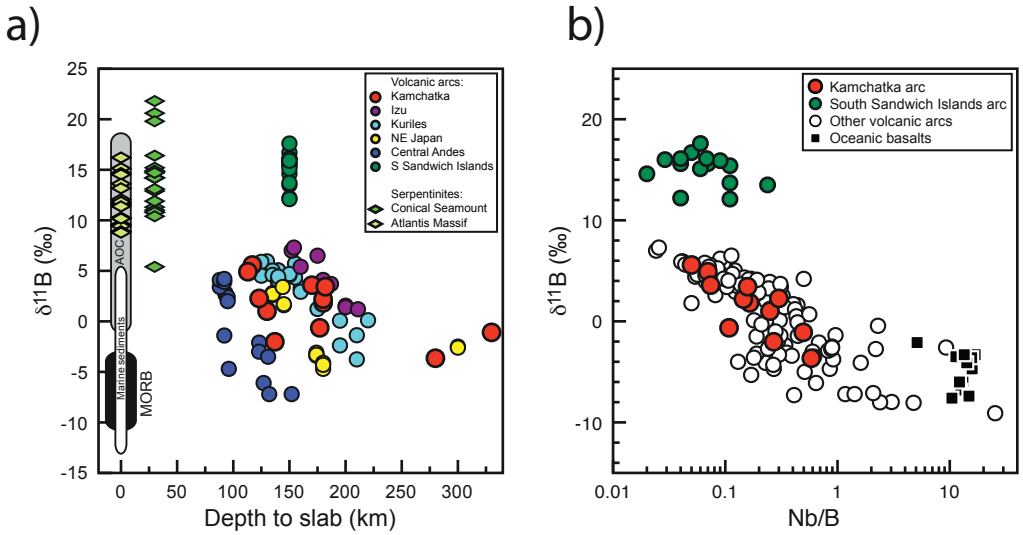
a)
b)
Volcanic arcs:
Kamchatka
Izu
Kuriles
NE Japan
Central Andes
S Sandwich Islands
Serpentinites:
Conical Seamount
Atlantis Massif
AOC
Marine sediments
MORB
δ11B (‰)
Depth to slab (km)
Kamchatka arc
South Sandwich Islands arc
Other volcanic arcs
Oceanic basalts
Nb/B

Fig. 02

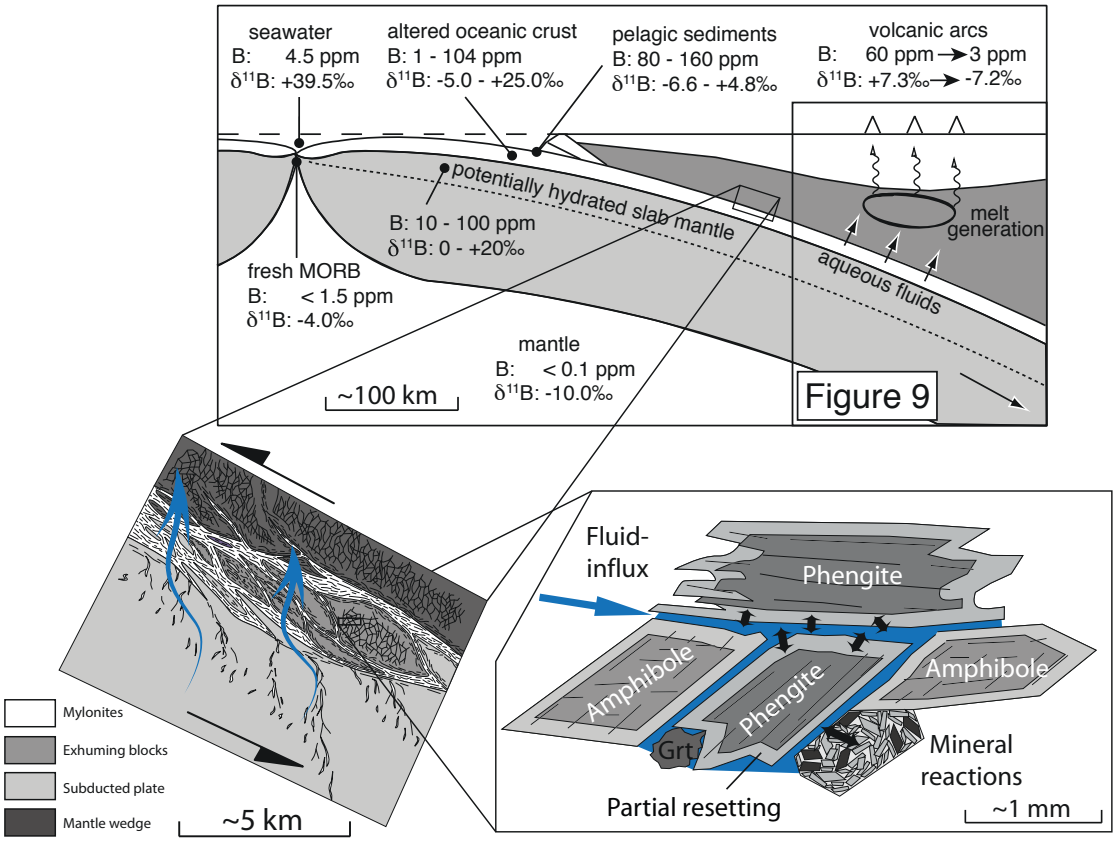
seawater
B: 4.5 ppm
δ11B: +39.5‰
altered oceanic crust
B: 1 - 104 ppm
δ11B: -5.0 - +25.0‰
pelagic sediments
B: 80 - 160 ppm
δ11B: -6.6 - +4.8‰
volcanic arcs
B: 60 ppm → 3 ppm
δ11B: +7.3‰ → -7.2‰
potentially hydrated slab mantle
B: 10 - 100 ppm
δ11B: 0 - +20‰
melt generation
aqueous fluids
fresh MORB
B: < 1.5 ppm
δ11B: -4.0‰
mantle
B: < 0.1 ppm
δ11B: -10.0‰
~100 km
Figure 9
Mylonites
Exhuming blocks
Subducted plate
Mantle wedge
~5 km
Fluid-influx
Phengite
Amphibole
Phengite
Amphibole
Grt
Mineral reactions
Partial resetting
~1 mm

Fig. 03

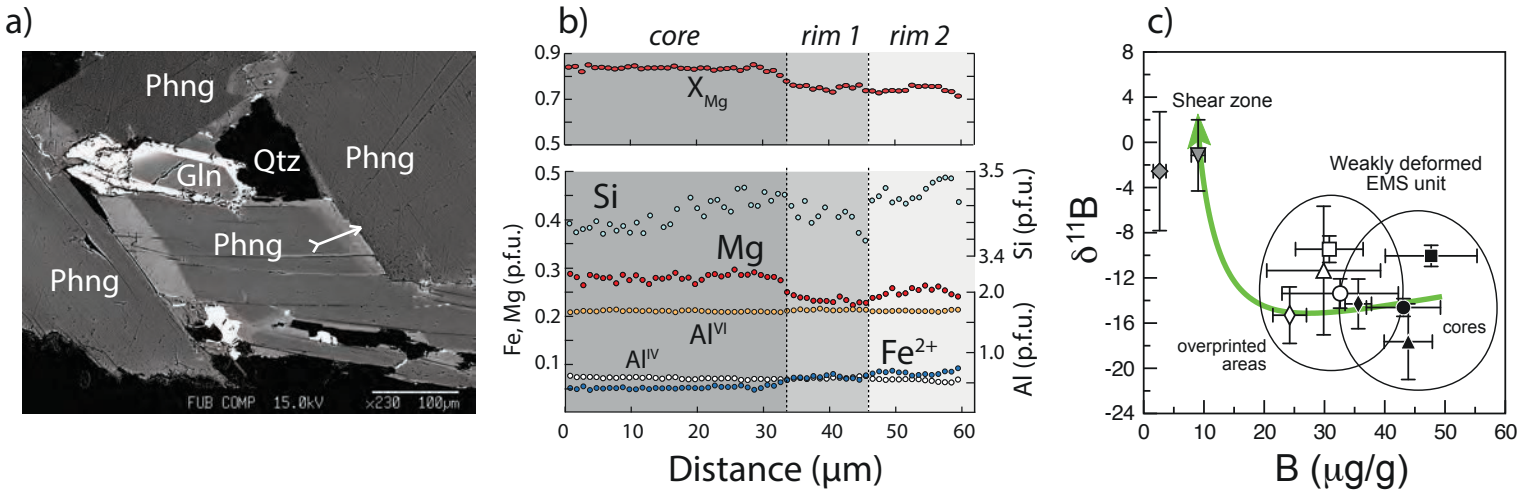
a)
Phng
Qtz
Gln
Phng
Phng
Phng
FUB COMP 15.0kV ×230 100µm
b)
core
rim 1
rim 2
X_Mg
Si
Mg
Al^VI
Al^IV
Fe^2+
Fe, Mg (p.f.u.)
Si (p.f.u.)
Al (p.f.u.)
Distance (µm)
c)
Shear zone
Weakly deformed EMS unit
overprinted areas
cores
δ11B
B (µg/g)

Fig. 04

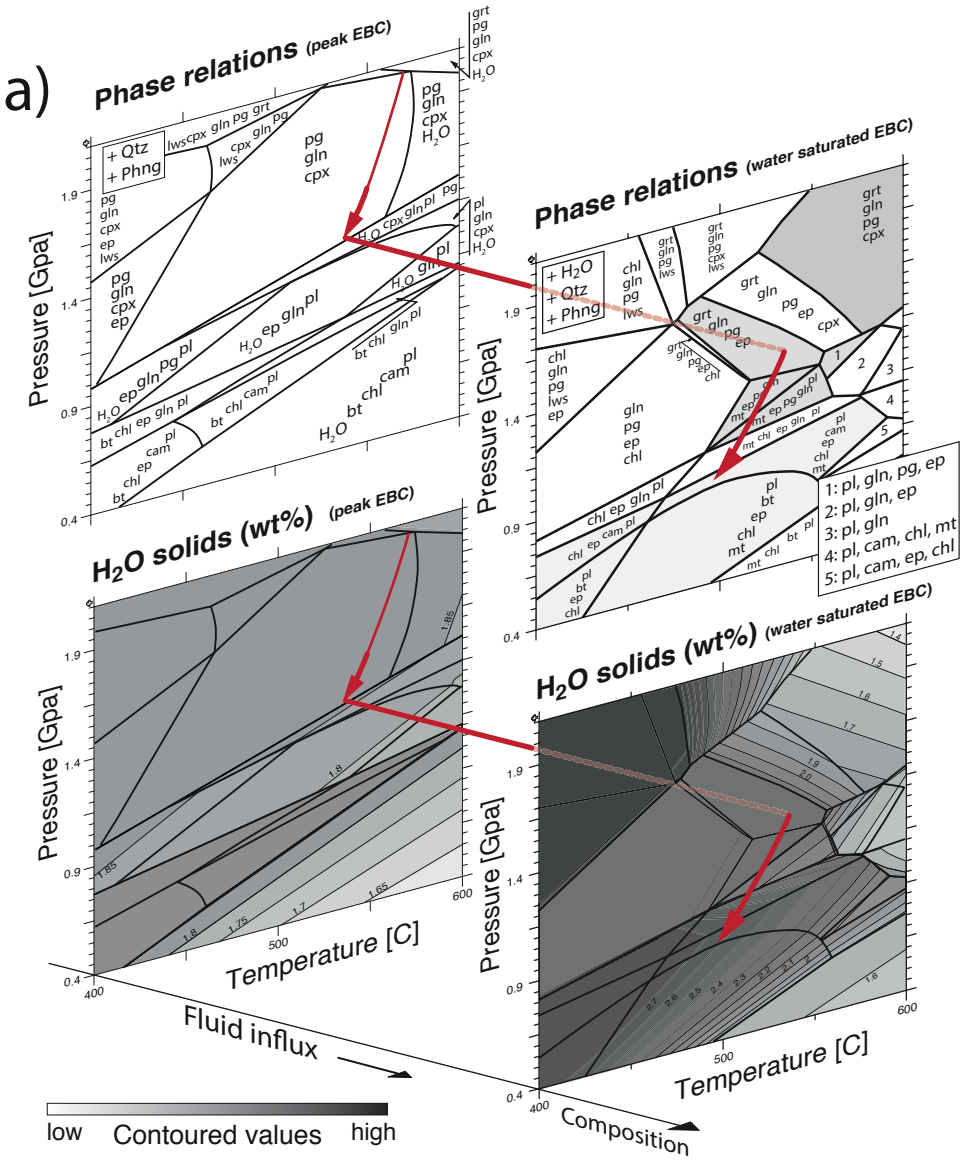
a)
Phase relations (peak EBC)
Phase relations (water saturated EBC)
+ Qtz
+ Phng
+ H2O
Pressure [Gpa]
H2O solids (wt%) (peak EBC)
H2O solids (wt%) (water saturated EBC)
Temperature [C]
Fluid influx
Composition
1: pl, gln, pg, ep
2: pl, gln, ep
3: pl, gln
4: pl, cam, chl, mt
5: pl, cam, ep, chl
low
Contoured values
high

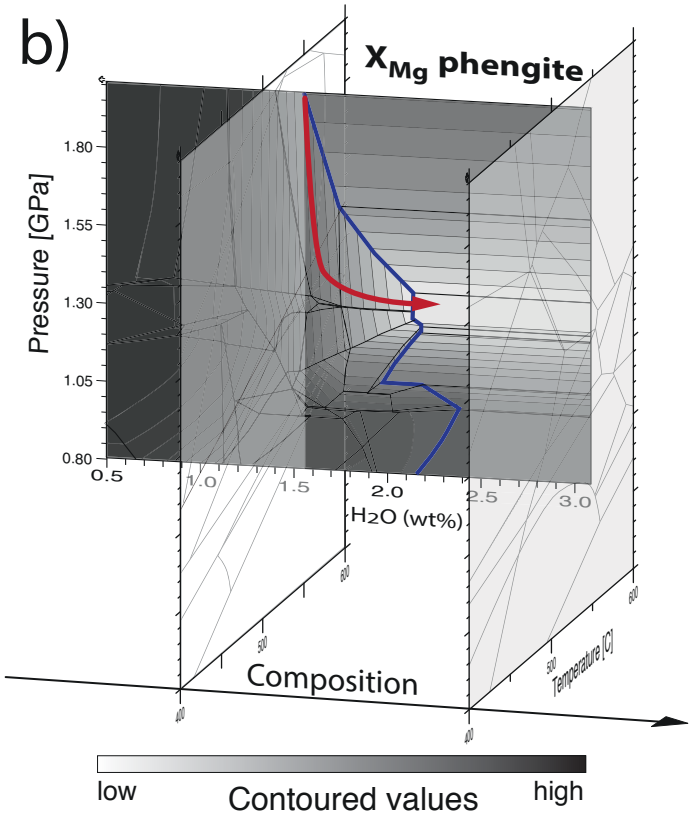
b)
XMg phengite
Pressure [GPa]
H2O (wt%)
Composition
Temperature [C]
low
Contoured values
high

Fig. 05

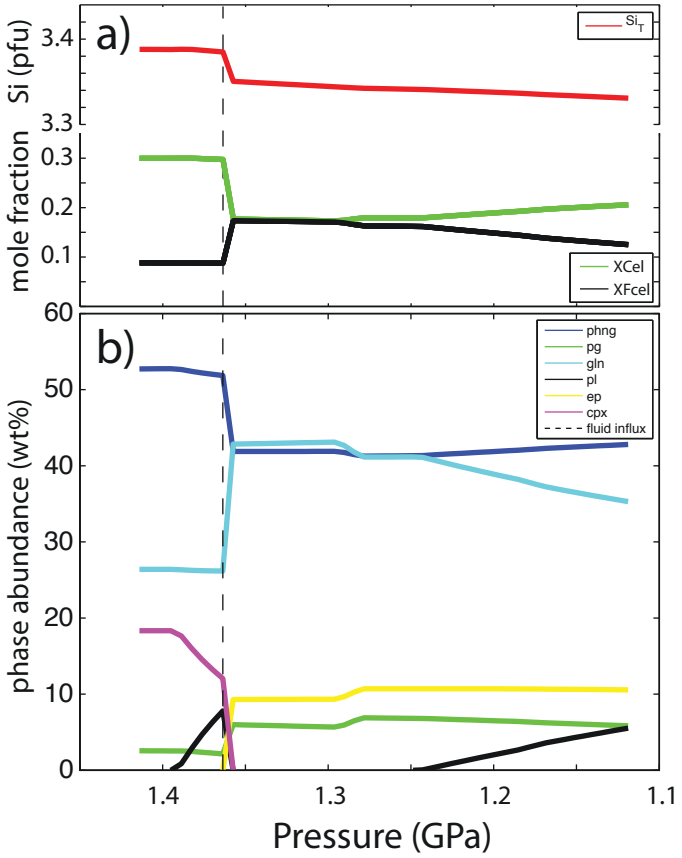
a)
b)
Si (pfu)
mole fraction
phase abundance (wt%)
Pressure (GPa)
Si_T
XCel
XFcel
phng
pg
gln
pl
ep
cpx
fluid influx
3.4
3.3
0.3
0.2
0.1
60
50
40
30
20
10
0
1.4
1.3
1.2
1.1

Fig. 06

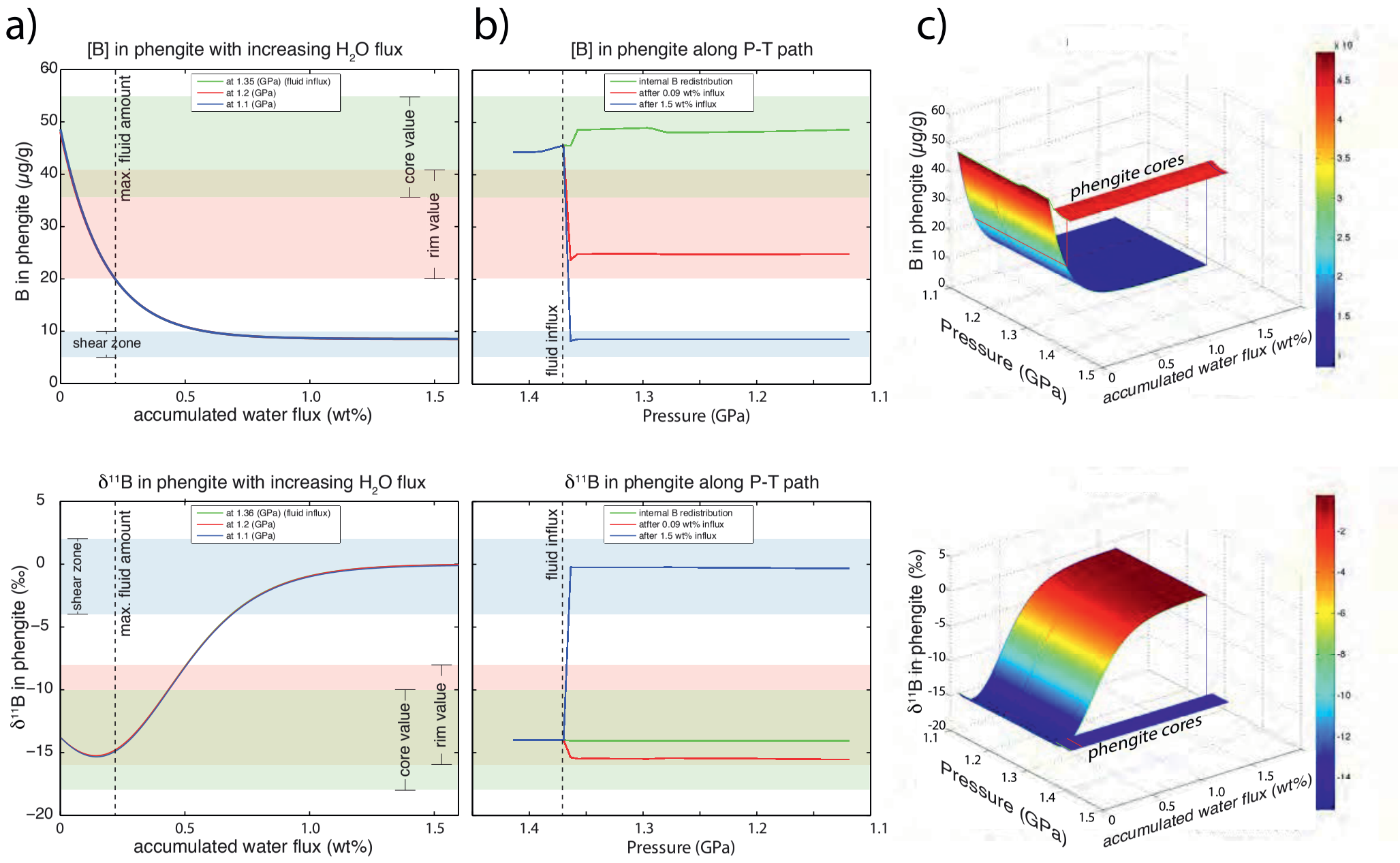
a)
[B] in phengite with increasing H2O flux
at 1.35 (GPa) (fluid influx)
at 1.2 (GPa)
at 1.1 (GPa)
max. fluid amount
core value
rim value
shear zone
B in phengite (µg/g)
accumulated water flux (wt%)
b)
[B] in phengite along P-T path
internal B redistribution
atter 0.09 wt% influx
after 1.5 wt% influx
fluid influx
Pressure (GPa)
c)
phengite cores
B in phengite (µg/g)
Pressure (GPa)
accumulated water flux (wt%)
δ11B in phengite with increasing H2O flux
at 1.36 (GPa) (fluid influx)
at 1.2 (GPa)
at 1.1 (GPa)
shear zone
max. fluid amount
core value
rim value
δ11B in phengite (‰)
accumulated water flux (wt%)
δ11B in phengite along P-T path
internal B redistribution
atter 0.09 wt% influx
after 1.5 wt% influx
fluid influx
Pressure (GPa)
phengite cores
δ11B in phengite (‰)
Pressure (GPa)
accumulated water flux (wt%)

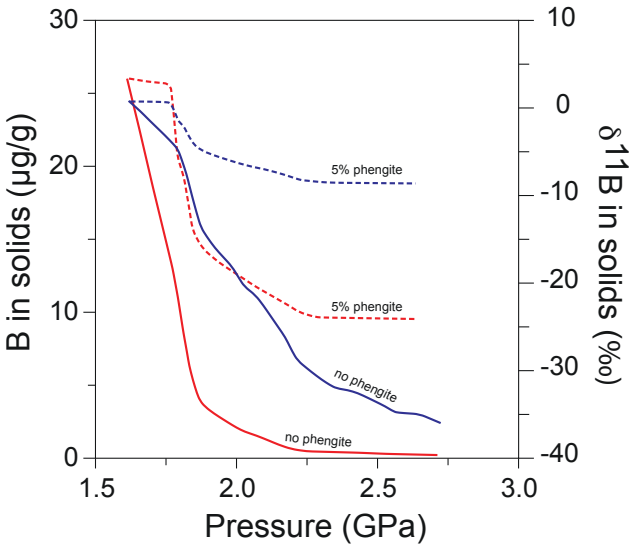
30
20
10
0
1.5
2.0
2.5
3.0
Pressure (GPa)
B in solids (µg/g)
10
0
-10
-20
-30
-40
δ11B in solids (‰)
5% phengite
5% phengite
no phengite
no phengite

Fig. 08

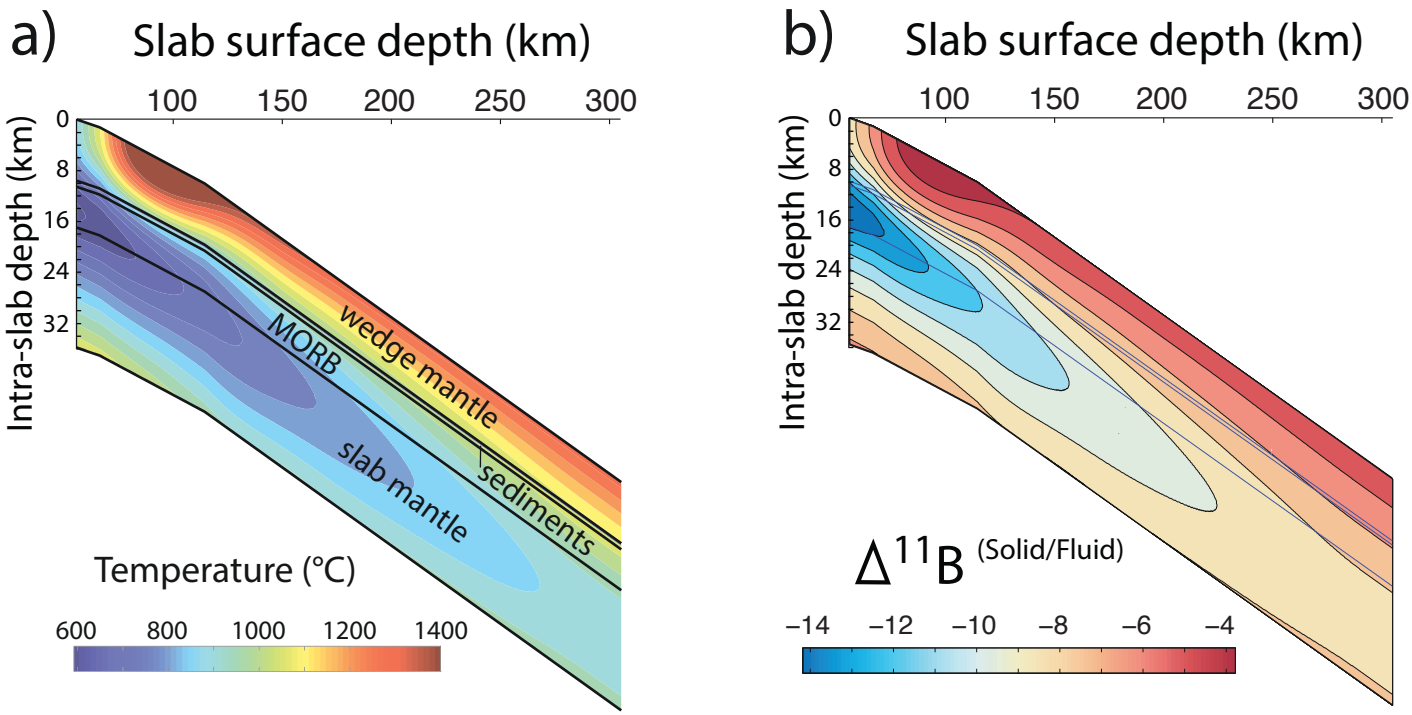
a)
Slab surface depth (km)
100
150
200
250
300
Intra-slab depth (km)
0
8
16
24
32
wedge mantle
MORB
slab mantle
sediments
Temperature (°C)
600
800
1000
1200
1400
b)
Slab surface depth (km)
100
150
200
250
300
Intra-slab depth (km)
0
8
16
24
32
Δ11B (Solid/Fluid)
−14
−12
−10
−8
−6
−4

Fig. 09

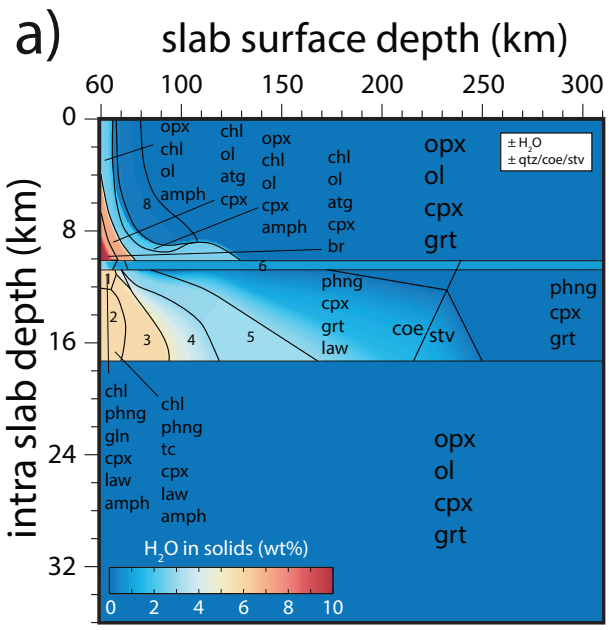

1: chl phng gln cpx law amph
2: chl phng tc cpx law amph
3: chl phng tc cpx law
4: chl phng tc cpx grt law
5: tc cpx grt law phng
6: phng cpx grt
7: chl phng cpx law
8: opx ol cpx grt amph

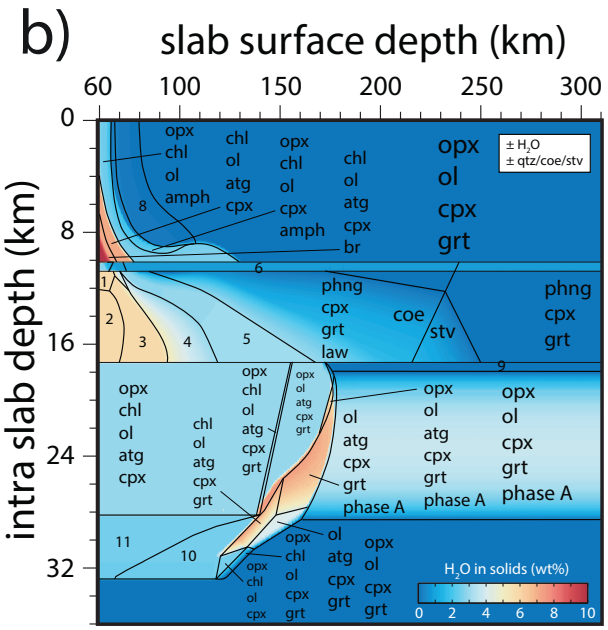

1: chl phng gln cpx law amph
2: chl phng tc cpx law amph
3: chl phng tc cpx law
4: chl phng tc cpx grt law
5: tc cpx grt law phng
6: phng cpx grt
7: chl phng cpx law
8: opx ol cpx grt amph
9: opx ol cpx grt
10: opx chl ol cpx grt
11: opx chl ol cpx

Fig. 10

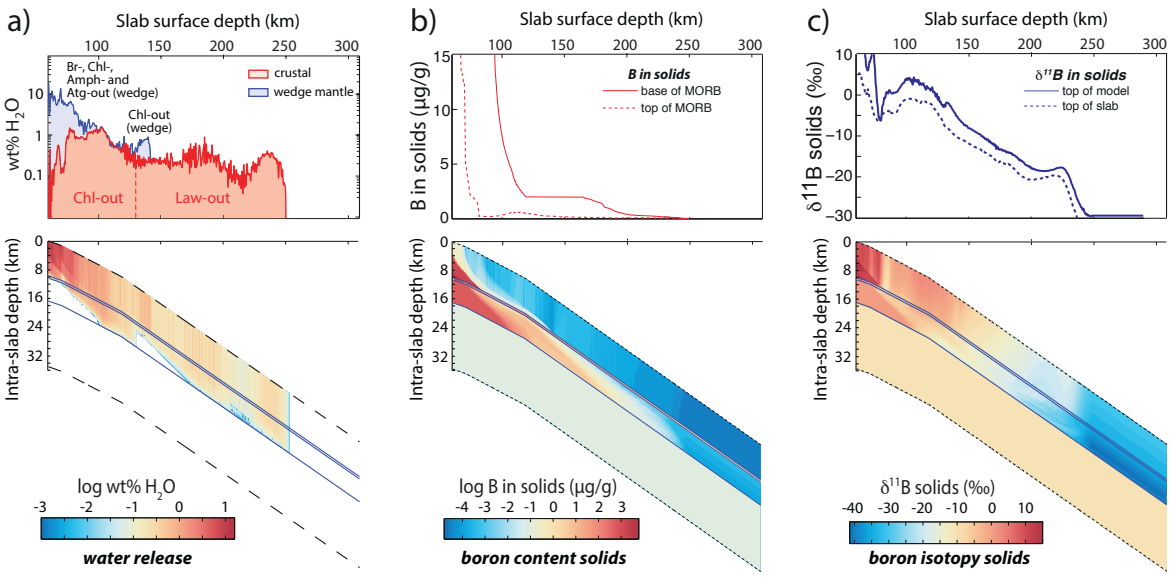
a)
Slab surface depth (km)
100 150 200 250 300
Br-, Chl-, Amph- and Atg-out (wedge)
crustal
wedge mantle
Chl-out (wedge)
wt% H2O
10
1
0.1
Chl-out
Law-out
Intra-slab depth (km)
0 8 16 24 32
log wt% H2O
-3 -2 -1 0 1
water release
b)
Slab surface depth (km)
100 150 200 250 300
B in solids (µg/g)
15 10 5 0
B in solids
base of MORB
top of MORB
Intra-slab depth (km)
0 8 16 24 32
log B in solids (µg/g)
-4 -3 -2 -1 0 1 2 3
boron content solids
c)
Slab surface depth (km)
100 150 200 250 300
δ11B solids (‰)
10 0 −10 −20 −30
δ11B in solids
top of model
top of slab
Intra-slab depth (km)
0 8 16 24 32
δ11B solids (‰)
-40 -30 -20 -10 0 10
boron isotopy solids

Fig. 11

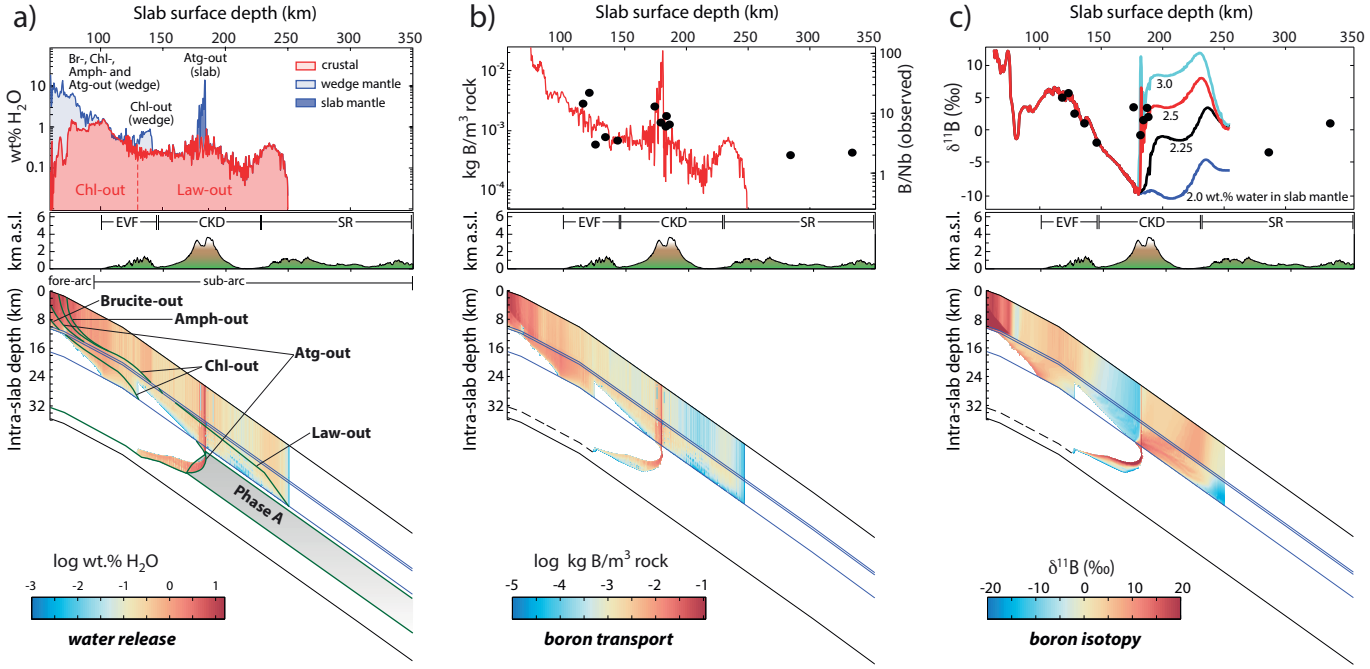
a)
Slab surface depth (km)
100 150 200 250 300 350
Br-, Chl-, Amph- and Atg-out (wedge)
Atg-out (slab)
Chl-out (wedge)
crustal
wedge mantle
slab mantle
wt% H2O
10
1
0.1
Chl-out
Law-out
km a.s.l.
6 4 2 0
EVF
CKD
SR
fore-arc
sub-arc
Intra-slab depth (km)
0 8 16 24 32
Brucite-out
Amph-out
Atg-out
Chl-out
Law-out
Phase A
log wt.% H2O
-3 -2 -1 0 1
water release
b)
Slab surface depth (km)
100 150 200 250 300 350
kg B/m3 rock
10-2
10-3
10-4
B/Nb (observed)
100
10
1
km a.s.l.
6 4 2 0
EVF
CKD
SR
Intra-slab depth (km)
0 8 16 24 32
log kg B/m3 rock
-5 -4 -3 -2 -1
boron transport
c)
Slab surface depth (km)
100 150 200 250 300 350
δ11B (‰)
10 5 0 -5 -10
3.0
2.5
2.25
2.0 wt.% water in slab mantle
km a.s.l.
6 4 2 0
EVF
CKD
SR
Intra-slab depth (km)
0 8 16 24 32
δ11B (‰)
-20 -10 0 10 20
boron isotopy

Fig. 12

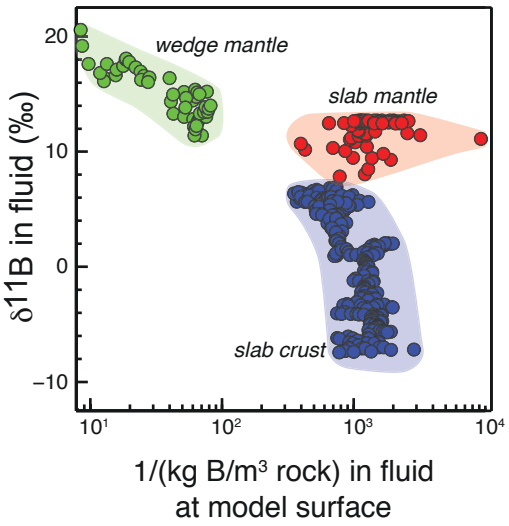
wedge mantle
slab mantle
slab crust
20
10
0
−10
δ11B in fluid (‰)
10¹
10²
10³
10⁴
1/(kg B/m³ rock) in fluid
at model surface

Fig. 13

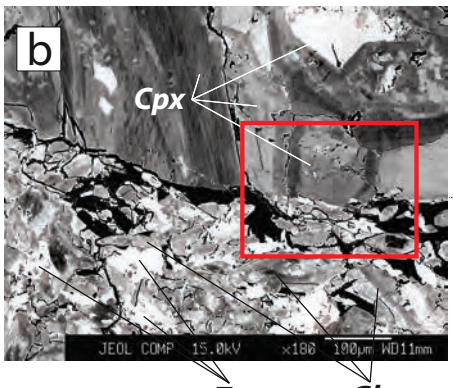

Eclogite
cpx + grt + rt

reaction front

Blueschist
gln + tn + plag

m-scale

mm-scale

Tn

Gln

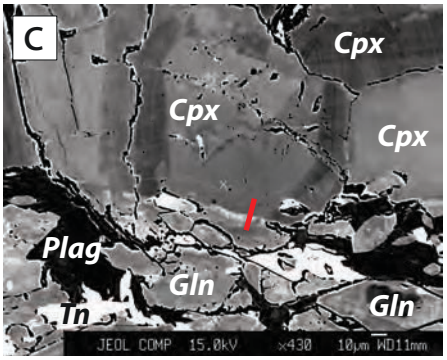

µm-scale

nm-scale

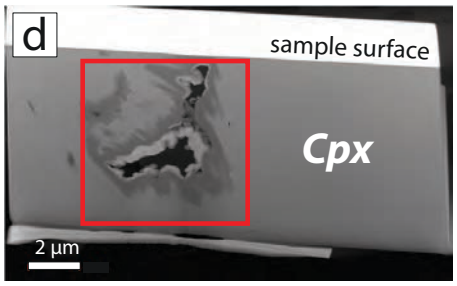

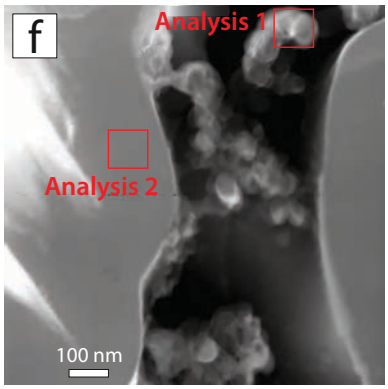

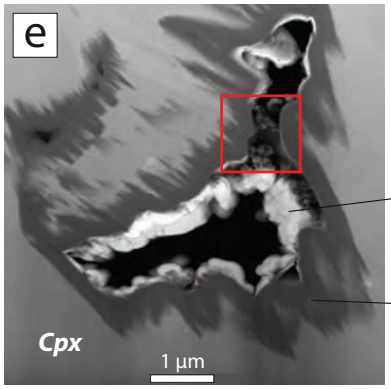

Ga precipitate (from FIB)

amorphous overprinting zone

Multi-stage reaction history in different eclogite types from the Pakistan Himalaya and implications for exhumation processes

Franziska D.H. Wilke[1]*, Patrick J. O´Brien[1], Uwe Altenberger[1],
Matthias Konrad-Schmolke[1], M. Ahmed Khan[2]

[1]Institut für Geowissenschaften, Universität Potsdam, D-14476 Potsdam, Germany.
[2]University of Sargodha, Sargodha, Pakistan.

Abstract

Metabasites were sampled from rock series of the subducted margin of the Indian Plate, the so-called Higher Himalayan Crystalline, in the Upper Kaghan Valley, Pakistan. These vary from corona dolerites, cropping out around Saif-ul-Muluk in the south, to coesite-eclogite close to the suture zone against rocks of the Kohistan arc in the north. Bulk rock major- and trace- element chemistry reveals essentially a single protolith as the source for five different eclogite types, which differ in fabric, modal mineralogy as well as in mineral chemistry. The study of newly-collected samples reveals coesite (confirmed by in situ Raman spectroscopy) in both garnet and omphacite. All eclogites show growth of amphiboles during exhumation. Within some coesite-bearing eclogites the presence of glaucophane cores to barroisite is noted whereas in most samples porphyroblastic sodic-calcic amphiboles are rimmed by more aluminous calcic amphibole (pargasite, tschermakite, edenite). Eclogite-facies rutile is replaced by ilmenite which itself is commonly surrounded by titanite. In addition, some eclogite bodies show leucocratic segregations containing phengite, quartz, zoisite and/or kyanite. The important implication is that the complex exhumation path shows stages of initial cooling during decompression (formation of glaucophane) followed by re-heating: a very similar situation to that reported for the coesite-bearing eclogite series of the Tso Morari massif, India, 450 km to the south-east.

Key words: Kaghan Valley, Himalaya, eclogites, multi-stage exhumation, coesite, glaucophane

*Corresponding author. Tel.: +49 331 9775853; fax: +49 331 9775700. Address: Karl-Liebknecht Str. 24-25, 14476 Potsdam. E-mail address: fwilke@geo.uni-potsdam.de

1. Introduction

The subduction of Tethys and subsequent collision of India with Asia is well evidenced in the record of crustal thickening, magmatism, multi-stage metamorphism, exhumation and finally extension (back sliding) in rocks of the former margin of the Indian Plate (e.g., Treloar & Searle, 1993; Khan et al., 2000). Although the main metamorphism of the crystalline complexes of the Indian Plate is of amphibolite to granulite facies there are numerous eclogite-facies rocks recognised as an integral part of the sequences thus pointing to a more complex evolution that is only partly preserved (Guillot et al., 1997; de Sigoyer et al., 1997; Lombardo et al., 2000; Lombardo & Rolfo, 2000; O'Brien et al., 2001). These volumetrically-minor eclogite bodies reveal a much greater part of the metamorphic history than their strongly overprinted hosts and are a key to the understanding of rates and magnitudes of dynamic processes active during deep collision and exhumation of continental crust in this archetypal collision orogen (Chemenda et al., 2000; Massonne & O'Brien, 2003; Guillot et al., 2003; Treloar et al., 2003).

The significance of high- (HP) and ultrahigh-pressure (UHP) metamorphism for the understanding of the Himalayan evolution has come about as a result of detailed petrological and geochemical studies initiated in the 1990's in Kaghan Valley, NW Pakistan (Pognante & Spencer, 1991) and Tso Morari, NE India (Guillot et al., 1995; de Sigoyer et al., 1997). Subsequent intensified investigation of the geochemical, petrological and geochronological features of the eclogites and related host rocks (Tonarini et al., 1993; de Sigoyer et al., 2000; Lombardo et al., 2000; Fontan et al., 2000; Kaneko et al., 2003; Treloar et al., 2003; Parrish et al., 2006; Rehman et al., 2007; Guillot et al., 2008) and especially the discovery of coesite, firstly in Kaghan Valley (O'Brien et al., 2001) and shortly after in Tso Morari (Sachan et al., 2004), have revolutionised ideas about the Himalayan subduction–collision process (e.g. Chemenda et al., 2000). The deduced pressure-temperature-time paths for both Kaghan and Tso Morari eclogites show many similarities (Massonne & O'Brien, 2003; Parrish et al., 2006; Guillot et al., 2008). The timing of coesite-grade metamorphism, the initial exhumation at cm/a rates, and the cooling below apatite fission track temperatures before the age of peak metamorphism in the typical Higher Himalayan crystalline series

of the central Himalaya are remarkably similar. However, there are distinct differences even within a single eclogite-bearing area in the compositions of post-peak pressure amphiboles, garnet compositional zoning patterns, garnet and omphacite grain size, degree of preservation of protolith texture, and in proportions of Ca-rich phases such as epidote, carbonates and titanite. In recent publications on the Kaghan Valley (Rehman et al., 2007, 2008) there is also a great discrepancy between the exhumation path presented for pelitic rocks and that already deduced from the eclogites (Lombardo et al., 2000; O'Brien et al., 2001). Here we present the results of a new, detailed geochemical and petrological investigation of macroscopically different eclogite types from a wide area of the Kaghan Valley with the aim of testing the validity of the existing, contrasting, pressure-temperature-time paths for the area. In addition, the possibility that eclogites in different nappe units show contrasting evolutions will also be investigated.

2. Geologic Setting

Eclogite facies rocks in northern Pakistan occur in the upper Kaghan and Neelum Valleys (Fig. 1) as part of the so-called Higher Himalayan Crystallines (HHC). This high-grade metamorphic sequence, part of the Indian plate, is bounded to the north by the Indus Suture (Main Mantle Thrust, MMT) from the mafic/ultramafic rocks of the Kohistan Island Arc, and to the south by the Batal Thrust from lower-grade sequences generally attributed to the Lesser Himalaya (Fig. 1). Three main units, which have firstly been described by Chaudhry & Ghazanfar (1987); Greco et al. (1989) and Greco & Spencer (1993), can be identified in the HHC; a basement complex made of metagranite and paragneiss, which is overlain by two sequences of meta-sedimentary cover rocks, a first predominantly metapelite–greywacke-bearing unit and a second stratigraphically younger series with marbles, schists and amphibolites. On the basis of a comparison with unmetamorphosed units in Kashmir, the carbonate-rich sequence is interpreted as Permo-Mesozoic platform cover and the mafic bodies, dykes, sills and lava flows correspond to the extensive Panjal Trap magmatism (Wadia, 1931; Greco & Spencer, 1993).

The large-scale structure in the Upper Kaghan Valley is of a stack of thrust sheets (Treloar et al., 2003; Kaneko et al., 2003). In the north, basement and first cover units structurally overlie rocks belonging to the second cover whereas in the south, at Saif-ul-Muluk, a further basement-bearing unit is tectonically lowermost. East–west-

trending open folds of this stacked sequence dominate the present day structural picture but a series of older isoclinal folds are recognised within the basement/first cover unit. The carbonate-rich units of the second cover thus appear as a series of domes protruding through the older sequences and not, as depicted by Kaneko et al. (2003), as a unit structurally overlying basement/first cover. Later deformation related to the exhumation of the high-grade units is reflected by a pervasive north-directed extensional shearing, at high structural levels, close to the MMT (Burg et al., 1996; Treloar et al., 2003). This latter stage is well evidenced by folds involving albite porphyroblasts (often several cm in length) representing a pervasive greenschist-facies overprint in pelitic, granitic and basic rocks.

A regional gradient in metamorphic grade (dominantly high amphibolite-facies with garnet, staurolite, kyanite and only very locally sillimanite in metapelites) is postulated by Rehman et al. (2007, 2008), based on a three-nappe structure for Upper Kaghan with the eclogite-bearing unit located between eclogite-free over- and underlying units. However, the tectonic pattern of Rehman et al. (2007, 2008) is inconsistent with several other mapping studies (e.g. Chaudhry & Ghazanfar, 1987; Treloar et al., 2003; Parrish et al., 2006), which indicate that the eclogite-bearing unit is uppermost. In the eclogites, now seen to be more extensive than previously realised, the much larger collection of material shows that fresh or strongly retrograded samples occur throughout the area with a rough relationship between size of body, position in the body and degree of retrogression. An obvious difference in formation conditions of the eclogites in the northern part of the area is not apparent and will be discussed in detail later. However, further south, near Naran and between Naran and Burawai, many metabasites preserve magmatic textures with only minor corona growth of garnet and no breakdown of plagoclase as would be expected for the conditions reached by the metabasites in the north. The implication is that there is a structural break between the basement units in the north and south.

3. Eclogites and coronitic metabasites of the Kaghan Valley

Several macroscopically distinct eclogite types were identified in the field. In the following section the key petrographic features of these eclogite types will be outlined.

3.1 Coarse grained, skarn-like eclogites

The most conspicuous garnet–clinopyroxene rocks in the Kaghan Valley are the skarn-like eclogites (mapped as ultramafic bodies) first recognised by Chaudhry & Ghazanfar (1987), and later studied in more detail by Pognante & Spencer (1991). Typical for this generally unaltered eclogite type are large, dark red garnets several cm in diameter set in a matrix of dark green clinopyroxene (Fig. 2A). Some varieties show quartz veins with cm-sized titanite (PKB3) or rutile (K4-60) crystals. Garnet contains abundant inclusions of clinopyroxene (partly replaced by hornblende), rutile (partly replaced by ilmenite and titanite), large idiomorphic titanites, and minor quartz and zircon. Many of these rocks also show irregular patches and streaks of garnetite (Fig. 2B), within which lightly-coloured, up to 0.1 mm garnet cores occur in a darker, net-like garnet matrix: minor rutile is the only other phase in such areas. In some examples garnet aggregates, showing pale cores and sharply-bounded, irregularly-shaped darker margins to individual grains, form a net-like structure around pyroxene domains. Matrix clinopyroxene, mostly 0.5 to 1 mm in length, and with minor inclusions of quartz, shows an irregular breakdown to fine-grained (innermost) or coarse-grained (outermost) symplectites of secondary clinopyroxene and plagioclase (with or without magnetite) or is replaced by hornblende. Some samples show abundant apatite as ca. 0.5 mm grains or clusters. Amphibole appears to be secondary with texturally earliest being olive-green hornblende and later rims or fracture fills comprising more aluminous, hence bluer varieties. This eclogite variety occurs in Purbinar (settlement Kaar) (PKB3), between Besal and Lake Lulusar, and in Joranar (K4-60&76).

3.2 Medium- to coarse-grained eclogites with inherited magmatic fabrics

This variety of eclogite represents the transition between corona dolerites and skarn-like eclogites. Typical for this type are clusters and networks of anhedral, irregularly- zoned garnet or skeletal coronas of garnet, with a range in size from 0.1 up to 1.5 mm which roughly pseudomorph the original feldspar fabric. Omphacite is 0.2-0.8 mm in longest dimension showing an irregular breakdown to fine and coarse-grained symplectites of clinopyroxene, amphibole and plagioclase. The inclusion content in omphacite varies between almost inclusion-free (with only minor quartz and rutile) to inclusion-rich varieties with an evenly-distributed dusting of fine-grained rutile. In addition, amphibole exists as large (cm-sized), green, poikilitic porphyroblasts, which are notably browner around rutile and ilmenite inclusions. Small (0.1 mm) nematoblastic amphibole in oriented clusters occurs together with epidote minerals (up to 0.5 mm), biotite, albite and

quartz and represents a later retrogression. Accessory minerals are apatite, as ca. 0.8 mm grains, and large rutile grains (up to 2 mm), mostly in chains or cluster, partly replaced by ilmenite. Eclogites in Joranar (K4-57 & -58) belong to this group.

3.3 Layered, clinozoisite and epidote bearing eclogites with leucocratic segregations

These generally strongly foliated and retrogressed eclogites exhibit a fine-grained, dark green to gray matrix, red garnet-rich layers, and cm-sized black amphiboles overgrowing this fabric (Fig. 2C). The macroscopically visible layers comprise alternating garnet–omphacite–symplectite, garnet–amphibole–symplectite and garnet-biotite–clinozoisite assemblages. Elongate omphacite, epidote minerals, and garnet bands, conspicuous around the margins of the large clinozoisites (Fig. 2D), define the foliation. In addition, the rock is cut by light-coloured veinlets containing phengite, albite, kyanite and locally also cm-sized rutile grains. In the microscope, garnet is generally 0.25 mm or less, pale pink, anhedral and mostly inclusion free. Relicts of omphacite occur mainly as tiny inclusions in clinozoisite although locally primary coarse omphacite-bearing bands are still preserved. Matrix omphacite, mostly smaller than 1 mm, contains minor inclusions of quartz or rutile needles, and is randomly replaced to varying degrees by fine-grained symplectites of pyroxene, amphibole and albite or large porphyroblastic amphiboles. Amphibole exists in several generations: as inclusions in clinozoisite; as large, pale green porphyroblastic grains with partly retrograded outer rims; in rough and fine symplectites after matrix omphacite and as euhedral nematoblastic amphibole of up to 0.1 mm in the leucocratic segregations. Phengite, up to 1 mm, occurs as inclusion in zoisite and in leucocratic sheets, partially transformed to lepidoblastic biotite and albite symplectites (Fig. 2G). Clinozoisite occurs as lense- or lath- like individuals within chain- or boudin-like structures. Grains up to 0.7 mm in length show the complete range of an eclogite mineral assemblage as inclusions whereas the foliation of the inclusions often differs from that defined by the same phases in the matrix. Epidote commonly appears as up to 2 mm long aggregates containing garnet, minor symplectised pyroxene and amphibole. Rutile, up to 2 mm in diameter, is partly replaced by ilmenite, which is itself rimmed by titanite. Apatite (mm-sized) occurs also. Leucocratic sheets of up to 1 cm thickness, most probably products of aqueous fluid migrations under HP conditions, contain quartz, zoisite (up to 2.5 mm), phengite, kyanite, and secondary biotite and albite after phengite. (Fig.2 E, F). This

eclogite type crops out in Gittidas Nala (K4-105, PK2-4), in Purbinar (settlement Kaar) (K4-98) and north (K4-84/87) and west of Jalkhad (J Nar 2).

3.4 Coesite-bearing UHP eclogites with secondary glaucophane and barrosite

The glaucophane- and coesite-bearing, commonly very fresh eclogites exhibit a massive, fine-grained (<1 mm) matrix with red garnet and dark green omphacite. Overgrowing this early fabric are larger (>1 mm) dark amphiboles. Anhedral, optically-zoned garnets (Fig. 2H) up to 0.8 mm in diameter sit within a weakly defined foliation formed by elongate omphacite, phengite and chains of rutile. Garnet contains tiny inclusions of rutile, minor quartz/ coesite, graphite and zircon. Omphacite is up to 1 mm in length and mostly inclusion poor, whereas some grains look dusty due to evenly distributed fine-grained rutile. Phengite, in 0.5 mm laths, is surrounded by a thin biotite-bearing breakdown rim. Amphiboles with a conspicuous lilac core and a dark green rim form small poikiloblasts (Fig. 2H) partly enclosing the earlier phases. Coesite occurs as inclusions in omphacite and garnet, showing in both cases the typical radiating network of fractures and partial breakdown to quartz. Coesite inclusions (Fig. 2I) are best preserved in omphacite and so far only one example has been found in garnet. Some of the glaucophane-bearing eclogites also contain the carbonate minerals magnesite and dolomite as matrix phases, apparently in equilibrium with the high-pressure assemblage, as well as ankerite as inclusions in garnet. Rutile, partly replaced by titanite, domains of pyrite/ chalcopyrite transformed to hematite, magnetite and goethite and a small amounts of epidote/clinozoisite, apatite and zircon are accessory phases. Coesite eclogites occur only a few hundred metres from the Indus Suture Zone north and northwest of Gittidas: at Saleh di Baihk (K4-106) as boulders close to the road and in situ at Saleh Gali (K4-120).

3.5 Very fine-grained eclogite

An unusual very fine-grained eclogite type exhibits a pale lilac hue in hand specimen whereby non-retrograded portions show only a very subtle red and green colouration. In the microscope, garnet is generally less than 100 μm, optically zoned, anhedral to semi-euhedral with locally inclusions of graphite and rutile in their interiors (Fig. 2J). Matrix omphacite, in places as aggregates of tiny, 20 μm grains, is mostly replaced to varying degrees by amphibole–clinopyroxene–plagioclase symplectites and secondary green amphiboles. Three generations of amphiboles occur. Yellow-green porphyroblastic amphibole grains significantly larger than primary phases randomly overgrow the fabric,

a second variety occurs in symplectites and the youngest variant is found in late cross-cutting veins. Rutile is about 10-20 µm in diameter and rimmed by titanite whereas fine distributed titanite and graphite give thin sections a dusty appearance. This eclogite type has been found within the metasediments close to Jalkhad in Jalkhad Nar (K3-11).

3.6 Coronitic metabasites

In addition to the eclogites exists a further metabasite variety exhibiting coronitic growth of garnet around plagioclase and recrystallisation of clinopyroxene. A wide variety of textures can be observed from only slightly modified magmatic rocks to completely recrystallised garnet+clinopyroxene+plagioclase+quartz±hornblende assemblages which pseudomorph the magmatic texture (Figs. 2K, L). The presence of stable plagioclase in the most recrystallised samples indicates a high-pressure amphibolite/granulite facies rather than eclogite facies conditions for these rocks. These coronitic metadolerites are found on both sides of lake Saif-ul-Muluk, in the area between Naran and Burawai, significantly further south than the outcrops of eclogite (Fig. 1) and have also been noted in the neighbouring Neelum Valley (Fontan et al., 2000).

4. Mineral chemistry

In the following section the chemistry of major minerals and their breakdown products will be outlined. Analyses were obtained using a 4 spectrometer Cameca SX100 electron microprobe at the GeoForschungsZentrum (GFZ) Potsdam operating at 15 kV and 20 nA with a 2-10 µm beam. Counting time were 10-30 s on peaks and half-peak on background, synthetic and natural standards were used. Representative point analyses are given in Table1-4.

4.1 Garnet

In addition to differences in grain size, distribution, texture, colour and inclusion density the garnet in the investigated samples shows variation in composition and in zoning pattern (Table 1; Fig. 3). Garnets from skarn-type eclogites and the rocks with inherited magmatic fabric (in both cases generally coarse-grained) are iron rich ($Alm_{60}Prp_{16}Sps_{1}Grs_{18}$) and show essentially homogeneous cores overgrown by smaller rims with increasing Prp, X_{Mg} and Sps associated with decreasing Ca content (Fig. 3A). In contrast, garnets in the epidote-bearing eclogites show a strong compositional zoning pattern with abrupt changes. In the inclusion-rich cores, garnets are Fe rich and Ca poor

($Alm_{55}Prp_{22}Sps_{1}Grs_{19}$) and only minor variation exists within cores of a single sample. These cores are surrounded by homogeneous overgrowths showing higher Ca and lower Fe with a sharp, step-like compositional change existing between the two zones (Figs.3 B, C &-D). In some examples three distinct zones are visible (Fig. 3B). Garnets in UHP- and very fine-grained eclogites are characterised by a complex multipart zoning (Figs.3 E, F). Small, irregular-shaped Fe+Ca-rich cores are surrounded by a zone with lower Ca and higher Fe+Mg, which is itself surrounded, by a wider zone with highest Fe and equal Ca and Mg. This outer zone is criss-crossed by vein-like structures, well depicted in the compositional map of Fig. 4, showing higher Ca and lower Fe+Mg as is usual for the outermost zones of such grains.

4.2 Clinopyroxene

Omphacite is an essential constituent of all the eclogites, but a large variation in grain size, modal abundance, inclusions and degree of breakdown is obvious. Jadeite content varies between 12 and 45 mol% for texturally eclogite facies clinopyroxene (Table 2; Fig. 5). In most samples this omphacite has been partially replaced by symplectitic intergrowths of secondary, less jadeitic clinopyroxene intergrown with plagioclase and commonly also amphibole. The skarn-like eclogites show lowest jadeite contents (generally below 20 mol%) whereas in the other coarse-grained eclogites even the secondary symplectitic clinopyroxene has a jadeite content above 20 mol% (Fig. 5). Epidote- and coesite-bearing eclogites contain matrix omphacites with X_{Jd} between 0.30 and 0.39 — tiny omphacites included in large clinozoisite porphyroblasts show a similar range — whereas secondary, symplectitic clinopyroxene especially in the epidote-rich varieties coexists with magnetite and has a significantly higher aegirine content (around 20 mol%). Conspicuously, the highest jadeite contents, up to 45 mol%, have been found in the tiny matrix omphacites of the very fine-grained eclogite (Table 2; Fig. 5).

4.3 Amphibole

Amphibole is a major phase in almost all studied samples and occurs in a number of compositional and textural modifications. The main varieties are calcic and sodic-calcic amphiboles but locally also sodic amphiboles occur. Different amphibole varieties may exist in a single sample as well as in a single zoned grain (Table 3; Figs. 6 A, B). Coarse-grained eclogites contain mainly large porphyroblasts of barroisite or

edenite/pargasite/Mg-hastingsite but inclusions in garnet and zone rims of such amphiboles adjacent to garnet are generally more aluminous. In comparison, large poikilitic amphibole porphyroblasts in epidote-bearing eclogites show a barroisite core and a rim of pargasite or tschermakite whereas tiny grains and inclusions in clinozoisite are edenite (Fig. 6 A). Symplectitic amphiboles tend to be edenitic or pargasitic in composition. Noticeable in many of these samples is a conspicuous brown halo around rutile inclusions marked by a 2- to 4-fold increase in TiO_2 content. Amphiboles in UHP eclogites are unusual in that they contain irregular patches of lilac glaucophane (already noticed by Lombardo et al., 2000) in the core surrounded by barroisite (Fig. 6 C) and with a thin outer rim of magnesio-hornblende. A typical example of core-rim compositional variation for such an amphibole is depicted in Fig. 6 D. Fine-grained eclogites contain less-aluminous amphiboles than the other eclogite types with the typical porphyroblasts plotting in the barroisite to Mg-katophorite fields.

4.4 Epidote minerals

As a common phase in the eclogite facies assemblage, fairly homogeneous epidote and clinozoisite (Table 4) occur as elongate lenses or individual grains. Eclogites with preserved magmatic texture contain zoisite most probably indicating the local influence of former magmatic Ca-plagioclase. The large clinozoisites overgrowing the eclogite fabric and preserving garnet and omphacite as inclusions are generally also unzoned. An additional epidote variety occurs in the leucocratic segregation zones where it is typically idiomorphic and optically and compositionally zoned to more Fe-rich rims. An important observation is the presence of feathery-textured quartz as inclusions in epidote of samples from the area of the coesite-bearing eclogites, which could represent pseudomorphs after coesite.

4.5 Mica phases

Phengite, grown during the UHP/HP-stage and in leucocratic sheets, is the dominant mica phase in the studied samples. Primary phengite is relatively homogeneous within a single sample with composition generally plotting between 3.44 and 3.55 Si p.f.u. (based on 11 oxygens), with low Ti but significant (around 5 mol%) paragonite content. In contrast, white micas in the leucocratic pockets contain lower Si in cores and are zoned to even lower Si values at the rim (Table 4). Breakdown of phengite produced phlogopite or biotite (Table 4).

4.6 Plagioclase

Plagioclase is only found as a secondary phase in the eclogites where it occurs in symplectites after omphacite intergrown with amphiboles and clinopyroxene and in leucocratic segregations together with biotite, phengite, kyanite and zoisite. Symplectite plagioclase is generally more sodic (albite-oligoclase) than the plagioclase of the segregation pockets (andesine)(Table 4).

5. Whole rock geochemistry

Major and trace element analyses for the five different eclogite groups are presented in Table 5. Analyses for major and trace elements were obtained using a Phillips PW-2400 X-ray fluorescence (XRF) spectrometer at the GeoForschungs-Zentrum Potsdam and the Geochemical Laboratory of the Institute of Geosciences in Mainz using internationally accepted rock standards yielding a determined precision better than 1–3% for major elements (depending on concentrations levels) and 2–3% for trace elements. The H_2O and CO_2 contents were analysed by quantitative high-temperature decomposition with an Elemental CHN analyser. Rare earth elements (REE) were determined by inductively coupled plasma–optical emission spectrometer (ICP-OES, Vista MPX) at the Geochemical Laboratory of the University of Potsdam. Sample preparation involved Na_2O_2 standard fusion and dilution techniques for dissolving rock powders into solution (Zuleger et al. 1988). Analytical precision was checked with international reference standards and found to be better than 12%.

5.1 Results

According to the classification of Winchester & Floyd (1977), based on contents of the relatively immobile high field strength elements Zr, Ti, Nb and Y (Fig. 7A), the eclogites are all of subalkaline to alkaline basaltic composition (assuming magmatic precursors). The maximum SiO_2 and Cr concentration of 51.6 wt.% and 170 ppm, respectively, are characteristic for the tholeiitic series according to the classification of Middlemost (1975). The non-skarn eclogites have total iron (as ferric) concentrations in the range 13.6 to 16.8 wt.%, low to moderate MgO (3.9–6.5 wt.%), mg# values of 23–31 ($mg\# = 100*Mg/(Mg + Fe_{tot})$ for SiO_2 concentrations between 48 and 52 wt.%, and TiO_2 concentrations in the range 2.1–2.8 wt.% which are significantly higher than

for modern subduction-related magmas (see compilation of modern analogues by Verma, 2006). Vanadium contents are 340–530 ppm but Ti/V is greater than 30, exceeding the limit of modern subduction-related basic melts significantly (Shervais, 1982). With one exception Cr concentrations are <110 ppm indicating that the melts parental to the eclogites could not have been in equilibrium with a mantle peridotite, and must have undergone pyroxene and spinel fractionation during their magmatic evolution. In contrast, the high Al_2O_3 (15.0 wt.%), total iron (as ferric) of 21.5 wt.%, TiO_2 (5.9 wt.%) and Nb (65 ppm) but low Na_2O (0.89 wt.%) and mg# (18) values of the skarn-like eclogites clearly distinguish them from the other eclogite samples.

In order to evaluate possible melt-generating and -modifying processes in a qualitative way, the measured incompatible elements were plotted normalised to chondrite (Fig. 7B: McDonough & Sun, 1995) primitive mantle (Fig. 7C: Hofmann, 1988), and E-MORB (Fig. 7D: Sun & McDonough, 1989). Three metabasic samples show similar behaviour with a moderate chondrite-normalized LREE enrichment (Fig. 7B) as expressed by chondrite-normalized La/Yb ratios between 2.1 and 4.6 and La/Sm ratios between 1.4 and 2.1. The fine-grained eclogite, despite comparable major and most minor element concentrations to those of the other eclogite types, shows significantly different trace element patterns with lower LREE contents, and La/Yb (1.3) and La/Sm (1.2) values similar to those of transitional mid-ocean ridge basalts (T-MORB, Schilling et al., 1983). The skarn-like eclogite is characterised by low LREE (La/Yb and La/Sm= 0.1) and displays a N-MORB like pattern (Fig. 7B).

Primitive mantle-normalised multi-element plots (Fig. 7C) show a pronounced enrichment in LIL elements and the lack of any Nb anomaly. The most significant anomaly of the metabasic samples is the PRIMA-normalized negative Sr anomaly, resulting from low concentrations, with an average of 140 ppm**.**

6. Metamorphic conditions and evolution

The petrographic descriptions and characteristic mineral compositions of the studied eclogites make it apparent that no single equilibrium assemblage is present in a sample. Instead, compositional zoning and reaction textures, especially with the evolution of different amphibole generations, allow an insight into the possible P-T path followed by the Kaghan eclogites. The peak-pressure parageneses in the eclogites are all plagioclase-free and garnet+omphacite+rutile-bearing. Additional phases such as phengite, quartz (locally coesite), carbonate(s), and epidote occur in various proportions in the assemblages pre-dating amphibole growth. Standard conventional geothermobarometers

for these assemblages are the garnet–clinopyroxene (Krogh, 1988), and garnet–phengite (Green & Hellman, 1982) Fe–Mg exchange thermometers and the garnet–clinopyroxene–phengite (Carswell et al., 1997) geobarometer which, together with the univariant coesite=quartz reaction for the samples with preserved coesite relics, allow a broad delimitation of metamorphic conditions.

The compositional profiles for garnet (Figs. 3 & 4) show significant variation in both Ca content and X_{Mg}. We interpret garnet cores with generally lowest X_{Mg} and high Ca (in some cases also high Mn) as belonging to part of the prograde evolution and have interpreted outer parts of grains (not necessarily the rims which in most cases show effects of decompression and resorption of garnet) with a plateau at maximum X_{Mg} as representing the peak eclogite facies stage. Based on this assumption for peak-pressure eclogite garnet composition, and taking the most jadeite-rich omphacite (Table 6), we deduced temperatures in the range 640-790°C for pressures in the range 30-36 kbar (Table 6, Fig. 8). Garnet–phengite thermometry, using the same garnet combined with the most silicic phengite, yielded a similar range (Table 6). For the selected phengite-bearing eclogites the pressures deduced by the garnet–clinopyroxene–phengite geobarometer plot above the coesite=quartz univariant curve (as already pointed out by O'Brien et al., 2001).

A significant new observation was the presence of glaucophane cores to sodic–calcic amphoboles in coesite-bearing eclogites. Porphyroblastic amphiboles post-dating the peak-pressure assemblage are characteristic for these eclogites and the presence of glaucophane has important consequences for possible exhumation paths. In order to investigate the possible growth conditions for glaucophane in these rocks we constructed phase diagrams for the effective bulk composition of the rock (i.e. taking the fractionation effect of the zoned garnet into consideration: Spear, 1988; Konrad-Schmolke et al., 2005) using the software Perple_X07, the thermodynamic data of the internally consistent and up-dated dataset of Holland & Powell (1998) and the solid-solution models (in file solut_07) of Dale et al. (2005: amphibole), Fuhrman & Lindsley (1988: feldspar), Berman (1990: garnet), Holland et al. (1998: chlorite), Holland & Powell (1990: phengite), Holland & Powell (1998: epidote) and Holland & Powell (1996: omphacite).

For the petrographically-determined amphibole-free eclogite facies stage, taking into consideration the Si per formula unit (p.f.u.) in phengite, pressures in the coesite

field (above 30 kbar) were deduced at around 700°C: values consistent with the results from conventional geothermobarometry (Fig. 9). The subsequent growth of glaucophane in the rock, monitored by the Na content on the A-site [Na(A)] in amphibole, requires conditions around 580-630°C at 10-17 kbar i.e., indicating significantly lower temperatures following a major amount of decompression. The observation that glaucophane-cored porphyroblasts enclose ragged omphacite relicts, points to breakdown of eclogite-facies pyroxene in the presence of water at this stage. Surrounding the glaucophane cores are amphiboles of sodic-calcic (barroisite) or calcic (magnesiohornblende) composition. The growth of these second-stage amphiboles requires a significant reheating from the conditions required for glaucophane. This is supported by temperatures derived from conventional amphibole-plagioclase thermometry (Holland & Blundy, 1994) of 650-720°C at around 12 kbar (Table 6; Fig. 9), taking the plagioclase composition from amphibole-plagioclase intergrowths and with the replacement of rutile by ilmenite. The resultant PT-path from this approach (Fig. 9) shows cooling during decompression from peak (coesite-field) pressures at mantle depths followed by a heating stage at normal crustal depths remarkably similar to the path proposed for Tso Morari coesite-bearing eclogites by de Sigoyer et al. (1997).

7. Discussion and conclusions

In the last decade, field studies have significantly extended the number of eclogite bodies known from the Upper Kaghan Valley. Together with the results of mapping of the neighbouring Neelum Valley (Fontan et al., 2000) it is clear that eclogite facies metabasites are generally small bodies, representing former dykes, sills and flows, but are widespread. Although significant variation in degree of retrogression can exist within a single metabasite body, it is still possible to assign all the eclogites to one of five major textural types. Analysis of major and trace element compositions showed, despite textural differences, that all investigated samples are subalkaline/alkaline basalts showing tholeiitic affinity and, apart from the very fine-grained and skarn-like type, exhibiting similar behaviour in REE thus strongly suggesting a genetic relation between the investigated samples. Minor differences in the REE pattern probably reflect different amounts of contamination during the emplacement in the continental crust. The deduced major and trace element trends, with key values such as high TiO_2 and Nb contents exclude a subduction-related origin whereas normalised La/Sm (1.25-2.0), La/Yb (1.3-

4.6) as well as Zr >>100 ppm, are essentially the same as those recognized for rift tholeiites and within-plate volcanism elsewhere (e.g. Deniel et al., 1994; Pearce & Norry, 1979; Verma, 2006) but, most importantly, also for analyses of non-metamorphosed Panjal Trap continental flood basalts (Bhat et al., 1981; Chauvet et al., 2008) with which the Kaghan metabasites have long been correlated (Papritz & Rey, 1989; Greco & Spencer, 1993; Spencer et al., 1995).

Despite the close similarity in bulk chemistry, other possibilities to explain the difference in eclogite appearance are the metamorphic PT-path or, alternatively, the protolith grain size (fine-grained, possibly hydrothermally-altered basalt versus coarse-grained less-altered dolerite or gabbro). The calculated equilibrium conditions for the different eclogite types do not show significant variation despite the fact that samples are widely spaced. It is highly likely that a continuation of the coesite-eclogite unit exists further north, still buried below Kohistan. The presence of coesite in eclogites only from the northern-most locations, close to the contact with the Kohistan arc, could merely be a problem of preservation potential in the other locations. Significantly, the garnet–clinopyroxene–phengite barometer, the prospecting tool used to locate the first coesite-bearing eclogite (O'Brien et al., 2001), yields coesite-field pressure conditions for samples collected much further south (Fig. 1) where no evidence for the former presence of coesite exists. This strongly suggests that a much larger area of the Upper Kaghan experienced pressures of around 30 kbar and that either evidence for the former presence of coesite has been completely obliterated or, alternatively, that these rocks underwent no significant garnet and/or clinopyroxene growth at eclogite-facies conditions such that there was no potential for trapping of coesite inclusions at high pressures. This latter alternative has been discussed for Norwegian eclogites by Konrad-Schmolke et al. (2008) and explained with reference to bulk-element fractionation (reflected in distinct compositional zoning patterns in garnets) during episodic rather than continuous garnet growth along a PT path. The important point is that slightly different parageneses and mineral compositions can be derived from the same protolith dependent on subtle variations in growth episodes of major minerals that, as long as non-equilibrated (i.e. zoned) phases exist, thus modifies the effective reacting bulk composition.

Pressure-temperature-time information for the Kaghan Valley metamorphic rocks exists from several previous studies. Peak metamorphic conditions for eclogites were derived by O'Brien et al. (2001: 27-29 kbar; 690-750°C), Kaneko et al. (2003: 27-

32 kbar; 700-770°C) and Rehman et al. (2007: 757-786°C; 28.6±0.4kbar; 2008: 28kbar; 762±46°C). A significant contrast exists between proposed decompression paths. Kaneko et al. (2003) show a clockwise PT-path with slight cooling during decompression (to 655±55°C; 11±1.4 kbar) whereas Rehman et al. (2008), based on the interpretation of assemblages in metapelites, suggested a distinct heating to 859±59°C at pressures around 18 kbar (high-pressure granulite facies) before subsequent cooling. This latter path is inconsistent with the presence of secondary glaucophane (as described by Lombardo et al. (2000) or in this work for the first time in coesite-bearing samples) or the survival of sharp compositional zoning profiles in garnet of several eclogites: features requiring relatively low temperatures following the peak. Although heating at lower pressures occurred it is likely that this was only a short-lived episode superimposed on a rapid exhumation path. Significantly, the S-shaped PT-path deduced here for the Kaghan eclogites (Fig. 9) is remarkably similar to that presented for the Tso Morari unit (de Sigoyer et al., 1997; Guillot et al., 1997; Guillot et al., 2008). This comparison is strengthened when the timescale of exhumation for these two areas is compared (Massonne & O'Brien, 2003; Treloar et al., 2003; Parrish et al., 2006). In both cases the exhumation from deep mantle to normal crustal depths occurs at rates of several cm per year before slowing to more normal mm per year rates thus suggesting a change in exhumation mechanism between these two stages. It is likely, based on the short time period between ocean closure and peak metamorphism of the subducted Indian Plate at coesite-eclogite conditions that the generally fine-grained nature of the eclogites, as well as the net-like garnet microstructure in many samples, is a product of nucleation–growth kinetics from variably altered protoliths.

The leucocratic segregations recognised in some of the eclogites are comparable with features documented from other eclogite locations around the world (e.g. Becker et al., 1999; Hermann et al., 2006). Such quartz-rich zones containing minerals such as phengite, zoisite, kyanite and rutile have been interpreted as products of metasomatic fluid flow driven by dehydration reactions in the metabasites and their surrounding pelitic gneisses (Spandler & Hermann, 2006; Castelli et al., 1998). In some eclogites there are distinct lens-like bodies of quartz-garnet-phengite-rutile fels most probably derived in the same manner. The possibility of a derivation by melting (e.g. Liebscher et al., 2007) is unlikely due to the complete absence of albite-rich plagioclase in the Kaghan examples although the PT-path for the rocks certainly passed through the necessary wet melting conditions.

In comparison to the metabasites with an obvious, despite retrogressive overprint, eclogite-facies evolution, meta-dolerites which crop out in the southern-most part of the study area show no indication that plagioclase was unstable and thus, despite the growth of metamorphic garnet coronas, probably experienced at most amphibolite facies conditions. Metabasic rocks with relicts of magmatic intergranular textures and growth of amphibole–garnet–biotite–chlorite-bearing assemblages were described by Fontan et al. (2000) from the SW Kalapani unit in the adjacent Neelum Valley. Formation conditions of 650-750°C at 8-9 kbar are consistent with the deduced third stage of metamorphism (producing pargasite, plagioclase and ilmenite) in the eclogite series (at 650-720°C at 12 kbar (Table 6, Fig. 9). The metamorphic conditions for the metadolerites are thus convergent with those of retrogression in the eclogite series and indicate a tectonic juxtaposition of these units after the eclogite facies stage. Such stacking of Indian Plate basement–cover units is well known further west in Pakistan (Treloar et al., 2003, DiPietro et al., 1993) where more extensive mapping has been undertaken, and is also a fundamental aspect of the subduction–exhumation models for ultrahigh-pressure metamorphic series (e.g. Chemenda et al., 2000; O'Brien, 2001).

8. Acknowledgements

We would like to thank Stéphane Guillot and Ian Buick for their helpful reviews and comments on the manuscript. This work received financial support from the Graduate School 1364, funded by the German Science Foundation (DFG). We thank Robert Reinisch for some of the samples and Roland Oberhänsli for helpful discussions. Excellent thin sections were prepared by Christine Fischer and microprobe analysis was supported by Oona Appelt (GFZ Potsdam). We are grateful to Antje Musiol (Potsdam) und Nora Groshopf (Mainz), for their chemical laboratory work.

9. References

Becker, H., Jochum, K.-P., Carlson, R.W., 1999. Constraints from high-pressure veins in eclogites on the composition of hydrous fluids in subduction zones. Chemical Geology, 160, 291-308.

Berman, R. G., 1990. Mixing properties of Ca-Mg-Fe-Mn garnets. American Mineralogist, 75, 328-344.

Bhat, M.I., Zainuddin, S.M., Rais, A., 1981. Panjal Trap chemistry and the birth of Tethys. Geological Magazine, 118, 367-375.

Burg, J.-P., Chaudhry, M.N., Ghazanfar, M., Anczkiewicz, R., Spencer, D., 1996. Structural evidence for back sliding of the Kohistan arc in the collisional system of northwest Pakistan. Geology, 24, 739-742.

Carswell, D.A., O´Brien, P.J., Wilson, R.N., Zhai, M., 1997.Thermobarometry of phengite-bearing eclogites in the Dabie Mountains of central China. Journal of Metamorphic Geology, 15, 239-252.

Castelli, D., Rolfo, F., Compagnoni, R., Xu, S., 1998. Metamorphic veins with kyanite, zoisite and quartz in the Zhu-Jia-Chong eclogite, Dabie Shan, China. The Island Arc, 7, 159-173.

Chaudhry, M.N., Ghazanfar, M., 1987. Geology, structure and geomorphology of upper Kaghan Valley, NW Himalaya, Pakistan. Geological Bulletin, Punjab University, 22, 13- 57.

Chemenda, A.I., Burg, J.-P., Mattauer, M., 2000. Evolutionary model of the Himalaya-Tibet system: geopoem based on new modelling, geological and geophysical data. Earth and Planetary Science Letters, 174, 197-409.

Chauvet, F., Lapierre, H., Bosch, D., Guillot, S., Mascle, G., Vannay, J.-C., Cotton, J., Brunet, P., Keller, F., 2008. Geochemistry of the Panjal Trap basalts (NW Himalaya): record of the Pangea Permian break-up. Bulletin de la Societé Géologique de France, 179, 383-395.

Dale, J., Powell, R., White, R.W., Elmer, F.L., Holland, T.J.B., 2005. A thermodynamic model for Ca-Na clinoamphiboles in Na_2O-CaO-FeO-MgO-Al_2O_3-SiO_2-H_2O-O for petrological calculations. Journal of metamorphic Geology, 23, 771-791.

Deniel, C., Vidal, P., Coulon, C., Vellutini, P., Piquet, P., 1994. Temporal evolution of mantle sources during continental rifting: the volcanism of Djibouti (Afar). Journal of Geophysical Research, 99, 2853-2869.

De Sigoyer, J., Guillot, S., Lardeaux, J.-M., Mascle, G., 1997. Glaucophane bearing eclogites in the Tso Morari dome (eastern Ladakh, NW Himalaya). European Journal of Mineralogy, 9, 1073-1083.

De Sigoyer, J., Chavagnac, V., Blichert-Toft, A., Villa, I.M., Luais, B., Guillot, S., Cosca, M., Mascle, G., 2000. Dating the Indian continental subduction and collisional thickening in the northwest Himalaya: Multichronology of the Tso Morari eclogites. Geology, 28, 487-490.

DiPietro, J., Pogue, K.R., Lawrence, R.D., Baig, M.S., Hussain, A., Ahmad, I., 1993. Stratigraphy south of the Main Mantle Thrust, Lower Swat, Pakistan. In: Treloar, P.J., Searle, M.P., (eds). Himalayan Tectonics. Geological Society, London, Special Publications, 74, 207-220.

Fontan, D., Schouppe, M., Hunziker, C.J., martinotti, G., Verkaeren, J., 2000. Metamorphic evolution, ^{40}Ar-^{39}Ar chronology and tectonic model for the Neelum valley, Azad Kashmir, NE Pakistan. In: Khan, M.A., Treloar; P.J., Searle, M.P., Jan, M.Q. (eds). Tectonics of the Nanga Parbat Syntaxis and the Western Himalaya. Geological Society, London, Special Publications, 170, 431-453.

Fuhrman, M.L., Lindsley, D.H., 1988. Ternary-feldspar modelling and thermometry. American Mineralogist, 73, 201-215.

Greco, A., Martinotti, G., Papritz, K., Ramsay, J.G., Rey, R., 1989. The crystalline rocks of the Kaghan Valley (NE-Pakistan). Eclogae Geologicae Helvetiae, 82, 629-653.

Greco, A., Spencer, D.A., 1993. A section through the Indian Plate, Kaghan Valley, NW Himalaya, Pakistan. In: Treloar, P.J., Searle, M.P., (eds). Himalayan Tectonics. Geological Society, London, Special Publications, 74, 221- 236.

Green, T.H., Hellman, P.I., 1982. Fg-Mg partioning between coexisting garnet and phengite at high pressure, and comments on a garnet-phengite geothermometer. Lithos, 15, 253-266.

Guillot, S., Lardeaux, J.M., Mascle, G., Colchen, M., 1995. Un nouveau témoin du métamorphisme de haute-pression dans la chaîne himalayenne: les éclogites rétromophosées du Dôme du Tso Morari, (Est Ladakh, Himalaya). Comptes Rendus de l´Académie des Sciences, Paris, 320, 931-936.

Guillot, S., de Sigoyer, J., Lardeaux, J.M., Mascle, G., 1997. Eclogitic metasediments from the Tso Morari area (Ladakh, Himalaya) evidence for continental subduction during India-Asia convergence. Contribution to Mineralogy and Petrology, 128, 197-212.

Guillot, S., Garzanti, E., Baratoux, D., Marquer, D., Mahéo, G., de Sigoyer, J., 2003. Reconstructing the total shortening history of the NW Himalaya. Geochemistry Geophysics Geosystems, 4, 1064, doi: 10.1029/2002GC000484.

Guillot, S., Mahéo, G., de Sigoyer, J., Hattori, K.H., Pêcher, A., 2008. Tethyan and Indian subduction viewed from the Himalayan high- to ultrahigh-pressure metamorphic rocks. Tectonophysics, 451, 225-241.

Hermann, J., Spandler, C., Hack, A., Korsakov, A.V., 2006. Aqueous fluids and hydrous melts in high-pressure and ultra-high pressure rocks: Implications for element transfer in subduction zones. Lithos, 92, 399-417.

Hofmann, A.W., 1988. Chemical differentiation of the Earth: the relationship between mantle, continental crust, and ocean crust. Earth and Planetary Science Letters, 90, 297-314.

Holland, T., Blundy, J., 1994. Non-ideal interactions in calcic amphiboles and their bearing on amphibole-plagioclase thermometry. Contribution to Mineralogy and Petrology, 116, 433-447.

Holland, T., Powell, R., 1996. Thermodynamics of order-disorder in minerals: II. Symmetric formalism applied to solid solutions. American Mineralogist, 81, 1425-1437.

Holland, T., Powell, R., 1998. An internally consistent thermodynamic data set for phases of petrological interest. Journal of metamorphic Geology, 16, 309-343.

Holland, T., Baker, J., Powell, R., 1998. Mixing properties and activity-composition and relationships of chlorites in the system MgO-FeO-Al_2O_3-SiO_2-H_2O. European Journal of Mineralogy, 10, 395-406.

Kaneko, Y., Katayama, I., Yamamoto,H., Misawa, K., Ishikawa, M., Rehman, H.U., Kausar, A.B., Shiraishi, K., 2003. Timing of Himalayan ultrahigh-pressure metamorphism: sinking

rate and subduction angle of the Indian continental crust beneath Asia. Journal of metamorphic Geology, 21, 589-599.

Kennedy, C.S., Kennedy, G.C., 1976. The equilibrium boundary between graphite and diamond. Journal of Geophysical Research, 81, 2467-2470.

Khan, M.A., Treloar, P.J., Searle, M.P., Jan, M.Q., 2000. Tectonics of the Nanga Parbat Syntaxis and the western Himalaya. Geological Society Special Publication, 170, pp 485.

Konrad-Schmolke, M.,Handy, M.R., Babist, J., O´Brien, P.J., 2005. Thermodynamic modelling of diffusion-controlled garnet growth. Contribution to Mineralogy and Petrology, 16, 181-195.

Konrad-Schmolke, M., O´Brien, P.J., de Capitani, C., Carswell, D.A., 2008. Garnet growth at high- and ultra-high pressure conditions and the effect of element fractionation on mineral modes and composition. Lithos, 103, 309-332.

Krogh, E.J., 1988. The garnet-clinopyroxene Fe-Mg geothermometer – a reinterpretation of existing experimantal data. Contribution to Mineralogy and Petrology, 99, 44-48.

Lambert, I. B., Wyllie, P. J., 1972. Melting of gabbro (quartz eclogite) with excess water to 35 kilobars, with geological applications. Journal of Geology, 80, 693–708.

Liebscher, A., Franz, G., Frei, D., Dulski, P., 2007. High-pressure melting of eclogite and the P-T-X history of tonalitic to trondhjemitic zoisite pegmatites, Münchberg Massif, Germany. Journal of Petrology, 48, 1001-1019.

Lombardo, B., Rolfo, F., Compagnoni,R., 2000. Glaucophane and barroisite eclogites from the Upper Kaghan nappe: implications for the metamorphic history of the NW Himalaya. In: Khan, M.A., Treloar; P.J., Searle, M.P., Jan, M.Q. (eds). Tectonics of the Nanga Parbat Syntaxis and the Western Himalaya. Geological Society, London, Special Publications, 170, 411-430.

Lombardo, B., Rolfo, F., 2000. Two contrasting types in the Himalayas: implications for the Himalaya orogeny. Journal of Geodynamics, 30, 37-60.

Massonne, H.J., O'Brien, P.J., 2003. The Bohemian Massif and the NW Himalaya. In Carswell, D.A., Compagnoni, R., (Ed.), Ultrahigh pressure metamorphism, 5, 145-187. European Notes in Mineralogy, Eötvös University Press, Budapest.

McDonough, W.F., Sun, S.-s., 1995. The composition of the Earth. Chemical Geology, 120, 223-253.

Middlemost, E.A.K., 1975. The basalt clan. Earth Science Reviews, 11,337-364.

Morimoto, N., 1988. Nomenclature of pyroxenes. Mineralogy and Petrology, 39, 55-76.

O'Brien, P.J., Zotov, N., Law, R., Ahmed Khan, M., Quasim Jan M., 2001. Coesite in Himalayan eclogite and implications for models of India-Asia collision. Geology, 29, 435-438.

Papritz, K., Rey, R., 1989. Evidence of the occurrence of permian Panjal Trap basalts in the Lesser- and Higher-Himalayas of the Western Syntaxis Area, NE Pakistan. Eclogae Geologicae Helvetiae, 82, 603-627.

Parrish, R.R., Gough, S.J., Searle, M.P., Waters, D.J., 2006. Plate velocity exhumation of ultrahigh-pressure eclogites in the Pakistan Himalaya. Geology, 34, 989-992.

Pearce, J.A., Norry, M.J. 1979. Petrogenetic implications of Ti, Zr, Y and Nb variations in volcanic rocks. Contributions to Mineralogy and Petrology, 69, 33-47.

Pognante, U., Spencer, D.A., 1991. First report of eclogites from the Himalayan belt, Kaghan valley (northern Pakistan). European Jounal of Mineralogy, 3, 613-618.

Rehman, H.U., Yamamoto, H., Kaneko, Y., Kausar, A.B., Murata, M., Ozawa, H., 2007. Thermobaric structure of the Himalayan Metamorphic Belt in Kaghan Valley, Pakistan. Journal of Asian Eaerth Sciences, 29, 390-406.

Rehman, H.U., Yamamoto, H., khalil, M.A.K., Nakamura, E., Zafar, M., Khan, T., 2008. Metamorphic history and tectonic evolution of the Himalayan UHP eclogites in Kaghan Valley, Pakistan. Journal of Mineralogical and Petrological Sciences, 13, 242-254.

Sachan, H.K., Mukhrjee, B.K., Ogasawara, Y., Maruyama, S., Ishida, H., Muko, A., Yoshioka, N., 2004. Discovery of coesite from the Indus Suture Zone (ISZ), Ladakh, India: Evidence for deep subduction. European Journal of Mineralogy, 16, 235-240.

Schilling, J.G., Zajac, M., Evans, R., Johnston, T., White, W., Devine, J.D., Kingsley, R., 1983. Petrologic and geochemical variations along the Mid-Atlantic Ridge from 27 N to 73 N. American Journal of Science, 283, 510-586.

Shervais, J.W., 1982. Ti–V plots and the petrogenesis of modern and ophiolitic lavas. Earth and Planetary Science Letters, 59,101-118.

Spandler, C., Hermann, J., 2006. High-pressure veins in eclogite from New Caledonia and their significance for fluid migration in subduction zones. Lithos, 89, 135-153.

Spear, F.S., 1988. Metamorphic fractional crystallization and internal metasomatism by diffusional homogenization of zoned garnets. Contribution to Mineralogy and Petrology, 99, 507-517.

Spencer, D.A., Tonarini, S., Pognante, U., 1995. Geochemical and Sr-Nd isotopic characterisation of Higher Himalayan eclogites (and associated metabasites). European Journal of Mineralogy, 7, 89- 102.

Sun, S.-s., McDonough, W.F., 1989. Chemistry and isotopic sytematics of ocean basalts: implications for mantle composition and processes. In: Saunders, A.D., Norry, M.J., (eds). Magmatism in the Ocean Basin. Geological Society, London, Special Publications, 42, 313-345.

Tonarini, S., Villa, I.M., Oberli, F., Meier, M., Spencer, D.A., Pognante, U., Ramsay, J.G., 1993. Eocene age of eclogite metamorphism in Pakistan Himalaya: implications for India-Eurasia collision. Terra Nova, 5, 13-20.

Treloar, P.J., Searle, M.P., (eds), 1993. Himalayan Tectonics. Geological Society, London, Special Publications, 74.

Treloar, P.J., O'Brien, P.J., Parrish, R.R., Khan, M.A., 2003. Exhumation of early Tertiary, coesite-bearing eclogites from the Pakistan Himalaya. Journal of the Geological Society, London, 160, 367-376.

Verma, S.P., 2006. Extension-related origin of magmas from a garnet-bearing source in the Los Tuxtlas volcanic field. International Journal of Earth Science, 95, 871-901.

Wadia, D.N., 1931. The syntaxis of the North-West Himalaya: Its rocks, tectonics and orogeny. Records of the Geological Survey of India, 65, 189-220.

Winchester, J.A., Floyd, P.A., 1977. Geochemical discrimination of different magma series and their differentiation products using immobile elements. Chemical Geology, 20,325-343.

Zuleger, E., Erzinger, J., 1988. Determination of the REE and Y in silicate materials with ICP-AES. Fresenius Zeitschrift für Analytische Chemie, 332,140-43.

Figure Captions

Fig.1 Simplified geological map of upper Kaghan Valley, north Pakistan (modified after Greco & Spencer, 1993; Lombardo et al., 2000) showing locations of investigated eclogites. Inset map shows the regional location.

Fig.2 A-L Textural features of the various eclogites. **A** Several cm-sized dark red garnets and cm-sized white titanite (ttn) grains set in a matrix of dark green clinopyroxene. Hand specimen, PKB3. **B** Cluster of zoned garnets (garnetite), showing pale inclusion rich cores with sharply-bounded, irregularly-shaped darker margins. Darker grains are rutile. Photomicrograph, plane polars, K4-76. **C** Strongly foliated and retrogressed eclogite containing a green to grey matrix (epidote and symplectite), layers of red garnet and large secondary black amphibole porphyroblasts. Hand specimen, K4-105. **D** Lens-like, inclusion-rich (mostly omphacite and garnet) clinozoisite (czo) crystal wrapped by bands of fine-grained garnet (grt) defining the strong foliation. Photomicrograph, crossed nicols, PK2-4. **E** Zoisite (zo) and quartz (qz) forming leucocratic segregations. Euhedral nematoblastic amphibole (amp) is restricted to such zones. Lepidoblastic biotite (bt) is secondary. Rutile is rimmed by ilmenite, which is itself surrounded by titanite. Photomicrograph, plane polars, K4-87. **F** Kyanite (ky) in a leucocratic segregation surrounded by biotite (bt). Photomicrograph, plane polars, PK2-4. **G** Phengite (phg) in a leucocratic segregation partially replaced by a biotite (bt) – albite (alb) intergrowth. Photomicrograph, crossed nicols, J Nar2. **H** Optically-zoned garnet, fresh omphacite, chains of rutile and lilac glaucophane core to dark green

barroisite. Vertical cracks relate to a later greenshist facies overprint. Photomicrograph, plane polars, K4-120. **I** Colour-coded Raman map showing coesite (green) rimmed and crosscut by quartz (blue) hosted in omphacite. K4-106. **J** Anhedral to semi-euhedral garnet (grt) sit in a very fine grained matrix of omphacite (omp: dark grey) relicts, replaced by symplectites of secondary clinopyroxene (medium grey), plagioclase (black) and amphibole. Porphyroblastic amphibole (amp) overgowth the matrix. BSE-image, K3-11. **K** Plagioclase laths preserving an original magmatic texture in metadolerite. Photomicrograph, crossed nicols, K3-3. **L** Garnet chains filled with quartz inclusions in metadolerite. Photomicrograph, plane polars, K3-47.

Fig.3 A-F Garnet compositional zoning profiles, show rim to rim or rim to core variations of Ca, Fe, Mg and Mn calculated per 24 oxygens. Distances in μm are given below the horizontal axes. X_{Mg}= Mg/(Mg+Fe^{2+}) See text for details.

Fig.4 Qualitative compositional map of garnet zoning in UHP eclogites (K4-120). Element concentrations (rainbow scale) rise from dark blue (low) to red (high).

Fig.5 Clinopyroxene analyses plotted in the Jd-Aeg-Quad (Quad: Ca-Mg-Fe pyroxene area) triangular diagram after Morimoto (1988). Open symbols represent primary omphacites whereas filled symbols are for secondary (symplectite) clinopyroxene.

Fig.6 A-D Representative plots of amphibole analyses. Different symbols indicate porphyroblastic amphiboles (black filled symbols), rims of porphyroblasts (open symbols), symplectitic types (small open symbols) and inclusions in clinozoisite (grey filled box). Each symbol (square, triangle, etc.) represents analyses from one sample. C and D are for coesite+glaucophane-bearing eclogite (K4-120) with D showing a typical core–rim compositional profile.

Fig.7 A-D Geochemical discrimination plots for the different eclogites. **A** after Winchester & Floyd (1977). **B** Chondrite-normalised REE abundances (after McDonough & Sun, 1995). **C** and **D** show incompatible elements normalized to (C) primitive mantle (PRIMA) (after Hofmann, 1988) and (D) enriched mid-ocean ridge basalt (E-MORB) (after Sun & McDonough, 1989).

Fig.8 Spatial distribution of temperatures (°C) at 30 kbar derived by standard geothermometry for studied eclogites, using Grt-Cpx (Krogh, 1988). Further methods and details are presented in Table 6 and Fig.1.

Fig.9 Phase diagram for garnet-fractionated bulk rock chemistry of the UHP eclogite (K4-120) calculated with Perple_X. Plotted are Si content in phengite (p.f.u.) and Na on A-site in amphibole. Also plotted are the water-saturated basalt solidus (Lambert &

Wyllie, 1972) and Graphite-Diamond curve (Kennedy & Kennedy, 1976). Coe-Qtz and Alb=Jd+Qtz equilibria are calculated within the phase diagram calculation. The ellipse indicates the field for the measured glaucophane composition whereas the grey-shaded area denotes the limits from corner Amp-Plag barometry. Large arrows show our preferred PT-path. Published PT-paths for Kaghan Valley (Rehman et al., 2008) and for Tso Morari coesite eclogites (Guillot et al., 2008) are shown for comparison.

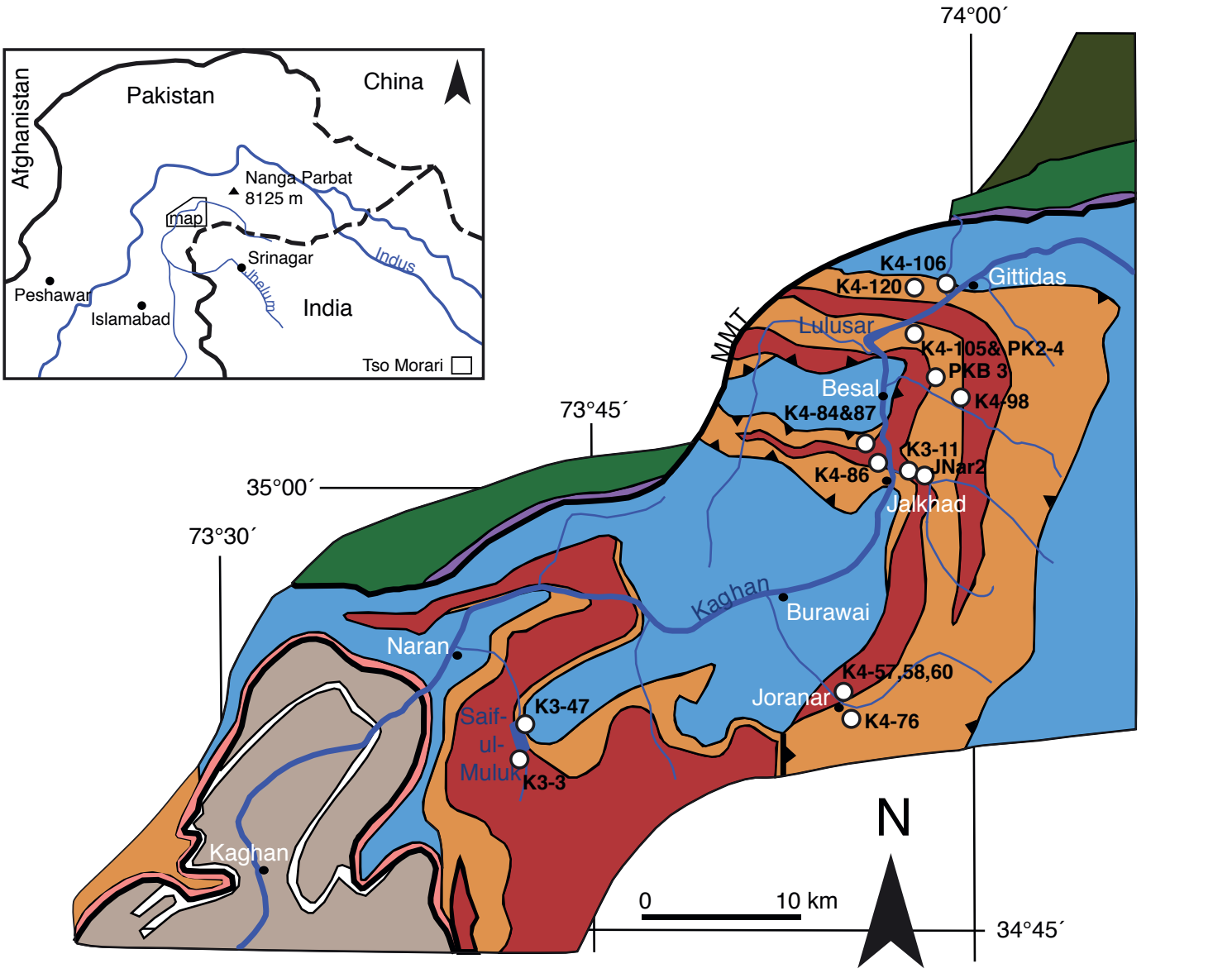

Kohistan Arc

- Metadiorite, Amphibolite
- Pyroxene granulites, Peridotites
- Serpentinites

Higher Himalayan Crystalline

- Carbonate and clastic metasedimentary cover
- Metapelite-rich cover
- Granitic basement
- Granitic mylonites

Lesser Himalaya

- Metapelites with marbles

- Faults (thrust marked with a Triangle)
- sample location

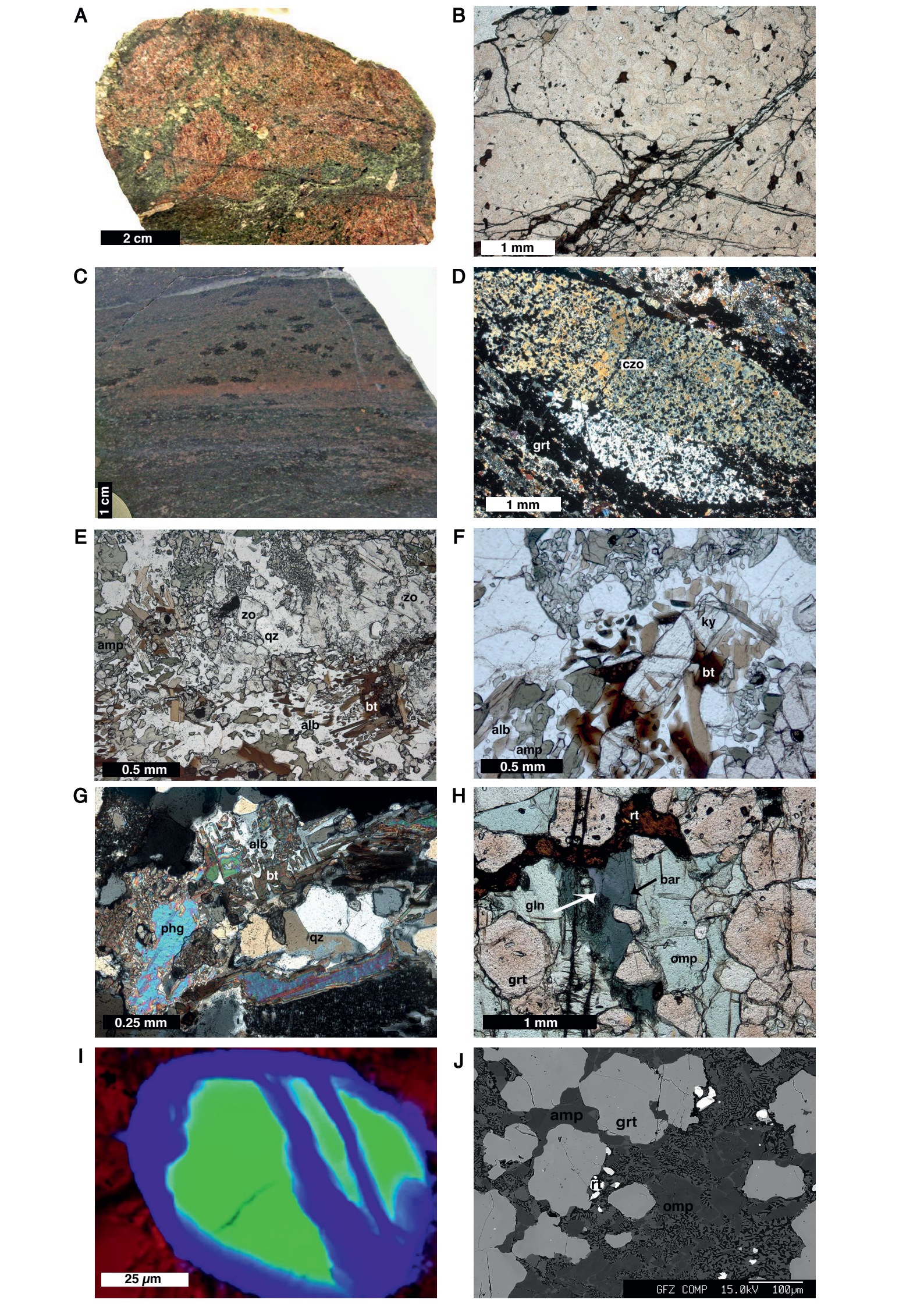
A
2 cm
B
1 mm
C
1 cm
D
czo
grt
1 mm
E
zo
zo
qz
amp
bt
alb
0.5 mm
F
ky
bt
alb
amp
0.5 mm
G
alb
bt
phg
qz
0.25 mm
H
rt
bar
gln
omp
grt
1 mm
I
25 µm
J
amp
grt
rt
omp
GFZ COMP 15.0kV 100µm

K

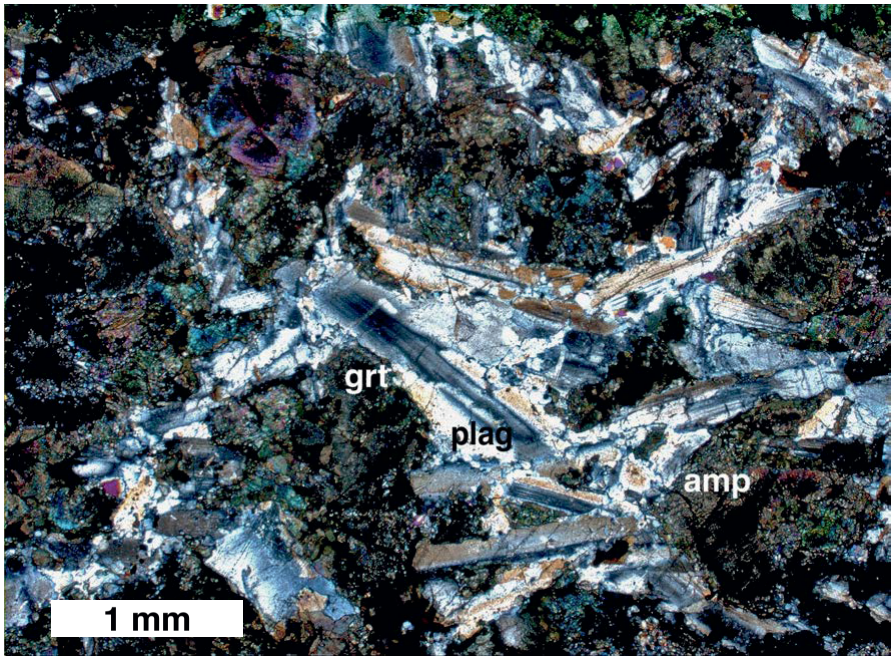

L

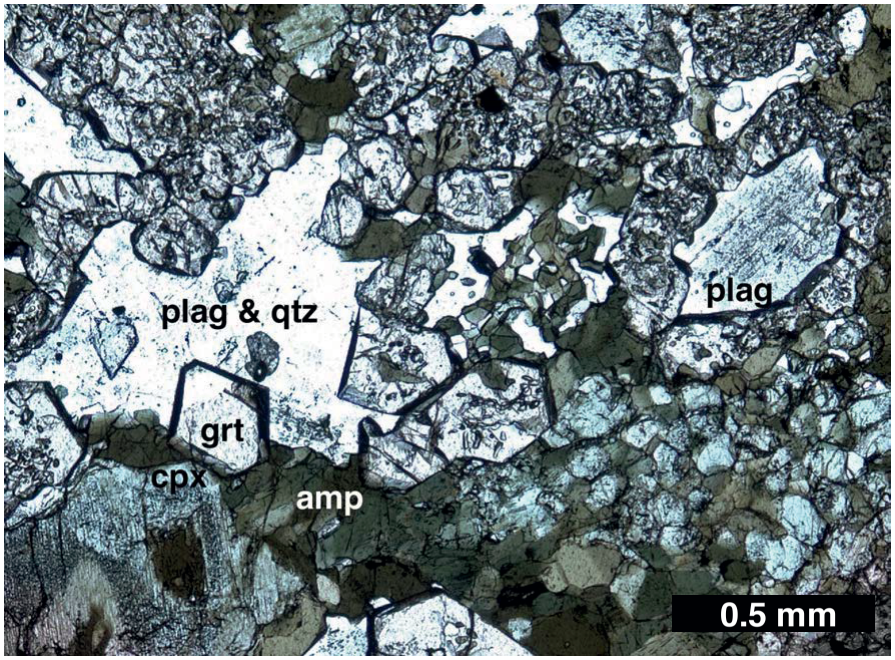

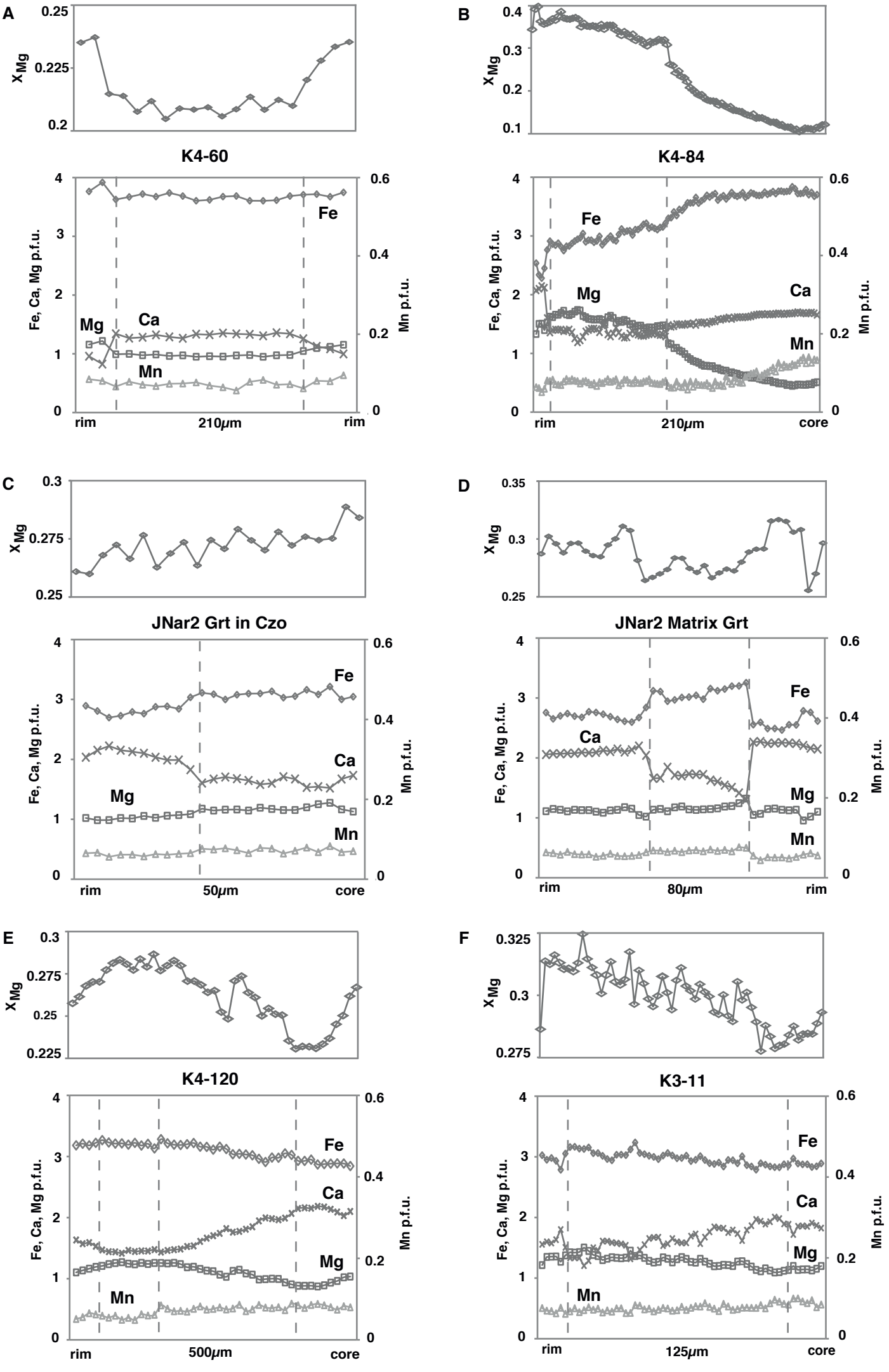
A
B
C
D
E
F
X_{Mg}
K4-60
K4-84
JNar2 Grt in Czo
JNar2 Matrix Grt
K4-120
K3-11
Fe, Ca, Mg p.f.u.
Mn p.f.u.
Fe
Ca
Mg
Mn
rim
core
210μm
50μm
80μm
500μm
125μm

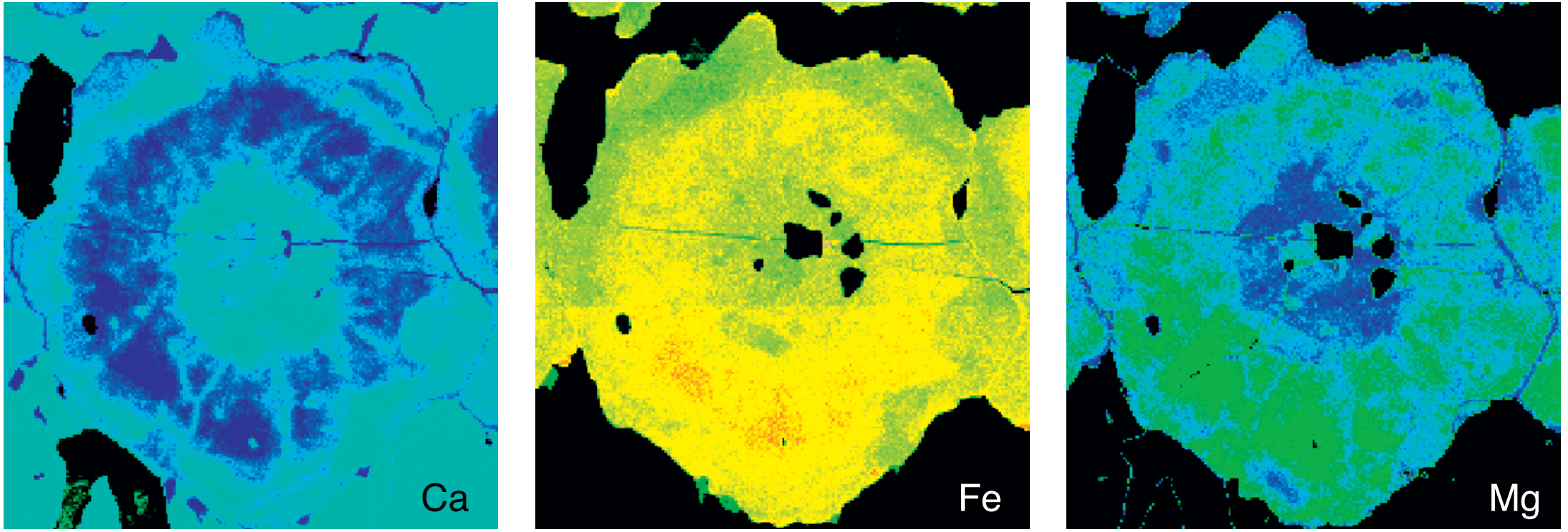
Ca
Fe
Mg

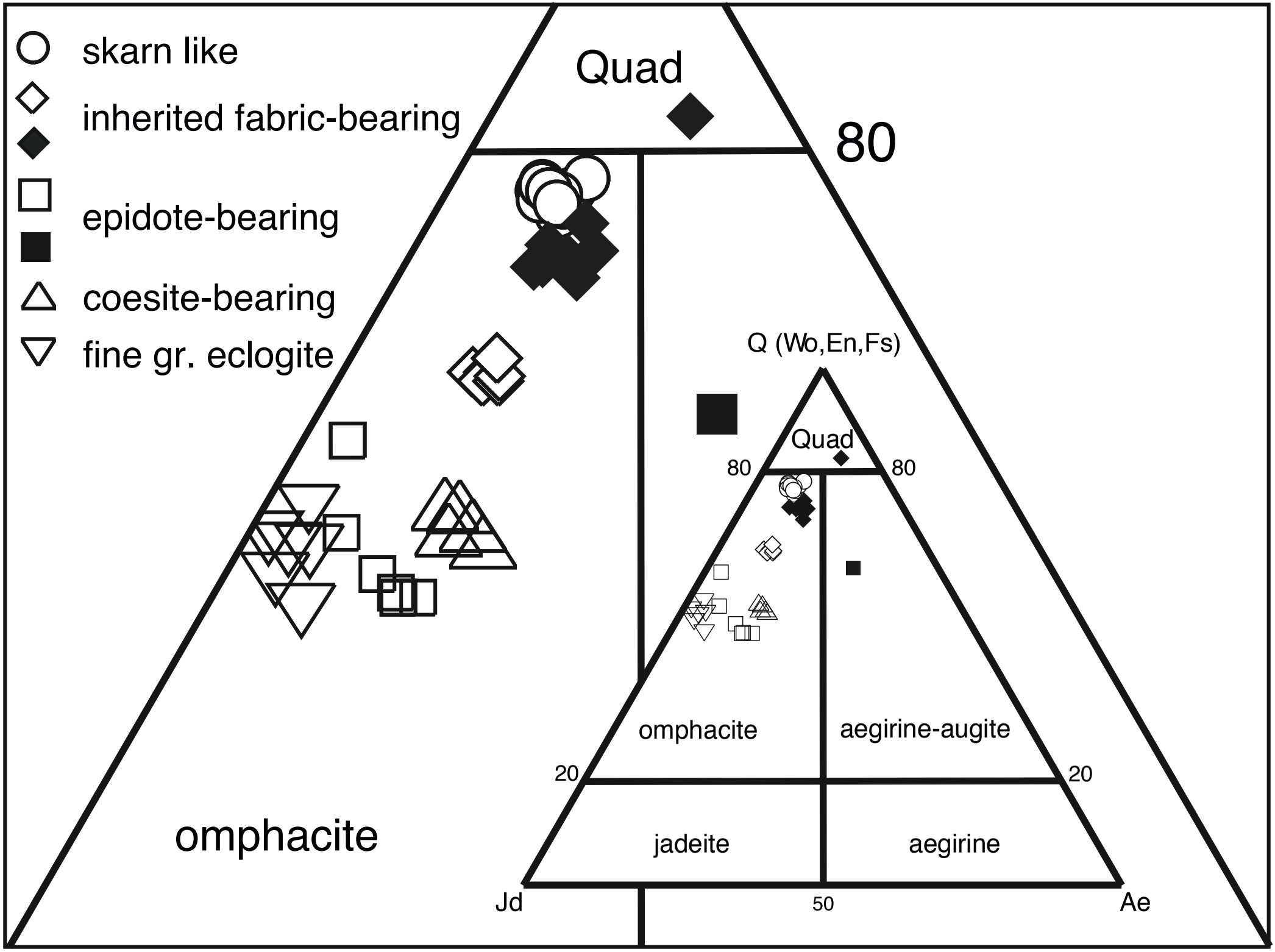
skarn like
inherited fabric-bearing
epidote-bearing
coesite-bearing
fine gr. eclogite
Quad
80
omphacite
Q (Wo,En,Fs)
Quad
80
80
omphacite
aegirine-augite
20
20
jadeite
aegirine
Jd
50
Ae

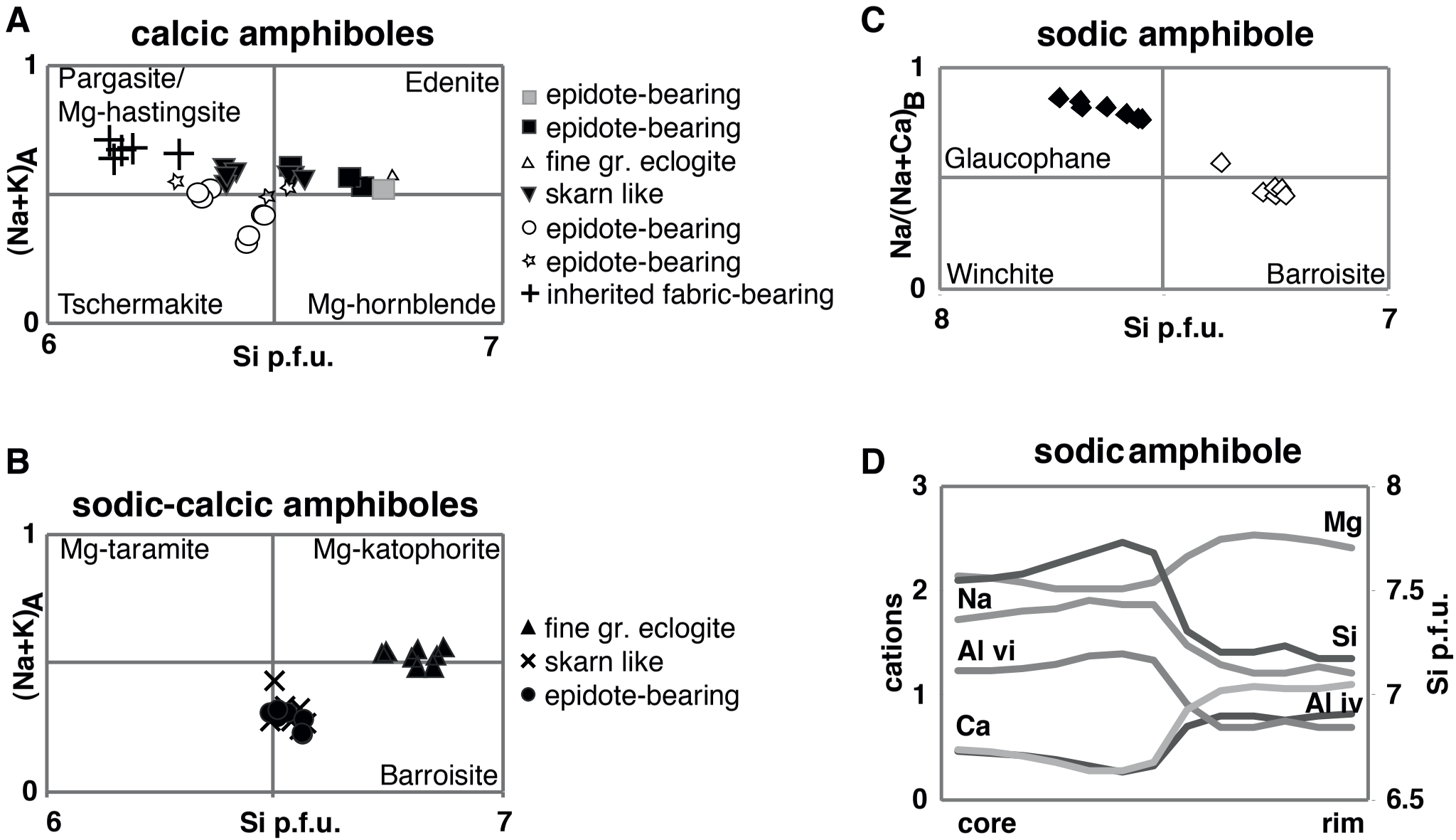
A
calcic amphiboles
Pargasite/
Mg-hastingsite
Edenite
Tschermakite
Mg-hornblende
(Na+K)A
Si p.f.u.
epidote-bearing
epidote-bearing
fine gr. eclogite
skarn like
epidote-bearing
epidote-bearing
inherited fabric-bearing
B
sodic-calcic amphiboles
Mg-taramite
Mg-katophorite
Barroisite
(Na+K)A
Si p.f.u.
fine gr. eclogite
skarn like
epidote-bearing
C
sodic amphibole
Glaucophane
Winchite
Barroisite
Na/(Na+Ca)B
Si p.f.u.
D
sodic amphibole
Mg
Na
Si
Al vi
Al iv
Ca
cations
Si p.f.u.
core
rim

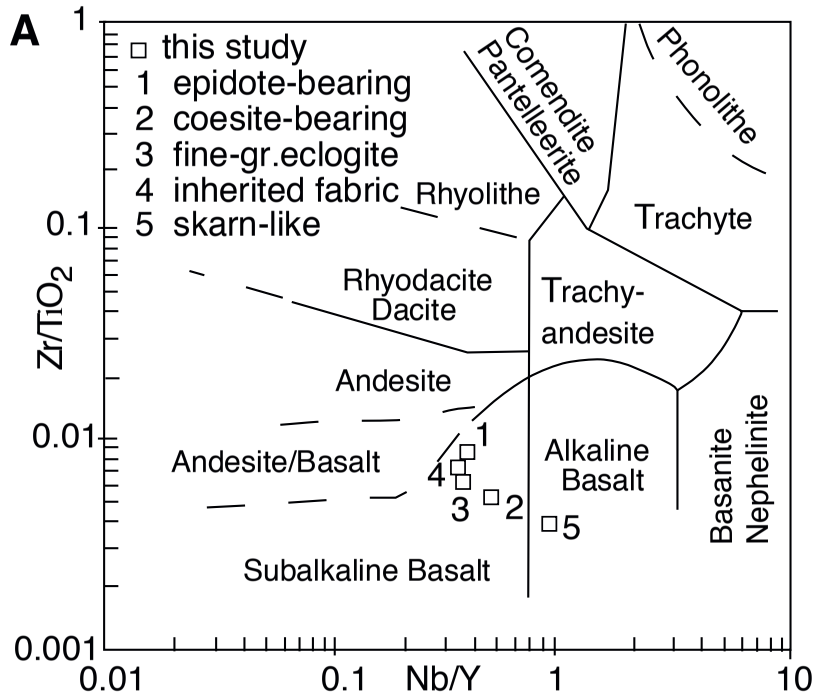
A
this study
1 epidote-bearing
2 coesite-bearing
3 fine-gr.eclogite
4 inherited fabric
5 skarn-like
Comendite
Pantelleerite
Phonolithe
Rhyolithe
Trachyte
Rhyodacite
Dacite
Trachy-
andesite
Andesite
Andesite/Basalt
Alkaline
Basalt
Basanite
Nephelinite
Subalkaline Basalt
Zr/TiO2
Nb/Y
0.001
0.01
0.1
1
10

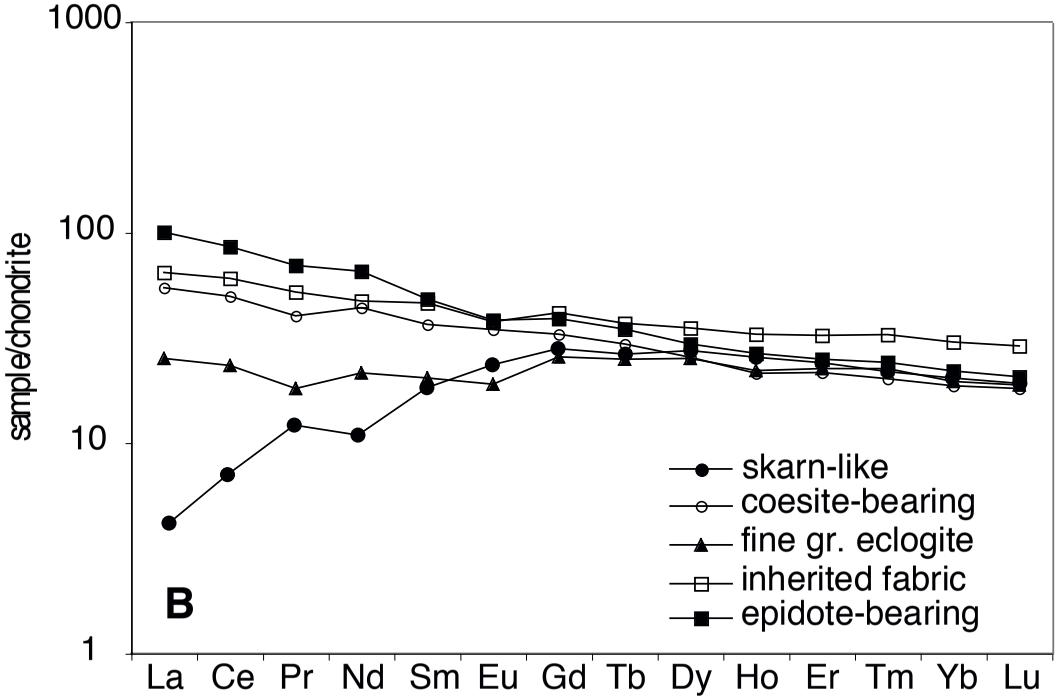
B
sample/chondrite
1000
100
10
1
La Ce Pr Nd Sm Eu Gd Tb Dy Ho Er Tm Yb Lu
skarn-like
coesite-bearing
fine gr. eclogite
inherited fabric
epidote-bearing

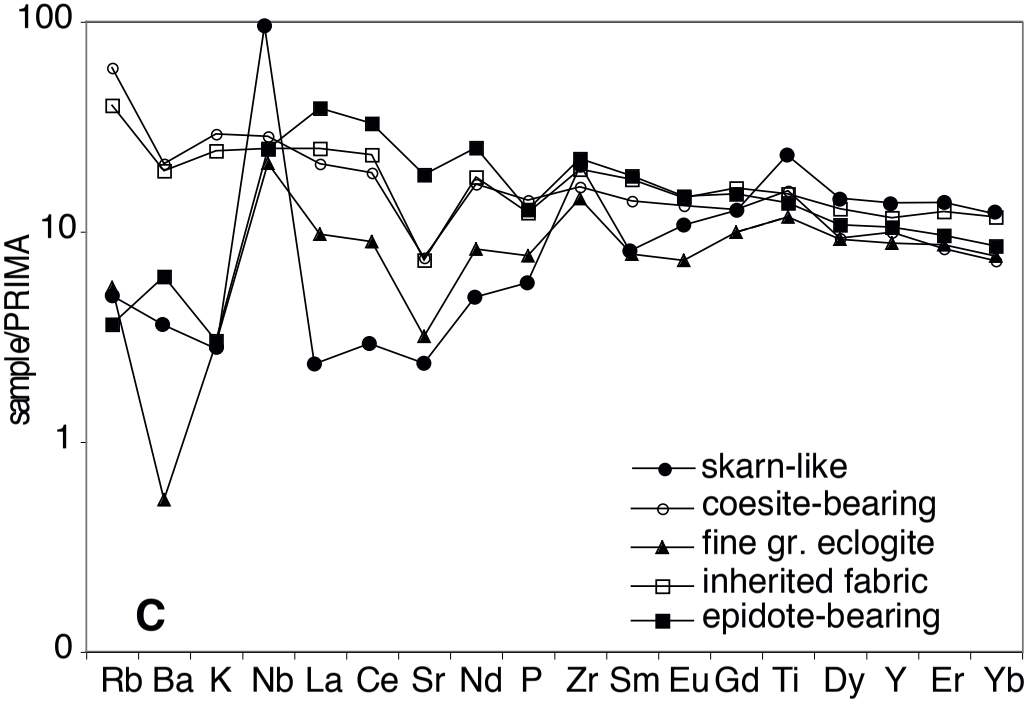
C
sample/PRIMA
100
10
1
0
Rb Ba K Nb La Ce Sr Nd P Zr Sm Eu Gd Ti Dy Y Er Yb
skarn-like
coesite-bearing
fine gr. eclogite
inherited fabric
epidote-bearing

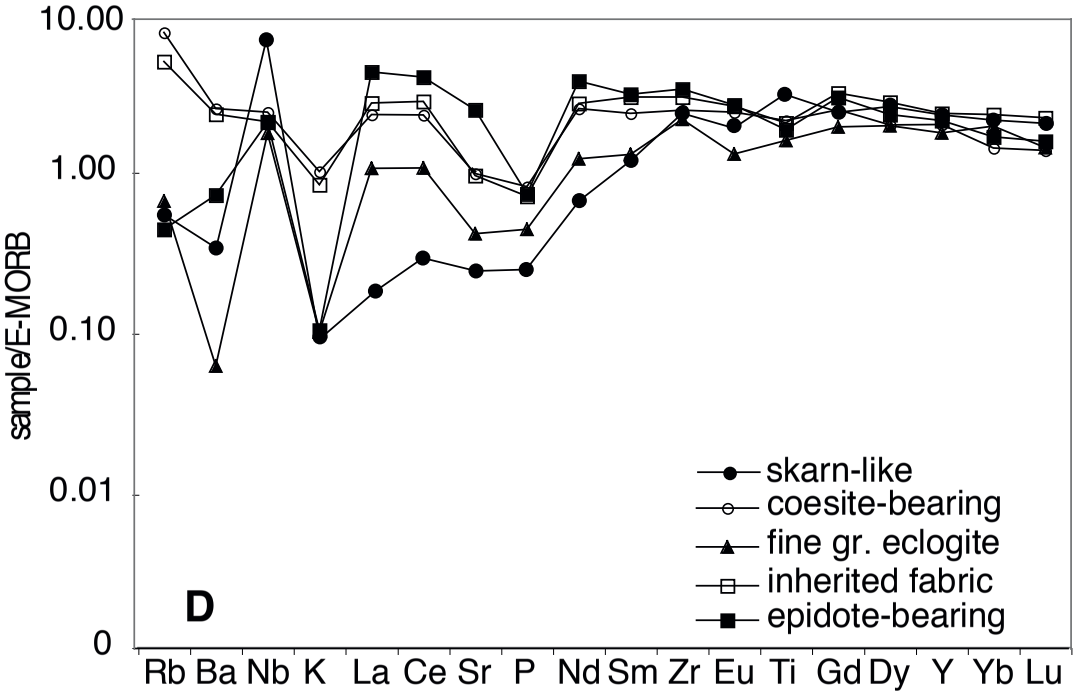
D
sample/E-MORB
10.00
1.00
0.10
0.01
0
Rb Ba Nb K La Ce Sr P Nd Sm Zr Eu Ti Gd Dy Y Yb Lu
skarn-like
coesite-bearing
fine gr. eclogite
inherited fabric
epidote-bearing

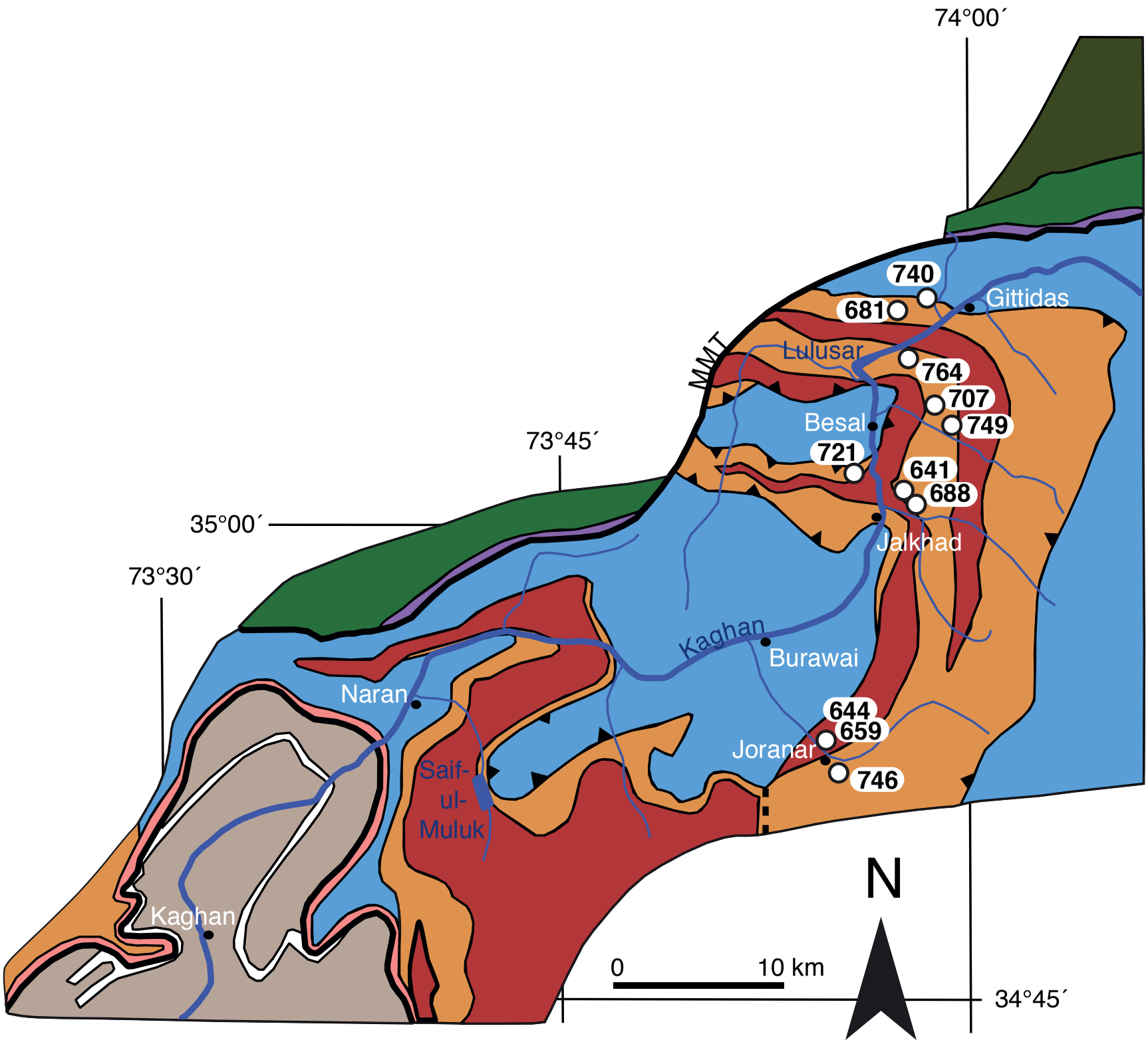
74°00´
740
681
Gittidas
MMT
Lulusar
764
707
749
Besal
721
641
688
Jalkhad
73°45´
35°00´
73°30´
Kaghan
Burawai
Naran
644
659
Joranar
746
Saif-
ul-
Muluk
Kaghan
N
0
10 km
34°45´

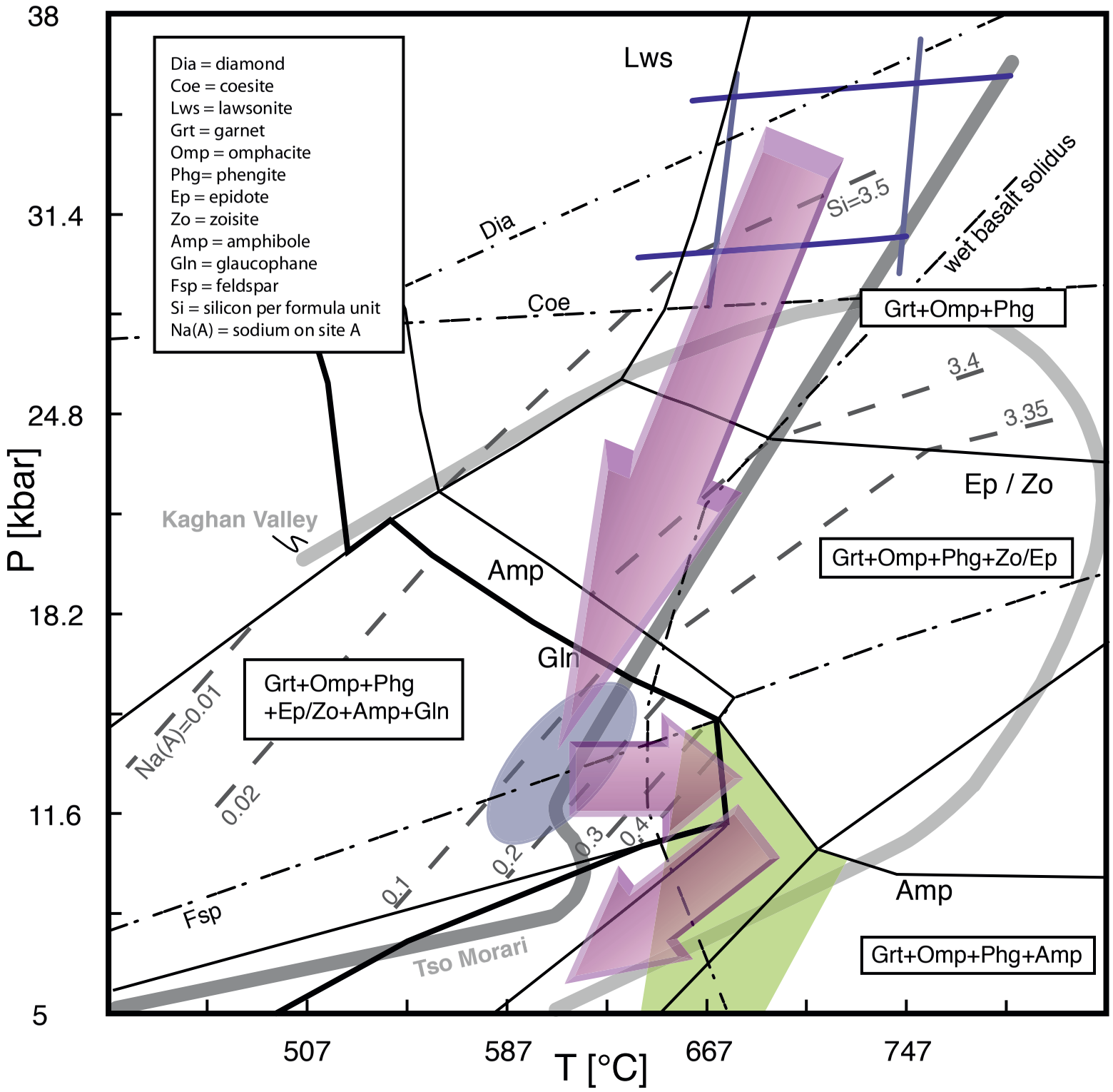
Dia = diamond
Coe = coesite
Lws = lawsonite
Grt = garnet
Omp = omphacite
Phg= phengite
Ep = epidote
Zo = zoisite
Amp = amphibole
Gln = glaucophane
Fsp = feldspar
Si = silicon per formula unit
Na(A) = sodium on site A
Lws
Dia
Coe
Si=3.5
wet basalt solidus
Grt+Omp+Phg
3.4
3.35
Ep / Zo
Grt+Omp+Phg+Zo/Ep
Kaghan Valley
Amp
Gln
Grt+Omp+Phg
+Ep/Zo+Amp+Gln
Na(A)=0.01
0.02
0.1
0.2
0.3
0.4
Fsp
Tso Morari
Amp
Grt+Omp+Phg+Amp
P [kbar]
38
31.4
24.8
18.2
11.6
5
507
587
667
747
T [°C]

sample	K4-60	K4-60	K4-76	K4-57	K4-98	K4-98	K4-84	K4-84	K4-84	JNar2	JNar2	JNar2	JNar2	PK2-4	K4-120b	K4-120	K4-120	K3-11	K3-11
wt%/position	core	rim	general	general	core	shell	core	shell	rim	incl core	incl rim	matrix core	matrix rim	rim	core	shell	rim	core	rim
SiO_2	37.84	38.28	38.08	38.32	39.98	38.70	37.34	38.61	38.70	38.60	38.24	38.49	38.74	38.66	38.48	38.56	38.53	38.73	38.79
TiO_2	0.13	0.04	0.06	0.10	0.05	0.03	0.11	0.02	0.05	0.14	0.10	0.10	0.09	0.11	0.04	0.08	0.06	0.07	0.03
Al_2O_3	20.46	20.94	21.35	21.15	21.79	21.95	20.20	21.32	21.43	21.54	21.50	21.69	21.93	21.68	21.39	21.34	21.11	21.59	22.23
Cr_2O_3	<0.01	0.02	0.02	0.02	0.07	0.06	0.04	<0.01	0.02	0.04	0.01	0.03	0.04	0.04	0.01	0.01	0.02	0.05	<0.01
FeO	28.63	29.50	24.79	26.09	21.60	21.85	28.28	22.39	19.01	21.71	24.96	24.02	20.43	22.80	22.64	25.50	25.31	22.81	22.47
MgO	4.15	4.94	5.80	5.23	9.26	9.88	1.95	7.43	6.38	4.28	5.16	4.90	5.05	6.70	3.76	5.45	4.76	4.66	5.56
MnO	0.59	0.72	0.69	0.29	0.35	0.35	0.88	0.44	0.39	0.43	0.60	0.53	0.39	0.54	0.41	0.59	0.61	0.42	0.59
CaO	7.85	5.94	8.96	8.34	7.79	7.06	10.65	9.16	13.75	13.42	9.17	10.36	13.68	9.23	13.09	8.90	9.79	11.72	10.97
Na_2O	0.01	0.02	<0.01	0.04	<0.01	<0.01	<0.01	<0.01	<0.01	0.03	0.01	0.03	0.01	n.d.	0.03	0.06	0.01	0.03	0.02
Sum	99.66	100.38	99.74	99.57	99.89	99.88	99.45	99.37	99.72	100.20	99.73	100.13	100.37	99.77	99.85	100.49	100.19	100.07	100.65
Si	5.99	6.00	5.92	6.00	5.92	5.87	5.98	5.96	5.93	5.97	5.97	5.97	5.94	5.96	5.99	5.97	6.00	6.00	5.95
Al	3.82	3.87	3.91	3.90	3.90	3.92	3.81	3.87	3.87	3.93	3.95	3.97	3.96	3.95	3.93	3.89	3.87	3.94	4.02
Ti	0.02	<0.01	0.01	0.01	0.01	<0.01	0.01	<0.01	0.01	0.02	0.01	0.01	0.01	0.01	0.01	0.01	0.01	0.01	<0.01
Cr	<0.01	<0.01	<0.01	<0.01	0.01	0.01	0.01	-	<0.01	<0.01	<0.01	<0.01	0.01	0.01	<0.01	<0.01	<0.01	0.01	<0.01
Fe^{2+}	3.61	3.75	3.00	3.33	2.52	2.44	3.58	2.68	2.17	2.70	3.16	3.04	2.49	2.83	2.87	3.13	3.18	2.92	2.79
Fe^{3+}	0.18	0.12	0.22	0.08	0.23	0.33	0.21	0.21	0.26	0.11	0.10	0.07	0.13	0.11	0.08	0.17	0.11	0.04	0.09
Mg	0.98	1.15	1.34	1.22	2.10	2.23	0.46	1.71	1.46	0.99	1.20	1.13	1.15	1.54	0.87	1.26	1.10	1.08	1.27
Mn	0.08	0.10	0.09	0.04	0.04	0.04	0.12	0.06	0.05	0.06	0.08	0.07	0.05	0.07	0.05	0.08	0.08	0.05	0.08
Ca	1.33	1.00	1.49	1.40	1.27	1.15	1.83	1.51	2.26	2.22	1.53	1.72	2.25	1.53	2.18	1.48	1.63	1.95	1.80
Na	<0.01	0.01	-	0.01	-	-	-	-	-	0.01	<0.01	0.01	<0.01	-	0.01	0.02	<0.01	0.01	<0.01
X_{Mg}	0.214	0.235	0.309	0.268	0.454	0.478	0.115	0.390	0.401	0.268	0.275	0.271	0.317	0.352	0.233	0.287	0.258	0.270	0.313
Alm	60.2	62.5	50.6	55.6	42.5	41.6	59.8	44.9	36.6	45.2	52.9	51.0	41.9	47.5	48.0	52.7	53.0	48.7	47.0
Adr	4.6	3.0	5.7	2.0	5.7	8.4	5.1	5.3	6.7	2.8	2.4	1.8	3.3	2.7	2.0	4.3	2.9	1.0	2.4
Grs	17.6	13.6	19.5	21.3	15.5	11.0	25.2	20.1	31.3	34.4	23.2	26.9	34.4	22.7	34.5	20.5	24.3	31.3	28.0
Prp	16.3	19.2	22.7	20.4	35.4	38.1	7.8	28.7	24.5	16.6	20.1	19.0	19.4	25.8	14.6	21.2	18.4	18.0	21.4
Sps	1.3	1.6	1.5	0.6	0.8	0.8	2.0	1.0	0.8	0.9	1.3	1.2	0.9	1.2	0.9	1.3	1.3	0.9	1.3

Table 2.1. Representative garnet analyses. n.d.=not determined. Normalised to 24[O], ferric iron calculated by charge balance. X_{Mg}= Mg/(Fe^{2+}+Mg)

sample	K4-60	K4-57	K4-76 p	K4-76 s	K4-98 p	K4-84 s	PK2-4 p	PK2-4 s	JNar 2	K4-120	K3-11
SiO_2	55.21	53.81	52.67	51.81	54.84	52.75	54.85	52.87	56.13	54.29	56.86
TiO_2	0.04	0.17	0.26	0.27	0.14	0.11	0.04	0.11	0.05	0.12	0.06
Al_2O_3	6.53	8.90	8.89	6.62	9.08	7.97	10.29	7.98	10.48	9.31	11.52
Cr_2O_3	0.05	<0.01	0.05	0.02	0.02	0.05	0.07	0.05	<0.01	0.04	0.05
FeO	9.30	9.36	8.58	9.41	4.92	8.57	7.04	7.57	4.67	7.95	2.46
MgO	8.20	8.48	8.15	9.53	9.62	9.27	7.66	10.17	8.55	8.22	8.85
MnO	0.03	0.02	0.06	0.06	0.02	0.04	0.03	0.04	0.01	0.04	<0.01
CaO	13.67	14.29	15,28	17.92	15.53	16.31	12.02	16.21	13.96	13.28	13.92
Na_2O	6.64	5.83	5.34	3.68	5.50	4.88	7.13	4.87	6.95	6.35	7.15
K_2O	<0.01	n.d.	<0.01	<0.01	n.d.	n.d.	<0.01	n.d.	n.d.	<0.01	n.d.
Sum	99.68	100.86	99.28	99.33	99.67	99.94	99.13	99.87	100.80	99.60	100.87
Si	2.00	1.94	1.92	1.91	1.97	1.91	1.97	1.91	1.98	1.96	1.99
Al^{IV}	<0.01	0.06	0.08	0.09	0.03	0.09	0.03	0.09	0.02	0.04	0.01
Al^{VI}	0.28	0.32	0.31	0.20	0.35	0.26	0.41	0.25	0.41	0.35	0.46
Ti	<0.01	<0.01	0.01	0.01	<0.01	<0.01	<0.01	<0.01	<0.01	<0.01	<0.01
Cr	<0.01	<0.01	<0.01	<0.01	<0.01	<0.01	<0.01	<0.01	<0.01	<0.01	<0.01
Fe^{2+}	0.09	0.12	0.13	0.16	0.09	0.09	0.10	0.06	0.05	0.12	0.04
Fe^{3+}	0.19	0.15	0.13	0.13	0.05	0.17	0.11	0.17	0.08	0.12	0.03
Mg	0.44	0.46	0.44	0.52	0.51	0.50	0.41	0.55	0.45	0.44	0.46
Mn	<0.01	<0.01	<0.01	<0.01	0.00	<0.01	<0.01	<0,01	<0.01	<0.01	<0.01
Ca	0.53	0.55	0.60	0.71	0.60	0.63	0.46	0.63	0.53	0.51	0.52
Na	0.47	0.41	0.38	0.26	0.38	0.38	0.50	0.34	0.47	0.44	0.48
X_{Mg}	0.82	0.79	0.77	0.77	0.85	0.84	0.80	0.91	0.89	0.79	0.92
Xjd	0.28	0.25	0.25	0.13	0.33	0.18	0.39	0.17	0.39	0.32	0.45
Xaeg	0.19	0.15	0.13	0.13	0.05	0.17	0.11	0.18	0.08	0.12	0.04
Quad	0.53	0.54	0.55	0.66	0.59	0.58	0.48	0.57	0.50	0.52	0.50

Table 2.2. Representative omphacite analyses. n.d.=not determined. Normalised to 6[O]. Ferric iron calculated by charge balance. X_{Mg}=Mg/(Fe^{2+}+Mg). p=primary; s=secondary

sample	PKB3	K4-60	K4-57	K4-76	K4-105	K4-105	PK2-4	PK2-4	K4-120b	K4-120b	K4-106	K3-11
wt%/type	pargasite	barroisite	Mg-hastingsite	Mg-hastingsite	barroisite	tschermakite	edenite	pargasite	glaucophane	barroisite	barroisite	barroisite
SiO_2	43.02	45.25	42.07	42.19	45.86	45.16	45.56	43.08	55.74	52.05	50.24	48.55
TiO_2	1.29	0.51	0.57	1.21	1.14	1.84	0.75	0.65	0.09	0.09	0.20	0.34
Al_2O_3	12.86	10.45	14.02	13.43	12.00	12.23	12.40	15.35	10.93	10.64	9.99	12.08
Cr_2O_3	0.02	0.02	0.02	<0.01	n.d.	<0.01	0.02	0.08	<0.01	0.04	0.07	0.01
FeO	15.97	16.77	16.90	16.16	11.60	10.31	12.52	10.42	12.84	14.67	12.91	9.41
MnO	0.03	0.09	0.04	0.04	0.05	0.01	0.02	0.03	0.02	0.07	0.04	0.01
MgO	10.36	12.00	10.53	11.03	13.98	14.14	13.08	12.76	9.61	10. 20	12.66	14.25
CaO	11.01	8.55	11.35	11.48	9.67	10.08	11.65	11.62	3.15	7.36	8.43	8.84
Na_2O	2.62	3.05	2.23	2.56	2.92	3.14	2.13	2.59	5.95	4.45	3.66	3.98
K_2O	0.50	0.49	1.60	0.86	0.37	0.15	0.67	0.24	0.06	0.23	0.22	0.40
Sum	97.66	97.26	99.33	98.95	97.57	97.06	98.80	96.82	98.39	99.80	98.42	97.86
Si	6.36	6.54	6.15	6.17	6.52	6.47	6.53	6.26	7.74	7.34	7.14	6.85
Al^{IV}	1.64	1.46	1.85	1.83	1.48	1.53	1.47	1.74	0.26	0.66	0.86	1.15
T	*8.00*	*8.00*	*8.00*	*8.00*	*8.00*	*8.00*	*8.00*	*8.00*	*8.00*	*8.00*	*8.00*	*8.00*
Al^{VI}	0.60	0.32	0.57	0.48	0.53	0.54	0.62	0.89	1.53	1.11	0.82	0.86
Ti	0.14	0.06	0.06	0.13	0.12	0.20	0.08	0.07	0.01	0.01	0.02	0.04
Fe^{3+}	0.43	1.43	0.67	0.60	0.89	0.59	0.40	0.31	0.10	0.03	0.24	0.39
Cr	<0.01	<0.01	<0.01	<0.01	<0.01	<0.01	<0.01	0.01	-	<0.01	0.01	<0.01
Mg	2.28	2.58	2.30	2.40	2.96	3.02	2.79	2.76	1.99	2.14	2.68	3.00
Fe^{2+}	1.55	0.60	1.40	1.37	0.49	0.65	1.10	0.95	1.37	1.70	1.23	0.72
Mn	<0.01	0.01	0.01	<0.01	0.01	<0.01	<0.01	<0.01	-	-	-	<0.01
C	*5.00*	*5.00*	*5.00*	*5.00*	*5.00*	*5.00*	*5.00*	*5.00*	*5.00*	*5.00*	*5.00*	*5.00*
Fe	-	-	-	-	-	-	-	-	0.02	-	0.06	-
Mn	-	-	-	-	-	-	-	-	<0.01	0.01	<0.01	-
Ca	1.74	1.32	1.78	1.80	1.47	1.55	1.79	1.81	0.47	1.11	1.28	1.34
Na	0.26	0.68	0.22	0.20	0.53	0.45	0.21	0.19	1.50	0.88	0.65	0.66
B	*2.00*	*2.00*	*2.00*	*2.00*	*2.00*	*2.00*	*2.00*	*2.00*	*2.00*	*2.00*	*2.00*	*2.00*
Na in A	0.49	0.18	0.41	0.52	0.28	0.42	0.38	0.54	0.10	0.34	0.36	0.42
K in A	0.10	0.09	0.19	0.16	0.07	0.03	0.12	0.04	0.01	0.04	0.04	0.07
A	*0.59*	*0.27*	*0.60*	*0.68*	*0.34*	*0.45*	*0.50*	*0.58*	*0.11*	*0.38*	*0.40*	*0.50*
sum	15.59	15.27	15.60	15.68	15.34	15.45	15.63	15.58	15.11	15.38	15.40	15.50
X_{Mg}	0.60	0.81	0.62	0.64	0.86	0.82	0.72	0.74	0.59	0.56	0.67	0.81

Table 2.3. Selected amphibole analysis. n.d.=not determined. Calculation is based on 23[O] with Fe^{2+}/Fe^{3+} calculation after charge balance assuming 13 cations excluding Ca, Na, K (except for K4-120 & K4-106 where Fe^{3+} is calculated by charge balance after normalisation to 15 excluding K, Na_A). Cations calculated after Leake et al., 1997. X_{Mg}= $Mg/(Fe^{2+}+Mg)$

sample	K4-76 Phl	K4-57 Phl	JNar2 Bt	PK2-4 Phl	JNar2 Phg core	JNar2 Phg rim	K4-120d Phg	sample	K4-76 Plag	JNar2 Plag	Pk2-4 Plag	PK2-4 Plag	sample	JNar2 Zo rim	JNar2 Zo core	PK2-4 Czo	K4-120 Ep
SiO_2	36.16	36.88	39.14	37.63	51.14	49.37	51.35	SiO_2	63.48	62.00	62.64	60.05	SiO_2	39.88	39.95	38.85	38.30
TiO_2	4.05	3.77	1.58	3.21	0.65	0.50	0.71	TiO_2	<0.01	0.03	0.02	0.01	TiO_2	0.11	0.07	0.07	0.15
Al_2O_3	15.53	15.74	23.83	17.86	28.27	31.15	25.37	Al_2O_3	22.30	23.38	23.56	25.32	Al_2O_3	31.45	31.91	27.86	23.62
Cr_2O_3	0.09	<0.01	<0.01	<0.01	<0.01	<0.01	<0.01	FeO	0.06	0.12	0.29	0.24	Cr_2O_3	0.04	0,02	<0.01	n.d.
FeO	16.50	15.67	10.71	13.14	1.54	1.51	3.25	MnO	<0.01	<0.01	0.02	<0.01	FeO	1.86	1.48	7.30	11.61
MgO	13.41	13.84	10.90	14.89	3.88	2.81	3.83	CaO	3.75	4.98	3.91	6.97	MnO	<0.01	0.01	0.05	0.05
MnO	0.02	<0.01	0.07	0.03	<0.01	<0.01	0.04	Na_2O	10.19	9.42	9.96	8.29	CaO	23.71	23.57	23.20	23.09
CaO	0.02	0.04	0.08	0.08	0.04	0.09	<0.01	K_2O	0.22	0.18	0.22	0.08	Na_2O	0.04	<0.01	<0.01	0.04
Na_2O	0.08	0.09	0.23	0.37	0.30	0.34	0.26	Sum	100.01	100.11	100.41	100.96	K_2O	<0.01	<0.01	0.01	0.01
K_2O	9.16	9.56	9.65	9.41	10.41	10.51	10.73						Sum	97.08	97.00	97.35	96.86
Sum	95.02	95.58	96.20	96.62	96.22	96.27	95.54										
													Si	3.25	3.26	3.07	3.12
Si	2.73	2.76	2.79	2.74	3.36	3.25	3.44	Si	2.81	2.75	2.77	2.66	Al	2.99	3.03	2.59	2.25
Al^{IV}	1.27	1.24	1.21	1.26	0.64	0.75	0.66	Al	1.17	1.22	1.23	1.32	Ti	0.01	<0.01	<0.01	0.01
Al^{VI}	0.11	0.14	0.79	0.27	1.55	1.67	1.44	Ti	<0.01	<0.01	<0.01	<0.01	Fe^{3+}	0.13	0.10	0.48	0.79
Ti	0.23	0.21	0.08	0.18	0.03	0.02	0.04	Fe	<0.01	<0.01	0.01	0.01	Mn	0.00	<0.01	<0.01	<0.01
Cr	0.01	<0.01	<0.01	<0.01	<0.01	<0.01	<0.01	Mn	<0.01	<0.01	<0.01	<0.01	Ca	2.07	2.06	1.96	2.02
Fe	1.04	0.98	0.64	0.80	0.08	0.08	0.18	Ca	0.18	0.24	0.18	0.33	Na	<0.01	<0.01	<0.01	0.01
Mg	1.51	1.54	1.16	1.61	0.38	0.28	0.38	Na	0.88	0.81	0.85	0.71	K	<0.01	<0.01	<0.01	<0.01
Mn	<0.01	<0.01	<0.01	<0.01	<0.01	<0.01	<0.01	K	0.01	0.01	0.01	<0.01	Sum	8.44	8.45	8.10	8.19
Ca	<0.01	<0.01	0.01	0.01	<0.01	0.01	<0.01	An	16.7	22.4	17.6	31.6	Al_2Fe (mol%)	0.13	0.10	0.82	3.23
Na	0.01	0.01	0.03	0.05	0.04	0.04	0.03	Ab	82.1	76.6	81.2	68.0	$Fe^{3+}/Al+Fe^{3+}$	0.04	0.03	0.16	0.26
K	0.88	0.91	0.88	0.87	0.87	0.88	0.92	Kfs	1.2	1.0	1.2	0.4					
X_{Fe}	0.41	0.39	0.36	0.33	0.18	0.23	0.32										
X_{Mg}	0.59	0.61	0.64	0.67	0.82	0.77	0.68										

Table 2.4. Selected microprobe analysis of primary and secondary mica phases, plagioclase and epidote minerals .n.d.=not determined. Normalisation based on 11oxygens for mica, 8 oxygens for plagioclase and 12.5 for epidote minerals. Al_2 Fe=Fe/(Al-2) (Franz et al., 1995)).

eclogite type wt. %	SiO_2	TiO_2	Al_2O_3	Fe_2O_3(tot)	MnO	MgO	CaO	Na_2O	K_2O	P_2O_5	CO_2	H_2O	Sum
coesite-bearing	48.03	2.85	13.20	14.25	0.21	6.53	10.29	2.65	0.91	0.29	0.09	1.09	100.39
fine-grained	49.56	2.14	13.89	14.44	0.21	6.23	10.28	2.02	0.09	0.16	0.05	0.67	99.74
inherited fabrics	48.27	2.75	12.47	16.78	0.26	5.27	9.86	2.50	0.75	0.25	0.06	1.02	100.26
epidote-bearing	51.58	2.50	13.58	13.56	0.16	3.93	11.81	1.71	0.09	0.26	0.05	0.67	99.91
skarn-like eclogite	39.62	5.94	14.99	21.46	0.26	4.83	11.00	0.89	0.07	0.04	n.d.	n.d.	99.68

ppm	La	Ce	Pr	Nd	Sm	Eu	Gd	Tb	Dy	Ho	Er	Tm	Yb	Lu
coesite-bearing	12.9	30.5	3.7	20.1	5.4	1.9	6.5	1.1	6.3	1.2	3.5	0.5	3.0	0.4
fine-grained	6.0	14.3	1.7	9.8	3.0	1.1	5.1	0.9	6.2	1.2	3.6	0.6	3.2	0.5
inherited fabrics	15.3	37.1	4.8	21.6	6.8	2.1	8.3	1.3	8.7	1.8	5.2	0.8	4.9	0.7
epidote-bearing	23.8	52.5	6.5	29.8	7.1	2.1	7.8	1.3	7.3	1.5	4.0	0.6	3.5	0.5
skarn-like eclogite	0.9	4.0	0.7	4.4	2.9	1.6	7.5	1.3	12.1	2.5	7.2	1.0	6.3	0.9

ppm	Ba	Cr	Nb	Rb	Sr	V	Y	Zn	Zr
coesite-bearing	127	170	18	33	137	400	39	96	159
fine-grained	3	60	13	3	58	428	35	90	139
inherited fabrics	37	<10	15	2	340	342	41	85	216
epidote bearing	118	39	15	22	133	526	46	272	193
skarn-like eclogite	<20	45	65	<3	32	528	65	119	210

Table 2.5. Major- and trace-elements of the different eclogite types. n.d.= not determined.

sample	Peak Grt X_{Mg} X_{Ca}	Cpx X_{Mg} X_{Jd}	Phg core X_{Mg} Si p.f.u.	Phg rim X_{Mg} Si p.f.u.	Amp secondary X_{Mg}	Plag secondary X_{An}	K_DGrt-Cpx Fe-Mg	Grt-Cpx T[°C] P[kbar]	lnKGrt-Phg-Cpx core Fe-Mg	Grt-Phg-Cpx T[°C] P[kbar]	K_DGrt-Phg Fe-Mg	Grt-Phg T[°C] P[kbar]	Amp-Plag T[°C] P[kbar]
K4-120	0.21	0.41	0.67					698		690		790	
	0.25	0.32	3.44				9.42	36	1.92	33	5.23	30	
K4-106	0.29	0.43						740					
	0.25	0.45					7.80	30					
K4-98	0.20	0.43						749					
	0.38	0.33					6.01	30					
PK2-4	0.26	0.42						764					654
	0.26	0.39			0.49	17.81	7.22	30					12
													717
					0.48	31.56							12
JNar2	0.18	0.43		0.75						690		763	
	0.35	0.39		3.25					4.77	33	7.12	33	
JNar2	0.19	0.43	0.78					703		690		759	
	0.38	0.37	3.43				13.54	36	2.66	36	8.10	36	
K4-84	0.29	0.41						721					
	0.25	0.18					8.33	30					
K3-11	0.21	0.43						641					
	0.30	0.45					13.50	30					
K4-58	0.19	0.38						659					
	0.19	0.22					8.12	30					
K4-57	0.20	0.40						644					
	0.23	0.26					10.28	30					
K4-76	0.23	0.38						746					
	0.25	0.25					7.58	30					
PKB3	0.15	0.37						707					
	0.29	0.15					9.91	30					

Table 2.6. Amalgamated mineral compositions and P-Testimates. Grt-Cpx: T from Krogh (1988) for given nominal P; Grt-Phg-Cpx: method of Carswell et al., 1997; Grt-Phg: calculation of Green & Hellman (1982); Amp-Plag: calculated after Holland & Blundy (1994).
X_{Mg}=Mg/Mg+Fe^{2+}+Ca+Mn; X_{Ca}=Ca/Ca+Fe^{2+}+Mg+Mn; X_{An}=Ca/Ca+Na+K

HIGH-*T*, LOW-*P* FORMATION OF OLIVINE-BEARING SYMPLECTITES IN VARISCAN ECLOGITES

JAMES SCOTT[1], MATTHIAS KONRAD-SCHMOLKE, PATRICK O'BRIEN, CHRISTINA GÜNTER

Insitut für Erd- und Umweltwissenschaften, Universität Potsdam, Karl-Leibknecht-Straβe 24, 14476 Potsdam, Germany

Correspondence to: james.scott@otago.ac.nz

phone: +64 3 479 3539

Running title: Eclogites with high-T, low-P olivine symplectites

[1] Now at: Geology Department, University of Otago, 360 Leith Walk, Dunedin, New Zealand

ABSTRACT

Extremely rare veinlets and reaction textures composed of symplectites of olivine (~Fo_{50})-plagioclase±orthopyroxene±spinel±ilmenite, associated with more common clinopyroxene-plagioclase±orthopyroxene and amphibole-plagioclase varieties, occur within eclogites and pyroxenites across the Moldanubian Zone of the Bohemian Massif. The distribution of each symplectite type broadly reflects reactions that took place in micro-scale domains with chemically distinct compositions at ~ 850ºC and ≤ 6 kbar. Breakdown of high-*P* garnet strongly influenced the formation of the olivine-bearing and the amphibole-plagioclase varieties, and breakdown of high-*P* clinopyroxene controlled the distribution of pyroxene-plagioclase symplectites. Isothermal *P-X* binary phase calculations for effective bulk compositions for micro-domains reveal that an influx of small volumes of an H- and Na-bearing fluid drove garnet dissolution-symplectite precipitation processes, even in symplectites that are now anhydrous. The olivine-bearing symplectites preferentially partitioned Fe and Mg from high-*P* garnet and clinopyroxene, but lost Si and Al to the simultaneously forming pyroxene-plagioclase and amphibole-plagioclase symplectites. Where Na was available to the reacting system, plagioclase in the olivine-bearing symplectites shifted from pure anorthite to bytownite with the less calcic feldspar partitioning Si and inhibiting the formation of orthopyroxene. Breakdown of garnet to an outer olivine-bearing symplectite and an inner amphibole-plagioclase symplectite generated asymmetrical and symmetrical chemical gradients depending on whether the H- and Na-bearing fluid migrated along the rim or through the interior, respectively, of garnet. The partial preservation of earlier high-*P* textures, the high-*T* and moderate-*P* of symplectite formation, the narrow Mn- and Fe- enriched garnet steps immediately adjacent to the symplectites, and the evidence for a limited fluid flux, point to the symplectite-forming stage as taking place during a short-duration anomalously hot event in the shallow to middle Variscan crust. As the studied samples are not associated with the aureoles of plutonic rocks, the symplectite-causing event may have been due to advective heat loss from rapidly exhumed high-*T* high-*P* granulitic bodies (Gföhl Unit) that were emplaced into and over the middle crust (Monotonous and Varied Series) during Carboniferous continent-continent collision.

KEYWORDS: olivine; symplectite; eclogite; thermodynamics; Variscan

INTRODUCTION

The sensitivity of metabasites to changes in pressure (*P*), temperature (*T*) and rock chemistry (*X*) makes them useful tools for the quantification of geodynamic and kinetic processes and aid the interpretation of the evolution of complex metamorphic terranes because they commonly preserve textures representing different stages of equilibration (*e.g.*, O'Brien, 1997a). Extraction of crucial P and T information in metamorphic rocks is possible with conventional exchange and net transfer thermobarometers that allow assessment of the precise pressure, temperature and chemical conditions for textures that contain key minerals such as pyroxene and garnet (*e.g.*, Clarke *et al.*, 2000). Further interpretations on such rocks can be drawn using thermodynamic equilibrium calculations based on internally consistent standard state datasets (e.g., Robie, Hemmingway and Fisher 1978, Robie and Hemmingway XXXX, Berman 1988). One issue with applying such thermodynamic equilibrium calculations to metamorphic rocks is that these (the rocks) often contain evidence for small-scale chemical disequilibrium, such as symplectite textures, which typically represent micro-scale element exchange and equilibration (*e.g.*, Monkoltip & Ashworth, 1983; Messiga & Bettini, 1990; Obata, 1994; Sassi *et al.*, 2004; Brouwer & Engi, 2005; Dégi *et al.*, 2010; Obata, 2011). It is therefore crucial to precisely determine compositionally equilibrated domains and volumes of effectively reacting bulk rock compositions. Conventional bulk rock chemical analysis used as the thermodynamic input composition are prone to homogenising domains that are in chemical dis-equilibrium, and so compromise interpretations made on the predicted stable minerals, compositions and proportions of phases. A solution to this problem is to calculate effective micro-domain compositions by counting the mineral modes from backscattered electron images and integrating the mineral percentages with microprobe analyses on the appropriate phases.

We provide a detailed description and micro-domain thermodynamic examination of the formation of extremely rare olivine-bearing symplectites and co-existing associated textures that overprint Variscan eclogites and pyroxenites from the Moldanubian Zone in the Bohemian Massif. The literature contains many examples of eclogites with metamorphic symplectites (*e.g.*, Messiga & Bettini, 1990; O'Brien & Vrána, 1995; Medaris *et al.*, 1995; Becker, 1997; O'Brien, 1997a; Nakamura

et al., 2004; Faryad *et al*., 2006; Faryad, 2009; Medaris *et al*., 2006a, 2006b, 2009; Obata, 2011; to name but a few for the Moldanubian Zone), but there appears very few worldwide examples of the occurrence of olivine+plagioclase±spinel±orthopyroxene symplectites. In one well documented case, zoned symplectite in a garnet peridotite in the Ronda Peridotite was interpreted to have formed by breakdown of high-P garnet and clinopyroxene at around 4-8 kbar and 620-700ºC during exhumation (Obata, 1994). In another case, earlier formed symplectites replacing garnet in granulite xenoliths within basalt in the Pannonian Basin were heated and replaced by olivine-bearing symplectites (Török *et al*., 2005) by the metasomatic addition Na, K, Ti and rare earth elements from the host basaltic melt during transport to the surface (Dégi *et al*., 2010).

Using the Gibbs energy minimisation algorithm THERIAK (De Capitani & Brown, 1987; De Capitani & Petrakakis, 2010) we attempt to model the formation of symplectite domains within samples of overprinted Variscan high-P rocks to ascertain which thermodynamic parameters played important roles in the symplectite formation, and then the geodynamic significance of the textures. The THERIAK algorithm is extremely useful because it calculates thermodynamically predicted stable assemblages, phase compositions and proportions for progressive steps in a chemically changing rock volume during its *P-T-X* evolution. This technique simulates the evolution of a chemically open system and enables simple comparison between the predicted results and the actual observed and measured phase compositions and proportions (*e.g*., Konrad-Schmolke *et al*., 2006, 2008). We aim to show that the rare olivine-bearing symplectites most likely formed from the replacement of high-*P* assemblages by fluid-assisted elemental diffusion during during an anomalously hot (granulite facies) event regionally affecting the shallow or middle crust. Such thermal spikes have been interpreted for the exhumation paths of ultra-high pressure rocks in the Karakoram Himalaya (De Signoyer *et al*., 1997; Guillot *et al*., 2008; Wilke *et al*., 2009), Western Gneiss Region (Walsch & Hacker, 2004) and the Swiss Alps (Tóth *et al*., 2000), as well as in some from Barrovian rocks (Vorhies & Ague, 2011), which implies that a thermal spike may be a common – but cryptic – orogenic feature.

GEOLOGICAL CONTEXT

84 The geologically complex Bohemian Massif, centred over the Czech Republic and extending into
85 Austria, Germany and Poland, is typically subdivided into several domains that were amalgamated
86 during Devonian-Carboniferous continent-continent collision (*e.g.*, Franke, 2000; Schulmann *et al.*,
87 2005; Kroner *et al.,* 2008; Schulmann *et al.*, 2008; Timmerman, 2008; and references therein). The
88 samples selected for study come from crystalline rocks of the Moldanubian Zone (Fig. 1), which
89 comprises the high-grade central core of the Bohemian Massif and separates the Brunia continental
90 margin from the Tepla-Barrandian Domian (*e.g.*, Konopásek, 2011). The Moldanubian Zone consists
91 of three principal subdivisions: the granulite complexes of the Gföhl Unit, the tectonically underlying
92 Monotonous and Varied Series, and widely distributed Carboniferous granitoids.
93 Because exposure is limited, the Gföhl Unit is differentiated from the Monotonous and Varied
94 Series on the basis of composition and metamorphic grade. Metamorphism in the Gföhl Unit granulite
95 complexes occurred at high-*T* (~850-1000°C) and high–*P* (~15-20 kbar) at ~ 354-345 Ma (Carswell &
96 O'Brien, 1993; Cooke, 2000; Cooke *et al.*, 2000; Cooke & O'Brien, 2001; Štípksá *et al.,* 2004; Racek
97 *et al.,* 2006; Tajčmanová *et al.,* 2006; Franěk *et al.*, 2011b), although there are some lower-P
98 exceptions such as the Lišov Massif (Janoušek *et al.,* 2006). The high metamorphic grades and the
99 inclusions of eclogite and spinel and/or garnet peridotite indicate the granulite rocks were often
100 subducted to upper mantle depths (*e.g.*, Beard *et al.,* 1992; O'Brien & Vrána, 1995; Medaris *et al.*,
101 1995, 1998, 2005, 2006a, 2006b, 2009). Integrated fabric-thermobarometry studies have proposed that
102 Gföhl Unit was initially exhumed rapidly in a subvertical channel(s) from the upper mantle, and then
103 laterally spread, folded and overturned as it reached the middle to shallow crust at c. 340 – 325 Ma
104 (*e.g.*, Štípksá *et al.,* 2004; Tajčmanová *et al.,* 2006; Schulmann *et al.,* 2005, 2008; Franěk *et al.,*
105 2011a).
106 The Monotonous and Varied Series – which lies tectonically beneath the Gföhl Unit – mainly
107 comprises metasedimentary rocks, amphibolites, orthogneisses and migmatites that record medium-*P*
108 (~ 8-9 kbar, 600-800°C) and/or low-*P* (4-6 kbar, 700-800°C) metamorphism (*e.g.*, Petrakakis, 1997;
109 Kalt *et al.,* 1999). However, the Monotonous and Varied Series contains rare fragments of eclogite and
110 spinel peridotite that indicate parts were exhumed from upper mantle depths (*e.g.*, Medaris *et al.*,
111 1995; O'Brien & Vrána, 1995; Faryad *et al.*, 2006). Some Monotonous Series eclogites contain

112 granulite facies overprints to former high-P assemblages that have been interpreted to either be due to
113 a short-lived heating event (O'Brien & Vrána, 1995; O'Brien, 1997a,b) or heating by an unspecified
114 mechanism during decompression (Faryad *et al*., 2006).
115 Plutons of syenite and S- and I-type granite were emplaced across the Bohemian Massif at
116 ~340 – 310 Ma (summarised in Finger *et al*., 1997; Schulmann *et al*., 2005; Timmermann, 2008).
117 These rocks are slightly younger than the earlier onset of Early Carboniferous vertical exhumation of
118 the Gföhl Unit, and some cut across the sub-horizontal fabrics in the Gföhl Unit therefore
119 demonstrating that transport from deep to shallow crustal levels was, in some places, complete before
120 granitoid intrusion had begun (*e.g*., Finger *et al*., 2007; Timmerman, 2008; Žák *et al*., 2010; and
121 references therein).
122
123 **SAMPLES**
124 There has been only brief mention of the olivine-plagioclase±spinel±orthopyroxene±ilmenite
125 symplectites from the Variscan (O'Brien, 1997a, b) and there is no published quantitative information
126 about these spectacular textures. A series of representative specimens containing the olivine-bearing
127 symplectites have been selected for detailed study. Mineral constituents indicate that sample BWI-45
128 and 42 are garnet pyroxenites, and samples 11, NM-1, and NOM1a and NOM1b are eclogites. These
129 rocks come from Winklarn (11, 42, BWI-45) and Niedermurach (NM-1) in the Oberpfalz of Germany,
130 and Weissenbrunn (NOM1a, NOM1b) in lower Austria (Fig. 1).
131 Characteristic features at the hand specimen scale, photomicrograph scale, and backscattered
132 electron image scale are shown in Fig. 2 (all mineral abbreviations in diagrams follow the scheme of
133 Whitney & Evans (2010)). In hand specimen, well-preserved reaction zones appear as dark veinlets
134 that dissect high-*P* mineral assemblages (Fig. 2A). Garnet and omphacite have been partially replaced
135 by these reaction zones, but the alteration compositions remain difficult to distinguish due to the very
136 fine grainsize (Figs. 2B, 2C). At the microscopic scale, individual garnet grains have clearly been
137 partially replaced by symplectites of olivine-plagioclase±spinel±ilmenite (in eclogites) or olivine-
138 plagioclase±spinel±orthopyroxene±ilmenite (in garnet pyroxenites) (Fig. 2D, 2E, 2F). The garnet
139 grains have also been partially replaced by amphibole-plagioclase symplectites, which typically occur

adjacent to the olivine-bearing symplectites. Omphacite in all samples has been partially to totally replaced by fine-grained diopside-plagioclase±orthopyroxene symplectites (*e.g.*, Fig. 2D). The symplectite textures occur in rocks of varying grainsize (Fig. 2E). In the following section, petrographic description of one complex but representative eclogite sample – NOM1a (Fig. 2G, 2H) – is presented.

Garnet in sample NOM1a is pale pink, anhedral, up to 5 mm diameter, and encloses pale green omphacite (< 1mm), dark brown rutile, and colourless apatite. Omphacite grains and coarse plates of optically continuous green amphibole are also present outside garnet (Figs. 2G, 2H). These coarse green amphibole plates commonly enclose ilmenite, which in most cases exhibits a red-brown halo in the amphibole. The most striking feature of NOM1a is the symplectites that dissect, or form at the rims of, garnet (Fig. 3A, 3B, 3C, 3D), the coarse plates of amphibole (Fig. 3B, 3C) and omphacite (Fig. 2H). Where replacing garnet, the most prominent symplectites are composed of extremely fine-grained olivine and plagioclase, usually with spinel and in places accompanied by ilmenite. The spinel is complexly intergrown with olivine and sharp grain boundaries are commonly indistinct (*e.g.*, Fig. 3C). Where the symplectites have not fully propagated through garnet, the crack tips contain a pale green amphibole that has exsolved small blebs of aluminous spinel (*e.g.*, Fig. 3D). The olivine-bearing symplectites almost always give way on their margins to either a granoblastic amphibole-plagioclase ± olivine (*e.g.*, Fig. 3A) symplectite or, more commonly, a wormy amphibole-plagioclase symplectite (*e.g.*, Fig. 3B, 3C, 3D). The wormy variety of amphibole is elongate and individual grains have grown perpendicular to the retreating garnet reaction front. Olivine and spinel can sporadically be found within the amphibole-plagioclase symplectites, and amphibole is rarely found in the olivine-plagioclase ± spinel symplectites. Omphacite grains have partially to totally recrystallised into lobate clinopyroxene-plagioclase ± orthopyroxene (Fig. 2D, 2H) or amphibole-plagioclase symplectites. Some omphacite inclusions in garnet contain a thin rim of amphibole. The garnet that hosts such omphacite grains is characterised by radial cracks that emanate from the inclusions.

SYMPLECTITE MINERAL CHEMISTRY

Mineral phases were analysed using a JEOL JXA-8200 Micro-analyser at the Institut für Erd- und Umweltwissenschaften at the Universität Potsdam, equipped with 5 wavelength dispersive spectrometers and operated with a 15 kV accelerating voltage, a 20 nA current, and beam diameters of between 1 and 5 μm. The analytical counting times were 20s for the element peak in question and 10s for background positions. Analyses were standardised against natural silicates obtained from the Smithsonian Institute and, for Fe in garnet, a synthetic metal provided by JEOL. Peak searches were conducted at the beginning and during each analytical session and secondary standards were analysed to check the accuracy of the analytical routine. All data were reduced using a ZAF correction. Qualitative element maps were measured using wavelength dispersion, a 1 to 4 μm step size and a dwell time of up to 350 ms. Clinopyroxene end-member components were recast following the method of Mysen & Griffin (1973). Amphibole classification follows Leake *et al*. (1997). Mineral chemistries, end-member calculations, and element ratios are presented for NOM1a in Table 1. Reconnaissance mineral analyses for three other samples are presented in Data Supplementary 1.

Garnet

Garnet within NOM1a is complexly zoned. In the most compositionally extreme garnet grains identified (Fig. 4A), there are low-Ca domains (*e.g.*, $Alm_{45}Prp_{36}Grs_{18}Sps_{1}$, XMg_{45}) dissected by relatively high-Ca zones (*e.g.*, $Alm_{40}Prp_{30}Grs_{29}Sps_{1}$, XMg_{43}). The transition between different domain-types is abrupt. High-Ca zones enclose omphacite (jadeite content?) and therefore most likely represent the peak eclogite facies equilibration stage. The high-Ca and low-Ca domains are in turn cross-cut by (amphibole-plagioclase symplectites that exhibit a parallel zoning with olivine-bearing zones in the centre of the symplectites. Is this what you mean?) the olivine-bearing and amphibole-plagioclase symplectites. Garnet is only rarely seen in direct contact with olivine-bearing symplectite variety because most boundaries are occupied by the amphibole-plagioclase symplectites. In the rare locations where the olivine-garnet contact is preserved (*e.g.* Fig. 4B), micro-stepping the microprobe beam shows that the garnet increases in Fe and Mn and decreases in Mg and Ca towards olivine (Fig. 4C) ($Alm_{43}Prp_{33}Grs_{23}Sps_{1}$, XMg_{43} → $Alm_{49}Prp_{26}Grs_{22}Sps_{2}$, XMg_{32}). Garnet within ~30 μm of the amphibole that occurs in the tips of some symplectite cracks also shows the same relationship (Fig.

195 3D, 4D), as does garnet within 10 μm of the 1-2 μm wide amphibole film that has grown around some
196 omphacite inclusions ($Alm_{42}Prp_{31}Grs_{29}Sps_1$, XMg_{43} → $Alm_{50}Prp_{24}Grs_{25}Sps_2$, XMg_{35}). Backscatter
197 imaging and element maps reveal that these narrow zones of modification are not symmetrical
198 adjacent to the symplectites, but instead form rather patchily and may occur in small channel-like
199 pathways (Fig. 4B, 4D, 4E).
200
201 *Pyroxene*
202 The earliest observed generation of clinopyroxene is omphacite. There is little systematic variation
203 within this mineral; the jadeite component is 21.6-26.8, the Ca-Tschermak component varies between
204 1.7 and 5.3, and aegirine ranges between 0.0-4.2. Omphacite encloses rare tiny quartz blebs (quartz
205 was sought but not found in the rock matrix in NOM1a). The pyroxenes in the pyroxene-plagioclase
206 symplectites that replace most omphacite (Fig. 2H) are diopside or Al-diopside and enstatite. The Al-
207 diopside variety tends to occur where there is less proximal plagioclase. Symplectite diopside has a
208 significantly lower jadeite component than omphacite, with compositions clustering around 3.5 $\pm$ 1.5
209 mol %. Enstatite forms a minor component (typically < 10 volume %) to the pyroxene-plagioclase
210 symplectites.
211
212 *Amphibole*
213 Amphibole grains are widely distributed and the textural position has strongly influenced composition.
214 The amphibole in amphibole-plagioclase symplectites that have formed within the interiors of garnet
215 generally has Ca $\leq$ 1.72 and Ti < 0.02 cations per formula unit (pfu), whereas amphibole in
216 symplectites that have formed on the margins of garnets has Ca $\geq$ 1.72 cations pfu and a variable Ti.
217 Amphibole replacing omphacite in the matrix has a lower XMg than amphibole that replaces
218 omphacite inclusions in garnet. One important feature of NOM1a is the presence of coarse plates of
219 amphibole within the matrix that have been partially replaced by olivine-plagioclase symplectites (*e.g.*
220 Fig. 3B, C). This variety of amphibole is easily differentiated from symplectite amphibole because of
221 a significantly lower Al and Na and markedly higher Mg (XMg = 75) content. The textural association

and chemical composition indicates that the coarse amphiboles must pre-date the symplectite forming stage.

Feldspar

Feldspar composition spans a spectrum from albite to anorthite and is strongly domain dependent (Fig. 5A). Plagioclase associated with the olivine-bearing symplectites varies from labradorite to anorthite, with compositions clustering around bytownite composition (Fig. 5A, 5B, 5C). Plagioclase in the amphibole-plagioclase symplectites is generally sodic labradorite or andesine, although in some places calcic labradorite or bytownite is found immediately adjacent to garnet (*e.g.*, Fig. 5B). The plagioclase within the symplectites that replace omphacite is a sodic variety that ranges from albite to andesine. Many plagioclase grains show narrow patches of slightly higher Ca (*e.g.*, Fig. 5B, Fig. 5C). All feldspars analysed contain a small component of Fe, the amount of which has a positive correlation against An content.

Olivine, Spinel, Ilmenite

Olivine and spinel $\pm$ ilmenite occur as intimate intergrowths within symplectites proximal to garnet and coarse amphibole in NOM1a, and replacing phlogopitic biotite in NOM1b (Fig. 3A, 3B, 3C, 3F, 4D, 4E). The olivine is very fine-grained. It has the compositional range over all domains of $Fa_{46}Fo_{54}$ to $Fa_{52}Fo_{48}$. The lowest Fo values are from locations where olivine coexists with amphibole (*e.g.* Fig. 3D). Olivine is typically complexly intergrown with fine-grained Fe-rich spinel ($Spl_{35\text{-}39}Her_{61\text{-}65}$). The most hercynite-rich compositions come from slightly coarser grains that are located within the centres of olivine-spinel-plagioclase symplectites (*e.g.*, Fig 4C). Ilmenite occurs as fine granules together with olivine and spinel, but also as a separate coarser generation that is surrounded by the coarse plates of amphibole. A systematic spatial correlation of distribution to ilmenite composition has not been established.

P AND *T* OF SYMPLECTITE FORMATION

Conventional geothermobarometry can be applied to several of the textures in NOM1a. Firstly, co-existing garnet-omphacite-rutile-apatite in NOM1A is characteristic of a basaltic rock metamorphosed at eclogite facies conditions (*e.g.*, Green & Ringwood, 1967). Eclogites within the Monotonous and Varied Series record a variety of temperatures and pressures, mostly at $P \geq 14$ kbar and T = 600-800ºC (*e.g.*, Medaris *et al.*, 1995; O'Brien & Vrána, 1995). As the eclogite facies high-Ca garnet and inclusions of omphacite in NOM1A appear to have been in equilibrium, and some omphacite is partially replaced by albite, a minimum pressure of 14 kbar at 600 ºC can be estimated from the reaction:

- jadeite + quartz = albite (Holland, 1980).

If the temperature for albite formation is raised to 800ºC, then a minimum pressure of eclogite facies metamorphism is 25 kbar. These results assume that the formation of secondary plagioclase has not modified the primary Fe-Mg ratio of omphacite. Application of the empirically re-calibrated garnet-clinopyroxene Fe-Mg exchange thermometer of Nakamura (2009) to these same minerals yields temperatures of 760ºC (at 14 kbar) and 810ºC (at 25 kbar).

The precise conditions of symplectite formation are commonly difficult to assess because of the varying degrees of local disequilibrium (*e.g.*, O'Brien & Vrána, 1995). Nevertheless, an approximate estimate can be made for both *T* and *P* of formation for the olivine-bearing symplectites using mineral compositions from the rare locations where these minerals are immediately adjacent to garnet because garnet has clearly attempted chemically adjust to the symplectite-forming stage by forming narrow Mn- and Fe-enriched zones (*e.g.*, Fig. 4B, 4C, 4D, 4E). The recently re-calibrated (Wu & Zhao, 2007) Fe-Mg exchange reaction:

- 3 fayalite (in olivine) + 2 pyrope (in garnet) = 3 forsterite (in olivine) + 2 almandine (in garnet)

coupled with the olivine-plagioclase-garnet equilibrium reaction:

- 3 fayalite (in olivine) + 3 anorthite (in plagioclase) = 2 almandine + grossular (in garnet)

yields conditions of ~ 860ºC and 6.0 kbar for olivine paired with bytownite and a garnet rim composition (Table 1). Although the microprobe beam is incapable of resolving the garnet composition at the very outermost (< 1 μm-wide) rim, micro-stepping of the beam shows that the utilised garnet composition is probably a very close approximation to this outermost composition. It is

277 also possible that the garnet rim represent a transient composition due to sluggish kinetics and so is out
278 of equilibrium with adjacent olivine and plagioclase. Therefore the garnet-olivine-plagioclase derived
279 *P-T* estimates are, at best, minimum temperatures and maximum pressures.
280 In the cases where pyroxene-plagioclase symplectites contain diopside and enstatite, various
281 two-pyroxene geothermometers can be applied. The Wells (1977) geothermometer applied to diopside
282 and enstatite in textural equilibrium (*e.g.*, Fig. 2H) yielded an average temperature of 856ºC. This
283 calibration is not pressure sensitive. The Taylor (1998) two-pyroxene geothermometer, set at pressure
284 of 6.0 kbar, yielded a similar averaged temperature of 843ºC. Changing the pressure by several kbar
285 has very little effect on temperature (> 10ºC). The apparent agreement between the two-pyroxene and
286 the olivine-garnet geothermometers suggests that a *T* of ~ 850ºC is a good assumption for the
287 formation of the symplectites. It is also worthy of note that thermodynamic modelling (discussed
288 below) also indicates that the symplectite textures can be generated at ≤ 6 kbar and 850ºC.
289
290 ***P-T-X* SYMPLECTITE EVOLUTION**
291 To ascertain the main petrological processes by which the olivine-bearing and related symplectites
292 formed, effective bulk compositions of a selection of micro-domains in NOM1a were calculated. This
293 was done by image analysis on high-contrast backscattered electron images and then integration of the
294 mineral modes in the images with microprobe analyses of phases. Two representative examples of
295 each symplectite type are shown in Table 2.
296 It is important to acknowledge that there are non-trivial uncertainties in calculating effective
297 domain compositions by image analysis. Firstly, this method assumes that a 2D image is
298 representative of 3D composition. This is difficult to verify but by selecting small 2D reaction
299 domains (*i.e.*, ≤ 100 μm across) the effect of variation in the 3D is hopefully minimised if we assume
300 that the symplectite textures are probably as thick as they are wide. Secondly, average mineral
301 compositions must be utilised where there is fine-scale heterogeneity (for example see the variation in
302 plagioclase compositions in Fig. 5). Images were therefore selected from areas that showed minimal
303 zoning. Thirdly, the location of the image will strongly affect the calculated composition. For
304 example, an image that is not located on the centre of the reacting domain will lead to an over-estimate

or an under-estimate of minerals on the margin or core of the reacting domain, respectively. Therefore, the selected backscattered electron images were taken from the interpreted centres of the reacting domains. A degree of confidence can be placed in several of the calculated effective compositions because pseudosections for particular domains were able to yield the approximate mineral assemblages, proportions and compositions that were actually observed. Brouwer & Engi (2005) followed a similar image analysis-mineral composition technique and found comparable results.

The thermodynamic properties of micro-domains were modelled in the system NCFMASHO using THERIAK with the Berman 92 thermodynamic database and following solution models: olivine (ideal), spinel (ideal with Margules-type excess function), amphibole (Dale *et al.,* 2005), cordierite and garnet (Berman, 1990), feldspar (Furhman & Lindsley, 1988), clinopyroxene (Meyre *et al.,* 1997), and orthopyroxene (Powell & Holland, 1999). Ti, Mn and K are not considered due to their very low amounts in the effective bulk domain compositions (Table 2). The chemical potential of oxygen was controlled utilising a quartz-fayalite-magnetite (QFM) buffer because this enables reproduction of the observed mineral assemblages.

Olivine-plagioclase-spinel symplectites

The effective bulk compositions of the olivine-plagioclase-spinel symplectites in NOM1a are broadly similar to that of garnet that they invariably replace (Table 2). The first symplectite (example 1), which is most common observed type of olivine-bearing symplectite, appears to have undergone little or no volume change during the replacement of garnet because symplectite Al is the same as in the garnet that it replaces (Table 2). This interpretation is partially supported by the minor density change (6 - 11%) in the transformation of garnet (density = 3.4) to olivine (3.27), spinel (3.95) and bytownite (2.7). Volume uncorrected mass balance calculations, and also those in which Al is held constant, therefore show clear gains in Mg, Fe and Na but losses in Si and Ca during symplectite formation. In the second symplectite example, Si is the same for garnet and symplectite. Mass balance calculations for Si held constant also show a gain in Mg, Fe, Ca and Na, but a distinct loss in Al.

The simple mass balance calculations also indicate that the ratios of certain elements have varied by the same amounts. In particular, garnet:symplectite Fe and Mg abundances appear to be

coupled (Table 2). Another important observation is that the formation of the symplectite must have occurred in an open chemical system because garnet contains no Na but the symplectite does. Further obvious chemical differences are that there is more plagioclase and less spinel in symplectites that have low Al, but more spinel and less plagioclase in domains with low Si. Ca content is domain variable; therefore its addition or subtraction from the garnet has not strongly influenced the stability of the olivine-bearing symplectites.

The allochemical breakdown of an initial garnet composition is confirmed by a pseudosection calculated for garnet composition as the effective (reacting) bulk composition. Isochemical breakdown of high-Ca garnet at 850ºC is predicted to produce co-existing olivine, anorthite and spinel accompanied by up to 25 weight % orthopyroxene (Fig. 6A). Isochemical breakdown of low Ca-garnet (not shown) yields almost exactly the same result. However, orthopyroxene is entirely absent from olivine-bearing symplectites in NOM1a (Fig. 3A, 3B, 3C, 3D, 3E). The main chemical factor controlling the presence or absence of orthopyroxene can be illustrated with a binary *P-X* phase diagram, as shown in Fig. 6B. In this diagram the x-axis represents a compositional vector starting with the high-Ca garnet composition and evolving towards garnet + Na. At very low added Na concentrations to the effective composition (in this case < 1.2 mol), orthopyroxene is stable. However, at slightly elevated Na concentration (>1.2 mol), the predicted mineral assemblage is olivine+spinel+plagioclase+magnetite. Na is partitioned into feldspar, which also takes up available Si, thus inhibiting orthopyroxene. Anorthite isopleths of the feldspar composition show that the addition of Na shifts feldspar composition from pure anorthite to bytownite (Fig. 6B), which is in accordance with the principal feldspar analysed within the olivine-bearing symplectites (Fig. 5). The even more sodic feldspar compositions measured represent areas that have had either more Na available during recrystallization and/or been modified during subsequent cooling, whereas occasional An-rich feldspar likely represents areas where very little Na was available to the reacting composition. Magnetite is predicted to form instead of ilmenite because Ti was not modelled in the system, although the small predicted magnetite volume could also be accounted for as a component dissolved within spinel. Alternatively fO_2 may have been slightly less than QFM, in which case no magnetite would form. Addition of Na to a low-Ca garnet starting composition also yields an

olivine+spinel+plagioclase+magnetite assemblage, except that in this case it requires more Na (~3.75 mol) to generate orthopyroxene-free assemblages than from a high-Ca composition. This relationship is verified in Na-poor samples presented in the Data Supplementary; garnet pyroxenites 42 and BWI-45 both contain orthopyroxene co-existing with olivine, spinel and anorthite. Fig. 6C demonstrates that the addition of Na to reacting garnet is not the only possible method of generating coexisting olivine-plagioclase-spinel at 850ºC. An orthopyroxene-free assemblage can also be achieved by extracting Si from garnet (Fig. 6C). However, if this was the case in NOM1a, the co-existing feldspar should be pure anorthite, which it is not.

Pseudosections also enable a broad independent estimate of the pressure of symplectite formation, assuming that the conventional geothermobarometry-derived *T* estimate of 850ºC is accurate. The olivine-plagioclase-spinel assemblage occurs without clinopyroxene or garnet at up to ~ 5.7 kbar (Fig. 6D), which is close to the $\leq$ 6.0 kbar estimate derived from conventional geobarometry. At 5.7 kbar, the thermodynamically predicted mineral compositions and abundances are: 42 % olivine (Fa_{53} Fo_{47}), 14.3 % spinel ($Spl_{38}Herc_{62}$), 43 % bytownite ($An_{84}Ab_{16}$), and 0.7 % magnetite. These modes and compositions are very similar to the measured compositions and abundances: *e.g.*, 48 % olivine (analysed as $Fa_{47\text{-}51}Fo_{53\text{-}49}$), 18 % hercynitic spinel (analysed as $Spl_{38\text{-}35}Herc_{62\text{-}65}$) and 34 % plagioclase (analysed as An_{93} to An_{51}, with an average bytownite composition (Fig. 5)). The second olivine-plagioclase-spinel effective composition (example 2 in Table 2) fails to reproduce this mineral assemblage in the *P* and *T* range examined; instead, orthopyroxene is predicted to co-exist with olivine-plagioclase-spinel. This issue can be remedied by reducing the Si in the effective composition, which then halts the formation of orthopyroxene. This result demonstrates that a low Si chemical potential is an important control on generating the olivine-plagioclase-spinel assemblage. Therefore, the addition of Na $\pm$ subtraction of Si from an initial garnet composition in conditions near to QFM at 850ºC and $\leq$ 6 kbar were fundamental parameters in forming the olivine-bearing symplectites.

Pyroxene-plagioclase symplectites

Because these symplectites form lobate textures entirely within omphacite, do not embay into the surrounding minerals, lack radial cracks, and are not zoned (*e.g.*, Fig 2H), there appears to have been

minimal volume change in the replacement of omphacite. This interpretation is supported by the very small (1-8%) density decrease from omphacite (3.35 cm^{-3}) to enstatite (3.2 cm^{-3}), diopside (3.4 cm^{-3}) and plagioclase (2.71 cm^{-3}). Mass balance calculations assuming no volume change therefore indicate that that the symplectites have gained Si, Al and Na but lost an approximately equivalent total amount of Fe, Mg and Ca. Al is extremely enriched relative to omphacite and has been added to the reacting system. It is notable that individually Fe, Mg and Ca all decrease by a similar ratio relative to these elements in the original omphacite.

An isothermal *P-X* diagram calculated from an initial omphacite composition illustrates the importance of addition of Si to reacting omphacite (Fig. 7). At low amounts of added Si, initial omphacite is predicted to be replaced by assemblages that are either olivine-bearing and/or orthopyroxene-free. Only with the addition of significant Si (in this case 6 mol) is the assemblage clinopyroxene-orthopyroxene-plagioclase stable. At 850ºC, the predicted assemblage has the calculated volumetric amounts of 61 % diopside, 33 % plagioclase ($An_{39}Ab_{61}$), and 6 % enstatite, which is similar to the observed volumes of 54 - 46 % diopside, 44 – 53 % plagioclase (An_{11} Ab_{88} to An_{42} Ab_{58}), and 1 – 2 % enstatite. Although Al and Na have been added to the chemical system, they do not stop the production of olivine and/or orthopyroxene; it is the role of Si that remains a key feature.

Amphibole-plagioclase symplectites

There was a 16 to 17 % density decrease in the replacement of garnet (3.4 cm^{-3}) by pargasite (3.1 cm^{-3}) and plagioclase (2.7 cm^{-3}). This change corresponds to either a mass decrease or a volume increase, or both. No cation concentration remains the same between garnet and symplectite, and both H and Na have been added in significant proportions to the reacting system (Table 2). Therefore, a constant volume during symplectite formation cannot be assumed. One pattern that emerges from the data is that the garnet:symplectite Al and Si ratios both increase by the same ratio. If Si and Al have not moved during symplectite formation and the effective composition is then normalised, there are significant cation losses in Fe and Mg and gains in Na and H $\pm$ Ca.

Through trial and error we find that the amphibole-plagioclase symplectites can be generated thermodynamically at 850ºC and $\leq$ 6 kbar from a starting high-Ca garnet reacting composition evolving towards garnet modified by olivine and spinel fractionation coupled to addition of Na and H (Fig. 8). This diagram shows that removal of these phases by fractional crystallisation will enrich Si and remove Fe, which along with the progressive addition of H and Na, promotes the co-existence of feldspar and amphibole. Incomplete fractional crystallisation would account for the presence of olivine in some symplectites (*e.g.*, Fig. 5C). This diagram also illustrates the important result that the addition of H and Na to a garnet does not necessarily immediately stabilise amphibole; rather, a component of free water remains until sufficient olivine and spinel has been removed from the reacting system.

The predicted composition of the amphibole-plagioclase symplectites after addition of Na (in this case 2 mol) and H (20 mol) and complete removal of olivine and spinel is 30% pargasitic amphibole and 70% bytownite plagioclase (An_{85}). The proportions of these phases are similar to the inspected micro-domains, although the bytownite is at the upper boundary of measured plagioclase composition in this textural position (Fig. 5A). As the binary phase diagram suggests that the compositional field for co-existing amphibole-plagioclase is very narrow but in reality such symplectites are extremely common in exhumed eclogites, the modelling and/or the amphibole solution models likely do not account for all factors in the generation of the amphibole-plagioclase symplectites. Nevertheless, the key point that can be taken from these results is that for the amphibole-plagioclase symplectites to form from garnet, Fe $\pm$ Mg must be removed and Na and H added.

DISCUSSION

Significance of olivine-plagioclase±spinel±orthopyroxene symplectites

Pyroxene-plagioclase and amphibole-plagioclase symplectite assemblages are common in mafic rocks but olivine-plagioclase±spinel±orthopyroxene assemblages are rare. This unusual assemblage has been described from some contact metamorphosed mafic rocks in the inner aureoles of gabbro and syenite plutons (*e.g.*, MacGregor, 1931; Sadashivaiah, 1950; Harry, 1952; Philips, 1959; Almond, 1964; Simmons *et al.*, 1974; Ferry *et al.*, 1987; Sakakibara & Isono, 1996) and as kelyphites in garnet peridotite (Obata, 1994) and granulite (Dégi et al., 2010). All scenarios described require that these

444 unusual assemblages form during at moderate-*T* or high-*T* at moderate or shallow crustal levels. This
445 is consistent with the estimated *P-T* conditions of ~850ºC and ≤ 6 kbar for the studied Variscan
446 symplectites. The mineralogy, temperatures and pressures of the olivine-bearing symplectites occur in
447 the granulite or pyroxene hornfels facies (*e.g.*, Turner, 1981).
448 Sample NOM1a (and all the samples listed in the Data Supplementary) records clear evidence
449 for attempts at metamorphic equilibration in two distinctly contrasting settings. The first event took
450 place at high-*P* and moderate-*T* upper mantle eclogite facies conditions (garnet-omphacite growth; ≥
451 14 kbar at ~700-800ºC), followed by high-*T* granulite facies conditions (symplectite formation, ~
452 850ºC and ≤ 6 kbar). The symplectite-forming stage in the studied rocks thus represents heating during
453 (Faryad, 2006) or after (O'Brien, 1997a) exhumation (Fig. 9). Although conditions of ~850ºC and < 6
454 kbar for the symplectite-forming stage fall just above the solidus for melting of gabbro in the presence
455 of water (Lambert & Wyllie, 1972), there is no sign of melt in-situ (as glass or its altered products)
456 that might be expected. A possible explanation for the lack of melting is that only small degrees of
457 water entered the rock and were immediately consumed in the formation of symplectite amphibole.
458 Texturally, the high-P event and the symplectite-forming stage are separated by a fluid-ingress
459 event that formed coarse plates of amphibole and, rarely, phlogopite. The spatial distribution to both
460 phases demonstrates that they formed by partial hydration of the eclogites and pyroxenites after the
461 high-*P* event but before the symplectite-forming stage (Fig. 3C, 3E). Reliable *P-T* conditions for the
462 coarse amphibole and biotite formation are not possible because neither mineral by itself is pressure or
463 temperature sensitive.
464 Clues to the significance of the symplectite textures are provided by (1) the sharp
465 compositional enrichment of Mn and Fe in garnet immediately adjacent to the symplectites and (2) the
466 general preservation of high-*P* compositions (Fig. 4). These two features are not consistent with a long
467 duration at a high temperature because solid-state volume diffusion would have homogenised the
468 garnet profiles. Strikingly similar textures have been shown to form due to short-duration granulite
469 facies events (< 1 Ma) by diffusion (see the detailed descriptions in O'Brien & Vrána, 1995; O'Brien,
470 1997a; Medaris *et al.,* 2006). If the garnet compositional change was also due to fluid-assisted
471 dissolution and precipitation, as is implied by the channel-like structures adjacent to some

symplectites (Fig. 4B, 4D), then the rate of garnet modification may have been even faster (Putnis, 2009; Putnis & John, 2010) than the results implied by diffusion modelling. Either way, the olivine-bearing and related symplectites in Variscan eclogites must represent a short-duration infiltration of fluid that immediately modified metastable eclogite facies textures to granulite facies symplectites.

Synchronous symplectite formation

Although the distribution of the symplectite varieties examined is strongly controlled by the pre-existing high-*P* minerals that they replaced, basic mass balance calculations and thermodynamic modelling indicates that the symplectites formed in an open system. Fe and Mg have been lost from the amphibole-plagioclase symplectites, for which the only sink is the olivine-bearing symplectites (which show a gain of Fe and Mg). In the case of adjacent amphibole-plagioclase and olivine-plagioclase-spinel symplectites, these chemical gradients represent the different rates of diffusion for certain elements during garnet consumption. Si and Al in symplectites are generally argued to generally be slower to diffuse, so probably remained closer to the reacting front (garnet surface) than the faster diffusing Fe and Mg (Mongkoltip & Ashworth, 1983). On the rims of garnet, an asymmetric chemical gradient has formed whereby Fe and Mg are higher at the outside (in olivine-bearing symplectite) but the slower diffusing Si, Al and Ca are higher on the inside (in amphibole-plagioclase symplectite) (Fig. 3A, 3B).

Where the symplectites have propagated through a garnet, there is a symmetrical chemical arrangement whereby Fe and Mg are enriched in the centre (olivine-bearing symplectite) and Si, Al, Ca and H enriched at the sides (amphibole-plagioclase symplectites) (Fig. 3A). The main sink for Mn was back-diffusion into garnet immediately adjacent to the retreating front (Fig. 4B, 4C, 4D, 4E). The relationship is not so clear when examining the pyroxene-plagioclase varieties; these have lost Fe, Mg and Ca and gained Al and Si, but are not part of a zoned symplectite. Fe and Mg must have been extracted out of the pyroxene-plagioclase symplectite and transported into another sink, most likely the olivine-bearing symplectites. Therefore, the symplectite textures in NOM1a appear to have formed synchronously.

The requirement of a fluid

The introduction of a fluid carrying alkalis and redistributing elements was important in driving symplectite reactions. Thermodynamic modelling shows that, despite its small volume, Na was a critical component in their formation but the source of this element is not immediately clear. The requirement for addition of Na to the pyroxene-plagioclase symplectites that replace omphacite (Table 2) demonstrates that omphacite cannot be the sole source of Na within the rock. This conclusion is supported by the calculations that show Na was also added to the olivine-bearing and amphibole-plagioclase symplectite varieties (Table 2). The only other local candidate that could have released Na is the dehydration and replacement of earlier-formed coarse amphibole plates (*e.g.*, Fig. 3B, 3D). However, as this early amphibole only occurs in small volumes (<1 % of the rock) it does not satisfy the observation of a sizeable influx of Na and so also cannot be the only source. Therefore Na must have been added to the rock during the symplectite stage.

Although the olivine-bearing symplectites and the pyroxene-plagioclase symplectites are anhydrous, several factors point to the infiltration of a fluid having being a catalyst to the symplectite-forming event. Firstly, the reaction zones commonly form veinlets that propagate through garnet grains (*e.g.*, Fig. 2A, 2G, 3A, 3B, 3D). Secondly, the eclogite facies mineralogy is essentially anhydrous, whereas the widespread distribution of amphibole-plagioclase symplectites records an influx of fluid. This fluid phase is therefore now probably partially represented by volatile components (*e.g.,* H) that are incorporated within amphibole chemical structure within the amphibole-plagioclase symplectites, and also in the patches of amphibole located at the tips of the symplectite-bearing fractures within garnet (*e.g.*, Fig. 3D). Like Na, the fluid source cannot be accounted for volumetrically by water that was bound within the earlier-formed coarse amphibole or phlogopite plates; thus, like Na, H must have been added to the rock during the symplectite-forming stage. There is no sign of graphite, but no fluid inclusion work has been undertaken to establish whether there are any CO_2-bearing inclusions. There is no petrographic evidence for the fluid phase being a melt; if it was present, it has now completely passed through the system. Therefore, all that can be stated with certainty at this stage is that that the infiltrating fluid carried H and Na.

The availability of a fluid controlled the distribution of the symplectites and therefore halting one part of the reacting system would have affected reactions elsewhere within the rocks. For example, if the available fluid was completely consumed in the production of the amphibole-plagioclase symplectites, then the olivine-bearing symplectites would lose the source of Fe and Mg that was being liberated by garnet breakdown, and these too would no longer form. The intimate association between a fluid and the symplectites indicates that reactions took place by fluid-aided dissolution of early phases (garnet, clinopyroxene, coarse amphibole, coarse phlogopite) and precipitation of new minerals (*e.g.*, Putnis, 2009; Putnis & Austrheim, 2010; Putnis & John, 2010). As none of the primary eclogite facies mineral phases (garnet, omphacite, apatite, rutile) have been entirely consumed, then the amount of fluid that infiltrated the rock was evidently an important parameter in controlling the extent of the symplectites. This is an important conclusion because water is a very effective transporter of heat (*e.g.*, Ferry, 1994) and in the absence of large volumes the heat source that imparted a regional ~850ºC event must have been very large indeed.

Implications for the Variscan Orogen

Regarding their regional occurrence and record of a short-duration infiltration of a small volume of fluid, the question that arises for the origin of the regional olivine-bearing symplectites is what was the heat source that promoted their formation? The partial preservation of metastable eclogite facies textures indicates that that the rocks are unlikely to have been subjected to heating for a prolonged period. A short duration regional heating event is inconsistent with the time scales required for heating of the crust by erosional thinning or extensional exhumation (*e.g.*, England & Thompson, 1986; Thompson & Connolly, 1995), or by conduction from asthenosphere upwelling following slab detachment (*e.g.,* Brouwer *et al.*, 2004). If any of these scenarios had taken place then the lower crust should have reached extreme temperatures that have yet to be documented. It is also important to note that none of the olivine-bearing symplectite samples studied are associated with the thermal aureoles of gabbros or within metres of granitoid intrusions as would be required to promote reactions at 850ºC.

554 Another heat source that is increasingly being recognised in complex orogenic systems is
555 advective heat loss from lower crustal rocks that are rapidly exhumed from mantle depths and over the
556 middle to shallow crust. Thermomechanical models for continent-continent collision predict that rocks
557 can be subducted to high- to ultra-high-*P* and then rapidly buoyantly extruded above the subducting
558 plate (*e.g.*, Warren *et al.*, 2008; Beaumont *et al.*, 2009; Butler *et al.*, 2011). When the exhumed high-*P*
559 rocks reach middle to shallow crustal levels and buoyancy contrast decreases, they are predicted to
560 form nappe complexes overtop of cooler middle crust (Beaumont *et al.*, 2009). This geological
561 association has been independently proposed to explain petrological associations in parts of the
562 Variscan Orogen: fabric studies of Gföhl Unit granulites show that they were exhumed rapidly in a
563 steep channel from mantle depths before flattening out over the middle crustal Monotonous and
564 Varied Series (*e.g.*, Schulmann *et al.*, 2005, Tajčmanová *et al.*, 2006; Schulmann *et al.*, 2008; Franěk
565 *et al.*, 2010a, b). There would have been a very short period of rapid advective heat loss upon the
566 granulite complexes reaching middle to upper crustal levels as the high-*P* rocks thermally equilibrated
567 with the surrounding crust (O'Brien, 2000). In the absence of hot proximal plutons or large amounts of
568 fluid, the olivine-bearing symplectites and related textures in eclogites in the Moldanubian Zone may
569 therefore have formed in response to heat expelled from the granulites as they "ironed" out over the
570 Monotonous and Variegated Series in the middle crust, with fluid sourced from heating and
571 dehydration of the adjacent Monotonous and Varied Series.
572
573 **CONCLUSIONS**
574 • Rare symplecites of olivine-plagioclase±orthopyroxene±spinel±ilmenite, as well as pyroxene-
575 plagioclase and amphibole-plagioclase, occur in eclogites and pyroxenites widely across the
576 Moldanubian Zone in the Bohemian Massif. Formation took place at high-*T* and moderate to
577 low *P* (~850ºC, ≤ 6 kbar).
578 • Breakdown of former high-*P* garnet, an influx of H and Na, and redistribution of Si was
579 important in generating the distinctive olivine-bearing symplectite varieties, although
580 replacement of rare amphibole and phlogopite also led to their formation. Fractional
581 crystallisation of olivine and spinel from a starting garnet composition and the addition of H

582 and Na promoted the simultaneous formation of amphibole-plagioclase symplectites. High-*P*
583 clinopyroxene also lost Fe and Mg, and was replaced by symplectites of diopside-enstatite-
584 plagioclase. All symplectites formed contemporaneously.
585 • Infiltration of a H-bearing fluid was critical in driving symplectite reactions, despite the fact
586 that the olivine-bearing and pyroxene-plagioclase symplectites are mainly anhydrous. This
587 fluid aided the dissolution of garnet and precipitation of olivine-plagioclase-spinel
588 symplectites.
589 • The lack of an associated fabric, the partial preservation of earlier peak-P minerals, and
590 formation of sharp compositional steps in garnet immediately adjacent to symplectites are
591 consistent with these rocks having been subjected to a short-duration heating event in the
592 middle Varican crust. The heat source could have been advective loss from rapidly exhumed
593 lower crust/upper mantle granulite sheets as they were juxtaposed over cooler upper crustal
594 rocks during Variscan continent-continent collision.
595
596 **SUPPLEMENTARY DATA**
597 **ACKNOWLEDGMENTS**
598 We thank A. Cooper, N. Daczko, J. Konopásek, H. Marschall, G. Medaris and A. Zeh for comments
599 and reviews.
600
601 **REFERENCES**
602 Almond, D. C. (1964). Metamorphism of Tertiary lavas in Strathaird, Skye. *Transactions of the Royal*
603 *Society of Edinburgh* **45**, 413-435.
604 Beaumont, C., Jamieson, R. A., Butler, J. P. & Warren, C. J. (2009). Crustal structure: A key
605 constraint on the mechanism of ultra-high-pressure rock exhumation. *Earth and Planetary Science*
606 *Letters*, 10.1016/j.epsl.2009.08.001.
607 Beard, B. L., Medaris Jr, L. G., Johnson, C. M., Brueckner, H. K. & Mısar, Z. (1992). Petrogenesis of
608 Variscan high-temperature Group A eclogites from the Moldanubian Zone of the Bohemian
609 Massif, Czechoslovakia. *Contributions to Mineralogy and Petrology* **111**, 468–483.

610 Becker, H. (1997). Petrological constraints on the cooling history of high-temperature garnet peridotite
611 massifs in lower Austria. *Contributions to Mineralogy and Petrology* **128**, 272-286.
612 Berman, R.G. (1990). Mixing properties of Ca–Mg–Fe–Mn garnets. *American Mineralologist* , 328–
613 344.
614 Brouwer, F.M., van de Zedde, D.M.A., Wortel, M.J.R. & Vissers, R.L.M (2004). Late-orogenic
615 heating during exhumation: Alpine PTt trajectories and thermomechanical models. *Earth and*
616 *Planetary Science Letters* **220**, 185-199.
617 Brouwer, F.M. & Engi, M. (2005). Staurolite and other aluminous phases in Alpine eclogite from the
618 central Swiss Alps: analysis of domain evolution. *The Canadian Mineralogist* **43**, 105-128.
619 Butler, J. P., Beaumont, C. & Jamieson, R. A. (2011). Crustal emplacement of exhuming (ultra)high-
620 pressure rocks: Will that be pro- or retro-side? *Geology*, doi: 10.1130/G32166.1
621 Carswell, D. A. & O'Brien, P. J. (1993). Thermobarometry and geotectonic significances of high-
622 pressure granulites: examples from the Moldanubian Zone of the Bohemian Massif in Lower
623 Austria. *Journal of Petrology* **34**, 427–459.
624 Clarke, G.L., Klepeis, K.A. & Daczko, N.R. (2000). Cretaceous high-P granulites at Milford Sound,
625 New Zealand: metamorphic history and emplacement in a convergent margin setting. *Journal of*
626 *Metamorphic Geology* **18**, 359-374.
627 Cooke, R.A. (2000). High-pressure/temperature metamorphism in the St. Leonhard Granulite Massif,
628 Austria: evidence from intermediate pyroxene-bearing granulites. *International Journal of Earth*
629 *Sciences* **89**, 631-651.
630 Cooke, R. A., O'Brien, P. J. & Carswell, D. A. (2000). Garnet zoning and the identification of
631 equilibrium mineral compositions in high-pressure–temperature granulites from the Moldanubian
632 Zone, Austria. *Journal of Metamorphic Geology* **18**, 551–569.
633 Cooke, R. A. & O'Brien, P. J. (2001). Resolving the relationship between high P–T rocks and gneisses
634 in collisional terranes: an example from the Gföhl gneiss-granulite association in the Moldanubian
635 Zone, Austria. *Lithos* **58**, 33–54.
636 Dale, J., Powell, R. , White R.W., Elmer, F.L. & Holland, T.J.B. & (2005). A thermodynamic model
637 for Ca-Na clinoamphiboles for Na_2O-CaO-FeO-MgO-Al_2O_3-SiO_2-H_2O-O for petrological

638 calculations. *Journal of Metamorphic Geology* **23**, 771-791.
639 De Capitani, C. & Brown, T. H. (1987). The computation of chemical equilibrium in complex systems
640 containing non-ideal solutions. *Geochemica et Cosmochimica Acta* **51**, 2639-2652.
641 De Capitani, C. & Petrakakis, K. (2010). **T**he computation of equilibrium assemblage diagrams with
642 Theriak/Domino software. *American Mineralogist* **95**, 1006-1016.
643 De Sigoyer, J., Guillot, S., Lardeaux, J-M. & Mascle G. (1997). Glaucophane bearing eclogites in the
644 Tso Morari dome (eastern Ladakh, NW Himalaya). *European Journal of Mineralogy* **9**, 1073–
645 1083.
646 Dégi, J., Abart, R., Török, K., Bali, E., Wirth, R. & Rhede, D. (2010). Symplectite formation during
647 decompression induced garnet breakdown in lower crustal mafic granulite xenoliths: mechanisms
648 and rates. *Contributions to Mineralogy and Petrology* **159**, 293-314.
649 England, P.C. & Thompson, A.B. (1984). Pressure-temperature paths of regional metamorphism 1.
650 Heat transfer during the evolution of regions of thickened continental crust. *Journal of Petrology*
651 **25**, 894-928.
652 Faryad, S.W., Perraki, M. & Vrána S. (2006). P-T evolution and reaction textures in retrogressed
653 eclogites from Svetlik, the Moldanubian Zone (Czech Republic). *Mineralogy and Petrology* **88**,
654 297-319.
655 Faryad, S.W (2009). The Kutná Hora Complex (Moldanubian Zone, Bohemian Massif): A composite
656 of crustal and mantle rocks subducted to HP/UHP conditions. *Lithos* **109**, 198-208.
657 Ferry, J. M., Mutti, L. J. & Zuccala, G. J. (1987). Contact metamorphism/hydrothermal alteration of
658 Tertiary Basalts on the Isle of Skye, northwest Scotland. *Contributions to Mineralogy and*
659 *Petrology* **95**, 166-181.
660 Ferry, J.M. (1994). A historical review of metamorphic fluid flow. *Journal of Geophysical Research*
661 **99**, 15487-15498.
662 Finger, F., Roberts, M.P., Haunschmid, B., Schermaier, A. & Steyrer, H.P. (1997). Granitoids of
663 central Europe: their typology, potential sources and tectonothermal relations. *Mineralogy and*
664 *Petrology* **61**, 67-96.
665 Finger, F., Gerdes, A., Janoušek, V., René, M. & Riegler, G. (2007). Resolving the Variscan evolution

of the Moldanubian sector of the Bohemian Massif: the significance of the Bavarian and the Moravo–Moldanubian tectonometamorphic phases. *Journal of Geosciences* **52**, 9 – 28.

Franěk, J., Schulmann K., Lexa, O., Tomek, C. & Edel J-B. (2011a). Model of syn-convergent extrusion of orogenic lower crust in the core of the Variscan belt: implications for exhumation of high-pressure rocks in large hot orogens. *Journal of Metamorphic Geology* **29**, 53-78.

Franěk, J., Schulmann K., Lexa, O., Ulrich, S., Štípksá, P., Haloda, J. & Týcová, P. (2011b). Origin of felsic granulite microstructure by heterogeneous decomposition of alkali feldspar and extreme weakening of orogenic lower crust during the Variscan Orogeny. *Journal of Metamorphic Geology* **29**, 103-130.

Franke, W. (2000). *The middle-European segment of the Variscides: tectonostratigraphic units, terrane boundaries and plate tectonic evolution*. In: Franke, W., Haak, U., Oncken, O. & Tanner, D. (eds.) *Orogenic Processes: Quantification and Modelling in the Variscan belt*. Geological Society of London Special Publication **179**, 35–61.

Fuhrman, M. L. & Lindsley, D. H., 1988. Ternary-feldspar modelling and thermometry. *American Mineralogist* **73**, 201–215.

Green, D. H. & Ringwood, A. E. (1967) An experimental investigation of the gabbro to eclogite transformation and its petrological applications. *Geochimica Cosmochimica Acta* **31**, 767–833.

Guillot, S., Mahéo, G., De Sigoyer, J., Hattori, K. H. & Pêcher, A. (2008). Tethyan and Indian subduction viewed from the Himalayan high- to ultrahigh-pressure metamorphic rocks. *Tectonophysics* **451**, 225–241.

Harry, W. T. (1952). Basic hornfels at a gabbro contact near Carlingford, Eire. *Geological Magazine* **89**, 411-416.

Holland, T.J.B. (1980). The reaction albite = jadeite + quartz determined experimentally in the rage 600-1200ºC. *American Mineralogist* **65**, 129-134.

Janoušek, V., Gerdes, A., Vrána, S., Finger, F., Erban, V., Friedl, G. & Braithwaite, C.J.R. (2006). Low-pressure granulites of the Lišov Massif, Southern Bohemia: Viséan metamorphism of Late Devonian plutonic arc rocks. *Journal of Petrology* **47**, 705-744.

Kalt, A., Berger, A. & Blümel, P. (1999). Metamorphic evolution of cordierite-bearing migmatites

694 from the Bayerische Wald (Variscan Belt, Germany). *Journal of Petrology* **40**, 601-627.
695 Konopásek, J. (2011). Tectonic position of eclogites and blueschists in the Bohemian Massif. *Geolines*
696 **23**, 11-17.
697 Konrad-Schmolke, M., Babist, J., Handy, M. R. & O'Brien, P. J. (2006). The physico-chemical
698 properties of a subducted slab from garnet zonation patterns (Sesia Zone, Western Alps). *Journal*
699 *of Petrology* **47**, 2123-2148.
700 Konrad-Schmolke, M., O'Brien, P. J., De Capitani, C. & Carswell, D. A. (2008). Garnet growth at
701 high- and ultra-high pressure conditions and the effect of element fractionation on mineral modes
702 and composition. *Lithos* **103**, 309-332.
703 Kroner, U., Mansy, J. L., Mazur, S., Aleksandrowski, P., Hann, H. P., Huckriede, H., Lacquement, F.,
704 Lamarche, J., Ledru, P., Pharaoh, T. C., Zedler, H., Zeh, A. & Zulauf, G. (2008). *Variscan*
705 *Tectonics*. In: McCann, T. (ed) *The Geology of Central Europe, Volume 1: Precambrian and*
706 *Palaeozoic*. Geological Society of London, 599-664.
707 Lambert, I.B. & Wyllie, P.J. (1972). Melting of gabbro (quartz eclogite) with excess water to 35
708 kilobars, with geological applications. *Journal of Geology* **80**, 693-708.
709 Leake, B. E., Woolley, A. R. & Arps, C. E. S., *et al*. (1997). Nomenclature of amphiboles: report of
710 the subcommittee on amphiboles of the International Mineralogical Association commission on
711 new minerals and mineral names. *The Canadian Mineralogist* **33**, 219–246.
712 MacGregor, A. G. (1931). Contact-metamorphosed Scottish igneous rocks of Tertiary age and their
713 bearing on the origin of the so-called beerbachites, gabbroporphyrites, and gabbro-pegmatites of
714 the Odenwald. *Geological Magazine* **68**, 506-521.
715 Medaris, L. G., Jelínek, E. & Mísaŕ, Z. (1995). Czech eclogites: terrane settings and implications for
716 Variscan tectonic evolution of the Bohemia Massif. *European Journal of Mineralogy* **7**, 7–28.
717 Medaris, L.G., Fournelle, J.H., Ghent, E.D., Jelínek, E. & Mísaŕ, Z. (1998). Prograde eclogite in the
718 Gföhl Nappe, Czech Republic: new evidence on Variscan high-pressure metamorphism. *Journal of*
719 *Metamorphic Geology* **16**, 563-576.
720 Medaris Jr, G., Wang, H., Jelínek, E., Mihaljevic, M. & Jakes, P. (2005). Characteristics and origins

721 of diverse Variscan peridotites in the Gföhl Nappe, Bohemian Massif, Czech Republic. *Lithos* **82**,
722 1-23.
723 Medaris Jr, L.G., Beard B.L. & Jelínek, E. (2006a). Mantle-derived, UHP garnet pyroxene and
724 eclogite in the Moldanubian Gföhl Nappe, Bohemian Massif: A geochemical review, new P-T
725 determinations, and tectonic interpretation. *International Geology Review* **48**, 765-777.
726 Medaris Jr, L. G., Ghent, E. D., Wang, H. F., Fournelle, J. H. & Jelínek, E. (2006b). The Spačice
727 eclogite: constraints on the P–T–t history of the Gföhl granulite terrane, Moldanubian Zone,
728 Bohemian Massif. *Mineralogy and Petrology* **86**, 203-220.
729 Medaris Jr, L.G., Ackermann, L., Jelínek, E., Toy, V., Siebel, W. & Tikoff, B. (2009). The Sklené
730 garnet peridotite: petrology, geochemistry and structure of a mantle-derived boudin in
731 Moldanubian granulite. *Journal of Geosciences* **54**, 301-323.
732 Messiga, B. & Bettini, E. (1990). Reactions behaviour during kelyphite and symplectite formation: a
733 case study of mafic granulites and eclogites from the Bohemian Massif. *European Journal of*
734 *Mineralogy* **2**, 125-144.
735 Meyre, C., de Capitani, C., Partzsch, J.H. (1997). A ternary solid solution model for omphacite and its
736 application to geothermobarometry of eclogites from the Middle Adula nappe (Central Alps,
737 Switzerland). *Journal of Metamorphic Geology* **15**, 687–700.
738 Mongkoltip, P. & Ashworth, J.R. (1983). Quantitative estimation of an open-system symplectite
739 forming reaction: restricted diffusion of Al and Si in coronas around olivine. *Journal of Petrology*
740 **24**, 635-661.
741 Mysen, B. & Griffin, W.L. (1973). Pyroxene stoichiometry and the breakdown of omphacite.
742 *American Mineralogist* **58**, 60-63.
743 Nakamura, D., Svojtka, M., Naemura, N. & Hirajima, T. (2004). Very high-pressure (>4 GPa) eclogite
744 associated with the Moldanubian Zone garnet peridotite (Nové Dvory, Czech Republic). *Journal of*
745 *Metamorphic Geology* **22**, 593-603.
746 Nakamura, D. (2009). A new formulation of garnet-clinopyroxene geothermometer based on
747 accumulation and statistical analysis of a large experimental data set. *Journal of Metamorphic*
748 *Geology* **27**, 497-508.

749 Obata, M. (1994). Material transfer and local equilibria in a zoned kelyphite from a garnet pyroxenite,
750 Ronda, Spain. *Journal of Petrology* **35**, 271-287.
751 Obata, M. (2011). Kelyphite and symplectite: textural and mineralogical diversities and universality,
752 and a new dynamic view of their structural formation. ISBN: 978-953-307-595-2del, InTech,
753 http://www.intechopen.com/articles/show/title/kelyphite-and-symplectite-textural-and-
754 mineralogical-diversities-and-universality-and-a-new-dynamic-
755 O'Brien, P. J. & Vrána, S. (1995). Eclogites with a short-lived granulite facies overprint in the
756 Moldanubian Zone, Czech Republic: petrology, geochemistry and diffusion modelling of garnet
757 zoning. *Geologische Rundschau* **84**, 473–488.
758 O'Brien, P. J. (1997a). Garnet zoning and reaction textures in overprinted eclogites, Bohemian Massif,
759 European Variscides: a record of their thermal history during exhumation. *Lithos* **41**, 119–133.
760 O'Brien, P. J. (1997b). *Granulite facies overprints of eclogites: short-lived events deduced from*
761 *diffusion modelling*. In: Qian, X., You, Z., Jahn, B-M., Halls, H. C. (eds) *Precambrian Geology*
762 *and Metamorphic Petrology*. Dordrecht, proceedings 30th International Geological Congress, 17,
763 pp. 157–171.
764 O'Brien, P. J. (2000). *The fundamental Variscan problem: high-temperature metamorphism at*
765 *different depths and high-pressure metamorphism at different temperatures*. In: Franke, W., Haak,
766 V., Oncken, O., Tanner, D. (eds) *Orogenic Processes: Quantification and Modelling in the*
767 *Variscan Belt*. Geological Society, London, Special Publications 179, 369–386.
768 Petrakakis, K. (1997). Evolution of Moldanubian rocks in Austria: review and synthesis. *Journal of*
769 *Metamorphic Geology* **15**, 203-222.
770 Phillips, E. R. (1959). An olivine-bearing hornfels from South-Eastern Queensland. *Geological*
771 *Magazine* **96**, 377-384.
772 Powell, R. & Holland, T. J. B., 1999. Relating formulations of the thermodynamics of mineral solid
773 solutions: activity modelling of pyroxenes, amphiboles and micas. *American Mineralogist* **84**, 1–
774 14.
775 Putnis, A. (2009). Mineral replacement reactions. In: Oelkers, E.H. & Schott, J. (eds)
776 Thermodynamics and kinetics of water-rock interaction. *Reviews in Mineralogy and Geochemistry*

70, 87-124.

Putnis, A. & Austrheim, H. (2010). Fluid induced processes: metasomatism and metamorphism. *Geofluids* **10**, 254-269.

Putnis, A. & John, T. (2010). Replacement processes in the Earth's crust. *Elements* **6**, 159-164.

Racek M., Štípksá, P., Pitra, P., Schulmann, K. & Lexa, O. (2006). Metamorphic record of burial and exhumation of orogenic lower and middle crust: a new tectonothermal model for the Drosendorf window (Bohemian Massif, Austria). *Mineralogy and Petrology* **86**, 221-251.

Sadashivaiah, M. S. (1950). Olivine-bearing and other basic hornfelses around the Insch Igneous Mass, Aberdeenshire. *Geological Magazine* **87**, 2, 121-130.

Sakakibara, M. & Isono, Y. (1996). Middle Miocene thermal metamorphism due to the infiltration of high-temperature fluid in the Sanbagawa metamorphic belt, southwest Japan. *Contributions to Mineralogy and Petrology* **125**, 341-358.

Sassi, R., Mazzoli, C., Miller, C. & Konzett, J. (2004). Geochemistry and metamorphic evolution of the Pohorje Mountain eclogites from the easternmost Austroalpine basement of the Eastern Alps (Northern Slovenia). *Lithos* **78**, 235-261.

Schulmann, K., Kröner, A., Hegner, E., Wendt, I., Konopásek, J., Lexa, O. & Štípská, P. (2005). Chronological constraints on the pre-orogenic history, burial and exhumation of deep-seated rocks along the eastern margin of the Variscan Orogen, Bohemian Massif, Czech Republic. *American Journal of Science* **305**, 407–448.

Schulmann, K., Lexa, O., Štípská, P., Racek, M., Tajčmanová, L., Konopásek, J., Edel, J-B., Peschler, A. & Lehmann, J. (2008). Vertical extrusion and horizontal channel flow of orogenic lower crust: key exhumation mechanisms in large hot orogens? *Journal of Metamorphic Geology* **26**, 273–297.

Simmons, E. C., Lindsay, D. H. & Papike, J. J. (1974). Phase relations and crystallization sequence in a contact-metamorphosed rock from the Gunflint Iron Formation, Minnesota. *Journal of Petrology* **15**, 539-565.

Štípksá, P., Schulmann, K. & Kröner, A. (2004). Vertical extrusion and middle crustal spreading of omphacite granulite: a model of syn-convergent exhumation (Bohemian Massif, Czech Republic). *Journal of Metamorphic Geology* **22**, 179–198.

805 Tajčmanová, L., Konopásek, J. & Schulmann K. (2006). Thermal evolution of the orogenic lower
806 crust during exhumation within a thickened Moldanubian root of the Variscan belt of Central
807 Europe. *Journal of Metamorphic Geology* **24**, 119-134.
808 Taylor, W.R. (1998). An experimental test of some geothermometer and geobarometer formulations
809 for upper mantle peridotites with application to the thermobarometry of fertile lherzolite and garnet
810 websterite. *Neues Jahrbuch für Mineralogie Abhandlungen* **172**, 381– 408.
811 Thompson, A.B. & Connolly, J.A.D. (1995). Melting of the continental crust: some thermal and
812 petrological constraints on anatexis in continental collision zones and other tectonic settings.
813 *Journal of Geophysical Research* **100**, 15565-15579.
814 Timmerman, M. J. (2008). *Palaeozoic magmatism*. In: McCann, T. (ed) *The Geology of Central*
815 *Europe*. *Volume 1: Precambrian and Palaeozoic*. Geological Society London, 665-748.
816 Török, K., Dégi, J., Szép, A. & Marosi, G. (2005). Reduced carbonic fluids in mafic granulite
817 xenoliths from the Bakony-Balaton Highland Volcanic Field, W-Hungary. *Chemical Geology* **223**,
818 93-108.
819 Tóth, T.M., Grandjean, V. & Engi, M. (2000). Polyphase evolution and reaction sequence of
820 compositional domains in metabasalt: a model based on local chemical equilibrium and
821 metamorphic differentiation. *Geological Journal* **35**, 163-183.
822 Turner, F. J. (1981). *Metamorphic petrology: Mineralogical, field, and tectonic aspects*. Hemisphere
823 Pub. Corp. (Washington and New York), 524 p.
824 Vorhies, S.H. & Ague, J.J. (2011). Pressure-temperature evolution and thermal regimes in Barrovian
825 zones, Scotland. *Journal of the Geological Society, London* **168**, 1147-1166.
826 Walsch, E. O. & Hacker, B. R. (2004). The fate of subducted continental margins: Two-stage
827 exhumation of the high-pressure to ultrahigh-pressure Western Gneiss Region, Norway. *Journal of*
828 *Metamorphic Geology* **22**, 671–687
829 Warren, C. J., Beaumont, C. & Jamieson, R. A. (2008). Formation and exhumation of ultra-high
830 pressure rocks during continental collision: role of detachment in the subduction channel.
831 *Geochemistry, Geophysics, Geosystems* **9**, Q04019.
832 Wells, P.R.A. (1977). Pyroxene thermometry in simple and complex systems. *Contributions to*

Mineralogy and Petrology **62**, 129-139.

Whitney, D. & Evans, B.W. (2010). Abbreviations for names of rock-forming minerals. *American Mineralogist* **95**, 185-187.

Wilke, F. D. H., O'Brien, P. J., Altenberger, U., Konrad-Schmolke, M. & Ahmed Khan, M. (2009). Multi-stage reaction history in different eclogite types from the Pakistan Himalaya and implications for exhumation processes. *Lithos* **114**,70-85

Wu, C.M. & Zhao, G.C. (2007). A recalibration of the garnet-olivine geothermometer and a geobarometer for garnet peridotites and garnet-olivine-plagioclase-bearing granulites. *Journal of Metamorphic Geology* **25**, 497-505.

Žák, J., Verner, K., Finger, F., Faryad, S. W., Chlupáčová, M. & Veselovsky, F. (2010). The generation of voluminous S-type granites in the Moldanubian unit, Bohemian Massif, by rapid isothermal exhumation of the metapelitic middle crust. *Lithos* **121**, 25-40.

845

846 **FIGURE AND TABLE CAPTIONS**

847 Figure 1. Simplified geological map of the Bohemian Massif. Black stars indicate the positions of
848 rocks with known olivine-bearing symplectites within the Moldanubian Zone. Figure modified
849 from Franke (2000).

850 Figure. 2A. Veinlets in a garnet pyroxenite that have crystallised olivine-bearing symplectites. Sample
851 42. 2B. Plane-polarised light photomicrographic image of the symplectites within the pyroxenite
852 shown in 2A. 2C. Plane-polarised image showing olivine-bearing symplectites replacing garnet in
853 an eclogite. Sample NM-1. 2D. Backscattered electron image of NM-1, showing symplectite
854 textures replacing omphacite and garnet. 2E and 2F. Plane-polarised light image of a fine-grained
855 eclogite with olivine-bearing symplectites and amphibole-plagioclase symplectites. 2G. Plane
856 polarized light image of olivine-bearing symplectites and pyroxene-plagioclase symplectites in an
857 eclogite. Sample NOM1a. 2H. Backscattered electron image of an omphacite partially replaced by
858 symplectites of clinopyroxene-orthopyroxene-plagioclase in NOM1a. An earlier coarse amphibole
859 occurs outside the omphacite.

860 Figure 3A. High-contrast backscattered electron images of olivine-bearing symplectites (NOM1a). 3B.
861 Olivine-bearing symplectites replacing garnet and amphibole (NOM1a). 3C. Assemblages from left
862 to right: garnet, amphibole-plagioclase symplectite, olivine-plagioclase-spinel symplectite, olivine-
863 plagioclase symplectite, coarse amphibole plate (NOM1a). 3D. The tip of the fracture within the
864 garnet grain is composed of amphibole that has exsolved small blebs of spinel. The garnet margin
865 has recrystallised to an amphibole-plagioclase symplectite with a little olivine and spinel (NOM1a).
866 3E. Phlogopite under replacement by olivine and spinel (NOM1b).

867 Figure 4A. Ca element map of a compositionally extreme garnet grain in NOM1a. High Ca zones
868 correspond to the dark narrow bands that traverse earlier formed low Ca domains (which
869 themselves enclose amphibole). 4B. A rare example of olivine-spinel-plagioclase symplectite
870 touching garnet. 4C. Micro-stepped element traverses across the contact between garnet and olivine
871 (line 1 in Fig. 4B). Note that Sps is plotted on the right-hand side, whereas Alm, Prp and Grs are
872 plotted on the lefthand side. 4D. High-contrast backscattered electron image in a compositionally

modified garnet adjacent to amphibole, at the tip of a symplectite-bearing vein. 4E. Mn element map across two symplectite-bearing cracks in garnet. Dark colours indicate higher concentrations. Note the limited alteration of earlier formed high-P garnet.

Figure 5A. Feldspar compositions in NOM1a. 5B and 5C. Inverted high-contrast backscattered electron images of feldspar within the olivine-plagioclase-spinel and the amphibole-plagioclase symplectites. Feldspar compositions correspond to microprobe analyses.

Figure 6A. Pseudosection illustrating the predicted phase assemblages for high-Ca garnet. 8B. *P-X* binary phase diagram of Na added to high-Ca garnet. Isopleths of anorthite content in plagioclase are plotted as solid grey lines. The diagram is constructed for 850ºC. 8C. Binary phase diagram illustrating phase transformations when Si is removed from high-Ca garnet starting composition. Isopleths for the mol % orthopyroxene show that this mineral volumetrically decreases as Si is removed. The diagram is constructed for 850ºC. 8D. Psuedosection calculated for the effective domain composition of an olivine-plagioclase-spinel symplectite (see: Example 1 in Table 2).

Figure 7. *P-X* binary phase diagram showing the results of addition of Si to the measured omphacite composition. The diagram is constructed for conditions of 850ºC.

Figure 8. *P-X* binary phase diagram with the starting composition of high-Ca garnet (on left) and the end composition of amphibole-plagioclase symplectite (at right). Na and H are added to the system while olivine and spinel are progressively removed. The amount of water present will control the vol % of amphibole that is stable. The diagram is constructed for 850ºC.

Figure 9. Interpreted *P-T* path for NOM1a. Two alternative *P-T* paths are shown to explain the metamorphic history. The exhumation path of the high-*P*, high-*T* (mantle depth) granulite facies Gföhl Unit is shown.

Table 1. Representative mineral analyses measured by wavelength dispersive techniques.

Table. 2. Representative effective bulk compositions and mass balance calculations for microscopic domains.

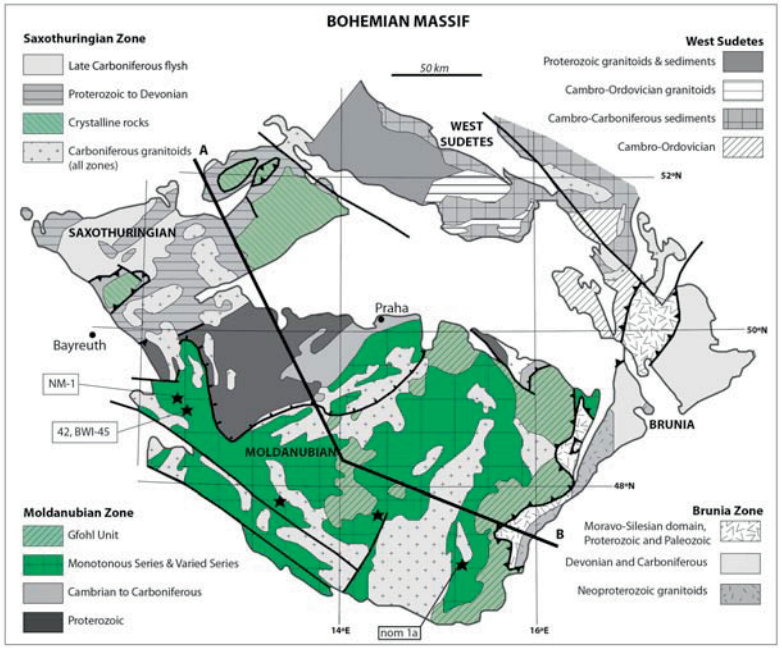

Figure 1. Simplified geological map of the Bohemian Massif. Black stars indicate the positions of mafic and ultramafic rocks with known olivine-spinel-plagioclase hornfels. Figure modified from Franke (2000).

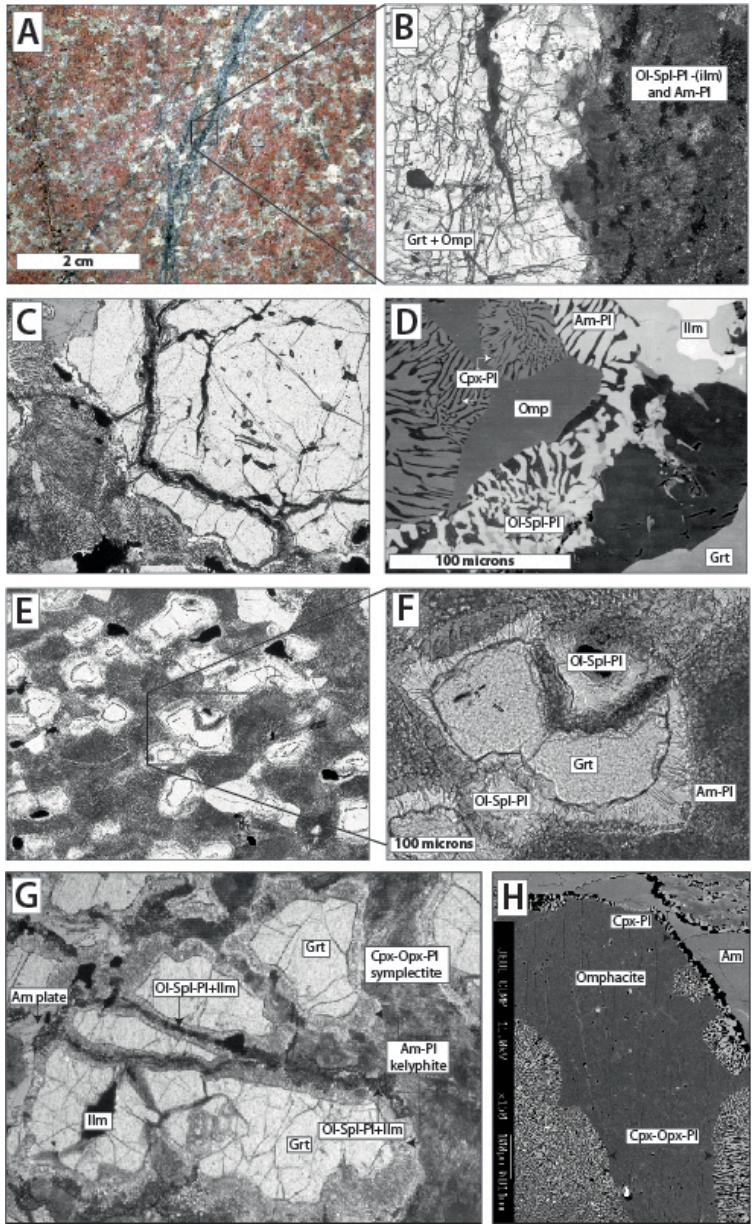

Figure. 2A. Veinlets that crystallised olivine-spinel-plagioclase (+ ilmenite) symplectites in a garnet pyroxenite. Sample 42. 2B. Plane-polarised light petrographic microscopic image of the symplectites within the pyroxenite shown in 2A. 2C. Plane-polarised image showing olivine-spinel-plagioclase symplectites replacing garnet. Eclogite, sample NM-1. 2D. Backscattered electron image of NM-1, showing symplectites replacing omphacite and garnet. 2E and 2F. Plane-polarised light image of a fine-grained ?ECLOGITE? with olivine-spinel-plagioclase symplectites and amphibole-plagioclase kelyphites. Sample XX. 2G. Plane polarized light image of olivine-spinel-plagioclase symplectites and pyroxene-plagioclase symplectites in an eclogite. Sample nom1a. 2H. Backscattered electron image of omphacite being replaced by symplectites of clinopyroxene-orthopyroxene-plagioclase in nom1a. Note the presence of an earlier coarse amphibole outside omphacite.

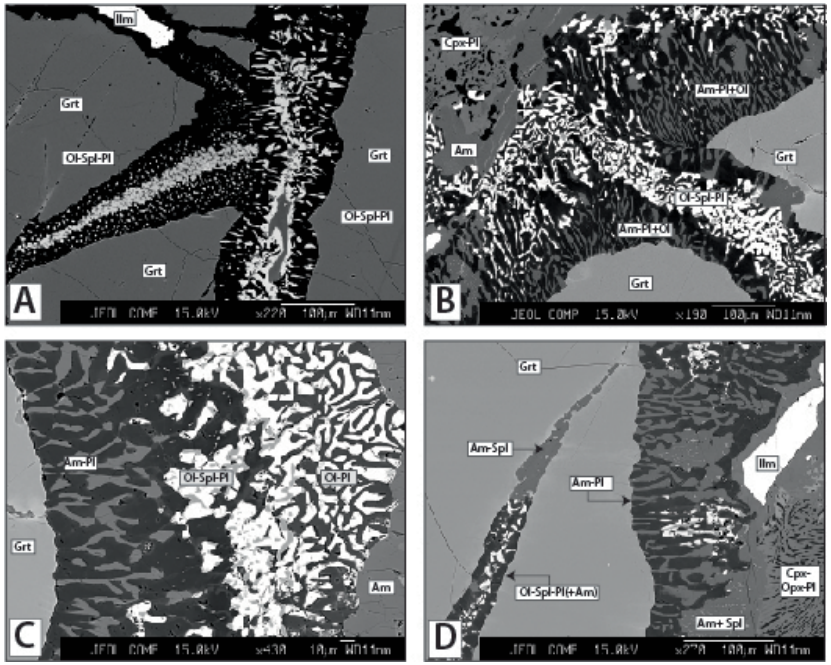

Figure 3A. High-contrast backscattered electron images of olivine-spinel-plagioclase symplectites in nom1a. There appears to be two generations of symplectite, with the coarser-grained veinlet truncating a fine-grained veinlet. and amphibole-plagioclase kelyphites in nom1a. 3B. Veinlet of olivine-spinel-plagioclase symplectite replacing garnet and amphibole. 3C, left to right. Garnet, amphibole-plagioclase kelyphite, olivine-spinel-plagioclase symplectite, olivine-plagioclase symplectite, coarse amphibole plate. 3D. The tip of a veinlet in garnet is here composed of amphibole and spinel.

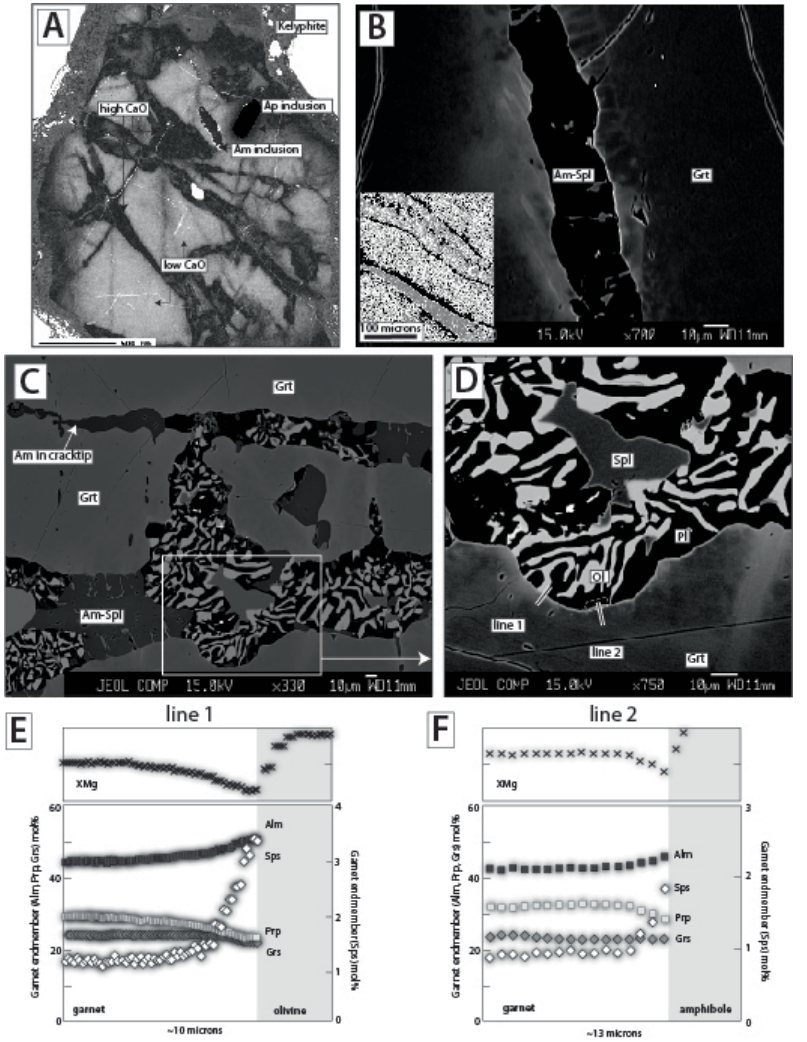

Figure 4A. A CaO element map of a garnet in nom1a. High CaO zones correspond to the dark narrow bands that traverse earlier formed low CaO domains (which themselves enclose amphibole). 4B. High-contrast backscattered electron image of diffusively modified garnet adjacent to an amphibole-bearing fracture. Inset shows a high-contrast Mn element map, with Mn in garnet distinctly increasing adjacent to the veinlets. 4C and 4D. A rare example of olivine-spinel-plagioclase symplectite touching garnet. 4E and 4F. Micro-stepped element traverses across the diffusively modified margins of garnet adjacent to olivine (line 1) and amphibole (line 2). Note that Sps scale is plotted on the righthand side. Positions of lines is indicated in Fig. 4D.

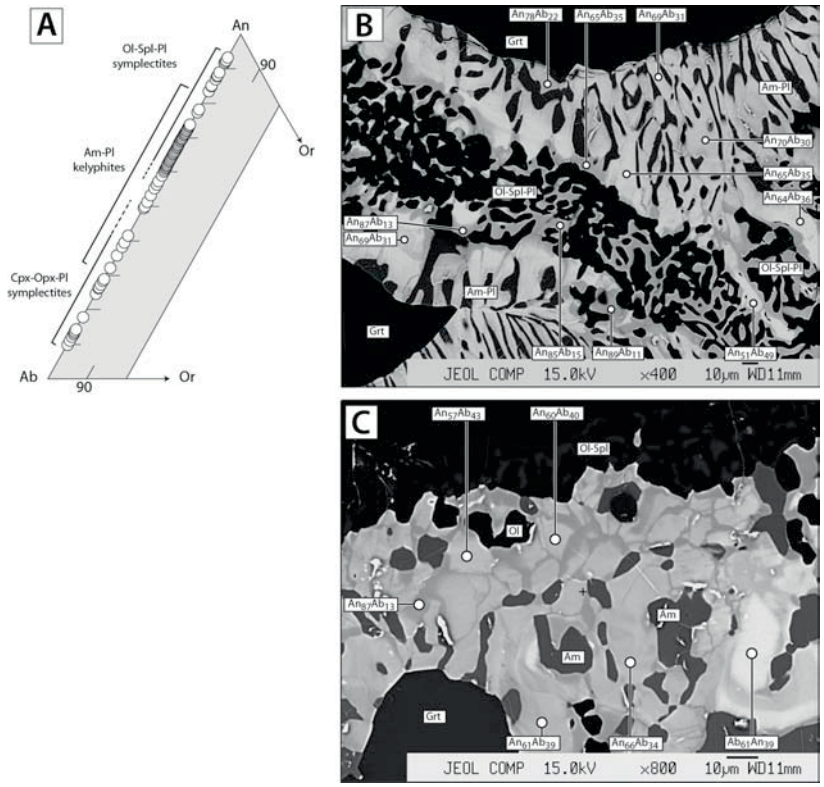

Figure 5A. Feldspar compositions in nom1a. 5B and 5C. Inverted high-contrast backscattered electron images of feldspar within the olivine-spinel-plagioclase symplectites and amphibole-plagioclase kelyphites.

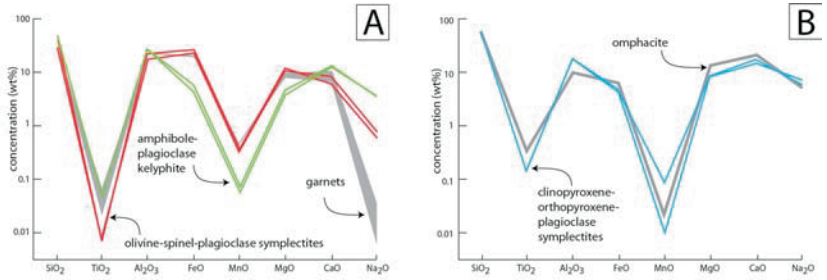

Figure 6A. Comparison of the micro-domain compositions of olivine-spinel-plagioclase symplectites and amphibole-plagioclase kelyphites versus the measured compositional range of garnet. 6B. Comparison between effective micro-domain compositions of clinopyroxene-orthopyroxene-plagioclase symplectites and the omphacite grains that they overgrow.

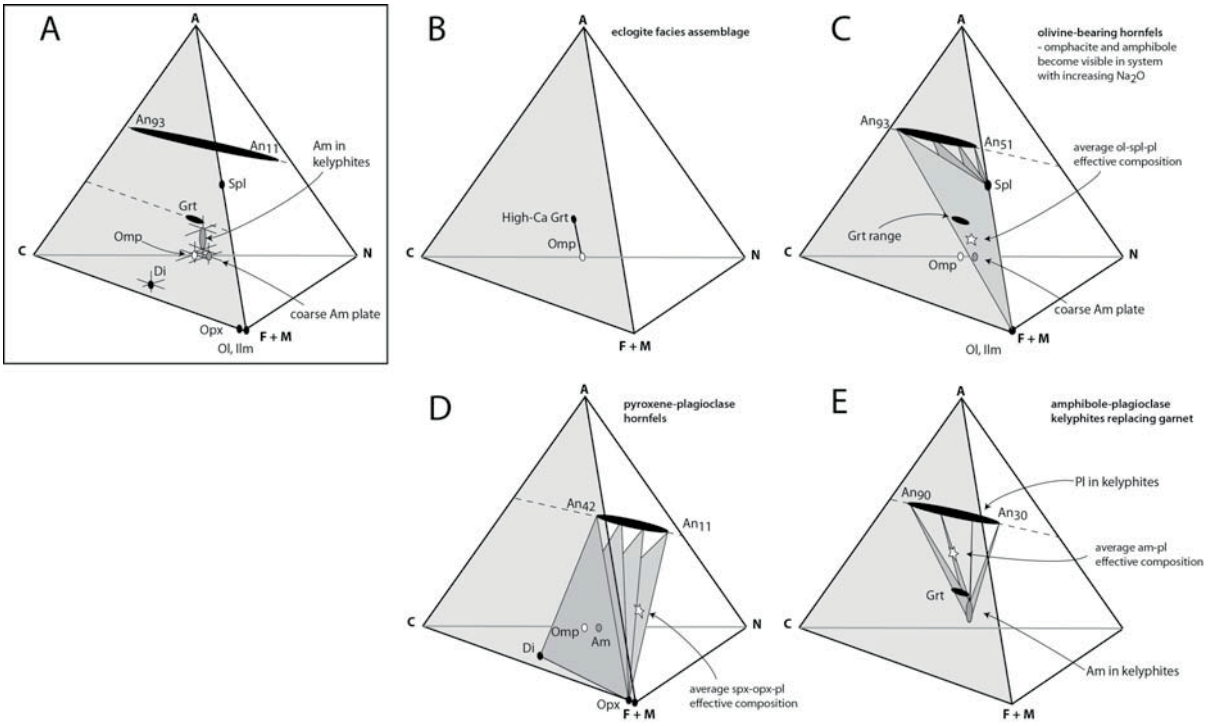

Figure. 7. ACFN diagrams of mineral compositions and effective bulk domain compositions for nom1a.

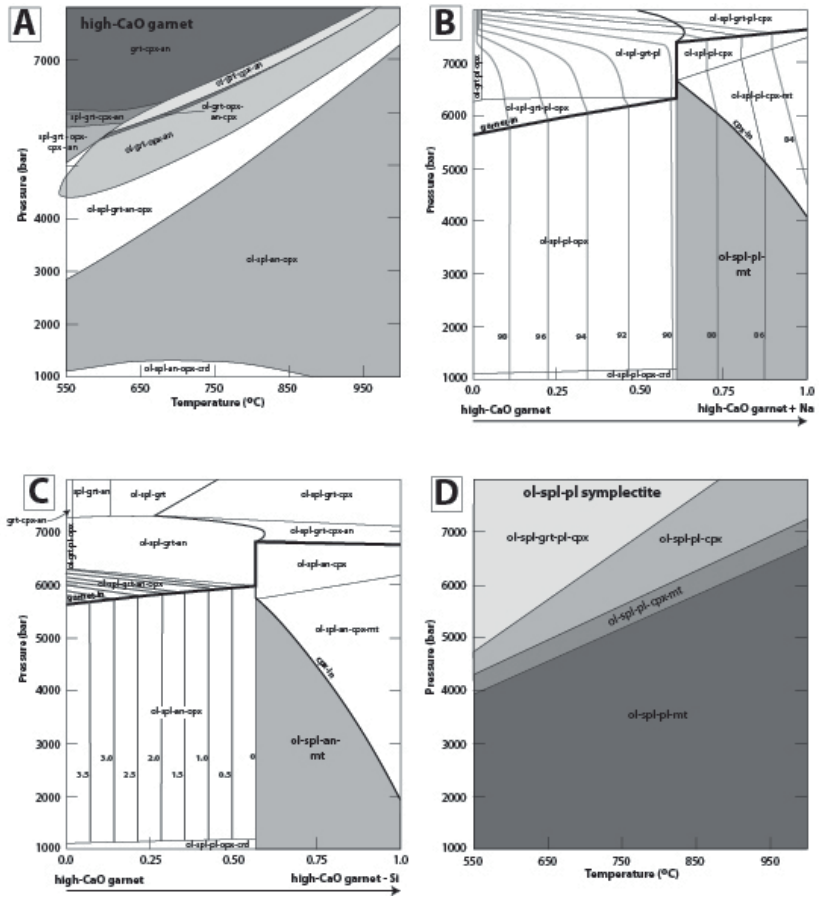

Figure 8A. Pseudosection for high-CaO garnet, illustrating the predicted phases. 8B.Binary phase diagram of Na added to high-CaO garnet. Isopleths of anorthite content in plagioclase are plotted as solid grey lines. The diagram is constructed for 850°C. 8C. Binary phase diagram illustrating transformations when Si is removed from the high-CaO garnet. Isopleths for the mol % orthopyroxene show how this element progressively decreases with decreasing Si. The diagram is constructed for 850°C. 8D. Representative psuedosection for the effective composition of one olivine-spinel-plagioclase symplectite.

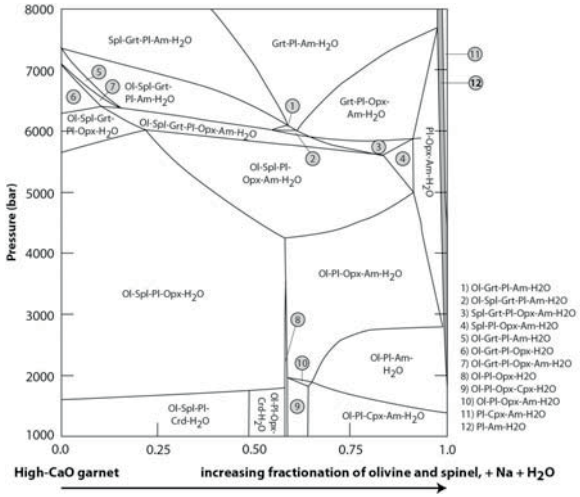

Fig. 9. Binary phase diagram with the starting composition of high-CaO garnet (on left) and the end composition of amphibole-plagioclase kelyphite (at right). Na and water are added to the system, olivine and spinel are progressively removed. The amount of water that is present controls the vol % of amphibole that is stable. The diagram is constructed for 850°C.

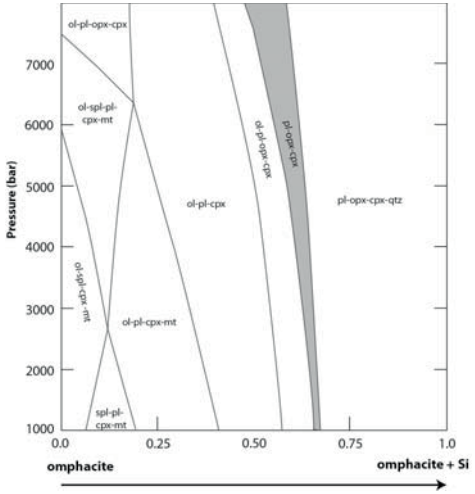

Figure 10. Binary phase diagram showing the results of addition of Si to the measured omphacite composition. The diagram is constructed for conditions of 850°C.

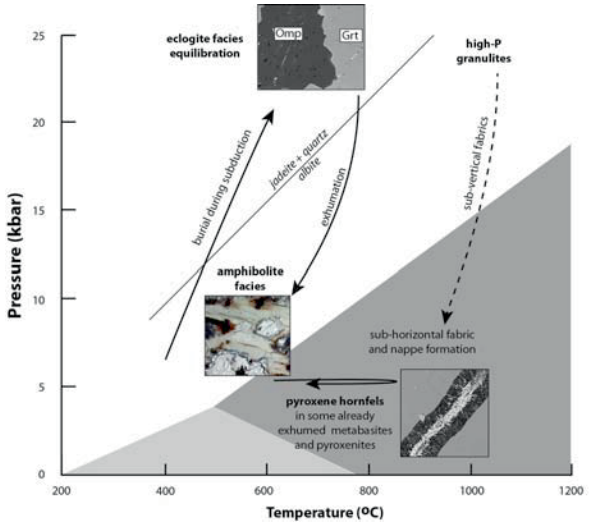

Figure 11. Interpreted P-T path for nom1a.

Table 1. Representative mineral analyses measured by wavelength dispersive techniques.

Mineral	Grt	Grt	Grt	Grt	Grt	Grt	Grt	Grt	Grt	Cpx	Cpx	Cpx	Opx	Am	Am	Am	Am	Am	Am	Am	Am	Am
Location	low Ca grt	high Ca grt	towards am on cpx margin	towards am on cpx margin	towards olivine	Adjacent to ol	reintegrated adjacent to ol	towards amp	towards amp	omphacite	Diopside repl. omp	al-diopside replacingomp	Enstatite replacing omp	parasite, plate, adjacent to omp	Pargasite incl in grt	Rim adjacent to omp incl	replacing omp	crack tip	Pargasite, kelyphite	Pargasite, kelyphite	parasite, outside grt	Pargasite, adjacent to ilmenite	Pargasite, outside garnat
analysis	c22-L-156	c22-L-137	c23-L1-4	c23-L1-21	c34-L-4	c34-L-20		c27-Line	Line 27	**c12-1**	**c12-14**	**c12-9**	**c12-3**	**c12-8**	c22-01	c23-L2-12	c1-23	c24-L-14	c13-34	c14-33	c13-38	c14-14	c28-20
SiO2	39.73	39.65	39.60	39.11	39.62	39.17	38.75	39.93	39.06	54.27	53.20	53.86	54.35	45.35	40.21	40.01	41.80	40.67	40.63	40.03	43.05	43.59	40.71
TiO2	0.07	0.02	0.05	0.01	0.04	0.07	0.07	0.06	0.02	0.13	0.18	0.05	0.06	0.67	0.05	0.01	0.30	0.05	0.13	0.10	0.48	0.56	2.50
Al2O3	22.53	22.62	22.58	22.28	22.34	21.95	21.62	21.71	21.14	7.64	2.91	3.11	1.10	11.76	19.64	19.96	16.00	17.00	18.02	19.30	14.88	14.17	16.08
FeO	21.06	19.05	20.16	23.33	20.35	22.37	23.50	20.41	23.66	4.64	5.57	5.68	20.78	9.42	13.55	10.22	13.31	14.25	12.45	12.98	12.49	12.87	11.79
MnO	0.47	0.40	0.42	0.94	0.45	0.81	1.49	0.39	1.17	0.00	0.04	0.08	0.12	0.05	0.08	0.06	0.16	0.24	0.14	0.17	0.16	0.17	0.16
MgO	9.62	7.97	8.47	6.23	8.76	7.22	6.70	8.54	6.13	10.92	14.25	14.20	23.26	15.59	11.09	12.52	11.63	11.45	11.34	10.82	12.64	12.82	11.38
CaO	6.59	10.54	9.58	9.03	8.48	8.48	8.25	8.75	8.04	17.93	22.92	22.07	0.86	11.56	9.82	10.82	11.10	10.19	11.30	11.20	11.24	11.11	11.32
Na2O	0.01	0.04	0.02	0.00	0.03	0.00	0.00	0.03	0.01	3.76	0.72	0.91	0.08	2.63	3.38	3.34	3.13	3.10	3.05	3.24	2.93	2.91	3.35
K2O	0.00	0.00	0.00	0.00	0.01	0.00	0.00	0.00	0.00	0.00	0.00	0.01	0.01	0.49	0.06	0.19	0.07	0.34	0.30	0.06	0.26	0.09	0.05
Total	**100.07**	**100.29**	**100.87**	**100.92**	**100.08**	**100.05**	**100.38**	**99.81**	**99.23**	**99.29**	**99.79**	**99.97**	**100.61**	**97.52**	**97.88**	**97.13**	**97.49**	**97.28**	**97.34**	**97.89**	**98.11**	**98.27**	**97.32**
Oxygens	12	12	12	12	12	12	12	12	12	6	6	6	6	23	23	23	23	23	23	23	23	23	23
Si	3.002	2.996	2.983	2.992	3.002	3.004	2.989	3.035	3.043	1.970	1.958	1.972	1.990	6.564	5.891	5.841	6.167	6.043	5.990	5.878	6.283	6.351	6.004
Al	2.007	2.014	2.004	2.008	1.995	1.984	1.966	1.945	1.941	0.327	0.126	0.134	0.047	2.007	3.392	3.435	2.781	2.977	3.131	3.340	2.559	2.433	2.794
Ti	0.004	0.001	0.003	0.001	0.002	0.004	0.004	0.003	0.001	0.004	0.005	0.001	0.002	0.073	0.005	0.002	0.034	0.005	0.015	0.011	0.052	0.061	0.277
Fe	1.331	1.204	1.270	1.492	1.290	1.435	1.516	1.297	1.541	0.141	0.171	0.174	0.636	1.140	1.660	1.248	1.642	1.771	1.535	1.594	1.524	1.568	1.454
Mn	0.030	0.026	0.027	0.061	0.029	0.053	0.097	0.025	0.077	0.000	0.001	0.002	0.004	0.006	0.010	0.007	0.020	0.031	0.017	0.021	0.019	0.021	0.019
Mg	1.083	0.897	0.951	0.711	0.990	0.825	0.770	0.967	0.711	0.591	0.782	0.775	1.270	3.363	2.422	2.725	2.557	2.536	2.493	2.369	2.751	2.784	2.501
Ca	0.533	0.854	0.773	0.740	0.688	0.696	0.682	0.713	0.671	0.697	0.904	0.866	0.034	1.793	1.541	1.692	1.755	1.622	1.785	1.762	1.758	1.734	1.788
Na	0.001	0.005	0.003	0.000	0.004	0.000	0.000	0.004	0.001	0.265	0.051	0.065	0.006	0.739	0.960	0.945	0.894	0.892	0.871	0.922	0.830	0.821	0.957
K	0.000	0.000	0.000	0.000	0.001	0.000	0.000	0.000	0.000	0.000	0.000	0.000	0.000	0.091	0.011	0.035	0.013	0.063	0.055	0.010	0.048	0.017	0.009
Total	**7.991**	**7.998**	**8.014**	**8.004**	**8.001**	**8.001**	**8.024**	**7.991**	**7.987**	**3.995**	**4.000**	**3.992**	**3.988**	**15.775**	**15.893**	**15.929**	**15.862**	**15.941**	**15.893**	**15.907**	**15.824**	**15.790**	**15.805**
Alm	45	40	42	50	43	48	49	43	51														
Sps	1.01	0.87	0.89	2.02	0.97	1.75	3.18	0.84	2.58														
Prp	36	30	31	24	33	27	25	32	24														
Grs	18	29	26	25	23	23	22	24	22														
XMg	45	43	43	32	43	37	34	43	32	81	82	82	67	75	59	69	61	59	62	60	64	64	63

Garnet end-members are: Alm = almandine = 100*Fe/(Fe+Mg+Ca+Mn); Prp = pyrope = 100*Mg/(Fe+Mg+Ca+Mn); Grs = grossular = 100*Ca/(Fe+Mg+Ca+Mn); Sps = spessartine = 100*Mn/(Fe+Mg+Ca+Mn).
XMg = 100*Mg/(Mg+Fe).
Plagioclase end-members are: An = anorthite = 100*Ca/(Ca+Na+K); Ab = albite = 100*Na/(Ca+Na+K); Or = orthoclase = 100*K/(Ca+Na+K).
Olivine end-members are: Fo = forsterite = 100*Mg/(Mg+Mn+Fe); Fa = fayalite = 100*Fe/(Fe+Mn+Mg).
Spinel end-members are: Spl = spinel = 100*Mg/(Mg+Fe); Her = 100*Fe/(Fe+Mg).

Table 1. continued

Mineral	Feld	Feld	Feld	Feld	Feld	Feld	Feld	Feld	Feld	Ol	Ol	Ol	Spl	Spl	Ilm
Location	Andesine, amp-pl	Labradorite, ol-spl-pl	Labradorite, amp-pl	Bytownite, amp-pl	Bytownite, ol-spl-pl	Anorthite, ol-spl-pl	oligoclase replacing omp	Oligoclase, replacing omp	Andesine, replaci	amp-pl-ol	amp-ol-pl	ol-spl-pl	ol-spl-pl	ol-spl-pl-il	ol-spl-pl-il
analysis	c28-23	c14b-9	c14b-4	c14b-12	c14b-3	c33-1	**c12-23**	c26-15	c26-21	c20-1	c25-3	c13-37	c20-15	c25-7	c25-9
SiO2	58.38	55.87	52.00	48.77	47.22	44.75	67.29	61.89	57.68	34.85	34.79	34.23	0.19	0.20	0.16
TiO2	0.00	0.00	0.02	0.00	0.00	0.03	0.03	0.00	0.00	0.02	0.00	0.00	0.02	0.27	52.83
Al2O3	26.98	27.74	30.02	32.10	33.51	35.26	20.57	24.61	27.50	0.20	0.17	0.04	62.73	62.34	0.12
FeO	0.25	0.68	0.38	0.39	0.55	0.77	0.24	0.29	0.48	40.42	42.53	43.97	27.03	28.05	44.65
MnO	0.01	0.02	0.01	0.00	0.01	0.00	0.00	0.01	0.00	0.75	0.78	0.62	0.20	0.21	0.99
MgO	0.00	0.02	0.00	0.00	0.00	0.00	0.42	0.04	0.00	23.21	21.88	20.98	9.31	8.62	0.76
CaO	8.16	10.33	13.27	16.09	17.51	18.66	2.45	5.49	8.53	0.25	0.25	0.11	0.05	0.11	0.16
Na2O	6.90	5.38	3.94	2.49	1.68	0.75	10.65	8.41	6.62	0.01	0.00	0.01	0.01	0.00	0.01
K2O	0.01	0.02	0.02	0.00	0.01	0.00	0.13	0.02	0.02	0.00	0.00	0.00	0.00	0.00	0.01
Total	**100.69**	**100.08**	**99.66**	**99.83**	**100.49**	**100.22**	**101.78**	**100.76**	**100.84**	**99.71**	**100.39**	**99.96**	**99.54**	**99.79**	**99.68**
Oxygens	8	8	8	8	8	8	8	8	8	4	4	4	4	4	3
Si	2.593	2.515	2.371	2.239	2.164	2.066	2.912	2.726	2.564	1.000	1.001	0.998	0.005	0.005	0.004
Al	1.412	1.472	1.613	1.737	1.810	1.919	1.050	1.278	1.441	0.007	0.006	0.001	1.998	1.991	0.003
Ti	0.000	0.000	0.001	0.000	0.000	0.001	0.001	0.000	0.000	0.000	0.000	0.000	0.000	0.005	0.998
Fe	0.009	0.026	0.014	0.015	0.021	0.030	0.009	0.011	0.018	0.970	1.024	1.072	0.611	0.636	0.938
Mn	0.000	0.001	0.001	0.000	0.000	0.000	0.000	0.000	0.000	0.018	0.019	0.015	0.005	0.005	0.021
Mg	0.000	0.002	0.000	0.000	0.000	0.000	0.027	0.003	0.000	0.993	0.939	0.912	0.375	0.348	0.028
Ca	0.388	0.498	0.648	0.791	0.860	0.923	0.114	0.259	0.406	0.008	0.008	0.003	0.001	0.003	0.004
Na	0.594	0.470	0.349	0.221	0.149	0.067	0.894	0.718	0.571	0.001	0.000	0.001	0.001	0.000	0.000
K	0.001	0.001	0.001	0.000	0.000	0.000	0.007	0.001	0.001	0.000	0.000	0.000	0.000	0.000	0.000
Total	**4.998**	**4.984**	**4.997**	**5.004**	**5.006**	**5.006**	**5.013**	**4.995**	**5.001**	**2.996**	**2.996**	**3.002**	**2.996**	**2.994**	**1.997**
An	40	51	65	78	85	93	11	26	42						
Ab	60	48	35	22	15	7	88	73	58						
Or	0	0	0	0	0	0	1	0	0						
Spl													38	35	
Her													62	65	
Fo										49	52	54			
Fa										51	48	46			

Table. 2. Representative effective bulk compositions for microscopic domains, as calculated from pixels in high-contrast backscattered electron images.

	ol-spl-pl symplectites	cpx-opx-pl symplectites	amp-pl kelyphites
SiO_2	32.56	57.61	48.15
TiO_2	0.01	0.08	0.05
Al_2O_3	22.51	15.24	26.51
FeO	26.14	2.96	4.17
MnO	0.37	0.00	0.06
MgO	11.79	6.33	3.63
CaO	6.04	12.44	12.37
Na_2O	0.59	5.43	3.56
K_2O	0.00	0.00	0.11

Data Supplementary 1. Mineral chemistry and ACFN examples of additional olivine-bearing hornfelses.

As noted in the main text and shown in Fig. 2, olivine-bearing hornfels occur in metabasites throughout the Bohemian Massif. They occur in mafic to ultramafic rocks of different composition. Representative mineral analyses of measured phases in three more samples (42, BWI-45, NM-1) are presented in DS Table 1.

The composition of the rocks prior to imposition of the hornfels event has strongly influenced the composition of feldspar within the hornfelses. This can be represented chemographically in the system ACF(N) (Figs. 1, 2, 3) - although it is strictly true that only NM-1 contains quartz and can therefore be truly be projected in this system. Nevertheless, several key points can be drawn from these diagrams. The main reaction driving the development of the olivine-spinel-plagioclase-orthopyroxene (-ilmenite) hornfelses in the pyroxenite 42 is shown chemographically as:

garnet = olivine-orthopyroxene-spinel-plagioclase

which is the petrographically observed reaction. BWI-45 is similar but also contains orthopyroxene-spinel-plagioclase symplectites. IN ACFN, this assemblage can be seen to have also formed from garnet breakdown. The two reported pyroxenites are more Mg-rich than the meta-eclogites (NM-1, nom1a), as indicated by the higher XMg ratios for olivine and spinel. NM-1 is similar to nom1a in that it is a metabasite that equilibrated at eclogite facies, crystallising omphacite and garnet, with a little quartz in the case of NM-1. Omphacite in NM-1 contains ~ 4.5 wt% NaO. As a result, when this mineral broke down during low-P and high-T, the Na component was partially housed within oligoclase in the plagioclase-clinopyroxene symplectite that replaced omphacite, but also as labradorite within the olivine-bearing hornfels. The controlling factor of the composition of the olivine-spinel-plagioclase symplectites is:

garnet + Na+ = olivine-spinel-plagioclase

This result is similar to what is seen in nom1a. NM-1, like nom1a, also contains an early amphibole that has grown before the hornfels assemblage, and this has also contributed Na to the hornfels because the amphibole is being overgrown by the olivine-spinel-plagioclase symplectites.

DS1 Table 1. Representative WDS mineral analyses of some other olivine-bearing metabasites

	42 – garnet pyroxenite								BWI-45 garnet websterite							NM1 - eclogite								
				symplectite							symplectite							symplectite					symplectite		
	grt	cpx	amp	olivine	opx	spinel	plag	Ilm	cpx	grt	olivine	opx	spinel	plag	ilm	cpx	amp	opx	cpx	plag	olivine	spinel	plag	
SiO2	39.91	54.44	44.39	34.98	52.35	0.03	43.31	0.01	54.63	40.79	34.1	55.67	0.05	43.48	0.01	53.23	39.68	48.38	51.7	61.29	33.59	0.05	50.65	0
TiO2	0.04	0.03	0.5	0.01	0.07	0.04	0	54.63	0.03	0	0.04	0.01	0.01	0.03	54.26	0.2	3.52	0	0.25	0	0.44	0.28	0.02	5
Al2O3	21.8	1.62	12.57	0	1.63	58.74	35.38	0	0.9	22.55	0	0.57	60.73	35.27	0	8.37	14.98	0	6.84	23.98	0.01	59.11	30.43	
FeO	19.94	4.05	11.86	38.31	22.22	27.62	0.75	42.56	3.4	17.17	42.24	13.93	26.57	0.73	40.34	6.48	14.01	39.93	7.26	0.26	48.56	33.85	1.08	4
MnO	0.44	0.04	0.19	0.65	0.49	0.18	0	0.64	0.08	0.45	1.21	0.13	0.21	0.01	0.41	0.04	0.06	0.72	0.13	0.03	0.68	0.26	0.01	0
MgO	11.95	15.78	13.87	26.34	23.08	9.59	0.01	1.28	16.67	14.05	22.11	29.36	10.6	0.01	3.46	9.97	11.36	10.98	11.6	0.07	20.55	7.74	0.04	0
CaO	5.36	23.34	11.07	0.05	0.34	0.1	19.84	0	23.72	5.3	0.06	0.2	0.04	20	0.04	16.66	11.46	0.9	20.24	5.56	0.07	0.04	13.36	
Na2O	0.02	0.8	1.88	0.01	0	0	0.26	0	0.24	0.02	0.01	0.01	0	0.09	0	4.67	3.49	0.02	1.82	8.63	0	0.02	3.96	0
K2O	-	0	0.17	0.01	0	0	0.01	0	0	0	0	0	0	0	0	0.01	0	0	0.01	0	0	0	0	
Cr2O3	0.11	0	0.09	0	0.02	2.01	0.01	0	0.06	0	0	0.03	1.04	0.01	0.18	-	-	0	-	-	0	0.4	-	0
Total	**99.57**	**100.10**	**96.59**	**100.36**	**100.20**	**98.31**	**99.57**	**99.12**	**99.73**	**100.33**	**99.77**	**99.91**	**99.25**	**99.63**	**98.70**	**99.63**	**98.56**	**100.93**	**99.85**	**99.82**	**103.90**	**101.75**	**99.55**	**10**
	12	6	23	4	6	4	8	3	6	12	4	6	4	8	3	6	23	6	6	8	4	4	8	
Si	3.01	1.99	6.53	0.99	1.95	0.00	2.02	0.00	1.99	3.01	0.99	1.99	0.00	2.03	0.00	1.94	5.87	1.96	1.91	2.73	0.96	0.00	2.33	0
Al	1.94	0.07	2.18	0.00	0.07	1.92	1.95	0.00	0.04	1.96	0.00	0.02	1.95	1.94	0.00	0.36	2.61	0.00	0.30	1.26	0.00	1.91	1.65	0
Ti	0.00	0.00	0.06	0.00	0.00	0.00	0.00	1.03	0.00	0.00	0.00	0.00	0.00	0.00	1.01	0.01	0.39	0.00	0.01	0.00	0.01	0.01	0.00	0
Fe	1.26	0.12	1.46	0.90	0.69	0.64	0.03	0.89	0.10	1.06	1.03	0.42	0.60	0.03	0.84	0.20	1.73	1.35	0.22	0.01	1.16	0.78	0.04	0
Mn	0.03	0.00	0.02	0.02	0.02	0.00	0.00	0.01	0.00	0.03	0.03	0.00	0.00	0.00	0.01	0.00	0.01	0.02	0.00	0.00	0.02	0.01	0.00	0
Mg	1.34	0.86	3.04	1.11	1.28	0.40	0.00	0.05	0.91	1.54	0.96	1.56	0.43	0.00	0.13	0.54	2.50	0.66	0.64	0.00	0.88	0.32	0.00	0
Ca	0.43	0.91	1.74	0.00	0.01	0.00	0.99	0.00	0.93	0.42	0.00	0.01	0.00	1.00	0.00	0.65	1.82	0.04	0.80	0.27	0.00	0.00	0.66	0
Na	0.00	0.06	0.54	0.00	0.00	0.00	0.02	0.00	0.02	0.00	0.00	0.00	0.00	0.01	0.00	0.33	1.00	0.00	0.13	0.75	0.00	0.00	0.35	0
K	0.00	0.00	0.03	0.00	0.00	0.00	0.00	0.00	0.00	0.00	0.00	0.00	0.00	0.00	0.00	0.00	0.00	0.00	0.00	0.00	0.00	0.00	0.00	0
Cr	0.01	0.00	0.01	0.00	0.00	0.04	0.00	0.00	0.00	0.00	0.00	0.00	0.02	0.00	0.00	0.00	0.00	0.00	0.00	0.00	0.00	0.01	0.00	0
Total	**8.02**	**4.01**	**15.61**	**3.01**	**4.02**	**3.01**	**5.02**	**1.97**	**3.99**	**8.02**	**3.01**	**4.00**	**3.01**	**5.01**	**1.99**	**4.04**	**15.93**	**4.04**	**4.00**	**5.01**	**3.03**	**3.03**	**5.03**	**2**
An							98							99						26			65	
XMg	52	87	68	55	65	38		5	90	59	48	79	42		13	73	59	33	74		43	29		

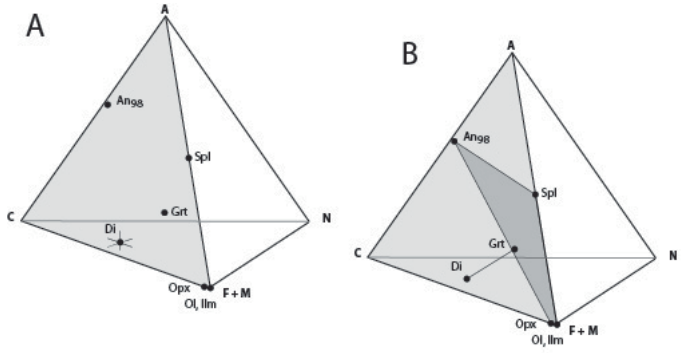

DS Figure 1: ACFN diagram of main hornfels minerals in 42. The mineral positions were calculated from data presented in DS Table 1.

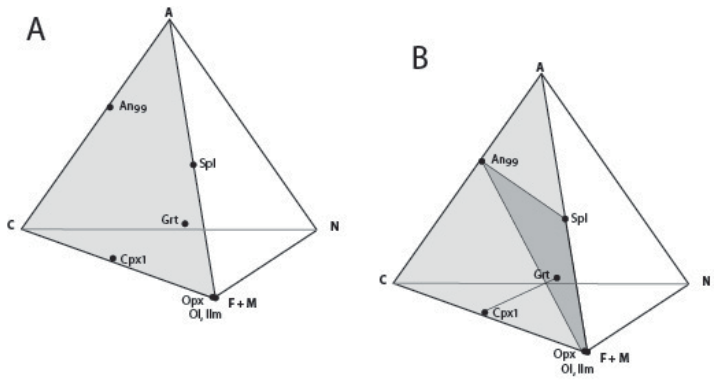

DS Figure 2: ACFN diagram of main hornfels minerals in BWI-45. There is virtually no NaO within this rock. The mineral positions were calculated from data presented in DS Table 1.

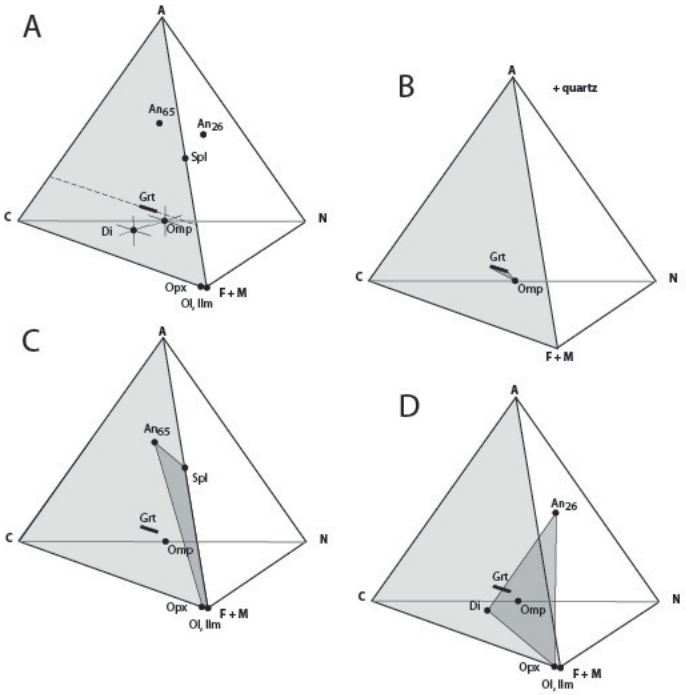

DS Fig. 3: ACFN diagram of main hornfels minerals in NM1. This inspected sample contains quartz, and can therefore be plotted with confidence in this system. The mineral positions were calculated from data presented in DS Table 1.

B illustrates the position of the eclogite facies assemblage garnet+omphacite.

C indicates the positions of representative olivine-spinel-plagioclase-ilmenite-orthopyroxene analyses.

D is the composition of the clinopyroxene-plagioclase-orthopyroxene assemblages.

Retrograde metasomatic effects on phase assemblages in an interlayered blueschist-greenschist sequence (Coastal Cordillera, Chile)

Ralf Halama[1,*], Matthias Konrad-Schmolke[1]

[1] Institute of Earth and Environmental Science, University of Potsdam, Karl-Liebknecht-Str. 24-25, 14476 Potsdam, Germany

* Corresponding author contact information:
Ralf Halama
University of Potsdam
Institute of Earth and Environmental Science
Karl-Liebknecht-Str. 24-25
14476 Potsdam
E-mail: rhalama@geo.uni-potsdam.de
Tel: +49-331-977-5783
Fax: +49-331-977-5700

Revised version, submitted to Lithos xx. November 2014

Abstract

Interlayered blueschists and greenschists of the Coastal Cordillera (Chile) are part of a Late Palaeozoic accretionary complex. They represent metavolcanic rocks with oceanic affinities based on predominantly OIB-type REE patterns and immobile trace element ratios. Amphibole is the major mafic mineral and varies compositionally from glaucophane to actinolite. The presence of glaucophane relicts as cores in zoned amphiboles in both rock types is evidence for a pervasive high-pressure metamorphic stage. During exhumation, a retrograde greenschist-facies overprint stabilized phengitic white mica + chlorite + albite ± K-feldspar at 0.4±0.1 GPa. Geochemical variability can be ascribed to primary, magmatic and secondary, metasomatic processes. We used several adjacent blueschist-greenschist pairs with similar protolith geochemistry to evaluate metasomatic changes due to retrograde fluid-rock interaction at greenschist-facies conditions. Isocon diagrams show that the most important geochemical changes are depletion of Si and Na and addition of water in the greenschists compared to the blueschists. Transition metals and LILE are mobilized to varying degrees. Both rock types of these adjacent pairs have a similar mineralogy, albeit with different mineral modal abundances, pointing to a selective infiltration overprinting process. We used pseudo-binary phase diagrams as a means to link bulk rock geochemical variability to changes in the modal abundance of minerals. These calculations show preferential formation of chlorite + albite and decrease in glaucophane abundance for greenschist compared to blueschist. Therefore, the fluid-induced metasomatic changes are the prime cause for the distinct visual appearance of the rocks as blue and green, respectively. Differences in protolith geochemistry become relevant when the entire outcrop-wide geochemical variation is considered. It is clear, however, that tectonic juxtaposition is an unlikely explanation for the cm-dm scale interlayering of blueschists and greenschists.

FULL GENETIC MODEL SHOULD BE SUMMARIZED

TERM LAYER-PARALLEL FLUID INFILTRATION SHOULD BE ADDED;

Keywords:

Fluid-rock interaction, metasomatism, element mobility, pseudo-binary phase diagrams, Coastal Cordillera (Chile)

1. Introduction

Interlayered sequences of blueschists, greenschists and/or eclogites frequently occur in subduction-related metamorphic terranes, such as the Cycladic Islands, Greece (Bröcker 1990), the Franciscan Belt, California (Oh et al. 1991), the Tauern Window, Eastern Alps (Selverstone et al. 1992), and Brittany, France (Barrientos and Selverstone, 1993; El Korh et al., 2009). Three distinct processes are commonly invoked to explain these apparent metamorphic heterogeneities within single units: 1) Equilibration at distinct pressure-temperature (P-T) conditions and late-stage tectonic juxtaposition (Ridley, 1984; Pognante and Kienast, 1987; Bousquet, 2008), 2) Chemical differences in the protolith (Dungan et al., 1983; Oh et al., 1991; El-Shazly et al., 1997; Baziotis and Mposkos, 2011; Pattison, 2013), occasionally combined with variable pre-metamorphic fluid overprinting (Dungan et al., 1983; El Korh et al., 2013), and 3) Variable retrograde overprinting resulting from different degrees of fluid infiltration during exhumation (Schliestedt and Matthews, 1987; Barrientos and Selverstone, 1993; Bröcker, 1990). Complete metamorphic equilibration is often inhibited by slow reaction kinetics and slow diffusion, so that deformation has a catalytic effect on re-equilibration (Pognante and Kienast, 1987; Konrad-Schmolke et al., 2011). The bulk rock composition of the protolith may also be directly linked to subsequent fluid-induced overprinting during metamorphism because compositions that are prone to dehydration are also more likely to re-equilibrate during retrogression (Baziotis et al., 2009). Variable bulk compositions can even cause changes in the mineralogy that mimic the progression of assemblages that undergo a facies transition during their metamorphic evolution (Kahl and Schumacher, 2000).

It is important to understand the processes that cause the occurrence of metamorphic heterogeneities within single units because each explanation provides distinct information about the tectonometamorphic history of the unit (e.g. Pattison, 2013) and constraints about

element transport during metamorphism. The occurrence of blueschist-facies assemblages without low-pressure overprint is interpreted to reflect retracing of the prograde P-T path during exhumation and upward motion of tectonically imbricated slices (Ernst, 1988). In contrast, the overprinting by greenschist and/or epidote-amphibolite facies assemblages is thought to involve rapid, nearly isothermal decompression and an approximately adiabatic rise of the subduction complex as consequence of deceleration/cessation of the subduction underflow (Ernst, 1988; 2006). Baziotis and Mposkos (2011) could show that the preservation of peak metamorphic blueschist assemblages also depends on bulk rock composition. In their example preservation is promoted in Fe-rich bulk compositions because dehydration ends earlier compared to relatively Fe-poor compositions (Baziotis and Mposkos, 2011). If distinct protolith compositions can be identified as major cause for metamorphic heterogeneities, these can be used to deduce pre-subduction tectonic settings and pre-metamorphic alteration processes (Becker et al., 2000; Bebout, 2007; John et al., 2010; Hyppolito et al., 2014). During high-pressure low-temperature (HP-LT) subduction zone metamorphism, rocks often retain the geochemical characteristics of their protoliths, including hydrothermal alteration before subduction (Dungan et al., 1983; Putlitz et al., 2000; El Korh et al., 2009; Halama et al., 2011; van der Straaten et al., 2012). Fluids are not only important during pre-metamorphic alteration, but they are particularly of interest during syn-metamorphic processes because they facilitate the attainment of equilbrium and are a key factor for the transport of elements in subduction zones. Hence, differences in the retrograde overprint and variable degrees of fluid infiltration during the metamorphic evolution of a rock provide crucial information about fluid release, fluid sources and element mobility during metasomatic processes and associated metamorphic reactions (Bebout and Barton, 1993; Halama et al., 2011; Marschall et al., 2009; Miller et al., 2009; Penniston-Dorland et al., 2010; van der Straaten et al. 2008; 2012). Fluids can be internally derived by dehydration or local dissolution (Heinrich 1982; Widmer and Thompson, 2001; Wangen and Munz, 2004; Baziotis et al., 2009; Verlaguet et al., 2011) with

106 metamorphic mineral growth occuring by small scale (mm-dm) diffusive mass transfer during
107 closed-system conditions (Philippot and Selverstone, 1991; Kohn et al., 1993). Alternatively,
108 fluids can be externally derived by large-scale advective mass transfer (Walther and Orville,
109 1982; Beitter et al., 2008; Bucholz and Ague, 2010). In the latter case, a significant
110 geochemical variability can be generated in the metamorphic rocks by interaction with
111 metasomatic fluids during high-pressure metamorphism (Halama et al., 2011) and such fluid-
112 rock interaction has significant effects on interpretation of geochronological data (Glodny et
113 al. 2002; 2008; Halama et al., 2014). Moreover, similarities in the geochemistry of the
114 rehydrated rocks can be related to geochemical patterns in arc volcanic rocks and the direct
115 examination of subduction zone metamorphic rocks provides insights about slab-derived
116 agents added to arc magma sources in the mantle wedge (e.g. Sorensen et al., 1997; Breeding
117 et al., 2004; El Korh et al., 2009; John et al., 2004; Spandler et al., 2004; Bebout, 2007;
118 Beinlich et al., 2010; van der Straaten et al. 2008). In the context of interlayered rocks with
119 apparently distinct metamorphic facies, it is important to note that syn-metamorphic
120 compositional changes influence phase relations and phase compositions. As a result, spatial
121 variations in the intensity of fluid-rock interaction and the amount of mass transfer may be
122 more important for determining the rock's mineralogy than changes in P-T conditions
123 (Goncalves et al., 2012). The effects of mass transfer, i.e. changes in composition due to
124 metasomatic overprinting, can be explored through pseudosection thermobarometry
125 (Goncalves et al., 2013; Evans et al., 2013).
126 This study investigates the causes of interlayering in a sequence of layered blueschists and
127 greenschist from the Coastal Cordillera in Chile. The first major objective is the distinction
128 between pre-subduction, inherited geochemical variability and elemental mobility during
129 metamorphic fluid-rock interaction based on the systematic evaluation of geochemical
130 differences between blueschists and greenschists in terms of pre- and syn-metamorphic
131 processes. The second aim is to understand the effect of fluid-rock interaction on the

mineralogy of the rocks and the link between metasomatic overprint and retrogression by quantifying the phase relations and compositions as a function of bulk rock chemical transformations. In the following we show that the interlayering of the investigated rocks results from compositional variations. The rocks experienced the same P-T evolution, but experienced different degrees of retrograde greenschist-facies overprinting.

2. Geological Setting

In the Coastal Cordillera of Chile, the crystalline basement of the Mesozoic and Cenozoic Andean sequences consists of metamorphic and associated magmatic rocks of Paleozoic to Triassic age (Hervé et al., 2007). Basement exposures in the Coastal Cordillera comprise fossil accretionary prisms, which are partly associated with a magmatic arc and high-temperature metamorphic belts (Hervé, 1988). Two units of this basement, the Western and the Eastern Series (Fig. 1), were recognized to constitute a classic Pacific-rim type paired metamorphic belt (Aguirre et al., 1972; Ernst, 1975). Geochronological studies in these units provided evidence for Late Paleozoic subduction along the western margin of South America (Munizaga et al., 1973; Hervé et al., 1974), corroborating the interpretation that the Western and Eastern Series constitute coeval parts of a Late Palaeozoic paired metamorphic belt (Willner, 2005).

Both, the Western and the Eastern Series, are dominated by metamorphosed and deformed siliciclastic sediments that represent former turbidite deposits. The Eastern Series comprise a very low-grade metapelite-metagreywacke sequence with minor calcsilicate rocks (Hervé, 1988; Willner et al., 2000), interpreted as frontally accreted sediments (Richter et al., 2007). Locally, the rocks of the Eastern Series experienced a thermal overprint at around 296-301 Ma at maximum temperatures of 720 °C (Willner, 2005) caused by the coeval Late

157 Palaeozoic magmatic arc batholith formation (Willner, 2005; Hervé et al., 1988). In contrast
158 to the Eastern Series, the Western Series comprise a mixture of continent-derived siliciclastic
159 rocks and subordinate slices of dismembered upper oceanic crust. The metabasites of the
160 oceanic crust, which partly exhibit relict pillow structures, form lenses of metre to kilometre
161 size. Minor rock types associated with the metabasites include serpentinite, marble,
162 metachert, black graphite-rich metapelite, and ferruginous metasediments with stilpnomelane
163 (Hervé, 1988; Hervé et al., 2007; Hyppolito et al., 2014). Among the metabasites,
164 greenschists are the most common rock type. They experienced peak P-T conditions of 0.70-
165 0.93 GPa at 380-420 °C, pointing to a geothermal gradient of 11-16 °C/km (Willner, 2005),
166 and are interpreted to reflect conditions of basal accretion in the accretionary prism (Willner
167 et al., 2009). Rare blueschists occur as lenses of 1-5 m thickness at only three locations within
168 the Western Series, scattered over a distance of ~60 km. These blueschists yielded peak P-T
169 conditions of 0.95-1.07 GPa and 350-385 °C (Willner, 2005), which are similar to those of the
170 more typical greenschists. The blueschists preserve a low metamorphic gradient of only 9-
171 11°C/km and are considered as fragments of the oceanic crust that were incorporated into the
172 subduction channel (Willner, personal communication). Both, greenschists and blueschists,
173 experienced a retrograde metamorphic stage at ~300-380 °C and ~0.4-0.8 GPa, indicating
174 pressure release with little cooling (Willner, 2005).
175 A $^{40}Ar/^{39}Ar$ phengite plateau age of 292±2 Ma from a blueschist was interpreted as peak HP
176 imprint coeval with the formation of the transposition foliation (Willner et al., 2005).
177 Throughout the Western Series, variability in the timing of the HP event (292-319 Ma) is
178 observed based on $^{40}Ar/^{39}Ar$ UV laser ablation phengite plateau ages (Willner et al., 2005).
179 The HP event is coeval with the main pulse of late Paleozoic arc magmatism (~305 Ma,
180 $^{207}Pb/^{206}Pb$ zircon evaporation). *In situ* $^{40}Ar/^{39}Ar$ analyses of phengite in microfolds yielded
181 an absolute age range from 257 to 321 Ma and are interpreted to record long-lasting
182 recrystallization (up to ~40 Myr for individual samples) during retrograde pressure release,

183 considering that there is no indication of a potential excess argon component on inverse
184 isochron diagrams (Willner et al., 2005). A retrograde metamorphic stage was identified in
185 various rock types and reflects a pressure release of 0.3-0.4 GPa accompanied by only slight
186 cooling to 300-380 °C (Willner, 2005). Later magmatic activity in the Western Series is
187 represented by isolated granite plutons with intrusion ages between 257 ($^{207}Pb/^{206}Pb$ zircon
188 evaporation; Willner et al., 2005) and 220 Ma (Rb-Sr mineral isochron; Lucassen et al.,
189 2004). Afterwards, the retreat of the subducting slab caused termination of accretionary
190 processes.
191 At Infiernillo Beach in Pichilemu (34°23.35 S, 72°01.33 W; Fig. 1), strongly foliated
192 blueschists occur interlayered with greenschists, producing a pronounced banding on the cm
193 to dm scale (Fig. 2). The sequence is interpreted to comprise various metavolcanic rocks
194 (metatuffs, meta-agglomerates and metalavas) that are associated with metasedimentary rocks
195 (pelitic schists, graphite-rich metapelites and quartzites; Hyppolito et al., 2014). Willner
196 (2005) described structures resembling hyaloclastites and suggested that the presence of white
197 mica in metabasite may point to former tuffitic deposits. The layering is parallel to the main
198 foliation, which has transposed an earlier foliation and the stratigraphic surface (Hyppolito et
199 al., 2014). Hyppolito et al. (2014) provide a detailed outcrop description of Infiernillo Beach
200 and an interpretation of geochemical data in terms of the geodynamic setting of protoliths and
201 the regional terrane assembly in central Chile. Here, we concentrate on several selected
202 blueschists and greenschists from this location in the context of retrograde metasomatic
203 overprinting.
204
205
206 # 3. Methodology
207 *3.1 Geochemistry*

208 In total, 11 samples from the layered sequences were analyzed for bulk rock major and trace
209 element contents. We selected three interlayered blueschist-greenschist pairs for detailed
210 microscopic and mineral chemical analyses. These sample pairs were taken either in direct
211 contact (<10 cm apart) in the outcrop (sample pair CH-1-18 and CH-1-19) or carefully cut
212 using the rock saw (samples CH-1-12 and CH-1-15) to ensure an accurate separation of blue
213 and green parts of individual pairs.
214 Major element compositions of rock-forming minerals were determined using a JEOL JXA
215 8900R electron microprobe at the University of Kiel, operated with 15 kV, a 15 nA beam
216 current and a beam diameter of 5 μm. Measurement times were 15s on the peak and 7s on the
217 background, except for Cl, which was measured 30s and 15s, respectively. Natural standards
218 were used for calibration and a CITZAF matrix correction was applied.
219 Whole rock major element contents were analyzed by X-ray fluorescence (XRF) on fused
220 glass discs with a Philips PW1480 XRF spectrometer at the University of Kiel. The relative
221 standard deviation (RSD) for all oxides is generally ≤ 1.3% based on multiple analyses of
222 reference material BHVO-1 (see van der Straaten et al., 2008, for details on precision and
223 accuracy). Concentrations of 37 trace elements were determined by inductively coupled
224 plasma mass spectrometry (ICP-MS), after HF-HNO_3-$HClO_4$ acid digestion in Teflon bombs
225 at 180°C, using an Agilent 7500c instrument at the University of Kiel. Details of sample
226 preparation and the analytical protocol are given in Garbe-Schönberg (1993) and John et al.
227 (2008). Analyses of the reference material and representative duplicate analyses are given in
228 Table 1, data for the procedural blank analyzed during the course of this study are given in
229 Halama et al. (2013). Instrumental precision, determined by multiple analyses of one sample
230 solution and expressed as relative standard deviation (RSD), is typically ≤1.5 % for most trace
231 elements, including the REE and Th, and up to 4 % for Sc, Cr, Co, Ni, Ta and Hf.
232
233 *3.2 Phase diagram calculations*

234 Phase diagrams were calculated using version 6.6.6 of the Perple_X software package
235 (Connolly, 1990, 2005) in the system CNKFMASHO (CaO-Na_2O-K_2O-FeO-MgO-Al_2O_3-
236 SiO_2-H_2O-O_2). Pseudosection calculations were performed at 300-500 °C and 0.2-1.2 GPa for
237 water-saturated conditions. The chemical potential of oxygen in the system was controlled by
238 the hematite-magnetite (HM) buffer. The advantage of buffering the oxygen fugacity is that
239 open-system processes can be investigated by assuming that the oxidation state is controlled
240 by a metamorphic stable mineral paragenesis and not by the amount of oxygen brought in or
241 removed from the system (Konrad-Schmolke et al., 2008; Scott et al., 2013). The HM buffer
242 assemblage seems appropriate because hematite is present in several samples, indicating
243 relatively oxidizing conditions. The P-T positions of water isopleths, showing the molar
244 percentage of water bound to 100% solids, were superimposed on the calculated
245 pseudosections to evaluate the hydration/dehydration behavior under closed-system
246 conditions. Pseudo-binary P-X_{H2O} diagrams were calculated to compare calculated mineral
247 assemblages and modal and chemical mineral variations in the two samples for water-
248 saturated and water-undersaturated conditions. Moreover, we calculated pseudo-binary P-X
249 diagrams, using the blueschist and greenschist bulk compositions as compositional end-
250 members, to evaluate the dependence of modal mineralogy and mineral chemistry on the
251 different bulk chemistry. For all calculations, we used the updated database from Holland and
252 Powell (1998) and solution models from Fuhrman and Lindsley (1988) for feldspar and from
253 Holland et al. (1998) for chlorite, potassic white mica, epidote, garnet and omphacite. For
254 amphibole, we used the solution model "GlTrTsMr" of Massonne and Willner (2008), which
255 is based on the four end-members glaucophane, tremolite, tschermakite and magnesio-
256 riebeckite and considers the incorporation of ferric iron into amphibole. We chose this model
257 because it was specifically developed to take into account the specific compositional
258 constraints of amphiboles at low-grade, medium-to-high pressure conditions, such as Si
259 contents close to 8 per formula unit and an almost vacant A site (Massonne and Willner,

2008). These compositional features are also present in the investigated samples, and this improved amphibole solution model has been successfully used to simulate the expected amphibole compositions for metabasites at low-grade metamorphic conditions (Massonne and Willner, 2008). We did not consider the andradite and acmite components in garnet and omphacite, respectively.

4. Petrography

All of the three blueschist-greenschist pairs investigated in detail are fine-grained with matrix minerals typically between 5 and 50 μm and rarely exceeding 100 μm in size. Major mineral phases are amphibole (amph), phengitic white mica (phg), chlorite (chl), and albite (ab) with subordinate amounts of titanite, epidote, hematite, apatite and K-feldspar (Fig. 3). Zircon and rutile occur as rare accessory phases. The mineralogy of blueschist and greenschist layers is similar, but the modal proportions of the major mineral phases differ (Table 2). Blue, sodic amphibole is significantly more abundant (>10%) in the blueschists compared to the greenschists. The proportion of blue amphibole as to all amphibole present is about 30-50% in blueschists, whereas it is <5% in greenschists. Modal chlorite increases in the greenschists to about 20-40% compared to the respective blueschists (~10%). Proportions of phengite and albite are variable and K-feldspar is typically lacking in the blueschists.

5. Mineral chemistry

Mineral chemical data of the four major mineral phases are given in the electronic appendix. The two feldspars are essentially pure albite (~$An_{0.002}Ab_{0.996}Or_{0.002}$) and K-feldspar (~$Ab_{0.02}Or_{0.98}$), respectively. White mica has Mg# (Mg# = $Mg/(Mg+Fe^{2+})$) of 0.54-0.75 and

285 Na/(Na+K) ratios <0.4. Silica content in white mica varies widely, both within and between
286 different samples, from 6.5 to 7.2 Si per formula unit (pfu). In chlorite, Si pfu is relatively
287 constant (5.6-6.0), whereas Mg# ranges from 0.55 to 0.67. Individual samples have a very
288 restricted range of chlorite compositions with a variation in Mg# ≤0.02.
289 Amphibole has very wide compositional range. Sodic, sodic-calcic and calcic compositions
290 are present (allocation of amphibole names following Locock (2014) based on Leake et al.
291 (1997)). The majority of amphiboles has close to 8 Si pfu, between 0.3 and 1.8 Na_B and Mg#
292 (Mg# = Mg/(Mg+Fe_T)) of 0.48-0.75 (Fig. 4). These amphiboles can be classified as
293 actinolites, winchites, ferri-winchites and glaucophanes and represent a compositional
294 continuum (Fig. 4). In both blueschist and greenschist samples, glaucophane cores are
295 overgrown by sodic-calcic or calcic amphibole (Fig. 3A-D). In some cases, however,
296 glaucophane appears to be surrounding sodic-calcic amphibole (Fig. 3E). Rare Ti-rich ferro-
297 pargasite with TiO_2 between 3.2 and 6.2 wt.% occurs in two samples (blueschist CH-1-18 and
298 greenschist CH-1-19), constituting the innermost parts of larger amphibole grains (Fig. 3F).
299 The Ti-rich ferropargasite most likely formed prior to subduction zone metamorphism and is
300 the only remnant of the pre-metamorphic evolution. The presence of glaucophane in
301 blueschists and greenschists provides evidence for a high-pressure metamorphic stage that
302 affected the whole sequence. Rare rutile in one of the blueschists also reflects a high-P
303 metamorphic stage (Table 2). In contrast, albite and alkali feldspar demonstrate
304 recrystallization on the retrograde path during exhumation. Two other major phases, chlorite
305 and phengite, may have been crystallizing and re-crystallizing over a wide P-T range on the
306 retrograde path.
307
308
309 # 6. Major and trace element chemistry

The eleven analyzed blueschists and greenschists are very variable in their major element composition, encompassing ultramafic, mafic and intermediate compositions (Table 1). The range in SiO_2 (40-56 wt.%), MgO (5.3-14.5 wt.%), $Fe_2O_3^T$ (9.1-16.5 wt.%), CaO (2.7-10.0 wt.%) and Na_2O (1.5-6.1 wt.%) is particularly large. Among the trace elements, Sr (23-681 µg/g), Li (20-56 µg/g), the large ion lithophile elements (LILEs), such as Rb (13-164 µg/g) and Ba (170-1360 µg/g), as well as the transition metals Cr (80-850 µg/g) and Ni (60-380 µg/g) show a considerable range. Whole-rock abundances of rare earth elements (REE) are also highly variable (La = 4-34 µg/g; Yb = 1.0-2.6 µg/g), resulting in distinct chondrite-normalized (CN) REE patterns (Fig. 5) and ratios ($(La/Yb)_{CN}$ = 1.5-12.6, $(La/Sm)_{CN}$ = 0.9-2.7 and $(Gd/Yb)_{CN}$ = 1.9-4.6). Compared to typical oceanic basalts, the REE patterns of most samples resemble ocean island basalts (OIBs) but are quite distinct from normal mid-oceanic ridge basalt (N-MORB). In contrast to volcanic rocks from the Chilean Volcanic Front, the main differences are the tendency to higher absolute REE contents and the lack of a flattening HREE slope. In the Th/Yb vs Nb/Yb diagram (Pearce, 2008), used to discriminate between oceanic basalts and subduction-related basalts, most samples broadly fall between the alkalic and tholeiitic OIB compositions (Fig. 6).

In adjacent blueschist-greenschist pairs, blueschist layers are typically enriched in SiO_2 and Na_2O and depleted in MgO, $Fe_2O_3^T$ (total iron as Fe_2O_3) and H_2O compared to the associated greenschist, whereas CaO and K_2O lack clear systematic relationships with respect to the rock type. The sequence CH-1-48, comprising a blueschist layer sandwiched in between two greenschists with distinctly different hues (Fig. 2), exhibits significant compositional differences not only between blueschist and greenschists but also between the two greenschists (Table 1, Fig. 5). In contrast, the adjacent blueschists and greenschists of three pairs have very similar REE slopes compared to the respective greenschist/blueschist counterpart (Fig. 5). Moreover, the blueschists of the two pairs CH-1-12 and CH-1-18/19 are

indistinguishable in terms of their Th/Yb and Nb/Yb ratios from the corresponding greenschists.

7. Discussion

7.1. Protolith composition

For altered and metamorphosed magmatic rocks, ratios of trace elements that are considered as immobile during low-grade alteration and metamorphism (Pearce and Cann, 1973; Pearce, 2008) can be used to determine the protolith composition. The Th/Yb versus Nb/Yb diagram combines Th/Yb as geochemical proxy for crustal input (via subduction, crustal recycling or magma-crust interaction) and Nb/Yb as proxy for mantle source/melting variance (Pearce, 2008). All samples fall into the field of oceanic basalts and do not show elevated Th/Yb ratios and low Nb/Yb ratios that are typical for the arc-related magmatic rocks from the Chilean volcanic front (Jacques et al., 2013). Hence, we exclude a subduction-related origin and favor formation in an oceanic setting. Hyppolito et al. (2014) also noted the lack of a subduction signature in blueschists and greenschists from the Coastal Cordillera of central Chile and attributed the observed N-MORB, E-MORB and OIB signatures to an oceanic origin.

On outcrop scale, blueschists and greenschists are interlayered with metasedimentary rocks, and hence a contribution of sedimentary material, either as detritus during deposition or by incorporation during subduction, has to be evaluated. In the Th/Yb vs. Nb/Yb diagram (Fig. 6) Chilean trench sediments (Lucassen et al., 2010) with high Th/Yb and low Nb/Yb ratios are geochemically distinct from the analyzed mafic samples. Therefore, we do not consider that admixing of a sedimentary component was a significant process in affecting the whole rock geochemistry of the blueschists and greenschists.

360 The overall heterogeneity in REE patterns from N-MORB-like to alkalic OIB-like (Fig. 5) is
361 evidence for chemically heterogeneous precursor rocks. Most samples, however, have
362 strongly negative REE slopes and correspondingly high (>5) $(La/Yb)_{CN}$ ratios, pointing to an
363 ocean island origin, consistent with relatively high Nb/Yb ratios (Fig. 6). The chemical
364 heterogeneity in the metavolcanic rocks can be explained by an origin as plume-influenced
365 ridge (Hyppolito et al., 2014) or as seamounts (John et al., 2010). Both scenarios can produce
366 the coexistence of chemically diverse meta-igneous rocks in HP subduction complexes. The
367 presence of Ti-rich ferropargasite relicts provides further support for an origin as igneous
368 oceanic lithosphere because similarly Ti-rich pargasitic amphibole has been observed in
369 ocean-floor ultramafic-mafic plutonic suites (Arai et al., 1997). Inclusions of hornblende in
370 metamafic rocks from the Attic-Cycladic blueschist belt were also assigned to an early, pre-
371 peak stage of metamorphism (Baziotis et al., 2009; Baziotis and Mposkos, 2011). In the
372 context of this study, the key observation is that the metavolcanic rocks exhibit primary
373 geochemical differences related to their magmatic origin, which are determined based on the
374 REE patterns and distinct immobile trace element ratios (Nb/Yb, Th/Yb). Since these
375 elemental features typically remain unchanged during subduction-related metamorphism and
376 retrogression (El Korh et al., 2009; 2013; John et al., 2004; 2010), additional, secondary
377 effects on the bulk rock geochemistry can be evaluated in sample pairs that show little or no
378 primary differences.
379
380 *7.2. Inheritance of chemical differences from igneous differentiation processes*
381 Variable REE patterns and distinct Nb/Yb ratios, as present in the sample sequence CH-1-48
382 (Figs. 2, 5), are clearly inherited from the pre-metamorphic precursor rocks, and these
383 adjacent samples are hence not suited to investigate subsequent metasomatic alterations. On
384 the other hand, three adjacent blueschist-greenschist pairs (samples CH-1-12, CH-1-15 and
385 CH-1-18/19) have almost identical REE patterns (Fig. 5) and similar key HFSE ratios (e.g.

386 Nb/Yb) and were hence selected for a more detailed investigation. First, pre-metamorphic
387 major and trace element variations that may have been caused by magmatic processes are
388 assessed by comparing general fractional crystallization trends to the blueschist-greenschist
389 pairs (Fig. 7). Some features of the major element abundances of individual blueschist-
390 greenschist pairs, such as higher Na_2O and lower MgO contents in the more SiO_2-rich
391 samples, are broadly compatible with a fractional crystallization relationship. However, there
392 is evidence that typical magmatic relationships between major elements are disturbed, both
393 for the entire sample set and individual blueschist-greenschist pairs.
394 Features that are inconsistent with igneous differentiation trends of ocean island volcanic
395 rocks include (Fig. 7): (i) For a given MgO content, several blueschists have significantly
396 higher SiO_2 and Na_2O contents compared to the igneous fractionation trend (ii) One
397 greenschist is displaced to very low SiO_2 and shows an unusual, extreme enrichment in FeO^T.
398 (iii) The slopes that connect matching blueschist-greenschist pairs in SiO_2-MgO space are
399 oblique to the differentiation trend. (iv) CaO is relatively depleted in all samples except one.
400 (v) The positive correlation of K_2O and Rb with MgO for two pairs is opposite to the igneous
401 differentiation trend. (vi) There is a general enrichment in Ni, whereas the Cr contents scatter
402 unsystematically. (vii) The behaviour of incompatible trace elements relative to major
403 elements is also difficult to explain with fractional crystallization alone because the more
404 SiO_2-rich blueschists have similar or lower Zr, La and U contents than the greenschists (Table
405 1), whereas higher contents of these elements would be expected if fractional crystallization
406 alone were responsible for the chemical variations. To conclude, many of geochemical
407 variations present require element mobilization subsequent to the magmatic/volcanic history.
408
409 *7.3. Chemical differences due to fluid-rock interaction*
410 If igneous differentiation cannot explain several of the major element features, seafloor
411 alteration and subduction and/or exhumation-related metamorphic processes remain as key

412 factors for the metasomatic overprint. The similarity of REE patterns combined with the
413 irregular major element contents of the selected blueschist-greenschist pairs show that
414 metasomatic changes affected the rocks subsequent to the magmatic history. Hydrothermal
415 alteration of oceanic crust is often observed in HP terranes (e.g., Putlitz et al., 2000; Spandler
416 et al., 2004; Halama et al., 2011; El Korh et al., 2013), and metasomatic processes specific for
417 ocean floor alteration, such as rodingitization and spilitization, have also been observed (Li et
418 al., 2004; Arghe et al., 2011; Halama et al., 2013). Regarding major elements, gains and
419 losses during seafloor alteration are highly variable and uncertainties in their quantification
420 are high (Staudigel, 2003). For instance, Na is lost during submarine glass alteration
421 (Staudigel and Hart, 1983), but spilitization leads to an increase in Na (Arghe et al., 2011).
422 Therefore, potential effects of pre-metamorphic seafloor alteration are evaluated based on
423 trace element abundances and ratios in diagrams that discern between seafloor alteration and
424 high-pressure metasomatic processes (Fig. 8; Bebout, 2007; 2014). Increasing degrees of
425 seafloor alteration in basaltic oceanic crust cause Ba/Rb and Th/U ratios to strongly decrease
426 and K/Th to strongly increase (Fig. 8). Importantly, these trends are distinct form those
427 observed for high-pressure metasomatic alteration (Bebout, 2007; 2014). None of the samples
428 investigated falls onto any of the seafloor alteration trends, suggesting that this process had a
429 neglibigle influence on the whole rock compositions. Instead, the samples plot close to typical
430 OIB compositions, as expected from their immobile trace element signatures, or along the
431 metasomatic alteration trends that illustrate chemical changes during subduction
432 metamorphism. In particular, the three blueschist-greenschist pairs with negligible magmatic
433 geochemical differences show trends that are subparallel to the general metasomatic alteration
434 trend (Fig. 8). The apparent lack of typical seafloor alteration trends suggests that fluid-rock
435 interaction during the subduction-related metamorphic evolution affected the whole rock
436 geochemistry.

For illustrative purposes, the chemical variations between individual blueschist-greenschist pairs are shown in isocon diagrams (Fig. 9). Isocon diagrams (Grant, 1986; 2005) are used to quantify chemical changes during metasomatism, and they have been successfully applied in elucidating tranformation of eclogites into epidote amphibolites (El-Shazly et al., 1997) and eclogite into blueschist (van der Straaten et al., 2012). For the graphic representation of isocon diagrams, altered compositions are plotted against an original composition, and species that have remained immobile in the investigated process define the isocon, which is a straight line through the origin (Grant, 2005). Here, the isocon diagrams reflect the integrated chemical variations of the rock's entire evolution and we use them to visualize geochemical variations and the general patterns of elemental behavior rather than the quantification of metasomatic changes. Although it is unlikely that blueschist and greenschist of individual pairs had exactly the same precursor, the near-identical REE patterns of the three selected pairs allows an evaluation of metasomatic changes superimposed onto the primary magmatic differences.

The isocon analysis is based on a set of selected "immobile" reference elements and robust isocons can be defined based on >10 trace elements for each blueschist-greenschist pair (Fig. 9). Based on petrographic observations, we assume that blueschists are the less overprinted equivalents to the greenschists. The following observations can be made independent from absolute concentrations in the rocks: (i) SiO_2, CaO, Na_2O are relatively depleted in the greenschist. As SiO_2 and Na_2O increase but CaO decreases during igneous differentiation, these combined effects must be related to the metasomatic overprint. (ii) Greenschists are enriched in H_2O, consistent with the assumption of more intense fluid-rock interaction. (iii) MgO, $Fe_2O_3^T$ and transition metals show variable behavior. The observed scatter is partly due to differences in degree of fractionation, but the strong relative enrichment in one greenschist (Fig. 9C) demonstrates metasomatic mobilization of transition metals, as observed in several other studies of metamorphic fluid overprinting (El Shazly et al., 1997; van der Straaten et al.,

2012) and presumably linked to interaction with ultramafic lithologies. (iv) The four LILE K, Ba, Rb and Cs follow a distinct, linear array in all three examples, and the slope of this linear array is distinct from the slope defined by the reference elements. These trends point to a mineralogical control by potassic white mica (Sorensen et al., 1997; Bebout et al., 2007) and is probably related to fluid equilibration with metasedimentary lithologies. In two cases (Fig. 9A, B), LILE were added during fluid infiltration together with H_2O, whereas in the third case (Fig. 9C), LILE were removed during fluid-rock interaction.

7.4. Pseudosections

The application of thermodynamic modeling to metasomatized rocks faces the difficulties that textures produced by fluid-rock interaction are difficult to distinguish from those caused by P-T changes and that the selection of equilibrated minerals may be hampered by the variability in the scale of mass transfer and equilibration (Goncalves et al., 2013). For the Pichilemu rocks, relict glaucophane cores in both blueschist and greenschist (Fig. 3) bear evidence for a high-pressure metamorphic stage of the whole sequence. The textural evidence suggests that glaucophane is not in equilibrium with albite and K-feldspar, pointing to a distinct retrograde metamorphic stage (see also Willner, 2005). To explore phase assemblage and compositional variations, we calculated pseudosections for the blueschist-greenschist pair CH-1-18 – CH-1-19. This sample pair was selected because of a distinct difference in visual appearance and negligible differences in REE abundances and patterns reflecting a similar igneous protolith. Key features observed for these two samples also occur in the pseudosections calculated for the two other sample pairs, so that showing the entire set of diagrams for all samples is deemed redundant. We assume that the rocks are water-saturated at peak conditions, which is likely if continuous dehydration occurred along the prograde path (Konrad-Schmolke et al., 2011). The pseudosections for the two samples show broadly similar topologies despite small

differences in detail (Fig. 10A-B). At peak conditions of around 1.0±0.1 GPa and 400±20 °C, the predicted equilibrium assemblage is chlorite + epidote + phengite + amphibole. Albite becomes stable below about 0.5±0.1 GPa and is joined by K-feldspar at still lower pressures. Maximum equilibration pressures during retrograde overprint are constrained by the presence of albite to about 0.4-0.6 GPa. The presence of K-feldspar in the greenschist constrains P to < 0.5 GPa, whereas minimum pressures are approximately 0.25 GPa based on the presence of phengite. Hence, the best estimate for the retrograde overprint is 0.4±0.1 GPa at ≤ 400°C. These estimates are clearly below peak pressure estimates of up to 1.1 GPa for blueschists from the region (Willner, 2005), demonstrating that incomplete greenschist-facies equilibration occurred after peak P-T on the retrograde path during exhumation. These findings are in accordance with a significant pressure release with only slight cooling during the retrograde P-T evolution (Willner, 2005). We suggest that the retrograde overprint is associated with layer-parallel fluid infiltration, causing the different degrees of metasomatism. It appears likely that the presence of a metasomatic fluid triggered the retrograde equilibration.

7.5. Influence of water on mineral assemblages and compositions

The amount of structurally bound water in minerals is critical for the formation and preservation of mineral assemblages during metamorphism (Guiraud et al., 2001; Clarke et al., 2006; Konrad-Schmolke et al., 2011). To examine the mineral assemblage evolution along the retrograde P-T path, we contoured the pseudosections for H_2O content of the mineral assemblage (Fig. 10 A-B). Moreover, we modeled isothermal (T = 400 °C) P-X_{H2O} pseudo-binary phase diagrams to study the influence of water undersaturation and water infiltration on mineral assemblages as well as modal and chemical mineral variations (Fig. 10 C-F).

The water isopleths patterns of the examined blueschist and greenschist are very similar, showing a positive slope above about 0.4-0.6 GPa, i.e. for all phase assemblages where albite

515 is lacking. (Fig. 10 A-B). In contrast, water isopleths have a negative slope where albite is
516 present in the calculated mineral assemblage. Along the retrograde P-T path of the blueschist-
517 greenschist sequence, successively lower isopleths are encountered within the 4 phase
518 assemblage field chlorite+epidote+phengite+amphibole. Hence, decompression from peak
519 pressure would result in dehydration because the capability of the rock to retain water
520 diminishes (cf. Heinrich 1982). Consequently, water saturation during decompression is
521 attained without external water influx. The rock would remain water-saturated until albite
522 joins the stable paragenesis where it becomes water-undersaturated as all the available water
523 will be incorporated into hydrous solid phases, rendered possible by the significant increase in
524 the modal chlorite abundance (Fig. 10 A-B).
525 As inferred from the water isopleth patterns, the rocks remain at or above the water saturation
526 line during decompression until pressures < 0.4 GPa are reached (Fig. 10 C-D). The absence
527 of garnet and omphacite and the presence of K-feldspar in the Pichilemu samples also suggest
528 crystallization conditions at or near water saturation. Only where the water saturation curve
529 has a negative slope, external water addition is required to maintain water saturation (see also
530 Konrad-Schmolke et al., 2011). The modal abundances of both chlorite (Fig. 10 C-D) and
531 amphibole (Fig. 10 E-F) are strongly dependent on the degree of water-undersaturation,
532 increasing with increasing water amounts, but show only moderate changes in water-saturated
533 regions. The amphibole composition shows distinct patterns for water-undersaturated and
534 water-saturated conditions (Fig. 10 E-F). The glaucophane component strongly decreases with
535 increasing water content and shows only minor pressure dependence at water-undersaturation.
536 However, once water saturation is reached, the amphibole composition solely depends on
537 pressure, with a significant decrease in glaucophane component below pressures of ~0.35
538 GPa, i.e. where two feldspars are coexisting.
539 In summary, water-saturated or water-oversaturated conditions on the retrograde P-T path and
540 the near-isothermal decompression are reflected in extensive albite crystallization and the

541 growth of sodic-calcic and calcic amphibole around glaucophane. The almost mylonitic
542 textures that reflect high strain also favor extensive recrystallization of the Pichilemu rocks on
543 the retrograde P-T path. Although these features do not necessarily require influx of external
544 water, they are certainly consistent with fluid influx during the final equilibration stage.
545 Supportive evidence for fluid influx comes from the sharp compositional boundaries between
546 glaucophane cores and winchite/actinolite overgrowths. The lack of a continuous
547 compositional trend in individual amphiboles suggests discontinuous growth, which can be
548 explained by a distinct fluid influx as observed in eclogite-facies rocks from the Sesia Zone
549 (Konrad-Schmolke et al., 2011; Halama et al., 2014).
550
551 *7.6. Compositional effects on mineral assemblages and compositions*
552 Previous studies have highlighted the important role of the bulk rock chemistry on amphibole
553 chemistry in interlayered blueschists and greenschists. Maruyama et al. (1986) proposed that
554 higher Fe contents expand the glaucophane stability, as glaucophane-bearing layers with
555 higher Fe contents were described (Oberhänsli et al., 1978; Dungan et al., 1983). Other
556 chemical variables, such as lower MgO and higher Na/Ca ratios in blueschists have also been
557 invoked to explain blueschist-greenschist interlayering (Baziotis et al., 2009; Dungan et al.,
558 1983). Evidently, phase stabilities depend on a complex interplay of major element
559 abundances. To accommodate for the complete major elemental variation of the rocks, we
560 calculated pseudo-binary phase diagrams for two selected blueschist-greenschist pairs in order
561 to evaluate the influence of bulk chemical properties on modal phase abundances and mineral
562 compositions.
563 Calculated modal phase changes show that the chlorite abundance increases towards the end-
564 member greenschist component (Fig. 11A), which can be related to the relative increase of
565 MgO compared to SiO_2. Modal amphibole contents are higher for the blueschist. Both of
566 these modeled features agree with the observed modal abundances and the restricted

567 occurrence of glaucophane in greenschist layers. Interestingly, the calculated glaucophane
568 component is higher for the greenschist composition at any given pressure, demonstrating that
569 the scarcity of glaucophane in the greenschist must be related to a more intense degree of
570 retrograde overprinting in the greenschist relative to the blueschist at low pressure where a
571 more Ca-rich amphibole becomes stable. The pseudo-binary phase diagrams demonstrate that
572 chemical variations in adjacent lithologies are the dominant factor in determining their
573 appearance as "blueschist" or "greenschist", without the necessity to invoke distinct P-T
574 equilibration conditions. Chemical variations can be related to two main causes, both of
575 which are observed in the Pichilemu rocks: 1) Primary compositional differences, inherited
576 from a pre-subduction stage, as in the sequence CH-1-48 A-B-C, and 2) Compositional
577 changes that are induced by fluid infiltration, affecting distinct layers to different degrees, as
578 observed in the sample pair CH-1-18/19.
579 Besides major element compositional variations, the oxidation state of metamorphic rocks
580 influences the stable mineral parageneses (Konrad-Schmolke et al., 2008; Diener and Powell,
581 2010) and their dehydration behavior (Massonne and Willner, 2008). For blueschist-facies
582 and greenschist-facies rocks, the preferential uptake of ferric iron by both sodic amphibole
583 and epidote relative to actinolite, chlorite and lawsonite exerts the most significant
584 compositional effect (Evans, 1990). Hence, the field of epidote and glaucophane is largest for
585 compositions rich in Fe^{3+}, i.e. for relatively oxidizing conditions (Evans, 1990), and the
586 addition of ferric iron moves the glaucophane-in boundary down to lower pressures (Diener et
587 al., 2007). In the Pichilemu samples, sodic amphibole is the major host of ferric iron because
588 epidote is only a minor phase and omphacite and garnet are absent. Hence, more oxidized
589 conditions would result in a larger stability field of sodic amphibole. However, we have
590 relinquished a more detailed discussion about the effects of oxygen fugacity because of two
591 reasons: First, despite recent improvements in the formulation of mineral solid solutions that
592 consider incorporation of Fe^{3+} (e.g. Diener et al., 2007), present knowledge about

593 thermodynamic properties of Fe^{3+} end-members is still incomplete and large uncertainties
594 exist about the Fe^{3+} standard state data and for the parameters of the mathematical
595 formulation of solid solution data (Scott et al., 2013). Second, it is difficult to relate observed
596 to modeled data because of the inability of the electron microprobe to resolve Fe valence
597 (Scott et al., 2013) and because bulk rock values of Fe_2O_3 may not reflect the oxidation state
598 during the main metamorphic evolution and may be modified by superficial alteration (López-
599 Carmona et al., 2013).
600
601 *7.7. Pre-metamorphic variability versus metamorphic overprinting*
602 The alternating layering on a cm-to-dm scale, the lack of structural breaks between the
603 different layers and the similar mineralogy of blueschists and greenschists suggest that the
604 whole sequence experienced a similar P-T evolution. If there is an appropriate spread in
605 whole rock compositions, reflected by mineral chemical variations along the exchange vectors
606 $Fe^{3+}Al_{-1}$ and $Fe^{2+}Mg_{-1}$, blueschists and greenschists can coexist over a pressure range of at
607 least 0.3 GPa and 400 °C (Evans, 1990). However, the Pichilemu rocks show abundant
608 evidence for retrogession in both rock types: Presence of albite ± K-feldspar, overgrowth of
609 winchite/ferrowinchite around glaucophane and actinolite and chlorite as abundant matrix
610 minerals. These observations and the pressure estimate of 0.4±0.1 GPa based on
611 pseudosection modeling demonstrate that an early blueschist event was followed by variable
612 retrograde overprint in the greenschist facies.
613 For several layers, exemplified in the chemically very heterogeneous sequence CH-1-48
614 (Figs. 2, 5, 7), the interlayering is best explained by metamorphism of layered volcanic rocks
615 (tuffs and/or basaltic lava flows) of different composition. In addition to primary, magmatic
616 compositional differences, some features of the interlayered sequence were acquired by pre-
617 and syn-metamorphic fluid overprining. Interlayering of blueschists and greenschists on a cm
618 scale may be due to heterogeneous alteration of pillow lavas and subsequent flattening during

619 metamorphism (Dungan et al., 1983). If metabasite layers are pervasively altered prior to
620 metamorphism, they are likely to show greater effects of retrogression because of enrichment
621 in Na and H_2O (El Korh et al., 2013). In the Pichilemu sequence, there is little evidence of
622 pre-metamorphic alteration based on trace element systematics (Fig. 8) and because the
623 blueschists, which are relatively enriched in Na, are also less retrogressed.
624 The detailed investigation of several blueschist-greenschist pairs revealed continuous
625 gradations from blueschist to greenschist facies mineralogies in parts of the interlayered
626 sequence and the persistence of blueschist-facies relicts in all rock types, pointing to an
627 important role of synmetamorphic fluid-rock interaction and incomplete re-equilibration
628 during uplift. Bröcker (1990) and Barrientos and Selverstone (1993) suggested that the
629 retrograde blueschist-to-greenschist transformation is catalyzed by the availability of
630 synmetamorphic fluid as the rocks pass through the greenschist facies by a selective
631 infiltration overprinting process. All of the Pichilemu rocks show evidence for retrograde
632 infiltration, but the effects were different in individual layers. We interpret these features as
633 channelled infiltration subparallel to pseudo-stratigraphic layering, most likely controlled by
634 differences in permeability (Bröcker, 1990).
635

636 # 8. Conclusions

637 Interlayered blueschists and greenschists occur in a fossil accretionary prism in the Coastal
638 Cordillera of Chile. Their close spatial association on a cm-to-dm scale and the lack of
639 structural breaks in between the layers argue against a large-scale tectonic transport of rocks
640 with different metamorphic facies. The geochemical differences between blueschist and
641 greenschist layers involve primary magmatic and secondary metasomatic processes. The
642 primary differences reveal that the rocks had oceanic basalts with dominantly OIB and
643 subordinately MORB affinities as protoliths. Glaucophane relicts occur in both blueschists

and greenschists, recording a high-pressure metamorphic event. The metasomatic overprint occurred under greenschist-facies conditions during exhumation and affected the rocks to different degrees. Gradational contacts between blueschists and greenschists on hand specimen and thin section scale and the persistence of blueschist-facies minerals in both rock types point to a selective infiltration overprinting during retrogression. Selected blueschist-greenschist pairs with similar REE patterns and immobile trace element ratios were used to evaluate geochemical effects of metasomatic overprinting. Key features of the metasomatic event include addition of water and depletion of Si and Na in greenschists relative to blueschists, mobilization and non-systematic behaviour of most major elements and transition metals, and concurrent mobilization trends for K, Ba, Rb and Cs. The application of equilibrium thermodynamics to the metasomatic rocks reveals that the variable bulk rock geochemistry is responsible for increasing modal abundance of chlorite and decreasing amounts of glaucophane in greenschists, which is ultimately responsible for the distinct visual appearance of the blue and green rocks.

Acknowledgments

We appreciate in particular the advice and information provided by Arne Willner about the general geology of the Coastal Cordillera as well as about specific outcrop locations. We also thank M. Büscher, I. Voß, H. Bobadilla and V. Schenk for help during sampling. We are grateful to D. Garbe-Schönberg and U. Westernströer for help with ICP-MS analyses, to P. Appel and B. Mader for assistance with the electron microprobe and to A. Weinkauf for XRF analyses. Moreover, we wish to thank Marco Scambelluri for editorial handling of the manuscript and Ioannis Baziotis and Michael Bröcker for their detailed and constructive reviews that served to greatly improve the manuscript. Funding of this work by the Deutsche

669 Forschungsgemeinschaft (SFB 574 “Volatiles and Fluids in Subduction Zones” at Kiel
670 University and grant KO-3750/2 to MKS) is gratefully acknowledged. This is contribution no.
671 274 of the SFB 574.
672

672 ## References

673 Aguirre, L., Hervé, F., Godoy, E., 1972. Distribution of metamorphic facies in Chile: an
674 outline. Krystallinikum 9, 7-19.

675 Arai, S., Matsukage, K., Isobe, E., Vysotskiy, S., 1997. Concentration of incompatible
676 elements in oceanic mantle: Effect of melt/wall interaction in stagnant of failed melt
677 conduits within peridotite. Geochimica et Cosmochimica Acta 61, 671-675.

678 Arghe, F., Skelton, A., Pitcairn, I., 2011. Spatial coupling between spilitization and
679 carbonation of basaltic sills in SW Scottish Highlands: evidence of a mineralogical
680 control of metamorphic fluid flow. Geofluids 11, 245-259.

681 Barrientos, X., Selverstone, J., 1993. Infiltration vs. thermal overprinting of epidote
682 blueschist, Ile de Groix, France. Geology 21, 69-72.

683 Baziotis, I., Mposkos, E., 2011. Origin of metabasites from upper tectonic unit of the Lavrion
684 area (SE Attica, Greece): Geochemical implications for dual origin with distinct
685 provenance of blueschist and greenschist's protoliths. Lithos 126, 161-173.

686 Baziotis, I., Proyer, A., Mposkos, E., 2009. High-pressure/low-temperature metamorphism of
687 basalts in Lavrion (Greece): implications for the preservation of peak metamorphic
688 assemblages in blueschists and greenschists. European Journal of Mineralogy 21, 133-
689 148.

690 Bebout, G.E., 2007. Metamorphic chemical geodynamics of subduction zones. Earth and
691 Planetary Science Letters 260, 373-393.

692 Bebout, G.E., 2014. Chemical and isotopic cycling in subduction zones. In: Rudnick, R.L.
693 (Ed.), The Crust. Treatise in Geochemistry 2nd Edition, vol. 4, pp. 703-747.

694 Bebout, G.E., Barton, M.D., 1993. Metasomatism during subduction: products and possible
695 paths in the Catalina Schist, California. Chemical Geology 108, 61-92.

696 Bebout, G.E., Bebout, A.E., Graham, C.M., 2007. Cycling of B, Li, and LILE (K, Cs, Rb, Ba,
697 Sr) into subduction zones: SIMS evidence from micas in high-P/T metasedimentary
698 rocks. Chemical Geology 239, 284-304.
699 Becker, H., Jochum, K.P., Carlson, R.W., 2000. Trace element fractionation during
700 dehydration of eclogites from high-pressure terranes and the implications for element
701 fluxes in subduction zones. Chemical Geology 163, 65-99.
702 Beinlich, A., Klemd, R., John, T., Gao, J., 2010. Trace-element mobilization during Ca-
703 metasomatism along a major fluid conduit: Eclogitization of a blueschist as a
704 consequence of fluid-rock interaction. Geochimica et Cosmochimica Acta 74, 1892-
705 1922.
706 Beitter, T., Wagner, T., Markl, G., 2008. Formation of kyanite-quartz veins of the Alpe
707 Sponda, Central Alps, Switzerland: implications for Al transport during regional
708 metamorphism. Contributions to Mineralogy and Petrology 156, 689-707.
709 Bousquet, R., 2008. Metamorphic heterogeneities within a single HP unit: Overprint effect or
710 metamorphic mix? Lithos 103, 46-69.
711 Breeding, C.M., Ague, J.J., Bröcker, M., 2004. Fluid-metasedimentary rock interactions in
712 subduction-zone mélange: Implications for the chemical composition of arc magmas.
713 Geology 32, 1041-1044.
714 Bröcker, M., 1990. Blueschist-to-greenschist transition in metabasites from Tinos Island,
715 Cyclades, Greece: Compositional control or fluid infiltration? Lithos 25, 25-29.
716 Bucholz, C.E., Ague, J.J., 2010. Fluid flow and Al transport during quartz-kyanite vein
717 formation, Unst, Shetland Islands, Scotland. Journal of Metamorphic Geology 28, 19-
718 39.
719 Clarke, G.L., Powell, R., Fitzherbert, J.A., 2006. The lawsonite paradox: a comparison of
720 field evidence and mineral equilibria modelling. Journal of Metamorphic Geology 24,
721 715-725.

722 Connolly, J.A.D., 1990. Multivariable phase diagrams: an algorithm based on generalized
723 thermodynamics. American Journal of Science 290, 666-718.
724 Connolly, J.A.D., 2005. Computation of phase equilibria by linear programming: A tool for
725 geodynamic modeling and its application to subduction zone decarbonation. Earth and
726 Planetary Science Letters 236, 524-541.
727 Diener, J.F.A., Powell, R., 2010. Influence of ferric iron on the stability of mineral
728 assemblages. Journal of Metamorphic Geology 28, 599-613.
729 Diener, J.F.A., Powell, R., White, R.W., Holland, T.J.B., 2007. A new thermodynamic model
730 for clino- and orthoamphiboles in the system Na_2O-CaO-FeO-MgO-Al_2O_3-SiO_2-H_2O-
731 O. Journal of Metamorphic Geology 25, 631-656.
732 Dungan, M.A., Vance, J.A., Blanchard, D.P., 1983. Geochemistry of the Shuksan greenschists
733 and blueschists, North Cascades, Washington: Variably fractionated and altered
734 metabasalts of oceanic affinity. Contributions to Mineralogy and Petrology 82, 131-146.
735 El Korh, A., Schmidt S.T., Ulianov, A., Potel, S. (2009). Trace element partitioning in HP–LT
736 metamorphic assemblages during subduction-related metamorphism, Ile de Groix,
737 France: a detailed LA-ICP-MS study. Journal of Petrology 50, 1107–1148.
738 El Korh, A., Schmidt, S.T., Vennemann, T., Ballèvre, M. (2013). Trace element and isotopic
739 fingerprints in HP-LT metamorphic rocks as a result of fluid-rock interactions (Ile de
740 Groix, France). Gondwana Research 23, 880-900.
741 El-Shazly, A.K., Worthing, M.A., Liou, J.G., 1997. Interlayered eclogites, blueschists and
742 epidote amphibolites from NE Oman: a record of protolith compositional control and
743 limited fluid infiltration. Journal of Petrology 38, 1461-1487.
744 Ernst, W.G., 1975. Systematics of large-scale tectonics and age progressions in Alpine and
745 Circum-Pacific blueschist belts. Tectonophysics 26, 229-246.
746 Ernst, W.G., 1988. Tectonic history of subduction zones inferred from retrograde blueschist
747 *P-T* paths. Geology 16, 1081-1084.

748 Ernst, W.G., 2006. Preservation/exhumation of ultrahigh-pressure subduction complexes.
749 Lithos 92, 321-335.
750 Evans, B.W., 1990. Phase relations of epidote-blueschists. Lithos 25, 3-23.
751 Evans, K.A., Powell, R., Frost, B.R., 2013. Using equilibrium thermodynamics in the study of
752 metasomatic alteration, illustrated by an application to serpentinites. Lithos 168-169,
753 67-84.
754 Fuhrmann, M.L., Lindsley, D.H., 1988. Ternary-feldspar modeling and thermometry.
755 American Mineralogist 73, 201-215.
756 Garbe-Schönberg, C.D., 1993. Simultaneous determination of 37 trace elements in 28
757 international rock standards by ICP-MS. Geostandard Newsletter 17, 81-97.
758 Glodny, J., Bingen, B., Austrheim, H., Molina, J.F., Rusin, A., 2002. Precise eclogitization
759 ages deduced from Rb/Sr mineral systematics: The Maksyutov complex, Southern
760 Urals, Russia. Geochimica et Cosmochimica Acta 66, 1221-1235.
761 Glodny, J., Kühn, A., Austrheim, H., 2008. Diffusion versus recrystallization processes in Rb-
762 Sr geochronology: Isotopic relics in eclogite facies rocks, Western Gneiss Region,
763 Norway. Geochimica et Cosmochimica Acta 72, 506-525.
764 Goncalves, P., Oliot, E., Marquer, D., Connolly, J.A.D., 2012. Role of chemical processes on
765 shear zone formation: an example from the Grimsel metagranodiorite (Aar massif,
766 Central Alps). Journal of Metamorphic Geology 30, 703-722.
767 Goncalves, P., Marquer, D., Oliot, E., Durand, C., 2013. Thermodynamic modeling and
768 thermobarometry of metasomatized rocks. In: Harlov, D., Austhreim, H. (Eds.),
769 Metasomatism and the chemical transformation of rock. Lecture Notes in Earth System
770 Sciences, Springer-Verlag Berlin Heidelberg, pp. 53-91.
771 González-Bonorino, F., 1971. Metamorphism of the crystalline basement of Central Chile.
772 Journal of Petrology 12, 149-175.

773 Grant, J.A., 1986. The Isocon diagram - a simple solution to Gresens' equation for
774 metasomatic alteration. Economic Geology 81, 1976-1982.
775 Grant, J.A., 2005. Isocon analysis: A brief review of the method and applications. Physics and
776 Chemistry of the Earth 30, 997-1004.
777 Guiraud, M., Powell, R., Rebay, G, 2001. H_2O in metamorphism and unexpected behaviour in
778 the preservation of metamorphic mineral assemblages. Journal of Metamorphic
779 Geology 19, 445-454.
780 Halama, R., John, T., Herms, P., Hauff, F., Schenk, V., 2011. A stable (Li, O) and radiogenic
781 (Sr, Nd) isotope perspective on metasomatic processes in a subducting slab. Chemical
782 Geology 281, 151-166.
783 Halama, R., Konrad-Schmolke, M., Sudo, M., Marschall, H.R., Wiedenbeck, M., 2014.
784 Effects of fluid-rock interaction on $^{40}Ar/^{39}Ar$ geochronology in high-pressure rocks
785 (Sesia-Lanzo Zone, Western Alps). Geochimica et Cosmochimica Acta 126, 475-494.
786 Halama, R., Savov, I.P., Garbe-Schönberg, D., Schenk, V., Toulkeridis, T., 2013. Vesuvianite
787 in high-pressure-metamorphosed oceanic lithosphere (Raspas Complex, Ecuador) and
788 its role for transport of water and trace elements in subduction zones. European Journal
789 of Mineralogy 25, 193-219.
790 Heinrich, C., 1982. Kyanite-eclogite to amphibolite facies evolution of hydrous mafic and
791 pelitic rocks, Adula Nappe, Central Alps. Contribution to Mineralogy and Petrology,
792 81, 30-38.
793 Hervé, F., 1988. Late Paleozoic subduction and accretion in southern Chile. Episodes 11, 183-
794 188.
795 Hervé, F., Faundez, V., Calderón, M., Massonne, H.-J., Willner, A.P., 2007. Metamorphic
796 and plutonic basement complexes. In: Moreno, T., Gibbons, W. (Eds.), The Geology of
797 Chile. The Geological Society, London, pp. 5-19.

798 Hervé, F., Munizaga, F., Godoy, E., Aguirre, L., 1974. Late Paleozoic K/Ar ages of
799 blueschists from Pichilemu, Central Chile. Earth and Planetary Science Letters 23, 261-
800 264.
801 Hervé, F., Munizaga, F., Parada, M.A., Brook, M., Pankhurst, R.J., Snelling, N.J., Drake, R.,
802 1988. Granitoids of the coast range of central Chile: Geochronology and geologic
803 setting. Journal of South American Earth Sciences 1, 185-194.
804 Holland, T., Baker, J., Powell, R., 1998. Mixing properties and activity-composition
805 relationships of chlorites in the system MgO-FeO-Al_2O_3-SiO_2-H_2O. European Journal
806 of Mineralogy 10, 395-406.
807 Holland, T., Powell, R., 1998. An internally consistent thermodynamic data set for phases of
808 petrological interest. Journal of Metamorphic geology 16, 309-343.
809 Hyppolito, T., Juliani, C., García-Casco, A., Meira, V.T., Bustamante, A., Hervé, F. (2014).
810 The nature of the Palaeozoic oceanic basin at the southwestern margin of Gondwana
811 and implications for the origin of the Chilenia terrane (Pichilemu region, central Chile).
812 International Geology Review 56, 1097-1121.
813 Jacques, G., Hoernle, K., Gill, J., Hauff, F., Wehrmann, H., Garbe-Schönberg, D., van den
814 Bogaard, P., Bindeman, I., Lara, L.E., 2013. Across-arc geochemical variations in the
815 Southern Volcanic Zone, Chile (34.5-38.0°S): Constraints on mantle wedge and slab
816 input compositions. Geochimica et Cosmochimica Acta 123, 218-243.
817 John, T., Klemd, R., Gao, J., Garbe-Schönberg, C.D., 2008. Trace-element mobilization in
818 slabs due to non steady-state fluid-rock interaction: constraints from an eclogite-facies
819 transport vein in blueschist (Tianshan, China). Lithos 103, 1-24.
820 John, T., Scherer, E., Haase, K.M., Schenk, V., 2004. Trace element fractionation during
821 fluid-induced eclogitization in a subducting slab: trace element and Lu-Hf/Sm-Nd
822 isotope systematics. Earth and Planetary Science Letters 227, 441-456.
823 John, T., Scherer, E., Schenk, V., Herms, P., Halama, R., Garbe-Schönberg, D., 2010.

824 Subducted seamounts in an eclogite-facies ophiolite sequence: The Andean Raspas
825 Complex, SW Ecuador. Contributions to Mineralogy and Petrology 159, 265-284.
826 Kahl, W.-A., Schumacher, J.C., 2000. Multiple pyroxene and amphibole assemblages in the
827 amphibolite facies: Bulk compositional controls. American Mineralogist 85, 1606-1616.
828 Konrad-Schmolke, M., O'Brien, P.J., de Capitani, C., Carswell, D.A., 2008. Garnet growth at
829 high- and ultra-high pressure conditions and the effect of element fractionation on
830 mineral modes and composition. Lithos 103, 309-332.
831 Konrad-Schmolke, M., O'Brien, P.J., Zack, T., 2011. Fluid migration above a subducted slab
832 – constraints on amount, pathways and major element mobility from partially
833 overprinted eclogite-facies rocks (Sesia Zone, Western Alps). Journal of Petrology 52,
834 457-486.
835 Leake, B.E. et al., 1997. Nomenclature of amphiboles: report of the subcommittee on
836 amphiboles of the International Mineralogical Association, Commisssion on New
837 Minerals and Mineral Names. Canadian Mineralogist 35, 219-246.
838 Li, X.-P., Rahn, M., Bucher, K., 2004. Metamorphic processes in rodingites of the Zermatt-
839 Saas ophiolites. International Geology Reviews 46, 28-51.
840 Locock, A.J., 2014. An Excel spreadsheet to classify chemical analyses of amphiboles
841 following the IMA 2012 recommendations. Computers & Geosciences 62, 1-11.
842 López-Carmona, A., Pitra, P., Abati, J., 2013. Blueschist-facies metapelites from the Malpica-
843 Tui Unit (NW Iberian Massif): phase equilibria modelling and H_2O and Fe_2O_3 influence
844 in high-pressure assemblages. Journal of Metamorphic Geology 31, 263-280.
845 Lucassen, F., Trumbull, R., Franz, G., Creixell, C., Vásquez, P., Romer, R.L., Figueroa, O.,
846 2004. Distinguishing crustal recycling and juvenile additions at active continental
847 margins: the Paleozoic to recent compositional evolution of the Chilean continental
848 margin (36-41°S). Journal of South American Earth Sciences 17, 103-119.

849 Lucassen, F., Wiedicke, M., Franz, G., 2010. Complete recycling of a magmatic arc: evidence
850 from chemical and isotopic composition of Quaternary trench sediments in Chile (36°-
851 40°S). International Journal of Earth Sciences 99, 687-701.
852 Marschall, H.R., Altherr, R., Gméling, K., Kasztovszky, Z., 2009. Lithium, boron and
853 chlorine as tracers for metasomatism in high-pressure metamorphic rocks: a case study
854 from Syros (Greece). Mineralogy and Petrology 95, 291-302.
855 Maruyama, S., Cho, M., Liou, J.G., 1986. Experimental investigations of blueschist-
856 greenschist transition equilibria: pressure dependence of Al_2O_3 contents in sodic
857 amphiboles – a new geobarometer. In: Evans, B.E., Brown, E.H. (Eds.), Blueschists and
858 Eclogites. Geological Society of America Memoir, vol. 164, pp. 1-16.
859 Massonne, H.-J., Willner, A.P., 2008. Phase relations and dehydration behaviour of
860 psammopelite and mid-ocean ridge basalt at very-low-grade to low-grade metamorphic
861 conditions. European Journal of Mineralogy 20, 867-879.
862 Miller, D.P., Marschall, H.R., Schumacher, J.C., 2009. Metasomatic formation and petrology
863 of blueschist-facies hybrid rocks from Syros (Greece): Implications for reactions at the
864 slab-mantle interface. Lithos 107, 53-67.
865 Munizaga, F., Aguirre, L., Hervé, F., 1973. Rb/Sr ages of rocks from the Chilean
866 metamorphic basement. Earth and Planetary Science Letters 18, 87-92.
867 Oberhänsli, R., 1978. Chemische Untersuchungen an Glaukophan-führenden basischen
868 Gesteinen aus den Bündnerschiefern Graubündens. Schweizerische Mineralogische und
869 Petrographische Mitteilungen 58, 139-156.
870 Oh, C.W., Liou, J.G., Maruyama, S., 1991. Low-temperature eclogites and eclogitic schists in
871 Mn-rich metabasites in Ward Creek, California; Mn and Fe effects on the transition
872 between blueschist and eclogite. Journal of Petrology 32, 275-301.
873 Okrusch, M., Bröcker, M., 1990. Eclogites associated with high-grade blueschists in the
874 Cyclades archipelago, Greece; a review. European Journal of Mineralogy 2, 451-478.

875 Pattison, D., 2013. Regional metamorphism in the Ballachulish area, SW Highlands,
876 Scotland: new perspectives on a famous old debate, with regional implications. Journal
877 of the Geological Society of London 170, 417-434.
878 Pearce, J.A., 2008. Geochemical fingerprinting of oceanic basalts with applications to
879 ophiolite classification and the search for Archean oceanic crust. Lithos 100, 14-48.
880 Pearce, J.A., Cann, J.R., 1973. Tectonic setting of basic volcanic rocks determined using trace
881 element analyses. Earth and Planetary Science Letters 19, 290-300.
882 Penniston-Dorland, S.C., Sorensen, S.S., Ash, R.D., Khadke, S.V., 2010. Lithium isotopes as
883 a tracer of fluids in a subduction zone mélange: Franciscan Complex, CA. Earth and
884 Planetary Science Letters 292, 181-190.
885 Philippot, P., Selverstone, J., 1991. Trace-element-rich brines in eclogitic veins: implications
886 for fluid composition and transport during subduction. Contributions to Mineralogy and
887 Petrology 106, 417-430.
888 Platt, J.P., 1993. Exhumation of high-pressure rocks: a review of concepts and processes.
889 Terra Nova 5, 119-133.
890 Pognante, U., Kienast, J.-R., 1987. Blueschist and eclogite transformations in Fe-Ti gabbros:
891 A case from the Western Alps ophiolites. Journal of Petrology 28, 271-292.
892 Putlitz, B., Matthews, A., Valley, J.W., 2000. Oxygen and hydrogen isotope study of high-
893 pressure metagabbros and metabasalts (Cyclades, Greece): implications for the
894 subduction of oceanic crust. Contributions to Mineralogy and Petrology 138, 114-126.
895 Richter, P.P., Ring, U., Willner, A.P., Leiss, B., 2007. Structural contacts in subduction
896 complexes and their tectonic significance: The Late Paleozoic coastal accretionary
897 wedge of central Chile. Journal of the Geological Society of London 164, 203-214.
898 Ridley, J., 1984. Evidence of a temperature-dependent 'blueschist' to 'eclogite' transformation
899 in high-pressure metamorphism of metabasic rocks. Journal of Petrology 25, 852-870.

900 Schliestedt, M., Matthews, A., 1987. Transformation of blueschist to greenschist facies rocks
901 as a consequence of fluid infiltration, Sifnos (Cyclades), Greece. Contributions to
902 Mineralogy and Petrology 97, 237-250.
903 Scott, J.M., Konrad-Schmolke, M., O'Brien, P.J., Günter, C., 2013. High-T, low-P formation
904 of rare olivine-bearing symplectites in Variscan eclogite. Journal of Petrology 54, 1375-
905 1398.
906 Selverstone, J., Franz, G., Thomas, S., Getty, S., 1992. Fluid variability in 2 GPa eclogites as
907 an indicator of fluid behavior during subduction. Contributions to Mineralogy and
908 Petrology 112, 341-357.
909 Sorensen, S.S., Grossman, J.N., Perfit, M.R., 1997. Phengite-hosted LILE-enrichment in
910 eclogite and related rocks: implications for fluid-mediated mass-transfer in subduction
911 zones and arc magma genesis. Journal of Petrology 38, 3-34.
912 Spandler, C., Hermann, J., Arculus, R., Mavrogenes, J., 2004. Geochemical heterogeneity and
913 element mobility in deeply subducted oceanic crust; insights from high-pressure mafic
914 rocks from New Caledonia. Chemical Geology 206, 21-42.
915 Staudigel, H., 2003. Hydrothermal alteration processes in the oceanic crust. In: Rudnick, R.L.
916 (Ed.), The Crust. Treatise on Geochemistry, vol. 3, pp. 511-535.
917 Staudigel, H., Hart, S.R., 1983. Alteration of basaltic glass: Mechanisms and significance of
918 the oceanic crust-seawater budget. Geochimica et Cosmochimica Acta 47, 337-350.
919 Vallis, F., Scambelluri, M., 1996. Redistribution of high-pressure fluids during retrograde
920 metamorphism of eclogite-facies rocks (Voltri Massif, Italian Western Alps). Lithos 39,
921 81-92.
922 van der Straaten, F., Halama, R., John, T., Schenk, V., Hauff, F., Andersen, N., 2012. Tracing
923 the effects of high-pressure metasomatic fluids and seawater alteration in blueschist-
924 facies overprinted eclogites: Implications for subduction channel processes. Chemical
925 Geology 292-293, 69-87.

926 van der Straaten, F., Schenk, V., John, T., Gao, J., 2008. Blueschist-facies rehydration of
927 eclogites (Tian Shan, NW-China): implications for fluid-rock interaction in the
928 subduction channel. Chemical Geology 225, 195-219.
929 Verlaguet, A., Goffé, B., Brunet, F., Poinssot, C., Vidal, O., Findling, N., Menut, D., 2011.
930 Metamorphic veining and mass transfer in a chemically closed system: a case study in
931 Alpine metabauxites (western Vanoise). Journal of Metamorphic Geology 29, 275-
932 300.
933 Walther, J.V., Orville, P.M., 1982. Volatile production and transport in regional
934 metamorphism. Contributions to Mineralogy and Petrology 79, 252-257.
935 Wangen, M., Munz, I.A., 2004. Formation of quartz veins by local dissolution and transport
936 of silica. Chemical Geology 209, 179-192.
937 Widmer, T., Thompson, A.B., 2001. Local origin of high pressure vein material in eclogite
938 facies rocks of the Zermatt-Saas Zone, Switzerland. American Journal of Science 301,
939 627-656.
940 Willner, A.P., 2005. Pressure-Temperature evolution of a late Palaeozoic paired metamorphic
941 belt in North-Central Chile (34°-35°30'S). Journal of Petrology 46, 1805-1833.
942 Willner, A.P., Hervé, F., Massonne, H.-J., 2000. Mineral chemistry and pressure-temperature
943 evolution of two contrasting high-pressure - low-temperature belts in the Chonos
944 Archipelago, Southern Chile. Journal of Petrology 41, 309-330.
945 Willner, A.P., Richter, P.P., Ring, U., 2009. Structural overprint of a late Paleozoic
946 accretionary system in north-central Chile (34°-35°S) during post-accretional
947 deformation. Andean Geology 36, 17-36.
948 Willner, A.P., Thomson, S.N., Kröner, A., Wartho, J.-A., Wijbrans, J.R., Hervé, F., 2005.
949 Time markers for the evolution and exhumation history of a late Palaeozoic paired
950 metamorphic belt in North-Central Chile. Journal of Petrology 46, 1835-1858.
951

952

Figure captions:

Fig. 1: Geological map of the Western and Eastern Series between 34° and 35°40’ S with the sample location at Pichilemu (modified from Willner et al., 2005; 2009).

Fig. 2: Photographs of layered blueschist-greenschist outcrops at Infiernillo Beach in Pichilemu. Note the distinct color difference between the blueschist and the greenschist layers.

Fig. 3: Back-scattered electron images of blueschist and greenschist layers. A) Blueschist layer comprising glaucophane cores overgrown by sodic-calcic to calcic amphibole (winchite-actinolite), together with larger winchites and small actinolites. Winchite contains inclusions of titanite. Albite, chlorite and phengite are present in the matrix. B) Greenschist layer showing the typical fine-grained texture of both greenschist and blueschist layers. Compared to the blueschist layer, albite occurs less frequently and large patches of chlorite are conspicuous. C) Blueschist layer with a patchy occurrence of glaucophane and winchite and aggregates of titanite. D) Greenschist layer that contains a relatively large glaucophane overgrown by actinolite. E) Amphibole porphyroblast comprising a core of ferro-winchite surrounded by glaucophane. Note that the porphyroblast is not aligned with the foliation, in contrast to actinolite in the matrix. F) Greenschist layer with relict Ti-rich ferropargasite in actinolite. Similar relicts, interpreted to derivd from the igneous protolith, occur in the corresponding blueschist sample. Mineral abbreviations: ab – albite, act – actinolite, ap – apatite, chl – chlorite, gln – glaucophane, phg – phengite, Ti-fpg – Ti-rich ferropargasite, ttn – titanite, win – winchite, zrn – zircon.

977 Fig. 4: Amphibole major element chemistry. A) Na_B versus Si_T. Note the large compositional
978 variation from almost pure actinolite to almost pure glaucophane. B) Mg#, defined as
979 $Mg/(Mg+Fe^{2+}+Fe^{3+})$, versus Ca_B. There is a general broad positive correlation, only the relict
980 Ti-rich ferropargasites fall off the trend.
981
982 Fig. 5: Chondrite-normalized (Boynton, 1984) REE diagrams. Panels A)-C) show three
983 blueschist-greenschist pairs with similar REE patterns. In contrast, panel D) shows large
984 compositional differences between the three adjacent layers of sample CH-1-48 and the
985 overall variability observed in the entire sequence. REE patterns of typical oceanic OIBs
986 (alkalic OIB and N-MORB from Sun and McDonough (1989), tholeiitic OIB is the standard
987 BHVO-1) and volcanic rocks from the Chilean volcanic front (Jacques et al., 2013) are shown
988 for comparison.
989
990 Fig. 6: Layered blueschists and greenschists plotted in the Th/Yb vs. Nb/Yb diagram of
991 Pearce (2008). All samples fall into the field of the oceanic basalts and are distinct from
992 volcanic rocks of the Southern Volcanic Zone (Jacques et al., 2013) and Quaternary trench
993 sediments from the Chilean coast (Lucassen et al., 2010). E-MORB and alkalic OIB
994 compositions are from Sun and McDonough (1989), tholeiitic OIB is the standard BHVO-1.
995
996 Fig. 7: Evaluation of igneous differentiation trends. In most cases, blueschist-greenschist pairs
997 show variations that are inconsistent with igneous differentiation alone as the compositions
998 plot either off typical differentiation trends, or they show compositional changes that are
999 oblique to the trends (see text for details). Typical ocean island igneous differentiation trends
1000 are shown as small grey dots, represented by 161 selected analyses from the island of Jan
1001 Mayen (North Atlantic) taken from the GEOROC database. Blue and green symbols represent
1002 blueschist and greenschists, respectively.

Fig. 8: Diagrams based on key trace element abundances and ratios to distinguish between seafloor alteration and subduction-related metasomatic alteration with trends from Bebout (2007). Data sources for MORB and OIB compositions as in Figs. 5 and 6.

Fig. 9: Isocon diagrams (after Grant, 2005) of three blueschist-greenschist pairs to illustrate the geochemical variability. The solid lines are the slopes based on the elements considered as immobile, dashed lines are the slopes for the four LILE K, Ba, Rb and Cs. The 1:1 line is shown for comparison.

Fig. 10: Thermodynamic calculations (see Methodology for details) for a representative blueschist-greenschist pair. A) and B) show pseudosections calculated for H_2O-saturated conditions buffered by the hematite-magnetite (HM) buffer. The molar percentage of water bound in solids is indicated by the contours and the corresponding black numbers. The white lines give the modal proportion of chlorite in vol%. The thick white arrow indicates the retrograde P-T path of Willner (2005). C) and D) show P-X_{H2O} diagrams with the appearance of major mineral phases indicated at the boundaries of the different phase assemblages and the modal abundance of chlorite shown by the grey contours. E) and F) show P-X_{H2O} diagrams with contours of modal amphibole abundance. To illustrate the compositional variation of amphibole, the glaucophane component is shown by the thin black lines. The glaucophane component was calculated as $Na_2O - 0.5 \times O_2$ based on the definition in the amphibole solution model. Mineral abbreviations: Ab – albite, Chl – chlorite, Phg – phengite, Ep – epidote, Law – lawsonite, Omph – omphacite, Amph – amphibole, Grt – garnet, Kfsp – alkali feldspar.

1028 Fig. 11: P-X diagrams of a representative blueschist-greenschist pair using the blueschist
1029 (left) and greenschist (right) composition as end-members on the x-axis. The appearance of
1030 key mineral phases shows only small differences between the two compositions. A) Diagram
1031 contoured for the modal proportions of chlorite. B) Diagram contoured for the modal
1032 proportion of amphibole (B) with the values for the glaucophane component shown by the
1033 white lines. Mineral abbreviations are as for Fig. 10.
1034
1035
1036
1037 **Tables:**
1038 Table 1: Whole-rock geochemical analyses of blueschist and greenschist samples from
1039 Pichilemu and basaltic reference material BHVO-2.
1040 Table 2: Modal mineral proportions of three selected blueschist-greenschist pairs.
1041
1042
1043 **Electronic Appendix:**
1044 Representative microprobe analyses of amphibole, white mica, chlorite and feldspar in
1045 blueschists and greenschists from Pichilemu.
1046

Fig. 1

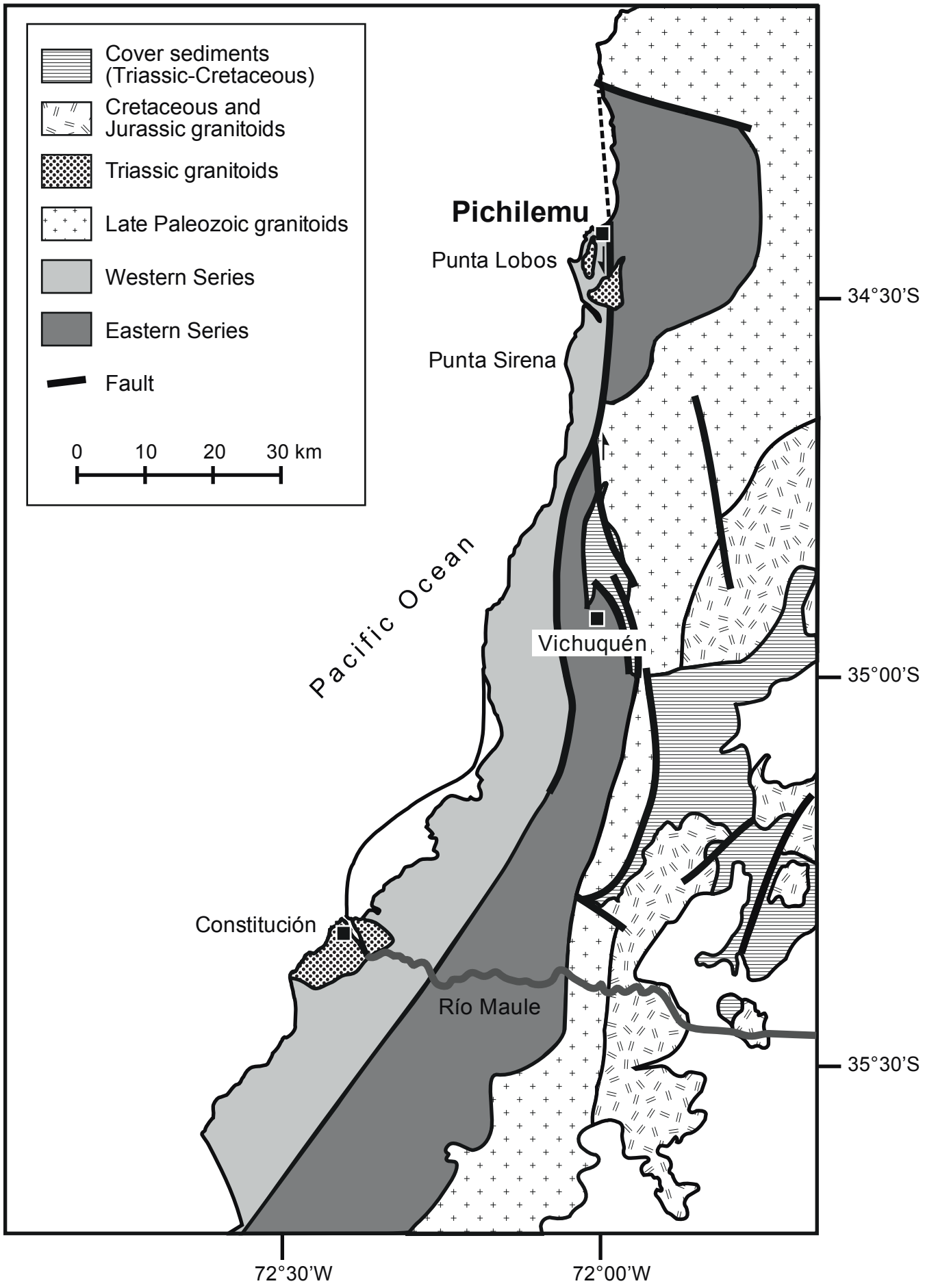
Cover sediments
(Triassic-Cretaceous)
Cretaceous and
Jurassic granitoids
Triassic granitoids
Late Paleozoic granitoids
Western Series
Eastern Series
Fault
0
10
20
30 km
Pichilemu
Punta Lobos
Punta Sirena
Pacific Ocean
Vichuquén
Constitución
Río Maule
34°30'S
35°00'S
35°30'S
72°30'W
72°00'W

Fig. 2

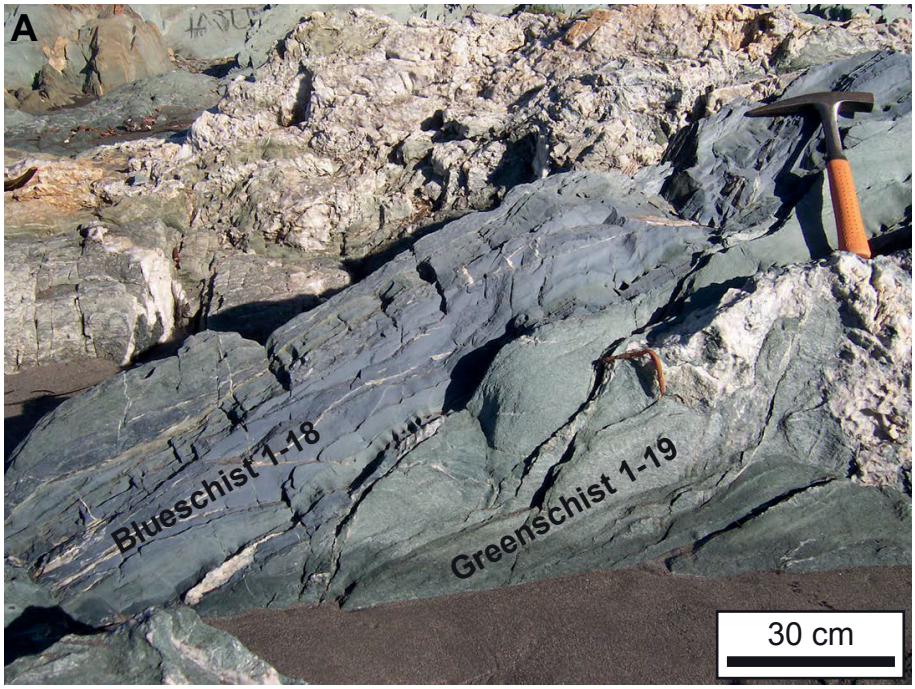
A
Blueschist 1-18
Greenschist 1-19
30 cm

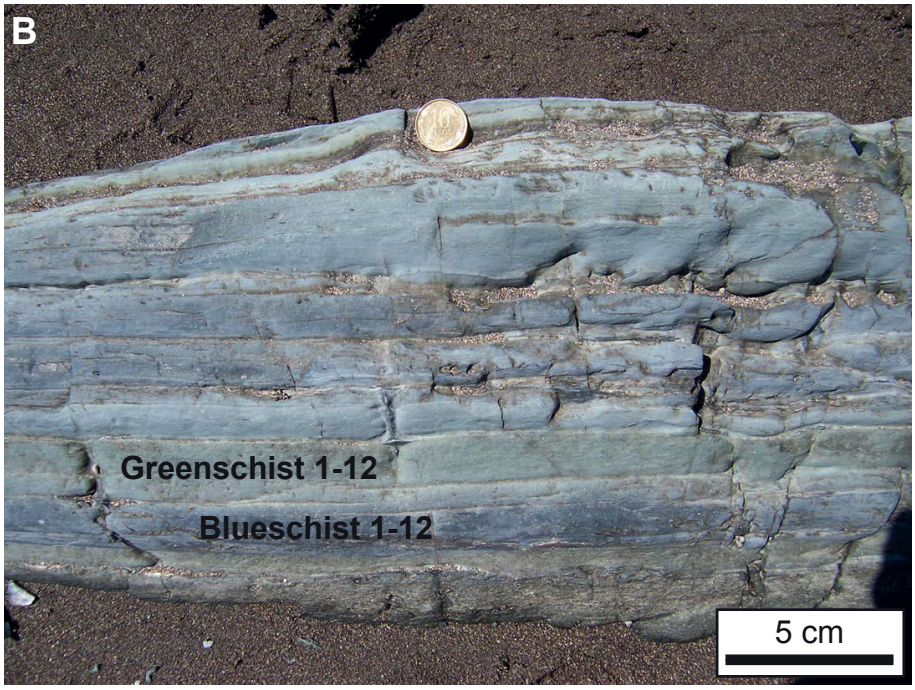
B
Greenschist 1-12
Blueschist 1-12
5 cm

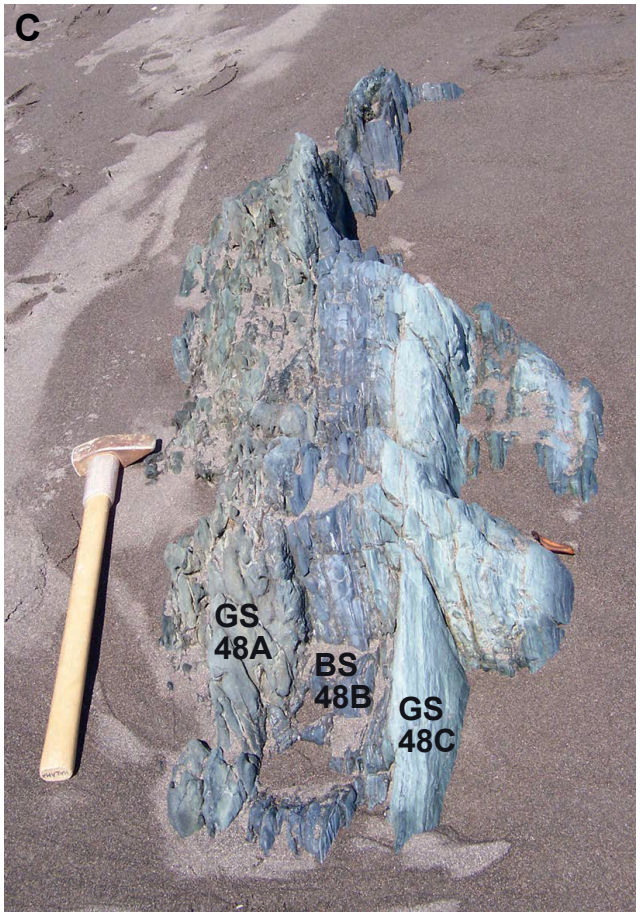
C
GS
48A
BS
48B
GS
48C

Fig. 3

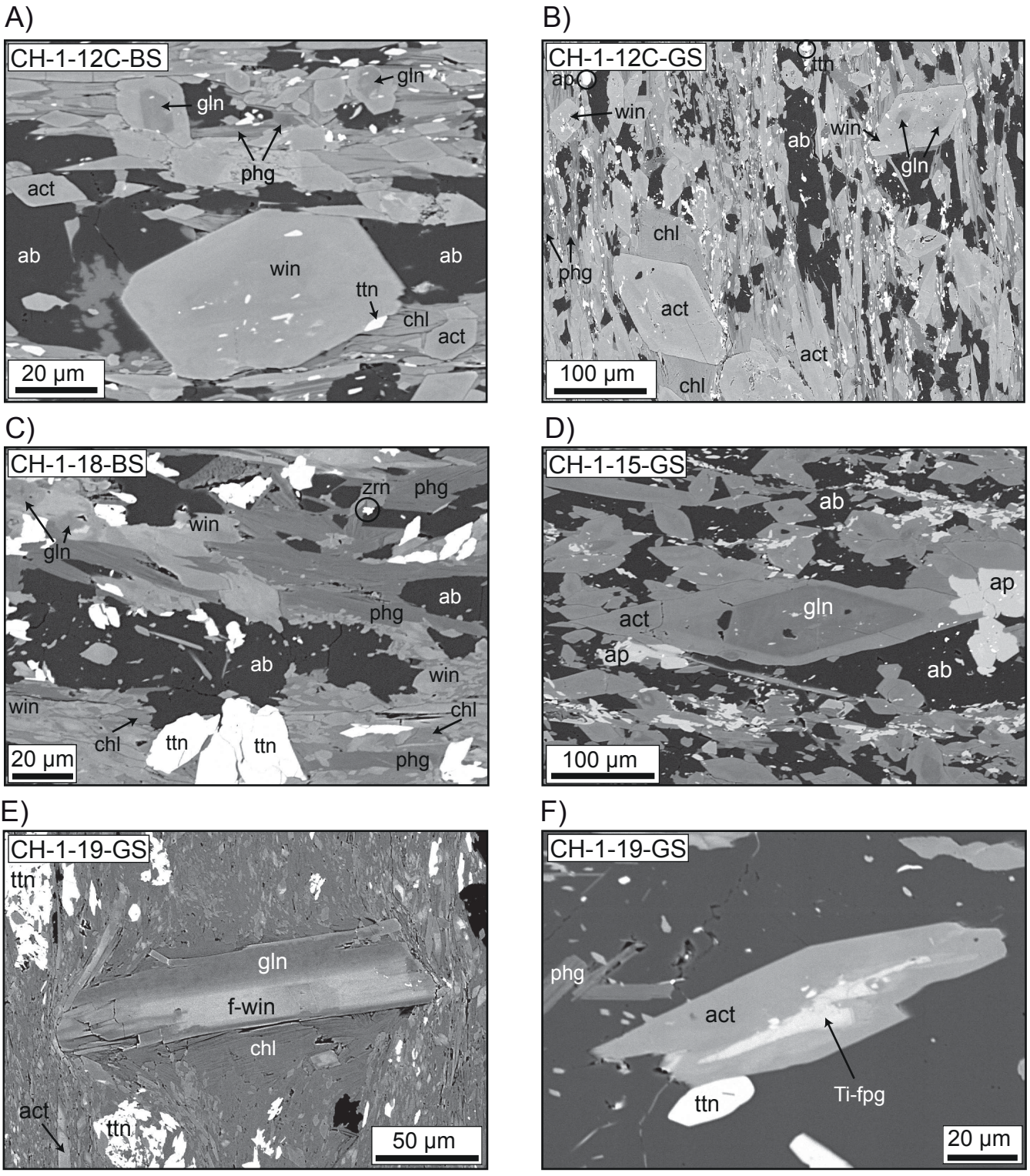
A)
CH-1-12C-BS
gln
gln
phg
act
ab
win
ab
ttn
chl
act
20 µm
B)
CH-1-12C-GS
ttn
ap
win
win
ab
gln
chl
phg
act
act
100 µm
chl
C)
CH-1-18-BS
zrn
phg
win
gln
ab
phg
ab
win
win
chl
chl
ttn
ttn
20 µm
phg
D)
CH-1-15-GS
ab
ap
act
gln
ap
ab
100 µm
E)
CH-1-19-GS
ttn
gln
f-win
chl
act
ttn
50 µm
F)
CH-1-19-GS
phg
act
Ti-fpg
ttn
20 µm

Fig. 4

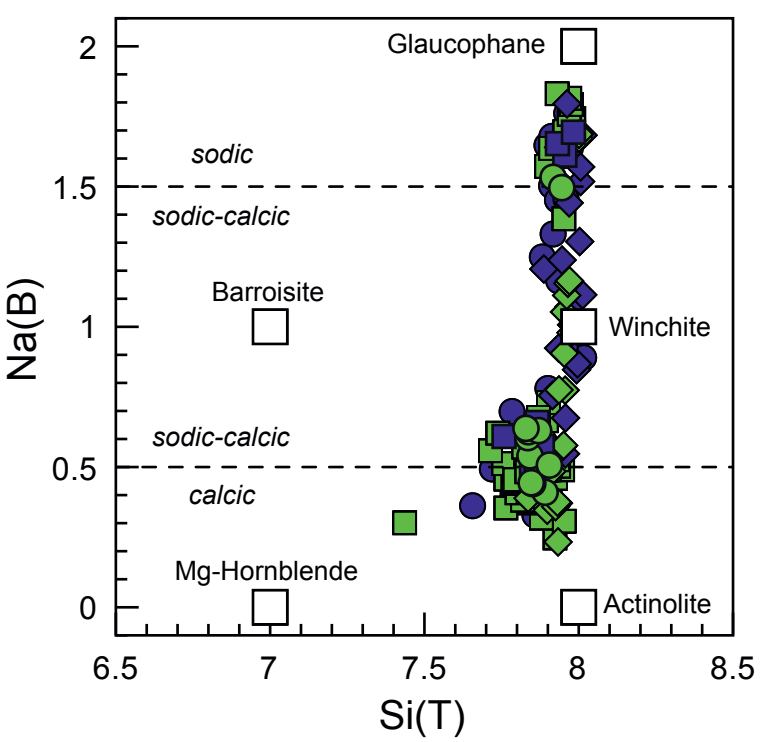
Glaucophane
sodic
sodic-calcic
Barroisite
Winchite
sodic-calcic
calcic
Mg-Hornblende
Actinolite
Na(B)
Si(T)
2
1.5
1
0.5
0
6.5
7
7.5
8
8.5

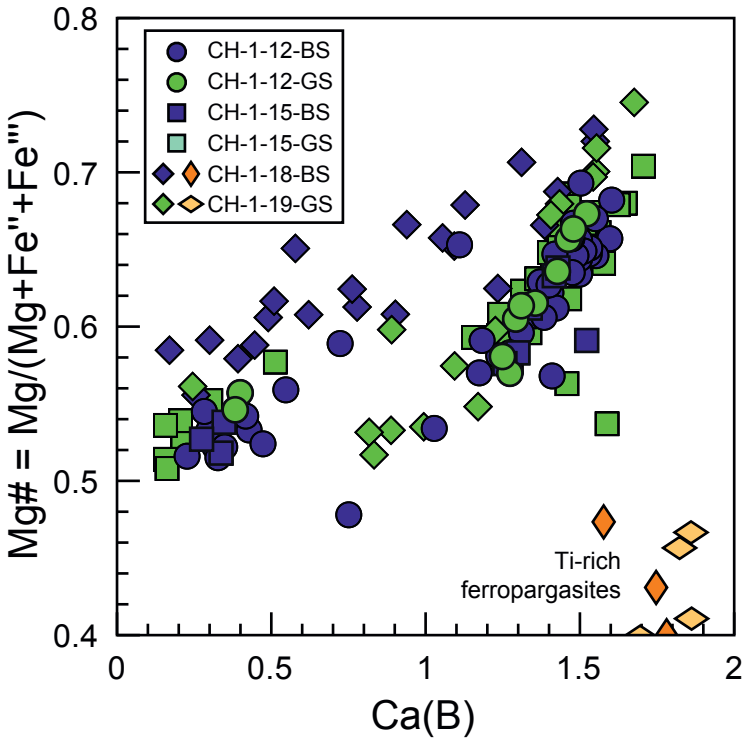
CH-1-12-BS
CH-1-12-GS
CH-1-15-BS
CH-1-15-GS
CH-1-18-BS
CH-1-19-GS
Ti-rich
ferropargasites
Mg# = Mg/(Mg+Fe"+Fe"')
Ca(B)
0.8
0.7
0.6
0.5
0.4
0
0.5
1
1.5
2

Fig. 5

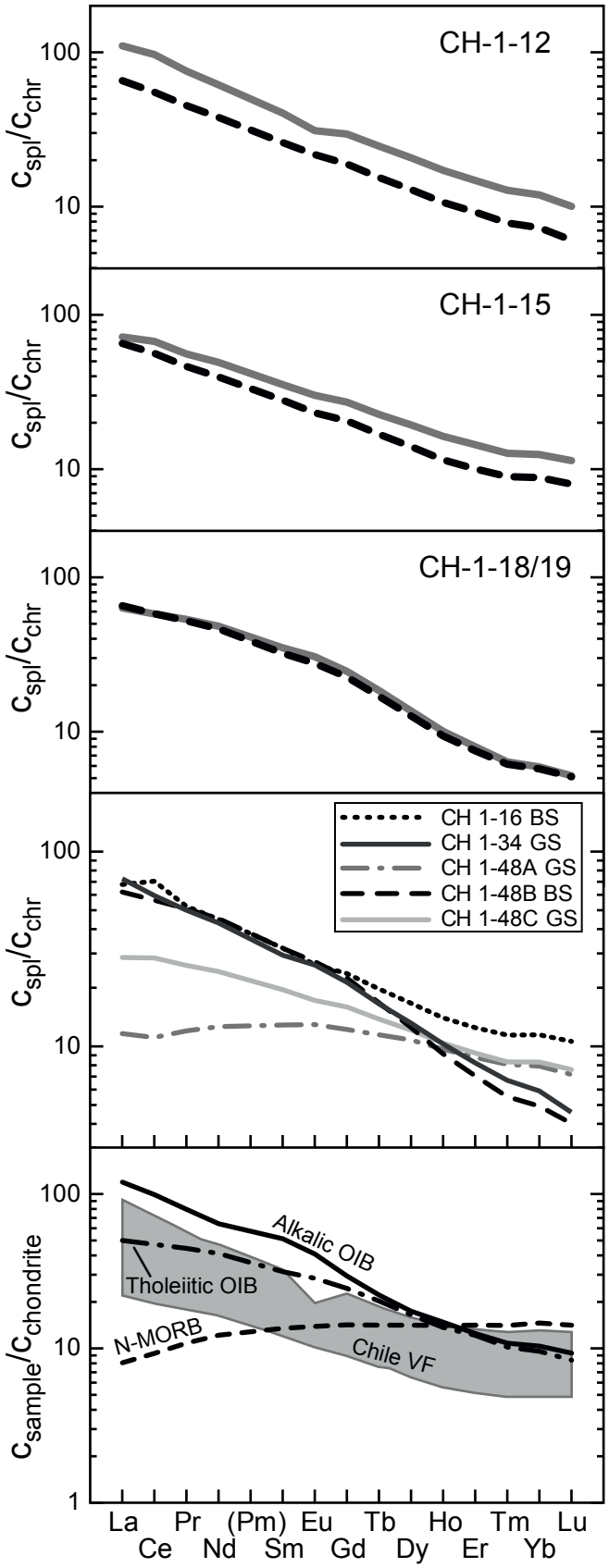
CH-1-12
CH-1-15
CH-1-18/19
CH 1-16 BS
CH 1-34 GS
CH 1-48A GS
CH 1-48B BS
CH 1-48C GS
Alkalic OIB
Tholeiitic OIB
N-MORB
Chile VF
100
10
1
La
Ce
Pr
Nd
(Pm)
Sm
Eu
Gd
Tb
Dy
Ho
Er
Tm
Yb
Lu

Fig. 6

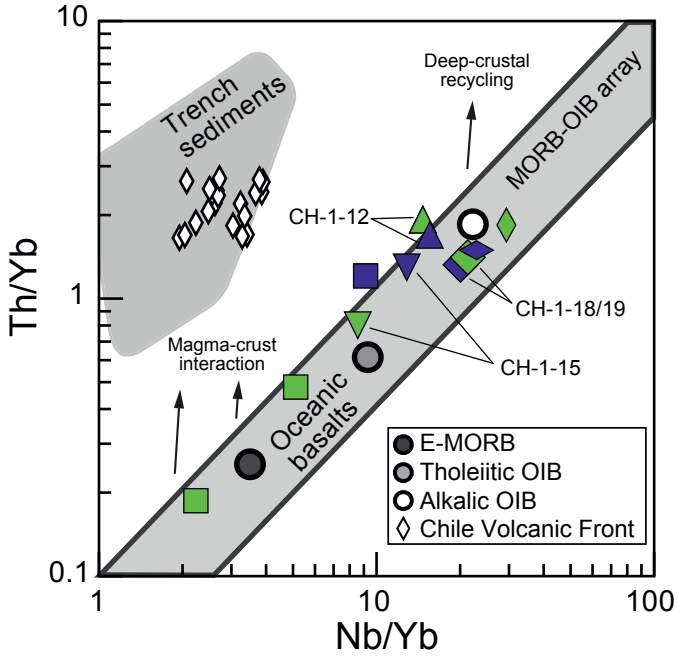
10
1
0.1
Th/Yb
1
10
100
Nb/Yb
Trench sediments
Deep-crustal recycling
MORB-OIB array
CH-1-12
CH-1-18/19
CH-1-15
Magma-crust interaction
Oceanic basalts
E-MORB
Tholeiitic OIB
Alkalic OIB
Chile Volcanic Front

Fig. 7

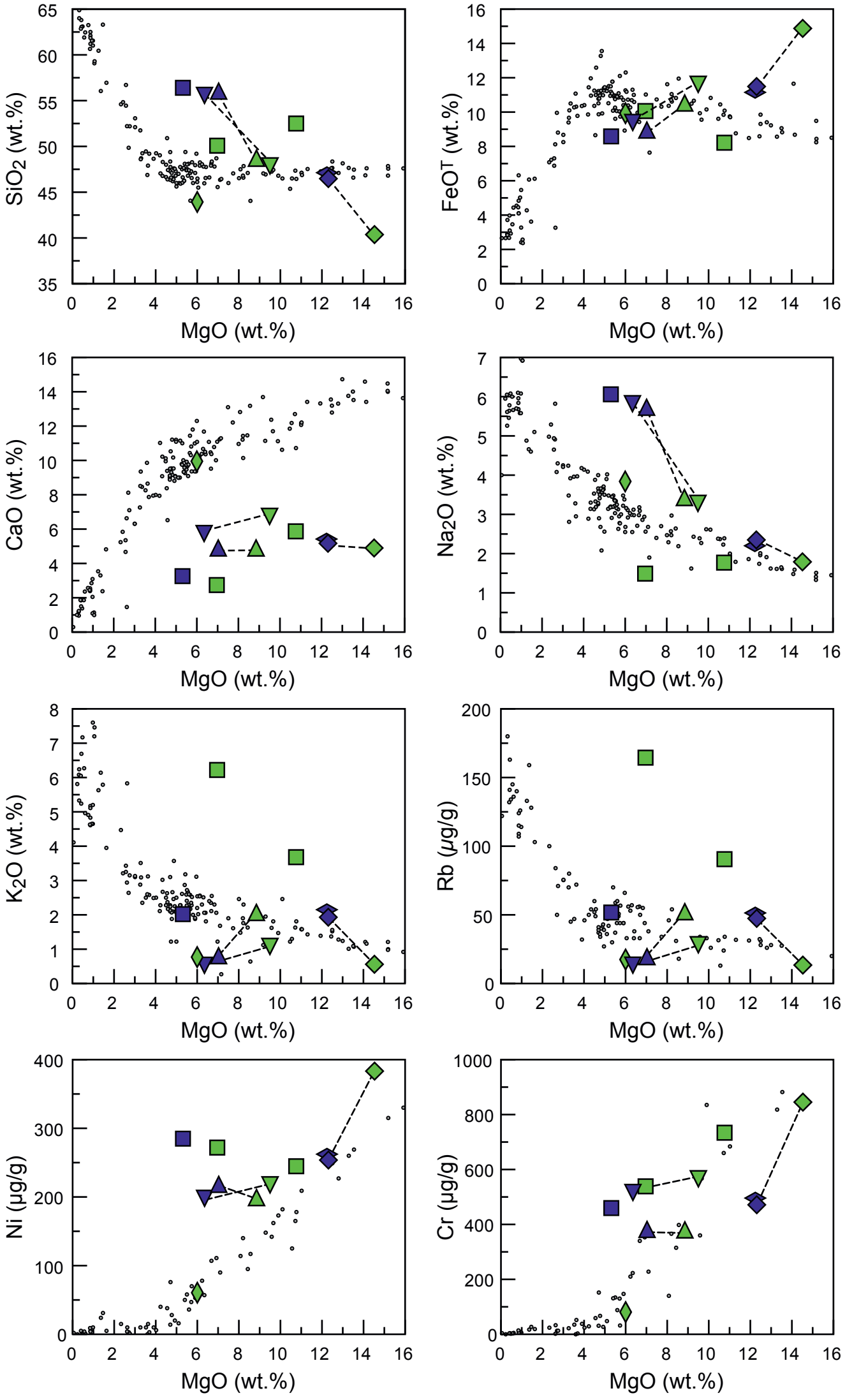

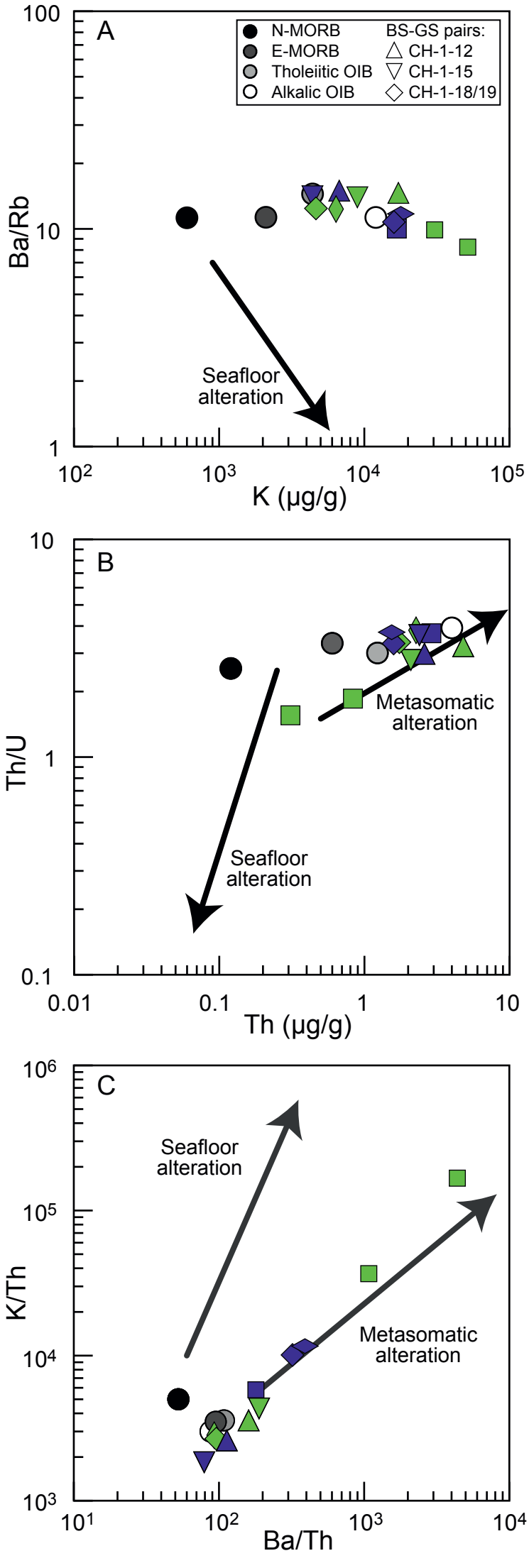
A
N-MORB
E-MORB
Tholeiitic OIB
Alkalic OIB
BS-GS pairs:
CH-1-12
CH-1-15
CH-1-18/19
Ba/Rb
K (μg/g)
Seafloor alteration
B
Th/U
Th (μg/g)
Metasomatic alteration
Seafloor alteration
C
K/Th
Ba/Th
Seafloor alteration
Metasomatic alteration

Fig. 8

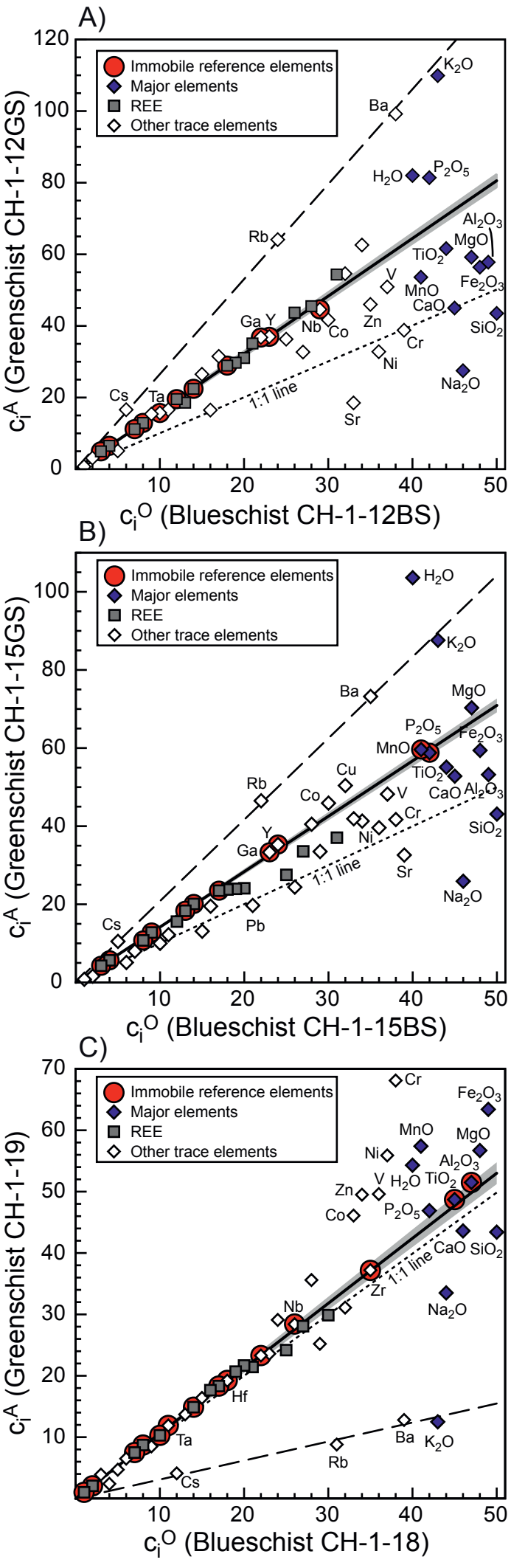
A)
Immobile reference elements
Major elements
REE
Other trace elements
K_2O
Ba
H_2O
P_2O_5
Al_2O_3
MgO
Rb
TiO_2
V
MnO
Fe_2O_3
CaO
Ga
Y
Nb
Co
Zn
SiO_2
Cr
Ni
Na_2O
Cs
Ta
1:1 line
Sr
c_i^A (Greenschist CH-1-12GS)
c_i^O (Blueschist CH-1-12BS)
B)
Immobile reference elements
Major elements
REE
Other trace elements
H_2O
K_2O
Ba
MgO
P_2O_5
Fe_2O_3
MnO
Cu
TiO_2
Rb
Co
V
CaO
Al_2O_3
Cr
SiO_2
Y
Ga
Ni
1:1 line
Sr
Na_2O
Cs
Pb
c_i^A (Greenschist CH-1-15GS)
c_i^O (Blueschist CH-1-15BS)
C)
Immobile reference elements
Major elements
REE
Other trace elements
Cr
Fe_2O_3
MnO
MgO
Ni
Al_2O_3
V
H_2O
TiO_2
Zn
Co
P_2O_5
CaO
SiO_2
1:1 line
Zr
Nb
Na_2O
Hf
Ta
Ba
K_2O
Rb
Cs
c_i^A (Greenschist CH-1-19)
c_i^O (Blueschist CH-1-18)

Fig. 9

Fig. 10

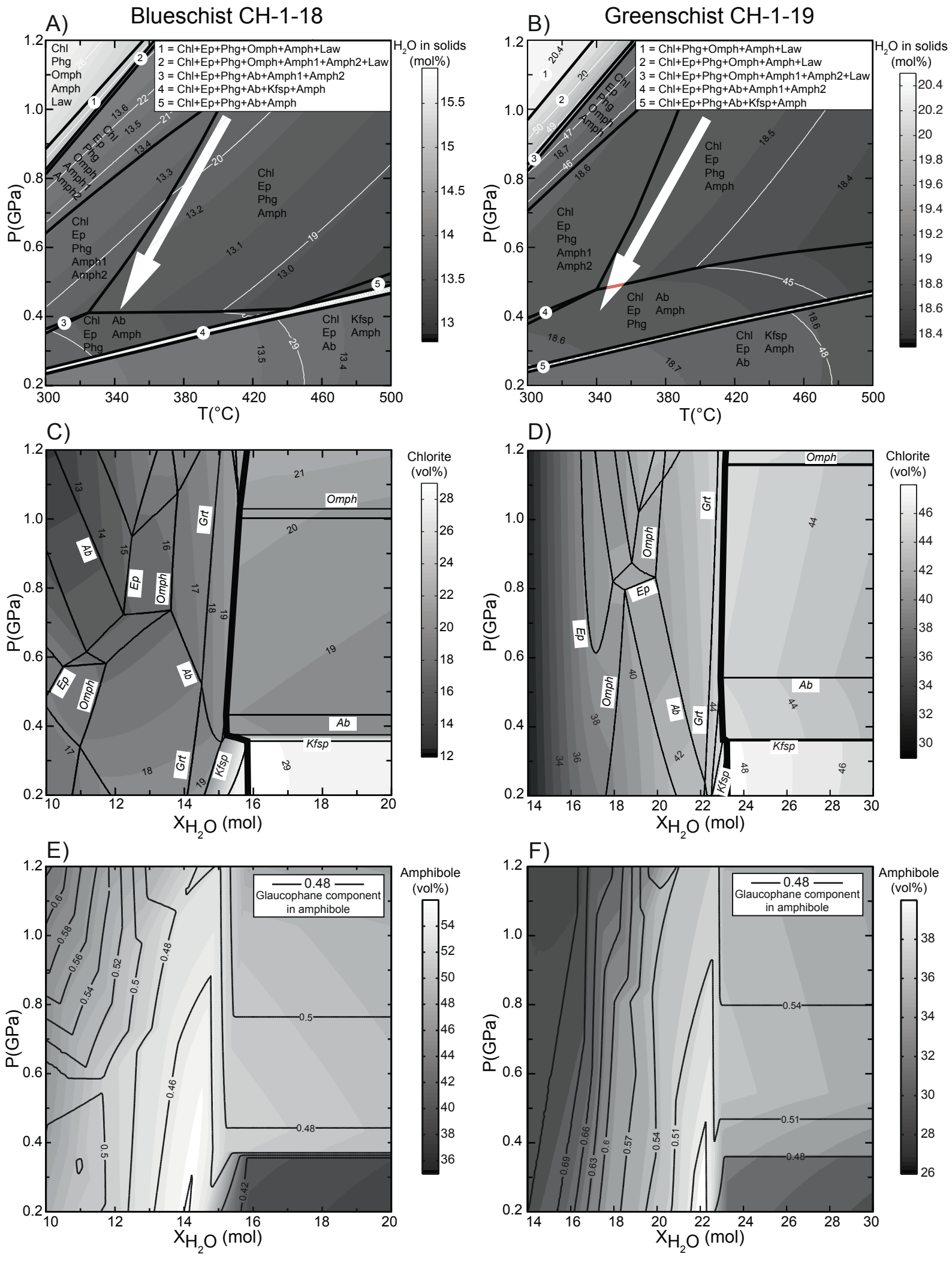
A)
Blueschist CH-1-18
1 = Chl+Ep+Phg+Omph+Amph+Law
2 = Chl+Ep+Phg+Omph+Amph1+Amph2+Law
3 = Chl+Ep+Phg+Ab+Amph1+Amph2
4 = Chl+Ep+Phg+Ab+Kfsp+Amph
5 = Chl+Ep+Phg+Ab+Amph
H2O in solids (mol%)
P(GPa)
T(°C)
B)
Greenschist CH-1-19
1 = Chl+Phg+Omph+Amph+Law
2 = Chl+Ep+Phg+Omph+Amph+Law
3 = Chl+Ep+Phg+Omph+Amph1+Amph2+Law
4 = Chl+Ep+Phg+Ab+Amph1+Amph2
5 = Chl+Ep+Phg+Ab+Kfsp+Amph
H2O in solids (mol%)
P(GPa)
T(°C)
C)
Chlorite (vol%)
P(GPa)
XH2O (mol)
D)
Chlorite (vol%)
P(GPa)
XH2O (mol)
E)
0.48 Glaucophane component in amphibole
Amphibole (vol%)
P(GPa)
XH2O (mol)
F)
0.48 Glaucophane component in amphibole
Amphibole (vol%)
P(GPa)
XH2O (mol)

Fig. 11

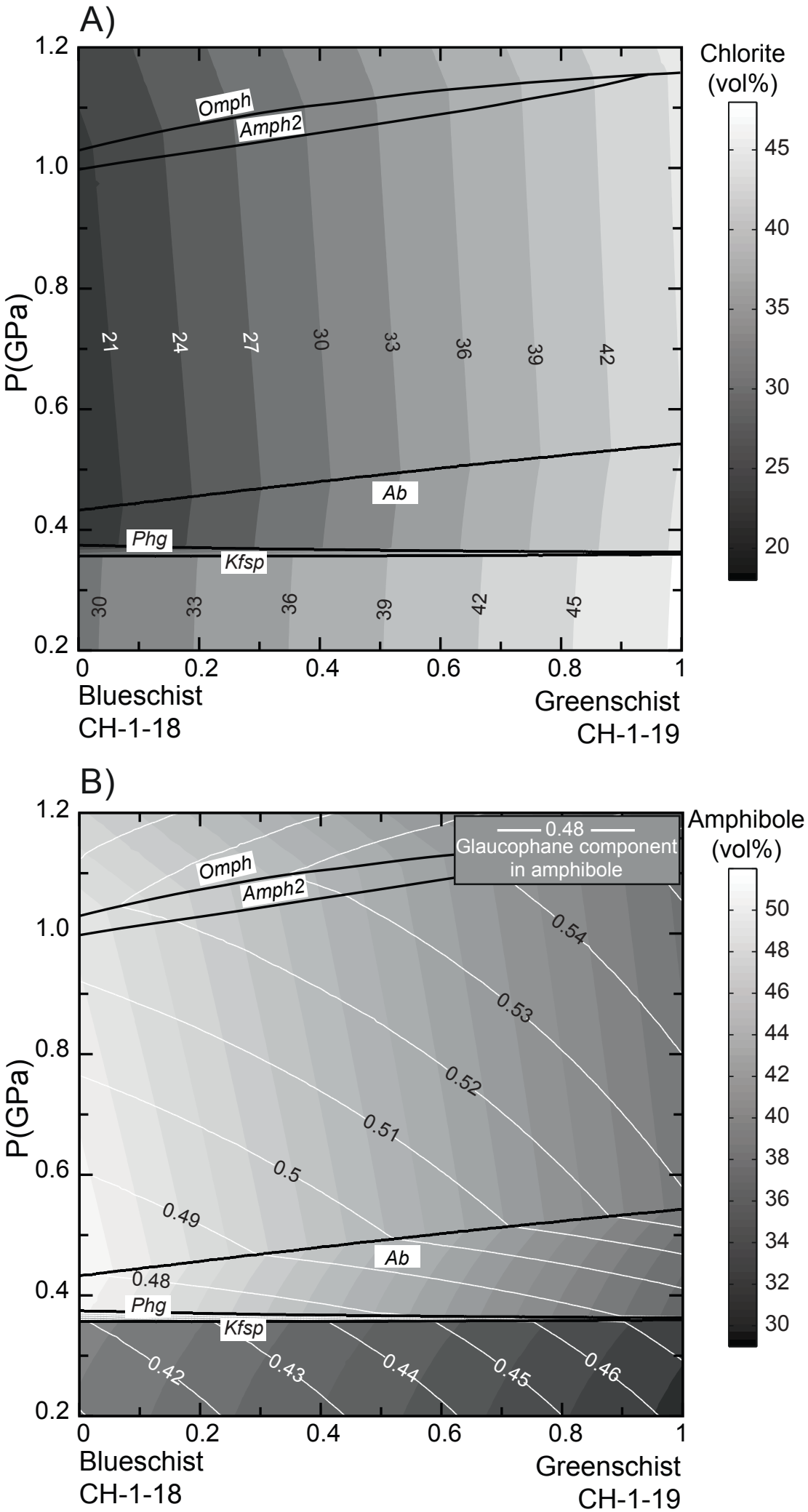
A)
Omph
Amph2
Ab
Phg
Kfsp
Chlorite (vol%)
P(GPa)
Blueschist CH-1-18
Greenschist CH-1-19
B)
0.48 Glaucophane component in amphibole
Amphibole (vol%)
P(GPa)
Blueschist CH-1-18
Greenschist CH-1-19